

The Evaluation of VIIRS Aerosol Retrievals Over Ocean

Ho-Chun Huang^{1,2*}, Shobha Kondragunta², Istvan Laszlo^{2,3}, Lorraine Remer⁴, Jingfeng Huang^{1,2}, Hai Zhang^{2,5}, and Alexander Smirnov^{6,7}
 * ho-chun.huang@noaa.gov ¹CICS-MD/ESSIC/UMD ²NOAA/NESDIS/STAR ³DAOS/UMD, ⁴JCET/UMBC, ⁵IMSG, ⁶Sigma Space Corp., ⁷NASA GSFC

VIIRS onboard Suomi-NPP and JPSS

- ❑ The Joint Polar Satellite System (JPSS) is the USA's next generation polar-orbiting operational environmental satellite system. JPSS will provide operational continuity of satellite-based observations and products currently obtained from the Suomi National Polar-orbiting Partnership (NPP) mission.
- ❑ Visible Infrared Imaging Radiometer Suite (VIIRS) is a multi-spectral scanning radiometer (22 bands between 0.4 μ m and 12 μ m) on-board the Suomi-NPP with spatial resolution for 16 bands at 750m and 5 bands at 325m. The spatial resolution of Intermediate Product (IP) output is 750 m at nadir. The spatial resolution of Environment Data Record (EDR) is 6 km at nadir compared to 10km at nadir for Moderate-Resolution Imaging Spectroradiometer (MODIS).
- ❑ The MODIS on-board Aqua and Terra are currently providing global aerosol coverage for research and operational activities in weather, climate, and air quality. The VIIRS on-board Suomi-NPP and future JPSS satellites are expected to continue daily global aerosol observations for operational and research communities.
- ❑ Separate algorithms are used for aerosol retrieval over land and ocean. The over-land aerosol algorithm is based on but a different scheme from MODIS Surface Reflectance algorithm (MOD09) and the over-ocean algorithm is derived from the MODIS Aerosol (MOD04 Collection 4) algorithm. In VIIRS, Aerosol Optical Thickness (AOT) and aerosol type are retrieved simultaneously by minimizing the difference between observed and calculated reflectance in multiple channels.

VIIRS Aerosol Products

- VIIRS aerosol products include AOT, Aerosol Particle Size Parameter (APSP), and Suspended Matter (SM).
- The VIIRS AOT and APSP products reached Provisional maturity level and the SM product reached Beta maturity level on January 23, 2013.
- The VIIRS AOT and APSP (both EDR and IP) products are now publicly accessible from NOAA's Comprehensive Large Array-data Stewardship System (CLASS at <http://www.class.ngdc.noaa.gov>).

Maritime Aerosol Network (MAN)

- MAN is a network of ship-borne aerosol optical thickness measurements using hand-held Microtops II sun photometers [Smirnov et al., 2009] with an uncertainty of AOT measurement no larger than 0.02.
- Collected MAN data follow AERosol RObotic NETwork (AERONET) protocol for data processing, http://aeronet.gsfc.nasa.gov/new_web/maritime_aerosol_network.html.
- The cruise measurements available from MAN offer an unprecedented opportunity to validate the VIIRS AOT and APSP over open Ocean, far from coastlines and islands as that AERONET site.

Comparisons between VIIRS Aerosol Retrievals and MAN Measurements

- Period from May 2, 2012 to February 28, 2014.
- MAN Level 2.0 Series Average Datasets.
- VIIRS AOT EDRs at three quality-flag (QF) levels;
 - High : used only high QF AOT.
 - Top2 : used both high and medium QF AOT.
 - All : used all retrieved AOT (QF = high, medium, and low).
- VIIRS APSP (Angstrom Exponent, AE) EDRs:
 - Used only high QF APSP.
 - AE computed at MAN's and MODIS's like wavelength pairs (445/865 versus 440/870 and 550/865 versus 500/870).
- Match-up criteria for VIIRS EDRs and MAN measurements:
 - The VIIRS-MAN match-up uses each MAN measurement as a reference point and finds the VIIRS retrievals within the spatial and temporal matching domain of 0.5° latitude-longitude and one hour time window centered on the MAN observation.
 - At least 12 (about 20%) selected quality VIIRS EDRs within the matching domain or any VIIRS EDR(s) within 3km of MAN measurements.
 - Multiple collocations within one-hour time window are averaged to a single match-up.
- Performance Statistics:
 - Accuracy : the mean difference between two datasets.
 - Precision : the standard deviation of the difference.
 - Separate AOT (τ) retrieval performance in the range of $\tau < 0.3$ and $\tau \geq 0.3$.

VIIRS and MAN Match-up

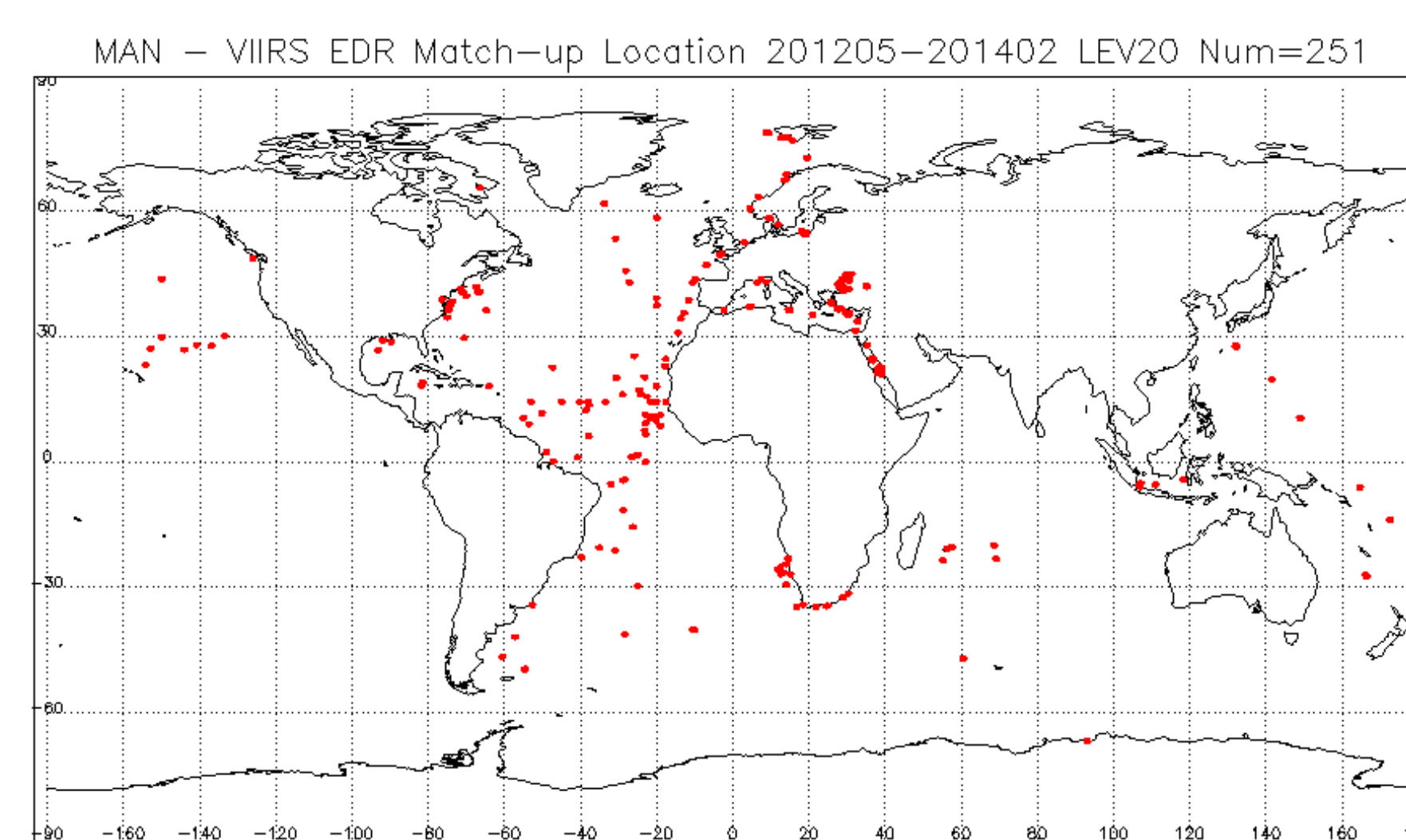


Figure 1 Locations of MAN measurements where match-ups were found with high quality VIIRS AOT EDRs during selected period.

VIIRS APSP EDR Performance

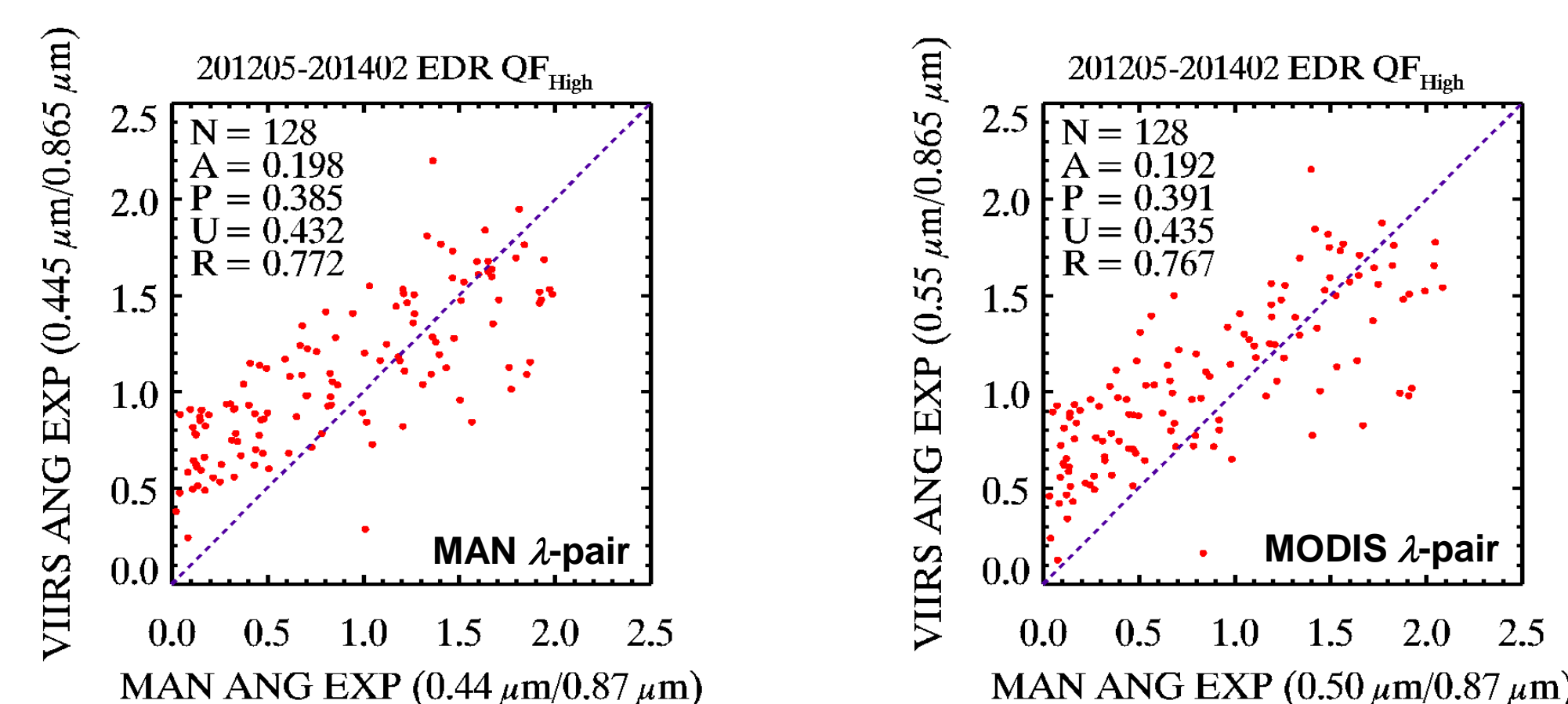


Figure 2 Comparisons between VIIRS high quality APSP EDRs and MAN measurements. Left panel shows the scatter plot of AE computed at MAN-like wavelength(λ)-pair and right panel shows the scatter plot of AE computed at MODIS-like λ -pair. N : number of match-ups, A : accuracy, P : precision, U : uncertainty, R : correlation coefficient

Attribute	QF Level	APSP λ -pair	VIIRS APSP Measurement	JPSS EDR Threshold	Achieved
Accuracy	High	MAN-like	0.20	0.3	✓
		MODIS-like	0.19		✓
Precision	High	MAN-like	0.39	0.6	✓
		MODIS-like	0.44		✓

Table 1 The performance statistics of VIIRS high quality APSP EDRs against JPSS requirement threshold at two AE λ -pairs.

VIIRS AOT EDR Performance

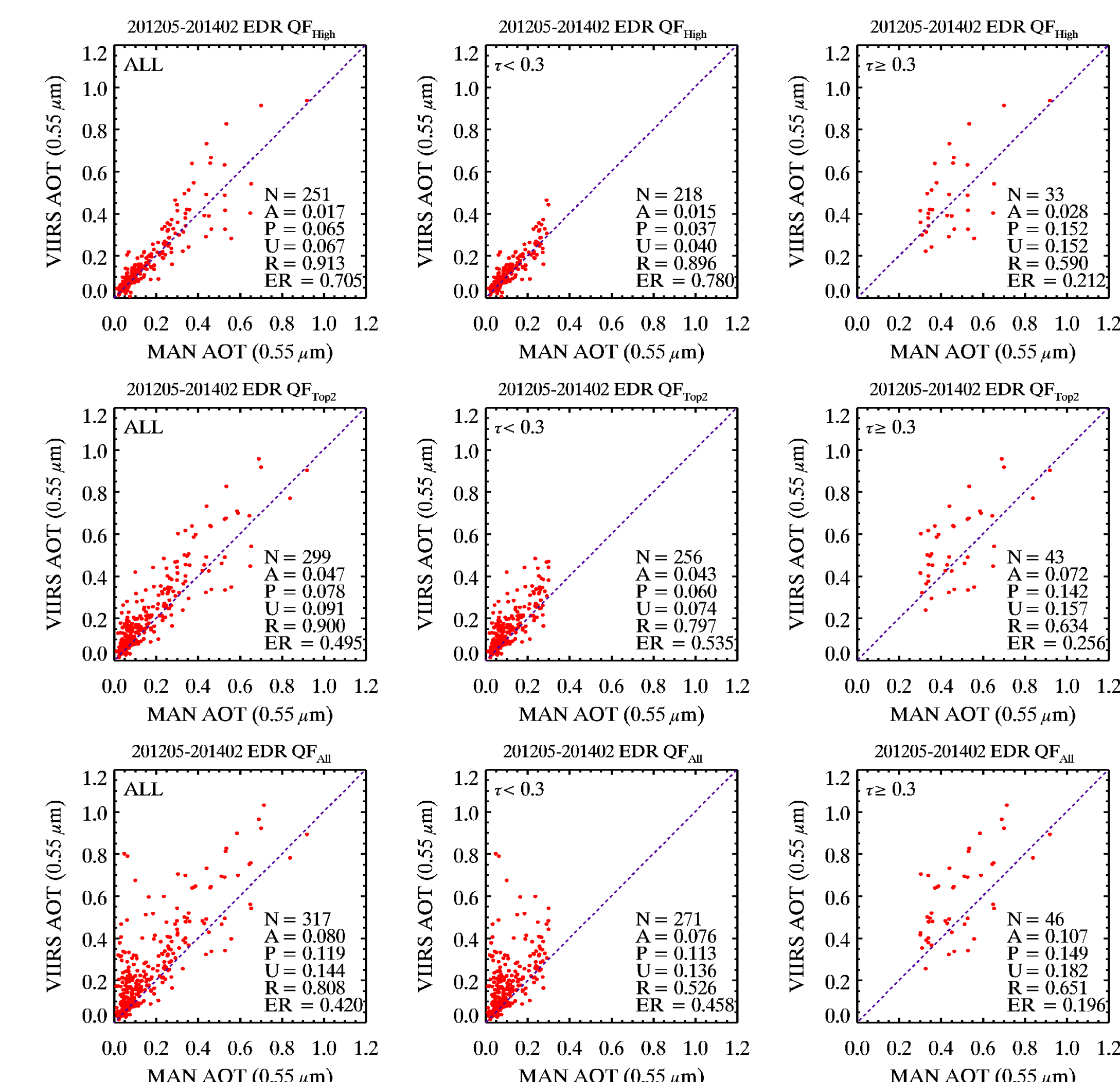


Figure 3 Comparisons between VIIRS AOT EDRs and MAN measurements. Figures in left, middle, and right columns are scatter plots of all match-ups, match-ups where MAN $\tau < 0.3$, and match-ups where MAN $\tau \geq 0.3$, respectively. Figures in upper, middle, and bottom rows are scatter plots of quality level equals to High, Top2, and All, respectively. N : number of match-ups, A : accuracy, P : precision, U : uncertainty, R : correlation coefficient, and ER : percentage of match-ups within MODIS expected error bars ($\pm 0.03 \pm 0.05\tau$).

Attribute	QF Level	τ -range	VIIRS AOT Measurement	JPSS EDR Threshold	Achieved
Accuracy	High	$\tau < 0.3$	0.02	0.08	✓
			0.04		✓
			0.08		✓
Precision	High	$\tau \geq 0.3$	0.03	0.15	✓
			0.07		✓
			0.11		✓
Accuracy	Top2	$\tau < 0.3$	0.04	0.15	✓
			0.06		✓
			0.08		✓
Precision	High	$\tau \geq 0.3$	0.15	0.35	✓
			0.14		✓
			0.15		✓

Table 2 The performance statistics of VIIRS AOT EDRs against JPSS requirement threshold at three quality levels.

Summary

- VIIRS AOT EDRs meet JPSS AOT thresholds at all three QF levels. It still needs some improvements to achieve the objective goal of 1% for both accuracy and precision at all τ values.
- VIIRS high quality APSP EDRs meet JPSS thresholds for APSP. It also needs improvements to achieve the objective goal of 0.1 unit for both accuracy and precision.
- Comparisons between VIIRS AOT and APSP over the land can be seen from poster session presented by J. Huang et. al., "Spatial and Temporal Characterization of the Difference between Multi-Sensor Aerosol Retrievals and AERONET measurements".

Acknowledgement: Authors thank PIs and their staff for establishing and maintaining MAN cruise measurements used in this study.
Disclaimer: The contents of this poster are personal view of authors and do not necessarily reflect any position of the Government or the National Oceanic and Atmospheric Administration.

INTRODUCTION

- The in-band and out-of-band responses refer to sensor spectral response contribution from within and outside the spectral bandwidth of the sensor bands, while total-band refers to the contribution from in-band as well as out-of-band regions (Wang et al., 2001).
- Most ocean color satellite sensors in addition to an in-band contribution, have a significant contribution from out-of-band region. Although the out-of-band effects can be small, it is not uniform over all bands hence can cause biases in derived biogeochemical variables.
- The out-of-band contributions for Sea-viewing Wide Field-of-view Sensor (SeaWiFS) and Moderate Resolution Imaging Spectroradiometer (MODIS) are relatively well characterized as compared to Visible Infrared Imaging Radiometer Suite (VIIRS).
- The objectives of this study are to analyze the sensor out-of-band effects for MODIS as well as VIIRS, and to determine their effective band center wavelengths using hyperspectral data from MOBY measurements. This study has been documented in our recent conference proceeding paper (Naik and Wang, 2014).

METHODS & DATA

- The hyperspectral normalized water-leaving radiance ($nL_w(\lambda)$) spectra from MOBY were convolved with respect to spectral response functions from the Moderate Resolution Imaging Spectroradiometer (MODIS) and the Visible Infrared Imaging Radiometer Suite (VIIRS) sensors to obtain the total-band and in-band averaged radiances as follows:

$$nL_w^{(Total)}(\lambda) = \frac{\int_{All} nL_w(\lambda) RSR(\lambda) d\lambda}{\int_{All} RSR(\lambda) d\lambda}$$

and

$$nL_w^{(In-Band)}(\lambda) = \frac{\int_{\pm 1\%} nL_w(\lambda) RSR(\lambda) d\lambda}{\int_{\pm 1\%} RSR(\lambda) d\lambda}$$

$RSR(\lambda)$ - sensor spectral response function.

- The out-of-band contribution can be calculated as the ratio of spectrally averaged radiances for total subtract in-band versus in-band as shown below:

$$OOB(\%) = \left(\frac{nL_w^{(Total)}(\lambda)}{nL_w^{(In-Band)}(\lambda)} - 1 \right) \times 100$$

- In situ data for this study were obtained from the Marine Optical Buoy (MOBY) in the waters off Hawaii (<http://coastwatch.noaa.gov/moby/>).
- MOBY is deployed in clear oligotrophic oceanic waters (chlorophyll-a is in the range of ~ 0.01 – 0.1 $mg\ m^{-3}$).
- Hyperspectral $nL_w(\lambda)$ data from MOBY covers wavelengths range from ~ 340 nm to 750 nm.
- The hyperspectral resolution of $nL_w(\lambda)$ from clear oceanic waters makes MOBY an optimum platform to analyze sensor out-of-band effects.
- Prior to the calculation of the band averages, the spectral response function values are interpolated to the $nL_w(\lambda)$ wavelength resolution.

Total-band and In-band averaged $nL_w(\lambda)$ – MOBY Site

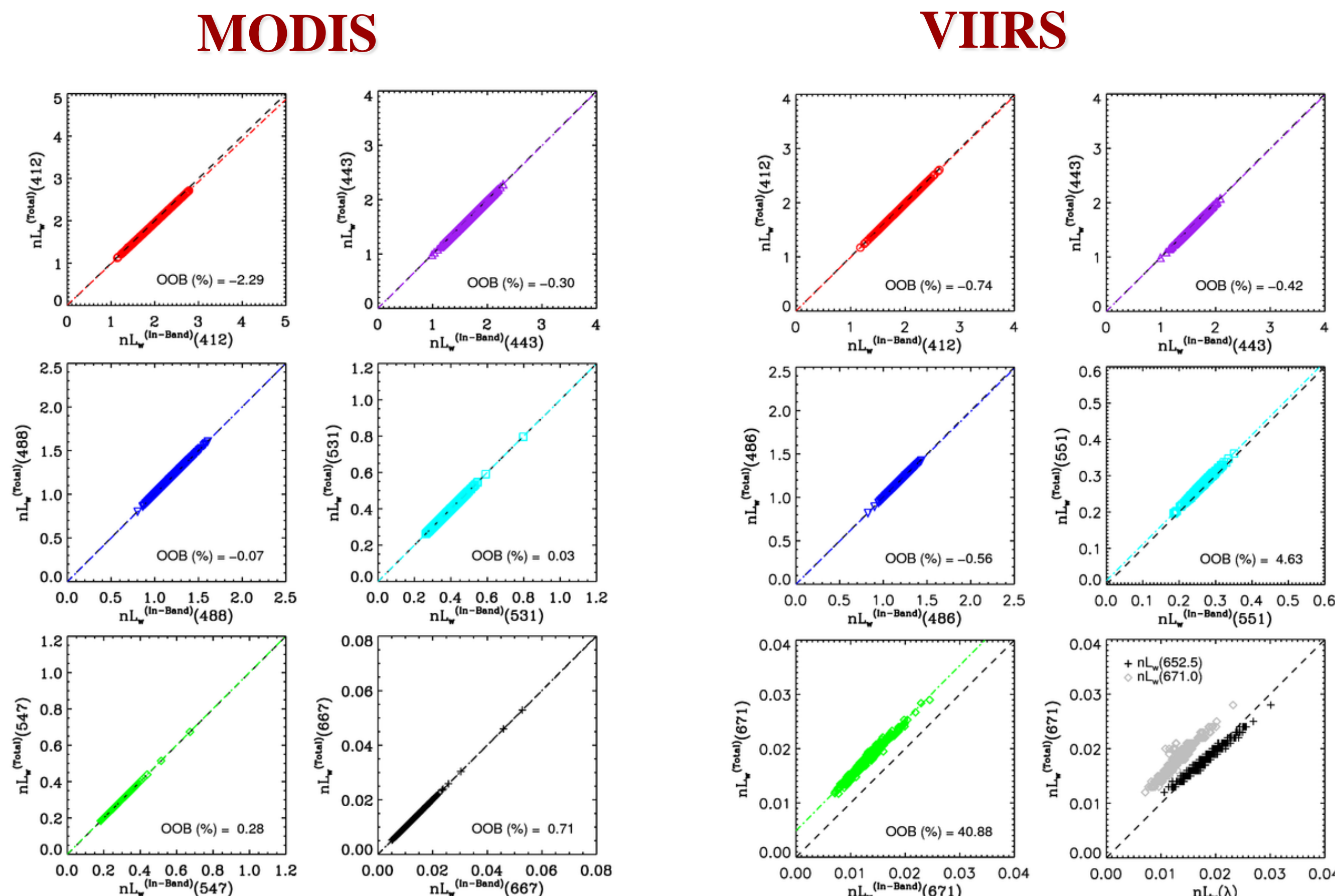


Fig.1 : Total-band and in-band averaged $nL_w(\lambda)$ comparisons at selected MODIS bands. The dotted line is the 1:1 fit.

Fig.2 : Total-band and in-band averaged $nL_w(\lambda)$ comparisons at selected VIIRS bands. The dotted line is the 1:1 fit.

- Figures 1 and 2 show the comparisons between total-band and in-band $nL_w(\lambda)$ averaged radiances at the MOBY site (open oceans) for MODIS and VIIRS, respectively.
- For the MOBY site (open oceans) the out-of-band contribution for MODIS is less than $\sim 3\%$ for the bands we have analyzed. While, for VIIRS, the out-of-band contribution is less than $\sim 5\%$ except for band M5 (671 nm).
- The high out-of-band contribution at the band M5 of VIIRS is due to a large leakage (out-of-band spectral distribution) from the blue region of the spectrum.
- In general, the out-of-band response is greater for VIIRS relative to MODIS, except at the blue band.

Effective band center wavelengths – MOBY Site

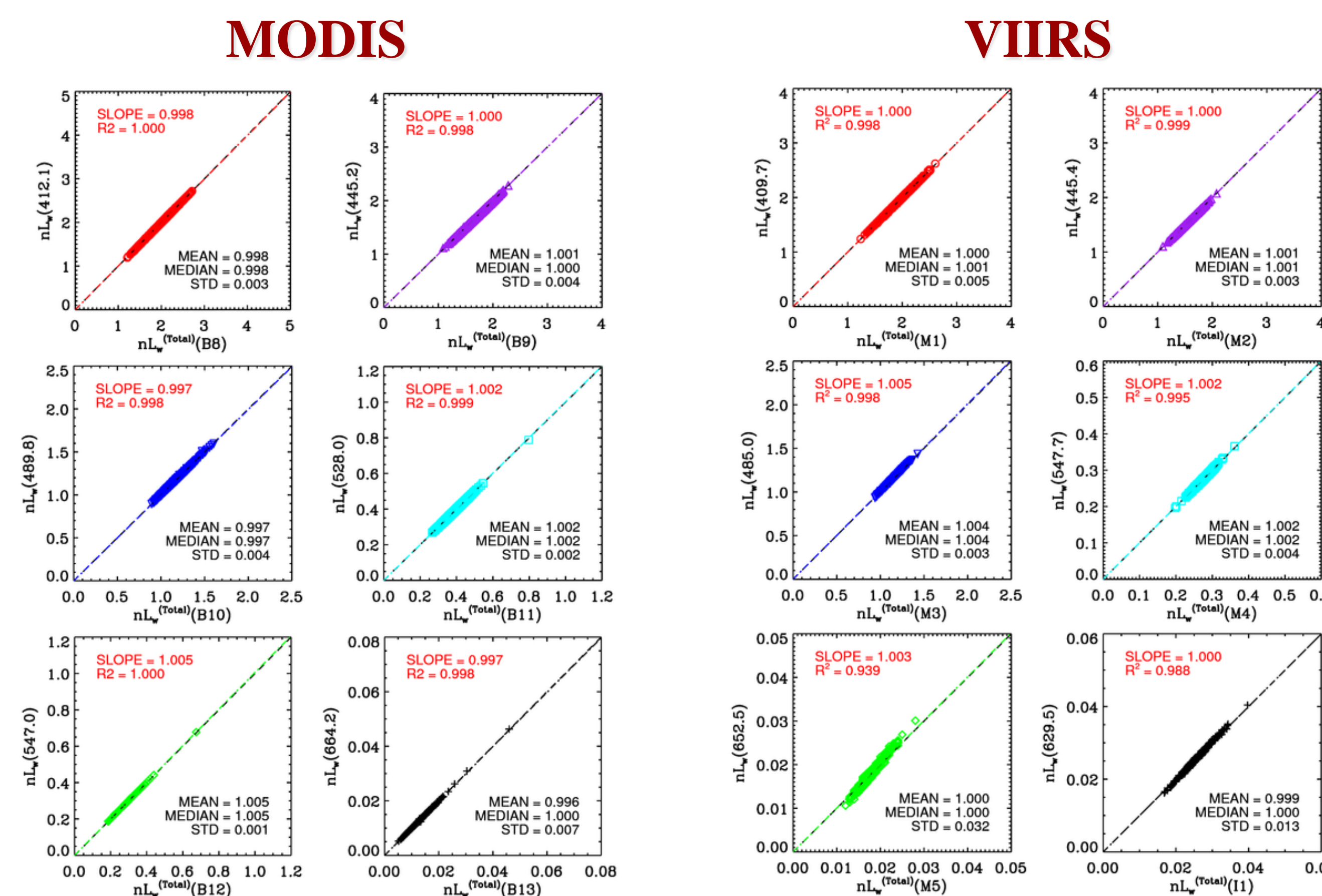


Fig.3 : Effective center wavelengths for selected MODIS bands. The dotted line is the 1:1 fit.

Fig.4 : Effective center wavelengths for selected VIIRS bands. The dotted line is the 1:1 fit.

Table 1. The ratio between $nL_w(\lambda)$ at the nominal band center and total-band averaged $nL_w(\lambda)$, and the effective band center wavelengths for MODIS and VIIRS.

MODIS			VIIRS		
Nominal Center Wavelength (nm)	$nL_w(\text{nominal})/nL_w(\text{Total})$	Effective Center Wavelength (nm)	Nominal Center Wavelength (nm)	$nL_w(\text{nominal})/nL_w(\text{Total})$	Effective Center Wavelength (nm)
412 (B8)	0.994	412.1	410 (M1)	1.022	409.7
443 (B9)	1.034	445.0	443 (M2)	0.959	445.4
488 (B10)	0.977	489.8	486 (M3)	1.072	485.0
531 (B11)	1.012	528.0	551 (M4)	1.078	547.7
551 (B12)	1.005	547.0	671 (M5)	1.399	652.5
667 (B13)	0.977	664.2	635 (I1)	1.070	629.5

- The significant out-of-band response that we noticed can cause an increase in the observed radiance above the measurement for the nominal center band.
- The ratio of the radiance at nominal center wavelength to total-band averaged radiances gives an estimate for out-of-band response on the derived $nL_w(\lambda)$ at nominal center wavelengths (Table 1). Ratio values greater than 1 indicate an underestimation, while ratio values less than 1 show an overestimation relative to the total-band averaged $nL_w(\lambda)$.
- For MODIS, except for bands 412 and 488 nm, all the other bands are biased low, whereas for VIIRS all the bands are biased low except for 443 nm (M2). The largest bias is seen in the VIIRS M5 band, consistent with the results from the total-band and in-band comparisons.
- We determined the effective band center wavelengths for MODIS and VIIRS by comparing the total-band averaged $nL_w(\lambda)$ to $nL_w(\lambda)$ at the individual wavelength measured by in situ radiometers at the MOBY site. In essence, the individual wavelengths are adjusted until the slope equals 1 between $nL_w(\lambda)$ radiance at the individual wavelengths and the corresponding total-band averaged values (Fig. 3 and Fig. 4).
- Figures 3, 4, and Table 1 show the effective band center wavelengths for MODIS and VIIRS determined using the scheme described in methods.
- The effective band center wavelengths are within ± 6 nm of the nominal center wavelengths for both MODIS and VIIRS, except for the VIIRS M5 band.

CONCLUSIONS

- From the results of the out-of-band correction, we show that there was up to $\sim 5\%$ out-of-band response (except for VIIRS M5 band with much large effect).
- This results in significant contribution from outside the nominal center wavelength of the sensor wavebands. A significant out-of-band response can cause an increase in the observed radiance above the measurement for the nominal center band.
- The effective band center wavelengths are significantly different from the nominal center wavelengths for both MODIS and VIIRS for some bands. It is noted that the effective band center wavelengths in Table 1 represent the center band wavelengths of MODIS and VIIRS-measured $nL_w(\lambda)$ for open ocean waters.

References:

- [1] M. Wang, B. A. Franz, R. A. Barnes, and C. R. McClain, "Effects of spectral bandpass on SeaWiFS-retrieved near-surface optical properties of the ocean," *Appl. Opt.*, vol. 40, pp. 342–348, 2001.
- [2] P. Naik and M. Wang, Evaluation of in situ radiometric data processing for calibration and validation of satellite ocean color remote sensing, SPIE Ocean Sensing and Monitoring VI, May 6-7, 2014, Baltimore, Maryland.

Acknowledgments: We thank the MOBY team (IP: Ken Voss) for providing the in situ data.

ABSTRACT

The Chesapeake Bay (CB) contains some of the most productive waters along the U.S. East Coast. Standard satellite algorithms for net primary production (NPP) for the open ocean are generally not applicable for the CB. In this presentation, we show NPP estimates from MODIS-Aqua by applying a new regional NPP model to satellite products. This NPP model for the CB incorporates an improved prediction of the photosynthetic parameter, P_{opt} , as a function of sea surface temperature (SST). These MODIS-Aqua NPP estimates agree well with in-situ measurements. NPP time series for CB using MODIS-Aqua data (2002–2011) with the new model are used to characterize spatial and temporal variability of NPP in CB. Spatial distributions show high NPP in the southern upper Bay and northern middle Bay, and low NPP values in the northern upper Bay, the eastern middle Bay, and the lower Bay. Lowest NPP occurred during winter over the entire Bay, and highest NPP occurred in late spring to summer. These results are consistent with NPP dynamics ascertained by shipboard studies. We conclude by demonstrating NPP derived using VIIRS products for CB. This study has been documented in our recent paper (Son et al., 2014).

DATA & METHODS

- In situ Primary Production and ancillary data ($Chl-a$, P_{opt}^B , Z_{eu} , PAR, SST, etc.) are obtained in the Chesapeake Bay by Harding et al.
- Total data number is 558 from April 1989 to November 2003 (data before April 1989 are excluded due to suspected data quality).
- MODIS-Aqua Level-2 ocean color data from July 2002 to December 2011 were generated using the NIR-SWIR combined atmospheric correction algorithm (Wang & Shi, 2007) with MODIS-Aqua Level-1B data from the NASA MODAPS website. MODIS PAR and SST data were obtained from the NASA OBPG website.
- Those Level-2 data were remapped and then processed to generate NPP composite images.
- Three regions in Chesapeake Bay are defined, i.e., the lower Bay, middle Bay, and upper Bay (shown as boxes, A, B, & C in Fig.1, respectively), following salinity gradients.

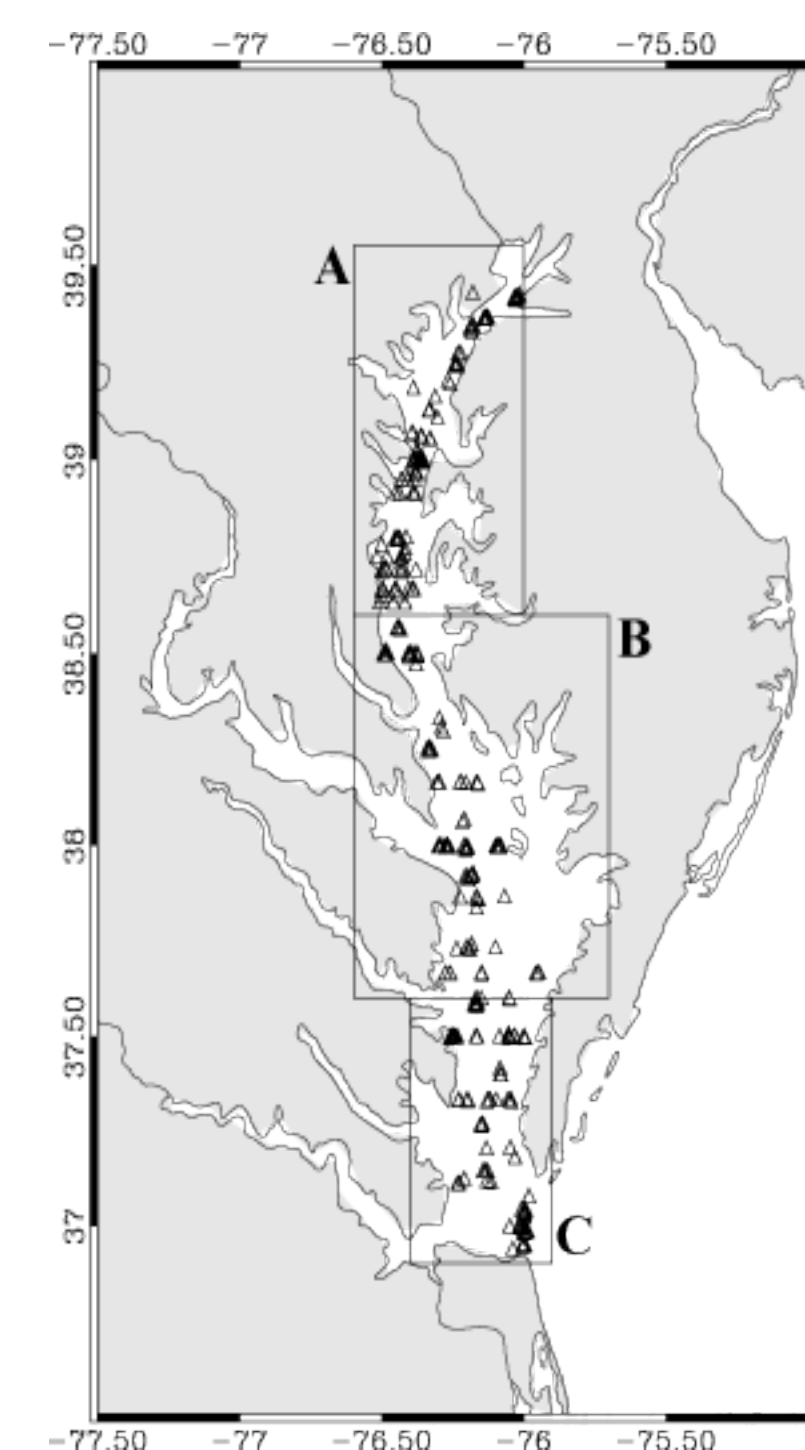


Fig. 1. Map of the Chesapeake Bay with locations of in situ PP data (triangles).

Chesapeake Bay Production Model

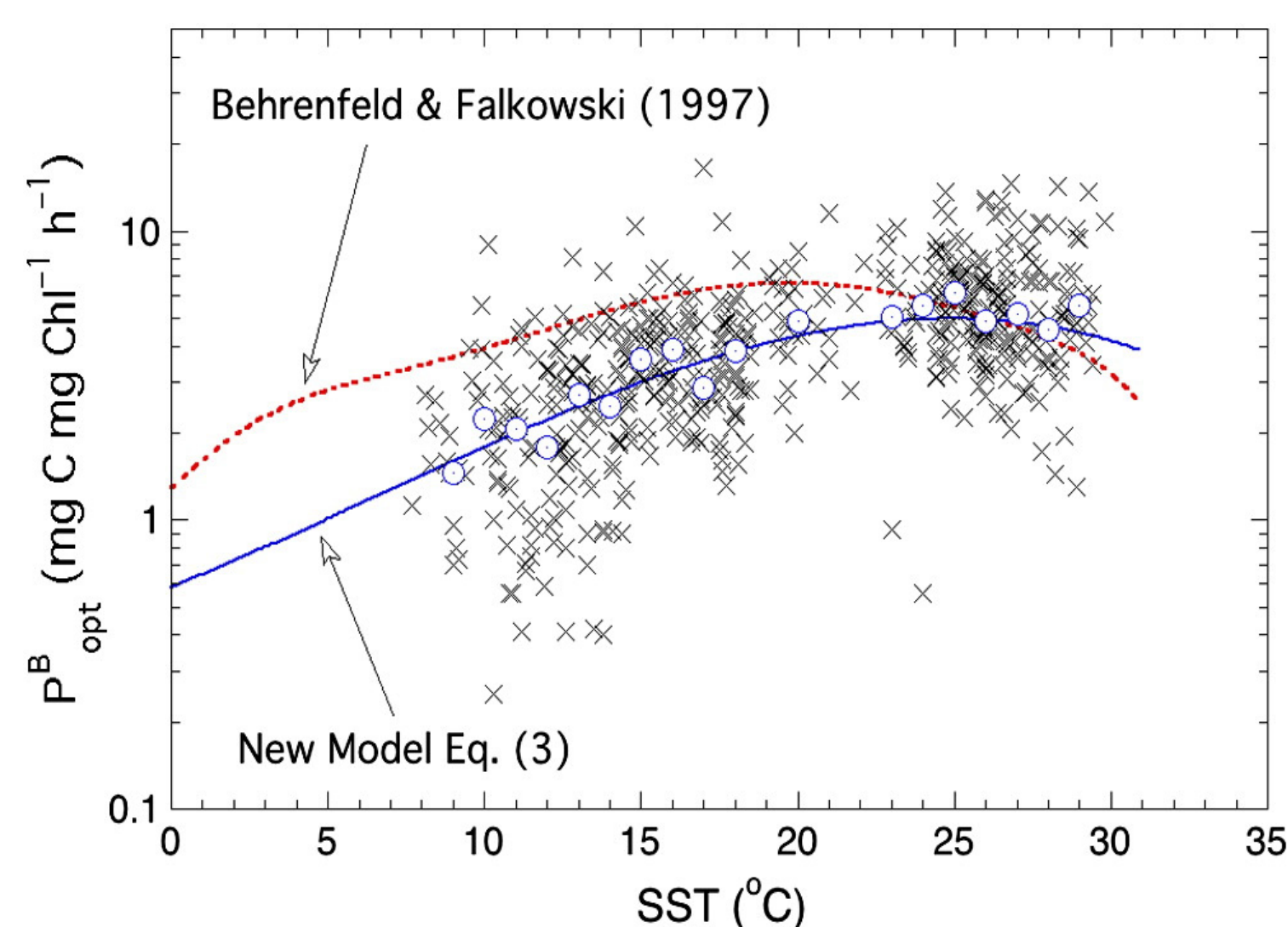


Fig. 2. Optimal photosynthetic carbon fixation rate (P_{opt}^B) as a function of SST for CB.

- The daily-integrated NPP model for CB, CBPM, (Harding et al., 2002) is described as:

$$\log_{10}(NPP) = 0.1329 + 0.964 \cdot \log_{10} P_{opt}^B + 1.0265 \cdot \log_{10} Chl-a + 0.9710 \cdot \log_{10} Z_{eu} + 1.4260 \cdot \log_{10} [E_0 / (E_0 + 4.1)] + 0.6645 \cdot \log_{10} DL,$$

where Z_{eu} is euphotic depth, E_0 is surface PAR, and DL is day length.

- A third polynomial regression relationship between P_{opt}^B and SST was derived to parameterize P_{opt}^B :

$$\log_{10} P_{opt}^B = -2.32 \times 10^{-1} + 4.34 \times 10^{-2} SST + 1.00 \times 10^{-3} SST^2 - 5.00 \times 10^{-5} SST^3$$

Validation of the CB NPP Model

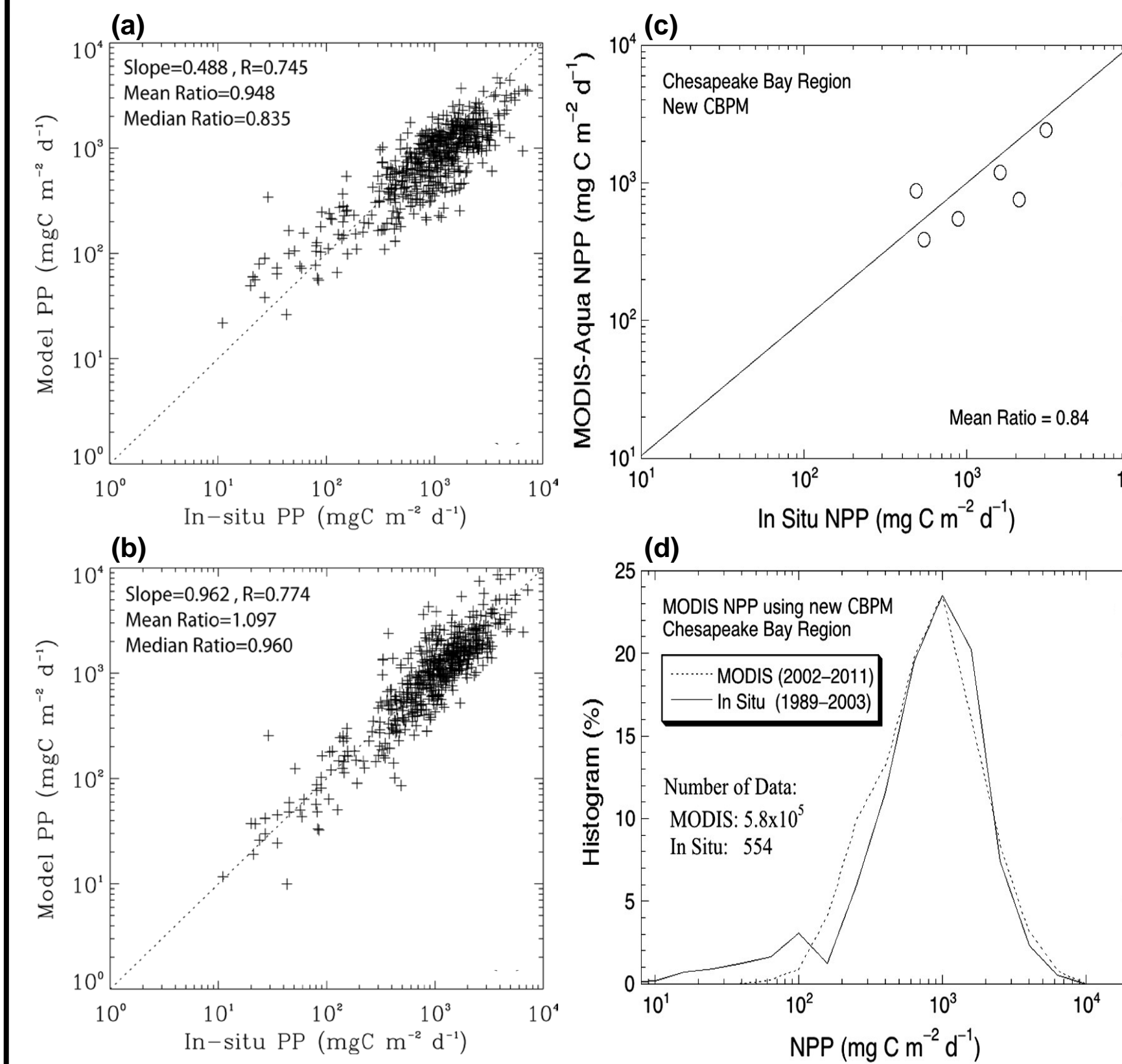


Fig. 3. Comparison of model-derived NPP with in situ NPP using (a) the original CBPM (Harding et al., 2002) and (b) the new CBPM. (c) matchup comparisons of MODIS-Aqua-derived NPP using the new CBPM with in situ NPP, and (d) histogram results for the MODIS-Aqua-derived and the in situ NPP measurements in the entire CB.

- Comparisons of model-derived and in situ NPP show the new approach to generate P_{opt} significantly improves retrievals for the Bay.
- The original CBPM-derived NPP are biased low by ~20%, while the new CBPM shows better agreement with NPP by ~4% for the median.
- Match-up analyses show that MODIS-derived NPP compares favorably with in situ NPP, despite limitations of sample size due to a short temporal overlap.
- Histogram results show MODIS-derived NPP is similar to in situ NPP. But there is decadal difference between MODIS-Aqua and in situ NPP measurements.

Seasonal Variability of MODIS-derived NPP

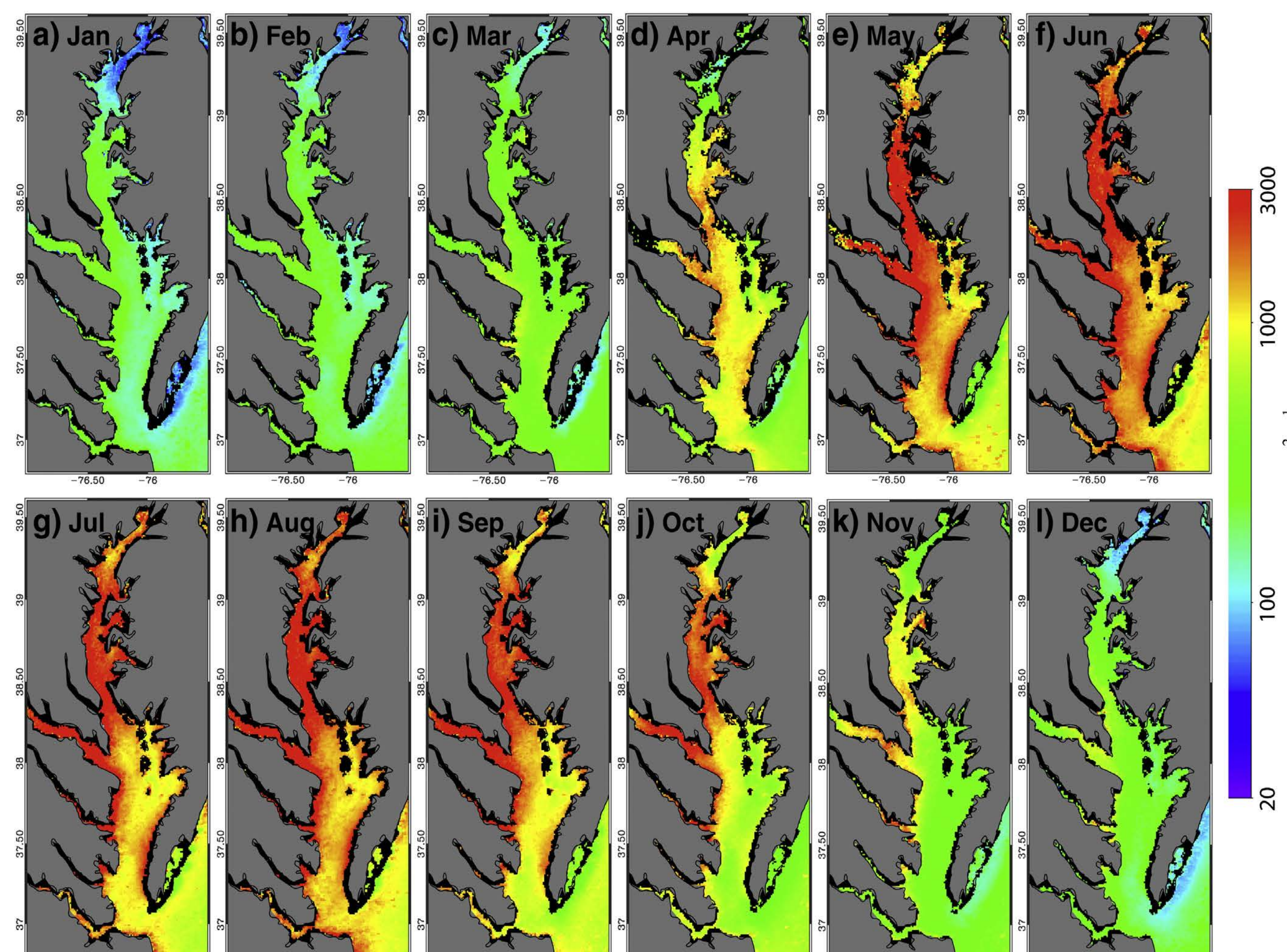


Fig. 4. MODIS-Aqua-measured (2002–2011) monthly NPP climatology images for the Chesapeake Bay for months of January to December.

- General spatial distributions from MODIS-Aqua NPP images are similar over most of months, showing high values in the southern upper Bay and the northern middle Bay, while relatively lower NPP values are in the northern upper Bay, the eastern area of the middle Bay, and the lower Bay.
- MODIS-derived NPP are lowest in winter (Dec–Feb) for the entire Bay, due to limited light availability. NPP is highest in late spring to summer (May–Aug), depending on location. In autumn, NPP decreases with seasonal reduction of solar energy.

Interannual Variability of MODIS-derived NPP

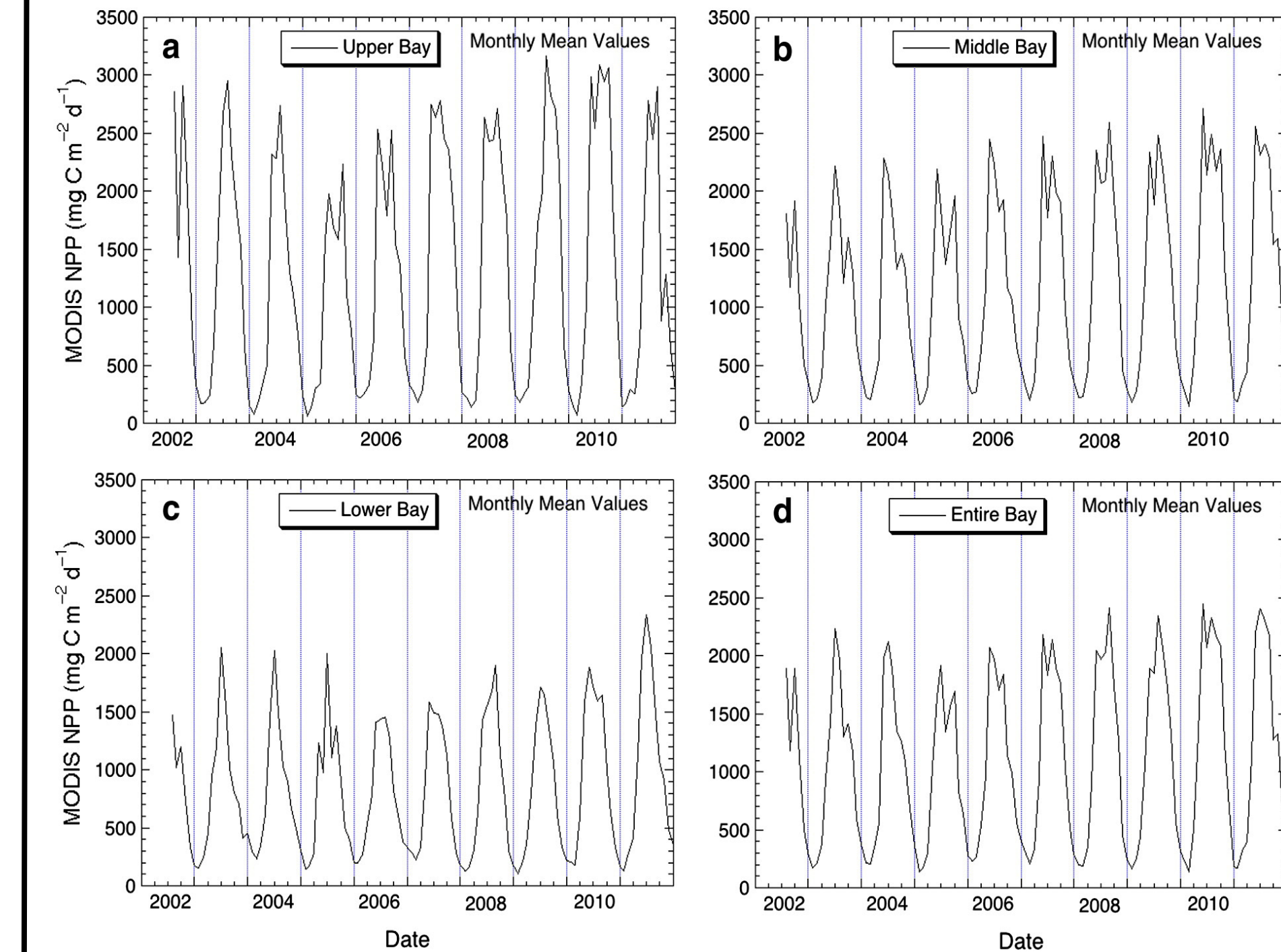


Fig. 5. Time series of MODIS-derived mean monthly NPP in the CB sub-regions of (a) upper Bay, (b) middle Bay, (c) lower Bay, and (d) entire Bay from July 2002 to December 2011.

- There is a strong interannual variability in the NPP for CB. In the upper Bay, highest NPP values appeared in summer of 2009 and 2010, while relatively lower seasonal peaks occurred in 2005 and 2006.
- In the lower Bay, the seasonal peak of NPP generally appears in June. But, an early seasonal peak appeared in 2007 and 2010 (May), and a late seasonal peak in 2008 (August). A relatively higher NPP peak occurred in June 2011.

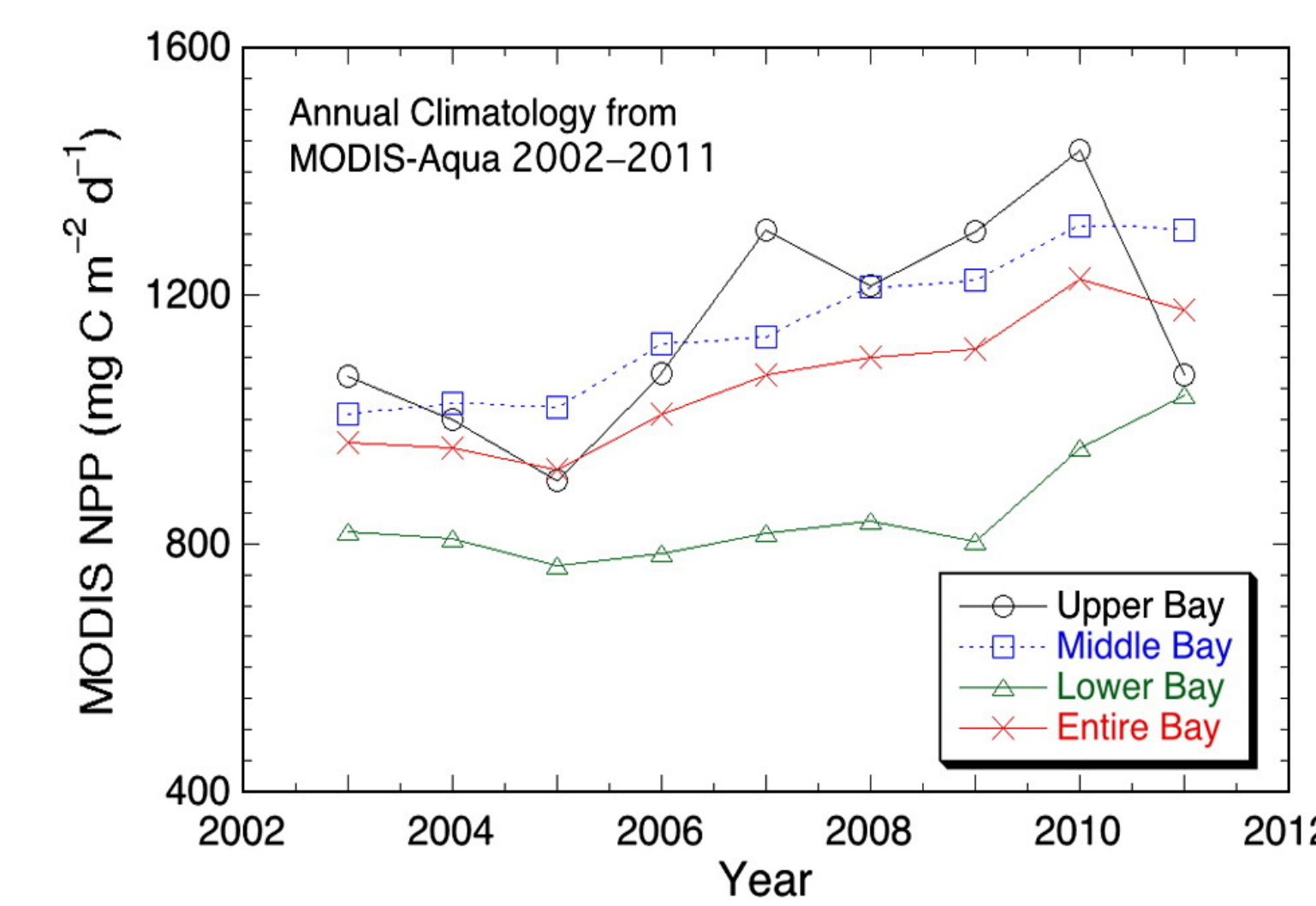


Fig. 6. MODIS-derived annual NPP time series from 2003 to 2011 for the upper Bay, middle Bay, lower Bay, and entire Chesapeake Bay.

- Results from mean values of the MODIS-derived annual NPP show that interannual variability of annual NPP is evident in the three sub-regions, with an apparent increasing trend from 2003 to 2011 in the all Bay regions. The increasing trend in NPP may be related to the increases in nutrient and phytoplankton biomass.
- Interannual variability in NPP in the Chesapeake Bay would be positively (lower Bay) or negatively (upper Bay) related to freshwater flow from the rivers, particularly the Susquehanna River.

CONCLUSIONS

- The regional daily NPP model for the Chesapeake Bay has been improved for use with satellite ocean color data.
- MODIS-derived NPP data correspond reasonably well to in situ measurements.
- MODIS-derived NPP products show that higher NPP values are found in southern upper Bay and northern middle Bay, while relatively low NPP values are in northern upper Bay, the eastern area of middle Bay, and lower Bay. Temporally, lowest NPP in winter over the entire Bay, while high NPP in later spring to summer depending on location.
- There is a strong interannual variability in NPP for CB, and an apparent increasing trend from 2003 to 2011.

Reference:

- Harding Jr., L. W., Mallonee, M. E., & Perry, E. S. (2002). Toward a predictive understanding of primary productivity in a temperate, partially stratified estuary. *Estuarine, Coastal and Shelf Science*, 55, 437–463.
- Son, S., Wang, M., & Harding Jr., L. W. (2014). Satellite-measured net primary production in the Chesapeake Bay. *Remote Sensing of Environment*, 144, 101–119.
- Wang, M., & Shi, W. (2007). The NIR-SWIR combined atmospheric correction approach for MODIS ocean color data processing. *Optics Express*, 15, 15722–15733.

Acknowledgments: This research was supported by the NOAA Ocean Remote Sensing (ORS) funding. LWH was supported the NSF Biological Oceanography Program and the NOAA Chesapeake Bay Program Office.

Abstract

A new approach that combines advantages of various existing near-infrared (NIR) ocean reflectance correction algorithms for satellite ocean color data processing, including Bailey et al. (2010) algorithm, Ruddick et al. (2000) "MUMM" algorithm, and Wang et al. (2012) algorithm, has been developed. The new algorithm is named BMW after Bailey, MUMM, and Wang. The results from the BMW algorithm are evaluated against those from the shortwave infrared (SWIR)-based atmospheric correction algorithm and also compared with results from various existing NIR ocean reflectance correction algorithms using data from MODIS-Aqua and VIIRS-SNPP, with emphasis on the performance in various coastal and inland turbid waters in the world. The new BMW algorithm provides improved satellite ocean color results compared with various existing NIR algorithms and can be incorporated into the official VIIRS ocean color data processing system, which does not have the NIR radiance correction algorithm that is required for the data processing in coastal and inland waters. Some detailed algorithm evaluations and discussions are provided.

Three different methods for estimation of ocean reflectance at the NIR bands

B: The bio-optical model described by Bailey et al. (2010) is used in the current NASA MODIS atmospheric correction algorithm, which is an improved version of the Stumpf et al. (2003) model. It exploits the relationships in the intrinsic optical properties (IOP) of the NIR and red/green bands. However, the disadvantage is that it cannot be applied to extremely turbid waters because the IOP relationship stops to work in those areas.

M: The MUMM algorithm described by Ruddick et al. (2000) is originally proposed for SeaWiFS. Its advantage is that it does not use any bio-optical model and it simultaneously solves for water-leaving reflectance and aerosol reflectance at the two NIR bands. However, it requires knowing *a priori* the reflectance ratios between the two NIR bands for both water (α) and aerosol (ϵ) contributions obtained from a scatter plot of the entire scene, which limits its operational usage.

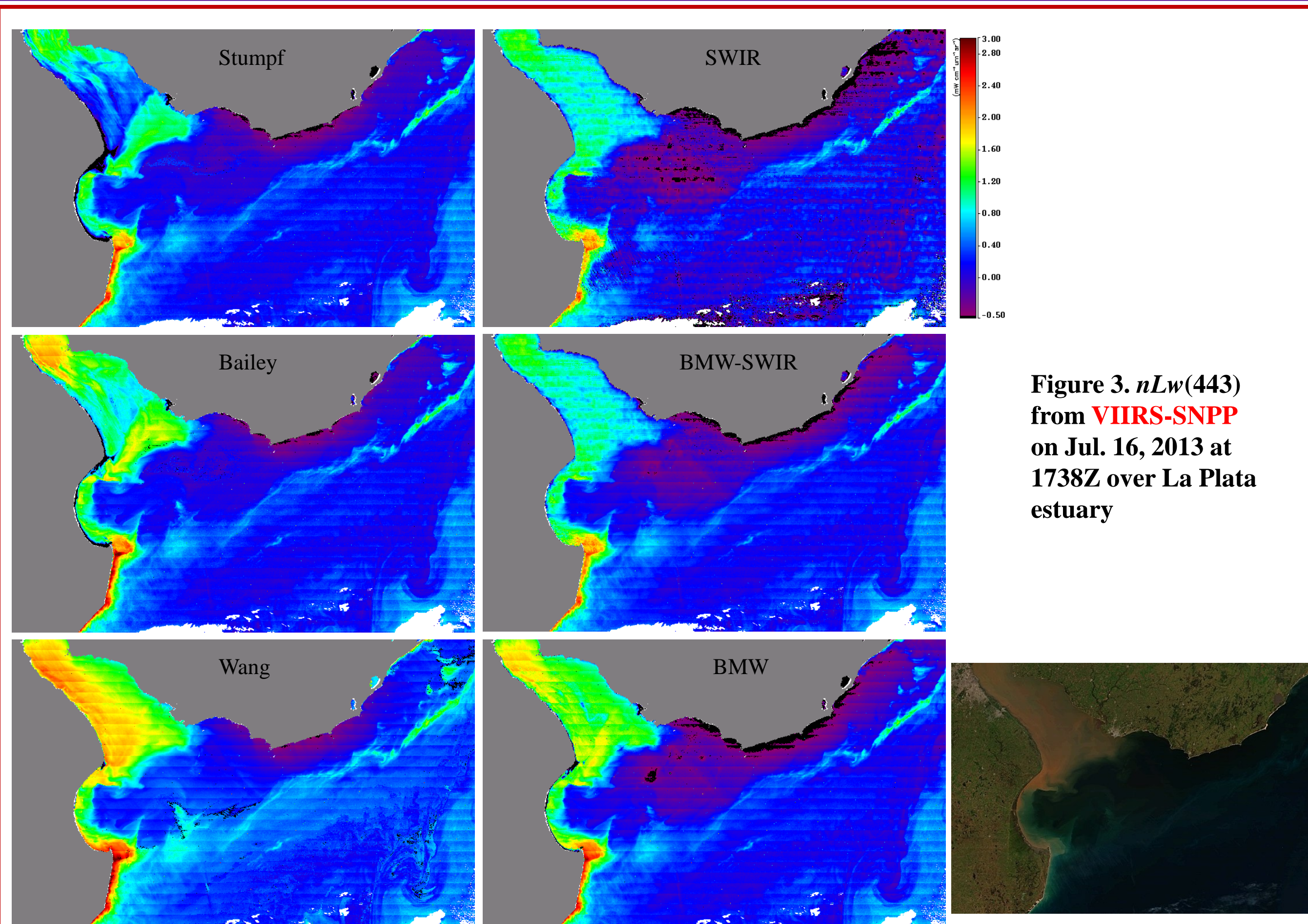
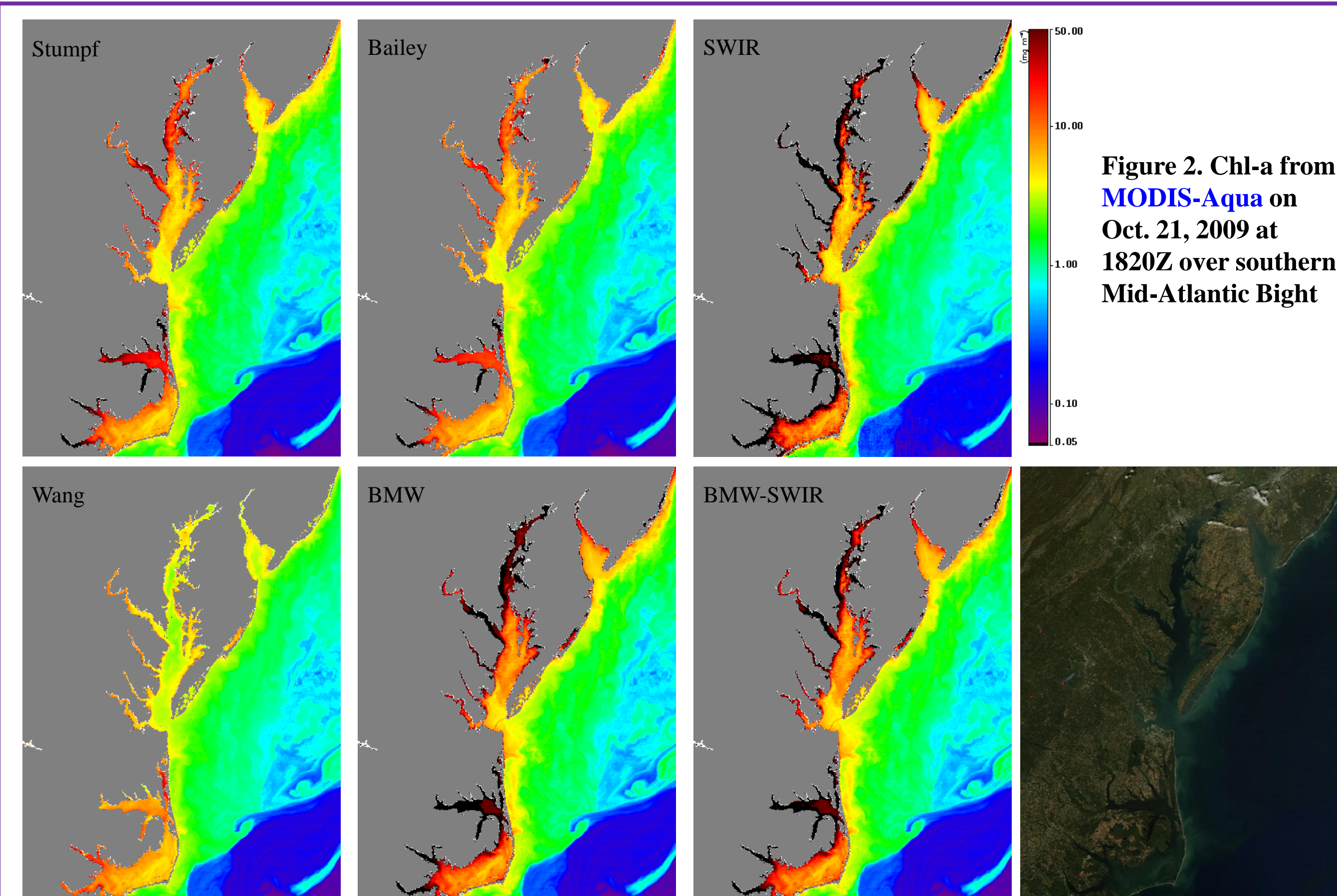
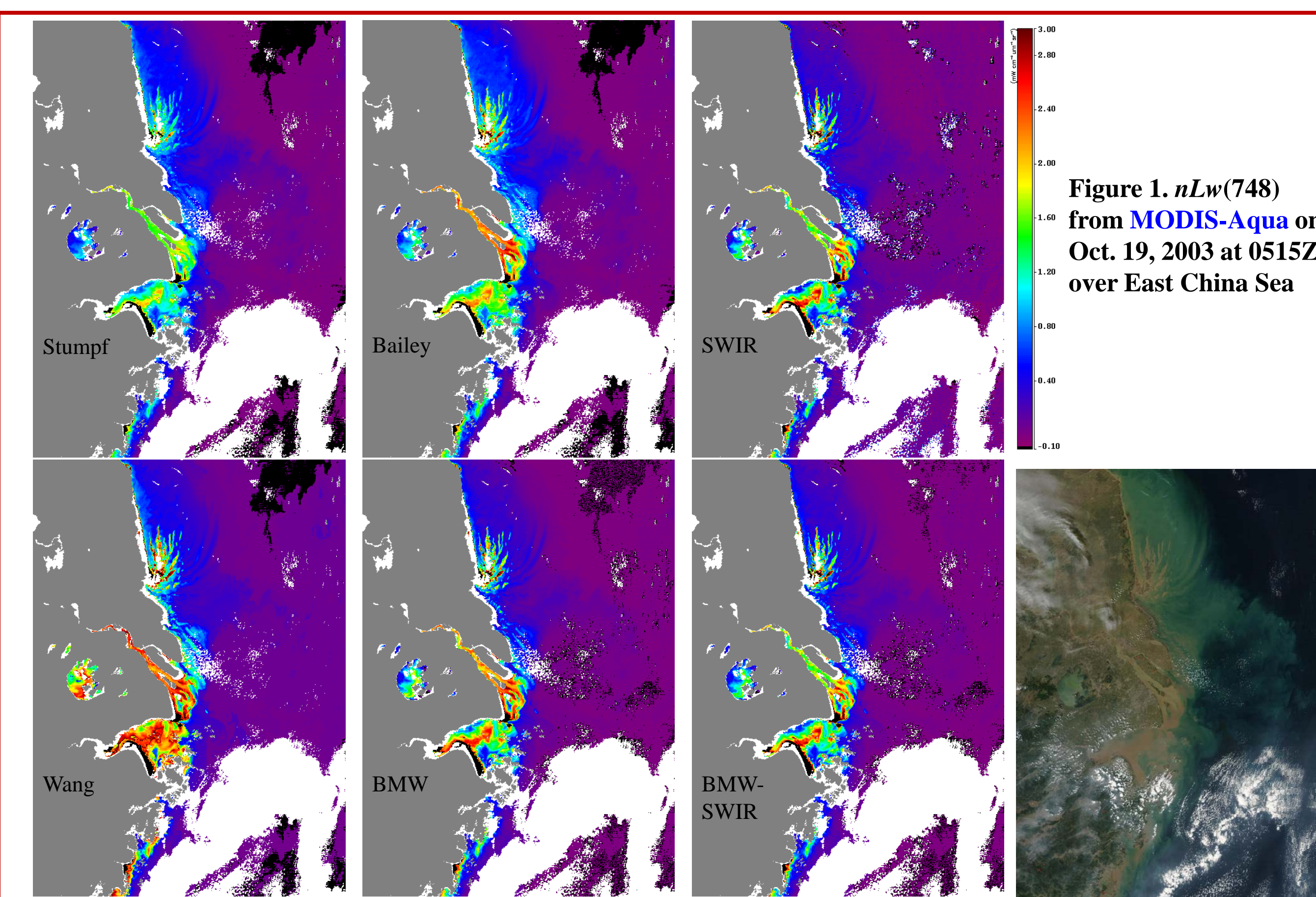
W: Wang et al. (2012) proposed a regional, iterative method for estimation of water reflectance at the NIR from diffuse attenuation coefficient $K_d(490)$, to be used in the atmospheric correction algorithm for the Korean geostationary ocean color sensor – the Geostationary Ocean Color Imager (GOCI). The NIR model (radiance relationship between two NIR bands) was derived from MODIS data using the SWIR approach. Its field of view include one of the most turbid areas in the world where the current MODIS algorithm will not work. GOCI does not have SWIR bands that can be used for atmospheric correction purpose.

BMW - the new blended algorithm

Simply speaking, the proposed blended algorithm uses **B** algorithm to identify and process clear water pixels and **M** algorithm to process the remaining turbid water pixels, and for the turbid water pixel processing **M** algorithm uses the NIR water reflectance relationship established by **W** algorithm and NIR aerosol reflectance ratio (ϵ) derived from nearby clear water pixels. In detail, the BMW algorithm works as follows:

1. Use **B** algorithm to perform a preliminary atmospheric correction, identify clear water pixels and save their corresponding NIR aerosol reflectance ratio ϵ (If a valid pixel is not a clear water pixel, it is regarded as a turbid water pixel).
2. For each turbid water pixel not yet assigned an ϵ value, assign it an ϵ value using the mean of the ϵ values of all clear or turbid water pixels (that have already been assigned an ϵ value) within the 101 pixels by 101 pixels box centered at this turbid water pixel. If no clear water pixel is found within the box, this turbid water pixel will wait for assignment of ϵ value in the next iteration.
3. Repeat Step 2 until no more turbid water pixels can find clear water pixels or turbid water pixels that has been assigned an ϵ value. The remaining turbid water pixels are assigned the mean ϵ value of all clear pixels in the image.
4. Use **M** algorithm incorporated with **W** algorithm's NIR water reflectance relationship to process all the turbid water pixels using their assigned ϵ values.

Results: case studies



The NIR-SWIR processing using BMW

Although the BMW algorithm works reasonably well in very turbid waters, there are circumstances where the SWIR algorithm is necessary. For example, in MODIS-Aqua images, 746 and 869 nm often get saturated in extremely turbid waters, such as in the La Plata estuary (Fig. 4), which will prevent the applicability of any NIR algorithm. Also, for highly turbid waters the NIR model is not accurate. Therefore, a NIR-SWIR processing algorithm using BMW as NIR component was developed to solve this problem. The BMW is first used to process all pixels, which is also used to identify turbid pixels with water-leaving radiances at ~865 nm band larger than a threshold (~0.2). For those turbid waters the SWIR algorithm is used, but there is a buffer zone 0.2-0.4 where the BMW and SWIR results are blended to create a smooth transition between the two algorithms.

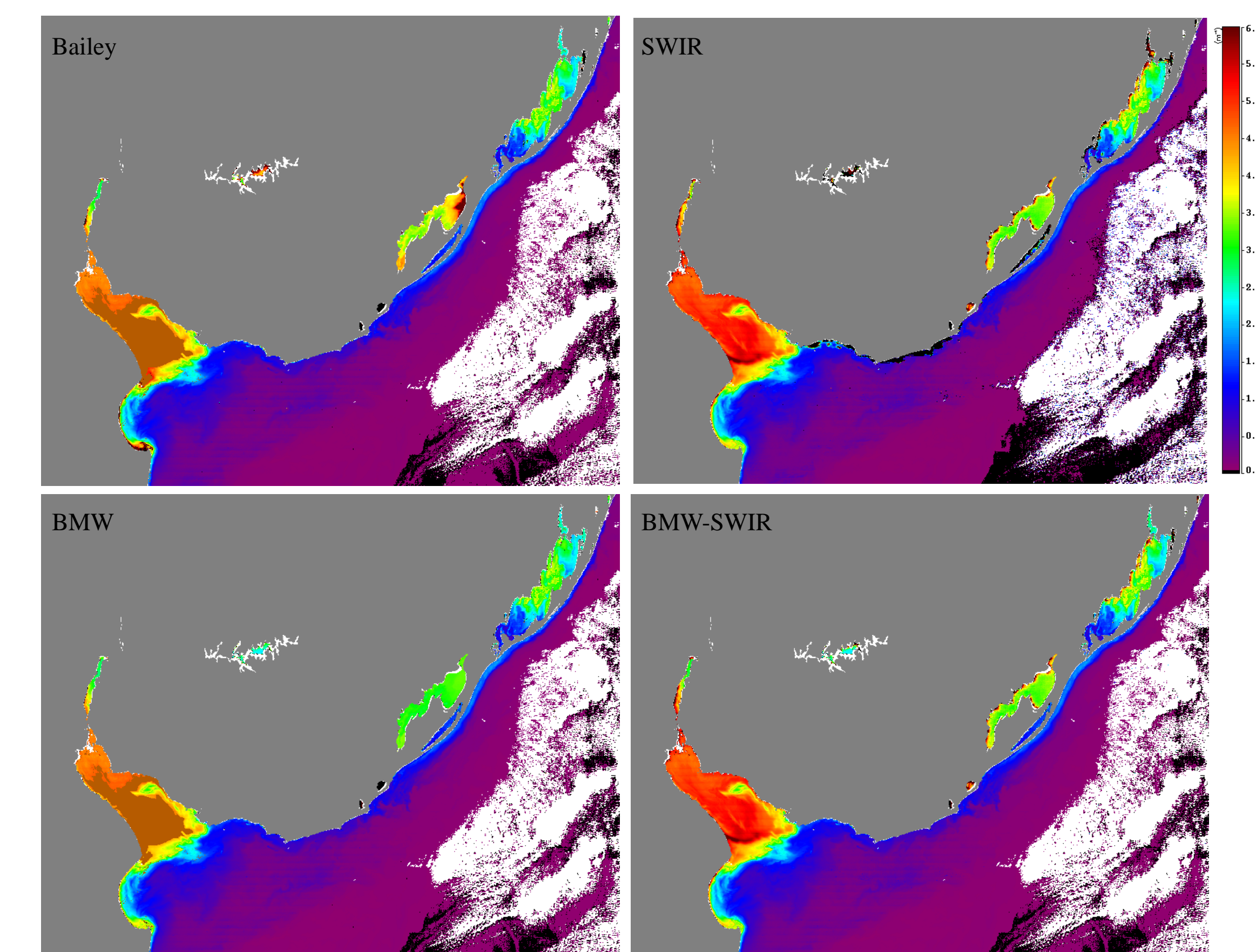


Figure 4. $K_d(490)$ from MODIS-Aqua on Mar. 30, 2006 at 1735Z over La Plata estuary

Results: match-ups

MOBY match-ups	NASA-NIR (Bailey) 794 match-ups		NOAA-NIR (BMW) 982 match-ups		
	Mean Ratio	STD	Mean Ratio	Median Ratio	STD
$nL_w(410)$	1.0428	0.120	1.0253	1.0147	0.149
$nL_w(443)$	1.0299	0.111	1.0170	1.0046	0.136
$nL_w(488)$	1.0143	0.098	1.0012	0.9967	0.120
$nL_w(551)$	0.9988	0.182	1.0045	0.9931	0.196
$nL_w(667)$	1.4125	0.559	0.9049	0.9392	1.050
Chlorophyll-a	0.9348	0.238	0.9712	0.9699	0.214

SeaBASS match-ups	NASA-NIR (Bailey)			NOAA-NIR (BMW)		
	Mean Ratio	STD	match-ups	Mean Ratio	STD	match-ups
$nL_w(410)$	0.9330	0.318	373	0.8173	0.359	369
$nL_w(443)$	1.0119	0.300	825	0.9445	0.309	863
$nL_w(488)$	0.9207	0.181	875	0.9440	0.193	931
$nL_w(551)$	0.8945	0.201	441	0.9485	0.209	487
$nL_w(667)$	0.7573	0.756	516	1.0498	0.823	560

References

- Bailey, S.W., B.A. Franz, and P.J. Werdell (2010). Estimation of near-infrared water-leaving reflectance for satellite ocean color data processing. *Optics Express*, 18 (7), 443-452, doi: 10.1364/OE.18.007521
- Ruddick, K.G., F. Ovidio, and M. Rijkeboer (2000). Atmospheric correction of SeaWiFS imagery for turbid coastal and inland waters. *Applied Optics*, 39 (6), 897-912, doi: 10.1364/AO.39.00897
- Stumpf, R.P., R.A. Arnone, J.R.W. Gould, P.M. Martinovich, and V. Ranisbrahmanakul (2003). A partially coupled ocean-atmosphere model for retrieval of water-leaving radiance from SeaWiFS in coastal waters, in Patt, F.S., et al., 2003: *Algorithm Updates for the Fourth SeaWiFS Data Reprocessing*. NASA Tech. Memo. 206892, National Aeronautics and Space Administration, Goddard Space Flight Center, Greenbelt, MD
- Wang, M., W. Shi, and L. Jiang (2012). Atmospheric correction using near-infrared bands for satellite ocean color data processing in the turbid western Pacific ocean region. *Optical Express*, 20 (2), 741-753, doi: 10.1364/OE.20.000741
- Acknowledgments:** This research was supported by NOAA funding. The MODIS L1B data were obtained from NASA/GSFC MODAPS Services website, and the in situ data were obtained from NASA SeaBASS and NOAA MOBY website.



Extension of NCEP/CPC's Ozone Monitoring Using OMPS Ozone Products



Craig Long¹, Jeannette Wild², Shuntai Zhou², Larry Flynn³, Eric Beach⁴

1 – NOAA/NWS/NCEP/Climate Prediction Center

2 – NOAA/NWS/NCEP/Climate Prediction Center – Innovim

3 – NOAA/NESDIS/STAR/ SMCD

4 – NOAA/NESDIS/STAR/ SMCD - IMSG

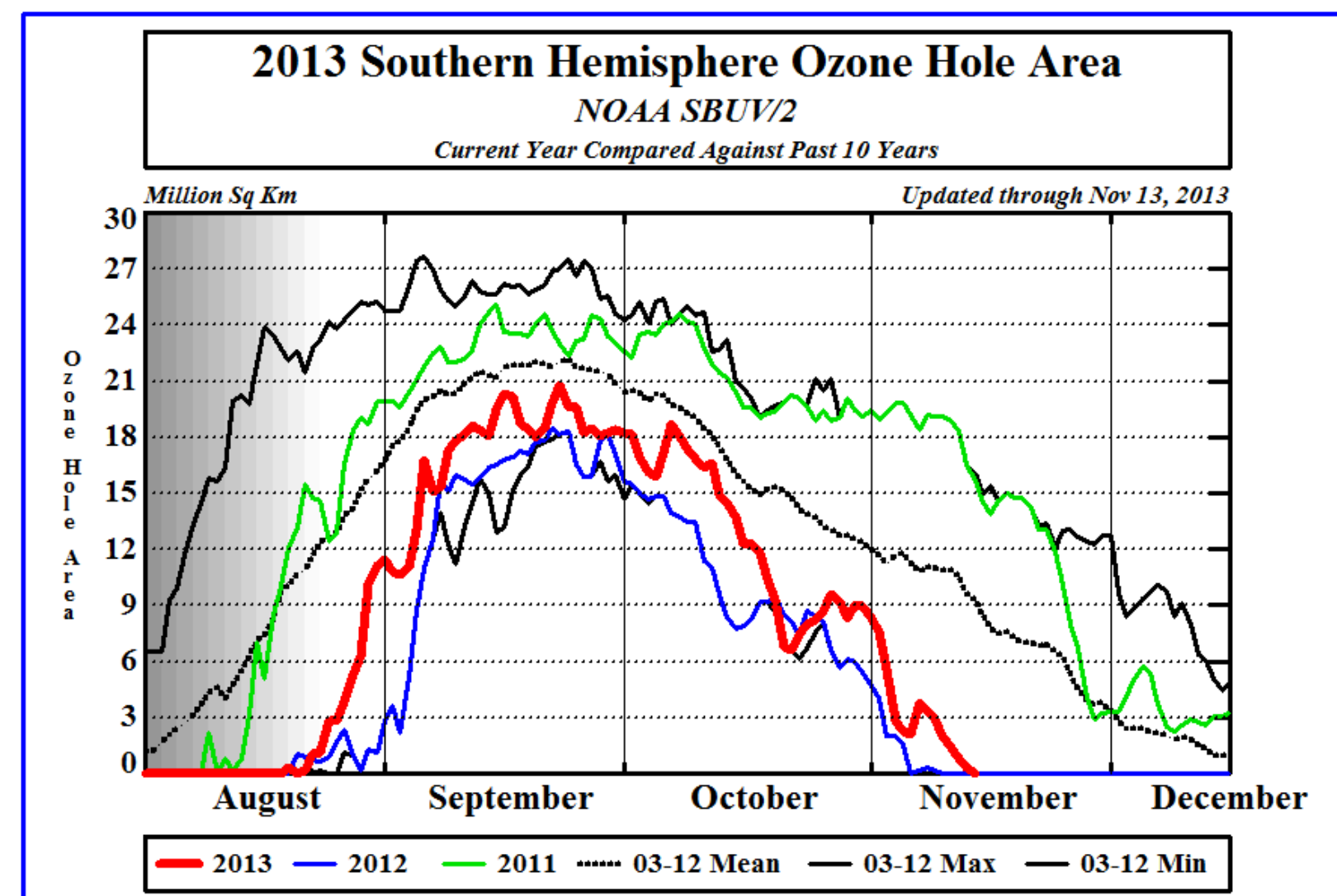
History of Ozone Monitoring at CPC

CPC worked along side NASA in the 1970's to determine the effects of Super Sonic Transport air liners flying on ozone in the stratosphere. CPC began using satellite data to monitor the ozone layer with the SBUV instrument on Nimbus-4 and the SBUV on Nimbus-7. NOAA chose to monitor the profile of ozone vs the total column and started using the SBUV/2 on NOAA-9. All together there have been 8 NOAA spacecraft with SBUV/2 instruments on them. CPC has worked hand-in-hand with NESDIS to utilize the best quality ozone data sets for its monitoring of the ozone depletion, the annual ozone hole, the determination of ozone trends, and assisting NCEP/EMC with the assimilation of ozone in NCEP's weather and climate models.

Ozone Monitoring at CPC

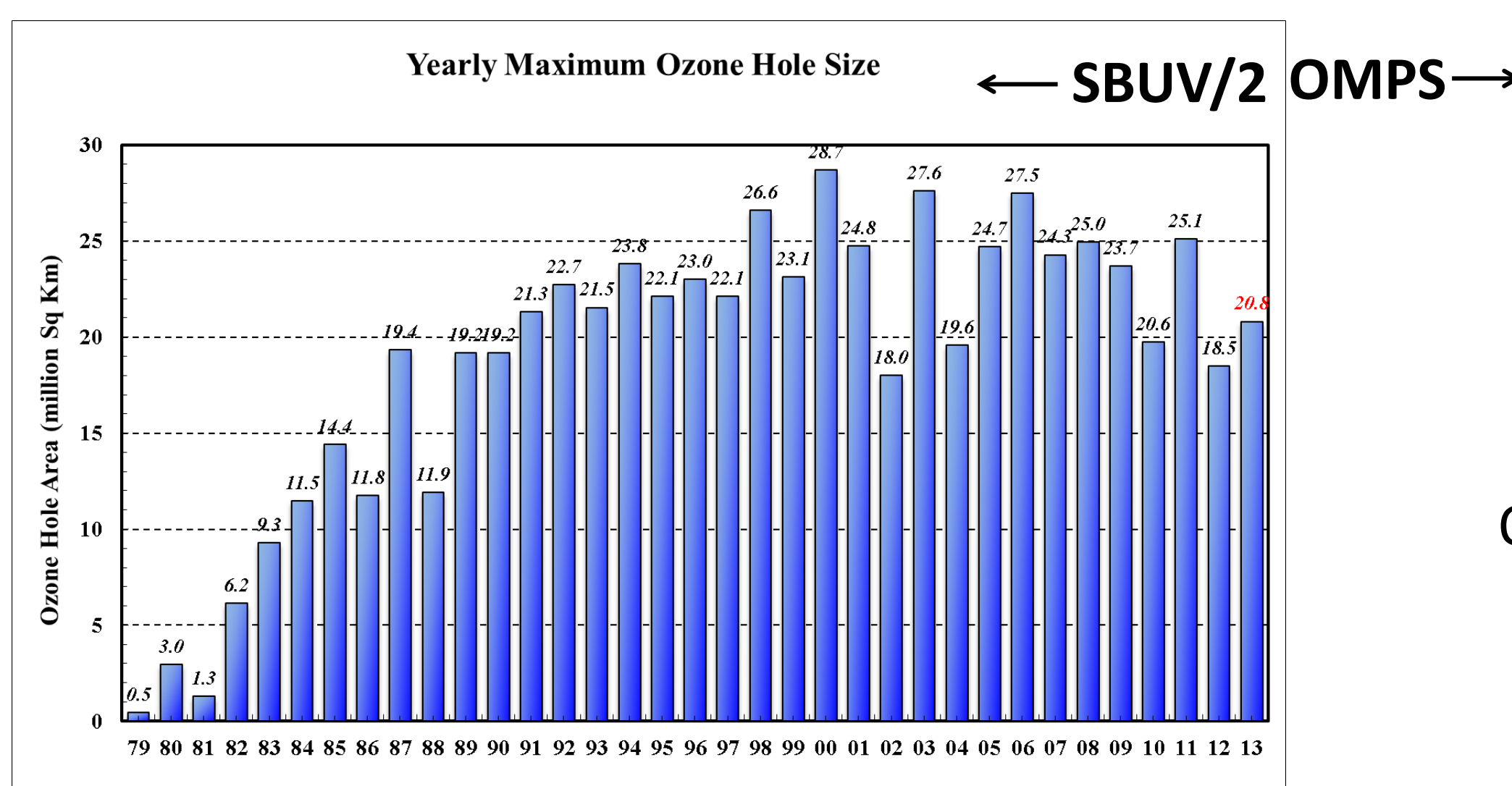
CPC monitors the total column of ozone as well as the ozone profile. CPC monitors ozone on various time scales. Short (day-to-day) time periods for phenomena such as the Antarctic (and occasionally Arctic) ozone hole. Seasonally, CPC monitors the ozone layer's relationship to the thermal and dynamical background. On the longer time scales (annual to decadal), CPC monitors trends in the ozone layer's profile and total column. CPC has used observations from the SBUV/2 instrument to perform this monitoring. The OMPS Nadir Mapper, Nadir Profiler, and Limb Profiler will continue and enhance CPC monitoring capabilities.

OMPS will allow CPC to Continuing to Monitor the Antarctic Ozone Hole



Last year's ozone hole in relation to previous years.

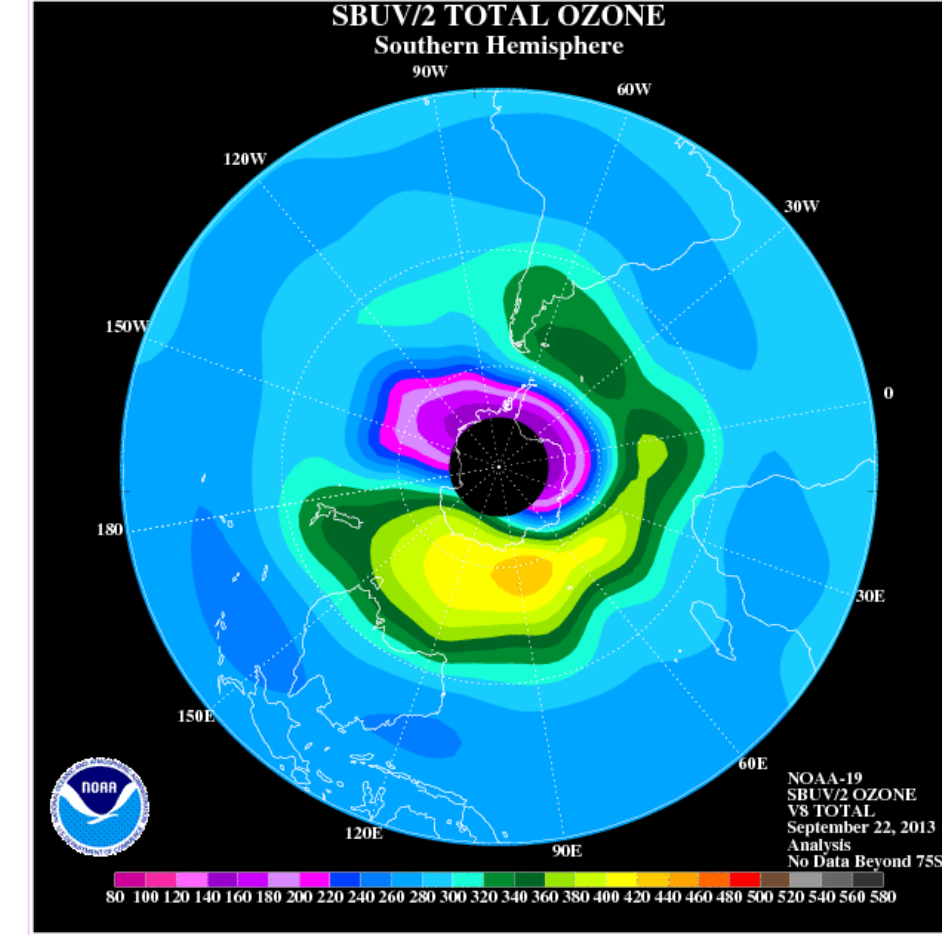
Monitor Inter-Annual Variability of Ozone Hole



Last year's single day maximum ozone hole size Compared to previous years. OMPS observations will continue this monitoring for the next couple decades.

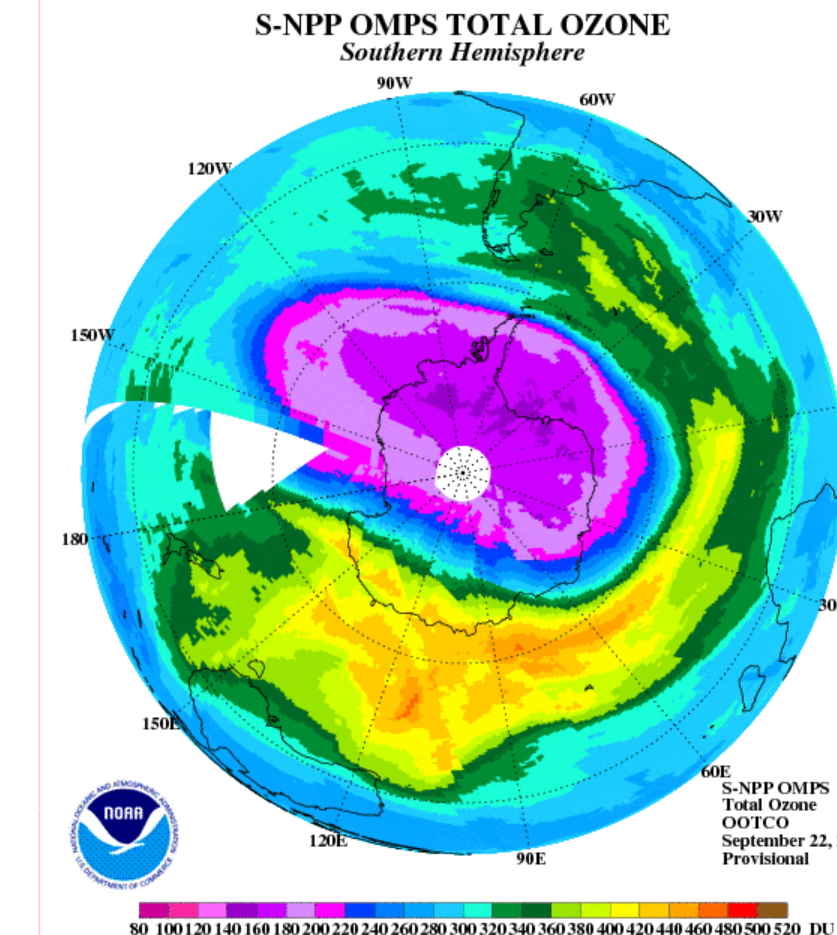
Monitoring Ozone Hole Peak Size

NOAA-19 Total Profile Analysis



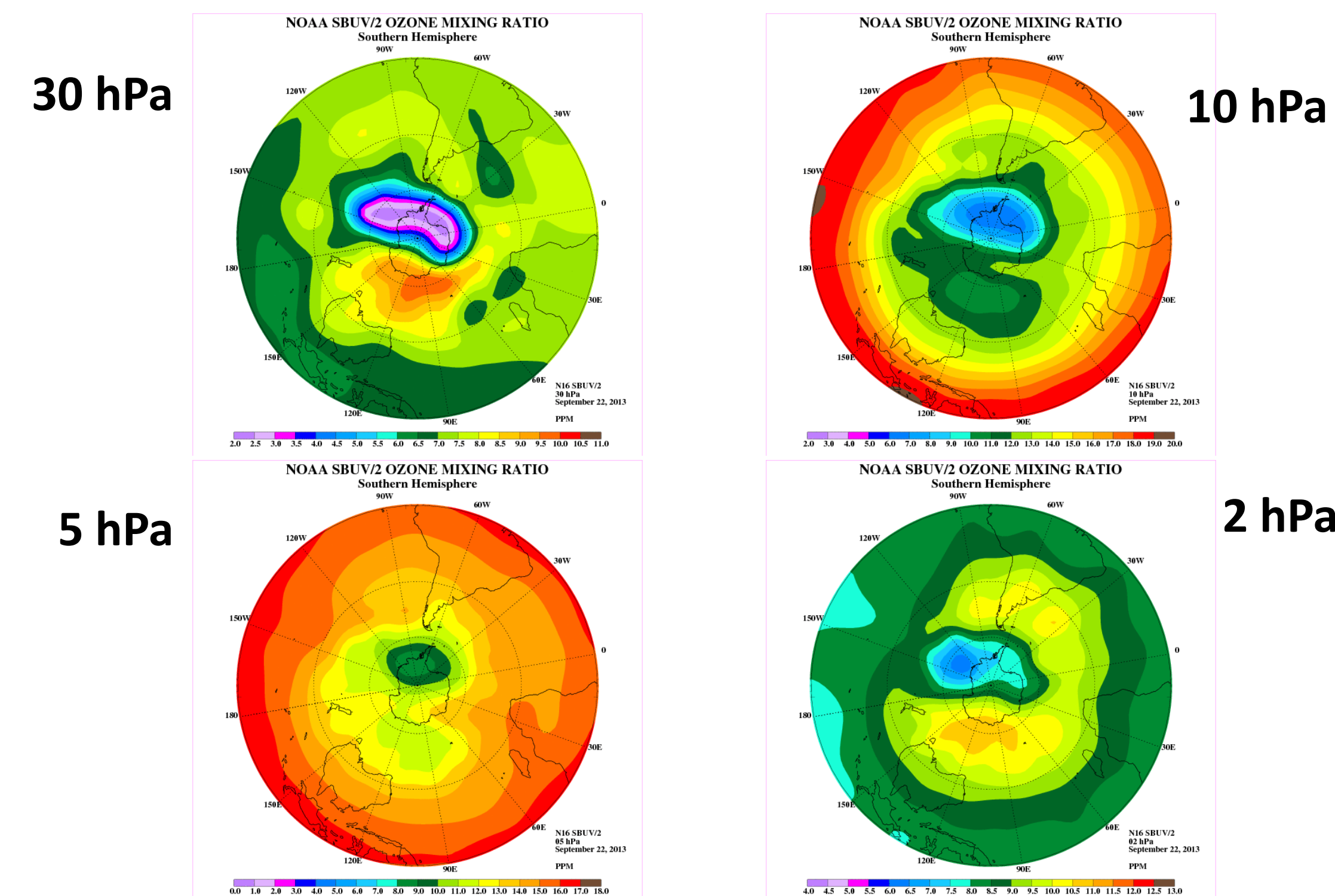
Analysis procedure smooths out features. Reduces Mins and Max values.

S-NPP OMPS NM



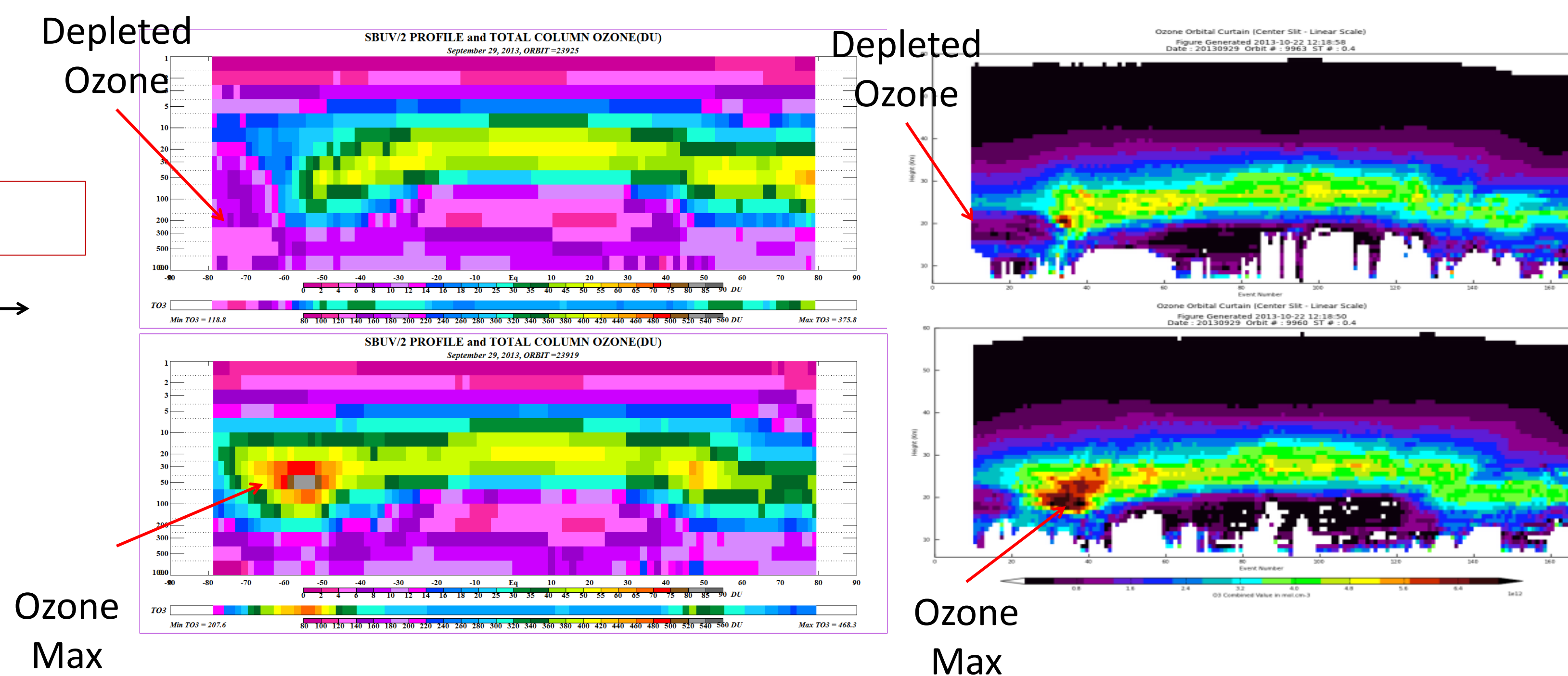
NM provides greater fidelity of features and maintains max and min values.

OMPS NP will continue to provide the structure of ozone in vertical



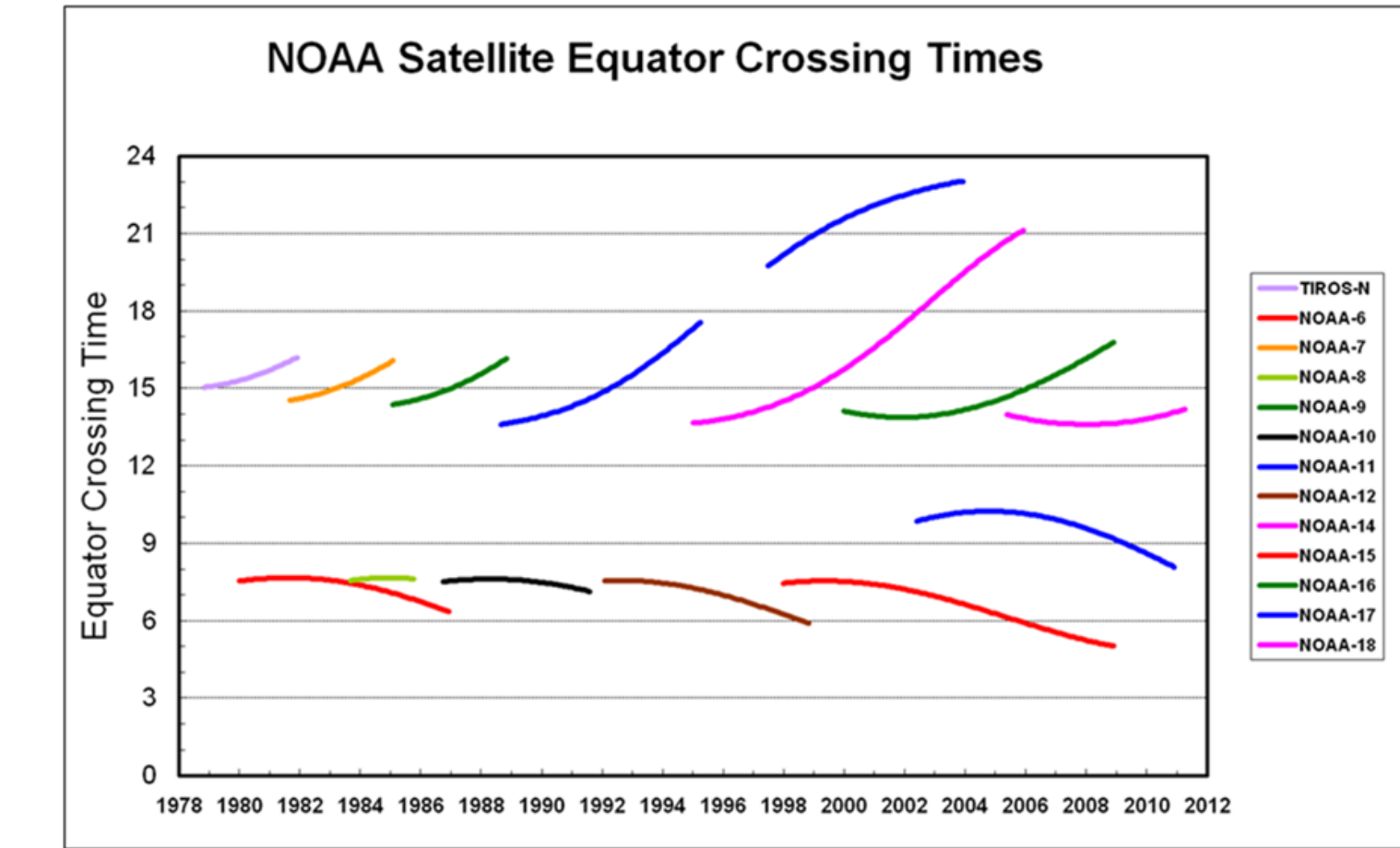
Peak ozone hole size day in 2013 at 30, 10, 5, 2 hPa from N19 SBUV/2

Finer Vertical Resolution of the OMPS Limb Provides Additional Information to the Ozone Profile in the Ozone Hole



Two sets of orbital curtain plots (SBUV/2 on Left and OMPS Limb on Right) of ozone concentration in October 2013. Top orbit shows low ozone values on the edge of the ozone hole on the left side. The bottom orbit passes through the ozone maximum region

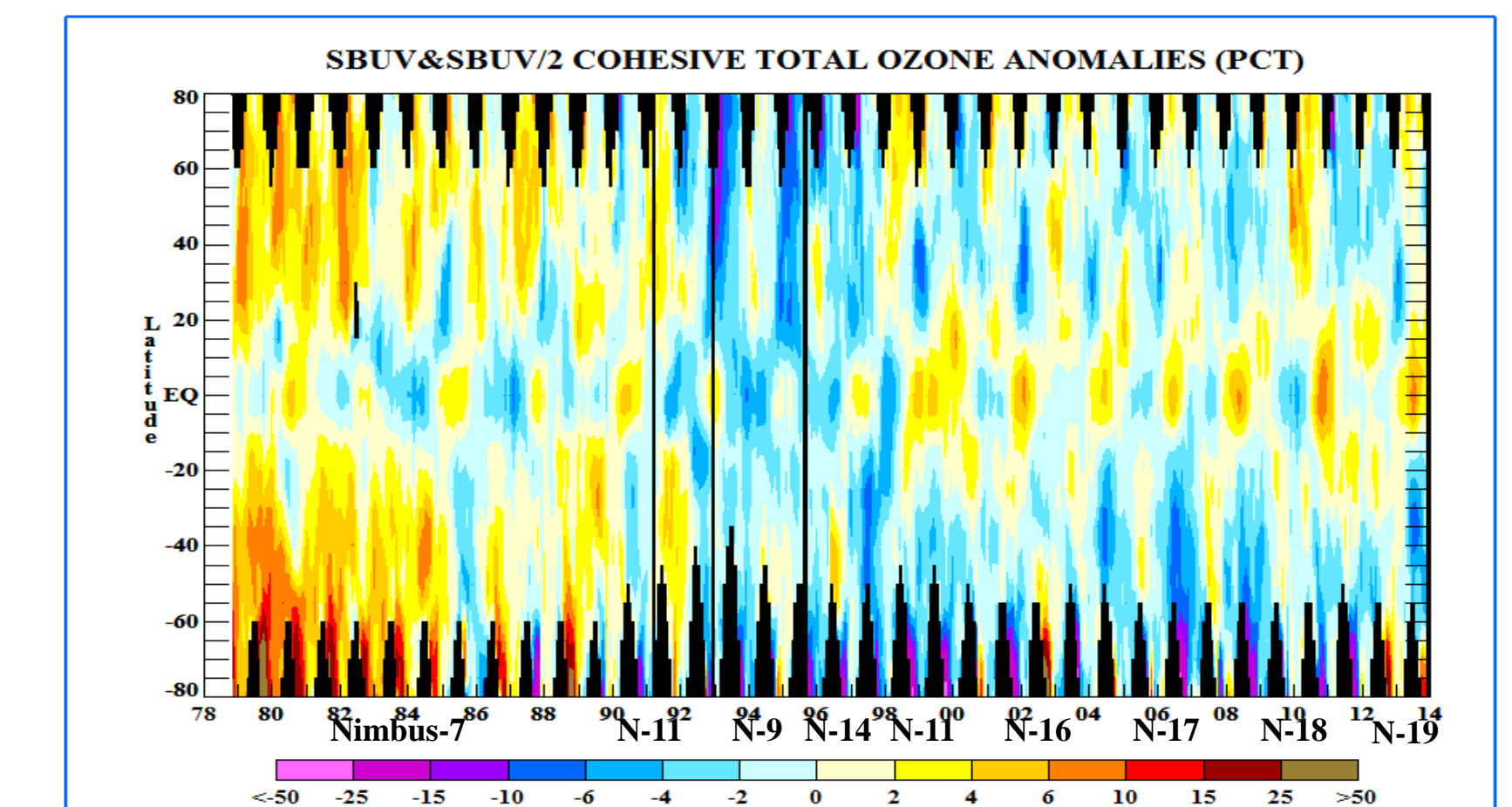
Long Term Monitoring Requires the Creation of a Cohesive Ozone Data Set



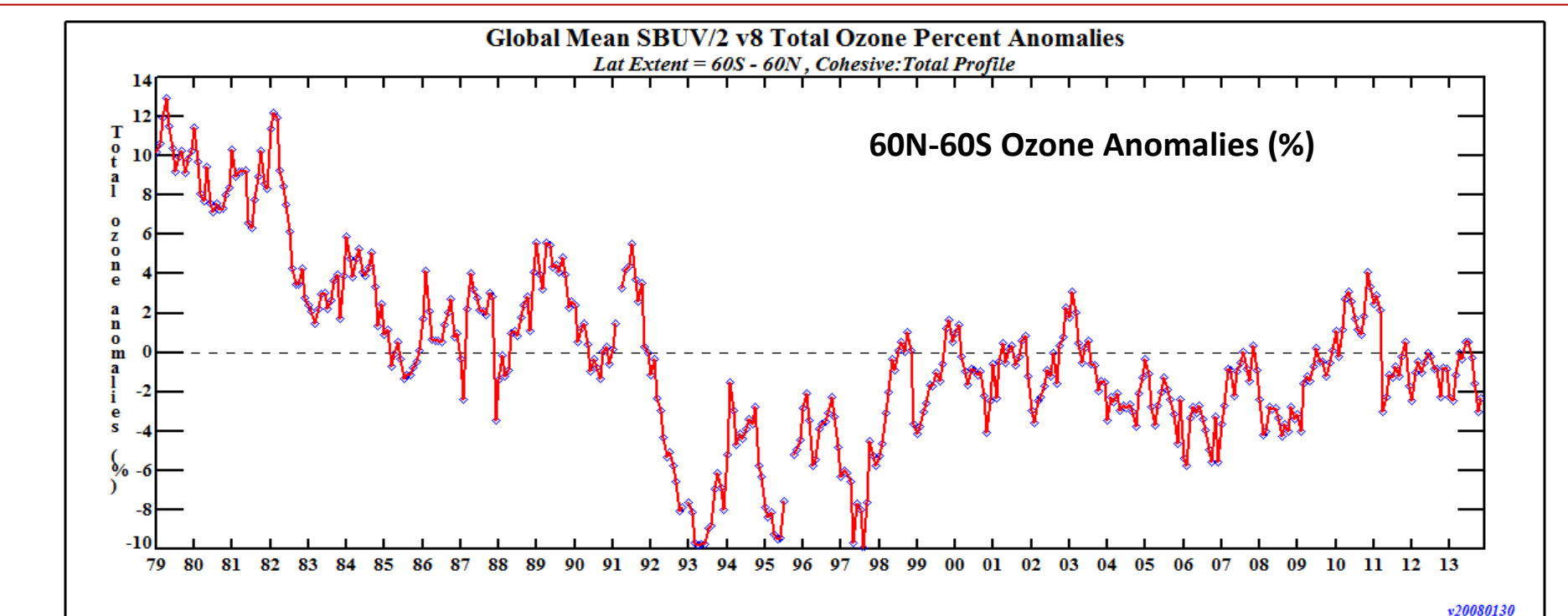
Satellite	Satellite dates
Nimbus 7	10/31/78 – 5/31/89
NOAA-11a	6/1/89 – 12/31/93
NOAA-9	1/1/94 – 2/4/95
NOAA-14	2/5/95 – 12/31/98
NOAA-11d	1/1/99 – 12/31/00
NOAA-16	1/1/01 – 12/31/02
NOAA-17	1/1/03 – 12/31/08
NOAA-18	1/1/09 – 12/31/10
NOAA-19	1/1/11 – 12/31/12

9 SBUV (/2) data sets (one for each satellite) are bias adjusted and trend adjusted to create a long term cohesive total and profile ozone data set to be used for climate and trend detection.

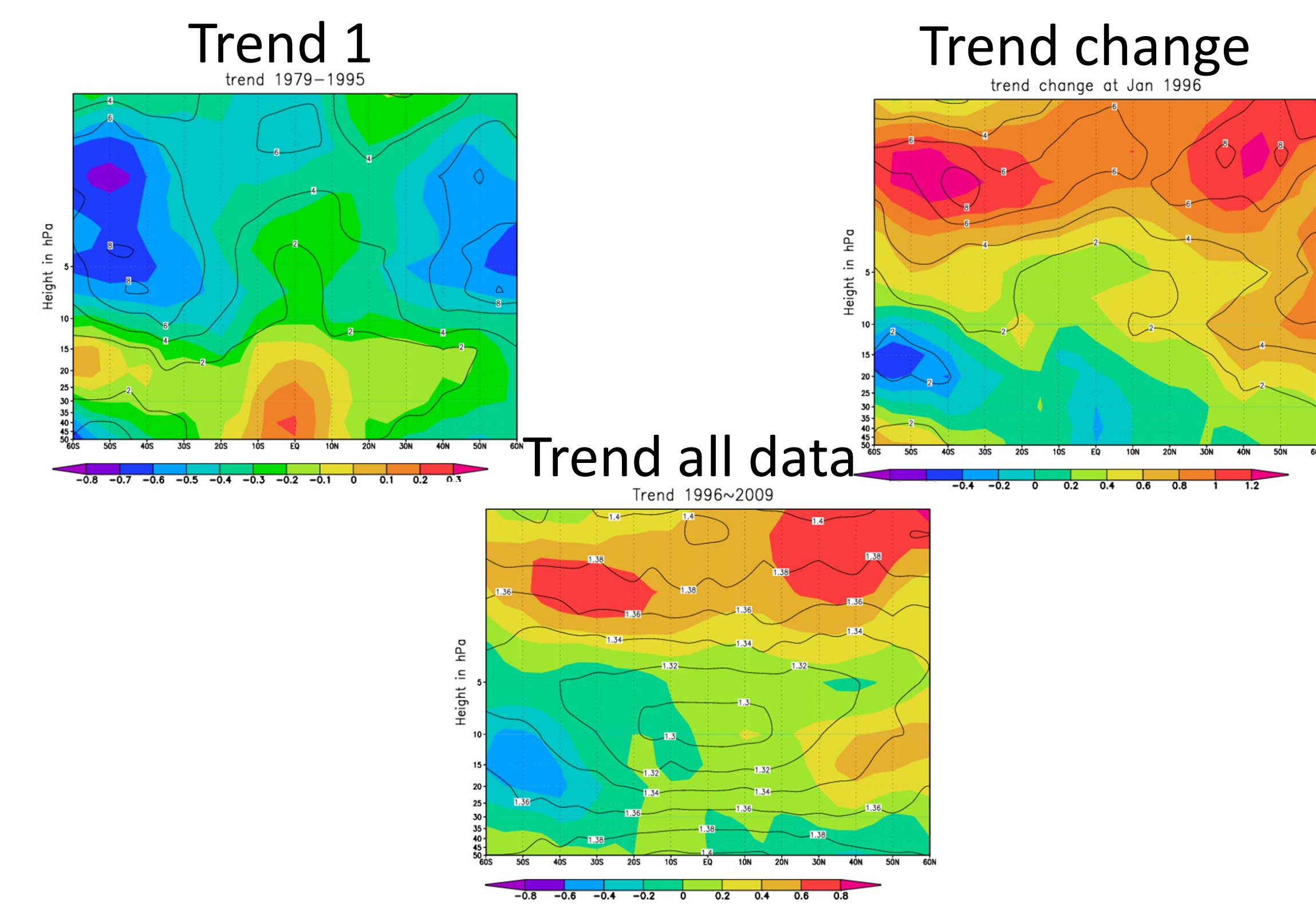
Inter-Annual Variability of Total Column Ozone



Long Term Monitoring of Total Column Ozone for Trend Detection



Using Regression Analysis to Determine Trends



A regression which removes the AO, AAO, QBO, and Solar cycles is used with the "hockey stick" model to determine the trend from 1979-1996, the trend change, and the linear trend from 1979-2009.

Suomi NPP/JPSS Cross-track Infrared Sounder (CrIS): Calibration Validation With The Aircraft Based Scanning High-resolution Interferometer Sounder (S-HIS)

Joe K. Taylor¹, D. C. Tobin¹, H.E. Revercomb¹, F.A. Best¹, R. K. Garcia¹, H. Motteler², and M. Goldberg³
 1. Space Science and Engineering Center, University of Wisconsin-Madison, 1225 West Dayton St., Madison, WI, 53706
 2. University of Maryland Baltimore County, Baltimore, Maryland, USA
 3. Joint Polar Satellite Systems Office, National Oceanic and Atmospheric Administration, Lanham, Maryland, USA

Summary

Climate change detection and potential attribution analyses, as well as Numerical Weather Prediction applications, require rigorous uncertainty analyses following established metrological principles. Using satellite radiance observations, these analyses start with understanding the uncertainties associated with the spectral radiance observations and propagate these and other sources of uncertainty into climate change radiance and geophysical product analyses.



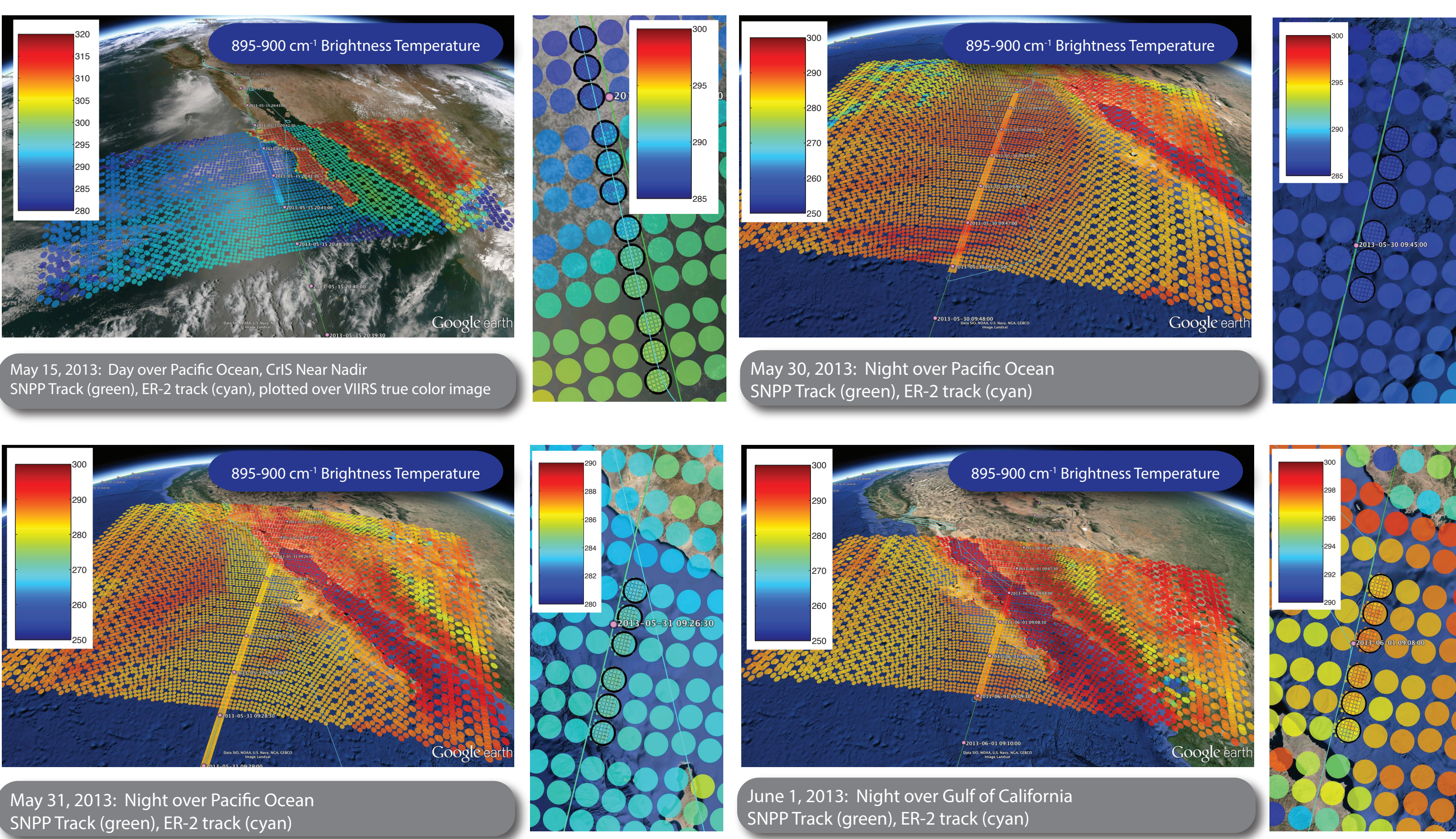
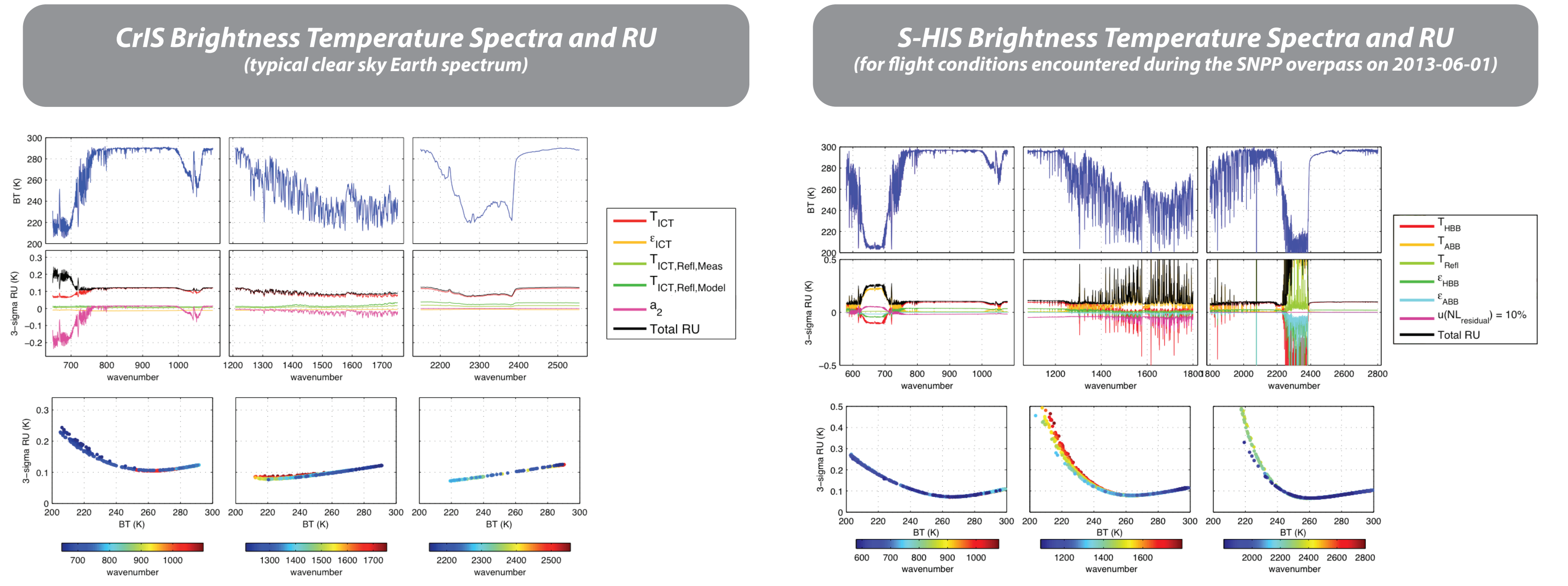
Considering the wide range of existing satellite cal/val approaches, the high accuracy of aircraft sensors, combined with the ability to perform pre- and post-campaign calibration tests to confirm the radiometric performance, make satellite underflight comparisons like those presented here uniquely capable of assessing infrared satellite observations with sufficient accuracy and traceability.

The first Suomi NPP dedicated airborne calibration validation campaign was conducted in May 2013 with a primary objective of providing detailed validation of CrIS radiance observations and meteorological products. During this calibration validation campaign, the NASA ER-2 aircraft instrument payload included the UW-SSEC Scanning-High resolution Interferometer Sounder (S-HIS), the NPOESS Atmospheric Sounder Testbed-Interferometer (NAST-I), the NPOESS Atmospheric Sounder Testbed-Microwave Spectrometer (NAST-M), the NASA MODIS/ASTER airborne simulator (MASTER), and the NASA JPL Airborne Visible / Infrared Imaging Spectrometer (AVIRIS).

Eleven ER-2 under-flights of the Suomi NPP satellite were conducted during the mission. The best conditions for radiance validation of CrIS with S-HIS were encountered for the 2013-05-15, 2013-05-30, 2013-05-31, and 2013-06-01 flights. During each of these flights, the ER-2 flew a straight and level flight leg at ~20.0 km altitude (50 mbar) along the suborbital track of Suomi NPP. This poster provides an overview of the radiometric calibration, calibration verification, and traceability of the S-HIS validation data. The S-HIS has proven to be an extremely well characterized and understood, carefully maintained, and accurately calibrated reference instrument with a well defined radiometric uncertainty and traceability path.

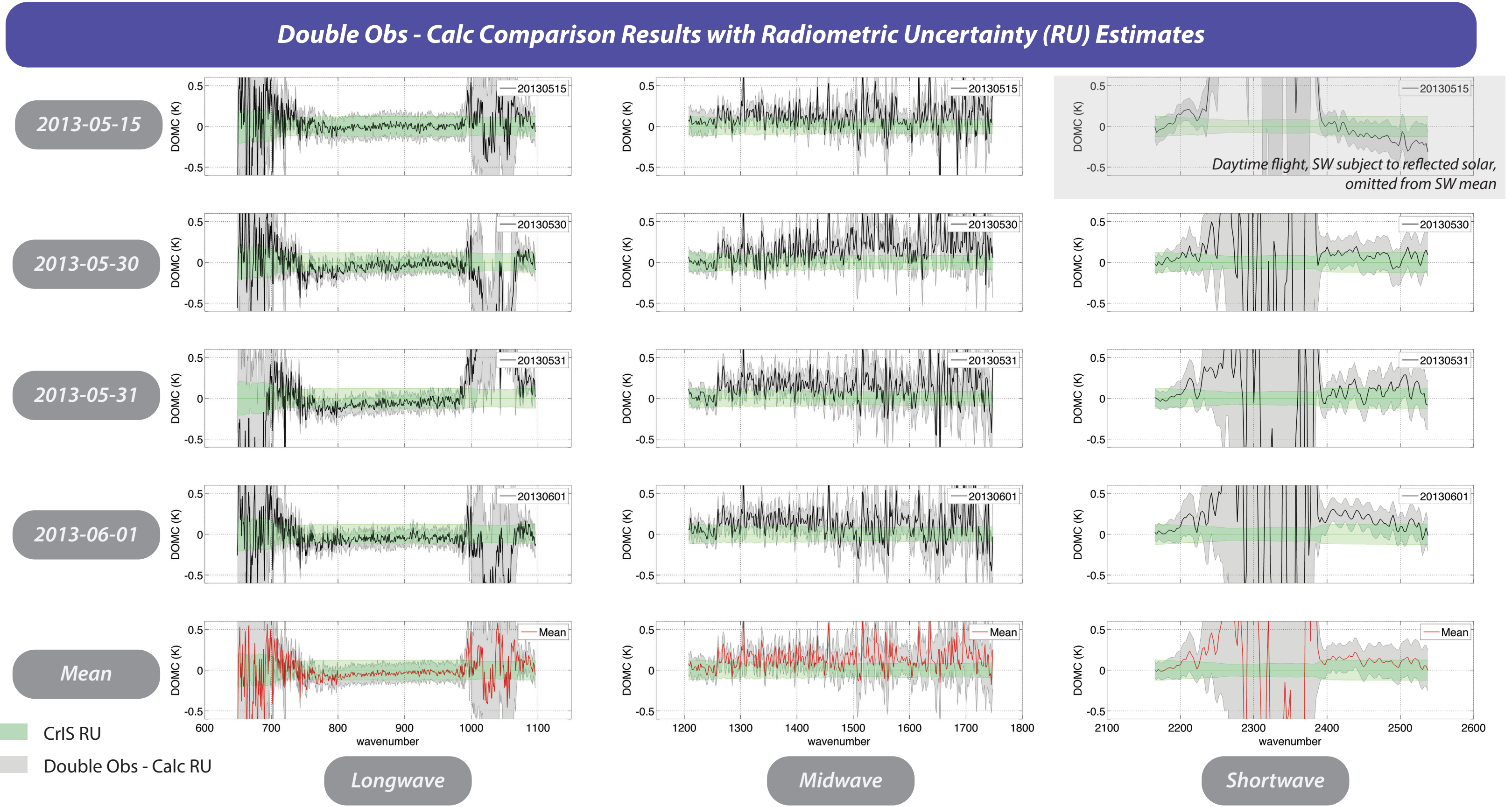
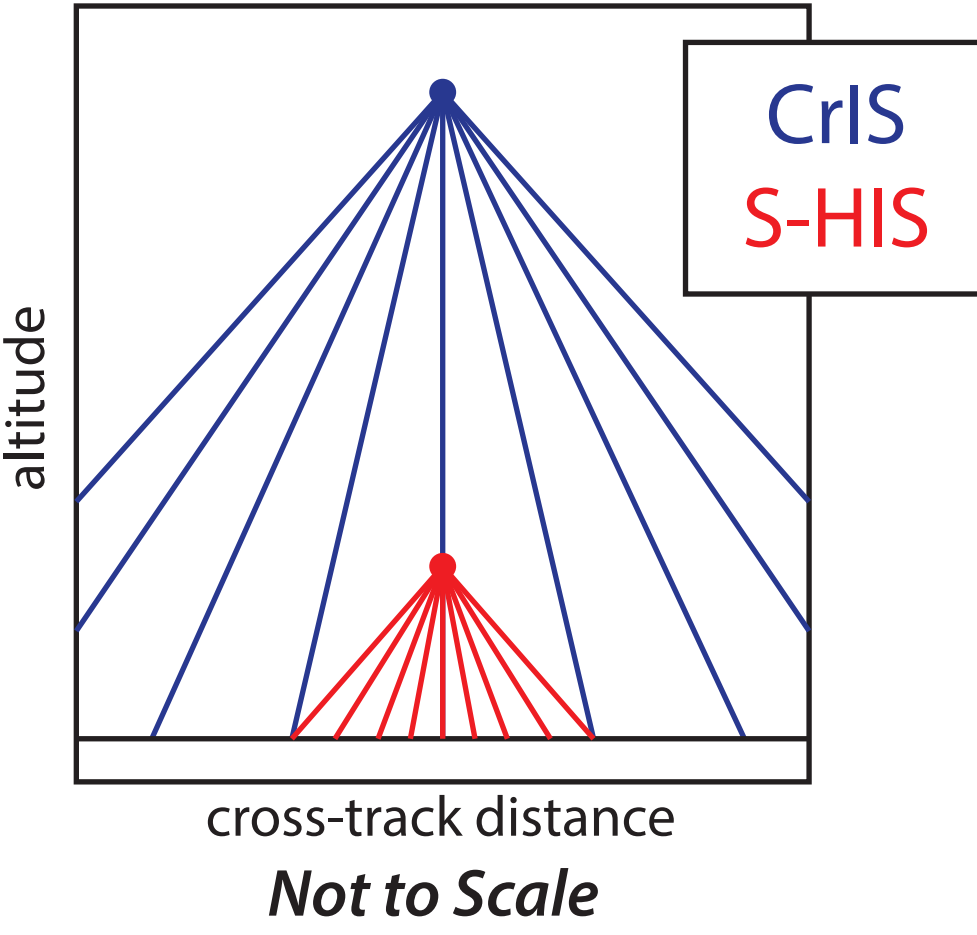
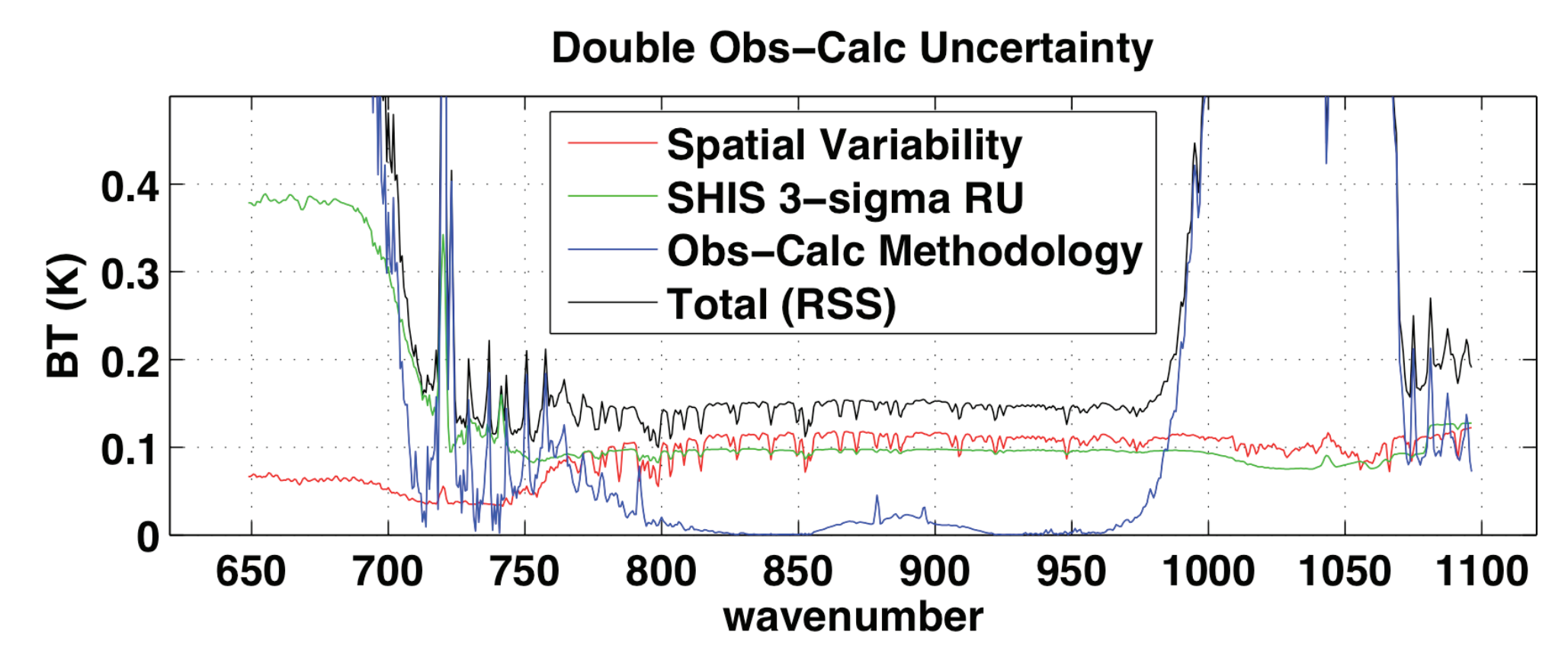
A detailed intercalibration assessment between the CrIS and S-HIS instruments for four under-flights from the 2013 SNPP airborne calibration validation campaign has been completed. The radiometric uncertainty contributions from both instruments, along with the radiometric uncertainty contribution associated with the comparison methodology are a critical component of the intercalibration and have been included in the analysis and summary result. The comparisons show excellent agreement, with residual differences less than 0.1K, and well within the combined radiometric uncertainty estimates.

Calibration Verification Results



Double Obs-Calc Comparison Methodology

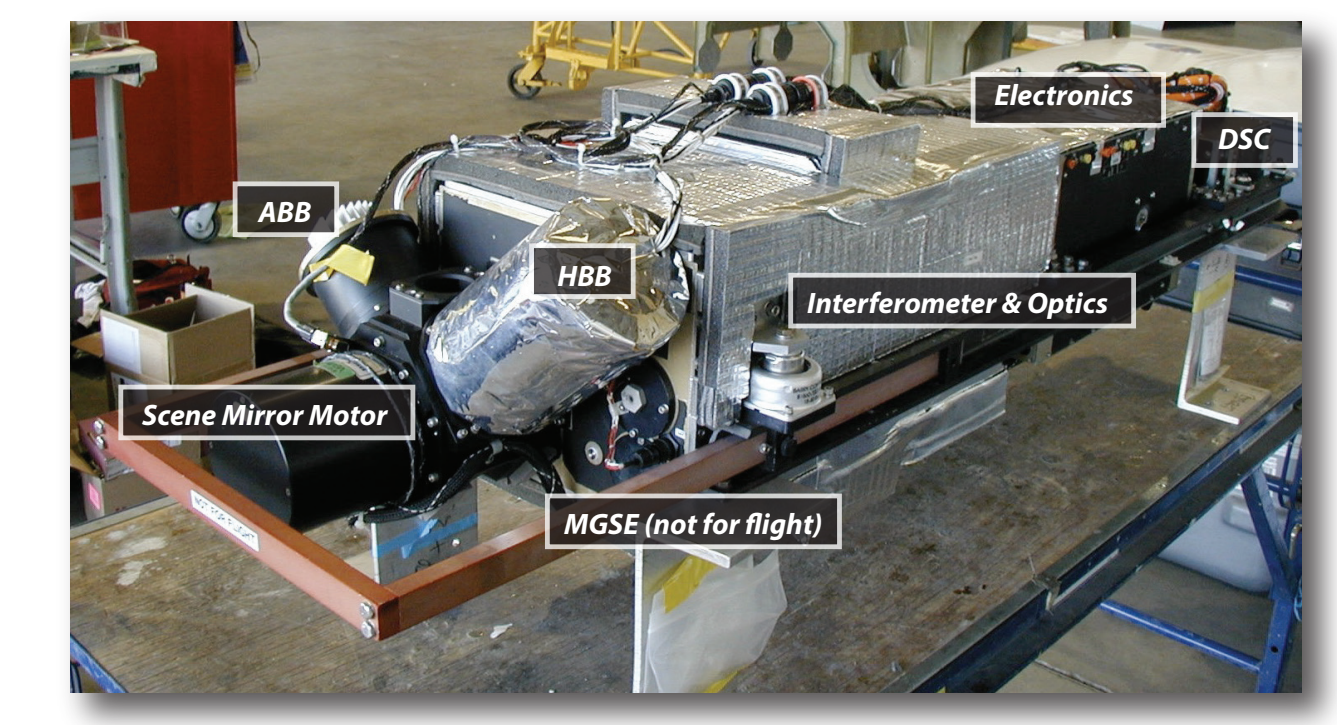
- The resulting residual difference in this method is essentially the difference between the CrIS and S-HIS respective observation minus calculation residuals, reduced to the lowest common spectral resolution for the two instruments.
- The radiance calculations for each instrument assume the same surface conditions, atmospheric state, and forward models. This results in systematic errors that are common to both sets of calculations, and to first order removes the fundamental effects of altitude and view angle differences.
- For methodology details, refer to: Tobin, David C., et al. "Radiometric and spectral validation of Atmospheric Infrared Sounder observations with the aircraft-based Scanning High-Resolution Interferometer Sounder." *Journal of geophysical research* 111.D9 (2006): D09S02.



S-HIS

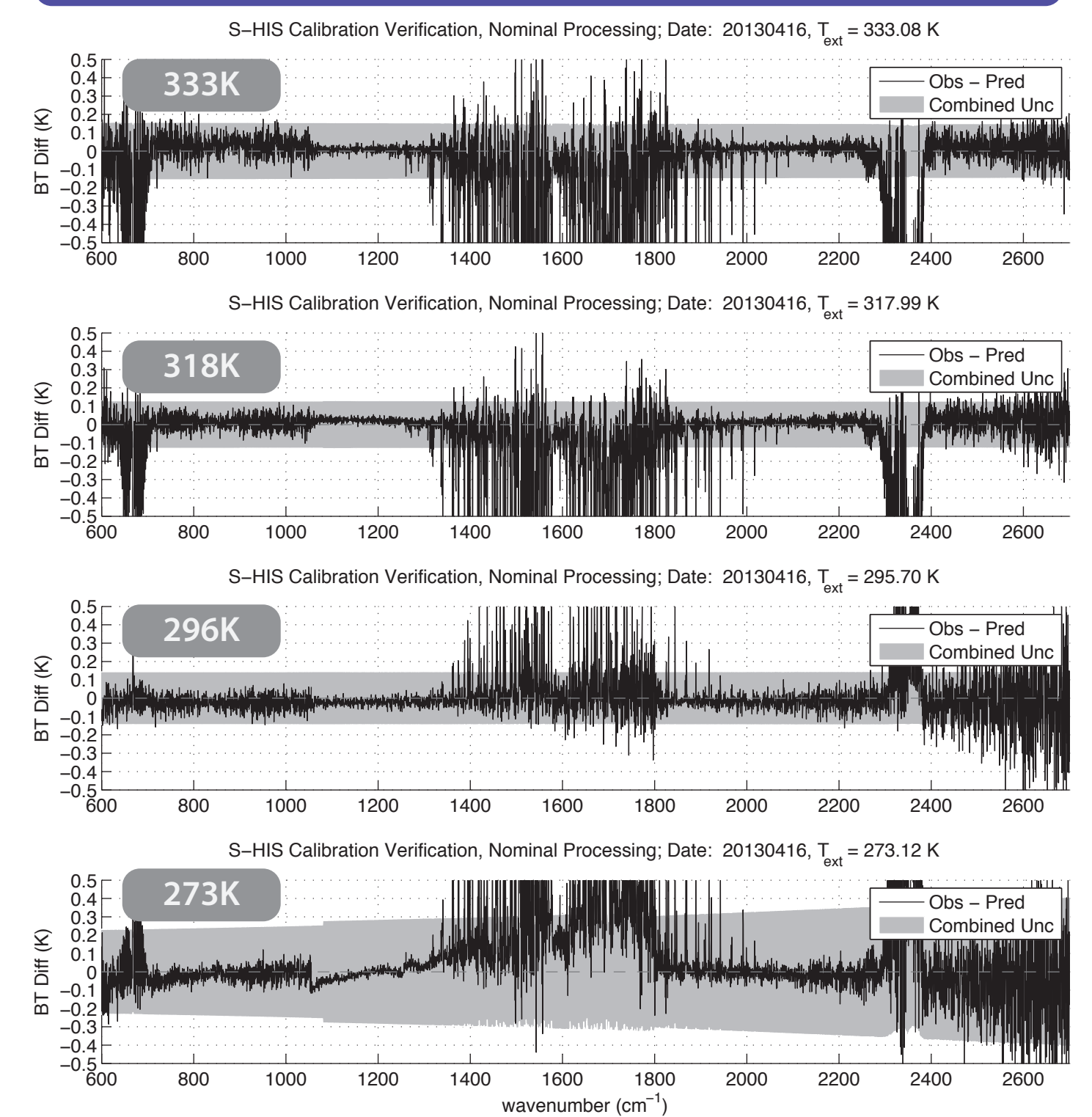
Calibration, Calibration Verification, and Traceability

- Pre-integration calibration of on-board blackbody references at subsystem level
- Pre and post deployment end-to-end calibration verification
- Instrument calibration during flight using two on-board calibration blackbodies
- Periodic end-to-end radiance evaluations under flight like conditions with NIST transfer sensors.

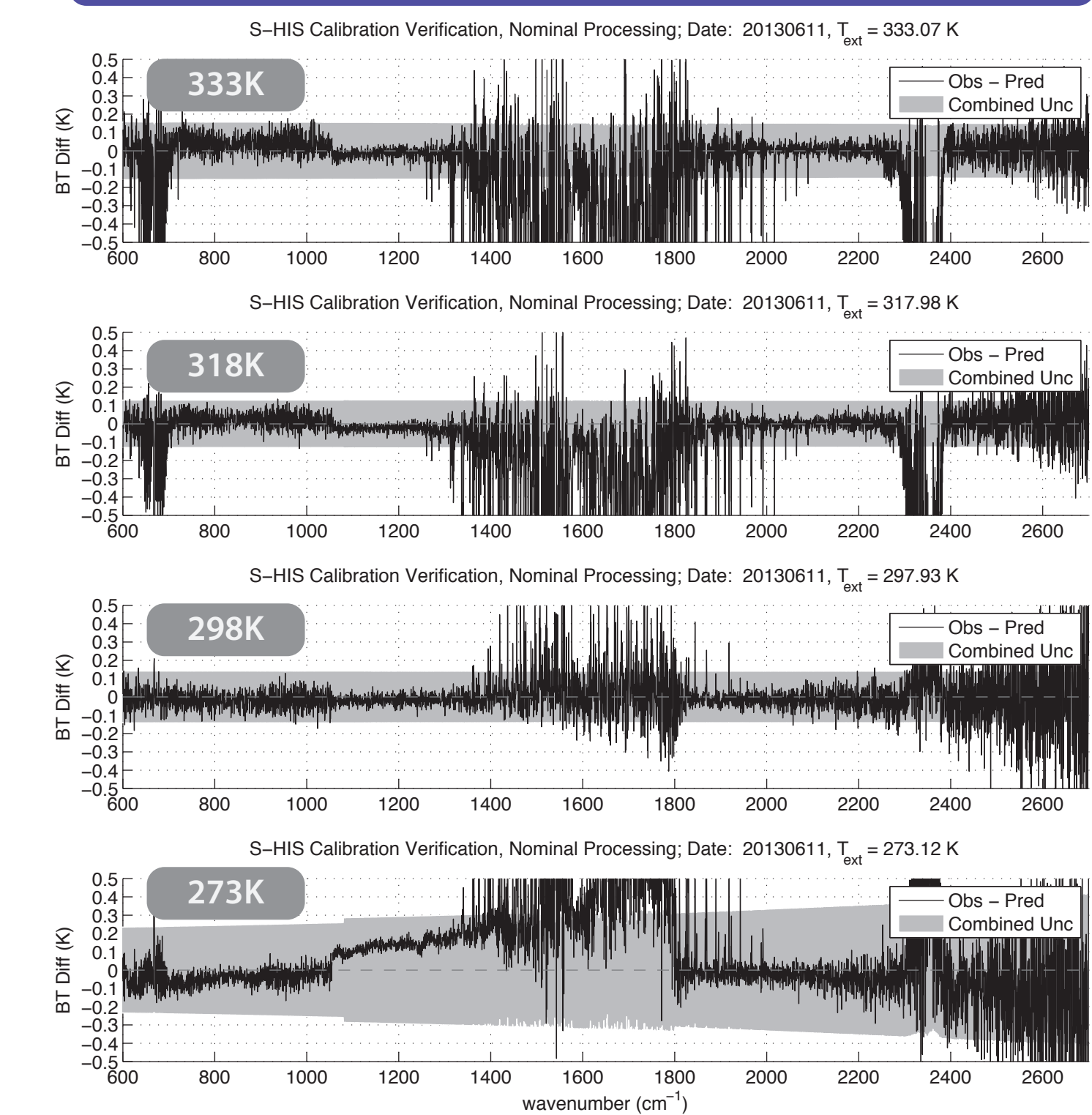


IFOV: 100 mrad (2km @ 20km, nadir)
 FOR: Programmable 45° scene mirror nadir ± 40° typical
 Spectral Coverage: 580 - 3000 cm⁻¹
 Spectral Resolution: 0.5 cm⁻¹

Pre-deployment End-to-end Cal Verification

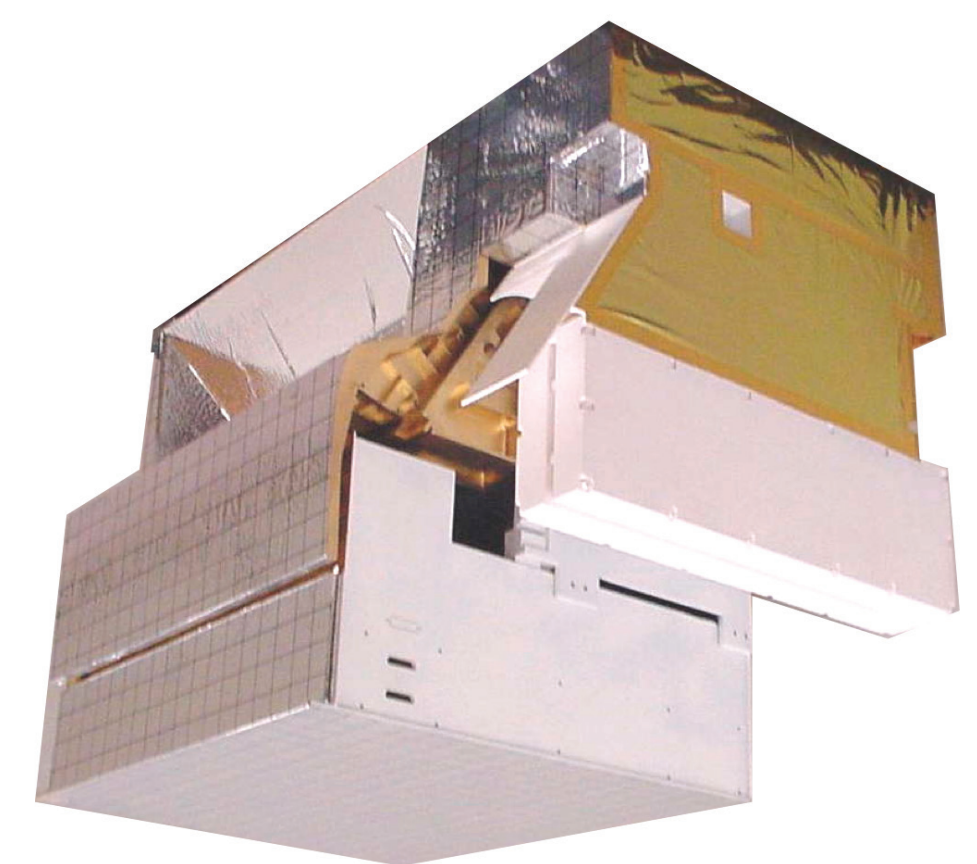


Post-deployment End-to-end Cal Verification



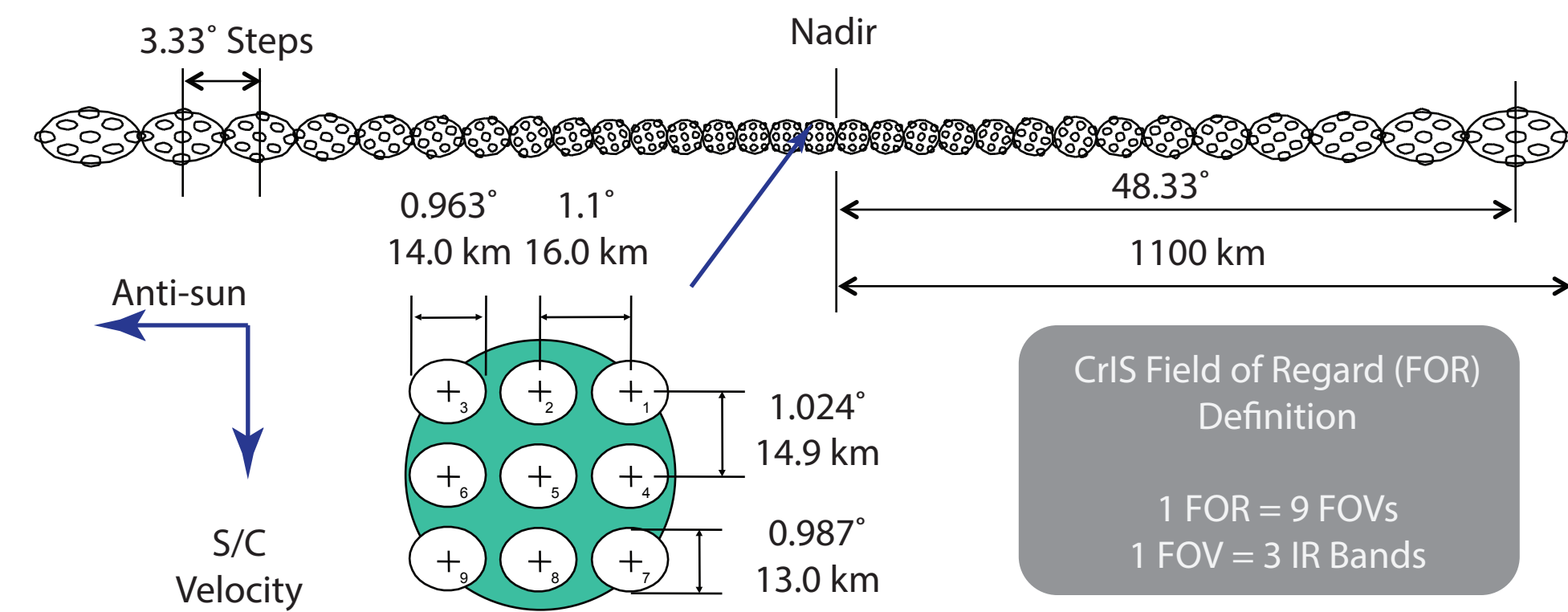
CrIS

- Infrared Fourier transform spectrometer with 1305 spectral channels; produces high-resolution, three-dimensional temperature, pressure, and moisture profiles. Designed to give scientists more refined information about Earth's atmosphere and improve weather forecasts and our understanding of climate.



- #### CrIS Sensor Features
- 8 cm clear aperture
 - 3 spectral bands
 - 3x3 FOVs, 14 km diameter at nadir
 - PV MCT detectors
 - 4-stage passive cooler
 - Plane mirror interferometer with DA
 - Internal spectral calibration
 - Deep-cavity calibration target

Single CrIS Scan Line (full sweep, 30 FORs)



CrIS Field of Regard (FOR) Definition
 1 FOR = 9 FOVs
 1 FOV = 3 IR Bands



The tool for the VIIRS LST Product monitoring and validation

Peng Yu¹, Yunyue Yu², Yuling Liu¹, and Zhuo Wang¹

¹ESSIC/CICS, UMD, College Park, MD ²STAR/NESDIS, NOAA, College Park, MD



Introduction

As one of the key products of VIIRS, land surface temperature (LST) is of fundamental importance to the net radiation budget at the Earth surface and to monitoring the state of crops and vegetation, as well as an important indicator of both the greenhouse effect and the energy flux between the atmosphere and the land. To better monitor the performance of the VIIRS LST product and evaluate different retrieval algorithms for potential algorithm improvement, a monitoring system has been developed and implemented for both the routine monitoring and the basic research.

It consists of two main components, the global cross-satellite comparison system and the one validating VIIRS LST against certain ground sites' LST observations. The third component for cross-satellite comparison at the granule level will be included in the near future. The global component generates daily global LST maps for both daytime and nighttime from VIIRS and MODIS-AQUA. Besides the satellite LST, additional variables such as the brightness temperature and the sensor zenith angle, etc. are included in the daily composite dataset, allowing not only the cross-satellite LST comparison, but also the cross-algorithm comparison. A series of subset datasets with respect to certain ground sites' locations are generated from this component. These will replace the subset data produced by LPEATE, which is currently being used by the satellite-ground validation component. The latter carries out the validation of VIIRS LST with observations from SURFRAD ground stations. It evaluates the satellite retrieval performance against the ground "truth" for the past week, the past month, and the past year. Warning messages will be generated and sent to the LST group if any of the prescribed criteria is met. A data table consisting of around 30 variables is generated with respect to each ground site. The data table is used to evaluate different retrieval algorithms and analyze the retrieval under different situations.

The monitoring system is automatically run at the background in a local Linux computer on a daily basis. The results are published via an FTP site and will be transitioned to a web site in the future. The tool currently includes two satellite sensors, VIIRS and AQUA, and will be extended to the monitoring of the LSTs from other satellites including the current GOES-13 and GOES-15 and the future GOES-R and Himawari/AHI.

Validation with ground sites

Index of /pub/smc/emb/pyu/VIIRS_monitoring/current/year/

Name	Size	Date Modified
ignat directory		
VIIRS-Bokeh_IL_2014116_yearly_coke_LPEATE.png	20.3 kB	5/14/12 12:00 AM
VIIRS-Bokeh_IL_2014116_yearly_coke_M37.png	20.2 kB	5/14/12 12:00 AM
VIIRS-Bokeh_IL_2014116_yearly_coke_M38.png	20.3 kB	5/14/12 12:00 AM
VIIRS-Bokeh_IL_2014116_yearly_diff_sensities.png	29.6 kB	5/14/12 12:00 AM
VIIRS-Bokeh_IL_2014116_yearly_LPEATE.png	21.0 kB	5/14/12 12:00 AM
VIIRS-Bokeh_IL_2014116_yearly_M37.png	21.0 kB	5/14/12 12:00 AM
VIIRS-Bokeh_IL_2014116_yearly_M38.png	21.1 kB	5/14/12 12:00 AM
VIIRS-Bokeh_IL_2014116_yearly_sensities.png	32.3 kB	5/14/12 12:00 AM
VIIRS-Bokeh_CO_2014116_yearly_coke_LPEATE.png	20.7 kB	5/14/12 16:00 AM
VIIRS-Bokeh_CO_2014116_yearly_coke_M37.png	20.7 kB	5/14/12 16:00 AM
VIIRS-Bokeh_CO_2014116_yearly_coke_M38.png	20.7 kB	5/14/12 16:00 AM
VIIRS-Bokeh_CO_2014116_yearly_diff_sensities.png	36.8 kB	5/14/12 16:00 AM
VIIRS-Bokeh_CO_2014116_yearly_LPEATE.png	21.0 kB	5/14/12 16:00 AM
VIIRS-Bokeh_CO_2014116_yearly_M37.png	21.1 kB	5/14/12 16:00 AM
VIIRS-Bokeh_CO_2014116_yearly_M38.png	21.1 kB	5/14/12 16:00 AM
VIIRS-Bokeh_CO_2014116_yearly_sensities.png	36.8 kB	5/14/12 16:00 AM
VIIRS-Desert_Rock_NV_2014116_yearly_LPEATE.png	20.0 kB	5/14/12 12:00 AM
VIIRS-Desert_Rock_NV_2014116_yearly_coke_M37.png	20.0 kB	5/14/12 12:00 AM
VIIRS-Desert_Rock_NV_2014116_yearly_coke_M38.png	20.0 kB	5/14/12 12:00 AM
VIIRS-Desert_Rock_NV_2014116_yearly_diff_sensities.png	26.2 kB	5/14/12 12:00 AM
VIIRS-Desert_Rock_NV_2014116_yearly_LPEATE.png	20.4 kB	5/14/12 12:00 AM

Flowchart of the site validation tool.

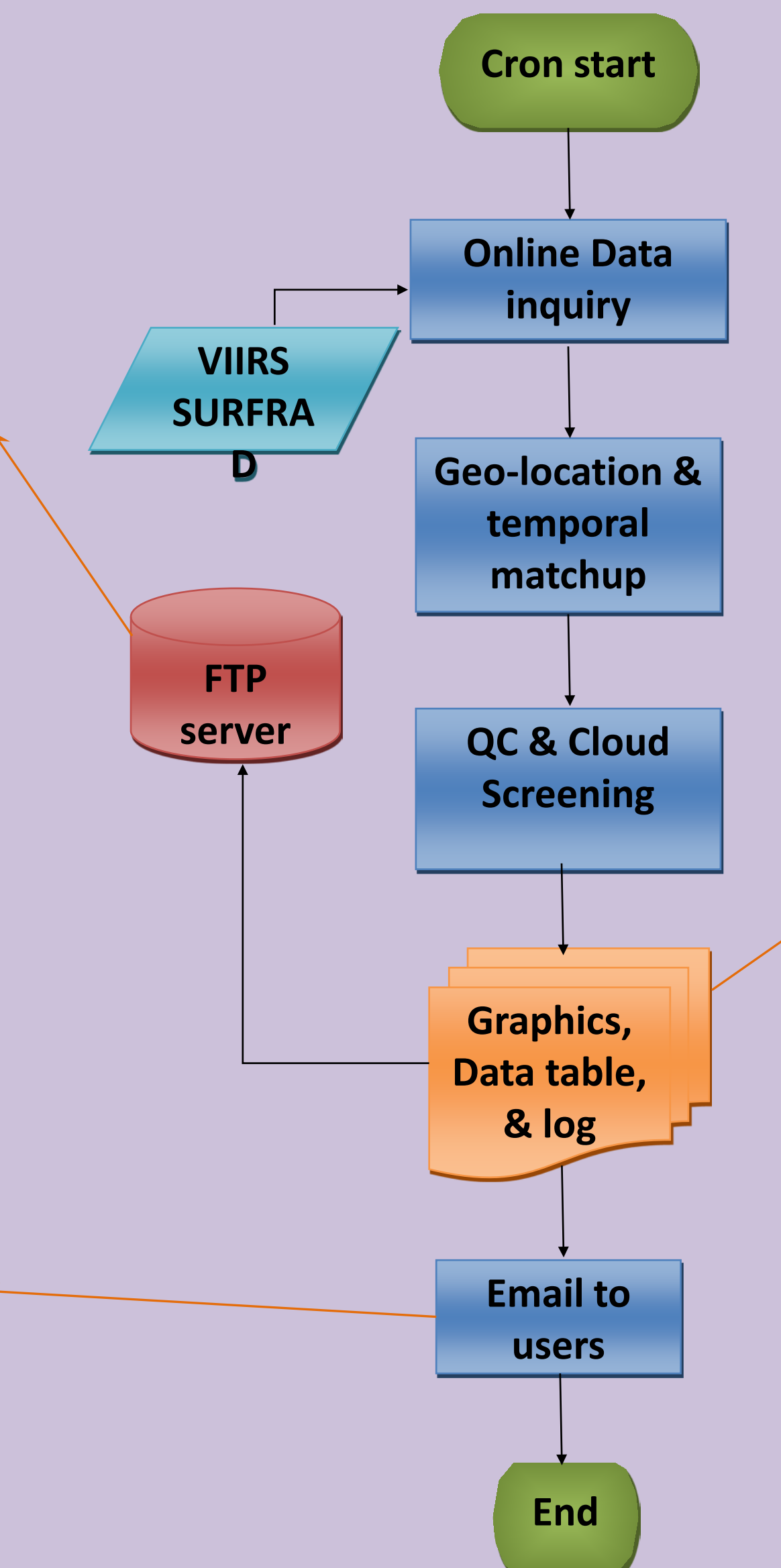


Fig. 1 Validation results are published via FTP server.

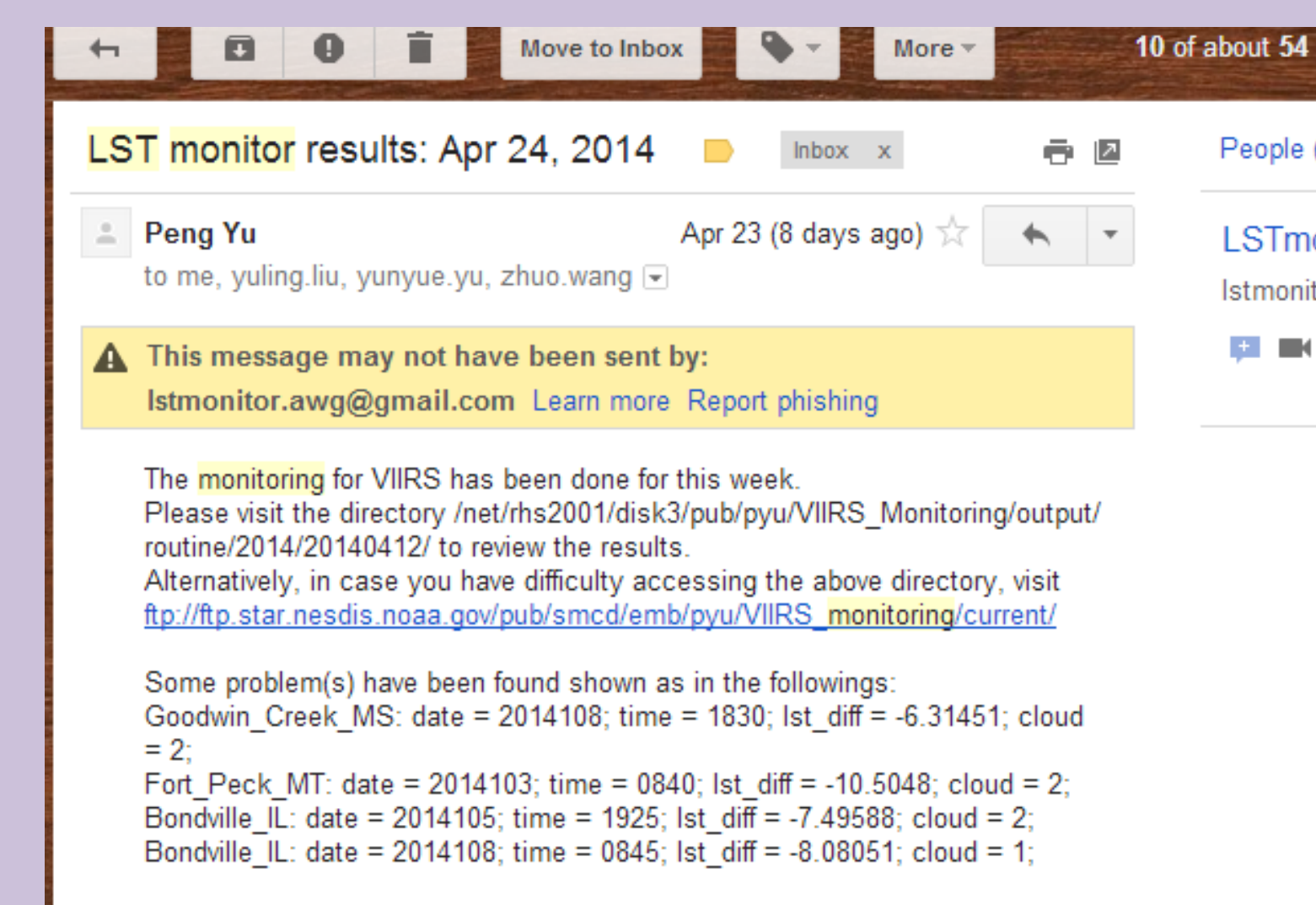


Figure 2. A message with summary and/or warning will be sent to the users once the validation is done.

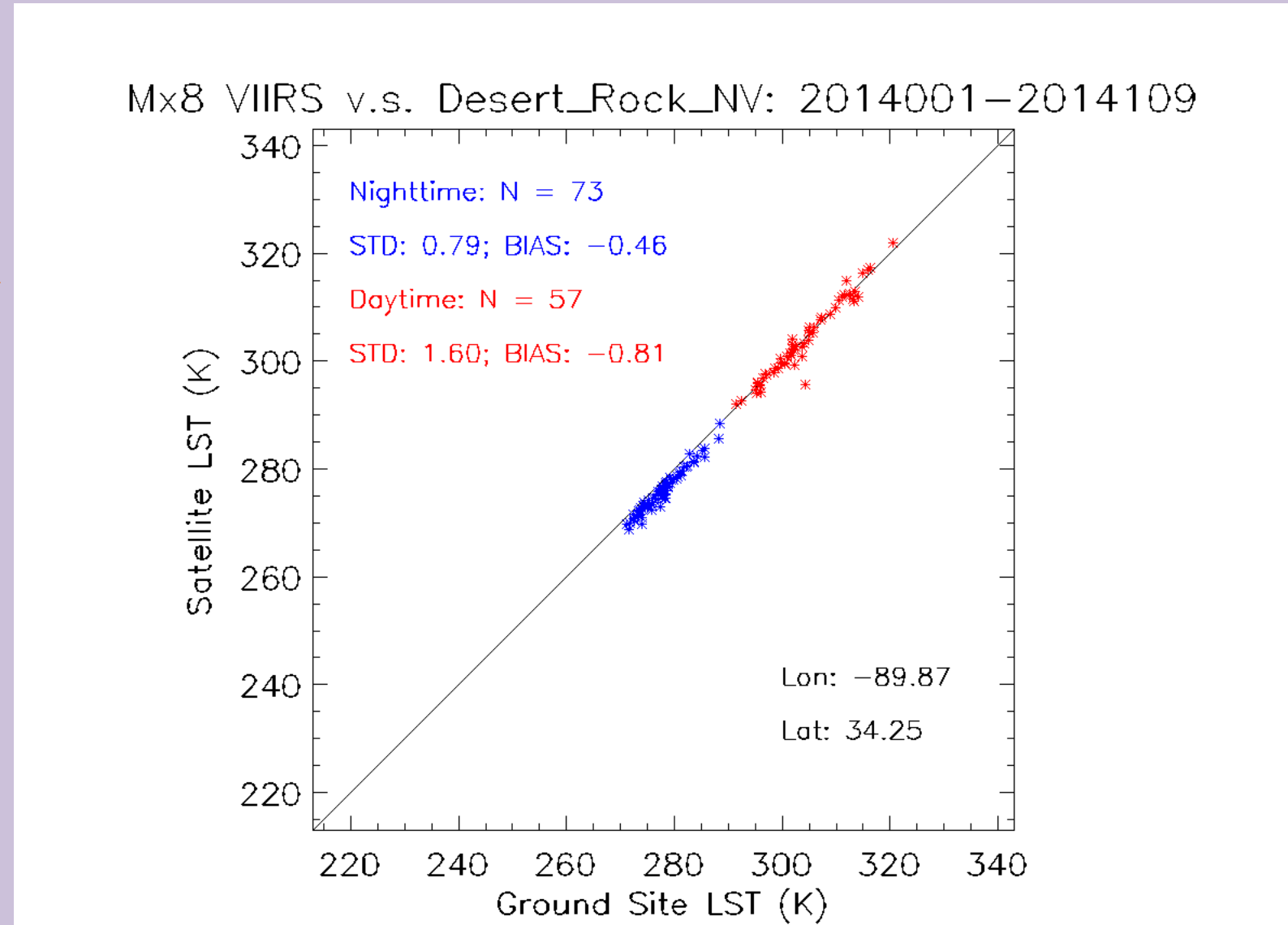
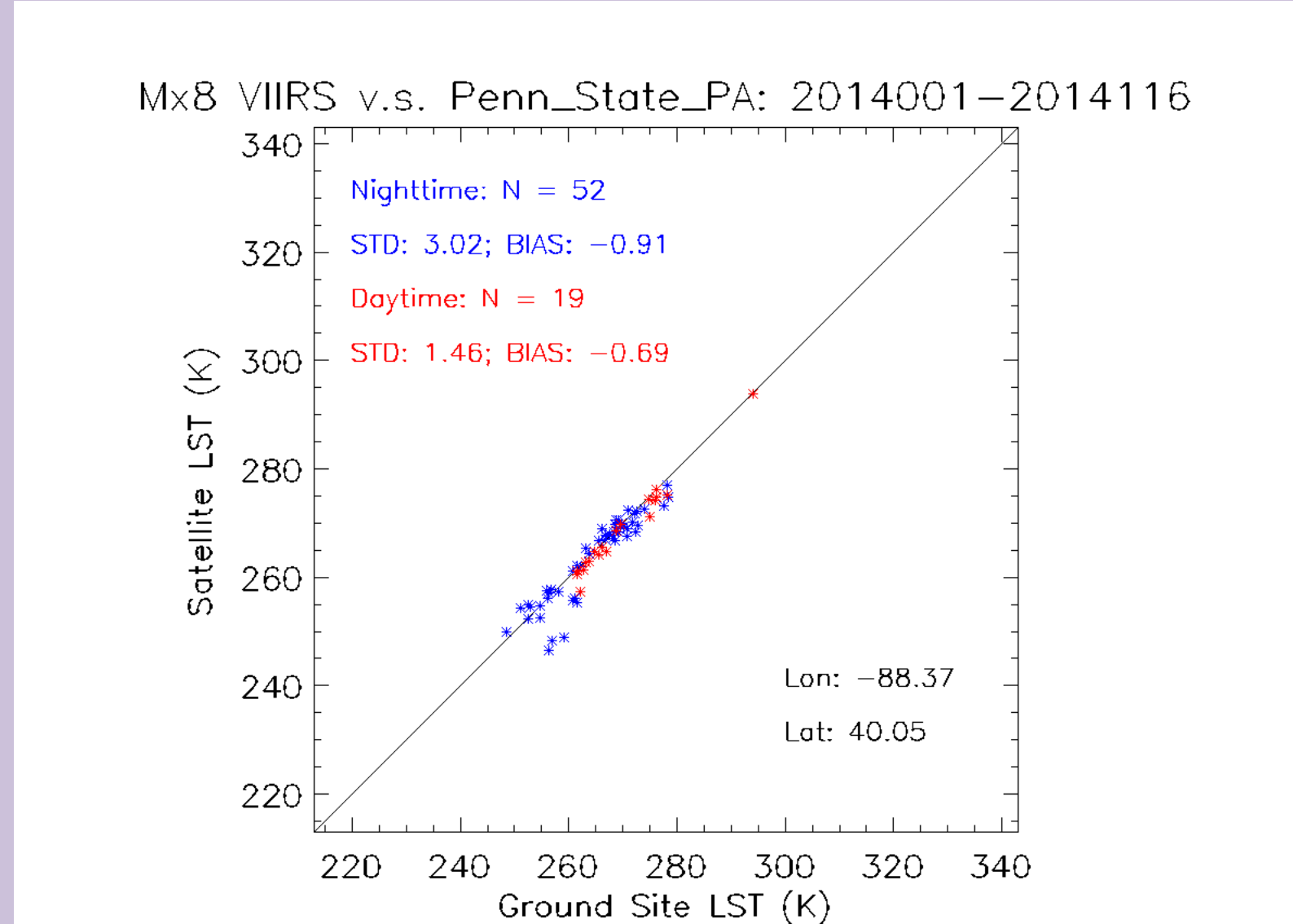
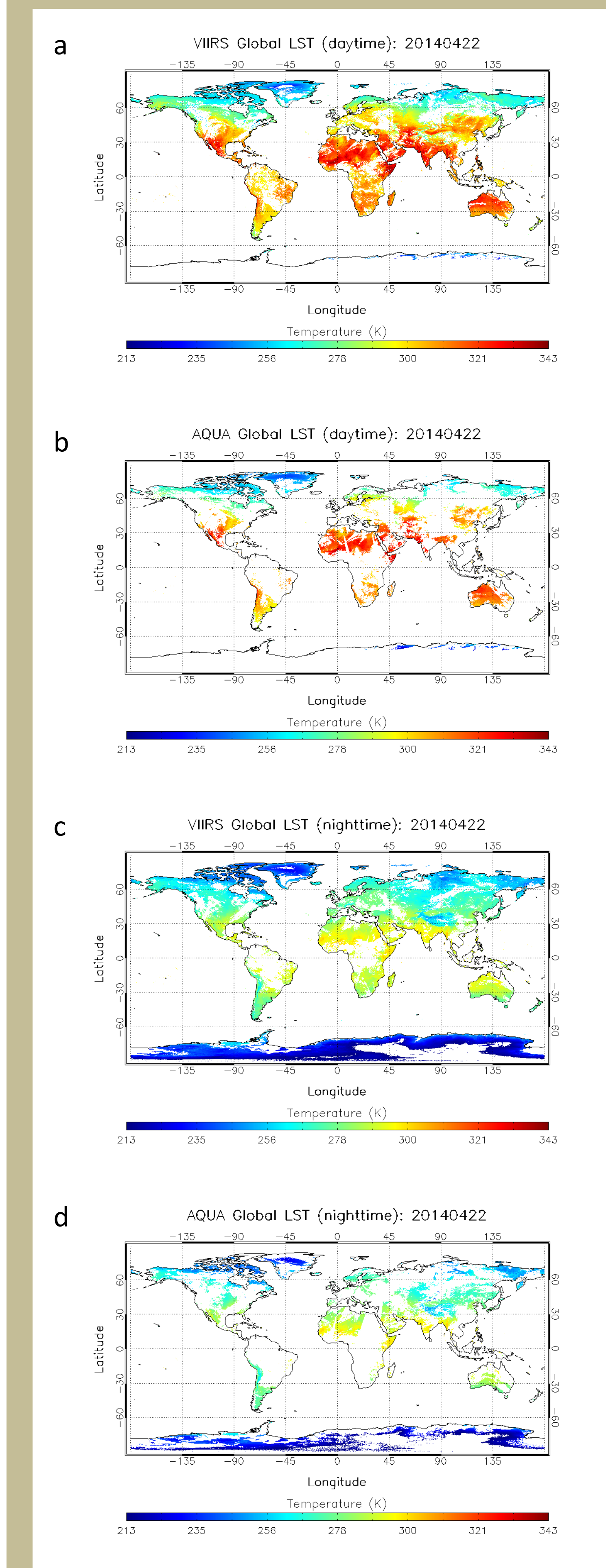


Figure 3. VIIRS LST and LST calculated with other algorithm are validated with SURFRAD sites' observations.

Global cross-satellite comparison

Daily data from SNPP-VIIRS and MODIS-AQUA are collected. Two global datasets based on different compositing procedure are generated for daytime/night and VIIRS/AQUA, allowing the cross-satellite comparison of the LST products. For dataset 1, satellite LST as well as data required for retrieval with other algorithm are stored. Different retrieval algorithms for VIIRS are tested for potential algorithm improvement.

Global LST maps for VIIRS and AQUA



Other variables of the global dataset

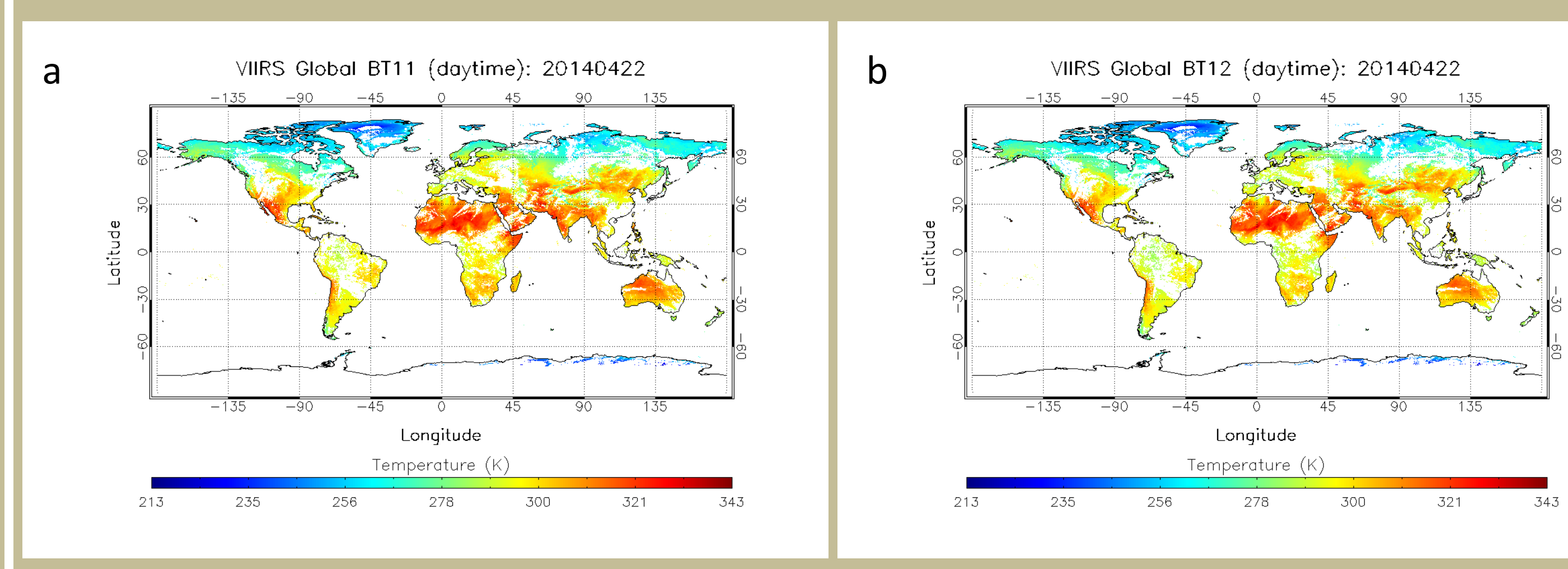


Figure 5. Different variables required for common LST retrieval algorithms are stored for evaluation of the performance of different algorithm. Variables included are bright temperature at the two split window bands, multi-channel emissivity, surface types, product quality flags, satellite view angle, solar zenith angle, and observation time.

A case study: the LST difference between VIIRS and AQUA

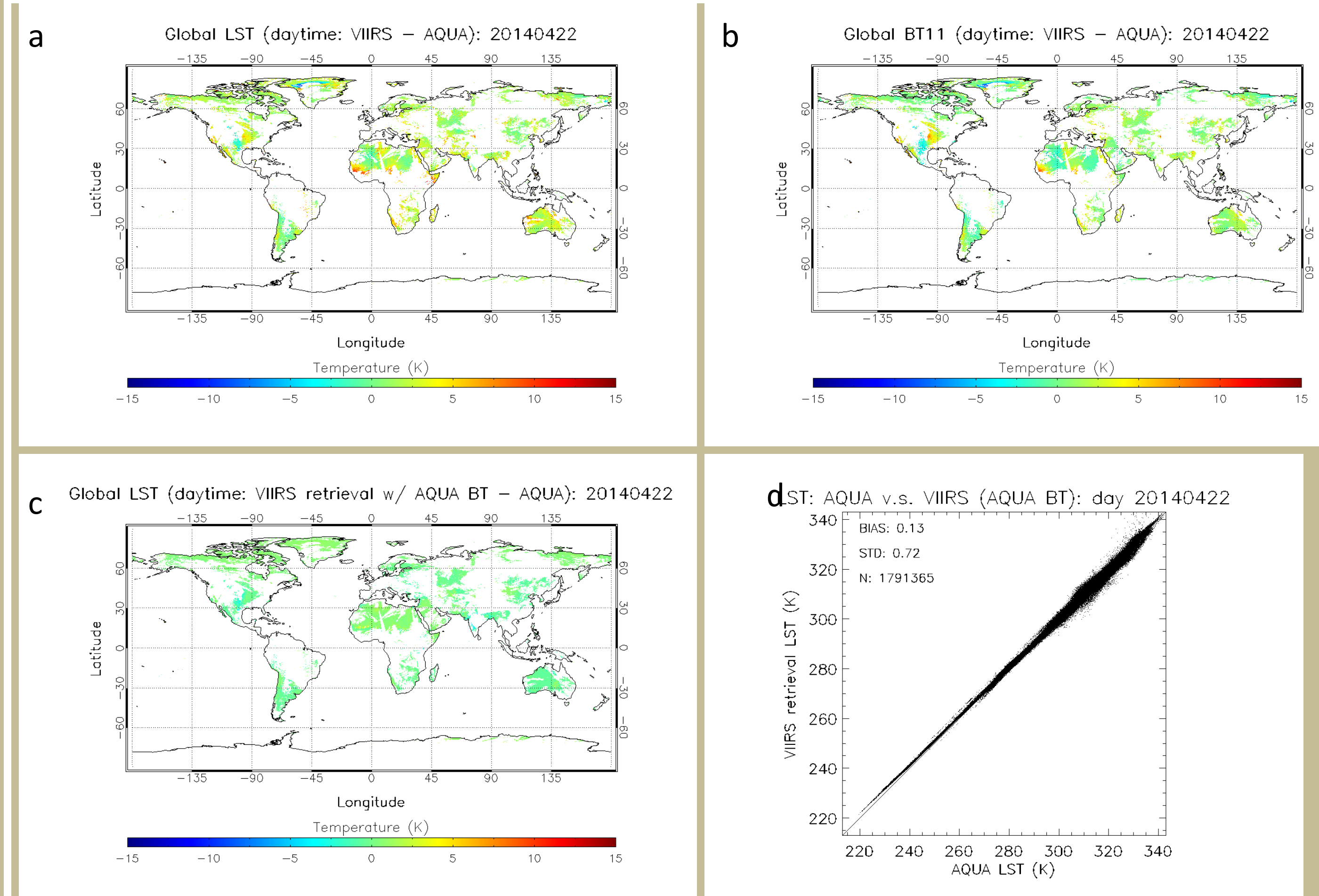


Figure 6. a) The LST difference between VIIRS and AQUA is shown. The difference can be as large as 10K in some areas. b) The BT (11 micron meter) difference between the two satellites is consistent with the LST difference. c) LST is calculated with MODIS BT data and VIIRS algorithm, its difference with AQUA LST is much smaller than that shown in a. This indicates the algorithm difference is not the main reason for the large LST difference. d) The scatter plot of the LST shown in c. Possible cause of the large LST difference: observation time, satellite view angle, which will be further studied.

Summary and future work

The routine satellite LST monitoring tool has been developed and implemented. Part of its functionalities has been automated for the goal of routine validation. The tool has been also utilized as a basic research tool to solve problems in the algorithm improvement and product validation.

The monitoring tool is still in development and testing mode. The global cross-satellite comparison component will be automated and the component to compare LST from different satellite LSTs at granule level is being developed. Further testing of the tool with different case studies will be needed. After the developmental phase, it will be also extended to other satellites such as GOES-R, etc.

Provisional Maturity

Yuling Liu¹, Yunyue Yu², Zhuo Wang¹, Peng Yu¹

¹CICS, University of Maryland, College Park; ²STAR/NESDIS/NOAA

Introduction

VIIRS LST EDR, the measurement of the skin temperature over global land coverage including coastal and inland-water, is derived utilizing the split-window technique. The regression based algorithm coefficients are surface type dependent, referring 17 International Geosphere-Biosphere Programme (IGBP) types. Since January 19th, 2012, VIIRS LST data has been generated at pixel level with 750m moderate spatial resolution at nadir.

VIIRS LST maturity has transitioned from beta to provisional status and the LST data calculated with the updated LUT is available in NOAA's Comprehensive Large Array-data Stewardship System (CLASS) archive since April 07, 2014. A lot of efforts have been devoted to the validation of the beta version LST and this study presents an evaluation of the provisional LST and addresses some issues in the algorithm development. The evaluation is mainly carried out using the conventional temperature-based approach by comparisons between the VIIRS LSTs and in-situ LSTs, and cross satellite comparison with MODIS LST.

The evaluation results suggest that the VIIRS LST EDR meets the provisional maturity criteria but the performance varies over surface types and day/night conditions. VIIRS LST agrees well with ground LST measurements and achieves comparable accuracy with MODIS LST over SURFRAD sites. Improvements are needed over open shrub land, snow/ice, barren surface and cropland surface. The cross satellite comparisons are mostly over Simultaneous Nadir Overpasses (SNO) between VIIRS and Aqua and the results show an overall close agreement between VIIRS and MODIS LST. However, we do observe some discrepancies between VIIRS LST and MODIS LST under some specific conditions, e.g., over Australia under circumstances of significant brightness temperature (BT) difference between the two split window channels, which is not observed in the ground evaluations. Although the BT difference correction has been applied to provisional LST and the impact of high BT difference on LST retrieval has been reduced compared to beta LST, VIIRS LST is degraded under this special situation. The possible causes of the LST degradation include: a very wide range of BT differences (can reach 16K over Australia, under hot and humid atmospheric condition with high water vapor content, or significant emissivity difference between the two split channels); limitations of the regression method and the radiative transfer simulation database being regressed; the VIIRS LST algorithm form, i.e., quadratic term of the BT difference. Efforts are made toward the investigation of the impacts of water vapor, emissivity, and sensor view angles on the LST retrieval, which will direct our focus on the further algorithm improvement.

VIIRS LST EDR Algorithm

❖ Baseline Split window algorithm

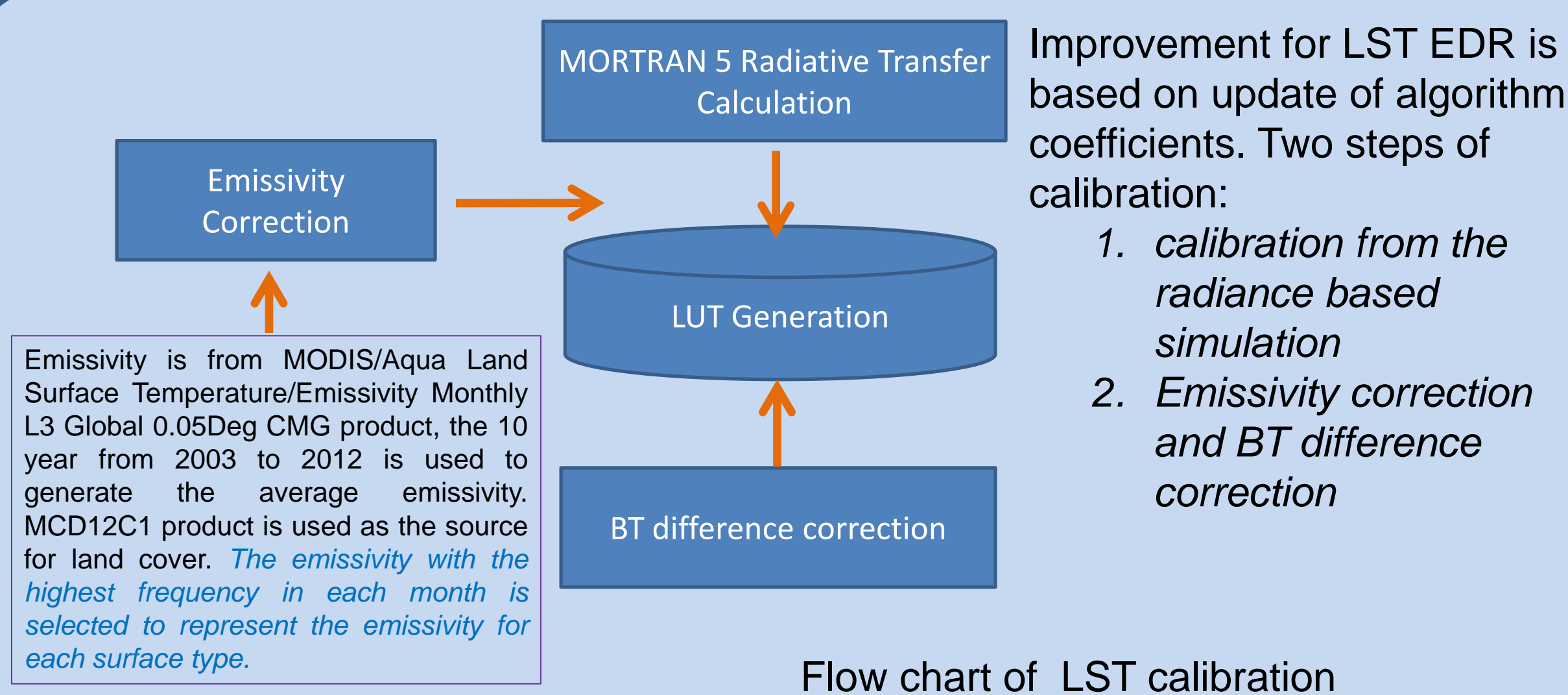
Establish the 2-band 10.76μm(M15) and 12.01μm(M16) split window algorithm for both day and night based on regression equation for each of the 17 IGBP surface types.

$$LST_{i,j} = a_0(i,j) + a_1(i,j)T_{15} + a_2(i,j)(T_{15} - T_{16}) + a_3(i,j)(\sec\theta - 1) + a_4(i,j)(T_{15} - T_{16})^2$$

Where

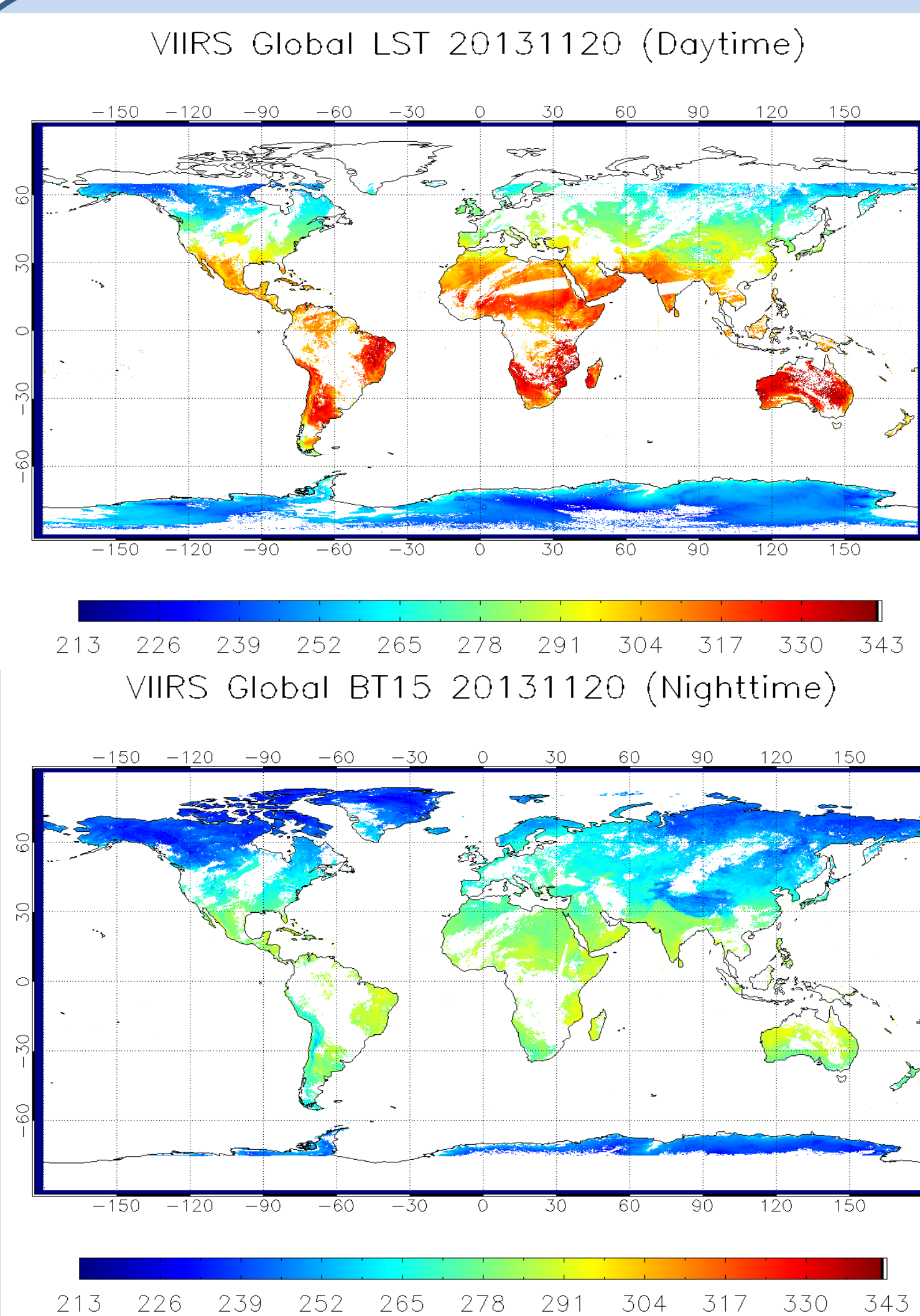
$a_k(i,j)$ (with $k=0$ to 4) depending on surface type (with $i=0$ to 16 for 17 IGBP surface types) and day/night condition (with $j=0$ to 1), are coefficients and θ is satellite viewing zenith angle.

VIIRS LST EDR Calibration



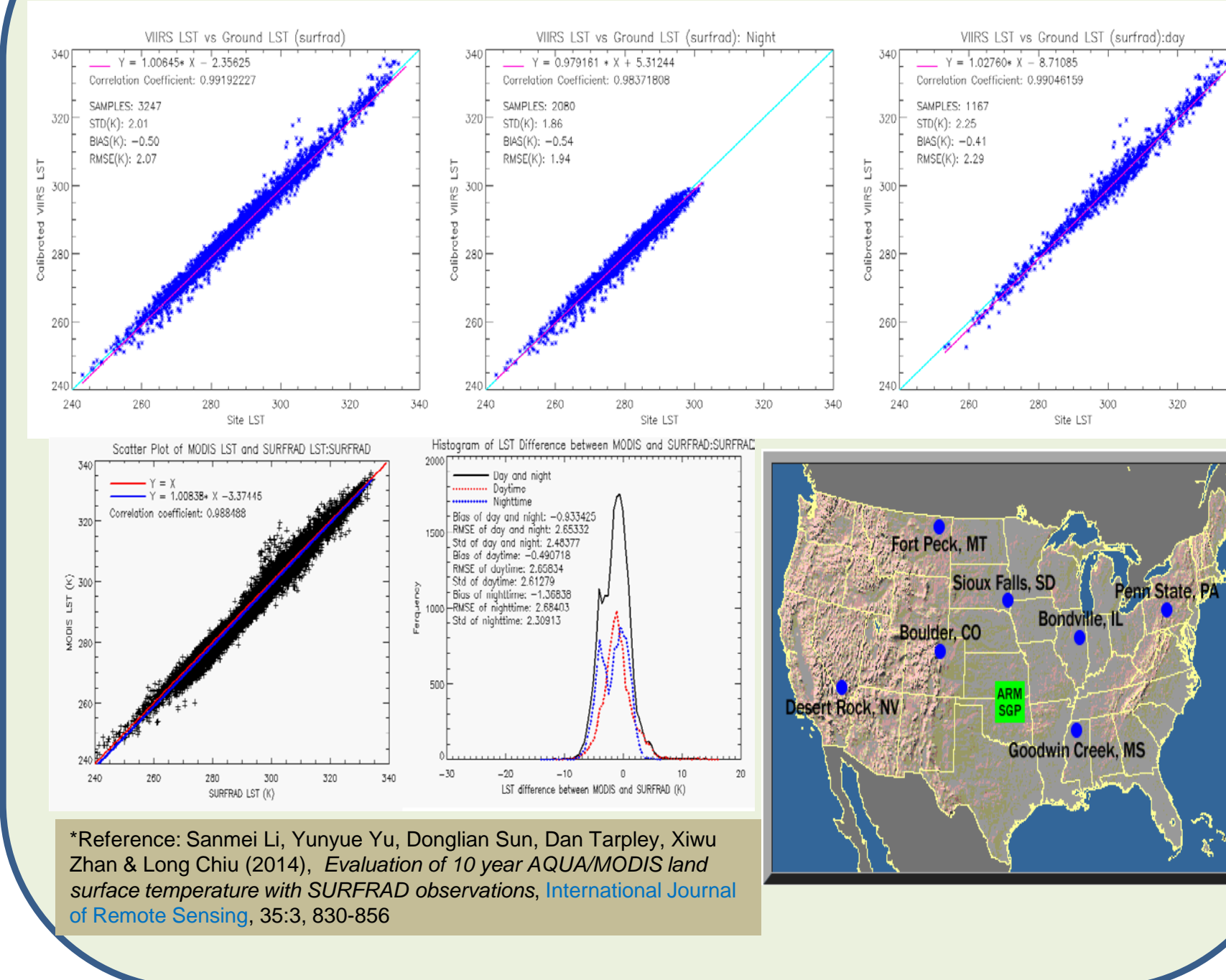
Flow chart of LST calibration

Global LST Image

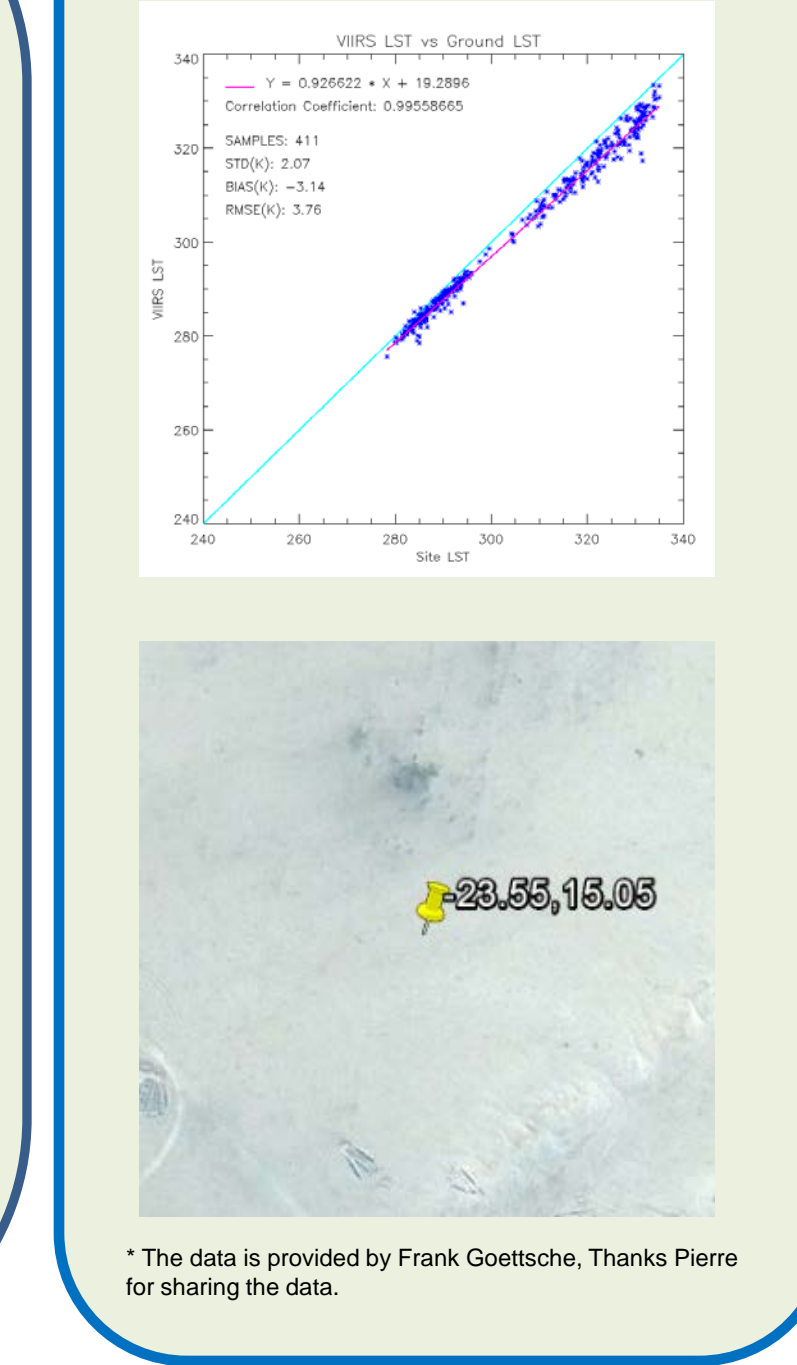


Ground Evaluation

The Surface Radiation Budget Network(SURFRAD): from Feb. 2012 to December 2013



Gobabeb in Namibia*: 2012



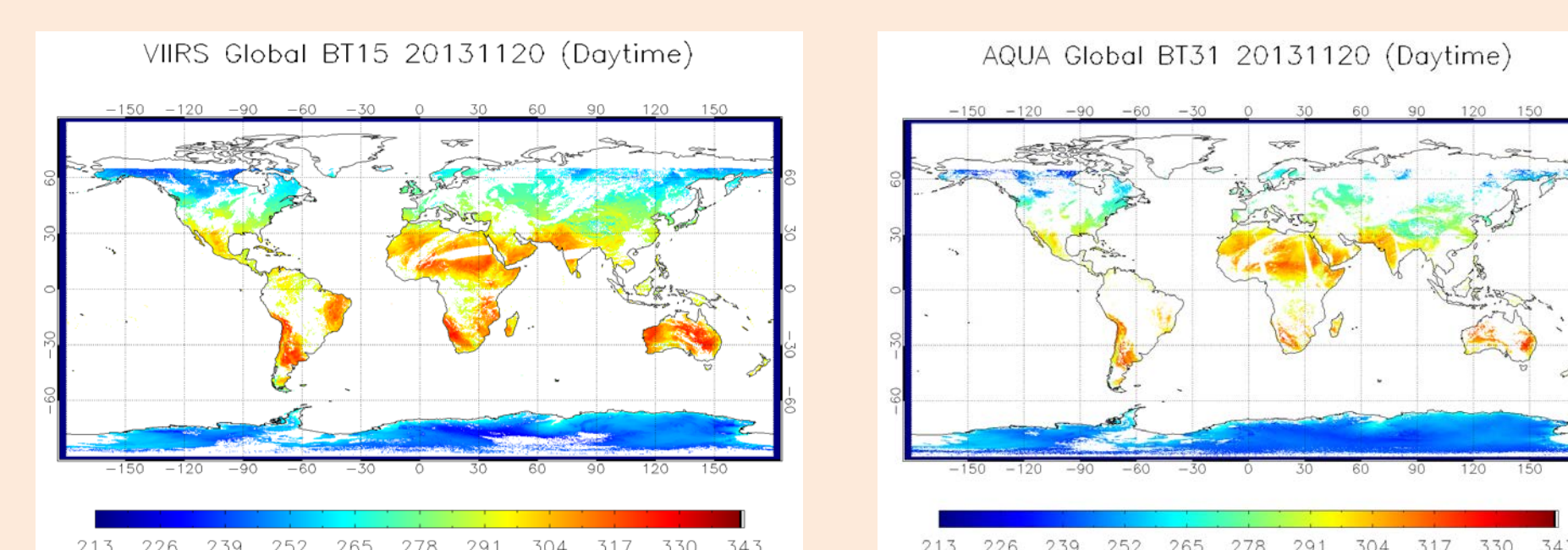
LST performance over surface types and day/night conditions (SURFRAD)

Surface type	Day/ni	Samples	Provisional LST		Beta LST	
			Bias	STD	Bias	STD
Deciduous Broadleaf	day	4	-0.67	0.80	0.31	3.10
	night	11	-0.13	1.60	-0.13	1.60
Forest	day	37	-0.81	1.77	-1.16	1.77
	night	57	-1.37	0.80	-2.48	0.63
Closed Shrub lands	day	277	-0.1	1.90	0.67	1.90
	night	327	-0.88	0.79	-2.38	0.79
Woody Savannas	day	46	-1.09	2.39	-0.34	2.81
	night	81	1.38	1.35	1.38	1.35
Grasslands	day	172	-0.38	1.90	1.11	2.36
	night	500	-0.35	1.41	-0.35	1.41
Croplands	day	266	0.14	2.95	2.39	3.54
	night	558	-0.21	1.58	-0.21	1.58
Cropland/Natural Vegetation Mosaics	day	208	-0.83	1.98	0.13	2.15
	night	459	0.47	1.94	0.47	1.94
Snow/ice	day	97	-1.16	1.67	-1.95	1.70
	night	87	-1.17	0.88	-2.67	0.88

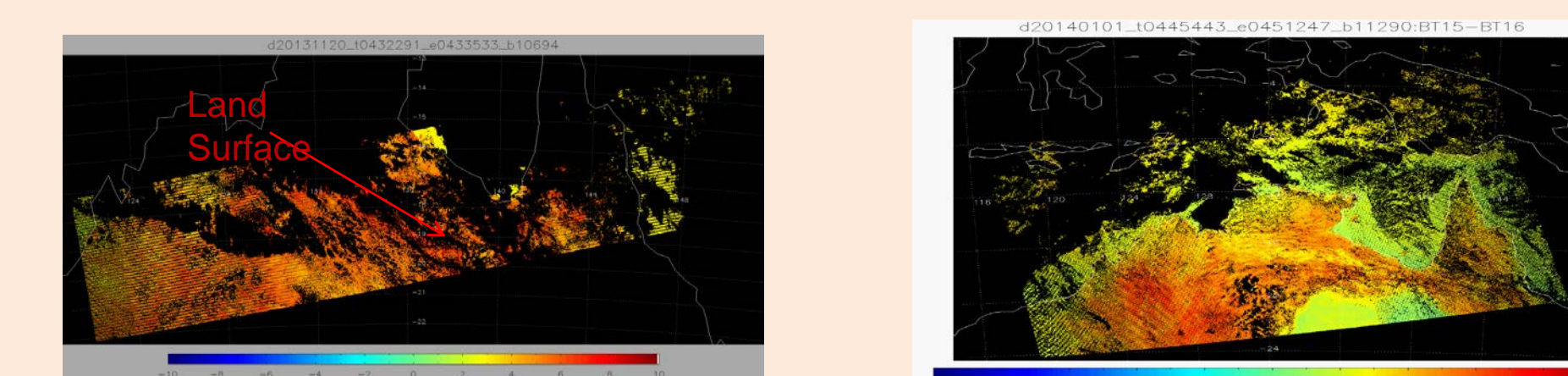
Issues

• Cross satellite comparisons at regional and global scale

- Temporal difference: BT change
- Composite process



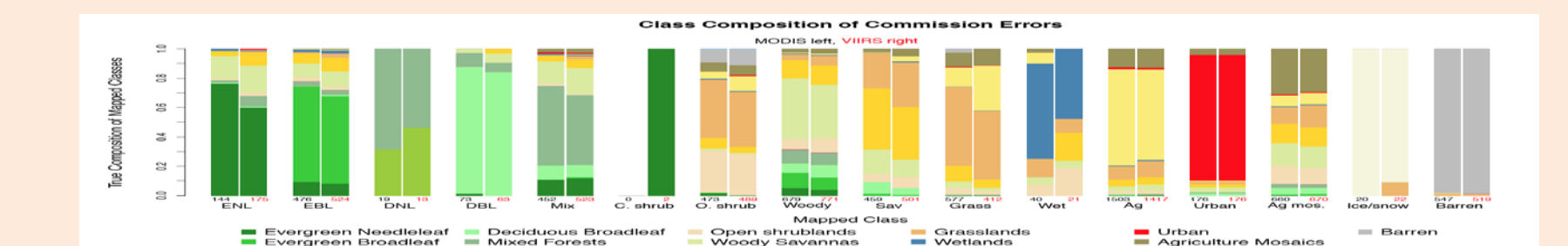
• BT difference over land and sea water



• Causes of the LST degradation

- Very wide range of BT difference for some surface types at global distribution. The BT difference can reach 16K over Australia under hot and humid atmospheric condition
- Limitations of the regression method and the radiative transfer simulation database being regressed
- VIIRS LST algorithm form, i.e. quadratic term of BT difference

• Surface type accuracy on LST performance: a case study



$$\Delta LST_i = \sum_{n=1}^N \sum_{j=1}^{17} (P_{ij} \epsilon_{ijn})$$

ΔLST_i is the LST error of surface type i , separately for day and night condition
 P_{ij} is the probability of mis-classification of surface type i ($i=1,2,...,17$) to be j ($j=1,2,...,17$)
 ϵ_{ijn} is the LST difference between LST calculated with the equation for surface type i and with the equation for surface type j for each pixel n with i surface type

Surface Type Accuracy on LST(Day)

Surface Type Accuracy on LST(Night)



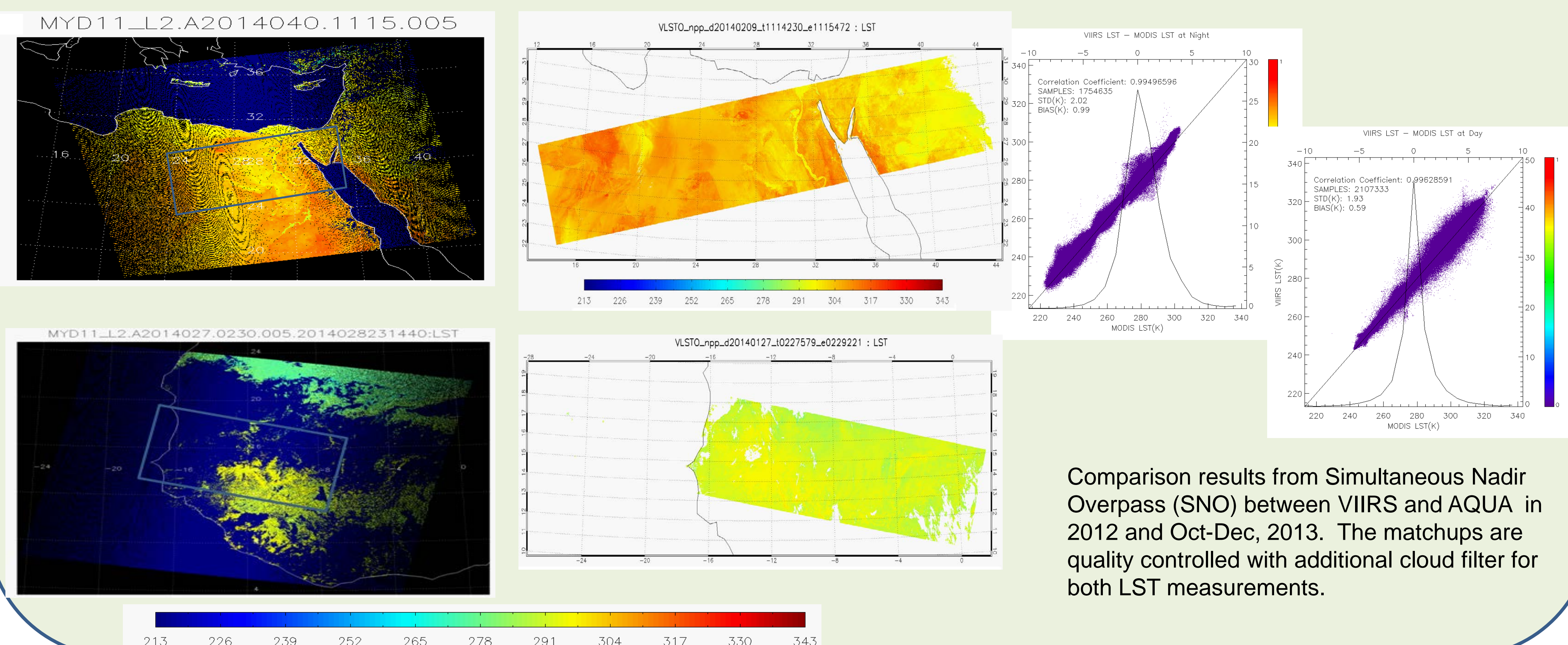
Emissivity impact to surface type dependent LST retrieval

- seasonal variation of some surface types
- Emissivity variation within cover types
- Appropriate emissivity setting for all surface types in building up the database for regression

Cross Satellite Evaluation

MYD11_L2, MODIS/Aqua Land Surface Temperature 5-Minute L2 Swath at 1 km is used as a reference for the cross satellite evaluation.

North east Africa on Feb. 09,2014 : daytime (top) and North west Africa at nighttime on Jan. 27,2014(bottom):



Comparison results from Simultaneous Nadir Overpass (SNO) between VIIRS and AQUA in 2012 and Oct-Dec, 2013. The matchups are quality controlled with additional cloud filter for both LST measurements.

Summary and Future Work

- VIIRS LST shows a good overall agreement with ground LST measurements, with a better performance achieved at nighttime than at daytime. However, the performance varies with surface type. LST is underestimated over closed shrub lands at both daytime and nighttime, open shrub lands and barren surface at nighttime, woody savannas and snow/ice surface at daytime. The evaluation results over barren surface at daytime conflict with the results obtained using measurements in Africa, the latter showing an obvious underestimation of VIIRS LST both at daytime and nighttime. Possible explanations for this apparent inconsistency include homogeneity of the site, ground in-situ quality control, emissivity used to calculate the ground LST and regional atmospheric condition that might affect LST retrieval.
- VIIRS LST is in close overall agreement with MODIS LST. Disagreements are shown over areas with large brightness temperature difference between the two retrieval channels, and these disagreements are reduced after calibration. However VIIRS LST is degraded under this special situation.
- Several issues need to be well addressed in the algorithm development. Since VIIRS LST algorithm is a surface type dependent algorithm, it underperforms over surface types that vary seasonally (which is not reflected in the surface type EDR), and misclassified surface types particularly if the misclassification happens between two surface types with distinct emission features. The appropriate emissivity setting for all IGBP surface types is very important for the simulation. The large variation of emissivity over surface types makes it difficult to determine the representative emissivity setting for each IGBP surface type and the uncertainty from the emissivity and land cover type product also introduce error into the procedure.

ESTIMATING SEA SURFACE SALINITY IN COASTAL WATERS OF THE GULF OF MEXICO USING VISIBLE CHANNELS ON SNPP VIIRS

Ryan A. Vandermeulen¹, Robert Arnone¹, Sherwin Ladner², Paul Martinolich³

¹University of Southern Mississippi, Department of Marine Science, Stennis Space Center, MS 39529

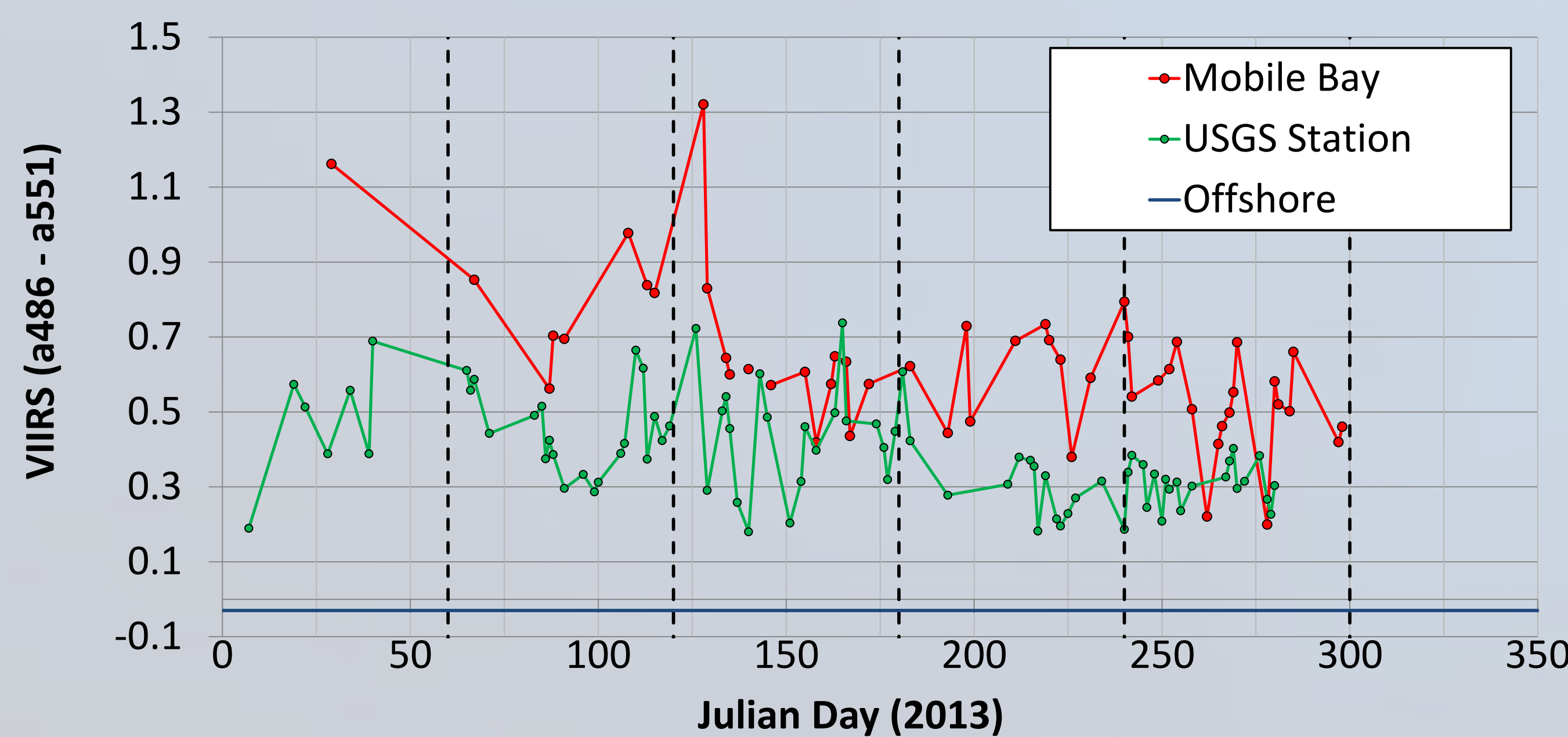
²Naval Research Laboratory, Stennis Space Center, MS 39529 ; ³QinetiQ North America, Stennis Space Center, MS 39529

ABSTRACT

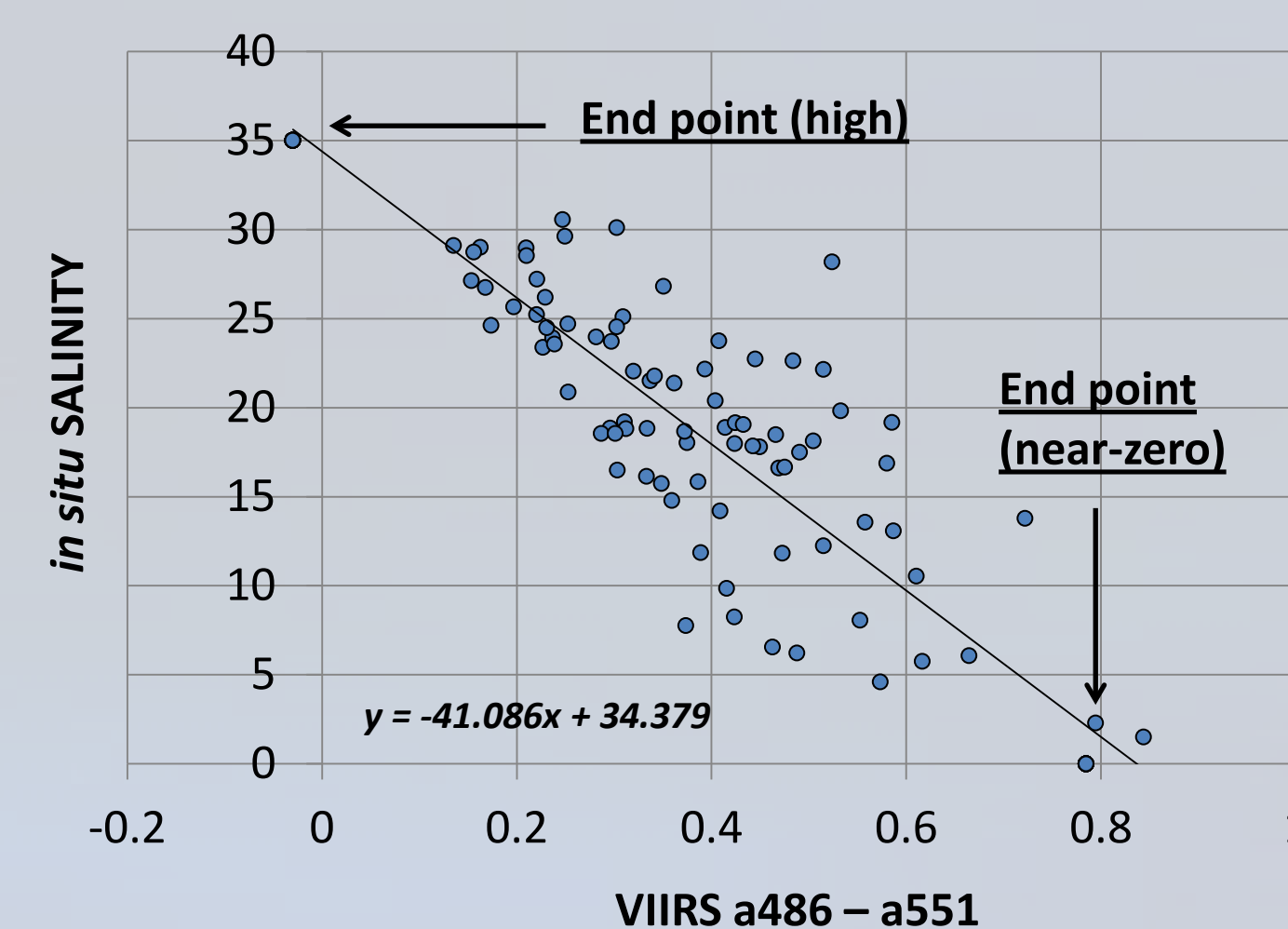
- Sea surface salinity is determined using the visible channels from the Visual Infrared Imaging Radiometer Suite (VIIRS) to derive a regional algorithms for the northern Gulf of Mexico. Data were collected over all seasons in the year 2013 in order to assess inter-annual variability. The seasonal spectral signatures at the river mouth were used to track the fresh water end members and used to develop a seasonal slope and bias between salinity and radiance.

APPROACH

- For salinity algorithm development, *in situ* salinity data (Jan–Oct 2013) obtained from five USGS platforms and one NOAA/NDBC platform in the Mississippi Sound were compared to VIIRS spectral Rrs and absorption (QAA).
- A time-series of satellite data monitoring NEAR-ZERO salinity points (mouth of Mobile Bay) shows changes *assumed* to be independent of salinity, indicating a change in water mass that can be normalized throughout the year.

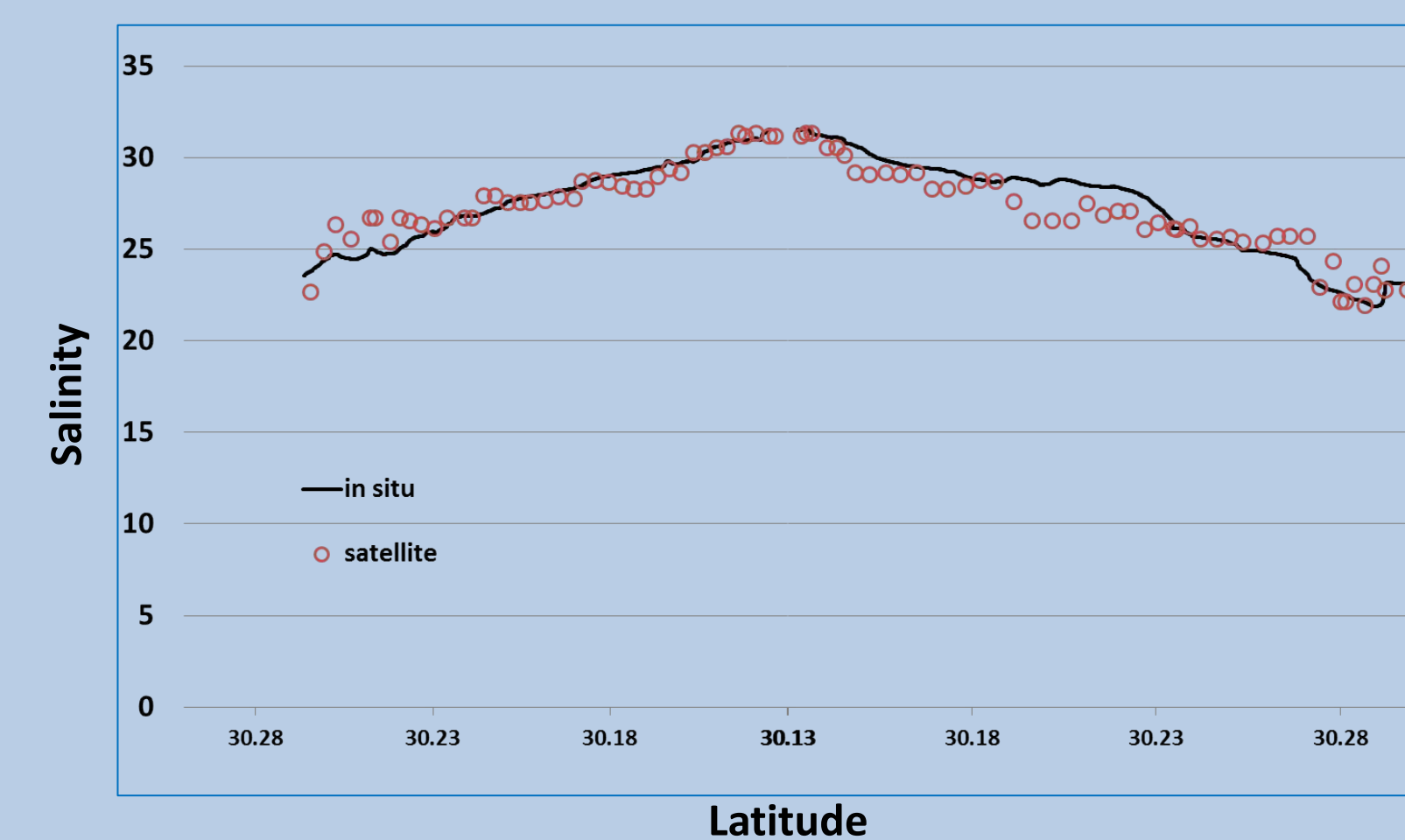


VIIRS absorption products (a486-a551, QAA), showed the highest consistent correlations. Bi-monthly means of VIIRS-derived products at the Mobile Bay mouth and oligotrophic waters (low and high end members, respectively) were used to constrain bi-monthly regression slopes of salinity to optical signatures.

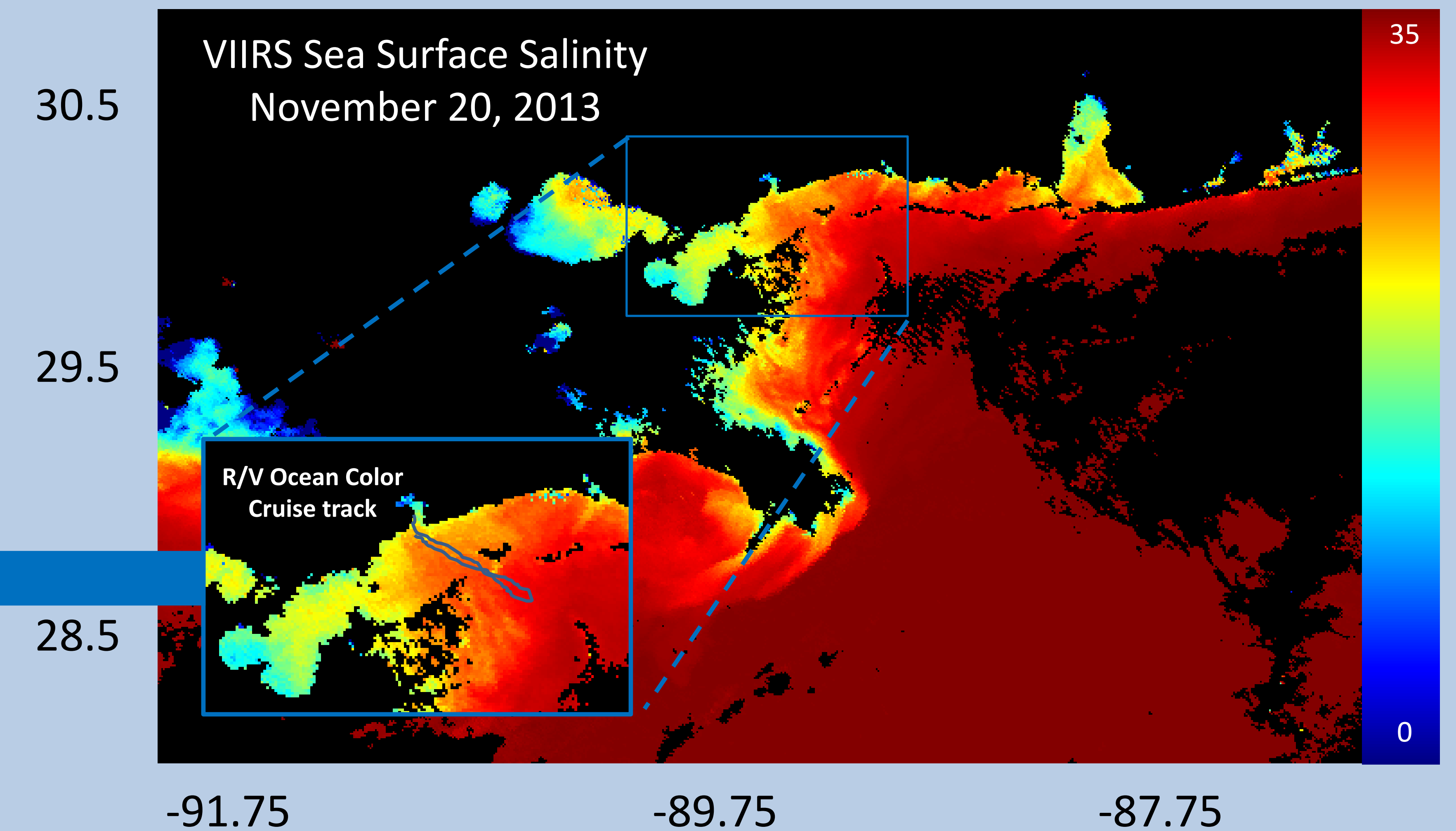
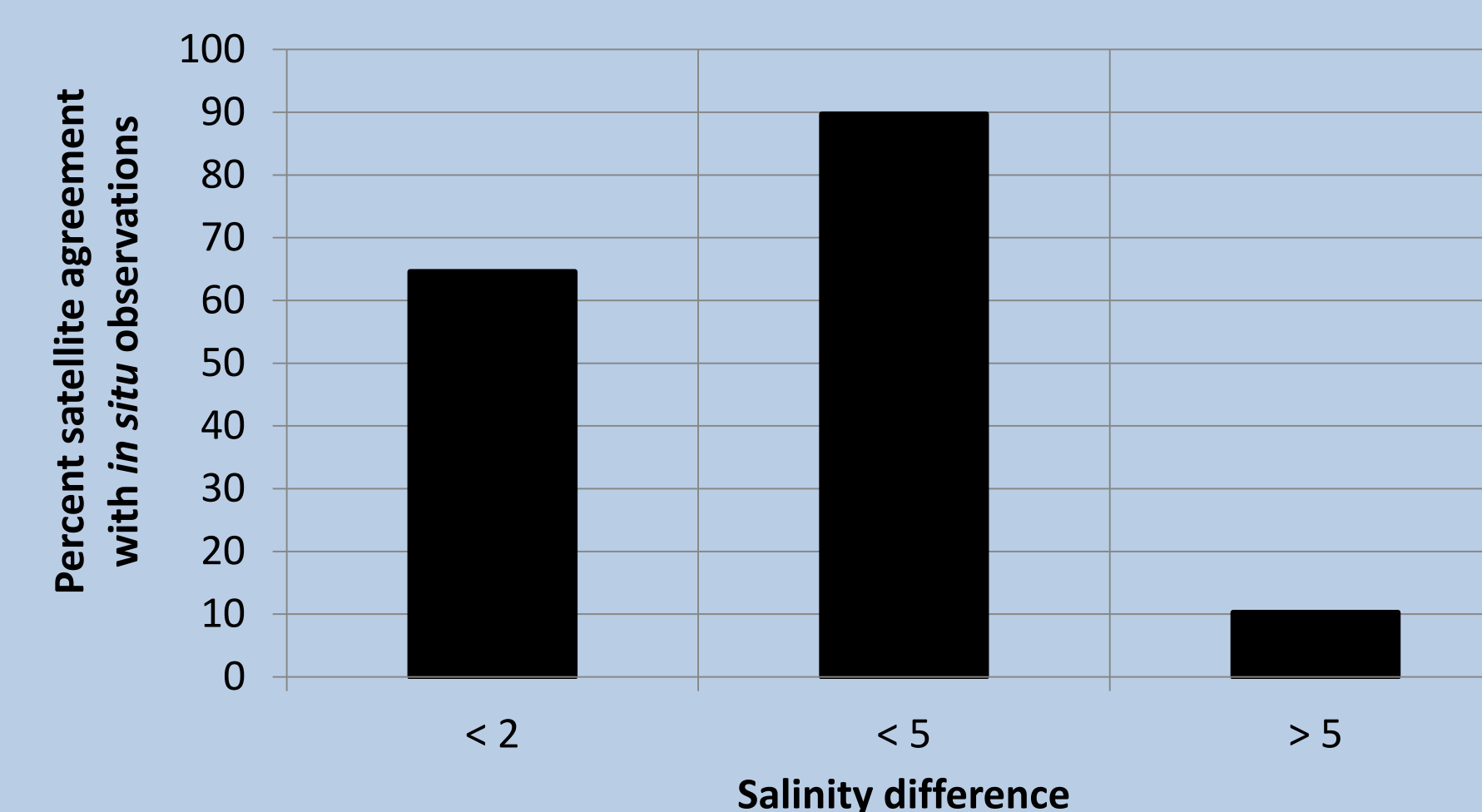
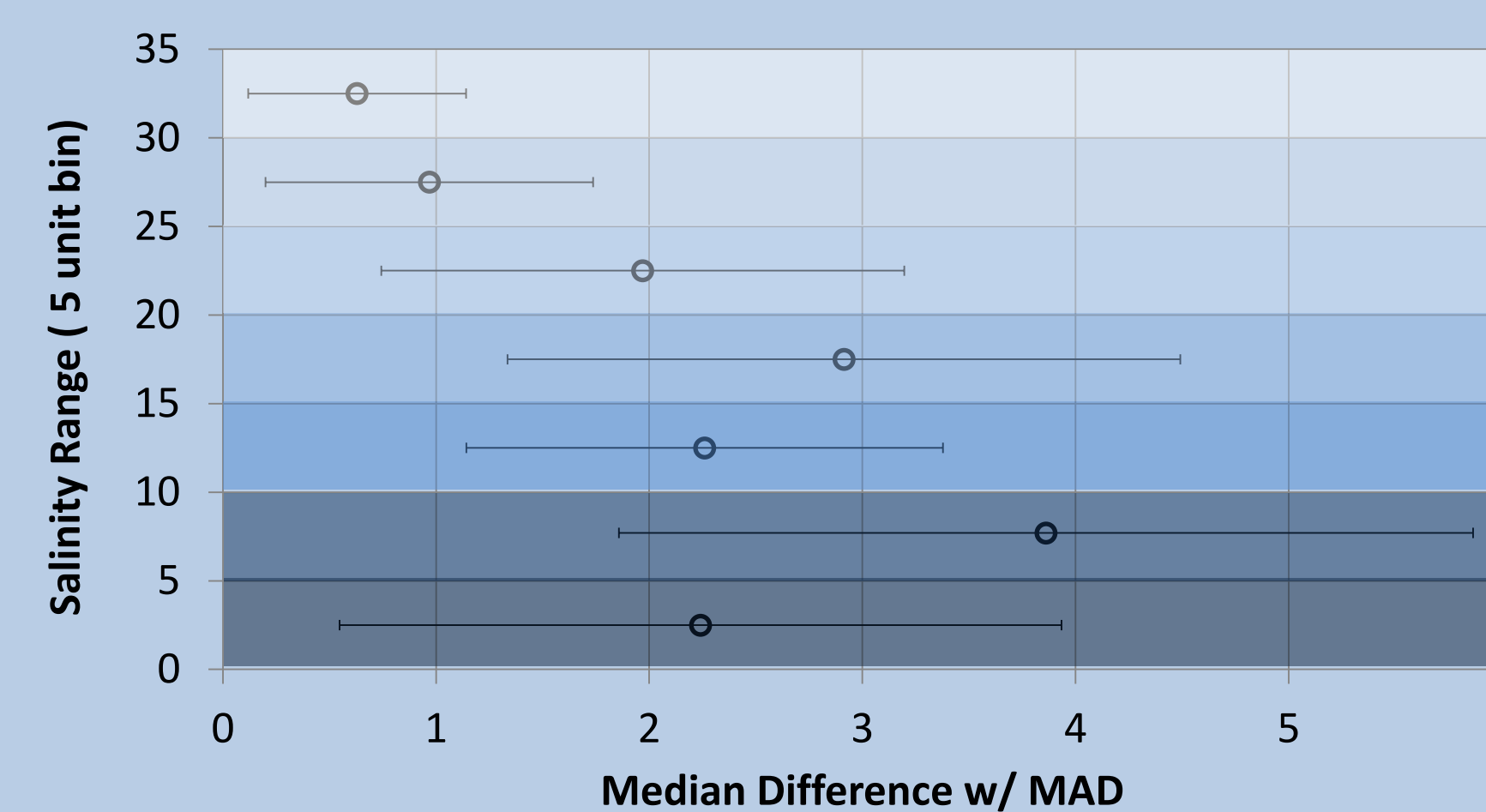


RESULTS & DISCUSSION

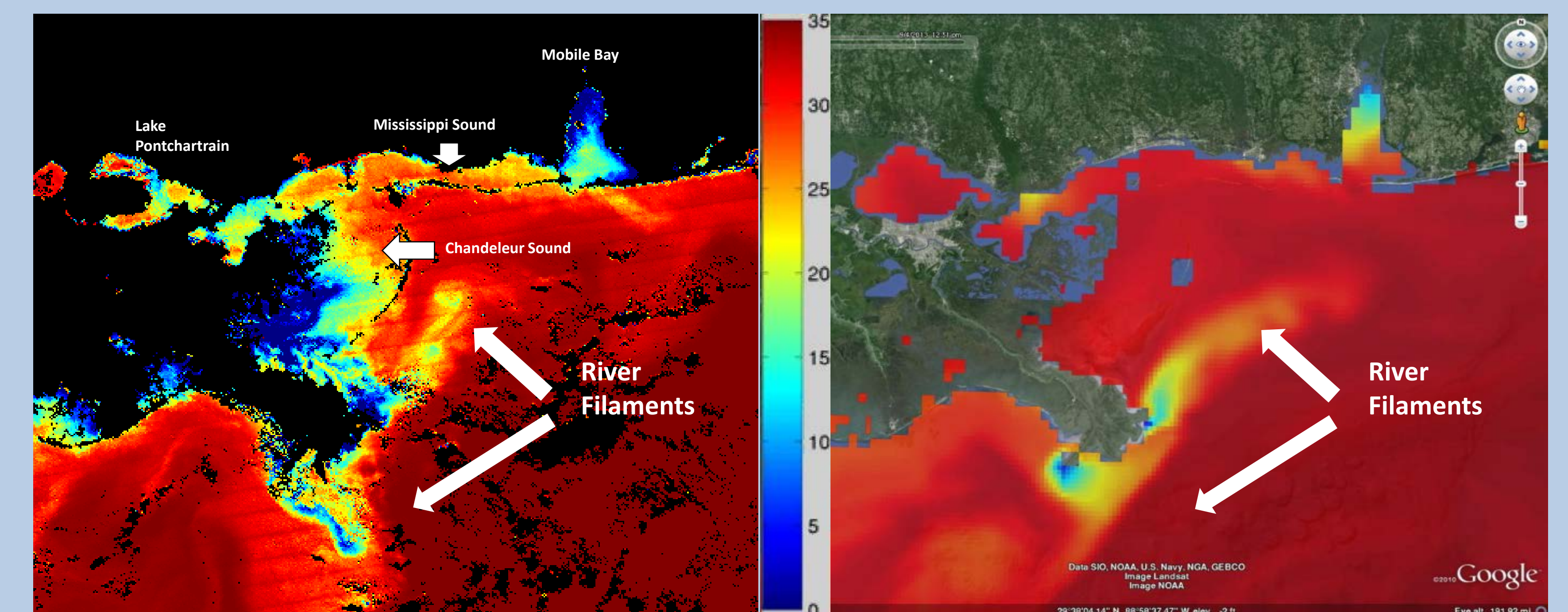
- Bi-monthly regression slopes were applied to VIIRS absorption data and evaluated using an *in situ* flow through data set in the MS Sound/Bight. Results (below) show good agreement of satellite data with *in situ* data along a range of salinity values.



- An qualitative analysis of errors (below) shows that higher uncertainties were present in the 5-10 and 15-20 psu range. Further evaluation shows that 65% of satellite data points (n=419) were within 2 psu of *in situ* measurements.



The river-mouth normalized regressions are applied to VIIRS absorption data (a486-a551, QAA) to obtain a salinity map for the Northern Gulf of Mexico (shown above). Even with higher inherent error than current microwave scatterometers (Aquarius/SAC-D, SMOS), the high spatial (750-m) and temporal (daily) resolution obtained from VIIRS offer significant improvements.



A comparison of VIIRS salinity product (left) with NAVY Coastal Ocean Model (NCOM, right) salinity product on September 04, 2013 shows the detection of episodic freshwater river plumes originating from the Mississippi River. The higher resolution satellite data product can potentially provide direct data for assimilation into physical circulation models in near-real time.

Summary

➤ Three-year (2009–2011) observations in highly turbid waters of the western Pacific from (MODIS) on the satellite Aqua are used to conduct this study. SWIR atmospheric correction with band set of 1640 nm and 2130 nm is conducted to derive $nL_w(\lambda)$ at the red, near-infrared (NIR), and shortwave infrared (SWIR).

➤ NIR ocean reflectance spectral shape represented by reflectance ratio of $\rho_{wN}(748)/\rho_{wN}(869)$ is highly dynamic in a large coverage of turbid waters.

➤ In turbid waters, ocean IOP modeling can be significantly simplified. It is feasible to analytically derive some IOP properties in turbid waters with combined visible-NIR $nL_w(\lambda)$ spectra data.

➤ IOP properties such as $b_{bp}(\lambda)$ can be derived from satellite $nL_w(\lambda)$ measurements in the NIR wavelengths. Backscattering spectral slopes can also be reasonably derived in the coastal turbid regions.

➤ This work is published in *Limnology and Oceanography* (Shi and Wang, 2014).

West Pacific Highly Turbid Waters

The BS, YS, and ECS are the three major marginal seas in the western Pacific Ocean bounded by China, Korea, and Japan (Fig. 1). They cover some of the most turbid waters in the world (Shi and Wang 2010, 2012). Major rivers in this region such as the Yangtze River and Yellow River transport large amounts of sediments into the BS, YS, and ECS.

In the coastal region of the YS (Sta. 1, 2 in Fig. 1), Subei Shoal of the YS (Sta. 3 in Fig. 1), Yangtze River estuary (Sta. 5 in Fig. 1), Hangzhou Bay (Sta. 6 in Fig. 1), and Lake Taihu (Sta. 7 in Fig. 1), normalized water-leaving radiance at the red band $nL_w(645)$ can be over $\sim 5 \text{ mW cm}^{-2} \mu\text{m}^{-1} \text{sr}^{-1}$ in the winter season (Shi and Wang 2012; Wang et al. 2011). Normalized water-leaving radiance at 859 nm ($nL_w(859)$) normally is also over $\sim 2 \text{ mW cm}^{-2} \mu\text{m}^{-1} \text{sr}^{-1}$ at these stations.

Three-year MODIS-Aqua observations from 2009–2011 are used to derive $nL_w(645)$, $nL_w(748)$, $nL_w(859)$, $nL_w(869)$, and $nL_w(1240)$ using the SWIR atmospheric correction with the band set of 1640 and 2130 nm (Wang 2007).

Spectral Features of $nL_w(\lambda)$ in the Red, NIR and SWIR

➤ NIR reflectance spectral shapes represented with $\rho_{wN}(748)/\rho_{wN}(869)$ is highly dynamic. It drops from ~ 1.8 – 2.0 for moderately turbid water to 1.1 – 1.2 for highly turbid waters.

$\rho_{wN}(748)/\rho_{wN}(869)$ vs. $\rho_{wN}(869)$ at Different Stations

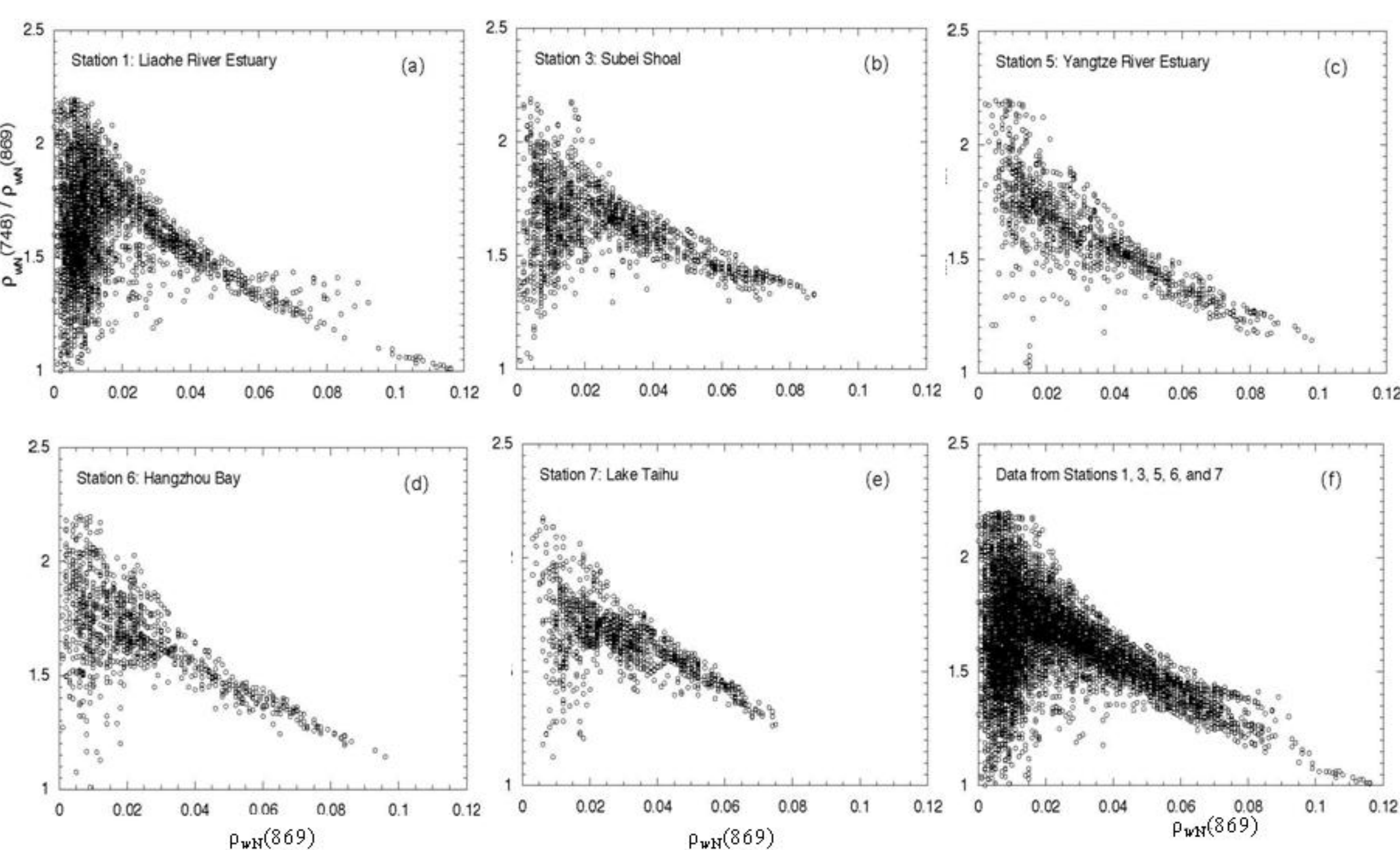


Figure 2. $\rho_{wN}(748)/\rho_{wN}(869)$ vs. $\rho_{wN}(869)$ between 2009 and 2011 in a 5x5 box centered at (a) Sta. 1, (b) Sta. 3, (c-e) Sta. 5-7, and (f) Sta. 1, 3, 5, 6, and 7.

Concept of NIR-based IOP Retrieval Modeling

NIR-based Reflectance Modelling and IOP Retrievals

In the NIR Wavelengths

$$a_{w}(\lambda) \gg a_{ph}(\lambda), a_g(\lambda), \text{ and } a_d(\lambda)$$

$$\left(\frac{b_s(\lambda)}{a(\lambda) + b_s(\lambda)} \right) \approx \left(\frac{b_s(\lambda)}{a_w(\lambda) + b_s(\lambda)} \right)$$

MODIS NIR-based Reflectance and IOP Modeling

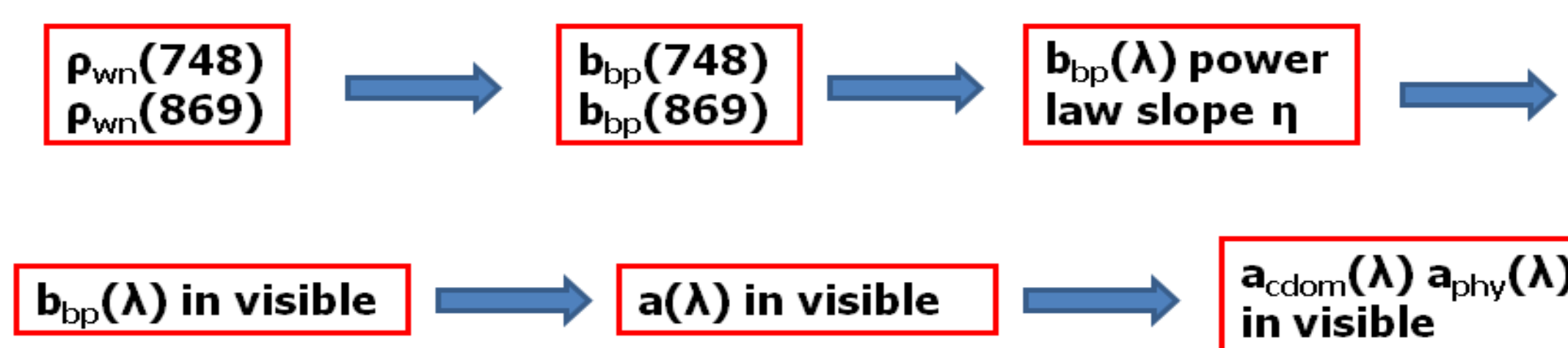


Figure 3. Schematic chart shows how the IOP properties are retrieved in coastal turbid waters.

NIR-based IOP Model Test with IOCCG Synthetic Data

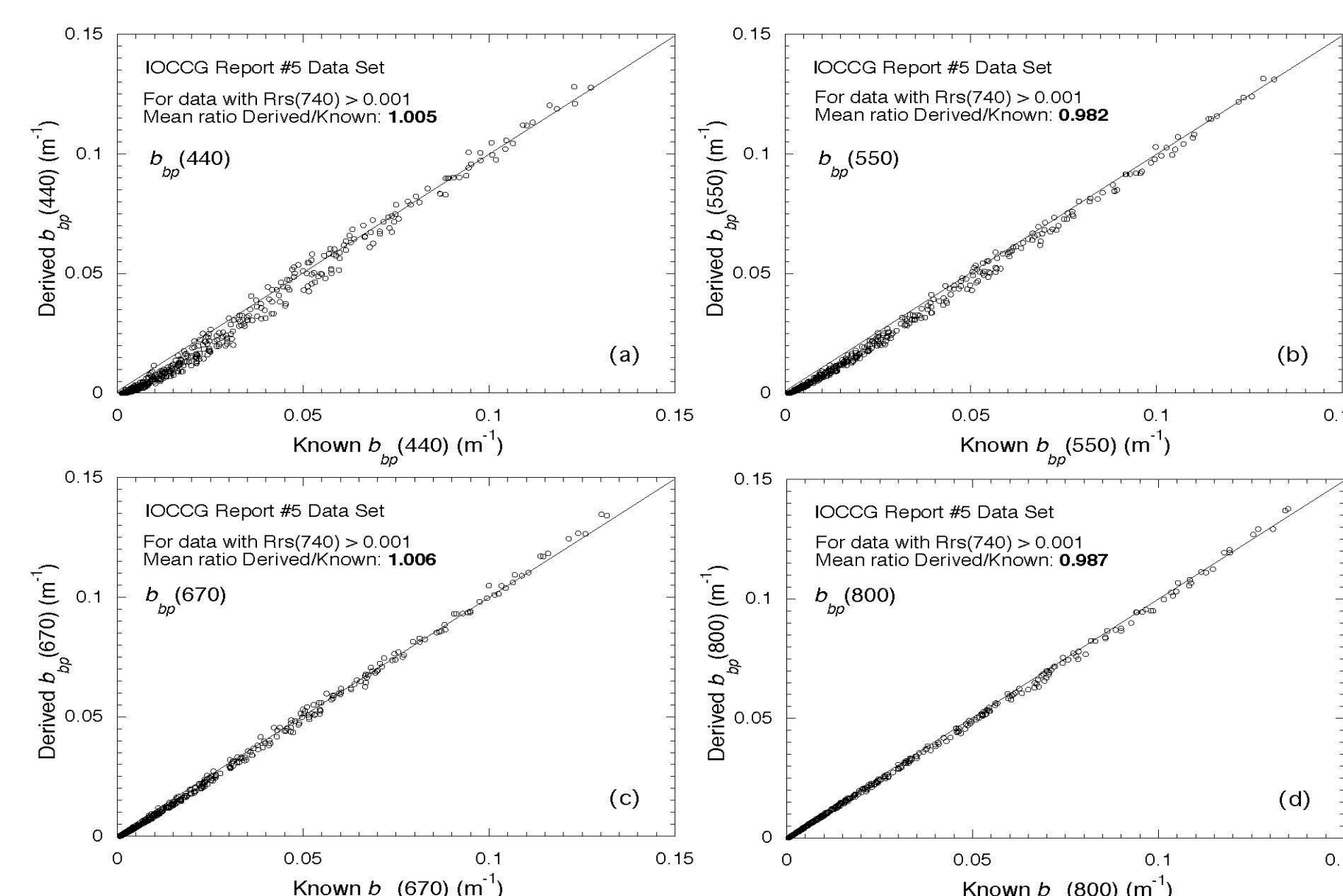


Figure 4. Comparison between the model-derived particle backscattering coefficient $b_{bp}(\lambda)$ and the true values from the IOCCG synthetic dataset for (a) $b_{bp}(440)$, (b) $b_{bp}(550)$, (c) $b_{bp}(670)$, and (d) $b_{bp}(800)$.

NIR-based IOP Retrievals in the Turbid Waters

$b_{bp}(859)$ Derived from MODIS-Aqua Measurements

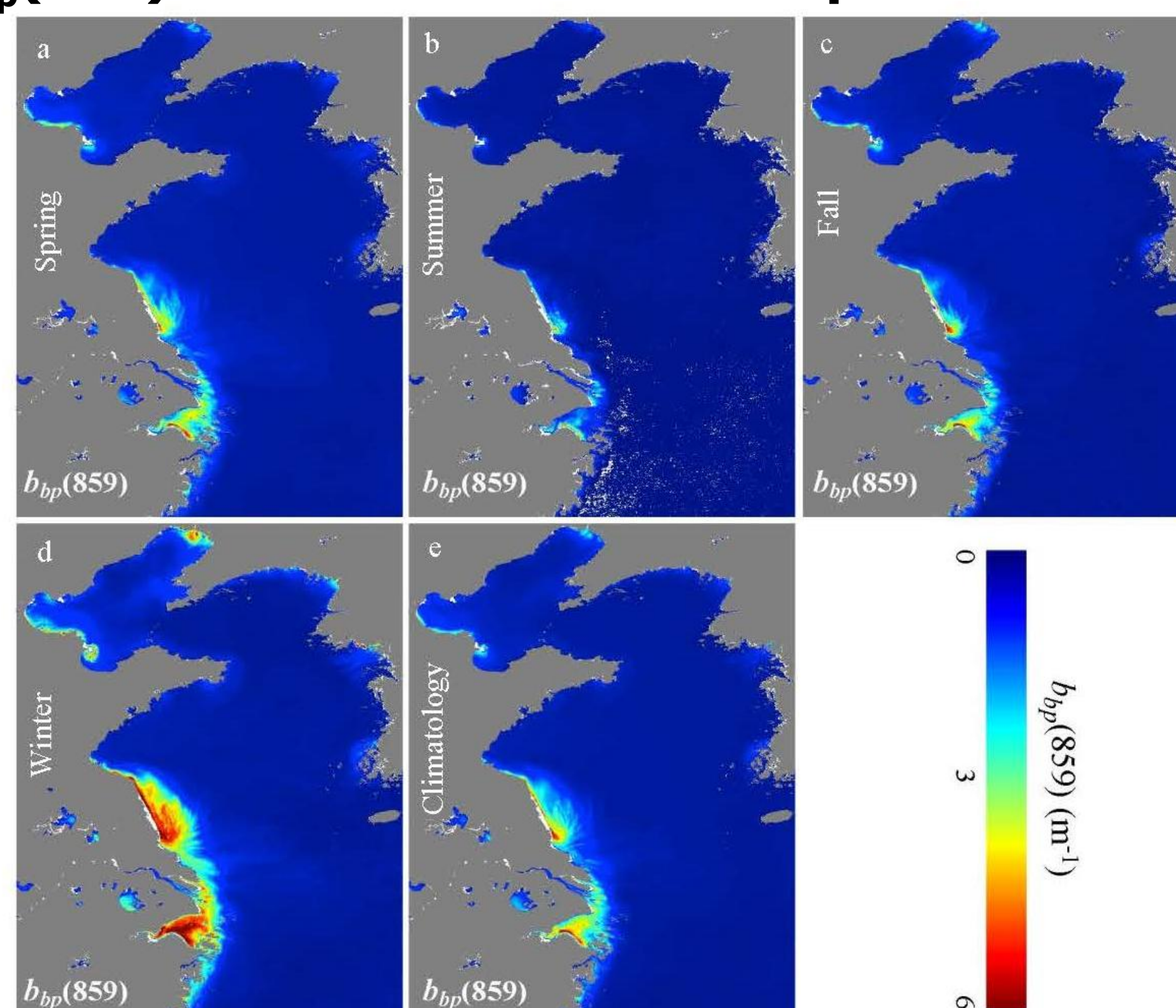


Figure 5. Three-year mean images of backscattering coefficient at the wavelength of 859 nm $b_{bp}(859)$ derived from MODIS-Aqua measurements from 2009 to 2011 for (a) spring (March–May), (b) summer (June–August), (c) fall (September–November), (d) winter (December–February), and (e) three-year climatology.

Backscattering Power Law Slope η vs. $b_{bp}(859)$

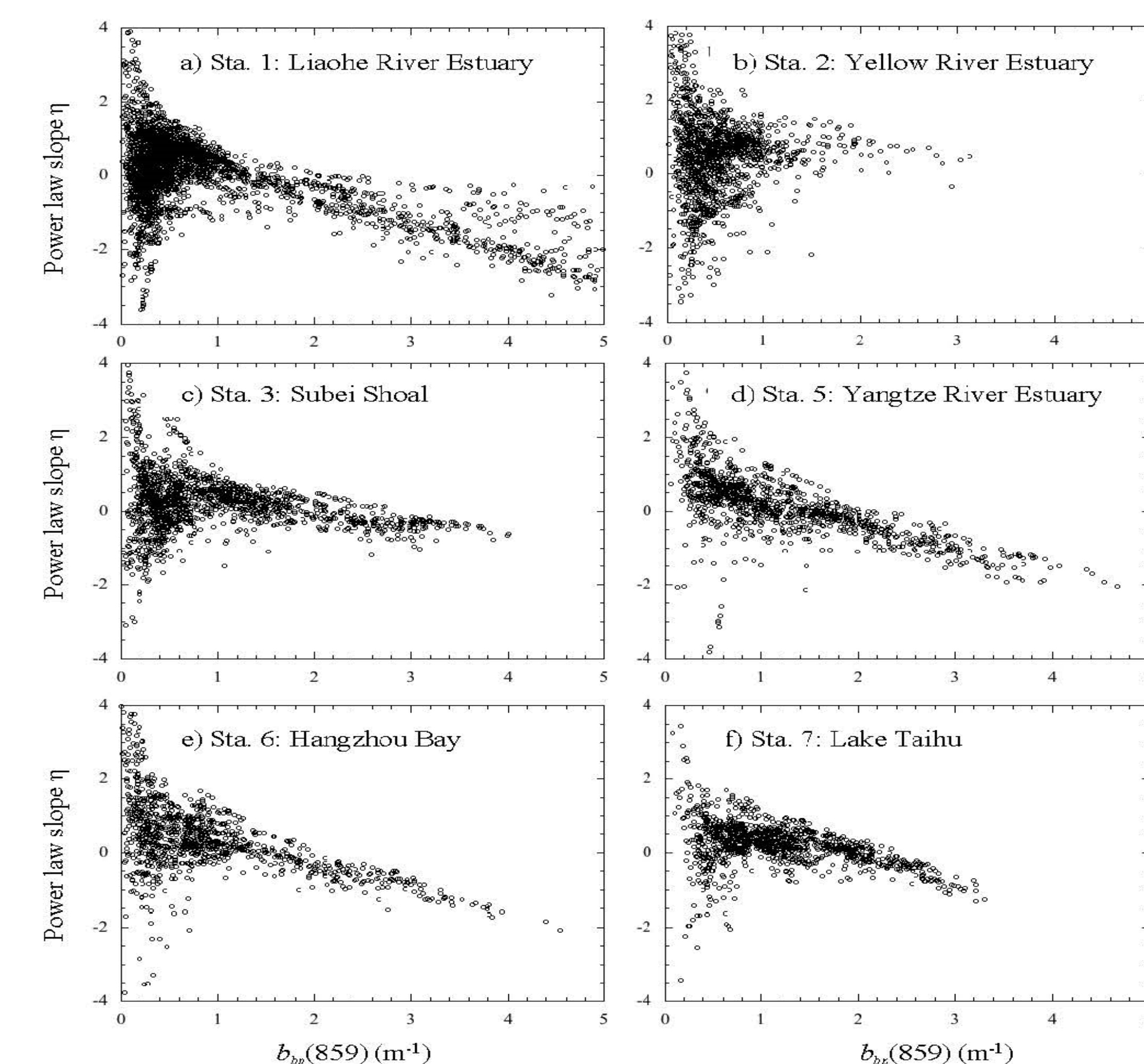


Figure 6. Scatter plots of MODIS-Aqua-derived power law slope η vs. $b_{bp}(859)$ from 2009–2011 in a 5x5 box centered at (a) Sta. 1, (b) Sta. 2, (c) Sta. 3, (d) Sta. 5, (e) Sta. 6, and (f) Sta. 7.

Conclusion Remarks

➤ This study quantifies and characterizes the normalized water-leaving radiance spectra $nL_w(\lambda)$ in wavelengths of the red, NIR, and SWIR in highly turbid coastal regions of the BS, YS, and ECS.

➤ NIR ocean reflectance spectral shape represented by reflectance ratio of $\rho_{wN}(748)/\rho_{wN}(869)$ is highly dynamic in a large coverage of turbid waters.

➤ In turbid waters, ocean IOP modeling can be significantly simplified. It is feasible to analytically derive some IOP properties in turbid waters with combined visible-NIR $nL_w(\lambda)$ spectra data.

➤ We demonstrate IOP properties such as $b_{bp}(\lambda)$ can be derived from satellite $nL_w(\lambda)$ measurements in the NIR wavelengths. Backscattering spectral slopes can also be reasonably derived in the coastal turbid regions.

➤ SWIR atmospheric correction with the MODIS SWIR band set of 1240 and 2130 nm can be safely used for $nL_w(\lambda)$ retrievals for waters with $nL_w(859)$ less than $\sim 2.5 \text{ mW cm}^{-2} \mu\text{m}^{-1} \text{sr}^{-1}$.

➤ Current existing algorithms for $Chl-a$, $K_d(490)$, TSM, and IOPs using the ocean reflectance at the red band for coastal regions are all limited and cannot be applied to highly turbid waters with $\rho_{wN}(859) > \sim 0.05$.

References

- SHI, W., and M. WANG. 2010. Characterization of global ocean turbidity from Moderate Resolution Imaging Spectroradiometer ocean color observations. *J. Geophys. Res.* **115**: C11022, doi:10.1029/2010JC006160
- SHI, W., and M. WANG. 2012. Satellite views of the Bohai Sea, Yellow Sea, and East China Sea. *Prog. Oceanogr.* **104**: 35–45.
- WANG, M. 2007. Remote sensing of the ocean contributions from ultraviolet to near-infrared using the shortwave infrared bands: simulations. *Appl. Opt.* **46**: 1535–1547.
- WANG, M., W. SHI, and J. TANG. 2011. Water property monitoring and assessment for China's inland Lake Taihu from MODIS-Aqua measurements. *Remote Sens. Environ.* **115**: 841–854.
- SHI, W., and M. WANG. 2014. Ocean reflectance spectra at the red, near-infrared, and shortwave infrared from highly turbid waters: A study in the Bohai Sea, Yellow Sea, and East China Sea, *Limnol. Oceanogr.* **59**: 427–444.

Acknowledgments: This research was supported by NASA and NOAA funding and grants. The MODIS L1B data were obtained from NASA/GSFC MODAPS Services website.

Regional Vicarious Gain Adjustment for Coastal VIIRS Products



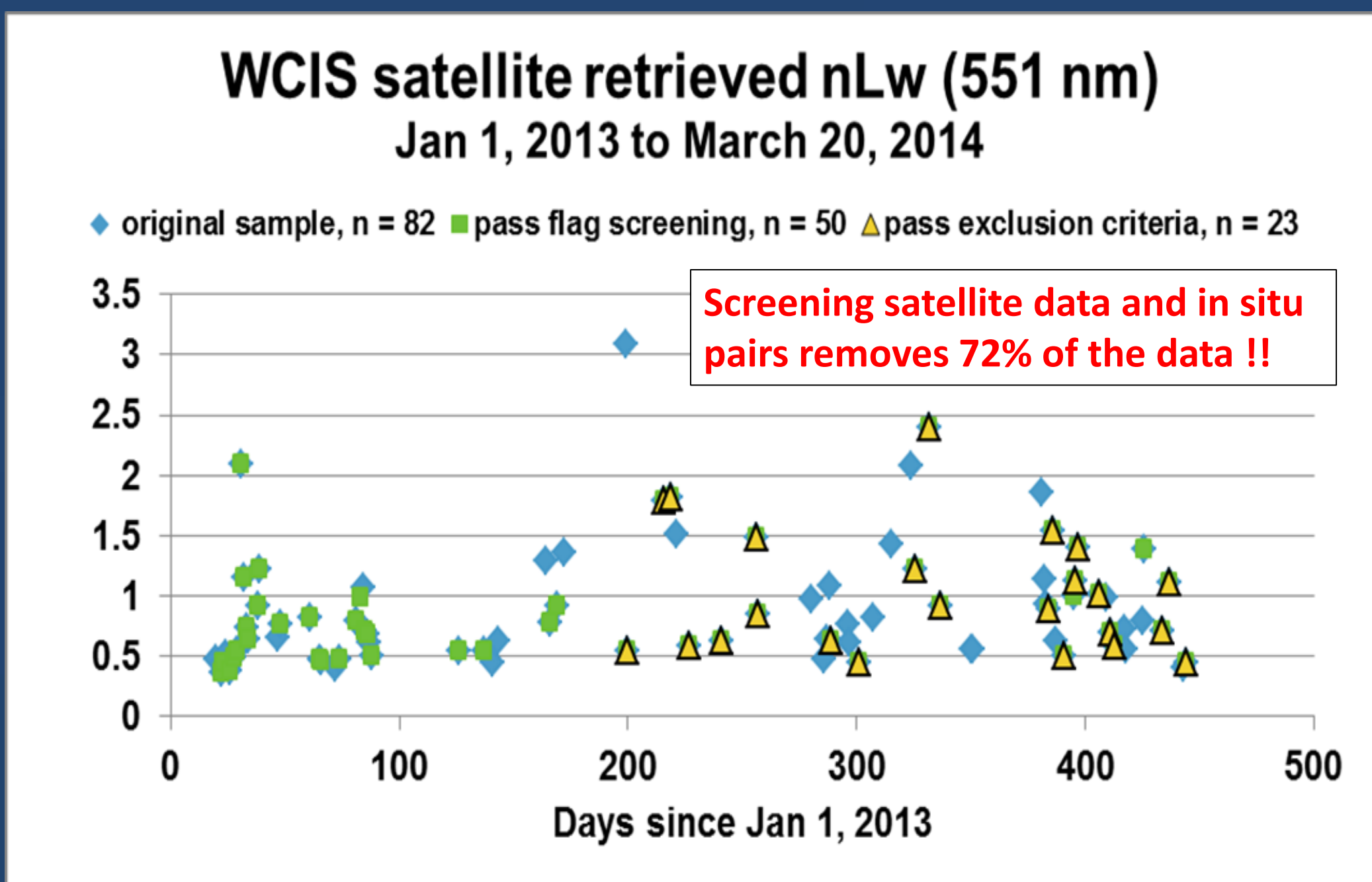
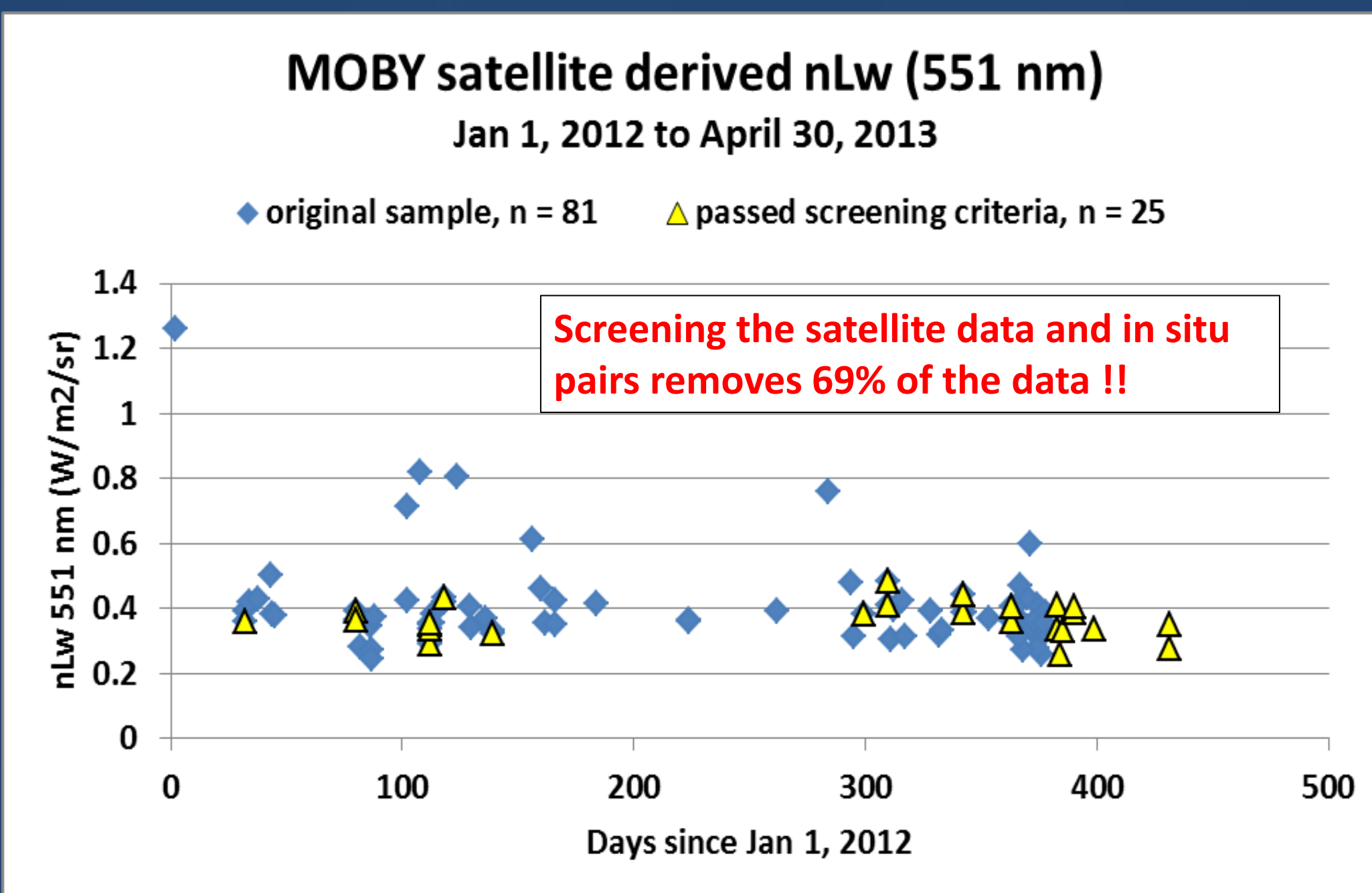
Jennifer Bowers¹, Robert Arnone², Sherwin Ladner³, Giuletta S. Fargion⁴, Adam Lawson³, Paul Martinolich¹, Ryan Vandermeulen²

¹ QinetiQ North America, Stennis Space Center, MS, ² University of Southern Mississippi, Stennis Space Center, MS, ³ Naval Research Laboratory, Stennis Space Center, MS, ⁴ San Diego State University, San Diego, CA

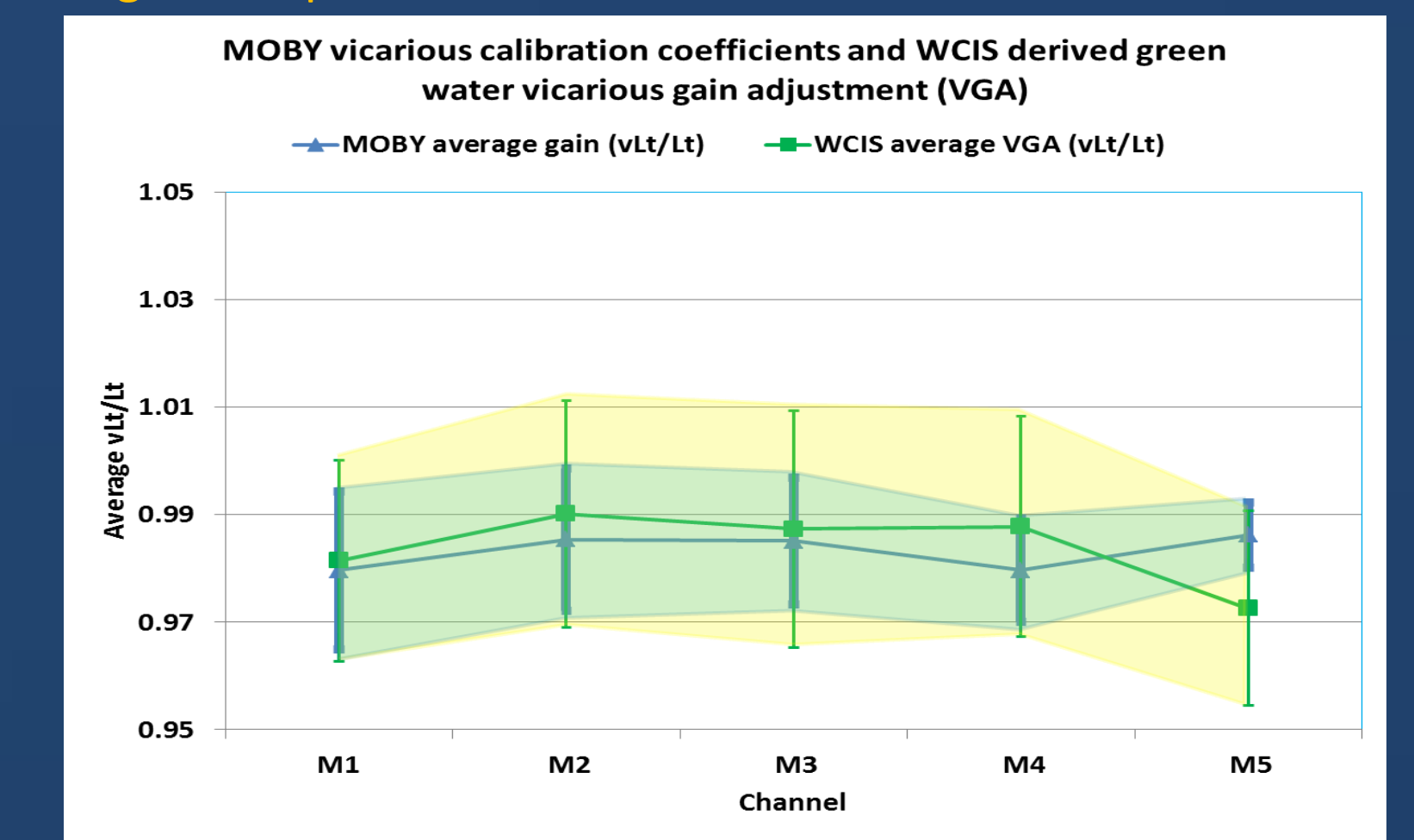
ABSTRACT: As part of the Joint Polar Satellite System (JPSS) Ocean Cal/Val Team, Naval Research Lab - Stennis Space Center (NRL-SSC) has been working to facilitate calibration and validation of the Visible Infrared Imaging Radiometer Suite (VIIRS) ocean color products. By relaxing the constraints of the NASA Ocean Biology Processing Group (OBPG) methodology for vicarious calibration of ocean color satellites and utilizing the Aerosol Robotic Network Ocean Color (AERONET-OC) system to provide *in situ* data, we investigated differences between remotely sensed water leaving radiance and the expected *in situ* response in coastal areas and compare the results to traditional Marine Optical Buoy (MOBY) calibration/validation activities.

An evaluation of the Suomi National Polar-Orbiting Partnership (SNPP)-VIIRS ocean color products was performed in coastal waters using the time series data obtained from the Northern Gulf of Mexico AERONET-OC site, WaveCIS. The coastal site provides different water types with varying complexity of CDOM, sedimentary, and chlorophyll components. Time series data sets were used to develop a vicarious gain adjustment (VGA) at this site, which provides a regional top of the atmospheric (TOA) spectral offset to compare the standard MOBY spectral calibration gain in open ocean waters.

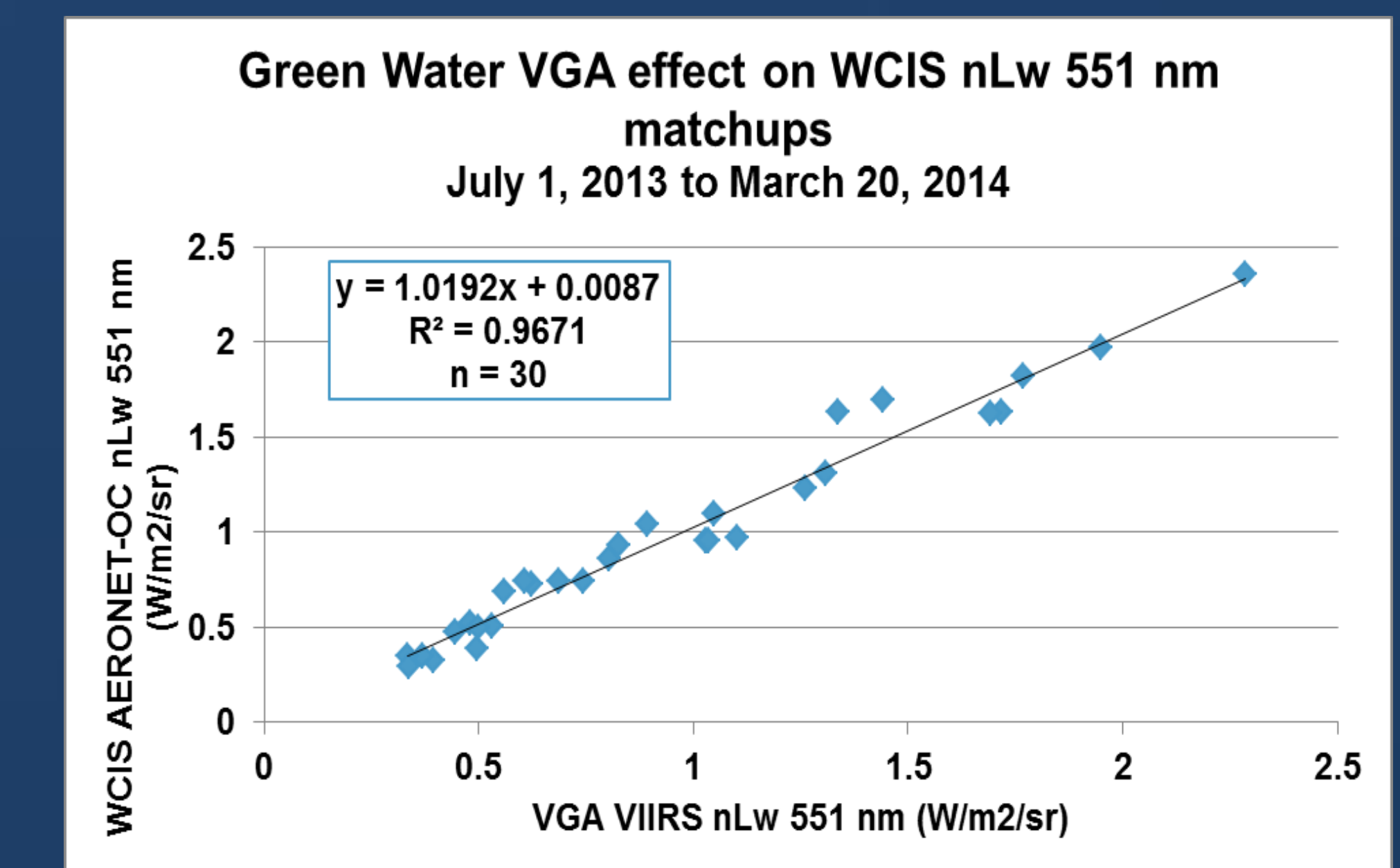
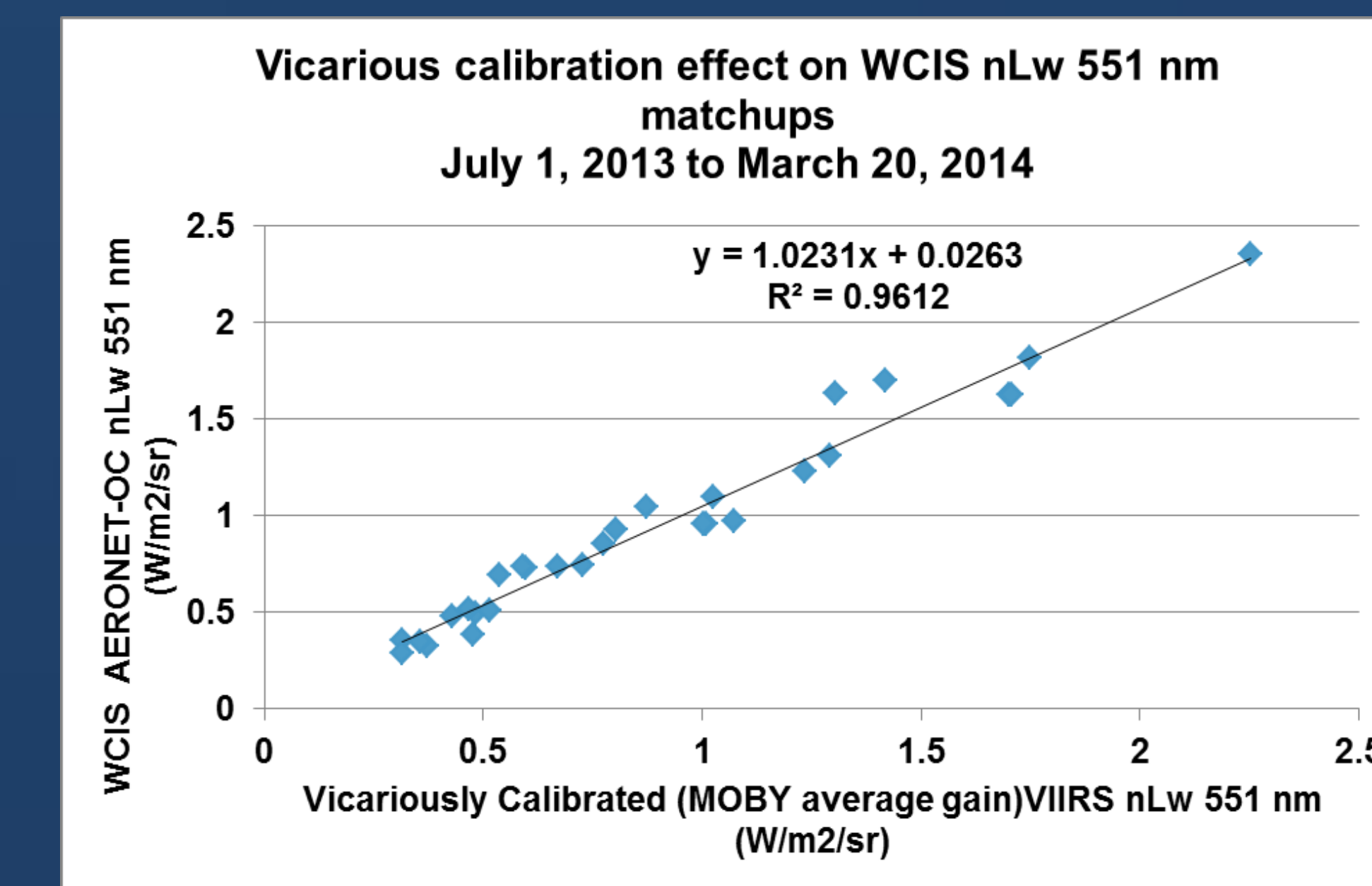
1. Accumulate coincident matchups (+- 3hrs) of satellite and in situ data (blue markers).
2. Apply screening criteria to coincident collections (green and yellow markers).



5. Calculate an average gain for each site: MOBY vicarious calibration and WCIS VGA. Although there is no statistical difference between the vicarious calibration and VGA gains, the MOBY site provides less uncertainty.



6. Apply Vicarious calibration and VGA using APS and look at effects on the nLw retrievals



SCREENING CRITERIA IS CRITICAL!
As mission average calibrations have been shown to reach stability after 20 – 40 high quality calibration samples^{4, 8} consideration is given to balance the strictness of removal criteria and preservation of sample size.

Vicarious calibration
MOBY (January 2012 to April 2013)
Satellite constraints: within 3 hours of over pass and **no** flags allowed on satellite imagery
Exclusion criteria: wind speed must be less than 8 m/s, the maximum aerosol optical thickness (AOT) must be less than 0.2 as measured by the MOBY buoy, the nLw values must be between 0.001 and 3.0, the maximum solar zenith angle = 70 degrees and maximum sensor zenith angle = 56 degrees.

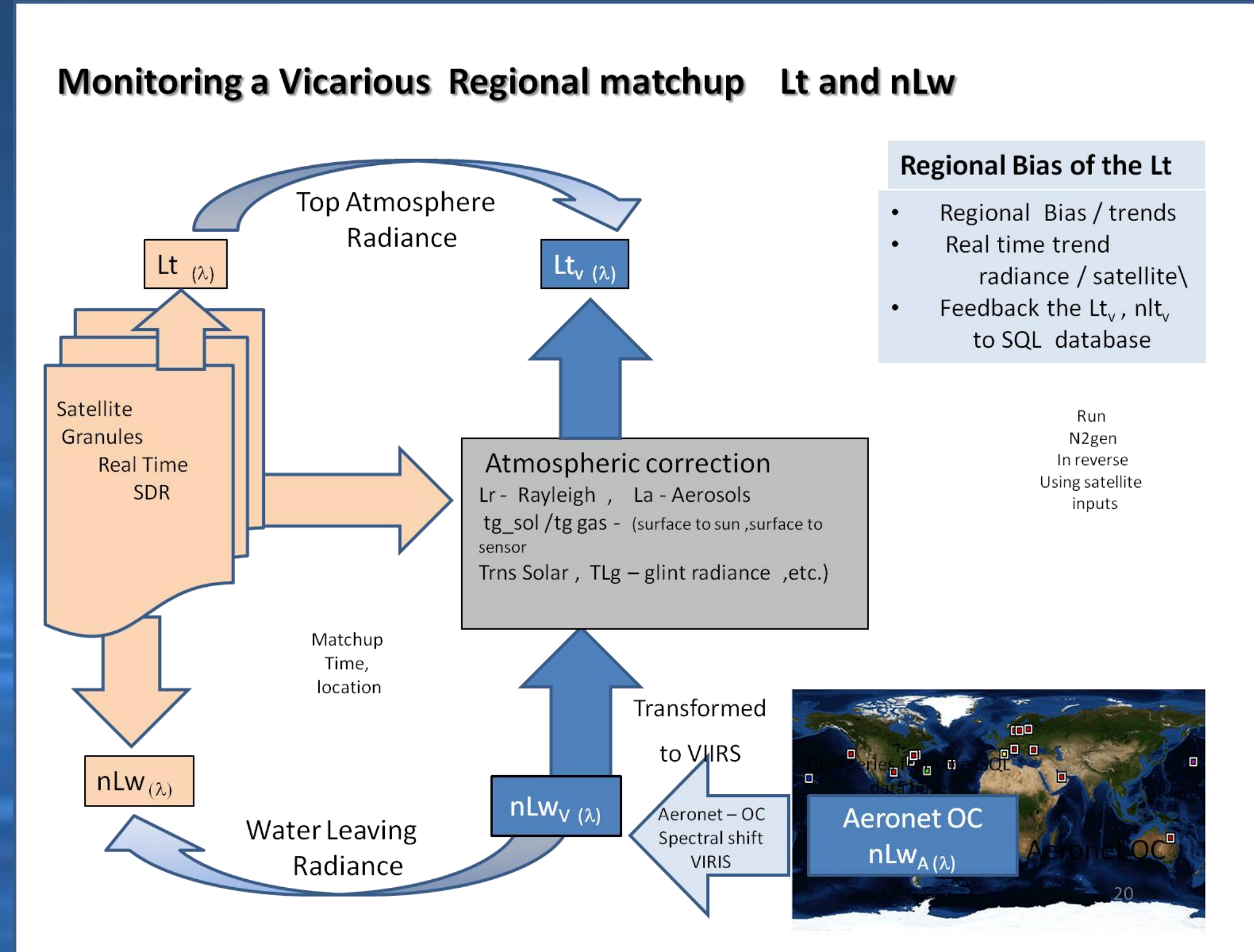
Regional VGA (relaxed constraints)
WaveCIS AERONET-OC (Jan 2013 to Mar 2014)
Satellite flags: within 3 hours of overpass, atmospheric failure, failure, cloud/ice, high LT, seaice, high satellite zenith angle, high solar zenith angle, epsilon out of range, high glint, max AER iteration, high polarization, moderate sun glint, and coccolithophores
Exclusion criteria: wind speed must be less than 8 m/s, the maximum aerosol optical thickness (AOT) must be less than 0.2 as measured by the AERONET, the nLw values must be between 0.001 and 3.0, the maximum solar zenith angle = 70 degrees and maximum sensor zenith angle = 56 degrees.

gain set	wavelength	regression equation	R ²
MOBY gains	nLw 410 nm	y = 0.6131x + 0.1962	R ² = 0.4085
WCIS gains	nLw 410 nm	y = 0.8684x + 0.1915	R ² = 0.2313
MOBY gains	nLw 443 nm	y = 0.8955x + 0.1248	R ² = 0.7199
WCIS gains	nLw 443 nm	y = 0.96x + 0.0819	R ² = 0.7745
MOBY gains	nLw 486 nm	y = 1.083x + 0.0225	R ² = 0.9096
WCIS gains	nLw 486 nm	y = 1.105x + 0.0215	R ² = 0.9317
MOBY gains	nLw 551 nm	y = 1.0231x + 0.0263	R ² = 0.9612
WCIS gains	nLw 551 nm	y = 1.0192x + 0.0087	R ² = 0.9671
MOBY gains	nLw 671 nm	y = 0.8689x + 0.0141	R ² = 0.9337
WCIS gains	nLw 671 nm	y = 0.8853x + 0.0389	R ² = 0.9453

The table to the left summarizes the regression statistics calculated for the MOBY and WaveCIS gains applied during image processing on the nLw retrievals by the satellite (x) compared to the *in situ* (y) as illustrated in the figures above. The results show minor improvements for using the green water VGA at all wavelengths except 486nm however, the slopes are not statistically different.

slopes closer to 1 indicate better calibration while higher r2 indicates better statistical fit of the regression

3. Calculate vLt/Lt for each matchup.



Extensively published by NASA's Ocean Biology Program Group (OBPG), the vicarious calibration is an inversion of the forward processing algorithm resulting in a ratio of predicted (vLt) to observed TOA radiance (Lt).

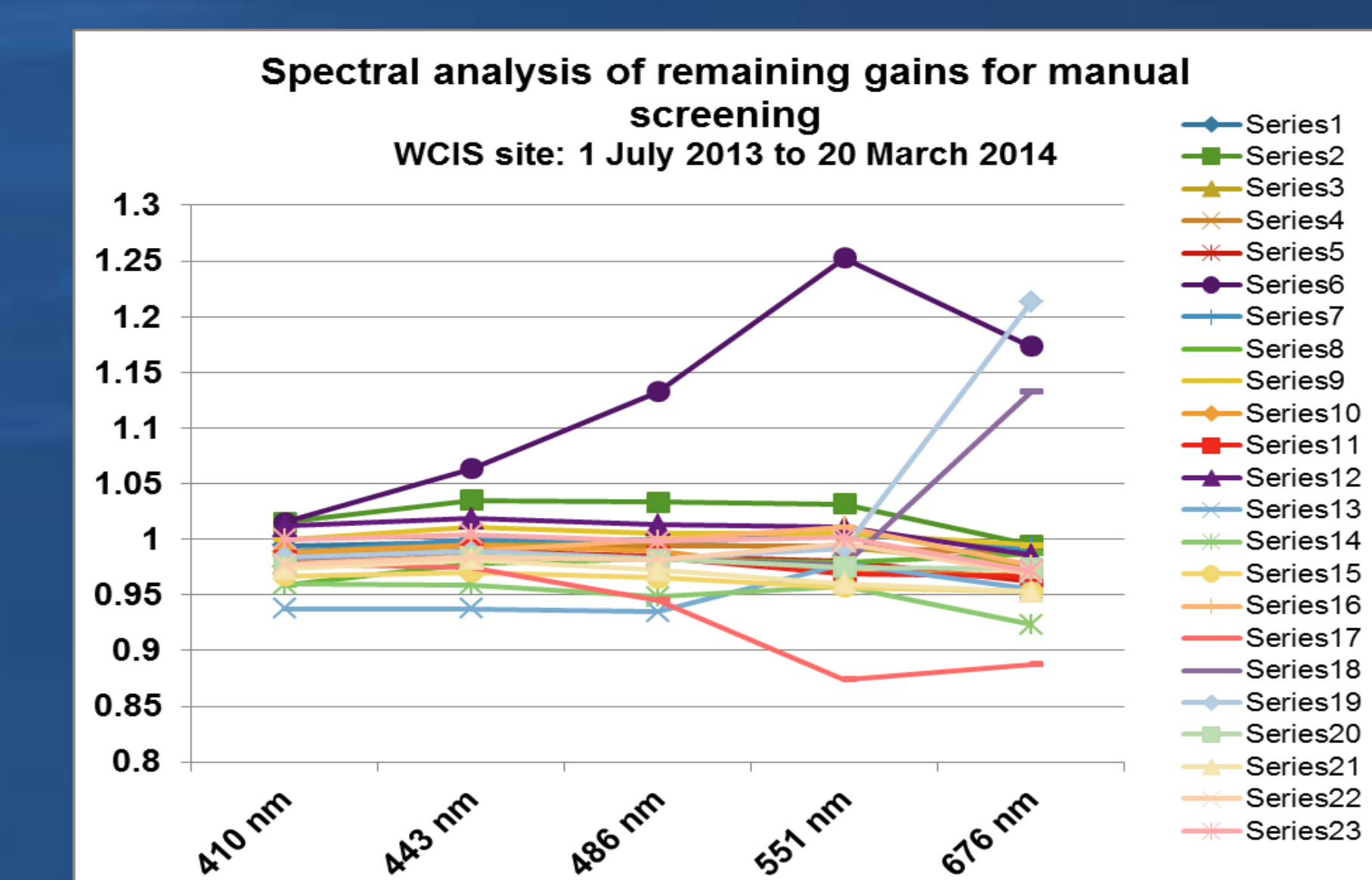
$$\text{gain}(\lambda) = \text{vLt}(\lambda) / \text{Lt}(\lambda)$$

- APS processing employs:
- standard atmospheric correction of Gordon/Wang
 - Stumpf NIR iteration
 - Initial processing assumes perfect sensor calibration (unity gains)
 - save the atmospheric components (Lr, La, transmittances, polarization correction, etc.) and pointing-angles
 - nLw from the *in situ* sensor is run through the inversion where the atmospheric components are added back creating an expected Lt from the view of the VIIRS (vLt(λ))

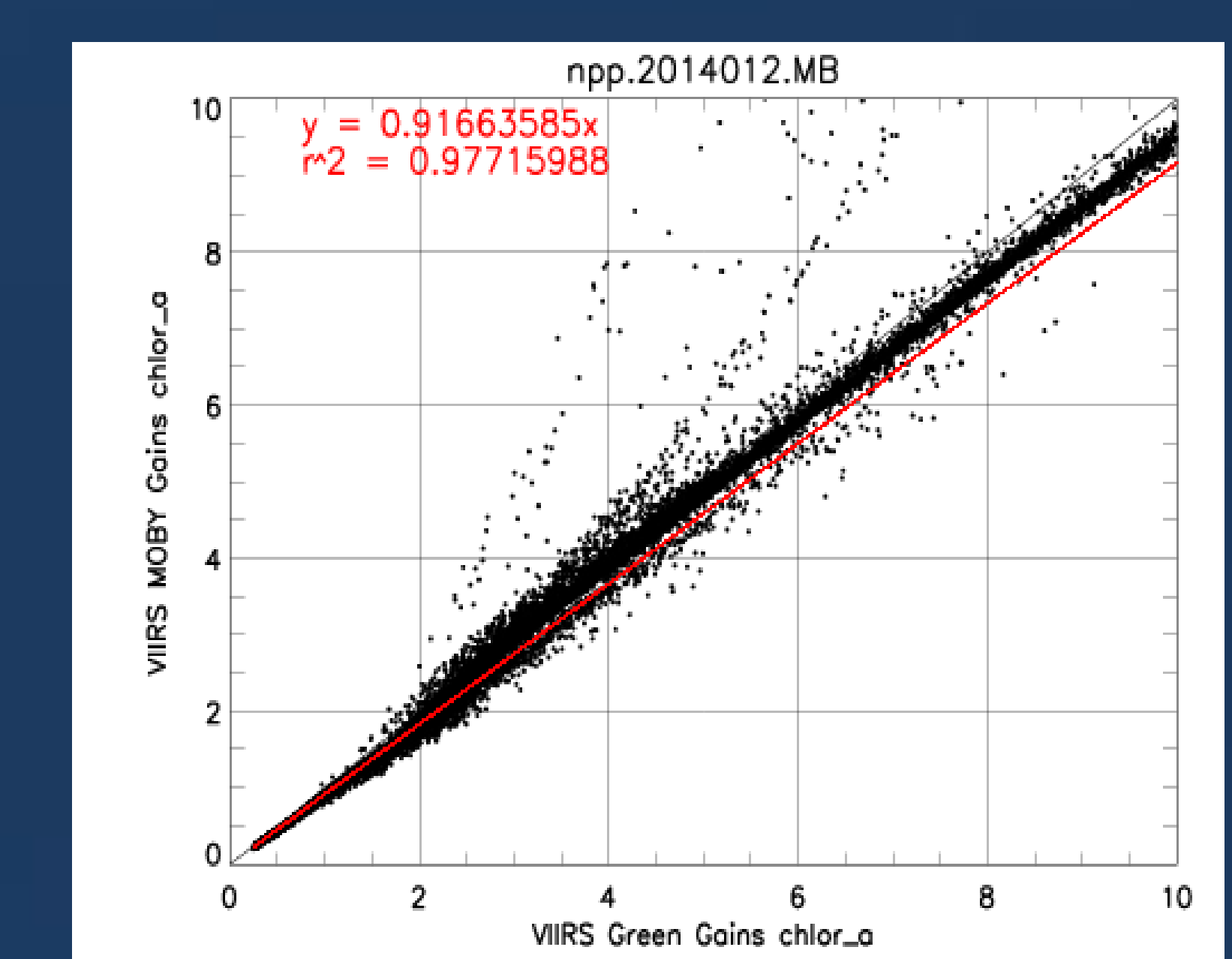
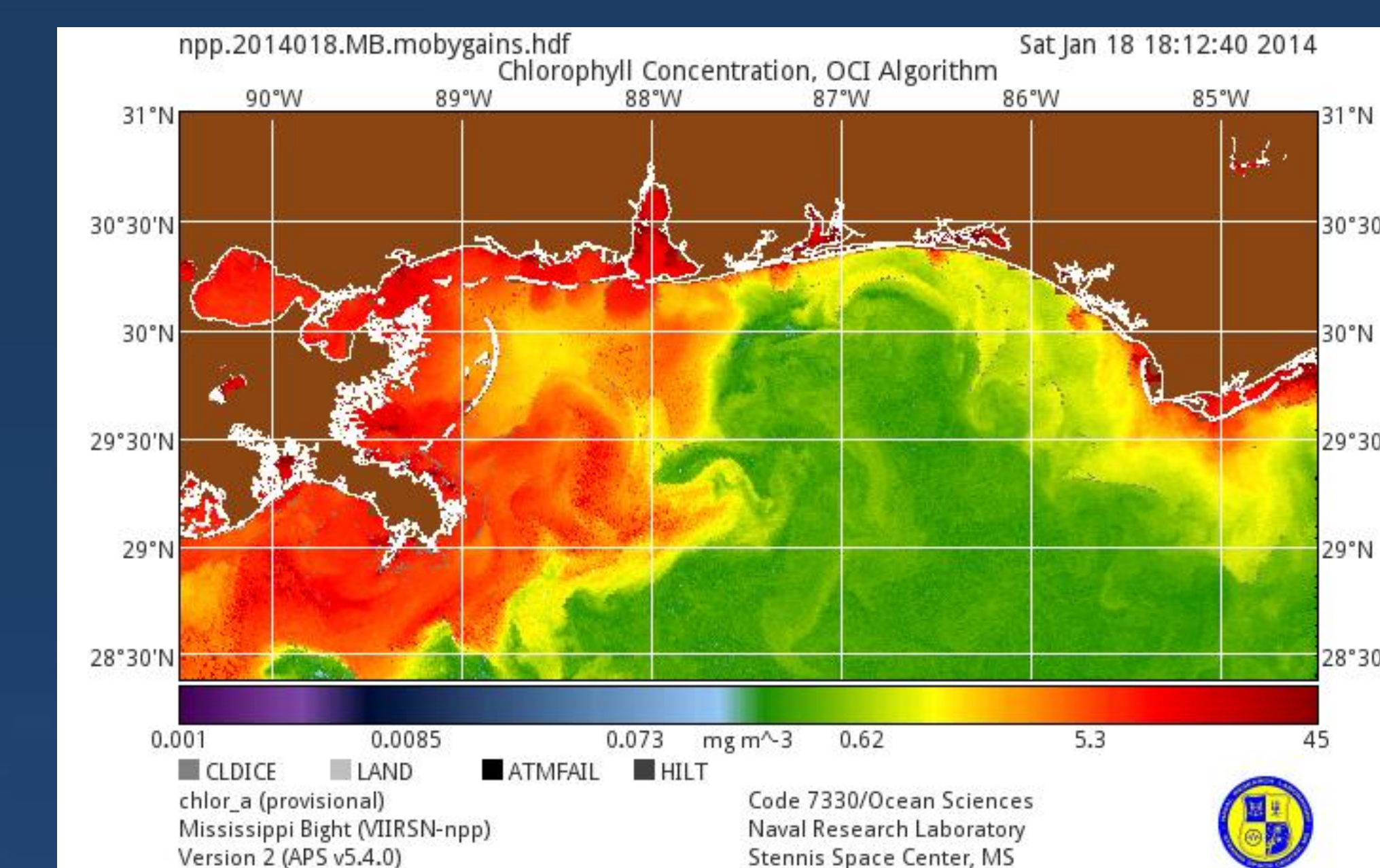
In a perfect system in which all components are computed accurately, the vLt and original Lt should have a ratio of 1.0.

4. Plot spectral gains and remove anomalies.

This leads to removal of Series 6, 17, 18, and 19.



7. Effects of Vicarious Calibration and VGA on chlorophyll products



8. Conclusions:

- The procedure addresses selection criteria for optimizing data quality in a near real-time situation, allowing for vicarious calibration and regional VGA to be established for each of the VIIRS visible channels.
- Assembling an optimum data set for determining vicarious gains is time consuming and excludes considerable data: 69% for MOBY and 72% for WaveCIS site
- The standard deviation of the adjustment gains was deemed acceptable and the screening procedure is critical for determining the adjustment.
- Due to the uncertainties in the vicarious calibration and VGA processes there was not a statistically significant difference in the blue water (g01) and green water (g02) gains, however; as expected, the blue water gains exhibit lower standard deviations per channel.
- Optimizing selection of matchup points provides a strong relationship between satellite and *in situ* nLw(λ) and chl for both gain set, MOBY or WaveCIS.

ACKNOWLEDGEMENTS: We would like to acknowledge the support of both our Navy and NOAA sponsors. We appreciate the efforts Dr. Ken Voss and the MOBY team for provision of MOBY site data and assistance with data quality determinations. We thank Dr. Bill Gibson and Dr. Alan Weidemann for their efforts collecting the WaveCIS AERONET-OC data. Additional assistance with establishing Level 1.5 data quality control was provided by Dr. Giuseppe Zibordi and Ilya Slutsker. Satellite data was provided by NOAA CLASS with calibration insight provided by the JPS SDR team.

REFERENCES

[1] Arnone, R., Fargion, G., Lawson, A., Martinolich, P., Lee, Z., Davis, C., Ladner, S., Bowers, J., Zibordi, G., "Monitoring and Validation of Ocean Water Leaving Radiance and Inter-Satellite Continuity," 2012 Ocean Sciences Meeting, Session 121, Salt Lake, UT, (2012).
 [2] Clark, D., et al., "MOBY: A Radiometric Buoy for Performance Monitoring and Vicarious Calibration of Satellite Ocean Color Sensors: Measurements and Data Analysis Protocols," NASA Tech. Memo. 2003-210004 Rev 4, Vol. VI, NASA Goddard Space Flight, Greenbelt, Maryland, 3-34, (2003).
 [3] Fargion, G., R. Arnone, et al., "Real Time VIIRS Cal/Val With Satellite Validation Navy Tool (SNAV-T)", 2012 Ocean Sciences Meeting, Session 121, B294, (2012).
 [4] Franz, B. S., Bailey, P., Werdell, C., McClain, C., "Sensor-independent approach to the vicarious calibration of satellite ocean color radiometry," Applied Optics 46 (22), 5068-5082, (2007).
 [5] Gordon, H. R. and M. Wang, "Retrieval of water-leaving radiance and aerosol optical thickness over the oceans with SeaWiFS: A preliminary algorithm," Applied Optics 33, 443-452 (1994).
 [6] Hooker, S.B., C. McClain and A. Manunno, "A Comprehensive Plan for the Long-Term Calibration and Validation of Oceanic Biogeochemical Satellite Data," NASA/SP-2007-214152, 1-40pp, (2007).
 [7] Shumpf, R. P., R. A. Arnone, J. R. W. Gould, P. M. Martinolich, and V. Rastrih-mahakul, "A partially coupled ocean-atmosphere model for retrieval of water-leaving radiance from SeaWiFS in coastal waters," NASA Tech. Memo. 206892, National Aeronautics and Space Administration, Goddard Space Flight Center, Greenbelt, MD (2005).
 [8] Werdell, P.J., S.W. Bailey, B.A. Franz, A. Morel, and C.R. McClain, "On-orbit vicarious calibration of ocean color sensors using an ocean surface reflectance model," Applied Optics 46 (23), (2007).

Assimilation of VIIRS AOT EDR for Air Quality Analyses and Forecasts: A Comparison with the Assimilation of MODIS AOT

Zhiqian Liu (liuz@ucar.edu), Junmei Ban, Hui-Chuan Lin

National Center for Atmospheric Research, Boulder, CO, USA

WRF/Chem and GSI Aerosol Data Assimilation

- WRF/Chem is an online-coupled meteorology-chemistry model
 - allow aerosol/chemistry feedback to meteorological fields.
- 3D mass concentrations of 15 aerosol variables from the GOCART aerosol module within the WRF/Chem model are analysis variables in GSI
 - Hydrophobic and hydrophilic organic carbon (OC₁, OC₂)
 - Hydrophobic and hydrophilic black carbon (BC₁, BC₂)
 - Sulfate, Dust in 5 particle-size bins, Sea salt in 4 particle-size bins
 - P₂₅: unspciated aerosols contributing to PM_{2.5}
- Aerosol background error covariance statistics
 - “NMC” method, univariate correlation, no cross-correlation b.w. variables
- Allow the assimilation of MODIS/VIIRS AOT/Radiance and surface PM_{2.5}/PM₁₀
- Observation operator: CRTM for MODIS/VIIRS AOT and visible-band radiances
- Multiple data assimilation methods can be used: 3DVAR, EnKF and Hybrid
- Also allow simultaneous assimilation of aerosol and meteorological observations

Experiment design

Domain : East Asia
 Resolution : horizontal 20km; vertical 57L
 grid points : 240x200
 Study Period : 2013-11-06 ~ 2013-12-06; 06 UTC analyses with 24h cycle
 Spin up : 10 days from 2013-11-01
 Background error : (48hfc-24hfc) from control experiment

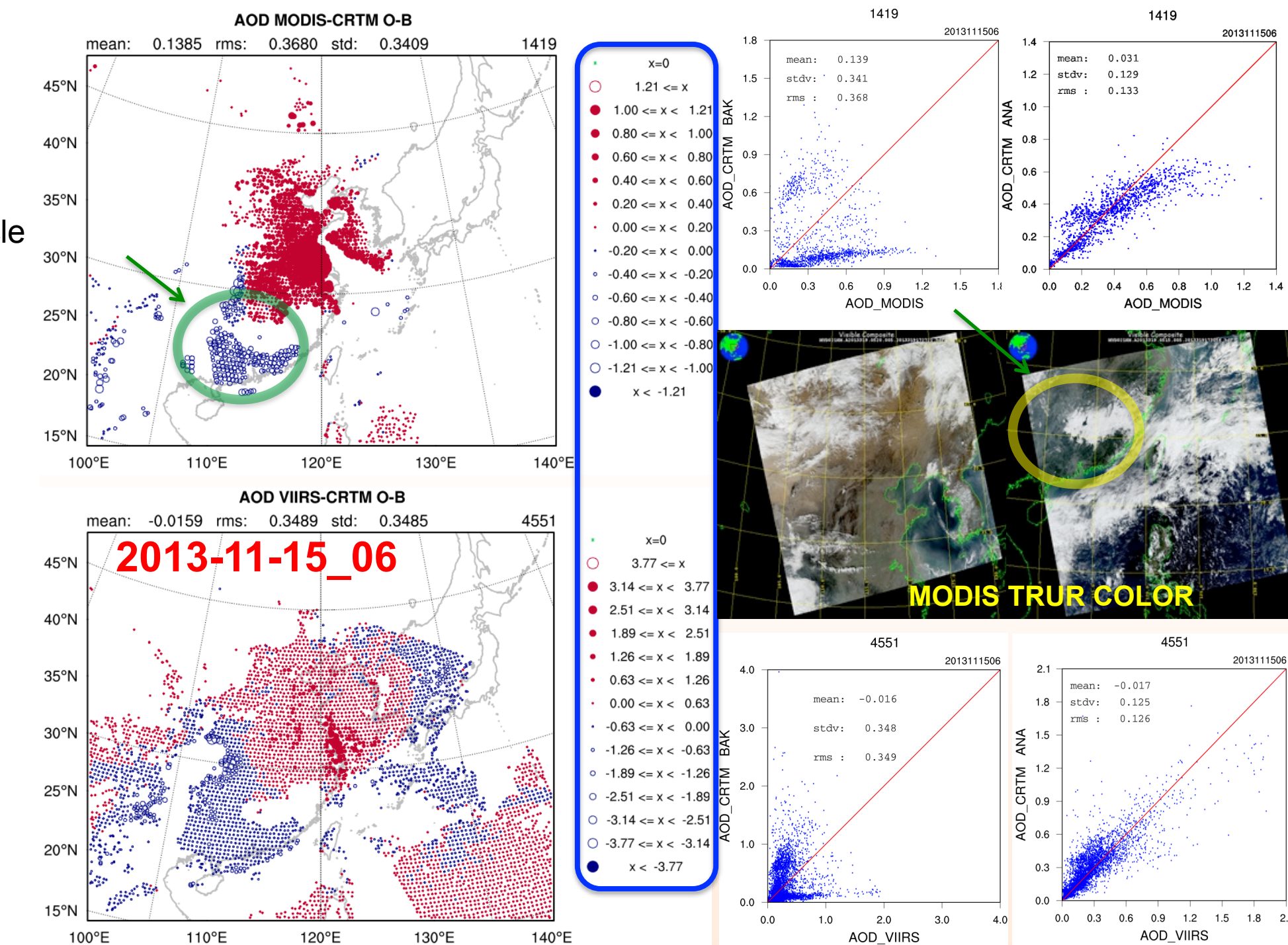
WRF/Chem Emission : Global EDGAR + Streets (monthly variation)

Satellites overpass : around 06 UTC
 Thinning : 40km
 Time window : ±1.5h

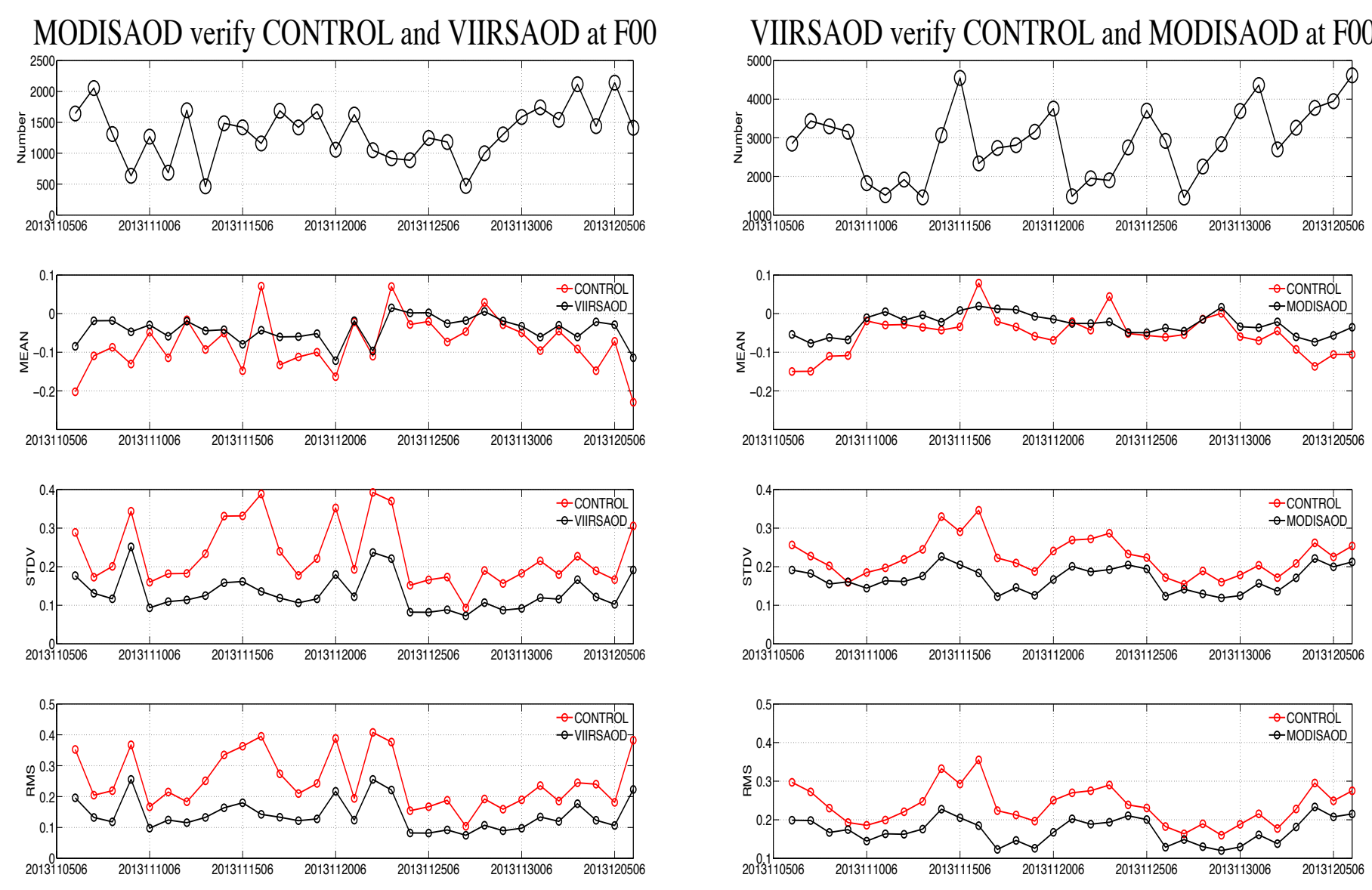
3 cycling experiments:

- Control: No AOT DA, continued aerosol forecasts
- VIIRS AOT DA: assimilate VIIRS Ch 4 AOT @555nm
- Aqua MODIS AOT DA: assimilate MODIS Ch 4 AOT @550nm

Meteor. initial conditions are the same for 3 exps (from GFS at 06 UTC).
 Ran 48-h forecasts from 06 UTC, 24-h forecast serve as the background for next cycle's analysis. Hourly forecast output for verification.

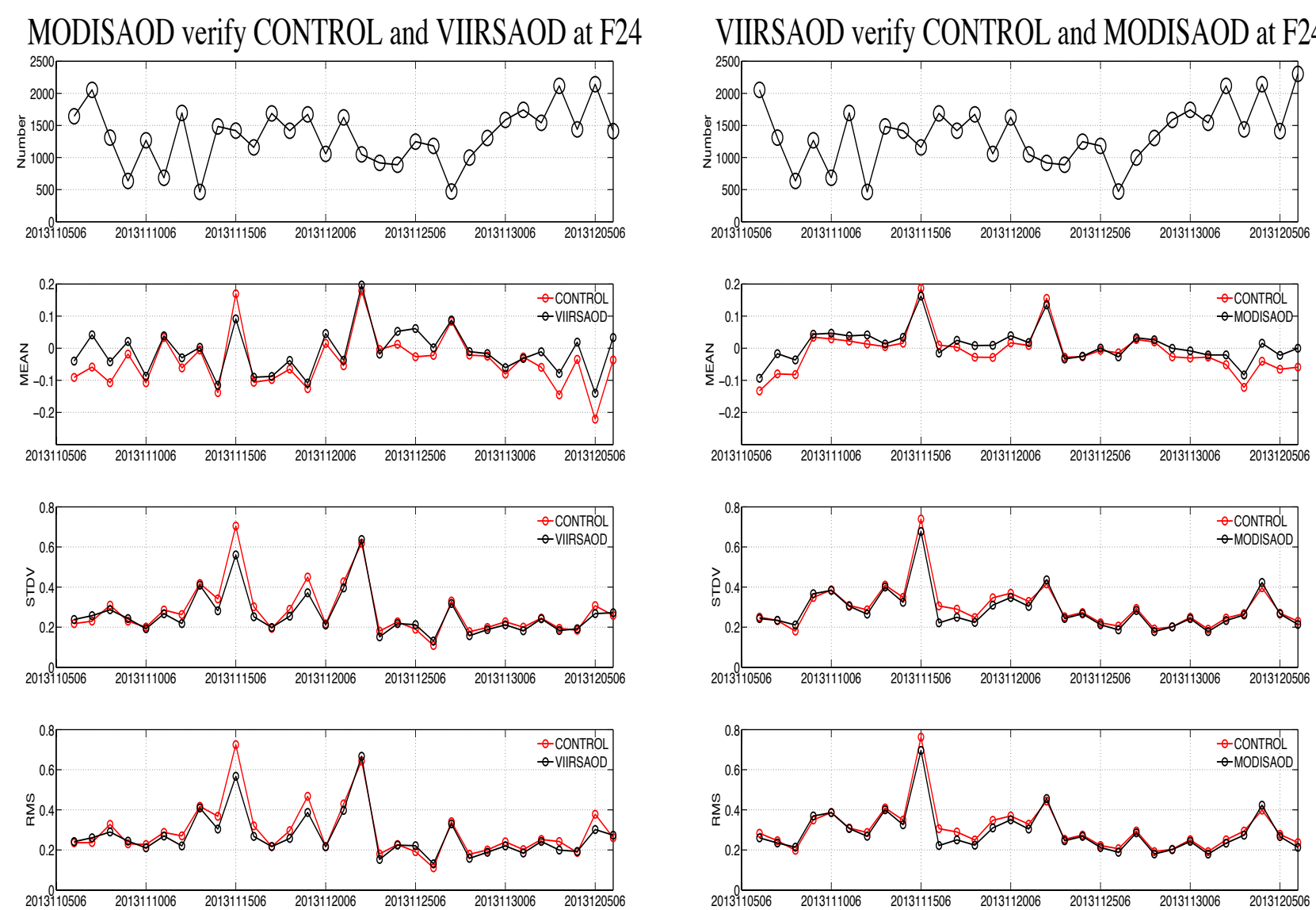


AOT Cross-Verification: analysis

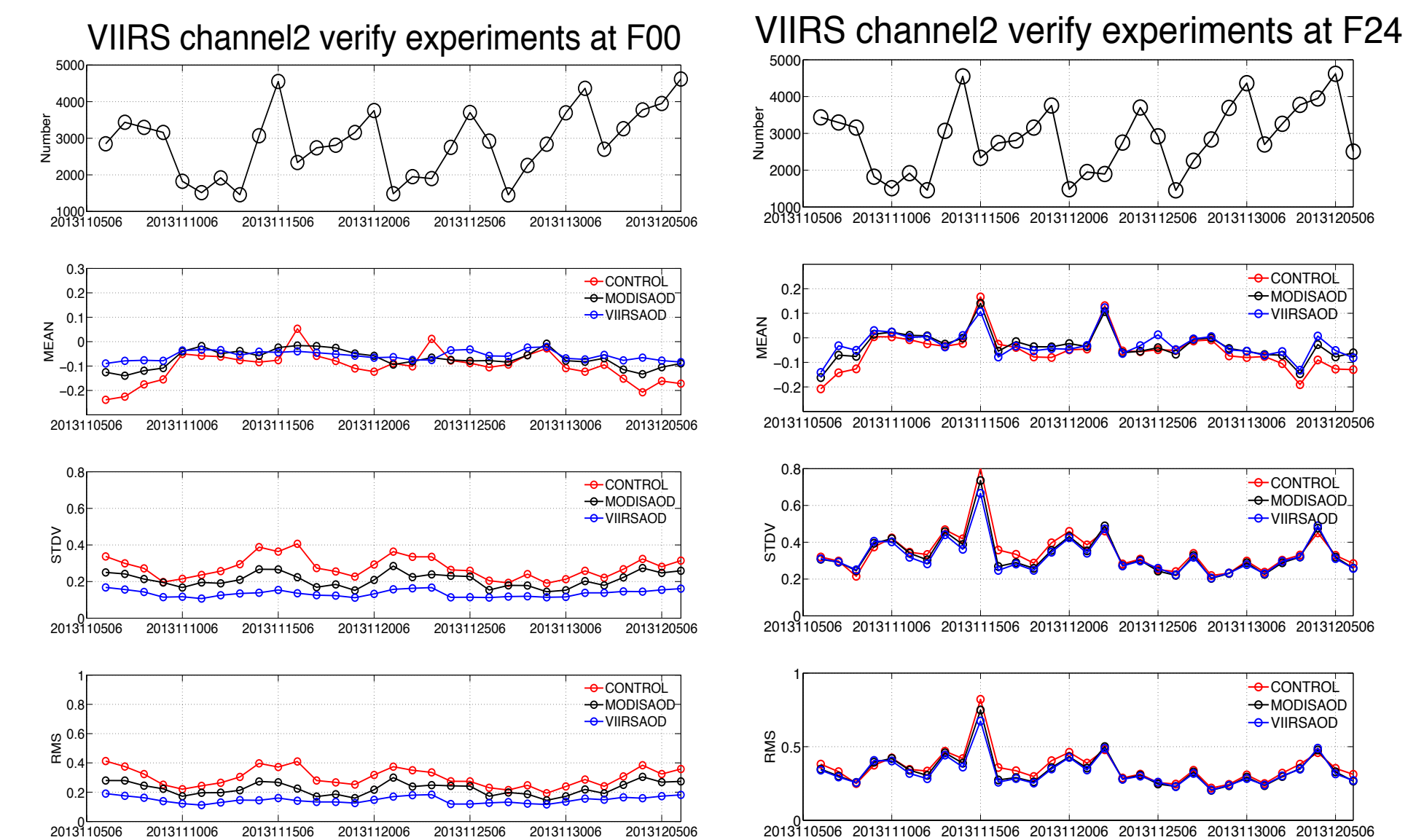


VIIRS AOT DA slightly better than MODIS AOT DA

AOT Cross-Verification: 24h FC



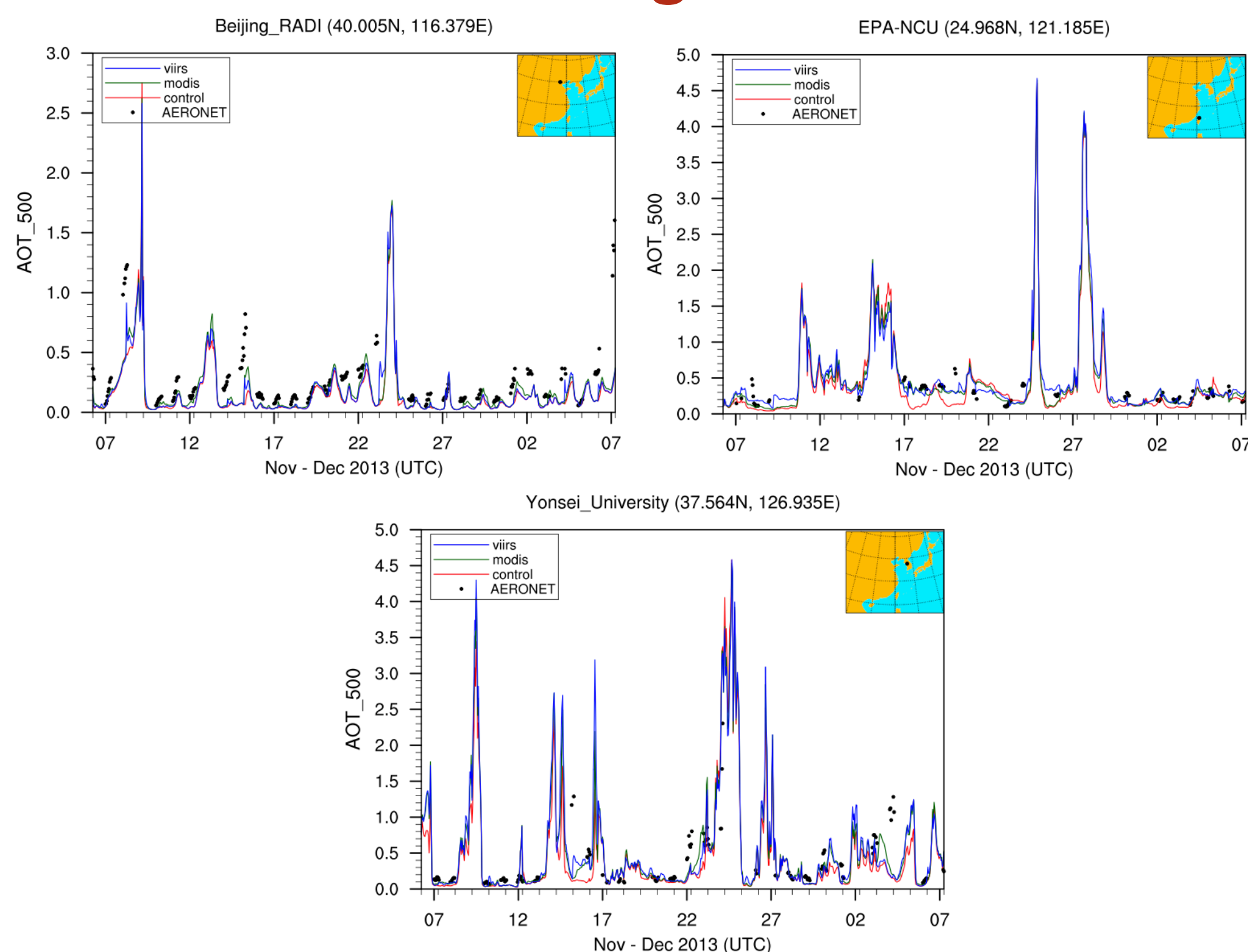
Verification using VIIRS Ch2 AOT



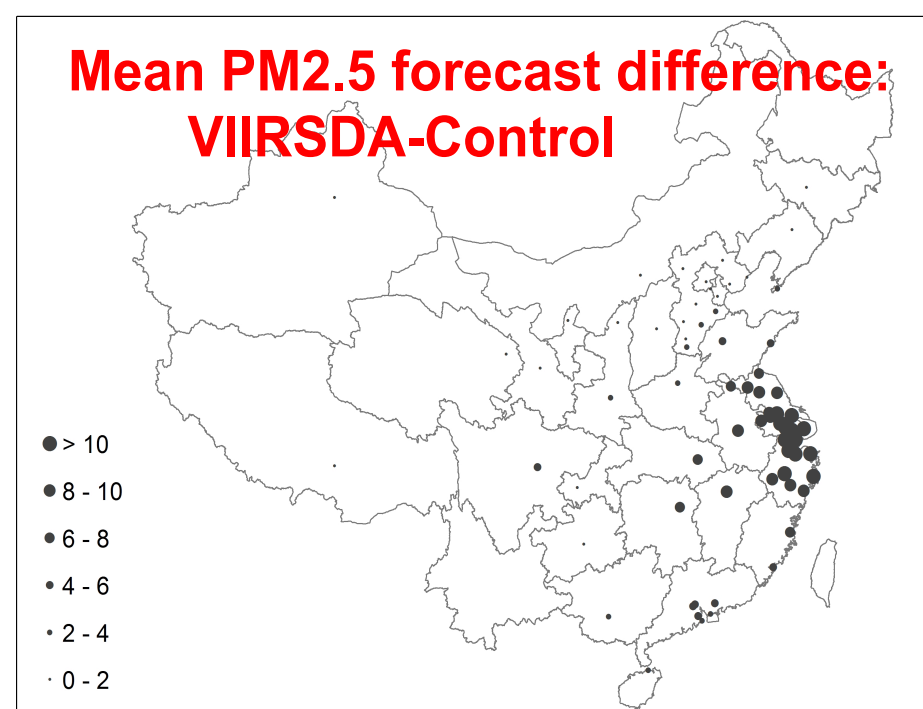
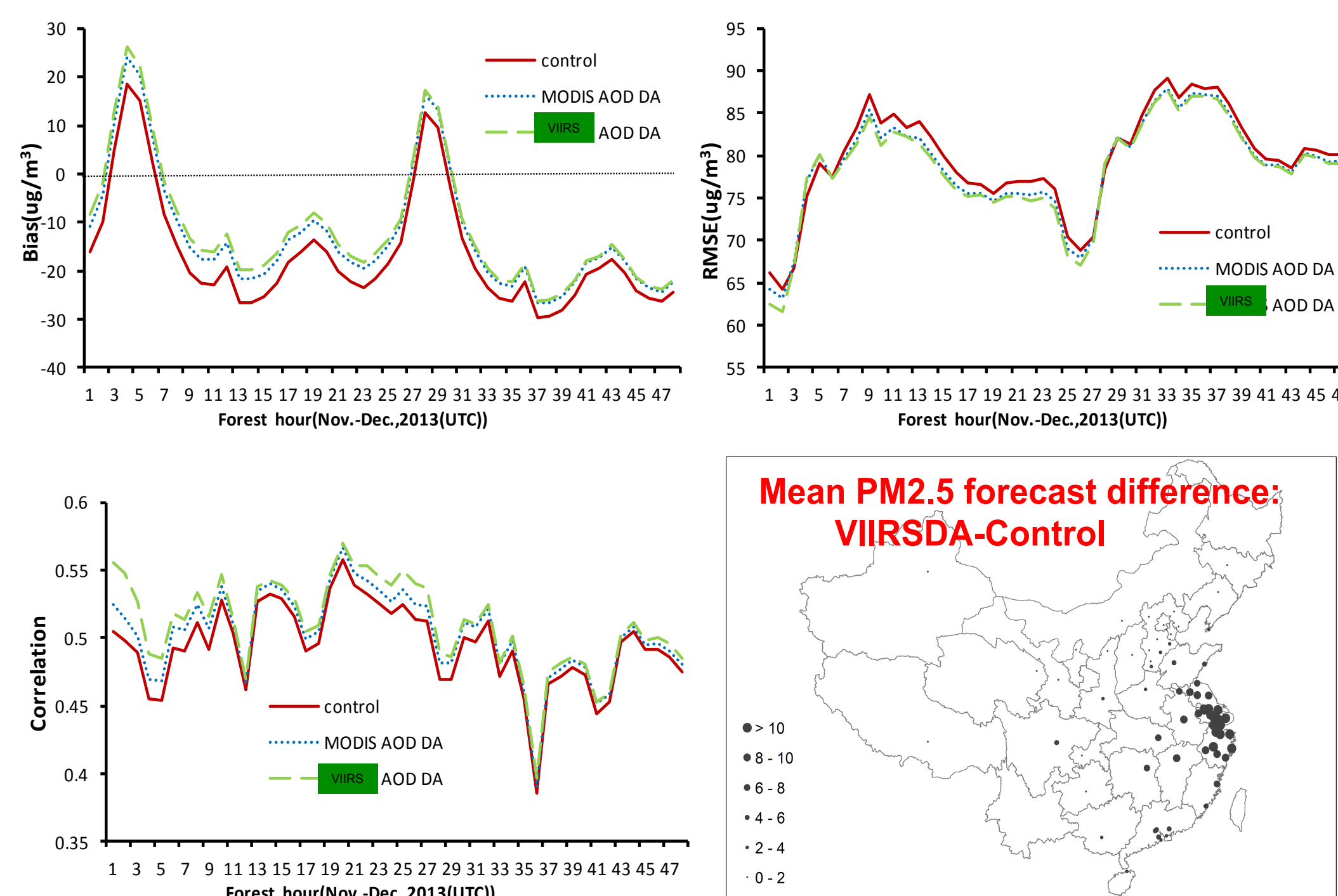
Summary

- VIIRS AOT generally has better coverage than MODIS AOT from Aqua over East Asia for the data marked as the best quality
- Assimilating MODIS (Aqua only) or VIIRS AOT improved aerosol analysis and subsequent forecasts
- Assimilating VIIRS AOT resulted in slightly better results than assimilating Aqua MODIS AOT.

Verification using AERONET AOD



Verification using surface PM2.5



Future Plan

- Assimilate MODIS and VIIRS AOT together
- Assimilate multiple channels VIIRS AOT
- Improve quality control and observation error specification
- Direct assimilation of VIS/NIR radiances
- Extend from regional to global applications

ENHANCED MONITORING OF BIO-OPTICAL PROCESSES IN COASTAL WATERS USING HIGH SPATIAL RESOLUTION CHANNELS ON SNPP-VIIRS

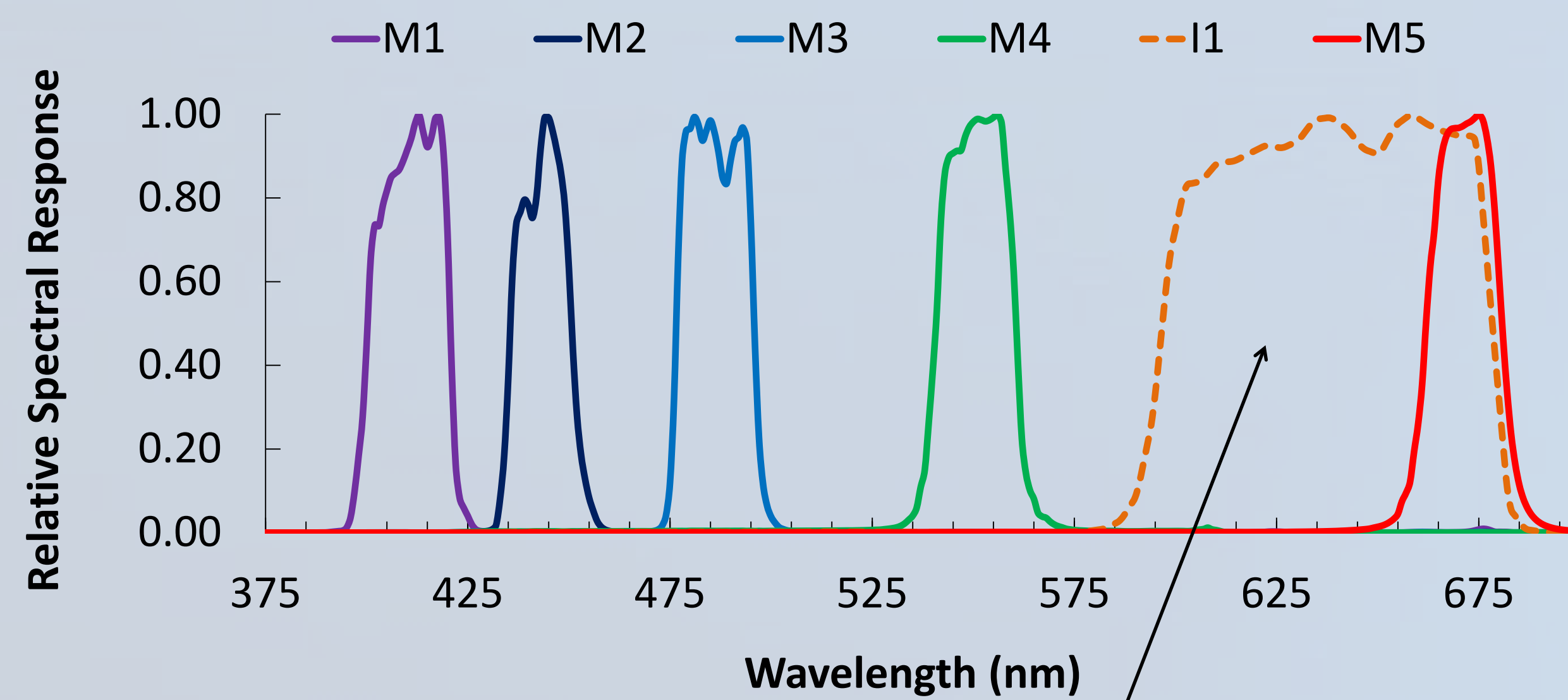
Ryan A. Vandermeulen¹, Robert Arnone¹, Sherwin Ladner², Paul Martinolich³

¹University of Southern Mississippi, Department of Marine Science, Stennis Space Center, MS 39529

²Naval Research Laboratory, Stennis Space Center, MS 39529 ; ³QinetiQ North America, Stennis Space Center, MS 39529

OBJECTIVES

- Demonstrate a spatially improved ocean color product by combining the VIIRS 750-meter (M- channels) with the 375-m (I1-channel) to produce an image at a pseudo-resolution of 375-m.
- Apply a dynamic wavelength-specific spatial resolution ratio that is *weighted* as a function of the relationship between proximate I- and M-band variance at each pixel.



Challenge:
I-1 band is not panchromatic, must account for *dynamic variance* across the spectrum based on differing absorption and scattering coefficients at each λ .

APPROACH

- Determine wavelength specific spatial resolution ratio, $R(\lambda)$, for every pixel in image:

$$R(\lambda) = ([(I - I^*) \times (M(\lambda)_{CV} / I_{CV})_{\text{thresh}=1}] + I^*) / I^*$$

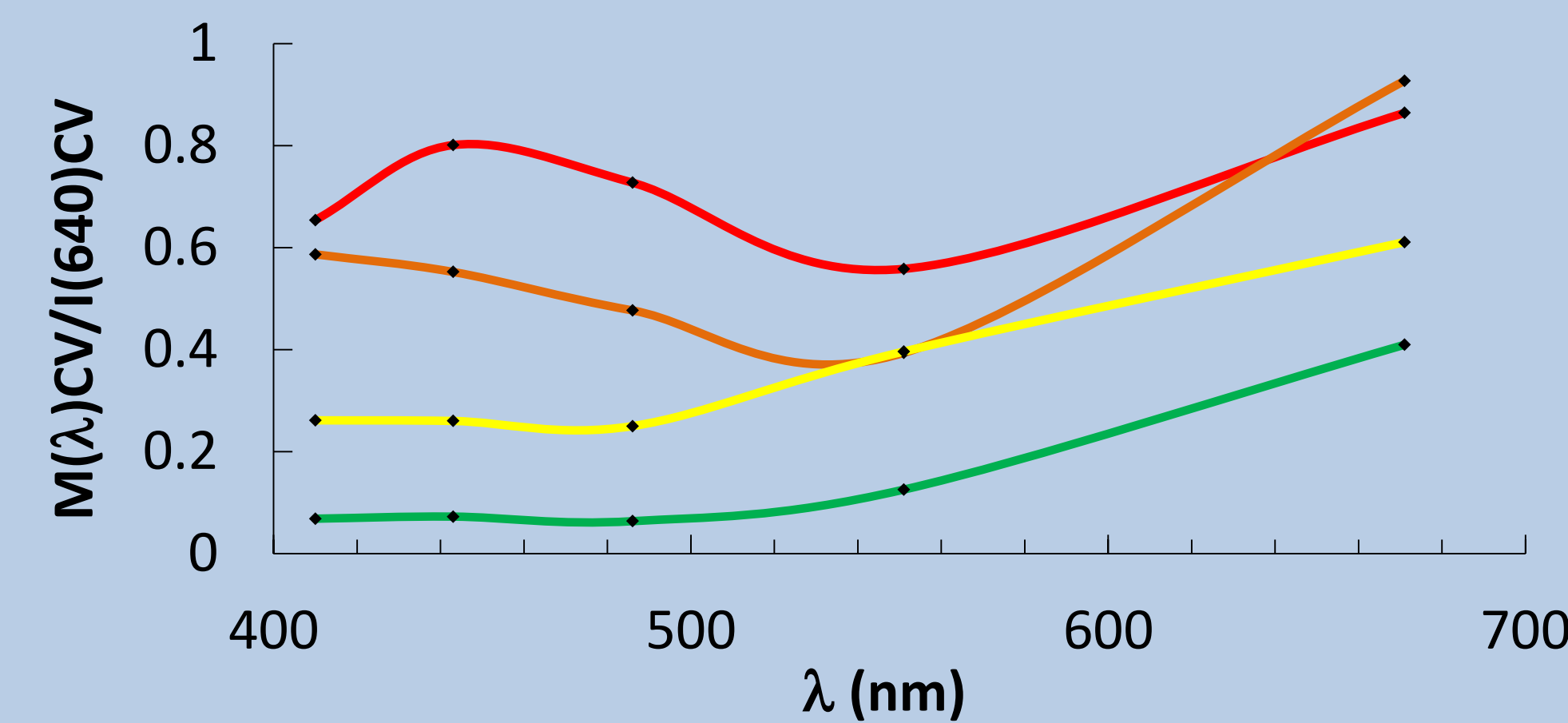
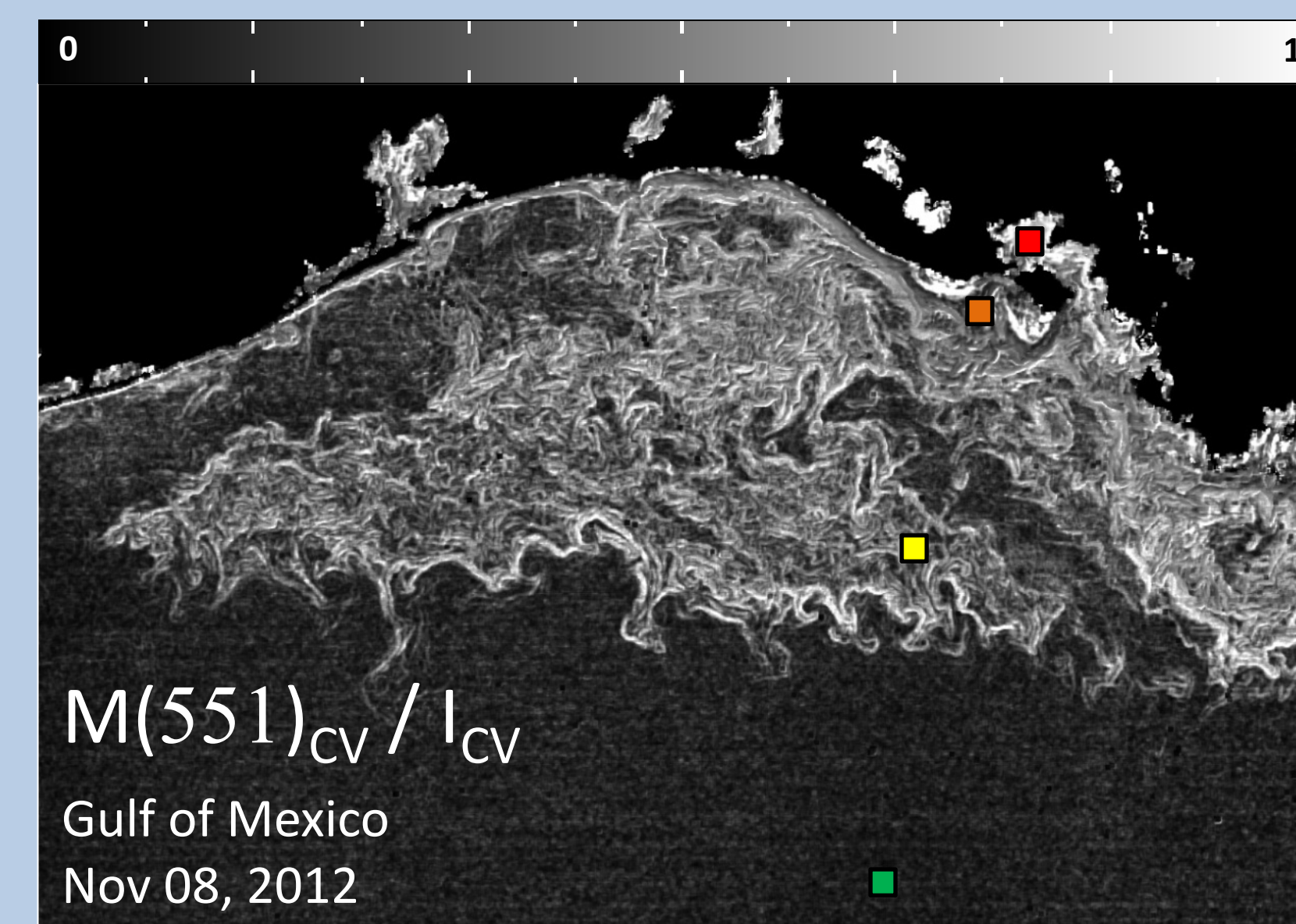
- I = VIIRS I1-Band (375-m resolution)
- I^* = VIIRS I1-Band (750-m resolution)
- $M(\lambda)_{CV}$ = VIIRS $M(\lambda)$ -Band coefficient of variance (5 x 5)
- I_{CV} = VIIRS I1-Band coefficient of variance (5 x 5)

- Apply *dynamic* ratio to each low-resolution M-band:



RESULTS & DISCUSSION

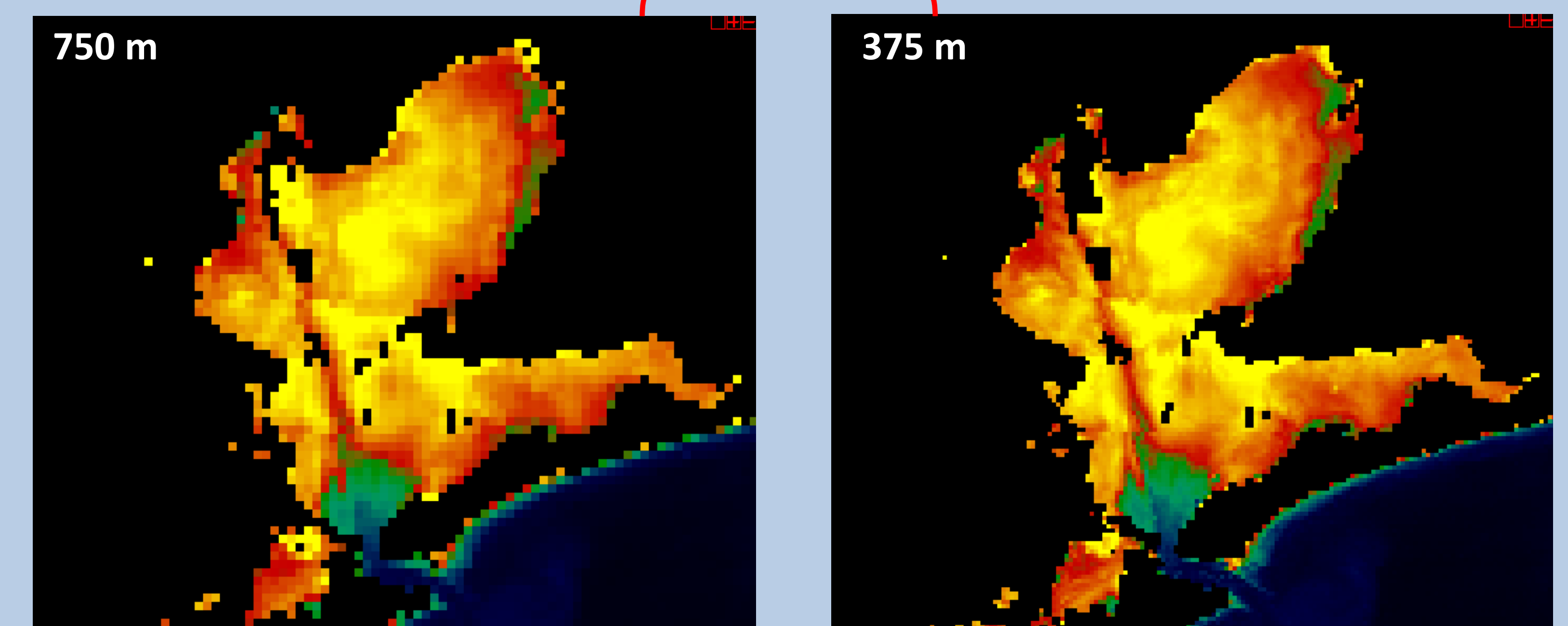
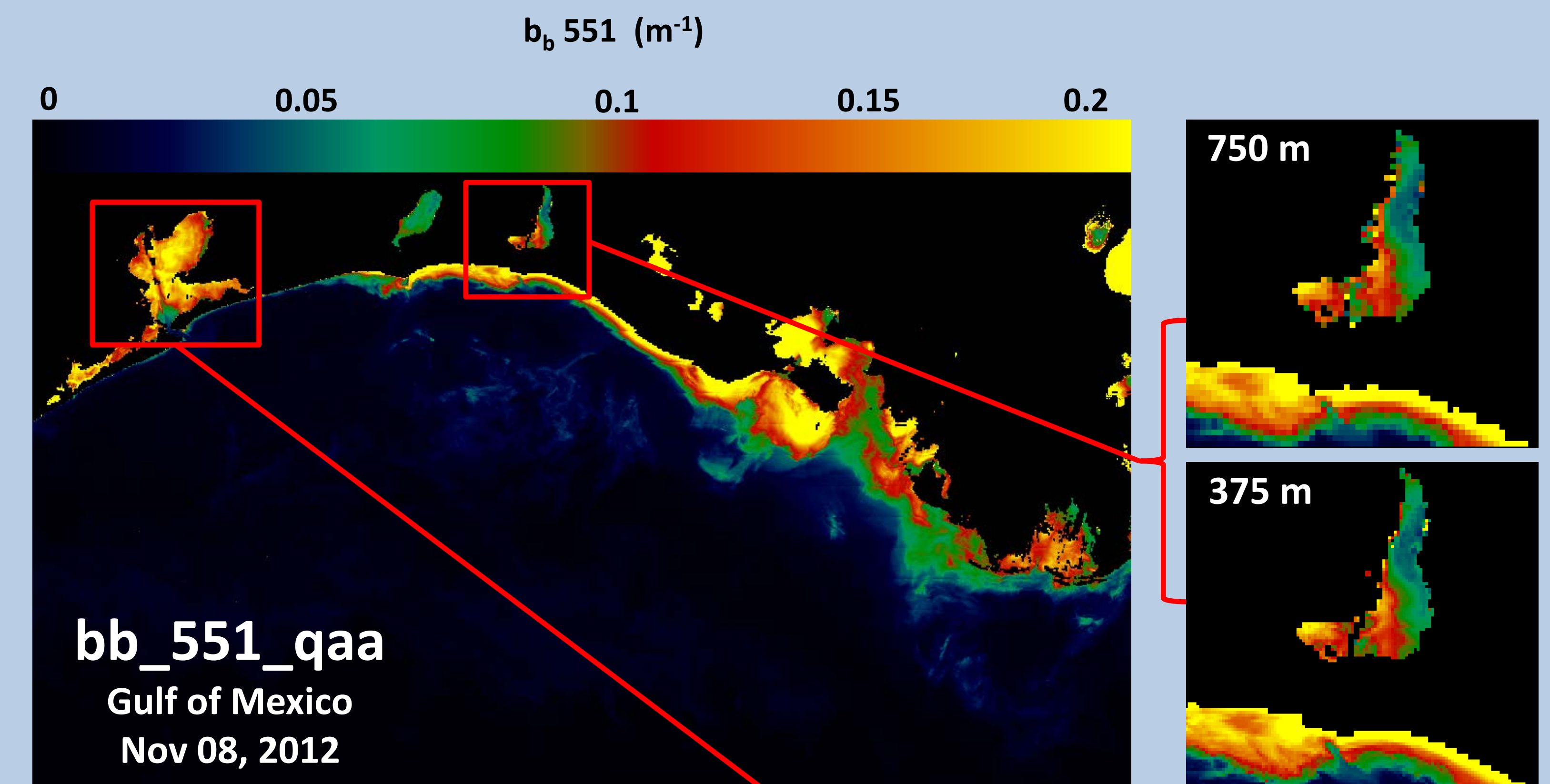
- By comparing variance across the interpolated spectrum with the variance of the high resolution band, a “sharpening probability map” is created.



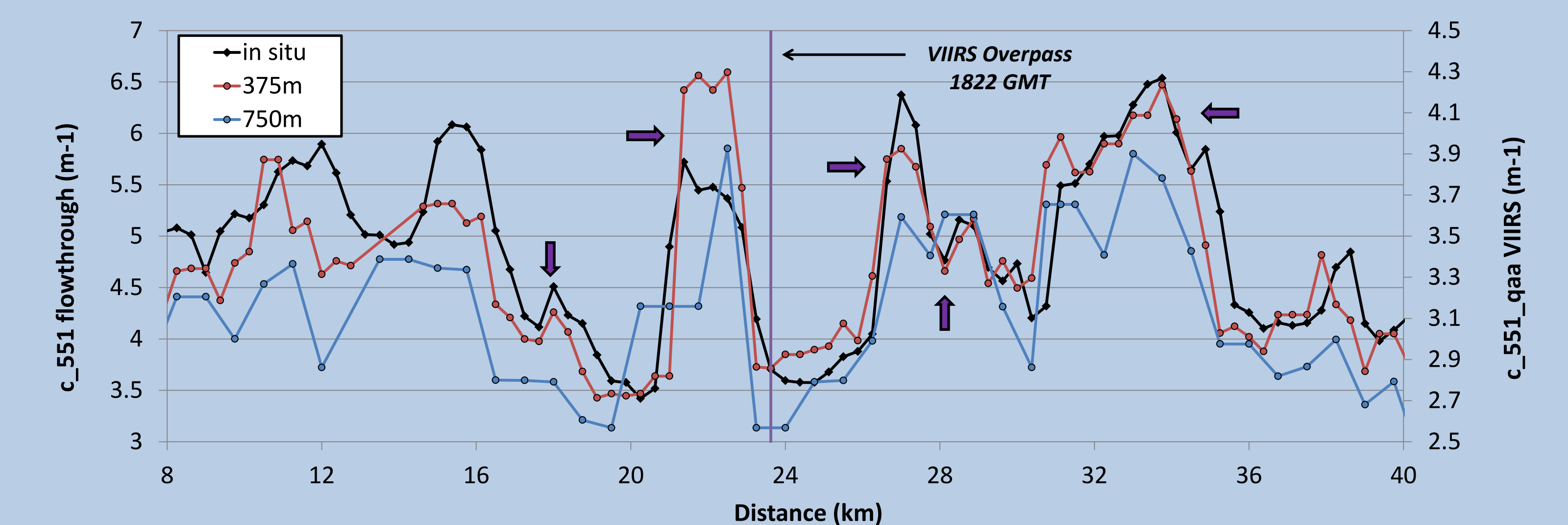
- At pixels where $M(\lambda)_{CV} / I_{CV}$ ratio is closer to 1 (i.e. covariance of M and I-channel), $M(\lambda)$ is sharpened according to I-band variance. Where divergence in variance occurs, the sharpening weight is adjusted in proportion to the difference in variance between the two bands.

λ	375-m		750-m	
	slope	r2	slope	r2
nLw_410	0.9943	0.8666	0.9892	0.8510
nLw_443	0.9746	0.9563	0.9688	0.9477
nLw_486	0.9648	0.9787	0.9823	0.9715
nLw_551	1.0092	0.9866	0.9941	0.9808
nLw_671	1.2532	0.9636	1.233	0.9528

- A scatter plot comparison of 44 *in situ* spectral reflectance measurements (Hyperpro, Sky-blocked approach [Lee et al. 2013], ASD, AERONET) to VIIRS satellite data processed at two different resolutions shows enhanced accuracy and precision at 375-m resolution compared to the native 750-m resolution of the sensor.



The sharpened water leaving radiance (nLw) radiance spectrum is placed into l2gen software, and processed to produce bio-optical products (bb_{551} shown above) at a higher spatial resolution. Notice the increased feature resolution for coastal bays and inland waters in the northern Gulf of Mexico.



An *in situ* flow through data set showing bean attenuation (551 nm) is binned to 375-m (black line) and compared to satellite products at 375-m (red) and 750-m (blue). Results show an increased feature detection for the VIIRS sensor.

Zhuo Wang¹, Yunyue Yu², Yuling Liu¹, Peng Yu¹

¹ University of Maryland, College Park; ² NOAA/NESDIS Center for Satellite Applications and Research, MD;

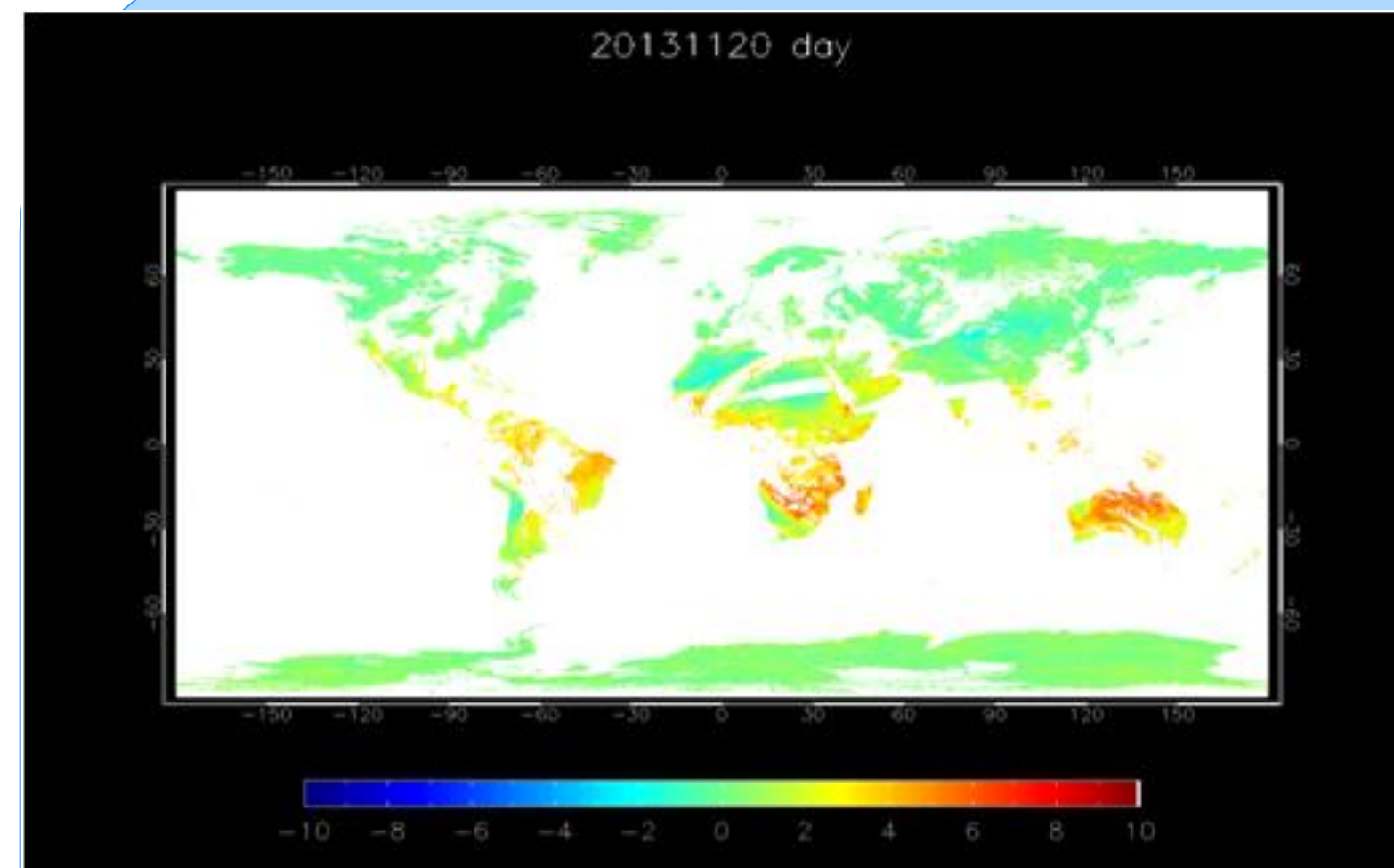
Introduction

The Visible Infrared Imager Radiometer Suite (VIIRS) on the Joint Polar Satellite System (JPSS) is one of the NOAA primary polar-orbiting satellite sensors. It can provide a series of Environmental Data Records (EDRs) including Land Surface Temperature (LST) product. The current VIIRS LST is generated from a surface-type dependent split window algorithm, which performs well for most surface types. There are still several issues which may cause uncertainties. Further improvements are necessary.

The satellites cross comparison between VIIRS and MODIS indicates that they agree with each other well under dry atmospheric condition, but there is some significant difference over wet regions mostly for daytime cases. In such regions, brightness temperature (BT) difference between split window channels is very large. We have performed some tests in different seasons over Australia to find the main factors related to high BT difference. We investigated the impacts of water vapor and emissivity on the LST retrieval. The results indicate that both water vapor and emissivity difference affect the BT difference, but water vapor is a dominant factor.

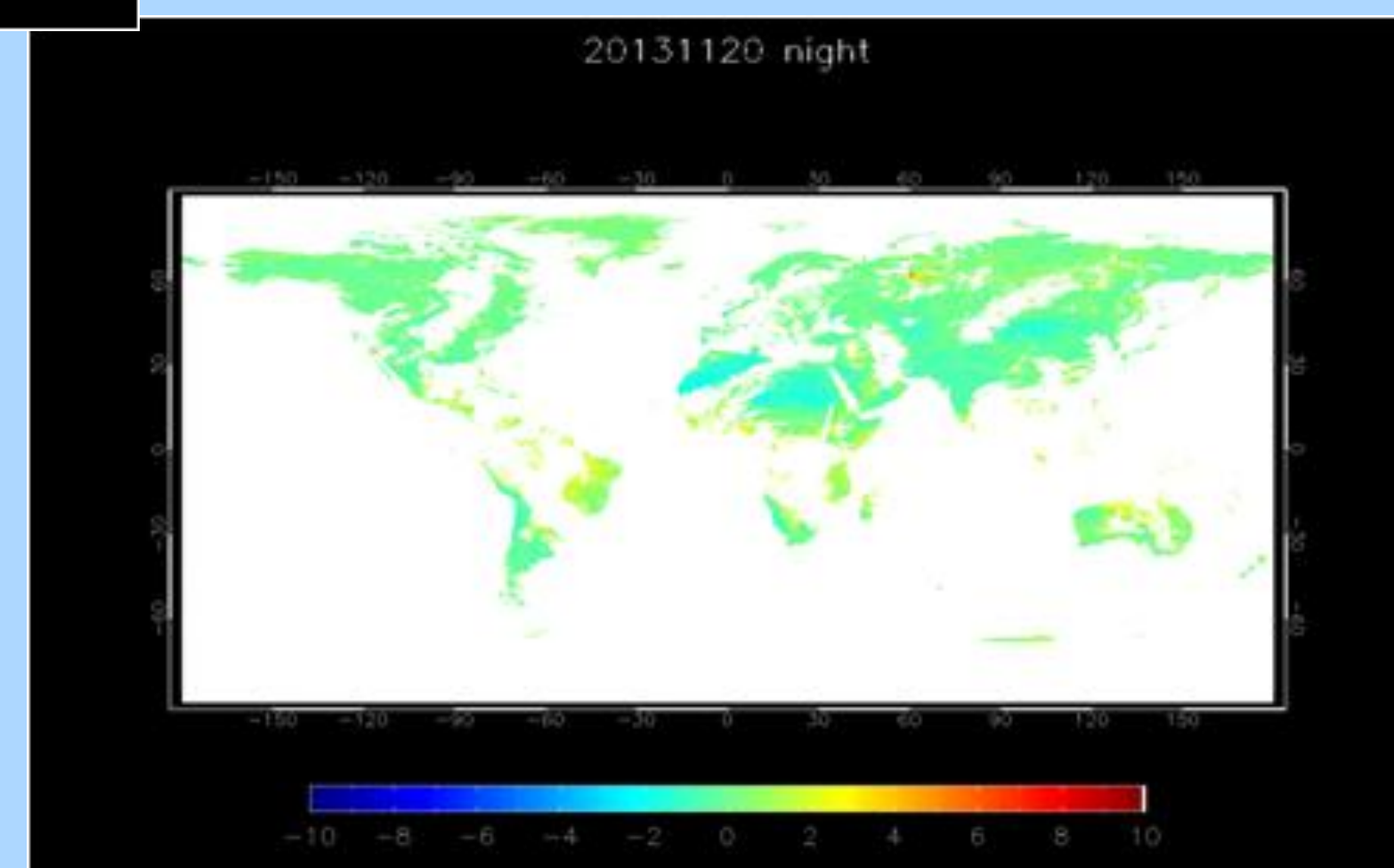
We have also tested an emissivity explicit algorithm in VIIRS LST retrieval, and its computed LSTs is more closer to Aqua LST than VIIRS beta version LSTs. The algorithms including water vapor terms in several different ways are tested. Some preliminary results are presented. All these studies provide a basis for our future algorithm improvements.

BT difference Issue



Brightness temperatures between the two split window channels on November 20, 2013.

Top Left: Day
Below right: Night

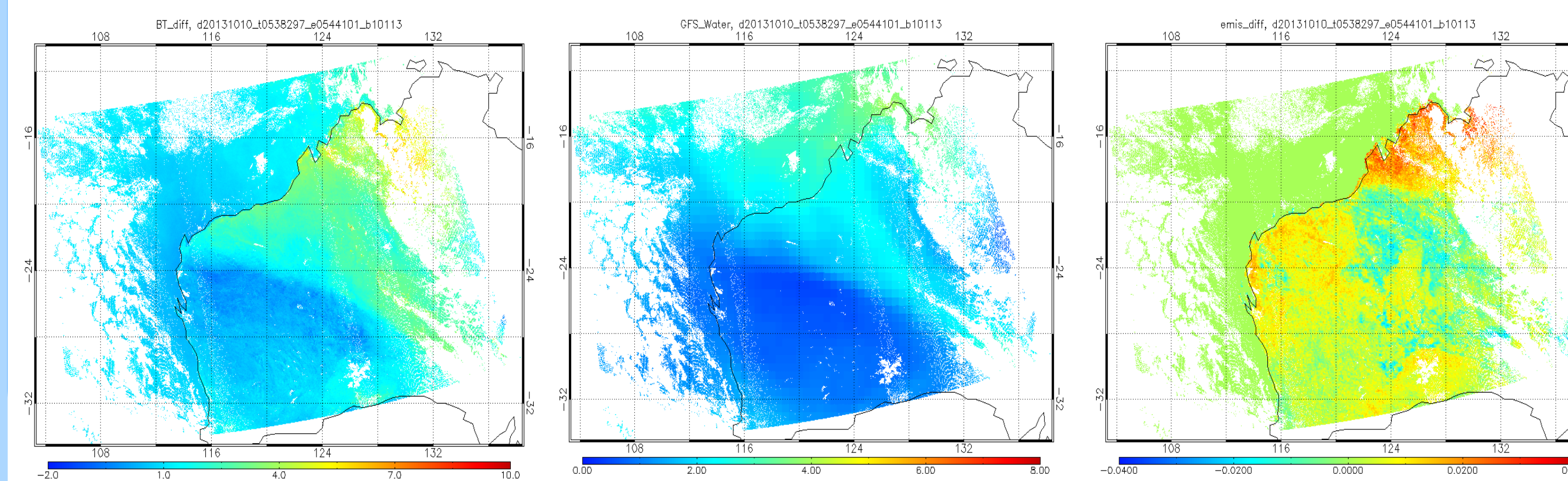


Significant difference found between VIIRS beta version LST and MODIS LST, mostly over wet regions; this is particularly true for daytime cases. In such regions, brightness temperatures difference between the two split window channels are very large. Investigation performed and found that additional correction should be made.

Further studies should be done in order to improve our LST product.

Water Vapor and Emissivity Impact on BT difference

The BT difference over land is usually larger than that over ocean, and it is affected by both water vapor and surface emissivity. The water vapor is a dominant factor, but the impact of emissivity is still under investigation. Left: BT difference, Middle: Water vapor, Right: emissivity difference.



Emissivity Impact on LST Algorithm Regression

In two emissivity datasets, IGBP types are represented by different emissivity pairs, which affects the simulation dataset regression process, and then affects the algorithm coefficients. The table shows the statistic comparison (Left: night; Right: day).

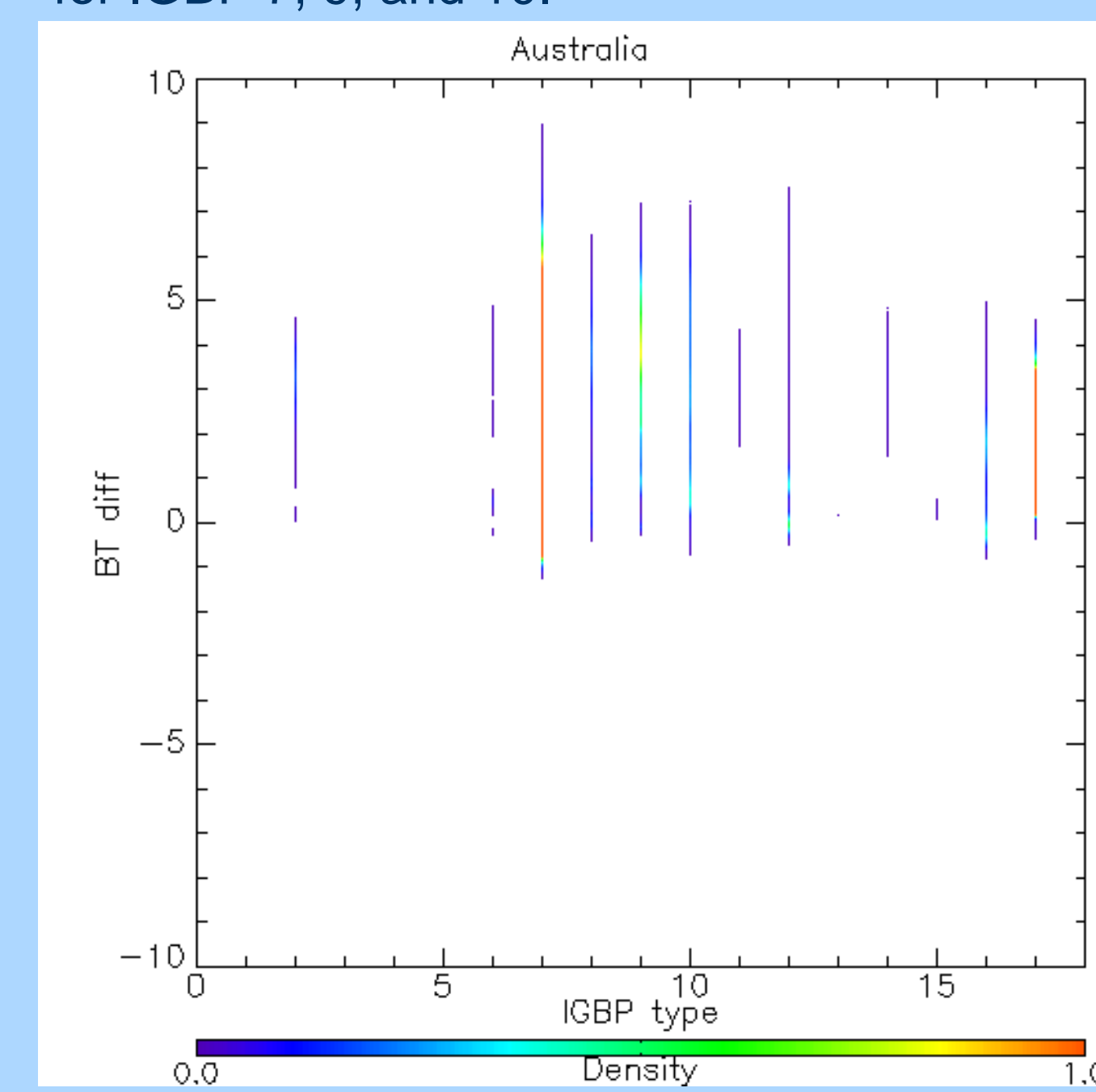
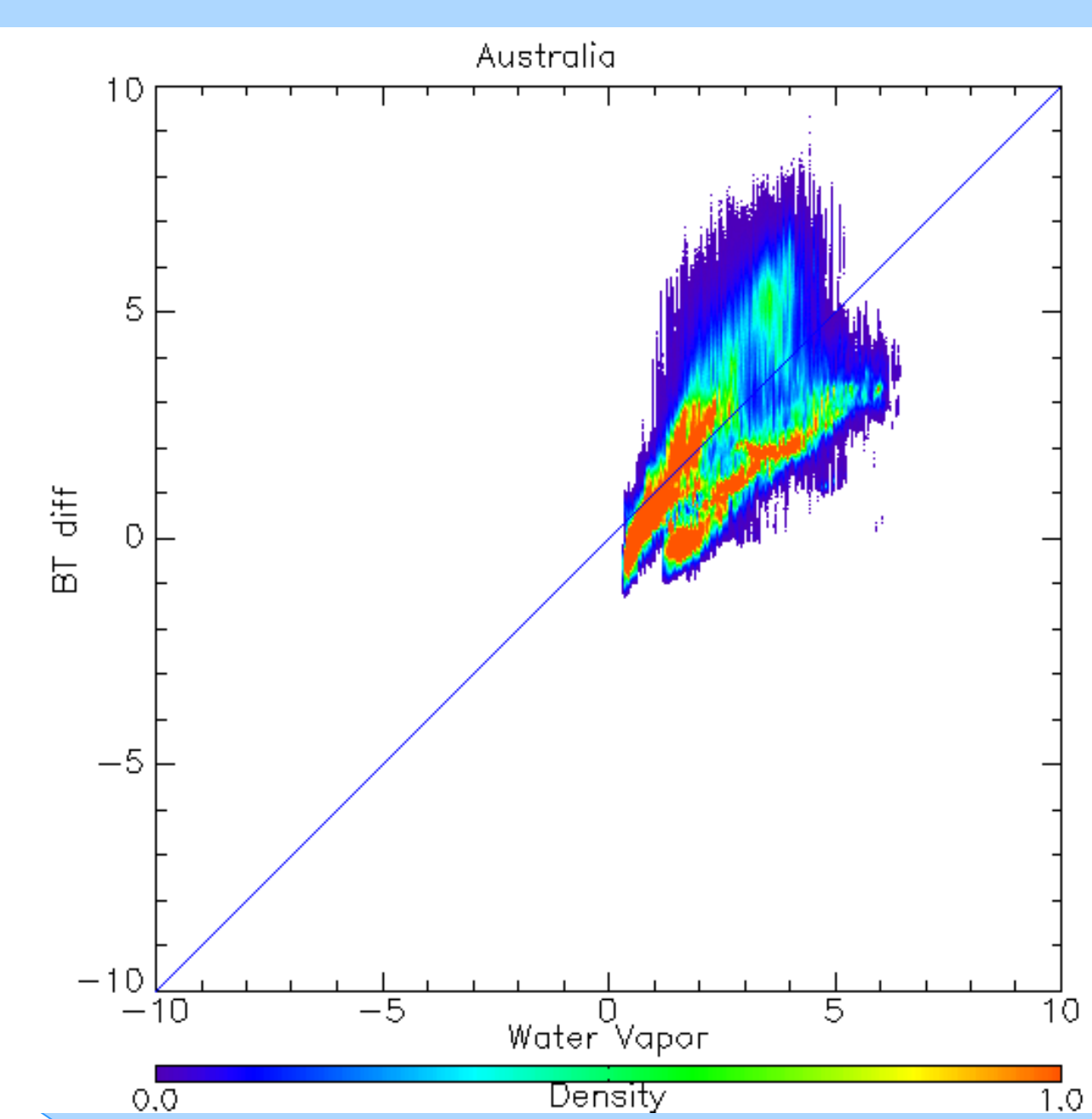
IGBP	Band-Averaged Emissivities in VIIRS testbed			MODIS 10-yr average Emissivity		
	Std	Min_dif	Max_dif	Std	Min_dif	Max_dif
1	0.483	-1.55	1.78	0.382	-1.42	1.49
2	0.335	-1.31	1.39	0.394	-1.47	1.64
3	0.447	-1.51	1.67	0.403	-1.41	1.48
4	0.461	-1.45	1.81	0.390	-1.45	1.59
5	0.418	-1.50	1.68	0.397	-1.40	1.52
6	0.695	-1.86	2.34	0.402	-1.41	1.60
7	0.485	-1.61	1.88	0.417	-1.45	1.59
8	0.409	-1.36	1.60	0.372	-1.40	1.52
9	0.375	-1.40	1.61	0.398	-1.43	1.66
10	0.502	-1.45	1.83	0.389	-1.43	1.60
11	0.462	-1.49	1.71	0.389	-1.44	1.53
12	0.367	-1.37	1.59	0.390	-1.44	1.58
13	0.462	-1.49	1.71	0.441	-1.45	1.76
14	0.656	-1.85	1.99	0.380	-1.40	1.58
15	0.398	-1.44	1.50	0.338	-1.25	1.38
16	1.332	-3.57	3.91	0.522	-1.68	1.98
17	0.327	-1.32	1.40	0.344	-1.27	1.41

Water Vapor and Surface Type Impact on BT difference

Some granules in different seasons over Australia are chosen to analyze the factors which may affect BT difference. Later will check more regions and global.

Scatterplot of BT difference vs. water vapor shows that water vapor related to BT difference positively.

The figure of BT difference vs. Surface Type shows that large BT difference occurs mainly for IGBP 7, 9, and 10.



Emissivity Explicit Algorithm

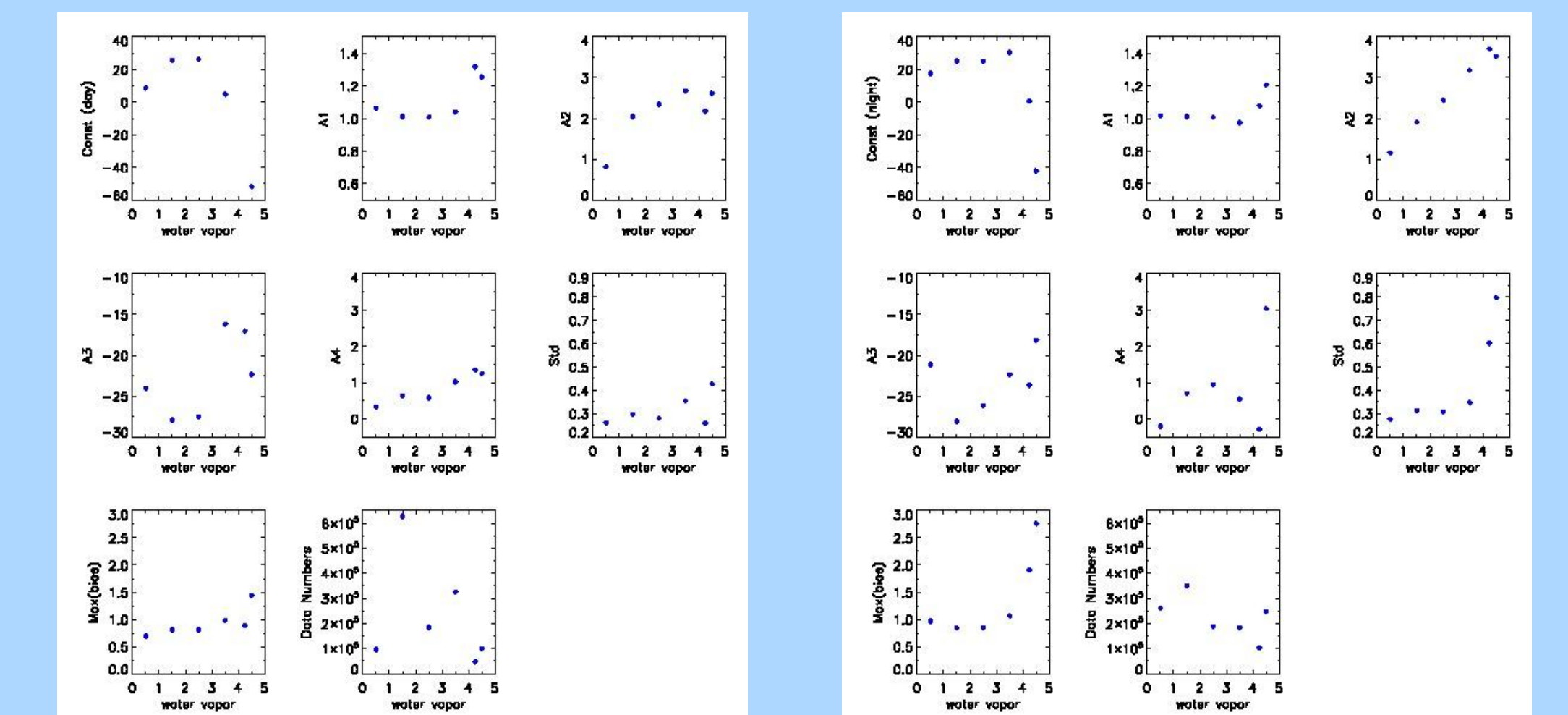
We have tested the emissivity explicit algorithm in VIIRS LST retrieval

$$LST = C + A_1 T_{11} + A_2 (T_{11} - T_{12}) + A_3 \varepsilon + A_4 (T_{11} - T_{12})(\sec \theta - 1) \quad (1)$$

Where T_{11} and T_{12} are the brightness temperatures in 11.2 μm and 12.3 μm bands, respectively. $\varepsilon = (\varepsilon_{11} + \varepsilon_{12})/2$, ε_{11} and ε_{12} are the spectral emissivity in the split window bands. C , A_1 , A_2 , A_3 , and A_4 are algorithm coefficients.

Water Vapor included Algorithm

To analyze how the water vapor affects the algorithm, I computed the algorithm coefficients for ABI algorithm for the following water vapor ranges: [0, 1], [1, 2], [2, 3], [3, 4], and [4, 4.5]. The following figures show that each coefficient in Eq. (1) varies with water vapor obviously (Left: daytime, Right: nighttime)



The algorithm coefficients in Eq. (1) are adjusted by a quadratic function of water vapor term ($b_0 + b_1 W + b_2 W^2$) one by one. The mean bias can decrease 0.5K. Further improvement is still needed.

Summary and Future Work

We have evaluated the VIIRS LST using SNO comparison with Aqua LST. In general, VIIRS LST matches Aqua data well for dry condition. There are some significant bias over the wet regions for daytime cases. In such regions, the brightness temperature differences between split window channels are very large. Our analysis indicates that BT difference is affected by both water vapor and emissivity. Water vapor is a dominant factor, but the emissivity effect is still under investigation. Additional correction should be made to improve our LST product.

Impact of emissivity on the LST algorithm regression is also investigated.

We have tested an emissivity explicit algorithm, and also add water vapor terms in the algorithm. The mean bias of LST is decreased.

All these studies provide a basis for our future algorithm improvements.

Algorithm Comparison

VIIRS granule	MODIS granule	Ts from ABI algorithm vs. MODIS		VIIRS Beta version Ts vs. MODIS	
		Mean bias	std	Mean bias	std
		d20131102_11704	2013306.1710	2.78	1.69
d20131121_0745	2013325.0755	0.95	2.87	1.08	3.24
d20131121_0746	2013325.0755	0.86	2.17	1.08	2.36
d20131126_11532	2013330.1540	0.27	1.51	0.20	1.51
d20131210_10624	2013344.0620	1.65	0.62	0.47	0.65
d20131201_1118	2013335.1145	1.80	2.62	2.49	3.27
d20140209_0608	2014040.0615	0.55	3.34	0.12	3.31
d20140209_1114	2014040.1115	-0.72	1.71	1.48	1.68
d20140209_1115	2014040.1115	0.27	1.34	-0.70	1.48

Simultaneous Nadir Overpass (SNO) comparison between AQUA and VIIRS computed LST from an emissivity explicit algorithm Eq. (1), as well as VIIRS beta LST.

In general, Ts from emissivity explicit algorithm is more closer to Aqua LST than VIIRS Beta version Ts.

1. INTRODUCTION

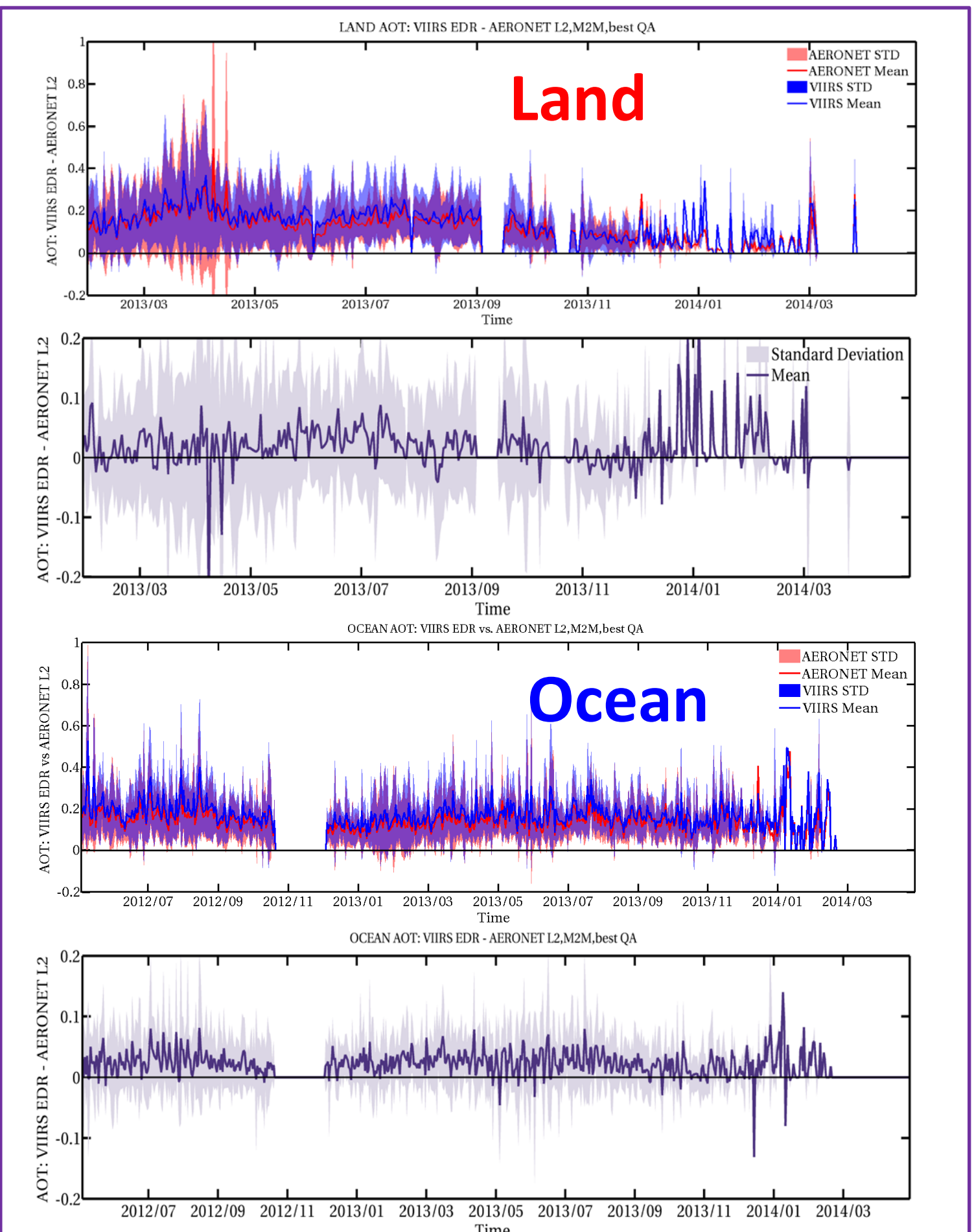
The Suomi National Polar-orbiting Partnership (S-NPP) Visible Infrared Imaging Radiometer Suite (VIIRS) provides the following aerosol Environment Data Records (EDRs):

- ☐ **Aerosol optical thickness (AOT)** (6km at nadir, released in Provisional from 01/23/2013)
- ☐ **Aerosol particle size parameter (APSP)** EDR (Angstrom Exponent (AE) herein, 6km at nadir, released in Provisional from 01/23/2013, not recommended over land)
- ☐ **Suspended matter (SM)** EDR (750m at nadir, released as Beta from 01/23/2013)

VIIRS Aerosol EDR validations were conducted for **1/23/2013-2/28/2014 over land** and **5/2/2012-2/28/2014 over ocean** (unless noted otherwise) by comparing VIIRS observations to their counterpart datasets from AERONET and heritage satellite sensors, such as Aqua/Terra MODIS and Terra MISR.

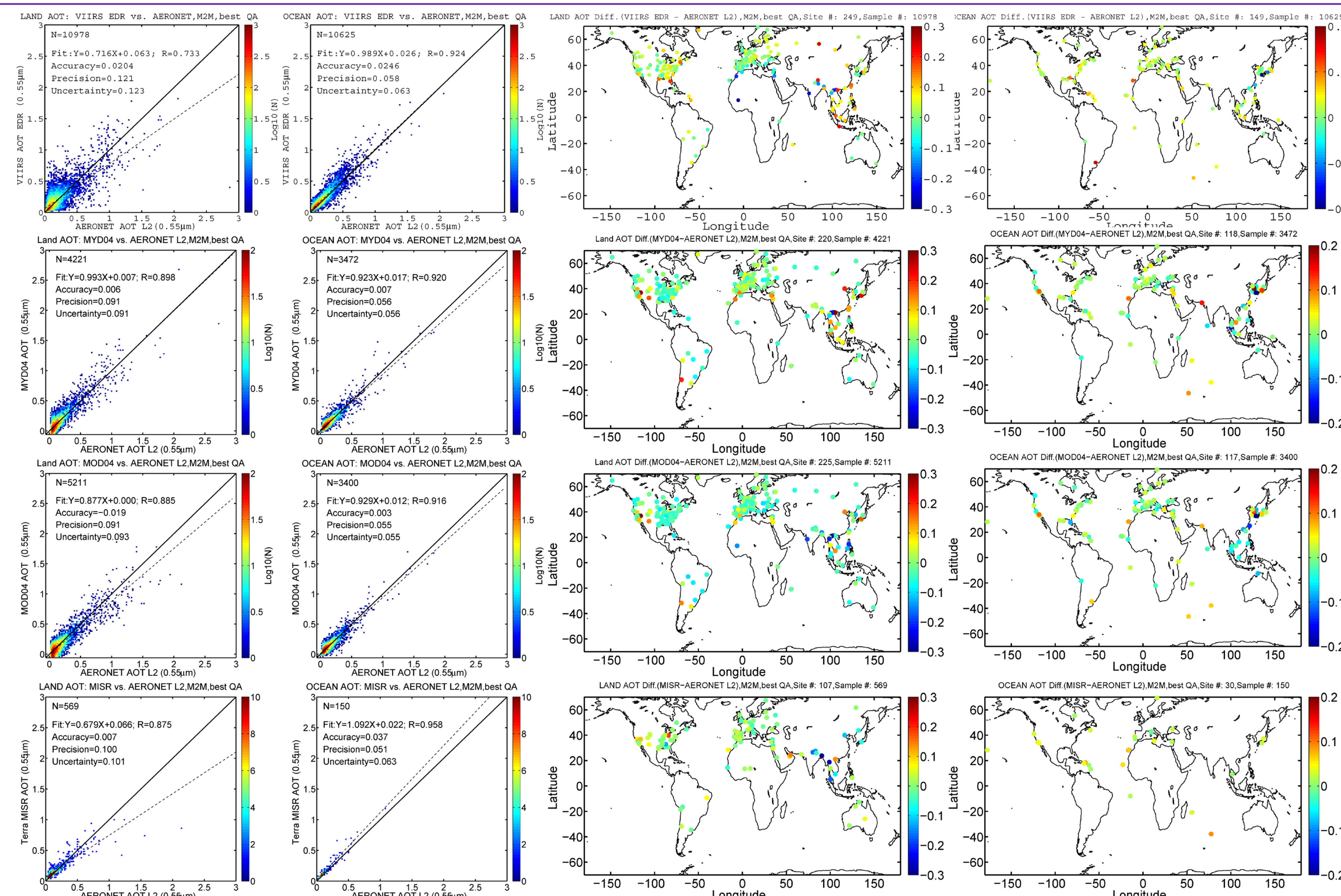
The focus of this study is finding the spatial and temporal patterns of the differences between the multi-sensor AOT retrievals and AERONET measurements.

2. VIIRS vs. AERONET L2: Time Series



The long term stability of the VIIRS vs. AERONET difference has been closely monitored. **The time series of the global AOT means from VIIRS and AERONET demonstrates strongly correlated temporal variability.**

3. Multi-Sensor (VIIRS, Aqua MODIS, Terra MODIS, MISR) vs. AERONET L2: Scatterplots and AOT difference maps



➤ With much larger sample sizes to match against AERONET, **VIIRS AOT retrievals over both land and ocean show levels of accuracy, precision, and uncertainty that are similar to heritage AOT products;**

➤ The relatively larger uncertainty over land in the VIIRS retrieval are attributed to the use of globally constant spectral surface reflectance ratios. **A set of NDVI-dependent spectral surface reflectance ratios or a location-specific spectral surface reflectance ratio database** will be implemented to further improve the products over land;

➤ **Satellite vs. AERONET AOT difference maps show notable regional patterns** related to the localized performance of the satellite algorithms that is sensitive to surface characteristics

4. Satellites vs. AERONET L2: Statistics

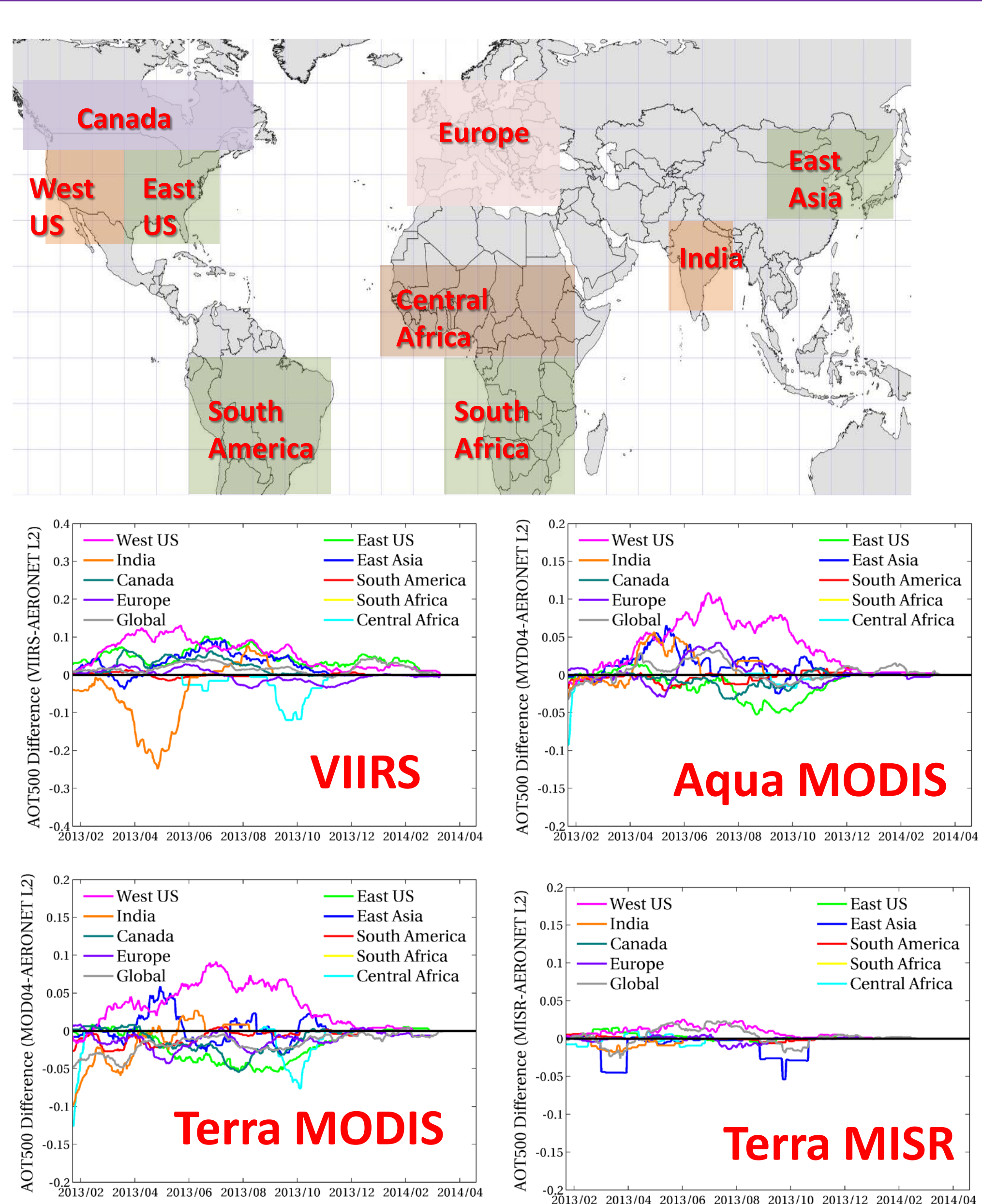
SAT. vs AERONET L2	VIIRS EDR	MYD04	MOD04	MISR	VIIRS EDR	MYD04	MOD04	MISR
AOT (550 nm)	LAND				OCEAN			
Sample Size	10978	4221	5211	569	10625	3472	3400	150
Accuracy	0.020	0.006	-0.019	0.007	0.025	0.007	0.003	0.037
Precision	0.121	0.091	0.091	0.100	0.058	0.056	0.055	0.051
Uncertainty	0.123	0.091	0.093	0.101	0.063	0.056	0.055	0.063
Cor Coef	0.733	0.898	0.885	0.875	0.924	0.920	0.916	0.958

LAND AOT EDR vs. AERONET L2	N	A/P	J1 Spec	VS1	Spec Achieved?
$\tau < 0.1$	5450	Accuracy	0.06	0.0374	✓
		Precision	0.15	0.0782	✓
$0.1 \leq \tau < 0.8$	5387	Accuracy	0.05	0.0087	✓
		Precision	0.25	0.1184	✓
$0.8 < \tau < 2.0$	137	Accuracy	0.20	-0.1260	✓
		Precision	0.45	0.3371	✓
$\tau > 0.8$	141	Accuracy	0.20	-0.1909	✓
		Precision	0.45	0.5533	✗
τ all	10978	Accuracy		0.0204	
		Precision		0.1230	

OCEAN AOT EDR vs. AERONET L2	N	A/P	J1 Spec	VS1	Spec Achieved?
$\tau < 0.3$	9485	Accuracy	0.08	0.0239	✓
		Precision	0.15	0.0418	✓
$\tau \geq 0.3$	1140	Accuracy	0.15	0.0302	✓
		Precision	0.35	0.1281	✓
τ all	10625	Accuracy		0.0239	
		Precision		0.0592	

The accuracy and precision of VIIRS AOT EDR meet JPSS-1 validation thresholds and demonstrate performance that is comparable to its counterparts from MODIS and MISR.

5. Satellites vs. AERONET L2 over Land: Regional and Seasonal Patterns



Among the 9 study regions over land, **VIIRS AOT appears to have larger biases over India, West US, and Central Africa**, when compared to the rest of the regions. Further, the overall bias trend shows significant seasonal cycles. In contrast, Aqua/Terra MODIS AOT tends to have smaller biases than VIIRS, with the largest biases over West US. Terra MISR AOT is the least biased dataset with the smallest seasonal variability; however, this dataset has the smallest sample size.

6. SUMMARY

- Results indicated that the performance of the VIIRS aerosol products on average is comparable to that of their counterparts from the heritage MODIS and MISR sensors
- Validation results showed that the VIIRS aerosol products meet the JPSS-1 threshold requirements
- Spatial and temporal patterns were observed when evaluating VIIRS AOT against AOT from other spaceborne sensors and AERONET. These findings will aid in improving VIIRS aerosol products as we transition from NPP to JPSS-1
- VIIRS aerosol EDRs are available from **NOAA's Comprehensive Large Array-data Stewardship System (CLASS)** at <http://www.class.ngdc.noaa.gov>
- **VIIRS Aerosol Products Users' Guide** is available at: <http://www.star.nesdis.noaa.gov/jpss/ATBD.php#S126472>
- **VIIRS Aerosol Products README** file is under "VIIRS Aerosol" at: <http://www.nsof.class.noaa.gov/saa/products/welcom>
- Other documents are available at: <http://npp.gsfc.nasa.gov/science/documents.html>

ACKNOWLEDGEMENT:

Support from NOAA JPSS Program, and NASA MODIS, MISR, AERONET and MAPSS teams are acknowledged.

Comparison of VIIRS SST fields obtained from differing SST equations applied to a region covering the northern Gulf of Mexico and western North Atlantic

Jean-François P. Cayula, QuinetiQ North America, Inc. (United States)

Robert A. Arnone, Ryan A. Vandermeulen, The Univ. of Southern Mississippi (United States)

INTRODUCTION

Sea Surface Temperature (SST) retrievals derived from data acquired by the Visible Infrared Imaging Radiometer Suite (VIIRS) sensor on-board the S-NPP satellite are produced using a number of SST equations. This study examines the effect on the produced SST fields of daytime SST equations that are or were used by the Naval Oceanographic Office (NAVOCEANO), NOAA/STAR, Météo France, the Integrated Data Processing Segment (IDPS) and the University of Miami. For the Météo France equation, coefficient values from NAVOCEANO, NOAA and Météo France are tested. To match a scene provided by the University of Miami, the region in this study covers the Northern Gulf of Mexico and part of the Western North Atlantic for a daytime scene which was captured on May 14, 2013. We attempt to validate the SST fields by comparing the satellite derived values with those of drifting or moored buoys. We also examine the end of scan region as it is the area where results of the SST equations differ most. Analyzing the difference in temperature at the overlap between swaths provides insight on how well the various equations and coefficients combinations perform at higher satellite zenith angles.

SST EQUATIONS (as of November 2013)

- IDPS (standard NLSST equation)

$$a_0 + a_1 T_{11} + a_2 T_f (T_{11} - T_{12}) + a_3 (T_{11} - T_{12}) \left(\frac{1}{\cos(\theta)} - 1 \right)$$

with first guess T_1 in Celsius.

- NL53deg - NAVOCEANO (expanded NLSST equation/operational)

$$a_0 + a_1 T_{11} + \left(a_3 + a_4 T_f + a_5 \left(\frac{1}{\cos(\theta)} - 1 \right) \right) (T_{11} - T_{12})$$

- NL+2 - NAVOCEANO (NLSST equation with extra angle terms)

$$a_0 + a_1 T_{11} + \left(a_3 + a_4 T_f + a_5 + a_7 T_f \left(\frac{1}{\cos(\theta)} - 1 \right) \right) (T_{11} - T_{12}) + a_6 \left(\frac{1}{\cos(\theta)} - 1 \right)$$

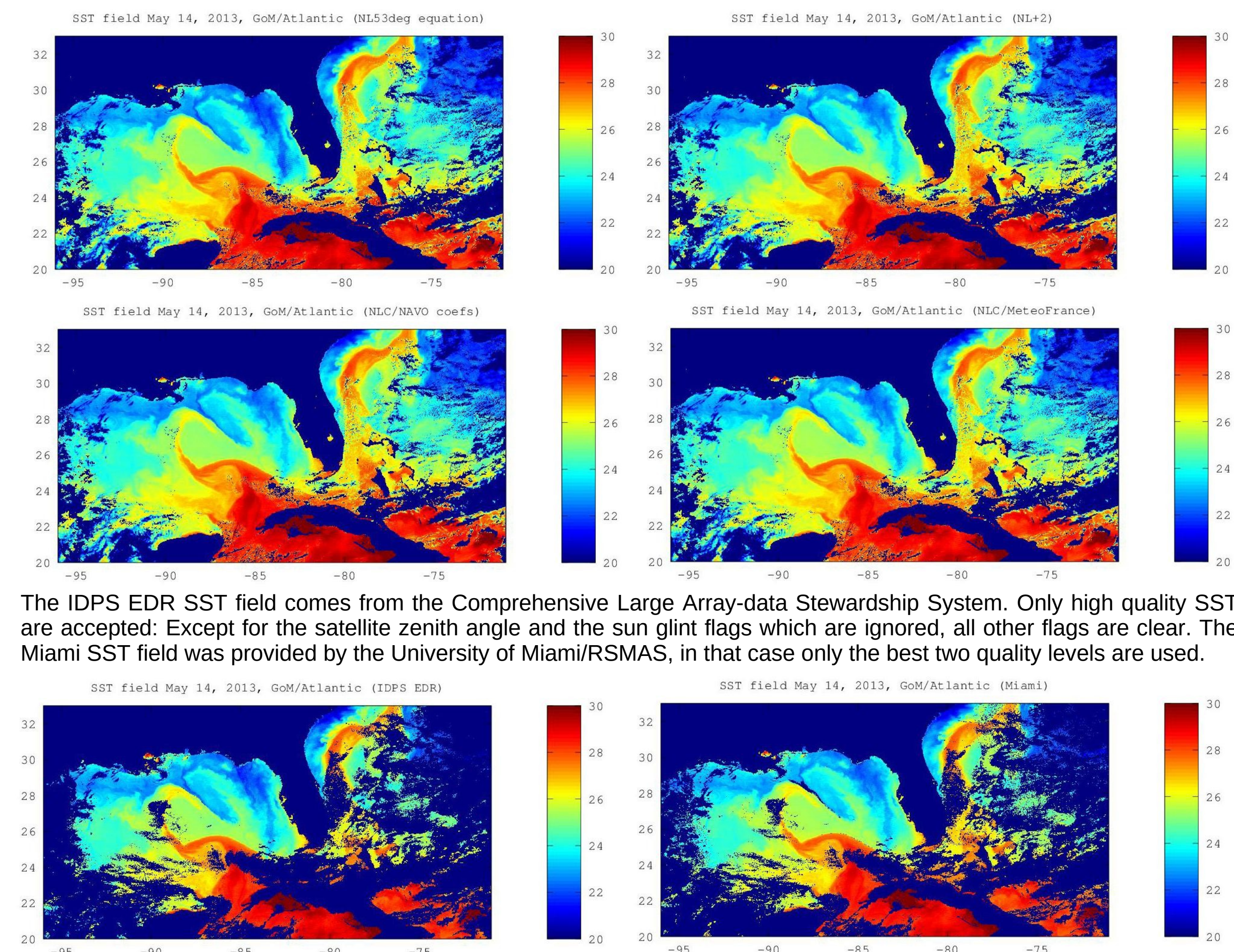
- NLC - OSI-SAF/Météo France (NLSST equation with extra angle terms)

$$a_0 + \left(a_1 + a_2 \left(\frac{1}{\cos(\theta)} - 1 \right) \right) T_{11} + \left(a_3 + a_4 T_f + a_5 \left(\frac{1}{\cos(\theta)} - 1 \right) \right) (T_{11} - T_{12}) + a_6 \left(\frac{1}{\cos(\theta)} - 1 \right)$$

- Miami: University of Miami uses the NLD equation with a domain divided by latitude bands

SST FIELDS

SST fields created with the NL53deg, NL+2, and NLC SST equations were all produced at NAVOCEANO with same minimal cloud detection. Coefficients derived at NAVOCEANO, and, provided by NOAA/STAR and Météo France were tested with the NLC equation.



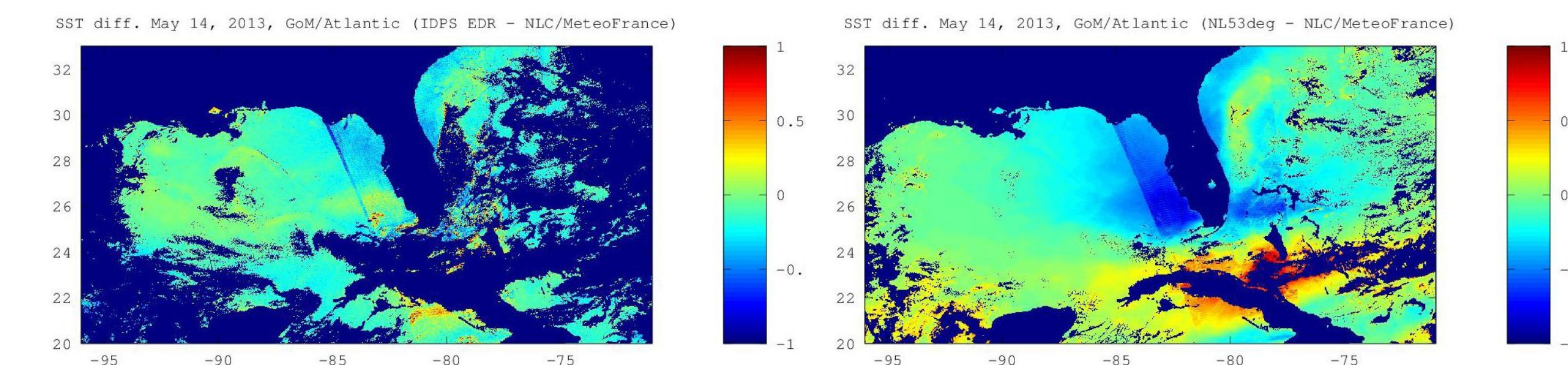
The IDPS EDR SST field comes from the Comprehensive Large Array-data Stewardship System. Only high quality SST are accepted: Except for the satellite zenith angle and the sun glint flags which are ignored, all other flags are clear. The Miami SST field was provided by the University of Miami/RSMAS, in that case only the best two quality levels are used.

REFERENCES

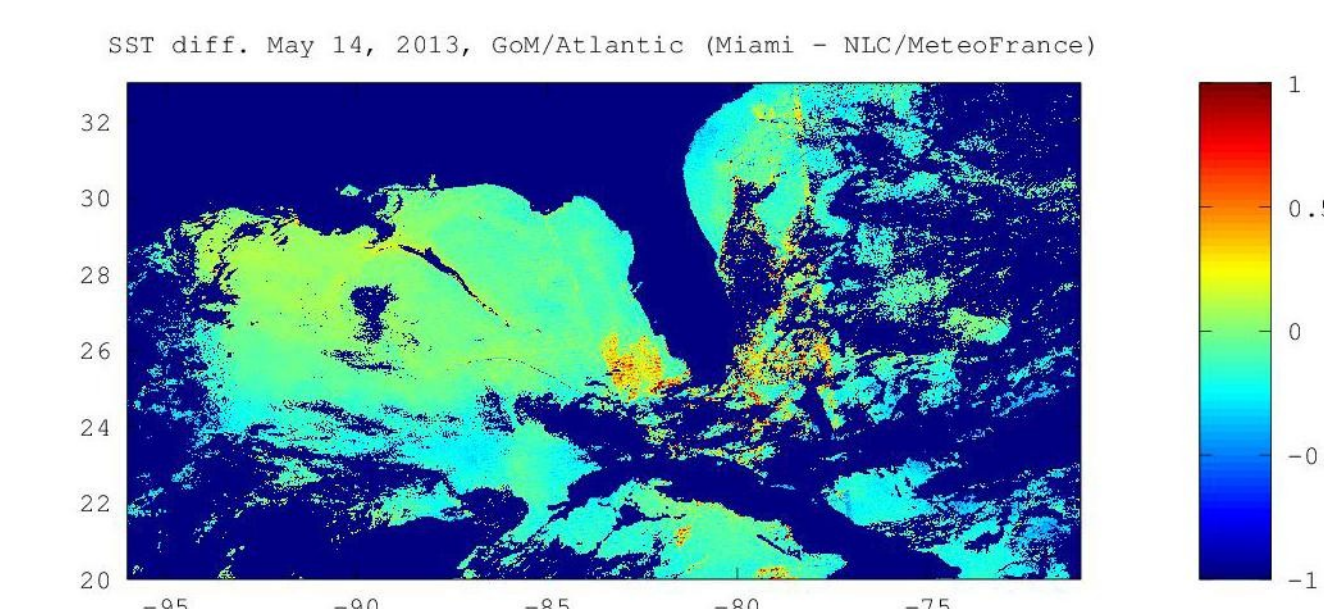
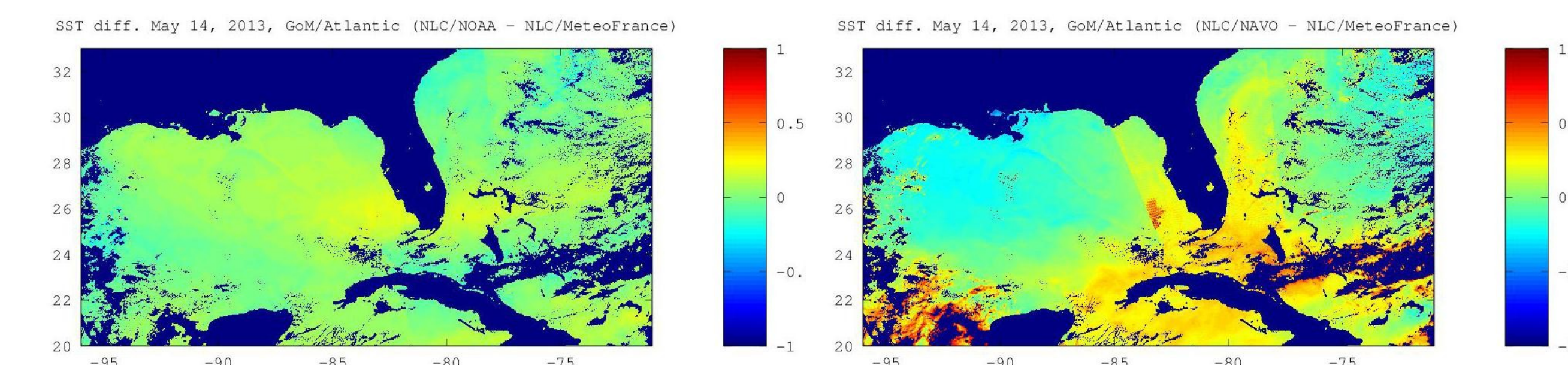
- Walton, C., Pichel, W., Sapper, J., and May, D., The Development and Operational Application of Nonlinear Algorithms for the Measurement of Sea Surface Temperatures with the NOAA Polar-Orbiting Environmental Satellites, J. Geophys. Res., 103(12), 27,999-28,012 (1998).
- Petrenko, B., A. Ignatov, Y. Kihai, J. Stroup, and P. Dash (2014), Evaluation and selection of SST regression algorithms for JPSS VIIRS, J. Geophys. Res. Atmos., 119, doi:10.1002/2013JD020637
- Cayula, J.-F., May, D., McKenzie, B., and Willis, K., "VIIRS-derived SST at the Naval Oceanographic Office: From evaluation to operation" Proc. SPIE 8724, Ocean Sensing and Monitoring V, 87240S (June 3, 2013); doi:10.1117/12.2017965; <http://dx.doi.org/10.1117/12.2017965>
- Jackson, S. and Siebels, P.D., "Operational Algorithm Description Document. VIIRS Sea Surface Temperature (SST) EDR", http://npp.gsfc.nasa.gov/science/sciencedocuments/022012/474-00061_OAD-VIIRS-SST-EDR-SW_RevA_20120127.pdf (2011).

Comparison between SST FIELDS

Both the IDPS and the NL53deg are designed to make SST retrievals at a maximum satellite zenith angle of 53 degrees, with IDPS flagging all data over 40 degrees as lower quality. Over that limit, their performance degrade rapidly. This is seen in the next two pictures of SST difference fields "IDPS minus NLC" and "NL53deg minus NLC" where we observe a cold bias in the swath overlap region.

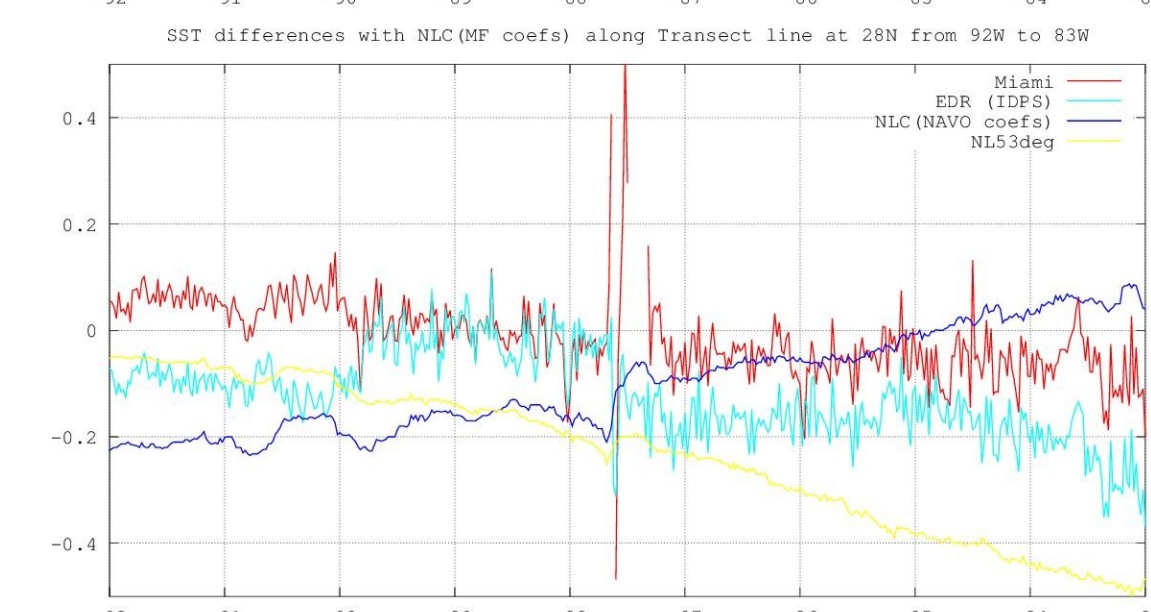
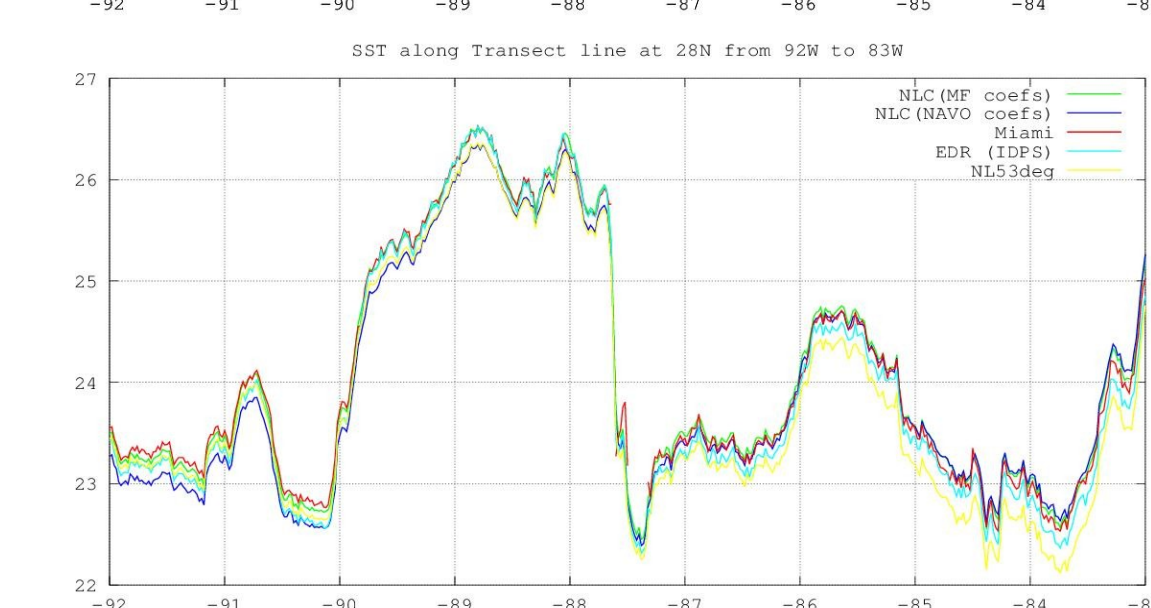
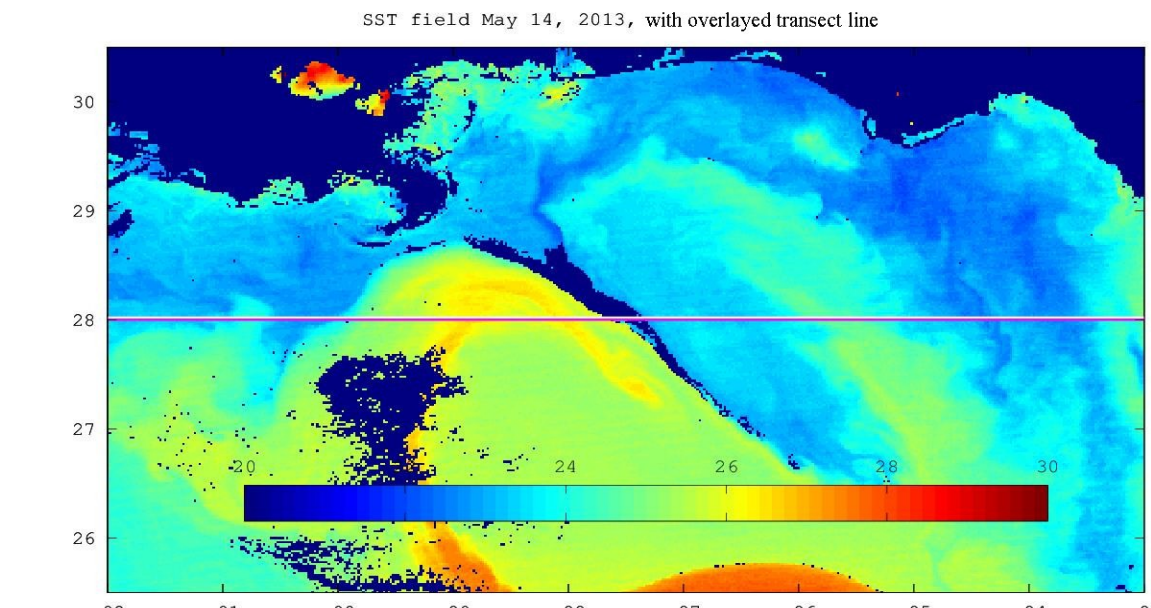
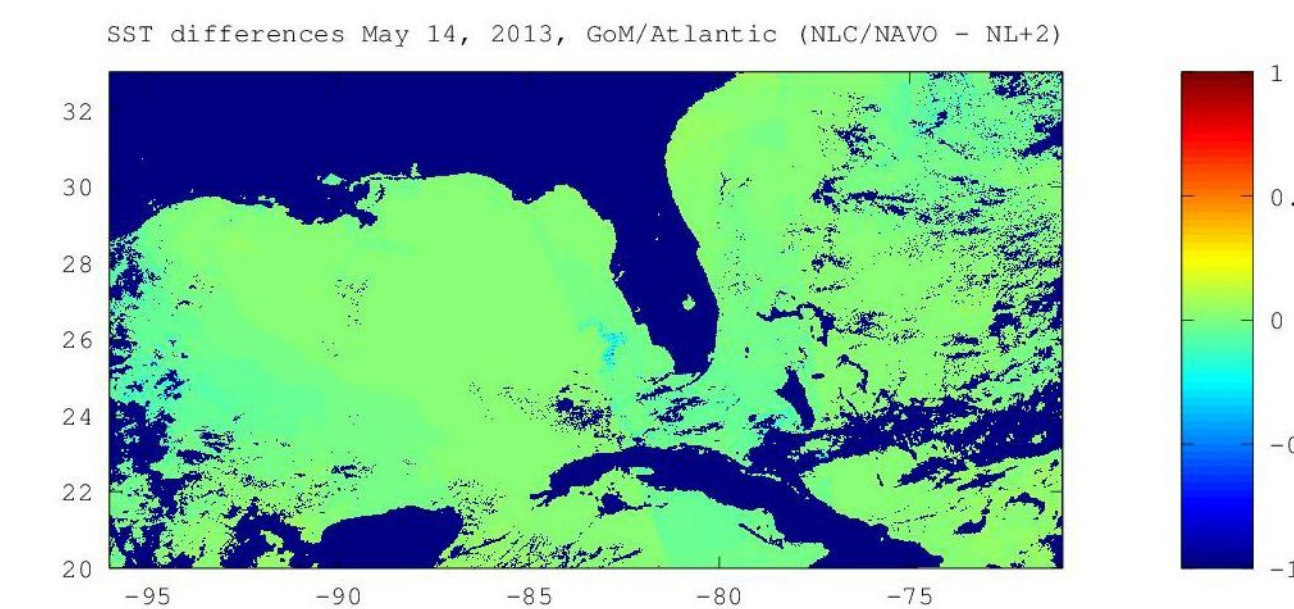


Between SST fields that are created with the NLC equation differences appear depending on which set of coefficients is used. There are relatively minor differences between fields with the Météo France and NOAA sets of coefficients. More significant differences are observed with the NAVOCEANO coefficients. In particular at high satellite zenith angle where the limb effect correction is more accentuated with the NAVOCEANO coefficients than with either the Météo France or NOAA coefficients.



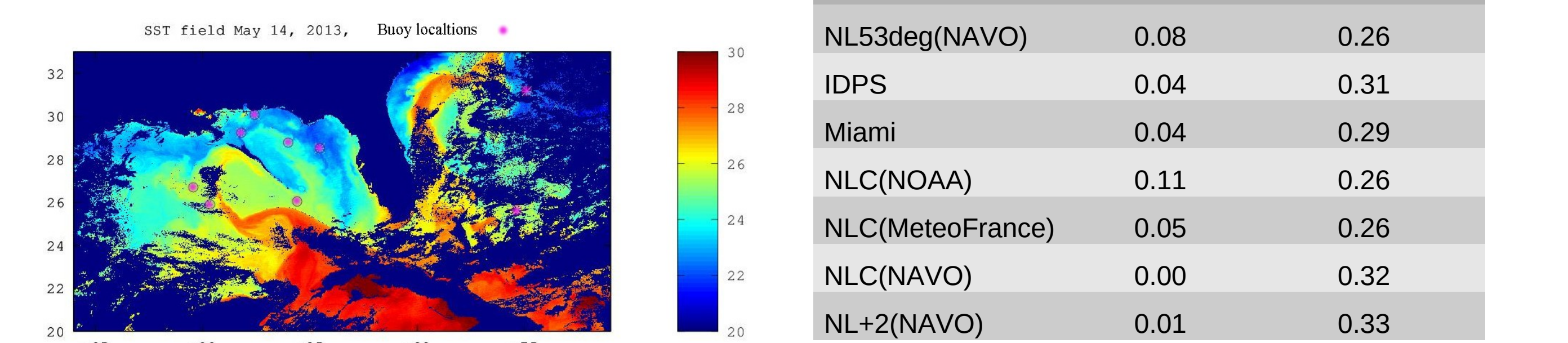
The Miami latitude bands algorithm produces fields which are close to those obtained the NLC equations and Météo France coefficients. This is surprising because the Miami algorithm relies on a standard NLSST equation like IDPS.

Comparison between the SST fields derived from the NLC and NL+2 equations, both with NAVOCEANO determined coefficients, show little differences, smaller than those observed with NLC with NOAA or Météo France coefficients.



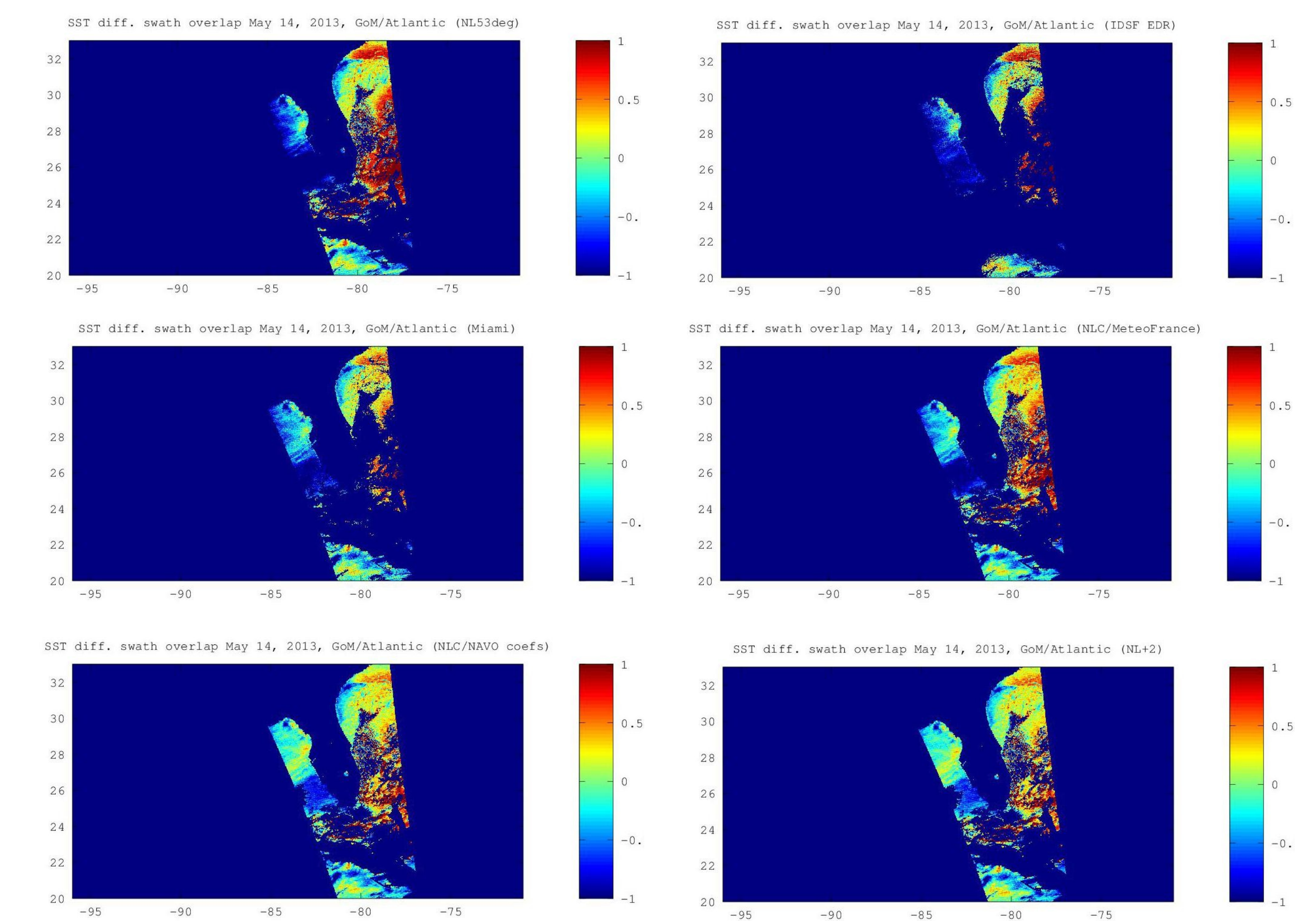
VALIDATION BY COMPARISON TO BUOYS

Because of the low number of buoys, results are not statistically significant. However they do offer a sanity check on all the SST fields. Of note, to better evaluate the SST equations and not the cloud detection, the closest SST retrieval to the buoy temperature, within the immediate neighborhood of the buoy, is selected as the match-up.



VALIDATION BY ANALYSIS OF OVERLAP BETWEEN SWATHS

The overlap between two successive satellite swaths allows the view of a scene at an interval of about 1 hour and 36 minutes. Here, the SST field of the later orbit is subtracted from that of the earlier orbit, and as such, a small cold bias can be expected because of daytime warming. The uncorrected limb darkening effect appears as a cold bias on west side of the overlap region and a warmer bias on the east side. As expected the NL53deg and IDPS equations perform poorly in the swath overlap region as they were not designed to work at a high satellite zenith angle.



The mean bias and the mean absolute bias are estimated on a common set of retrievals that are cloud free in all SST fields. They confirm the good performance of NLC and the poor performance of NL53deg and IDPS at high satellite zenith angle. Results from a March 31, 2014 scene (same region but clouded west side) show IDPS better performance after the switch to the NLC equation.

May 15, 2013	bias °C	mean abs bias °C	March 31, 2014	bias °C	mean abs bias °C
NL53deg(NAVO)	-0.23	0.51	NL53deg(NAVO)	0.19	0.35
IDPS	-0.23	0.52	IDPS	0.14	0.30
Miami	-0.15	0.39	Miami		
NLC(NOAA)	-0.12	0.41	NLC(NOAA)	0.10	0.25
NLC(MeteoFrance)	-0.13	0.38	NLC(MeteoFrance)	0.18	0.32
NLC(NAVO)	-0.09	0.27	NLC(NAVO)	0.10	0.27
NL+2(NAVO)	0.07	0.26	NL+2(NAVO)	0.07	0.24

CONCLUSION

The NLC equation has been shown to perform well, although the choice of coefficients can significantly affect results. As expected NL53deg and IDPS (standard NLSST) perform poorly at high satellite zenith angles as they were not design to process such data. Full swath processing results in large regions where successive orbits overlap even at low latitude. Those overlap regions allow new ways to evaluate and analyze the SST fields. Beside Météo France; NOAA/STAR, IDPS and NAVOCEANO are using or plan to use the NLC equation.

Suomi-NPP VIIRS Radiometric Performance Validation using Lunar Band Ratio Time Series

Taeyoung (Jason) Choi¹, Xi (Sean) Shao¹, Changyong Cao², Fuzhong Weng²
¹Earth Resource Technology (ERT), ²STAR/NESDIS/NOAA

Abstract

Operational radiometric calibration of reflective solar bands (RSBs) of Suomi-NPP VIIRS relies on using onboard Solar Diffuser (SD) together with Solar Diffuser Stability Monitor (SDSM). As an independent validation of RSB calibration of VIIRS, lunar calibration is employed through observing moon in Earth View during scheduled spacecraft maneuver with lunar phase being nearly the same. These lunar calibrations often rely on using lunar irradiance models and it requires the model to be highly accurate.

Here, we present a simple lunar band ratio (LBR) approach to trend radiometer stability of VIIRS so that the usage of lunar irradiance model is not required. Using scheduled lunar observations, digital numbers (DN) of the lunar signal are aggregated in each band after the removal of bias. One of the most stable bands such as M4 is chosen as the reference band for calculating the band ratios.

The LBR analysis reveals that M6 and M7 degrade the fastest and agrees well with the trending independently determined from onboard solar diffuser ratios. For stable bands such as M2-M4 of VIIRS, the variation range of M2/M4 and M3/M4 are all within 0.5%, indicating the LBR can reveal the sub percent band to band stability. It is demonstrated that long-term stability monitoring of VIIRS solar bands using LBR is an important part of the VIIRS lunar calibration and can reveal the relative degradation of instruments.

Introduction

- VIIRS scheduled lunar observations are performed approximately monthly.
 - ✓ With the roll angle limitation between 0 to -14 degrees for safety.
- Lunar roll maneuver views the moon in the day side through the earth view sector near the nadir angle as shown in Figure 1.
- The dual gain bands are set to high gain mode during the collection.
- For radiometric stability and repeatability, the lunar phase angles are maintained between -51.1 to -50 degrees.
 - ✓ Negative phase angle means that VIIRS views waxing moon.
 - ✓ Initially, phase angle limit was from -56 deg to -55 deg in the first three scheduled lunar observations [1].

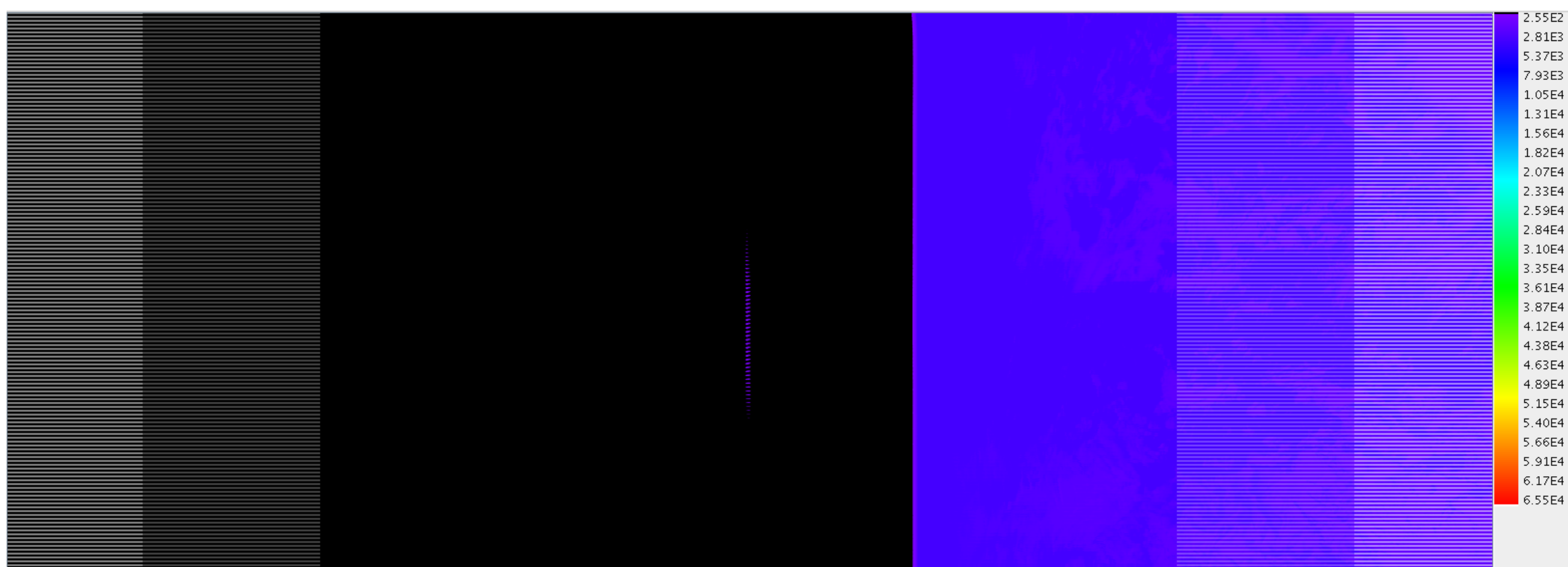


Figure 1. VIIRS band 1 image of the scheduled lunar collection on November 23rd 2012.

Data Sets

- VIIRS scheduled lunar observation data: 15 collections listed in Table 1.
- NASA LAADS (L1 Atmospheric Archive Distribution System) provides Verified Decompressed Raw Instrument Packets 5-min L0 RDR (vRDR).

Table 1. VIIRS scheduled lunar collection list

Date	Target time	Roll angle	Date	Target time	Roll angle
4/2/2012	23:05:11	-3.989	10/14/2013	21:39:19	-1.305
5/2/2012	10:20:06	-3.228	11/13/2013	6:57:41	-7.981
10/25/2012	6:58:15	-4.048	12/12/2013	19:35:46	-9.438
11/23/2012	21:18:20	-9.429	1/11/2014	9:59:45	-6.727
12/23/2012	15:00:50	-7.767	2/10/2014	5:34:12	-3.714
2/21/2013	9:31:25	-1.712	3/12/2014	1:11:43	-3.945
3/23/2013	3:29:00	-3.32	4/10/2014	20:53:15	-4.977
4/21/2013	19:47:54	-3.882			

Data Processing

- Lunar Band Ratio (LBR) calculation
 - ✓ This methodology was originally developed and applied to monitor long-term normalized difference vegetation index (NDVI) stability for AVHRR [2].
 - ✓ From the vRDR data sets, lunar area is properly trimmed including deep space in each band as shown in Figure 2.
 - ✓ Before summation of the all the DN values, bias level is calculated and removed in each line by the averaged value from either sides of the moon.
 - ✓ Lunar Band Ratios (LBR) are calculated by reference band M4 as shown in following equation.

$$LBR_{band} = \frac{\sum_{pixels} (DN_{band, pixel} - \langle bias \rangle_{band, line})}{\sum_{pixels} (DN_{band M4, pixel} - \langle bias \rangle_{band M4, line})}$$

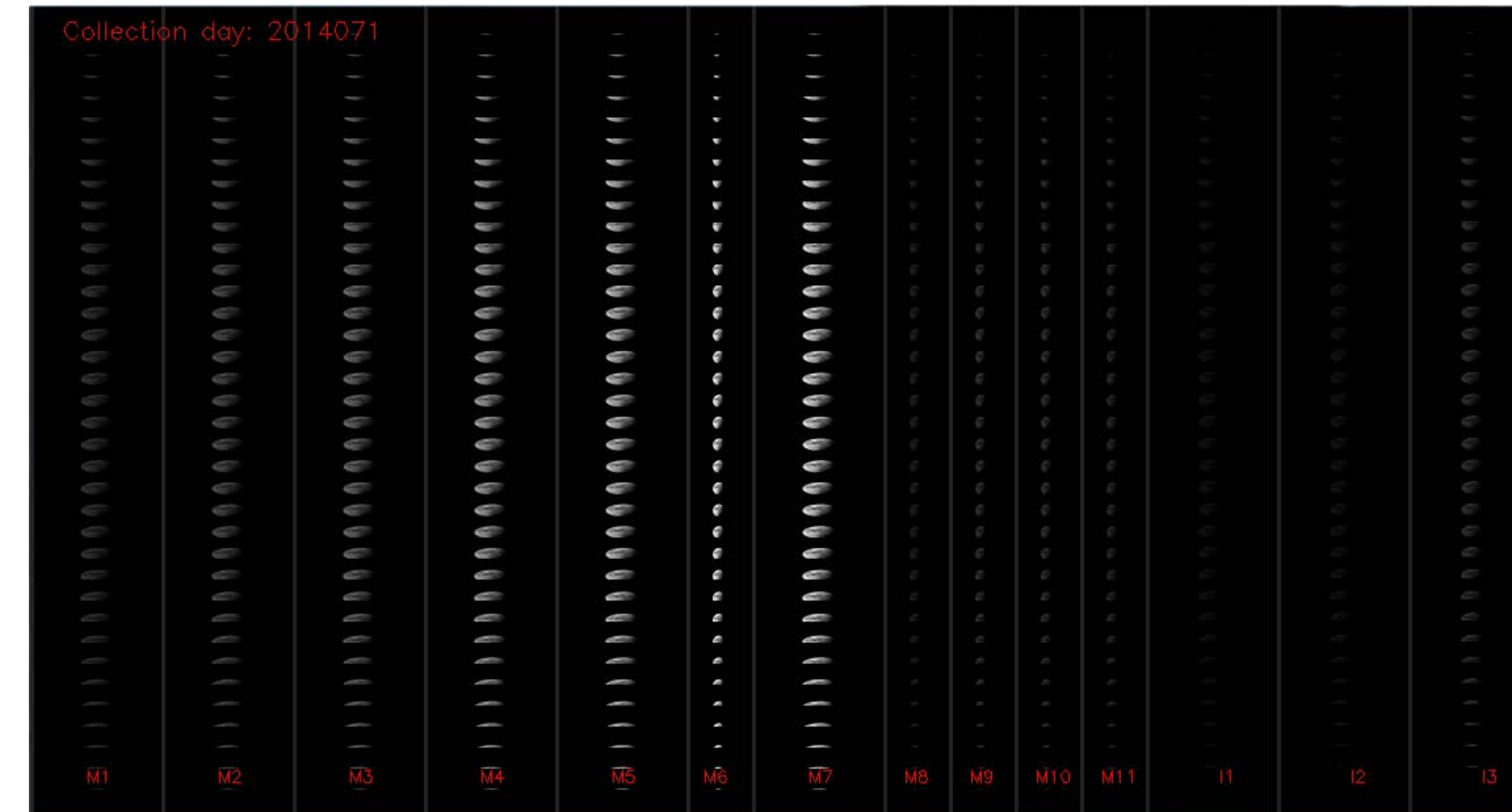


Figure 2. VIIRS trimmed lunar images in the reflective solar bands on March 12th 2014.

- Operational F factors are shown in Figure 3.
 - ✓ The band M4 provides reasonably stable F factors over the VIIRS lifetime.
 - ✓ The F factors are normalized by band M4 before comparing the LBR.

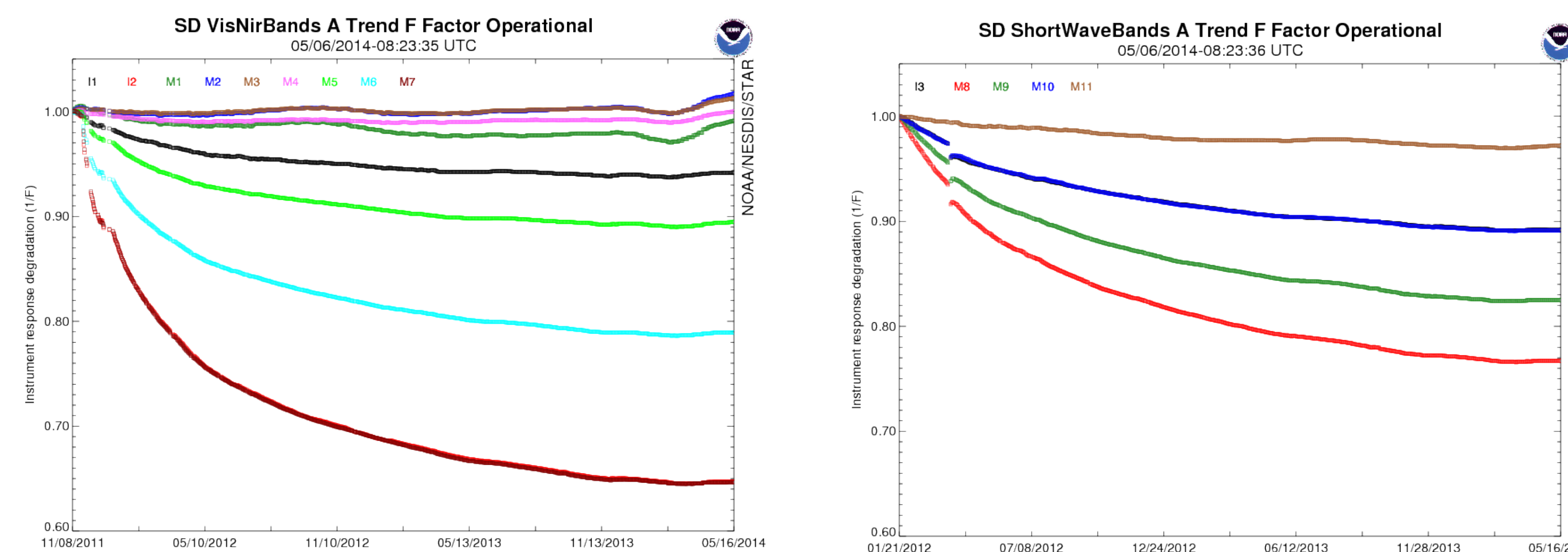


Figure 3. VIIRS operational F factors from VISNIR and short wave bands. These plots are taken from NOAA ICVS VIIRS long-term monitoring (LTM) website at http://www.star.nesdis.noaa.gov/icvs/status_NPP_VIIRS.php

Results and Analysis

- The LBRs versus SD F factor Ratios normalized by band M4 (Figure 4)
 - ✓ The LBRs are normalized by the first scheduled lunar collection on 4/2/2012.
- VisNIR bands M1~M4 (400 to 600 nm)
 - ✓ The LBRs are following the annual oscillation pattern but not as strong as F factor ratios.

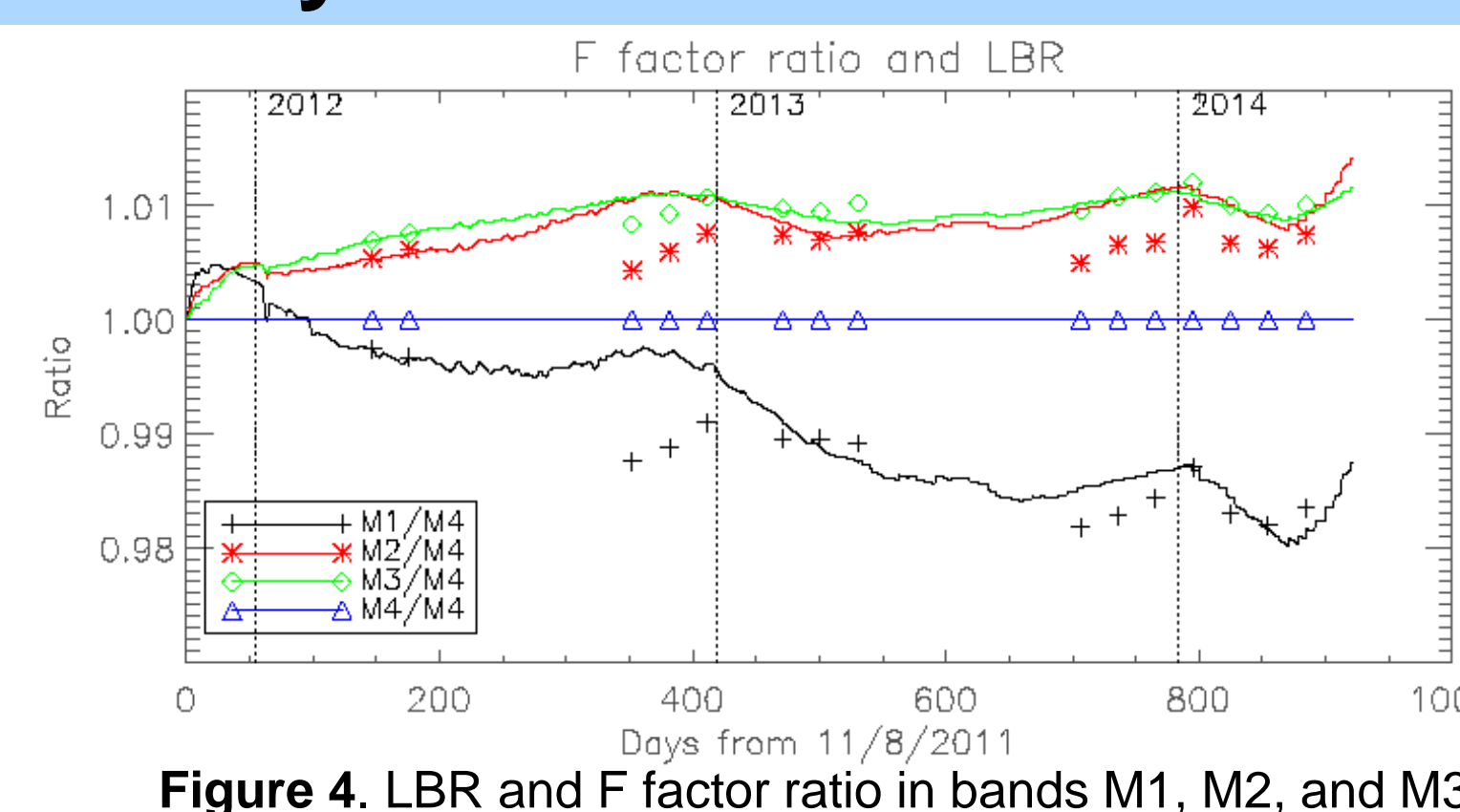


Figure 4. LBR and F factor ratio in bands M1, M2, and M3.

- VisNIR bands M5, M6, M7, I1 and I2 (Figure 5)
 - The LBRs are following general F factor ratio trends.
 - Differences between LBRs and F factor ratios are growing.
 - With time and center wavelength
 - I2 and M7 ratios are almost identical.
- S/WWIR bands M8~M11 and I3 (Figure 6)
 - There is no SD degradation applied in these bands.
 - There are noticeable differences between F factor ratios and LBR.
- I2/M7 and I3/M10 ratios consistency (Figure 7)
 - The LBRs and F factor ratios are consistent approximately within 0.2%.
- LBR / F factor ratio @ Lunar collection plot (Figure 8)
 - The differences are increasing by time.
 - With wavelength dependency.
- Wavelength dependency of LBR / F factor ratio (Figure 9)
 - Used results on 3/12/2014 (2nd from the last).
 - Ratios are increasing in the M5 ~ M8 wavelength range below 1µm bands.
 - Ratios are decreasing in the short wave IR bands.

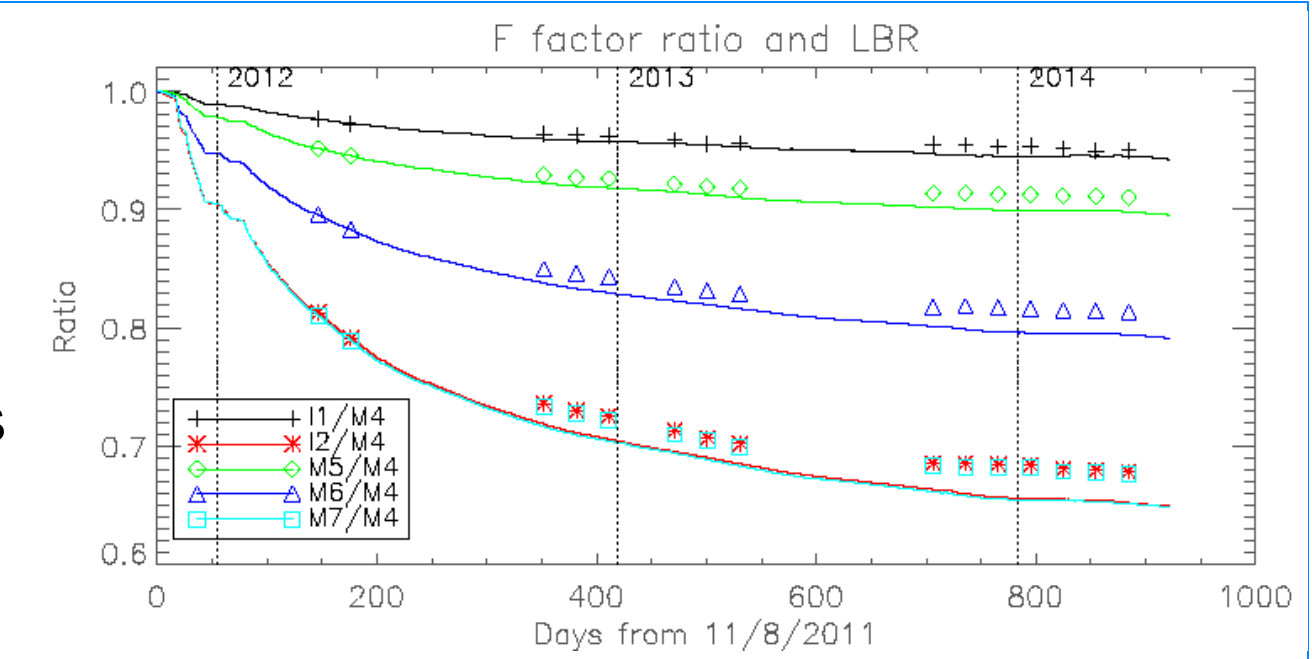


Figure 5. LBR and F factor ratios in bands M5, M6, M7, I1, and I2.

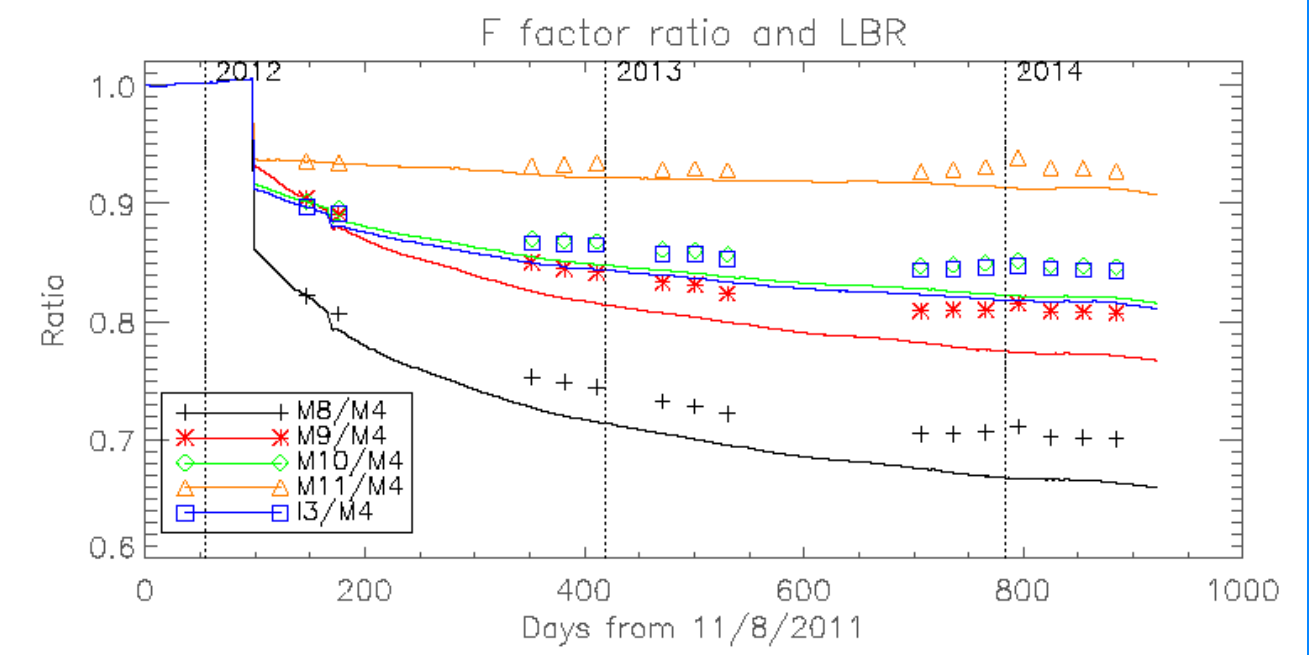


Figure 6. LBR and F factor ratios in bands M8-M11 and I3.

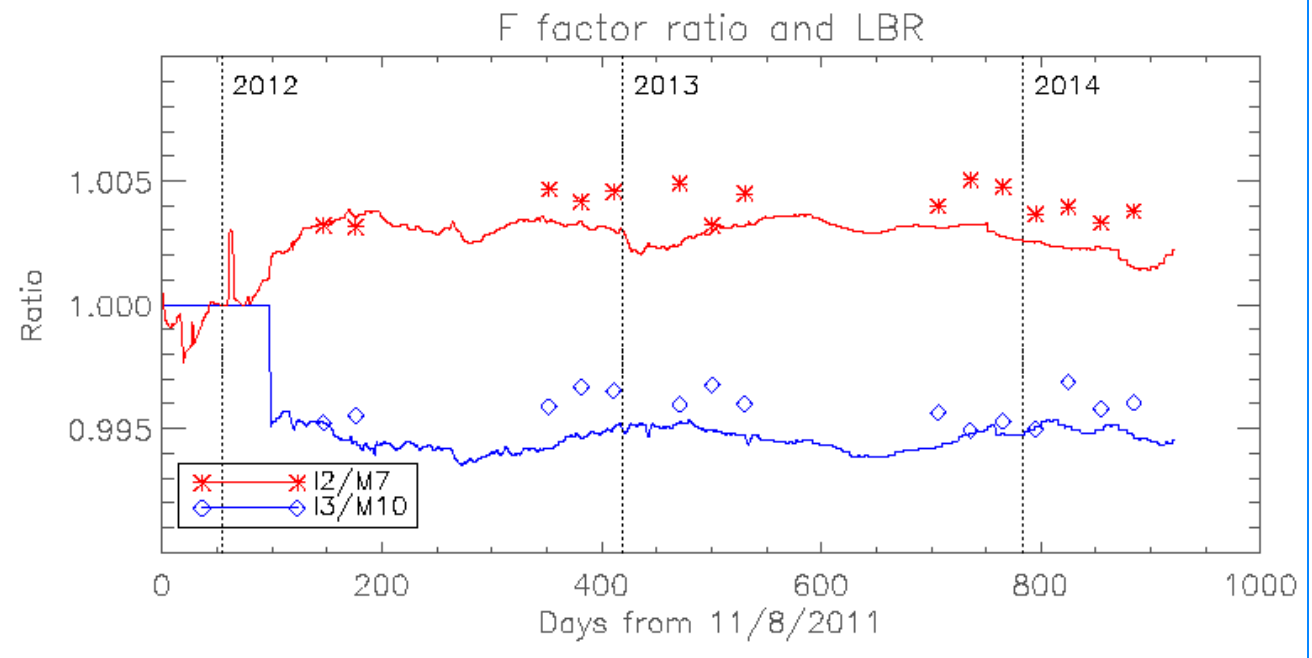


Figure 7. I2/M7 and I3/M10 consistency

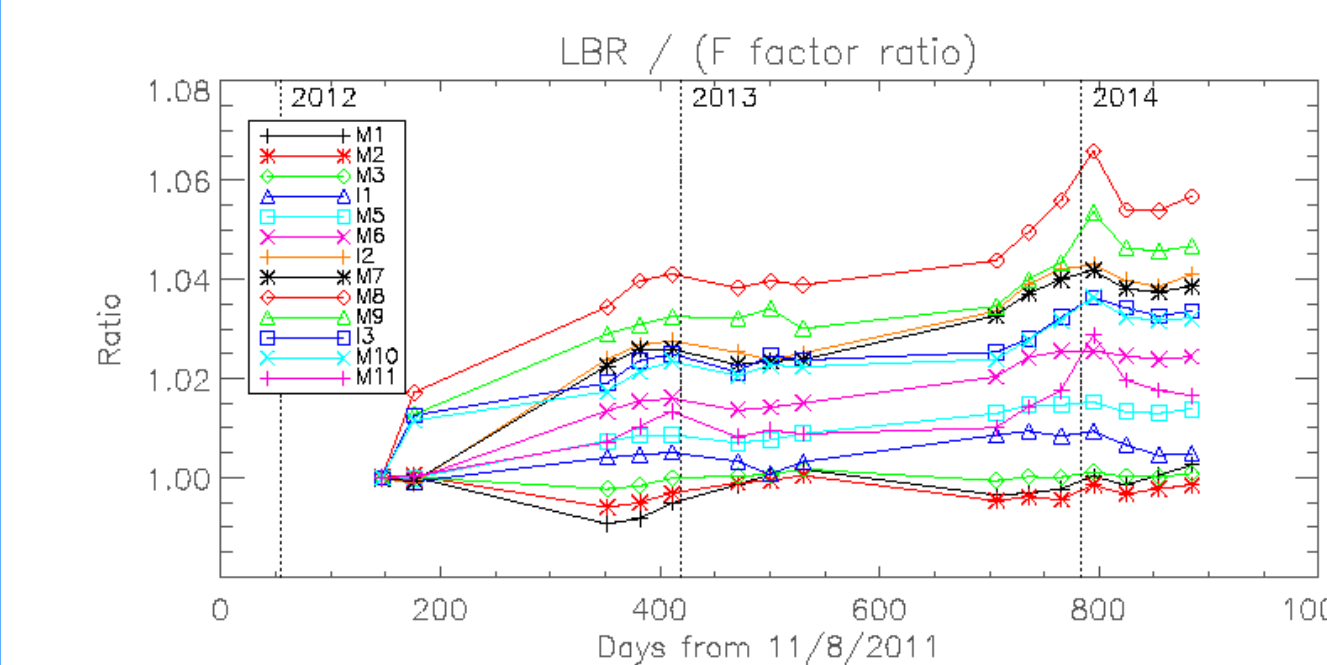


Figure 8. LBR / F factor ratio at lunar collection time

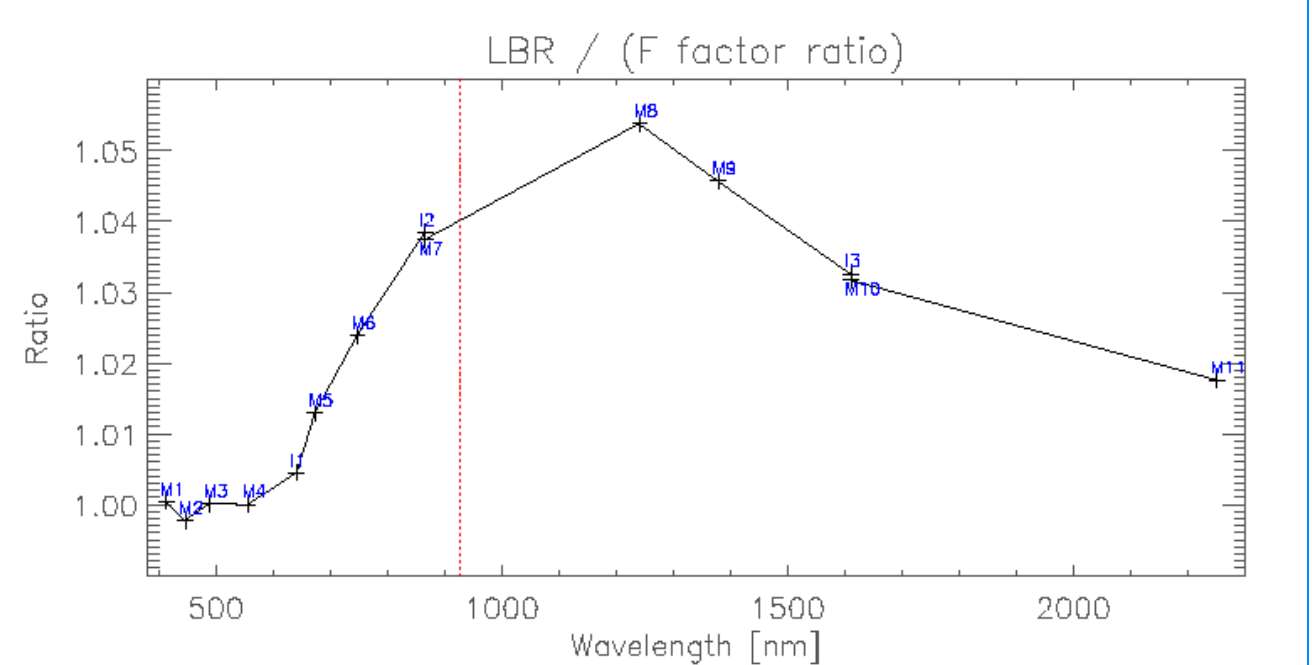


Figure 9. Wavelength dependency of LBR / F factor ratio using collection on 3/12/2014

Summary

- The LBR method is developed and applied to measure relative accuracy of VIIRS radiometric calibration coefficients (F factors).
- The LBRs are generally following the annual oscillation pattern of the F factor ratio within 0.5% especially in the bands M2 and M3.
 - ✓ Growing differences over time are observed in bands of M5, M6, M7, I1 and I2.
- The S/WWIR band LBRs also suggest time dependent ratio differences.
- The direct ratios of I2/M7 and I3/M10 are very consistent within 0.2% in both LBRs and F factors.
- Strong wavelength dependencies are observed in longer wavelength bands beyond M5 at 672nm.
- The LBR demonstrated the radiometric stability and consistency in short wavelength bands in M1, M2, M3, and I1.

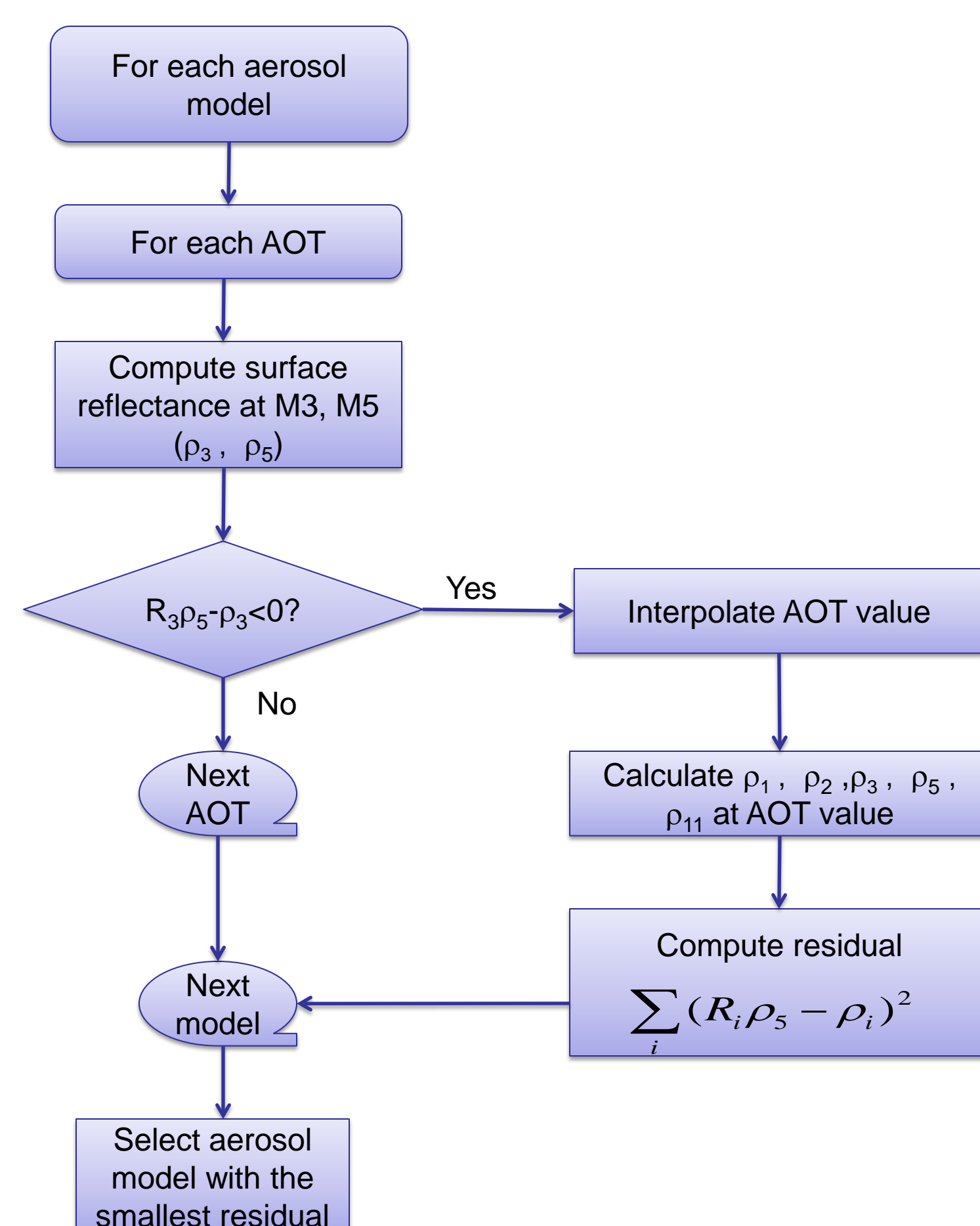
Reference

- [1] J. Sun, X. Xiong, J. Butler, "NPP VIIRS On-Orbit Calibration and Characterization Using the Moon," SPIE 2012: San Diego, CA; U.S.
- [2] C. Cao, E. Vermote, X. Xiong, "Using AVHRR lunar observation for NDVI long-term climate change detection," JGR, Vol. 114, D20105, 2009.

Introduction

Surface reflectance ratios of M1/M5, M2/M5, M3/M5, and M11/M5 are crucial to the VIIRS AOT retrieval over land. Having better estimates of these ratios can improve AOT retrievals. Current VIIRS aerosol retrieval algorithm uses constant ratios over the whole globe. We present an investigation of the surface reflectance ratios over the global AERONET sites and show that we can improve the AOT retrieval by using more accurate surface reflectance ratios. Surface reflectance in the M1, M2, M3, M11 and M5 channels were retrieved at a large number of AERONET sites using AERONET-retrieved AOT. M1/M5, M2/M5, M3/M5, and M11/M5 surface reflectance ratios were then calculated for each site separately. These ratios vary strongly from site to site. This variability is the reason for the biases and standard deviations in the AOT retrieval when a single fixed value of the ratio is used. When instead the individual ratios are used in the AOT retrieval, their statistics (naturally) improve. In order to obtain these ratios without the help of the AERONET AOT, we tested a clear sky method, which assumes a low AOT and looks for the lowest atmospheric corrected M3/M5 ratio over a period of time. The clear sky ratios were obtained for each AERONET sites, which were then applied in land AOT retrieval. The resulting AOT retrievals also showed improvements over those from the original algorithm.

VIIRS Aerosol Retrieval over Land



In the flow chart, the ratios R_i are surface reflectance ratios between each band and band M5 (672nm).

The accuracies of the AOT retrievals over land are dependent on the accuracies of the surface reflectance ratios used in the algorithm.

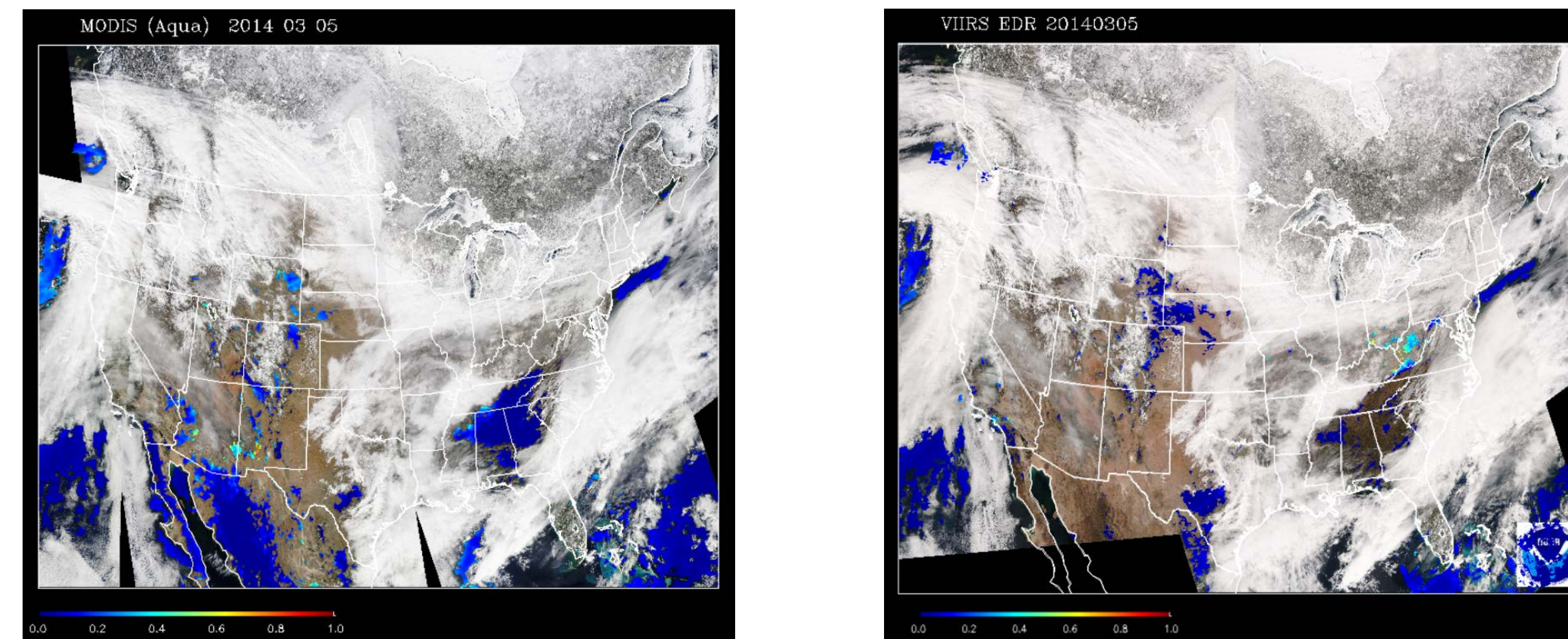
The ratio between M3 (488nm) and M5 determines the AOT value. AOT will usually be underestimated if a higher ratio is used and vice versa.

Current official VIIRS aerosol algorithm uses constant values globally.

On IDEA (Infusing satellite Data for Environmental Applications), NDVI dependent ratios are used.

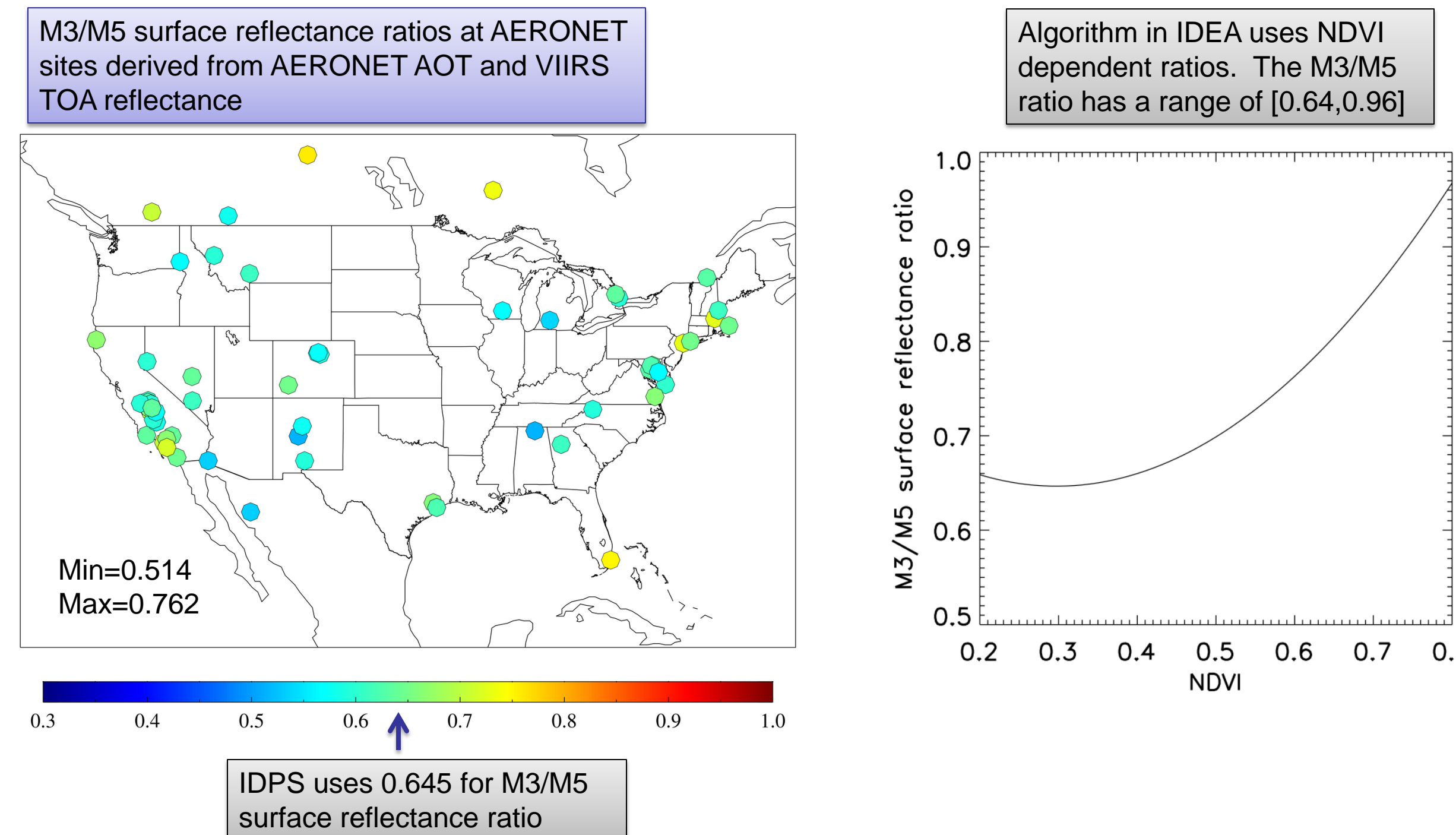
Figure 1. VIIRS AOT retrieval over land algorithm flow chart

VIIRS AOT data coverage



A comparison between MODIS Aqua (left) and VIIRS high quality EDR AOT (right) coverage over land: VIIRS AOT has less data coverage. Two reasons contribute to it: (1) VIIRS uses higher M3/M5 ratio than real value and therefore those no retrieval regions have negative AOT retrievals less than -0.05; (2) VIIRS does not have high quality AOT retrieval over soil dominated regions, which is defined as NDVI < 0.2.

Surface reflectance ratios



Many sites have M3/M5 surface reflectance ratio less than 0.64. When AOT is close to 0, negative AOT will be retrieved on those locations.

Estimate surface reflectance ratios at AERONET site

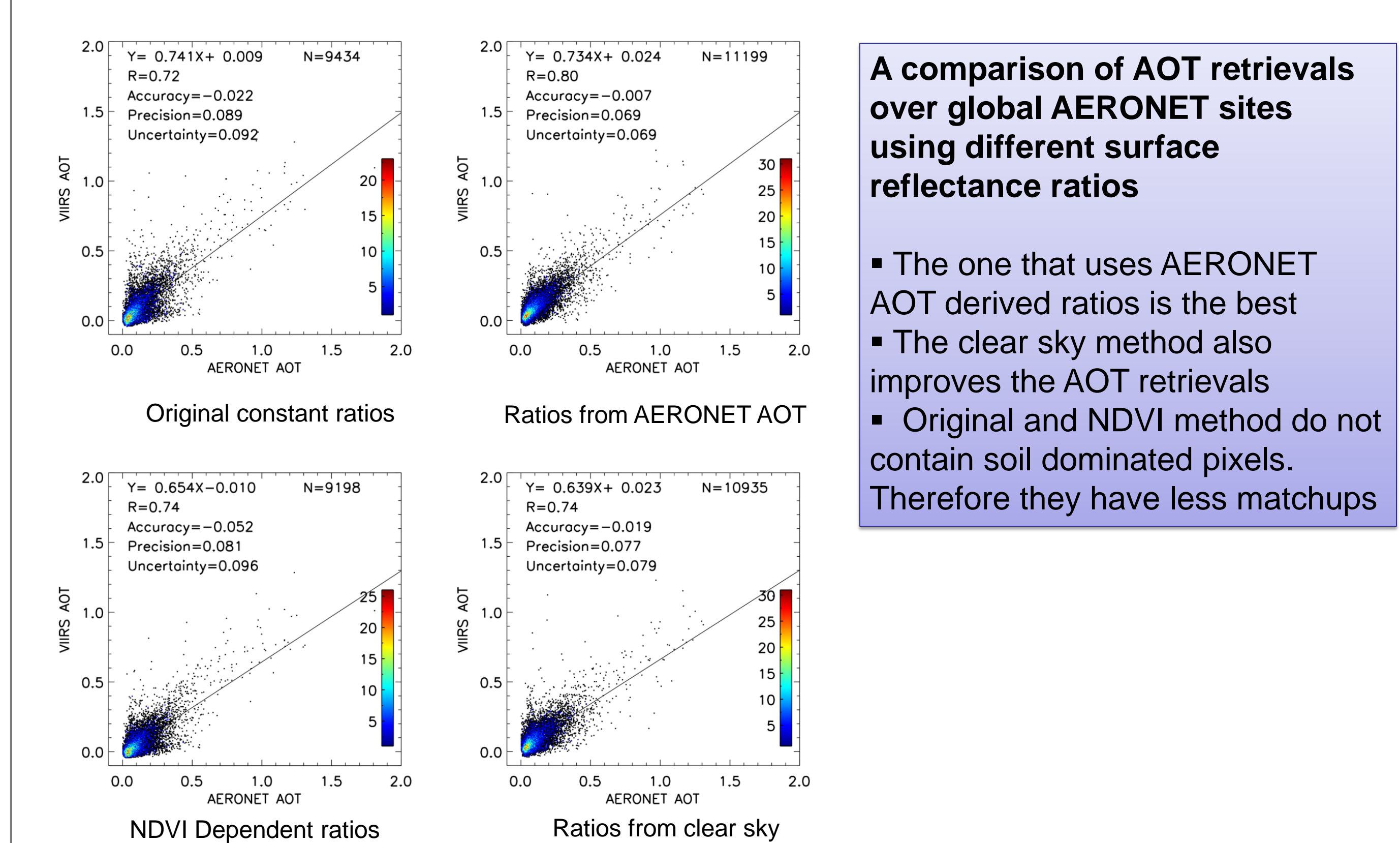
Method 1 (Use AERONET AOT)

- 2013 AERONET matchup dataset
- 25 km region
- Pixels with VIIRS IP AOT QF high or out of bound AOT (negative)
- AERONET AOT < 0.1
- Retrieve surface reflectance at M1, M2, M3, M5, M11 using TOA reflectance, AERONET AOT and LUT (look-up-table)

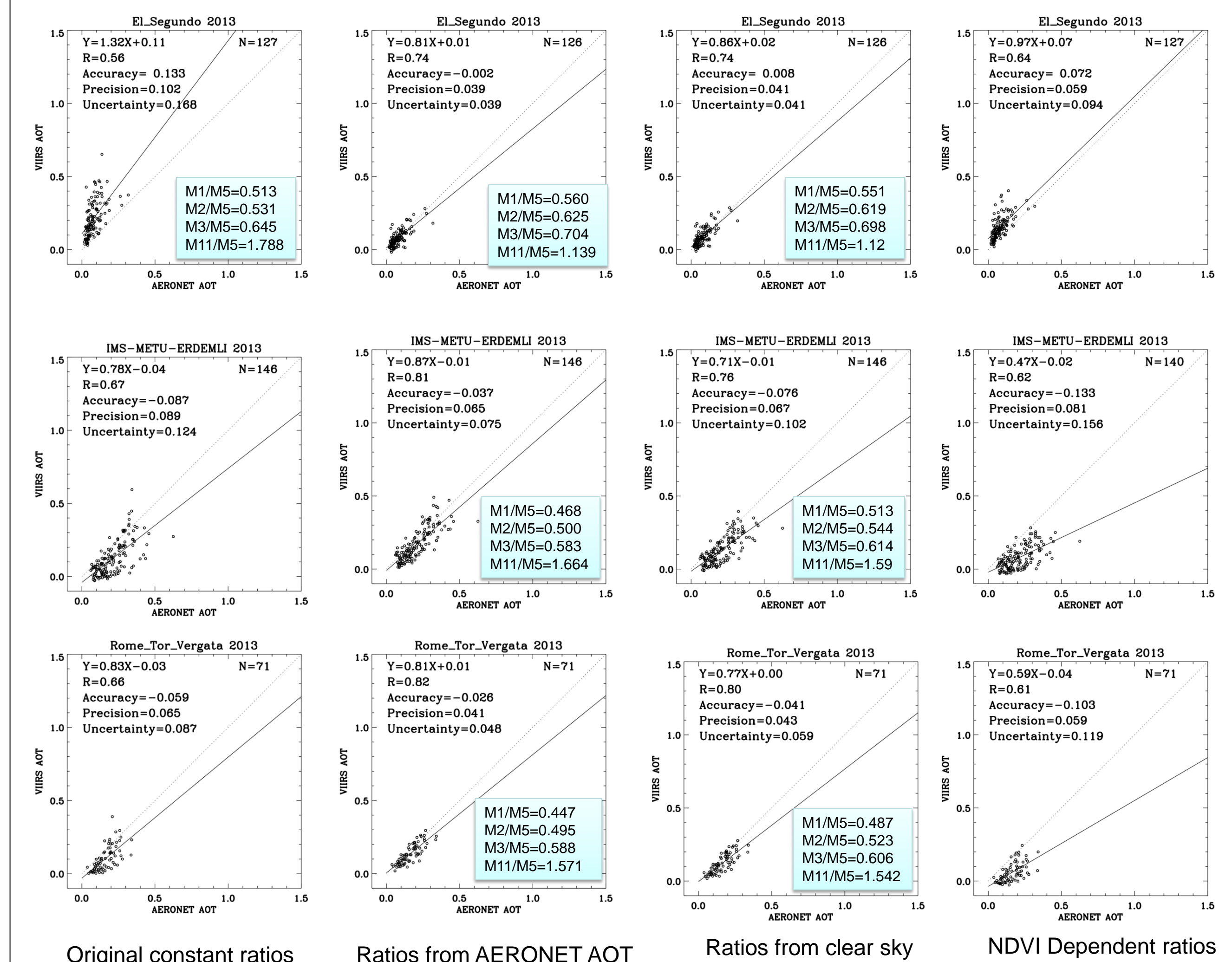
Method 2 (Clear sky)

- 2013 AERONET matchup dataset
- 25 km region
- Get surface reflectance ratios for each day, assuming AOT=0.05
- 20%+ pixels are high quality (high IP AOT quality or out of bound)
- Select the day with minimum M3/M5 ratio over the 30 day period
- Total 12 days over the whole year (Maybe less for the AERONET matchup dataset)
- Use the pixels from those 12 days to derive the ratios for each site

- Both methods add soil dominated pixels as high quality.
- The estimated surface reflectance ratios are then used for the AOT retrievals



AOT retrievals at selected sites using different ratios



Improvements of AOT retrievals are observed at the sites where the difference of the surface reflectance ratios are large. Between those from AERONET AOT and the constant ratios used in the official algorithm.

Summary

- Using site specific surface reflectance ratios can improve AOT retrieval statistics
- Including soil dominated pixels does not degrade AOT statistics
- Future work:
 - Expand clear sky method to the whole globe
 - Develop surface ratio database
 - Include seasonal variation of the surface ratios
 - Test the algorithm sensitivity to the choice of the clear sky AOT (currently 0.05)

Acknowledgment

The project is supported by NOAA.

VIIRS SST at the Naval Oceanographic Office analyses at NAVO/USM

Jean-François Cayula

QinetiQ North America,inc

Douglas May, Bruce McKenzie, Keith Willis

Naval Oceanographic Office

NAVOCEANO Milestones

- Operational with NPP VIIRS SST: March 2013
- Official Distribution in GDS 2.0 format: September 2013 (first GDS 2.0 SST product on JPL/GDAC)
- Monitoring NAVO SST statistics for over 2 years

NAVOCEANO SST Evaluation

- Statistics for April based on match-up buoys (count)
- NAVO VIIRS SST (Best quality):

	Count	Bias	RMS error
day	19780	-0.06	0.41
night	32470	-0.02	0.37

- NAVO VIIRS SST Statistics have remained stable and within requirements.
- Similar or better than NAVO AVHRR SST

NAVOCEANO SST EDR Evaluation

- For comparison, IDPS SST EDR (Best quality):

	Count	Bias	RMS error
day	8199	0.06	0.50
night	9476	-0.08	0.29

- Much smaller domain because of satellite zenith angle limit  can be relaxed with new equations
- Daytime RMS error varies 0.45-0.50°C due to missed aerosol and cloud contamination

Evaluation of Clear Sky determination on SST accuracy

- Accuracy of the VIIRS Cloud Mask (VCM) “cloud-free” SST retrievals
- Comparison with NAVOCEANO Cloud Mask (NCM)

NCM is a good comparison standard as it produces very clean SST for assimilation by oceanographic models.

VCM only handles the detection of clouds and not other contaminants → needs extra tests for a valid comparison.

Evaluation of Clear Sky determination on SST accuracy

- Added contamination tests: Simple tests to be considered as proof of concept
 - Daytime:
 - Reflectance test contingent on field test
 - Nighttime:
 - NCM aerosol test
 - Adjacency to cloud test contingent on field test

Evaluation of Clear Sky determination on SST accuracy

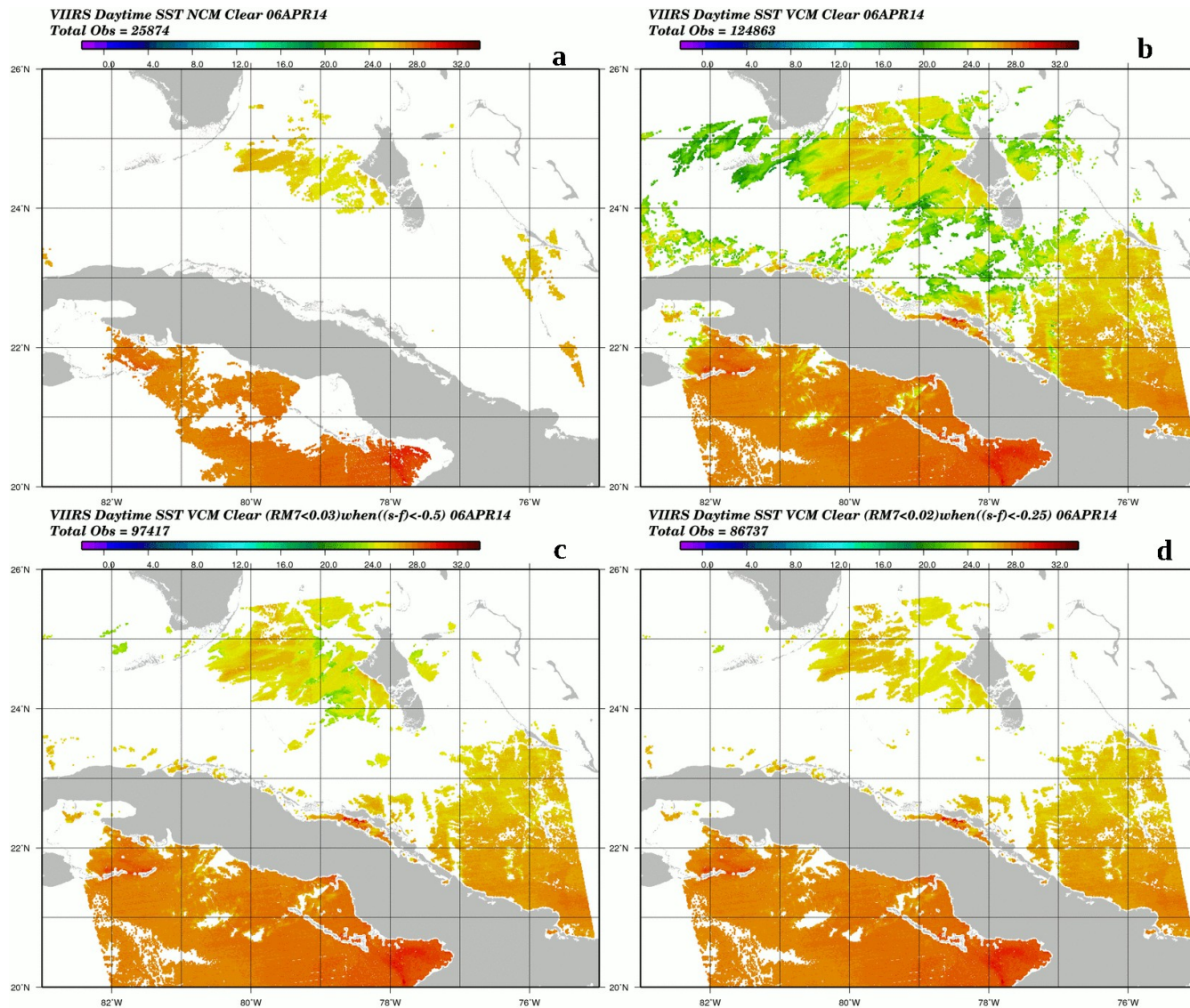
Daytime / February	Buoy matches	RMS error °C
NCM / NCM + test	4967 / 4901	0.51 / 0.50
VCM / VCM + test	16844 / 14863	0.70 / 0.51

Nighttime / February	Buoy matches	RMS error °C
NCM	6785	0.36
VCM / VCM + tests	21052 / 17171	0.56 / 0.34

- Additional tests mostly flagging adjacent retrievals to detected clouds  cloud leakage w/ original VCM
- VCM with additional tests performs as well as NCM, and allows increased coverage

Example of Clear Sky SST

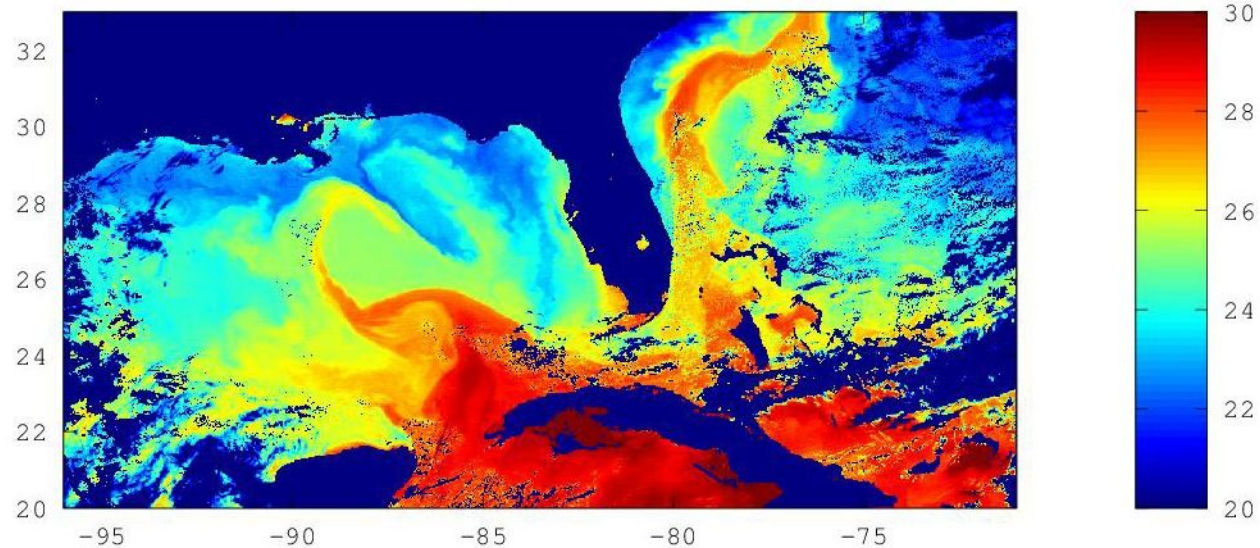
Daytime SST fields on April 6, 2014 a) for NCM clear, b) for VCM clear, c) for VCM clear with additional test, d) with a tightened additional test to remove remaining cloud leakage



SST analyses with Swath Overlap

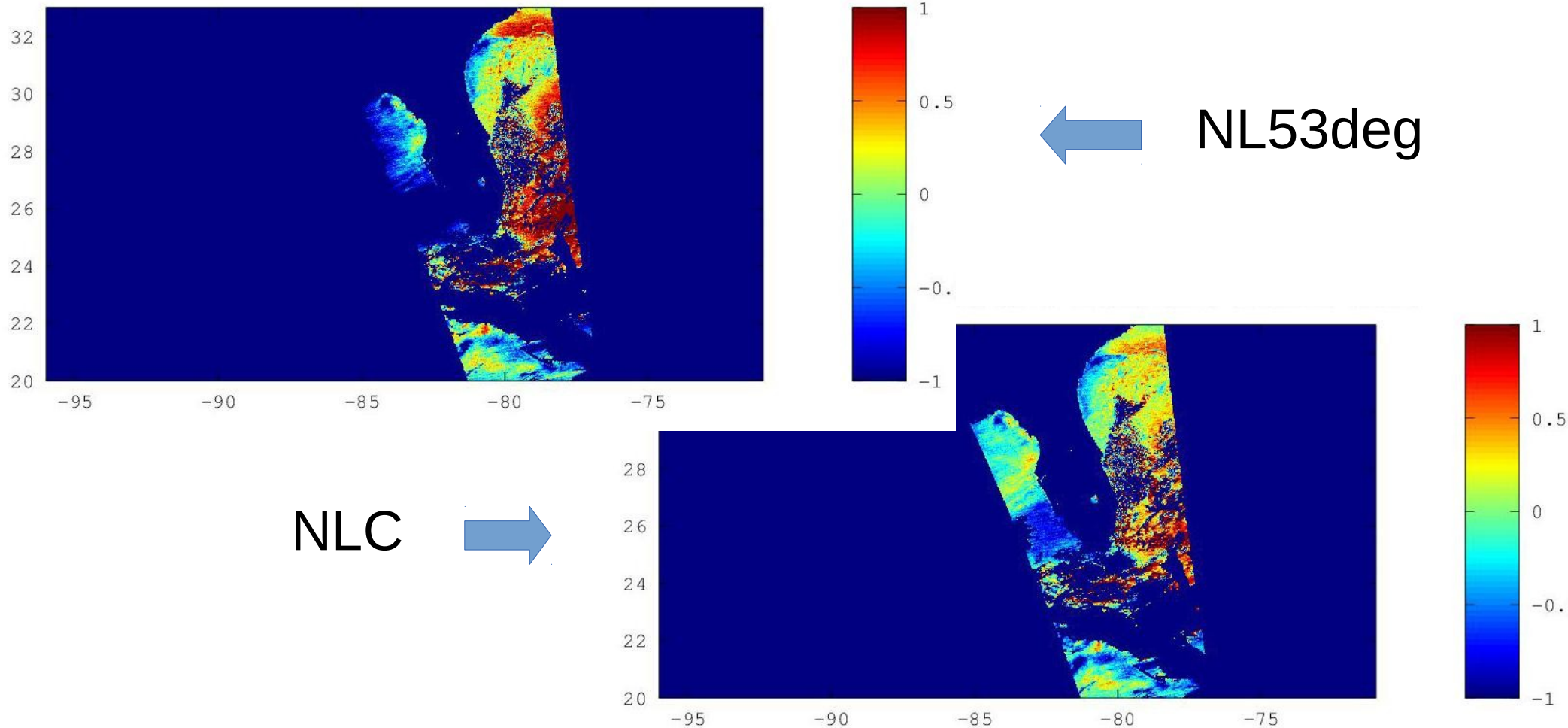
- With full swath processing, significant swath overlap even at low latitudes
- The overlap between swath can help evaluate SST equations at higher satellite zenith angle (SZA).
- Three types of equations:
 - Standard Non Linear SST – NL53deg (designed for SZA < 53°)
 - NLSST equation with additional SZA terms – “Non Linéaire Complet” (NLC) which is OSI/SAF daytime equation
 - Miami Lat-band algorithm v6
- For NLC: coefficients from NAVO, STAR, Météo France.

SST field May 14 2013



SST analyses with Swath Overlap

- SST field of later orbit is subtracted from that of earlier orbit
- Uncorrected limb darkening effect appears as a cold bias on west side of the overlap region and a warmer bias on the east side



SST analyses with Swath Overlap

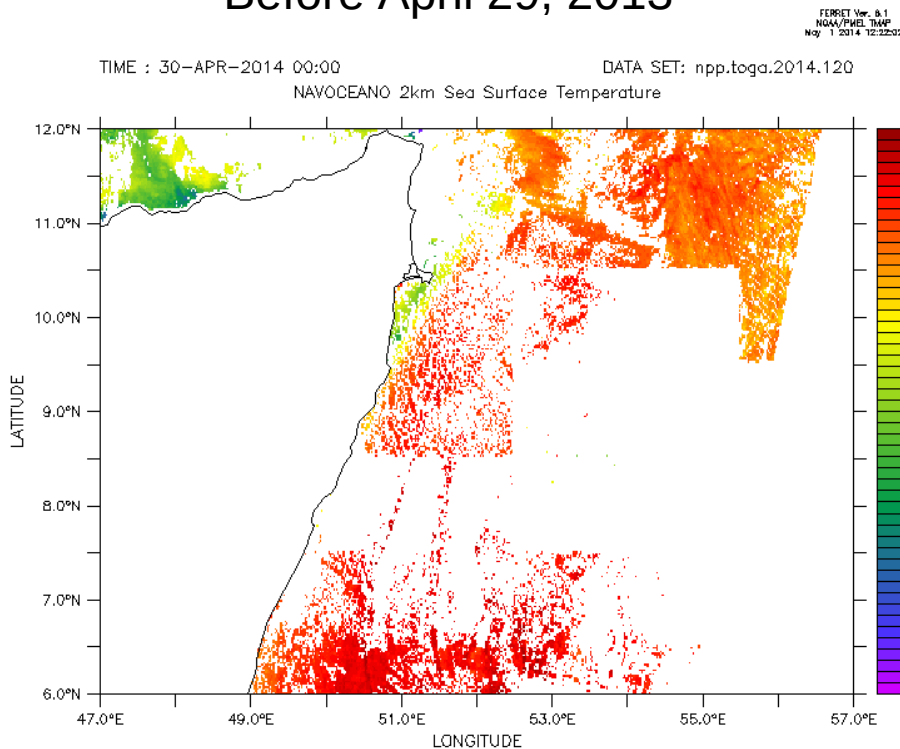
- Numerical results for domain shown in previous two slides
- As expected at high satellite zenith angle NL53deg performs significantly worse than NLC.

May 14, 2013	bias °C	mean absolute bias °C
NL53deg	-0.23	0.51
IDPS (old equations)	-0.23	0.52
Miami	-0.15	0.39
NLC (NOAA coefs 10/2013)	-0.12	0.41
NLC (Météo France coefs)	-0.13	0.38
NLC (NAVO coefs)	-0.09	0.27

NAVOCEANO improvements

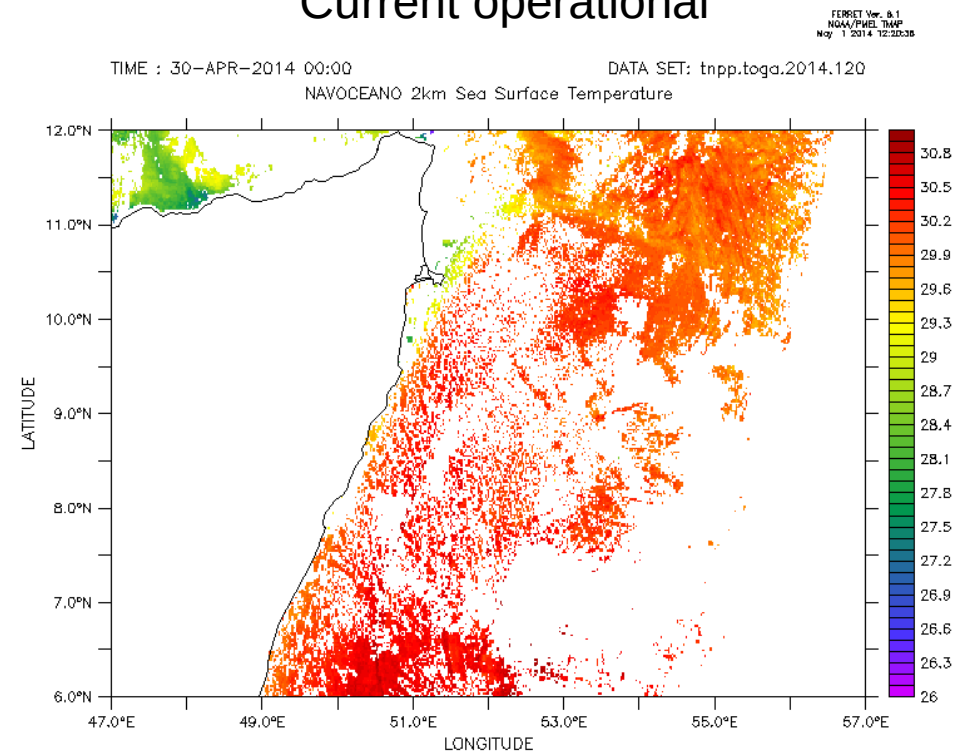
- NAVOCEANO is investigating the use of VCM or improvements to NCM for SST production
- Example: Recent improvements address coverage and cloud detection artifact issues in nighttime SST

Before April 29, 2013



Nighttime Sea Surface Temperature (celsius)

Current operational

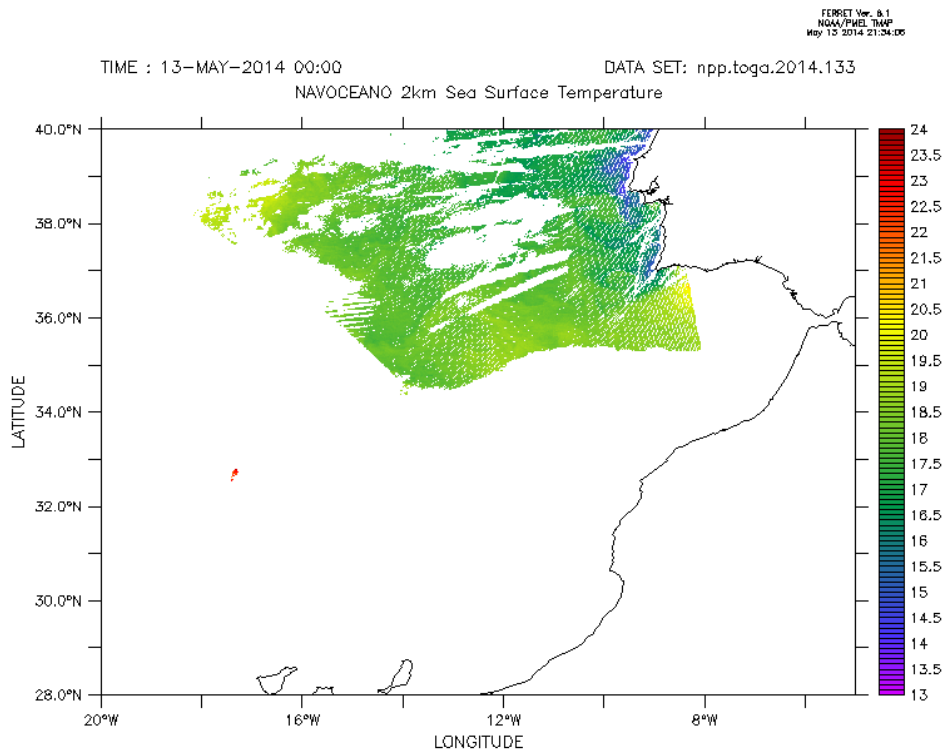


Nighttime Sea Surface Temperature (celsius)

NAVOCEANO improvements

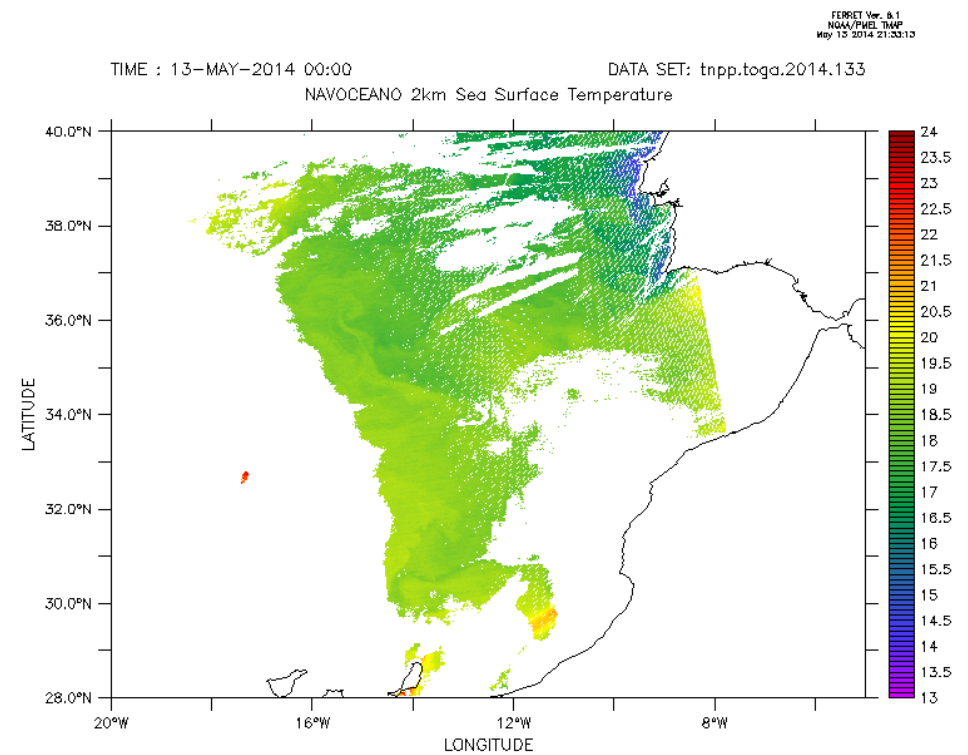
- Example: Proposed modification to address coverage and cloud detection artifact issues in daytime SST

Current operational



Daytime Sea Surface Temperature (celsius)

In testing



Daytime Sea Surface Temperature (celsius)

Conclusion

- VIIRS is an excellent sensor which allows the production of quality SST retrievals.
- VCM with additional tests performs well for SST production. VCM would benefit from access to computed SST retrievals and a good previous day SST field.
- Full swath processing allows overlap analyses even at low latitudes but requires the switch to an NLC (NL with extra SZA terms) type equation.

Direct Estimation of Land Surface Albedo from VIIRS Data

Algorithm Improvement and Preliminary Validation

Dongdong Wang¹, Shulin Liang¹, Yuan Zhou¹, Tao He¹, Yunyue Yu²
¹Department of Geographical Sciences, University of Maryland, College Park, MD 20742
²NOAA/NESDIS/STAR, Camp Springs, MD 20746

Overview

- Surface albedo is the ratio between outgoing and incoming shortwave radiation at the Earth surface. It is an essential component of the Earth's surface radiation budget.
- Surface albedo EDR is combination of land surface albedo (LSA), ocean surface albedo (OSA) and sea-ice surface albedo (SSA).
- Two algorithms (Dark Pixel Sub-Algorithm (DPSA) and Bright Pixel Sub-Algorithm (BPSA)) implemented for LSA; DPSA derives the BRDF information from the 17-day gridded surface reflectance IP, and then calculates spectral albedoes which then are converted to broadband albedo using empirical models. BPSA directly estimate broadband albedo from VIIRS TOA radiances.
- BPSA is also applied to sea ice pixel to estimate SSA with a separate LUT specifically developed for sea-ice surfaces.
- The BPSA is currently used to generate LSA. Several improvements have been made since the S-NPP launch.

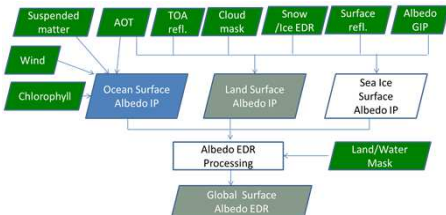


Fig. 1. A flowchart showing the major inputs data to surface albedo EDR algorithm

Example of VIIRS LSA maps

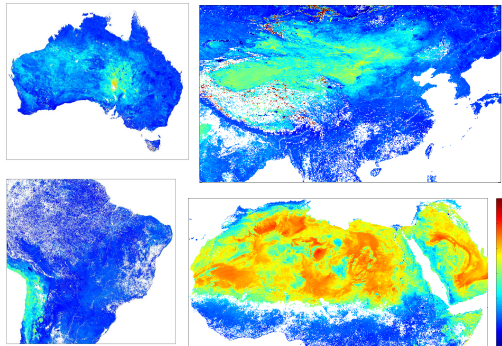


Fig. 2. Temporal averaged maps of surface albedo, May 8-23, 2012

Publication

Wang, D., S. Liang, T. He, and Y. Yu (2013), Direct estimation of land surface albedo from VIIRS data: Algorithm improvement and preliminary validation, *J. Geophys. Res. Atmos.*, 118, 12,577–12,586, doi:10.1002/2013JD020417

Refinement to the BPSA algorithm

- A new LUT of LSA BPSA regression coefficients was developed:
 - Using updated spectral response function;
 - Considering multiple aerosol types;
 - Including surface BRDF in radiative transfer simulation;
 - Developing surface-specific LUTs.
- The new BRDF LUT has not been implemented in the NOAA operational system yet.
- Analysis of results from the new BRDF LUT is based on the data generated at the UMD local facility.

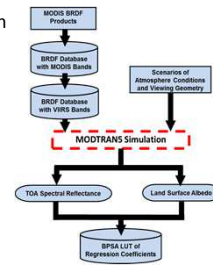


Fig. 3. A brief flowchart showing how the BPSA LUT of regression coefficients is generated

Temporal stability of LSA retrievals

The LSA retrievals in the summer of 2012 over two Libya desert sites (Site 1: 24.42°N 13.35°E and Site 2: 26.45°N, 14.08°E) are used to illustrate the issue of temporal variability of LSA.

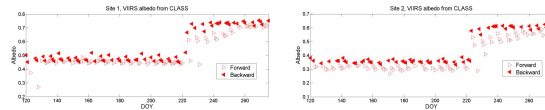


Fig. 4. Time series of beta release data. Jumps around 8/9 were caused by the bugs in an early version of the operational codes. "Forward" means pixels with relative azimuth angle >90° and "backward" means those with relative azimuth angle <90°.

New albedo estimated with the BRDF LUT has improved in temporal stability

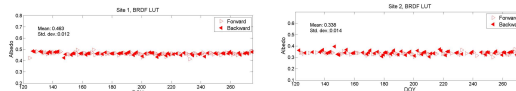


Fig. 5. LSA retrieved from new BRDF LUT. The spurious retrievals caused by undetected cloud and cloud shadow are excluded with the threshold of mean \pm 0.05.

Compare residual variations with those from alternative methods

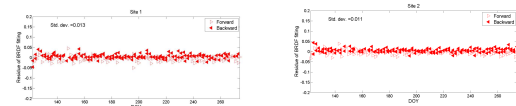


Fig. 6. Residue of BRDF fitting, calculated as the difference between MODIS surface reflectance and BRDF predicted from MODIS BRDF. The narrow-to-broadband conversion residues are used to convert spectral residues to the broadband residue.

Validation at SURFRAD

- Surface Radiation Budget Network, established in 1993

Table 1. List of seven SURFRAD sites.

Name	Location	Latitude	Longitude	Land cover
DRR	Desert Rock, NV	36.63	-116.02	Desert
BDN	Bondville, IL	40.05	-88.37	Cropland
FPK	Fort Peck, MT	48.31	-105.10	Grassland
GWN	Goodwin Creek, MS	34.25	-89.87	Forest/Pasture
PSU	Penn State, PA	40.72	-77.93	Cropland
SXF	Sioux Falls, SD	43.73	-96.62	Grassland
TBL	Boulder, CO	40.13	-105.24	Grassland

- Bondville is not used due to great spatial heterogeneity
- Instantaneous measurements of downward and upward shortwave radiation at the surface every minute

Site	VIIRS (BRDF LUT)			VIIRS (beta release)			MODIS		
	R ²	RMSE	Bias	R ²	RMSE	Bias	R ²	RMSE	Bias
Boulder	0.96	0.029	0.011	0.91	0.034	0.012	0.79	0.047	0.002
Fort Peck	0.89	0.070	0.001	0.72	0.138	0.076	0.98	0.043	-0.020
Goodwin Creek	0.01	0.040	-0.033	0.19	0.122	0.066	0.11	0.051	-0.048
Desert Rock	0.10	0.032	0.026	0.11	0.157	0.116	0.02	0.025	-0.023
Penn State	0.60	0.040	-0.020	0.27	0.127	0.073	0.02	0.079	-0.054
Sioux Falls	0.89	0.064	0.004	0.59	0.149	0.088	0.87	0.059	-0.001
Overall	0.84	0.046	0.001	0.48	0.143	0.090	0.80	0.050	-0.023

Table 2. Summary of validation results at seven SURFRAD sites (Top: 2012, bottom: 2013). Three satellite albedo data (VIIRS LSA from the Lambertian LUT, VIIRS LSA from the BRDF LUT and MODIS albedo) are validated against field measurements.

Site	VIIRS (BRDF LUT)			VIIRS (beta release)			MODIS		
	R ²	RMSE	Bias	R ²	RMSE	Bias	R ²	RMSE	Bias
Fort Peck	0.97	0.042	-0.006	0.94	0.063	0.001	0.99	0.064	-0.038
Goodwin Creek	0.02	0.037	-0.031	0.03	0.086	-0.010	0.02	0.048	-0.046
Desert Rock	0.06	0.038	0.029	0.07	0.101	0.048	0.29	0.013	-0.010
Sioux Falls	0.98	0.081	-0.066	0.92	0.097	-0.069	0.98	0.066	-0.062
Penn State	0.86	0.114	0.048	0.82	0.142	0.057	0.91	0.062	-0.007
Boulder	0.97	0.050	0.020	0.89	0.087	0.029	0.27	0.134	-0.037
Overall	0.88	0.061	0.010	0.77	0.099	0.024	0.82	0.068	-0.026

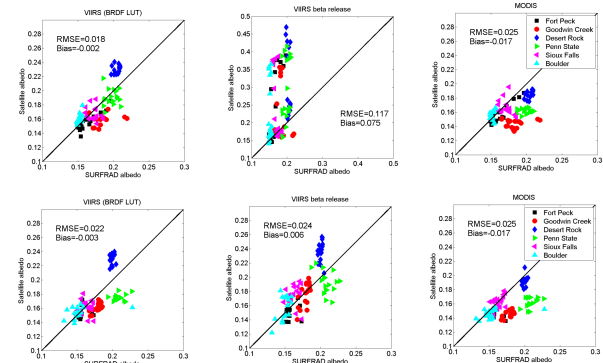


Fig. 7. Validation results of 16-day mean albedo from VIIRS BRDF LUT, CLASS VIIRS data and MODIS, using data from 2012(top) and 2013 (bottom) non-snow seasons (May-September) at six SURFRAD sites.

Summary

- Validations are performed with comparisons to MODIS LSA, in-situ LSA, LSA map monitoring, evaluation of LSA temporal stability.
- Validation results demonstrate the VIIRS BPSA algorithm can reliably retrieve LSA over both dark and bright surfaces.
- Continuous efforts have been put to improve the BPSA LSA algorithm. The refined algorithm will be able to provide more stable and consistent LSA with higher accuracy for the J1 mission.
- Comprehensive validation will be carried out to better understand uncertainties of LSA products.

Repair for VOCCO Coastal Products

Evaluation of the IDPS (VOCCO) ocean color products in Coastal regions



Robert Arnone¹, R. Vandermeulen¹, S. Ladner², G. Fargion³, P. Martinolich⁴, Jen Bowers⁴

¹University of Southern Mississippi Department of Marine Science, ²Naval Research Laboratory Stennis Space Center, ³San Diego State University, ⁴QNA- Corporation

Objectives:

- Define Limitations of the present IDPS VIIRS processing for ocean color in high scattering waters (VOCCO failures)
- Evaluate the impact of negative radiance in high Scattering waters for VOCCO
- Demonstrate how VIIRS IDPS products can be improved
- Show need for a DR to be established for the NIR processing

Atmospheric correction:

- Correctly partitioning the contribution of various atmospheric components from the total radiance signal is necessary to retrieve confident ocean measurements (Lu):

$$L_t(\lambda) = L_r(\lambda) + L_a(\lambda) + L_o(\lambda)$$

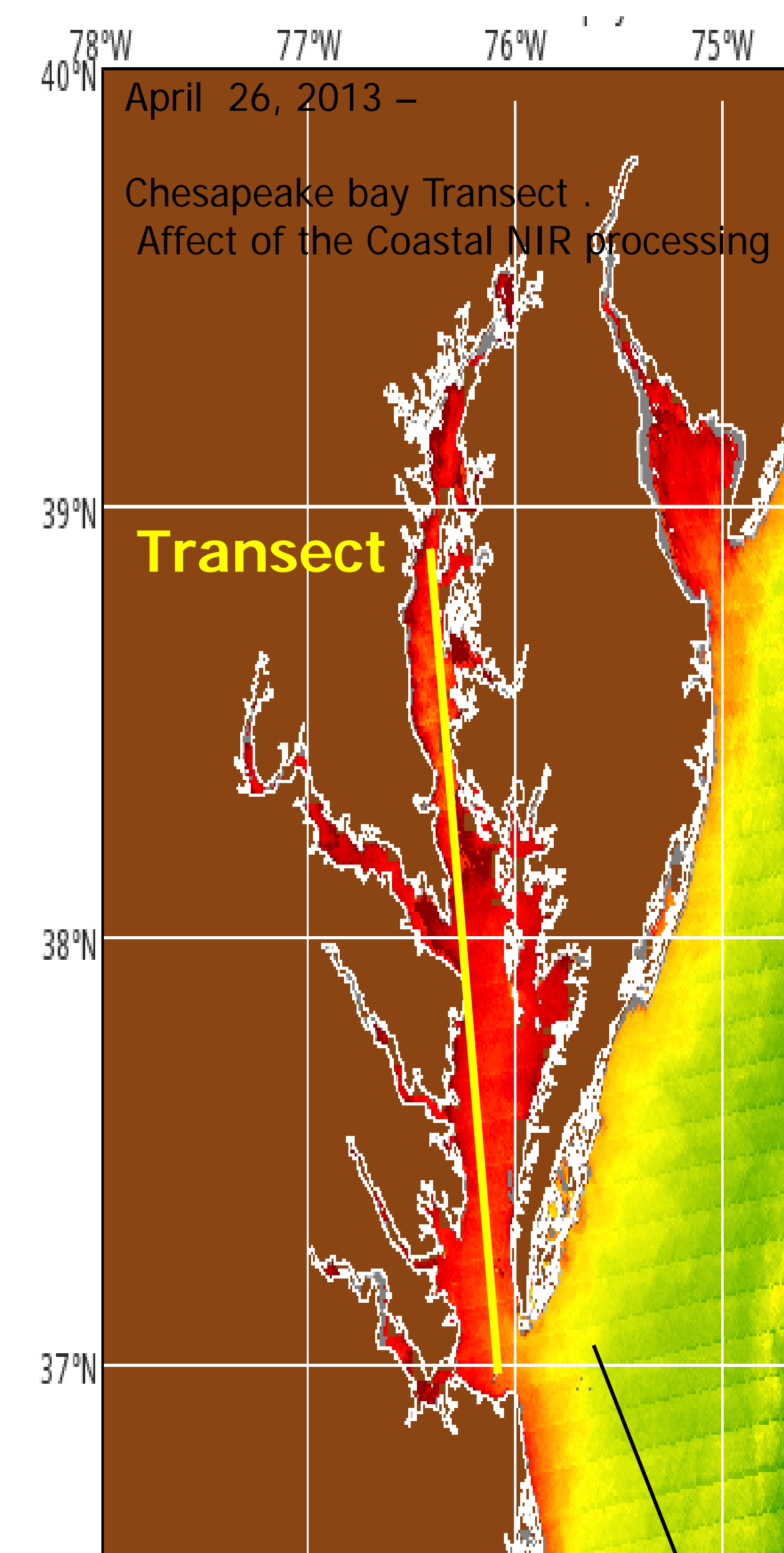
Total = Rayleigh + Aerosol + Ocean

Black Water Assumption

$$L_a(865) = L_t(865) - L_r(865) - L_o(865) \rightarrow 0$$

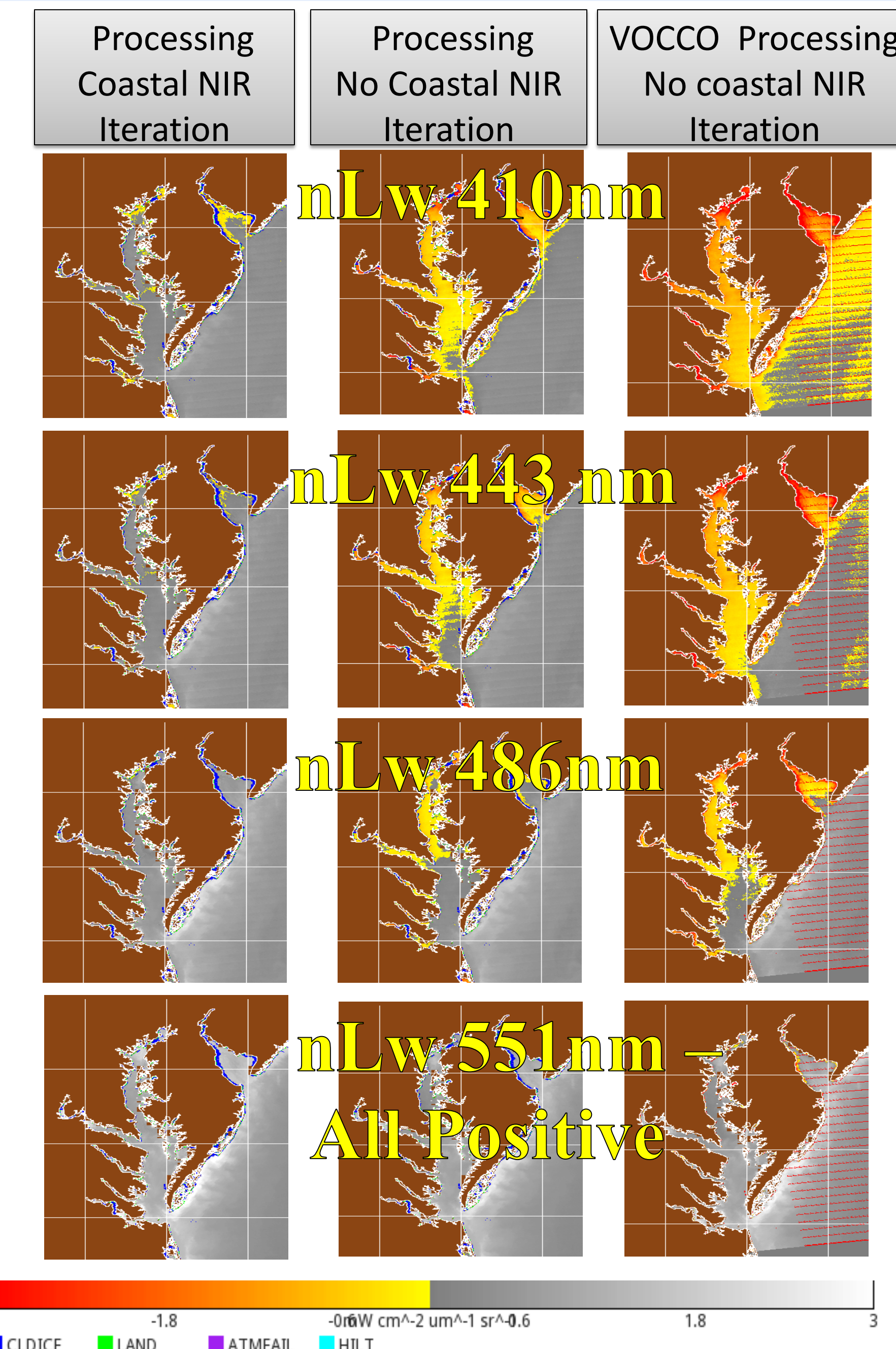
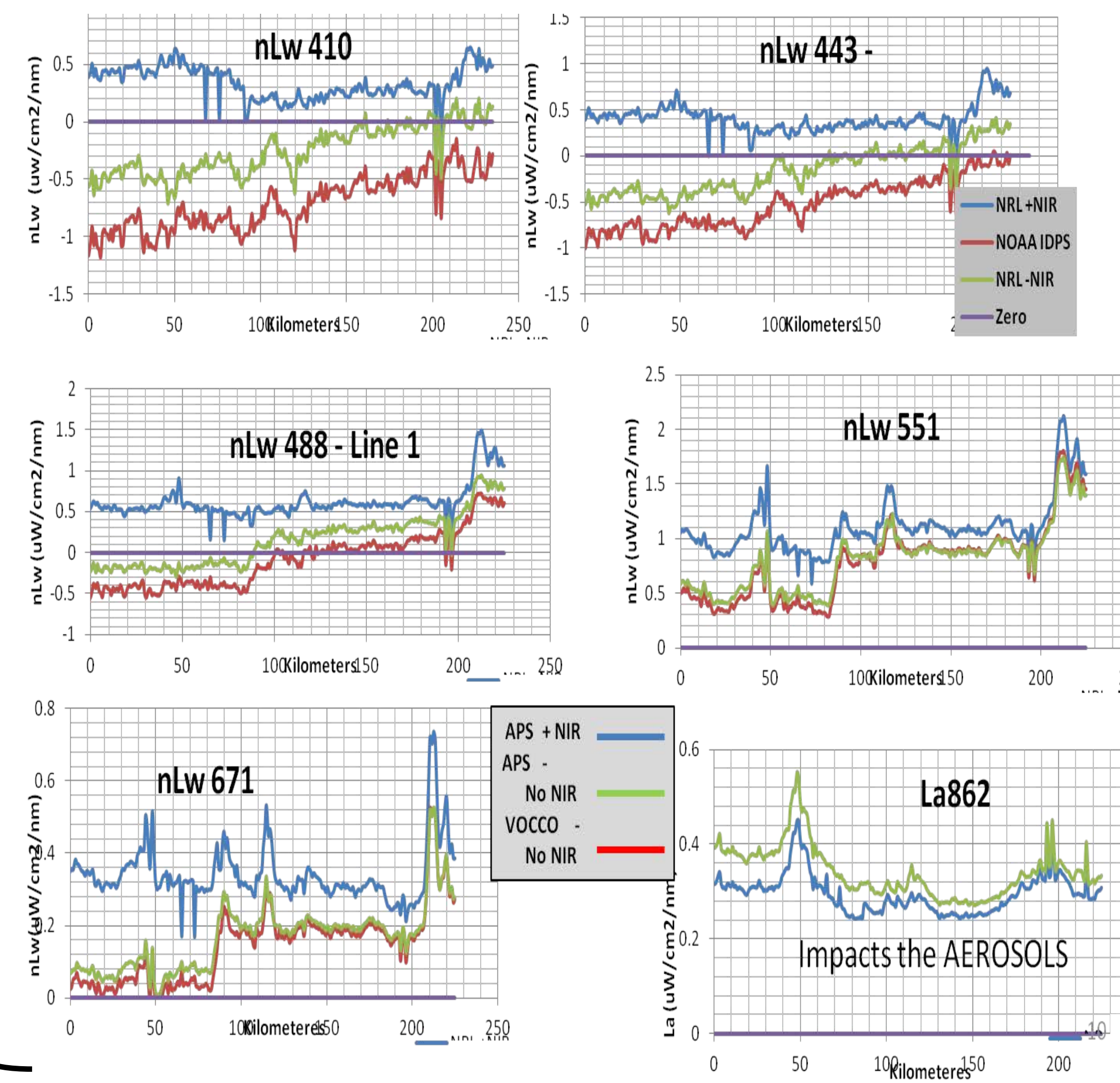
In high scattering water the $L_u(865) > 0$

- Black pixel assumption violations can be handled using an "iteration" or Coastal NIR processing procedure
- Uses the spectral water backscattering to derive the $L_u(865)$



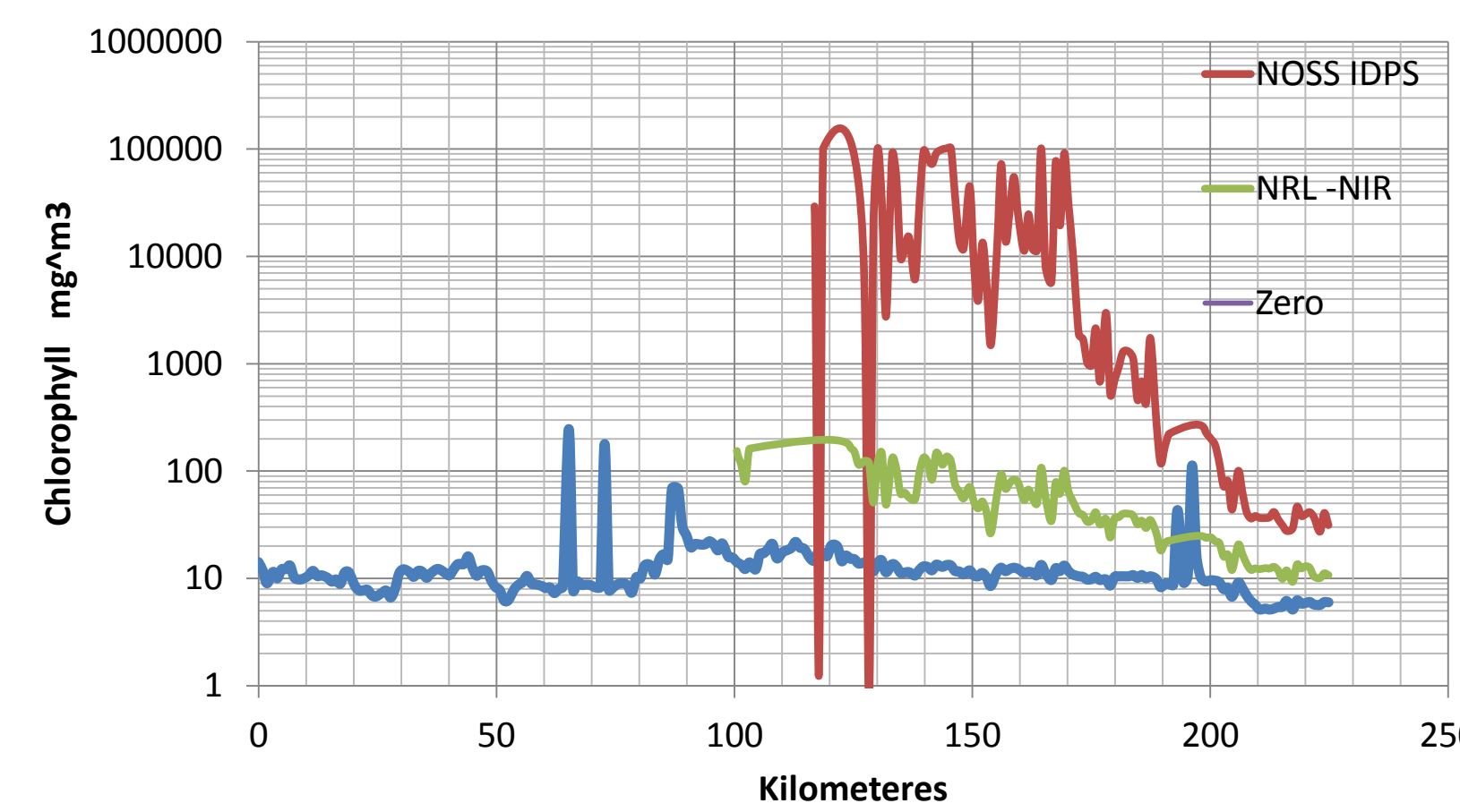
Evaluation of Coastal NIR implementation

Chesapeake Bay Transect NASA, NOAA, and NAVY processing



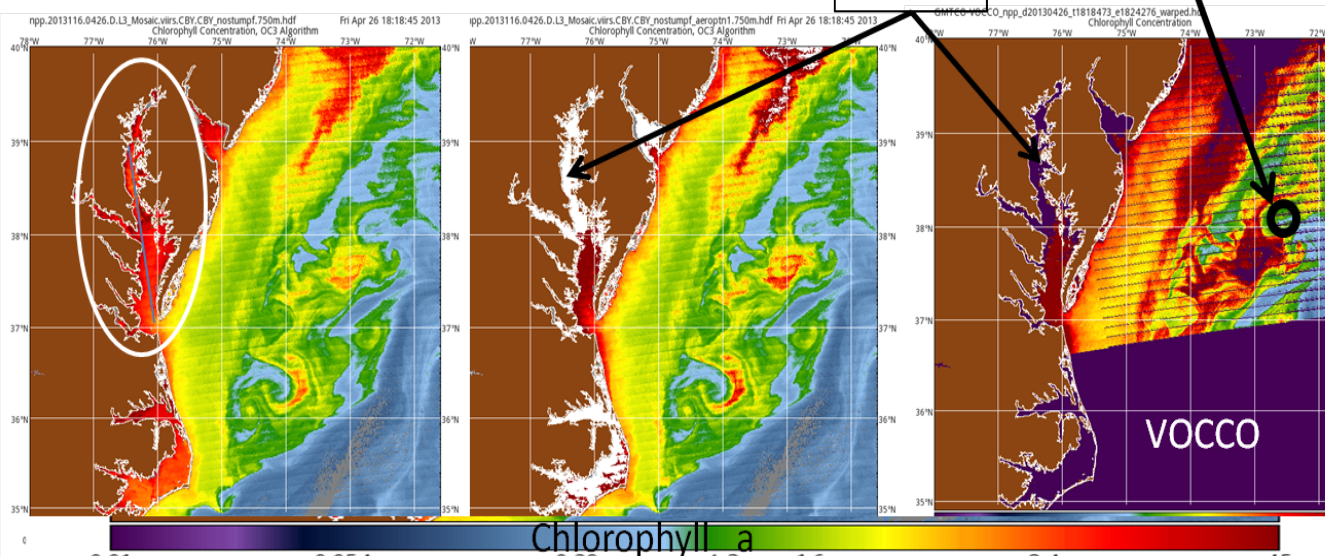
Impact of "non-zero" nLw 865 on coastal products

Chlorophyll - Along Transect



Evaluation of the IDPS VOCCO ocean products Failures

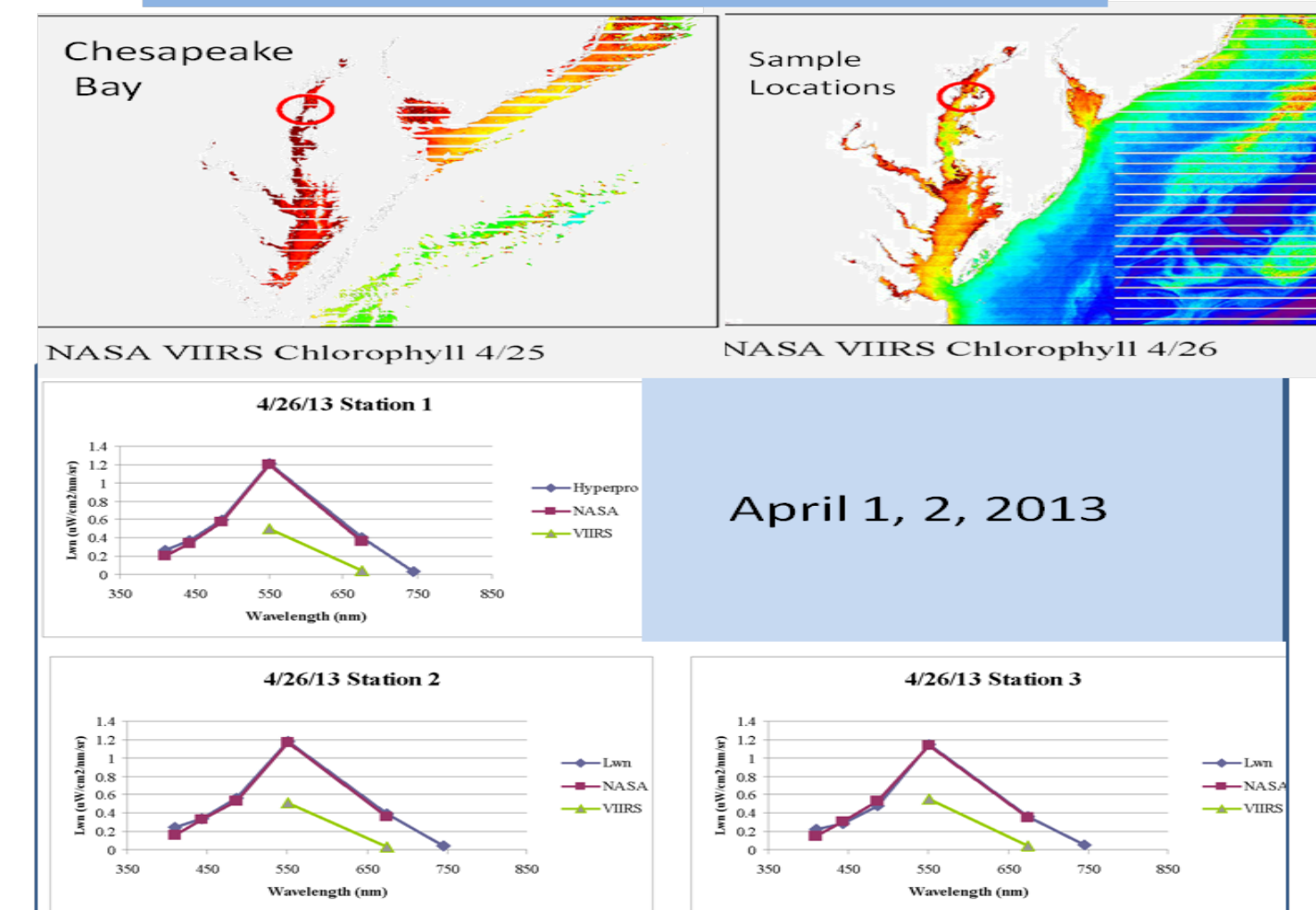
April 26, 2013
Focus on the Chesapeake Bay Retrievals



Validation of NIR Coastal Products

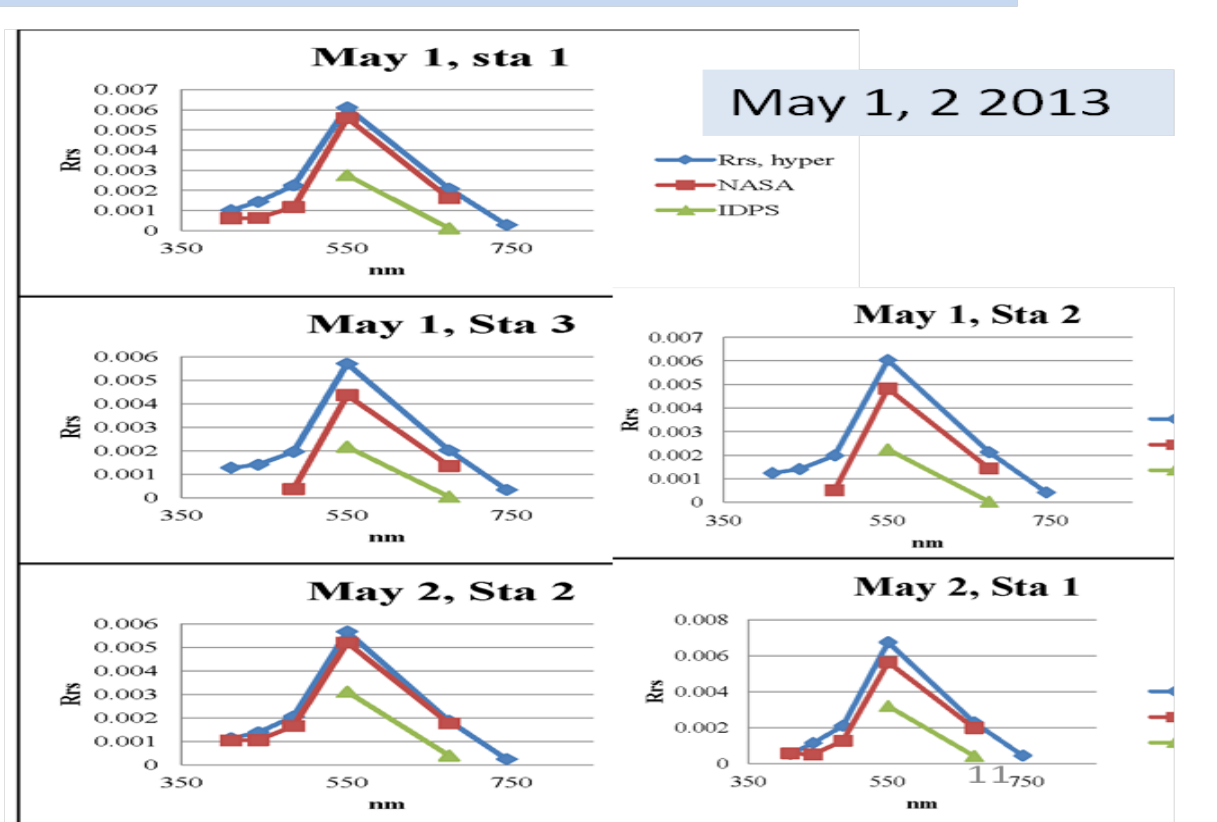
STAR Coastal Data sets Upper Chesapeake Bay (Mike Ondrusek)

4 Cruises show similar results
4/25, 4/26, 5/1, 5/2 2013



Validation of the Coastal IR using NASA and APS processing

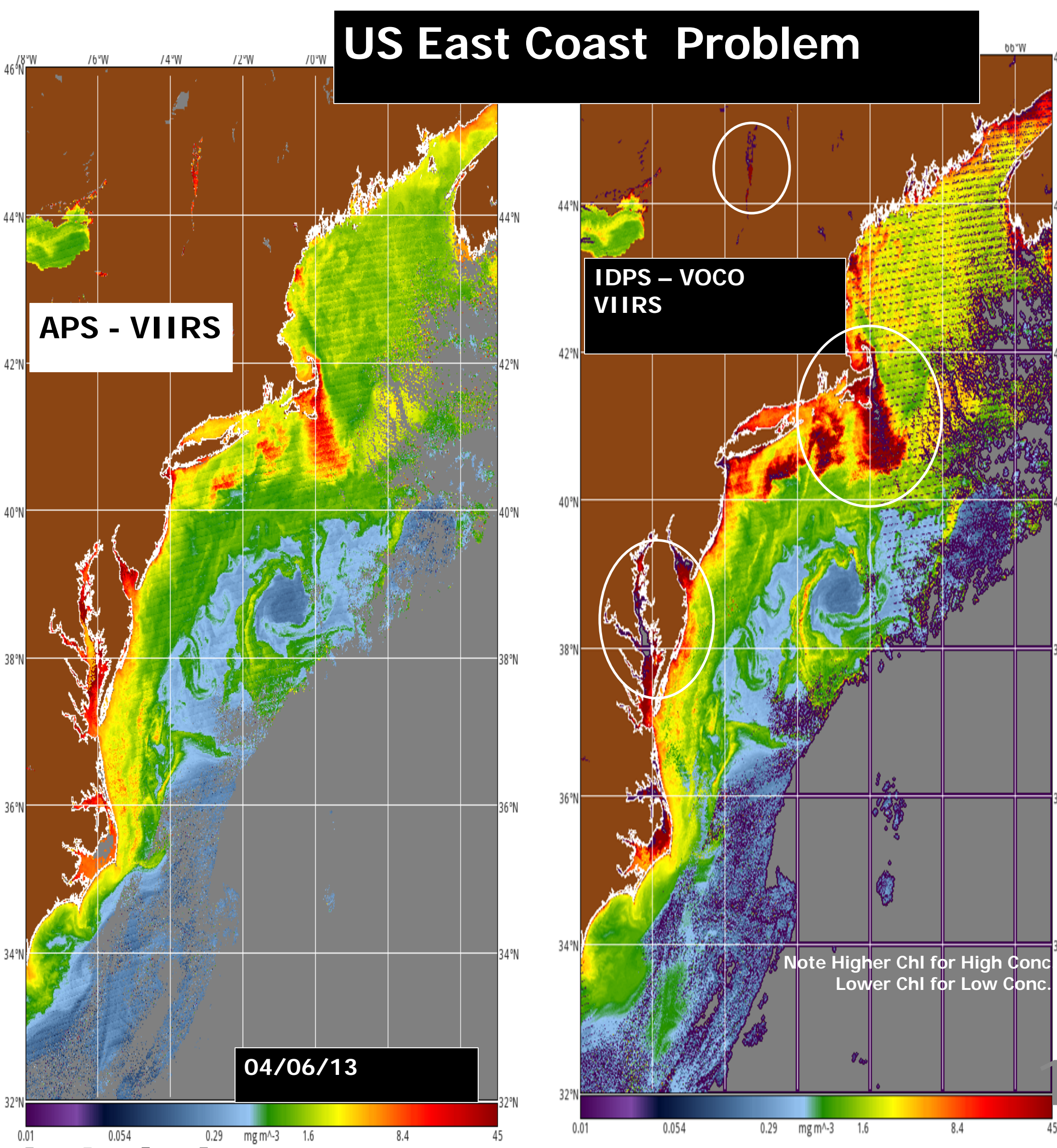
Results
April 25, 26, May 1, 2 - Matchup
VOCCO 410, 440, 488 Negative
nLw(555) ~ 56% low
nLw(672) ~ 89% low



Summary: It Works - Major Improvement

Black Water assumption and Coastal NIR Affects coastal and Shelf waters

- Produces Negative or "NO" nLw retrievals Greater in 410, 443, 488
- Produces reduced values in "certain areas"
- Impacted the Aerosol (L_a) atmospheric correction removal
- Impacts - Lower nLw (radiance) and Higher Chlorophyll values
- Accounts for differences of VIIRS and MODIS products
- Results in VIIRS not meeting Ocean requirements.



Current and Future Marine Optical BuoY (MOBY)

Kenneth Voss, University of Miami
 Mark Yarbrough, Moss Landing Marine Laboratory
 Carol Johnson, National Institute of Science and Technology (NIST)
 Kent Hughes, NOAA/NESDIS

Abstract

The MOBY system has provided vicarious calibration data for virtually all ocean color satellites since the launch of NASA's SeaWiFS instrument. MOBY has been operating continuously since 1997 in an operational manner, and the current system is described in this poster. Recently we have been funded to "refresh" the internal systems in MOBY with a new optical system and updated control electronics (MOBY-Refresh). This updated system will lead to improved data quality and reliability.

History

The Marine Optical BuoY (MOBY) (Clark et al. 1997, 2002) is the primary ocean measurement site for vicarious calibration of satellite ocean color sensors (Barnes et al. 2001, Eplee et al. 2001). Since late 1996, the time series of normalized water-leaving radiances $nL_w(\lambda)$, determined from the array of radiometric sensors attached to MOBY, has been the primary basis for the on-orbit vicarious calibrations of the USA Sea-viewing Wide Field-of-view Sensor (SeaWiFS), the Japanese Ocean Color and Temperature Sensor (OCTS), the French Polarization Detection Environmental Radiometer (POLDER), the German Modular Optoelectronic Scanner on the Indian Research Satellite (IRS1-MOS), and the USA Moderate Resolution Imaging Spectrometers (MODIS, Terra and Aqua). MOBY support has been provided to Japanese and European Space Agency calibration teams for the Global Imager (GLI) and the Medium Resolution Imaging Spectrometer (MERIS), respectively. The MOBY vicarious calibration $nL_w(\lambda)$ reference is an essential element in the international effort to develop a global, multi-year time series of consistently calibrated ocean color products using data from a wide variety of independent satellite sensors (Franz et al., 2007a).

Description of Present System

MOBY is a 16 m spar buoy (including the lower instrument bay) uniquely designed as an optical bench for measurements of $E_d(z, \lambda)$ and $L_u(z, \lambda)$ at depths of 1 m, 5 m, 9 m, and 12 m. Meteorological sensors for wind speed, wind direction, air temperature, relative humidity, and barometric pressure are mounted on the MOBY Mooring Buoy (MMOB). The Marine Optical System (MOS), the heart of MOBY, consists of two single-grating CCD spectrographs connected via an optical multiplexer and fiber optic cables to the $E_d(z, \lambda)$ and $L_u(z, \lambda)$ optical heads mounted at the ends of the buoy's three standoff arms. To provide low-loss transmission at ultraviolet wavelengths, 1 mm diameter silica fiber optic cables are used to connect the optical heads to MOS. $L_u(12, \lambda)$, at $z = 12$ m, is measured through a window in the bottom of the MOS housing itself. A seventh fiber optic cable connects a surface irradiance, $E_s(\lambda)$, cosine collector, mounted at the top of the MOBY above-water mast, to the spectrographs. Each pair of in-water optical heads is mounted on a standoff arm to minimize radiometric artifacts due to shadows or reflections from the buoy.

MOBY is continuously moored approximately 20 km west of the island of Lanai in a water depth of 1200 m. During prevailing trade wind conditions, this location is sheltered in the lee of the island, yet it is far enough offshore to minimize atmospheric perturbations associated with the island's wake. The MOBY Operations Site, located at the University of Hawaii (UH) Marine Facility in Honolulu, is staffed full time by personnel from the Moss Landing Marine Laboratories (MLML) for buoy maintenance, for instrument maintenance and calibration, and for staging buoy relief. The University of Hawaii's research vessels are used for cruises to support buoy deployments, and interim maintenance and quality control operations. A subset of the MOBY data is transmitted daily, via web linked cellular telephone, to the University of Miami (UM) in Florida. The MOBY data are transferred from UM to MLML for processing to produce and extract weighted band-averaged $nL_w(\lambda)$. These data are made available to NOAA via an MLML web host and ftp server, and are openly available through the NOAA Coastwatch site.

The current MOBY optical system has two spectrometers, one which covers the region from 350-620 nm (Blue spectrograph or BSG, and another which covers the region from 620 nm to 750 nm (red spectrograph or RSG). The light from each sensor head comes to the MOBY Optical System (MOS) over a fiber which is sequentially introduced to the spectrographs. A dichroic mirror separates the light into the two spectral regions. Along with the measurement fibers, there are internal calibration sources that can measure the instrument stability.

An example of the use of the MOBY system in determining the absolute calibration of a relatively stable satellite sensor (SeaWiFS) is shown in the figures on the right (Franz et al., 2007a). The SeaWiFS project used lunar views to determine the relative temporal drift of the sensor, while the absolute gain factor was determined through a vicarious calibration using the MOBY time series. One aspect of both the noise in the satellite retrieval and the inherent environmental noise in the MOBY system, is that multiple measurements are required for the satellite data to converge to the "true" gain factor. Presumably, if the noise in either of these systems was reduced, the number of data points required to attain convergence would also be reduced in a corresponding manner.

MOBY-Refresh Optical System

In the new optical system, as currently designed, we will be measuring the optical signal from all of the sensors simultaneously using an imaging optical system. The new spectrometers are based on a volume phase grating, and have the imaging capabilities to do this simultaneous imaging. A picture of the spectrograph is shown on the right along with an image taken from a prototype system displaying the imaging capabilities, with 14 individual channels displayed on the spectrograph.

An example comparison of the straylight in the current MOBY instrument vs the MOBY-Refresh prototype, is shown on the right. This figure is normalized by the peak in the central band. The stray light in the figure is due to scattering and imperfect imaging in the optical system. As can be seen, the new system will exhibit straylight approximately two orders of magnitude less than the current system. This improved characteristic will increase the accuracy of the data by decreasing the importance and reliance on the stray light correction in the data.

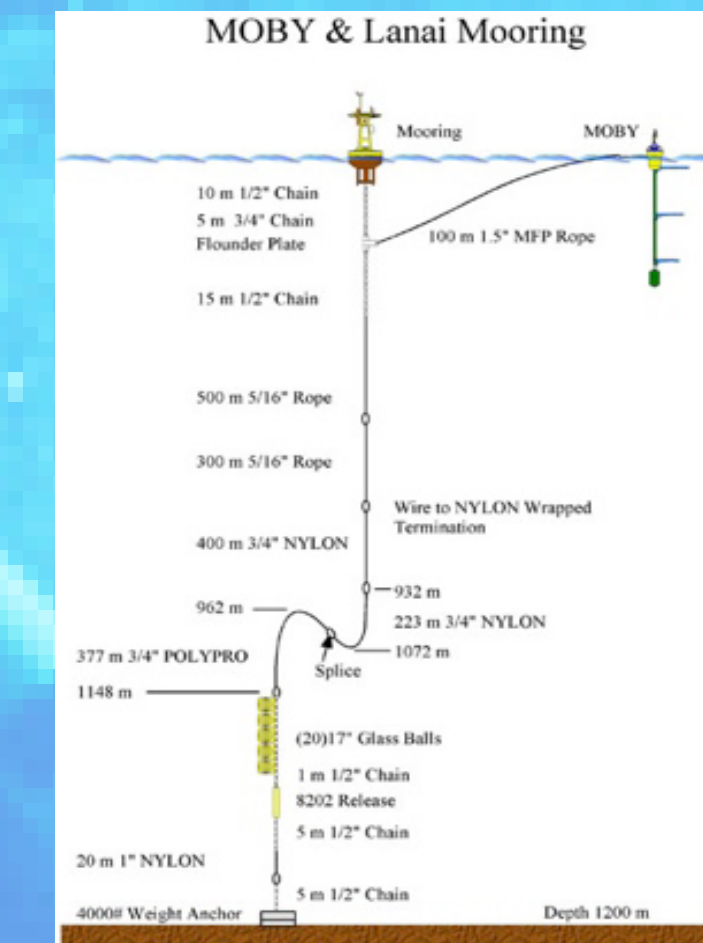
The other advantage of the new optical system is shown in the figure below, which shows some results derived from an experiment with the prototype optical system, deployed off of Hawaii (Yarbrough et al., 2007)). Here the water leaving radiance is derived in two ways. First the data were binned and used in a manner similar to the current system, where each measurement depth can only be determined in a sequential manner. The water leaving radiance determined in this way is shown with the large black dots. The scatter in these dots is similar to that seen in the MOBY data set. The data were then used to determine the water leaving radiance using each simultaneously acquired data set to determine an individual data point for the water leaving radiance. In this way the environmental noise is greatly reduced, resulting in less noise for the reported water leaving radiance. Additionally, with the simultaneous data, it is possible to make many more individual measurements, which through averaging will provide a more accurate representation of the natural light field viewed by the satellite. With this data set, the number of calibration points will be greatly reduced, allowing more rapid initialization of a new satellite sensor and the possibility of correcting a sensor which has more frequent instabilities (such as MODIS Terra (Franz, 2007b).

Conclusion

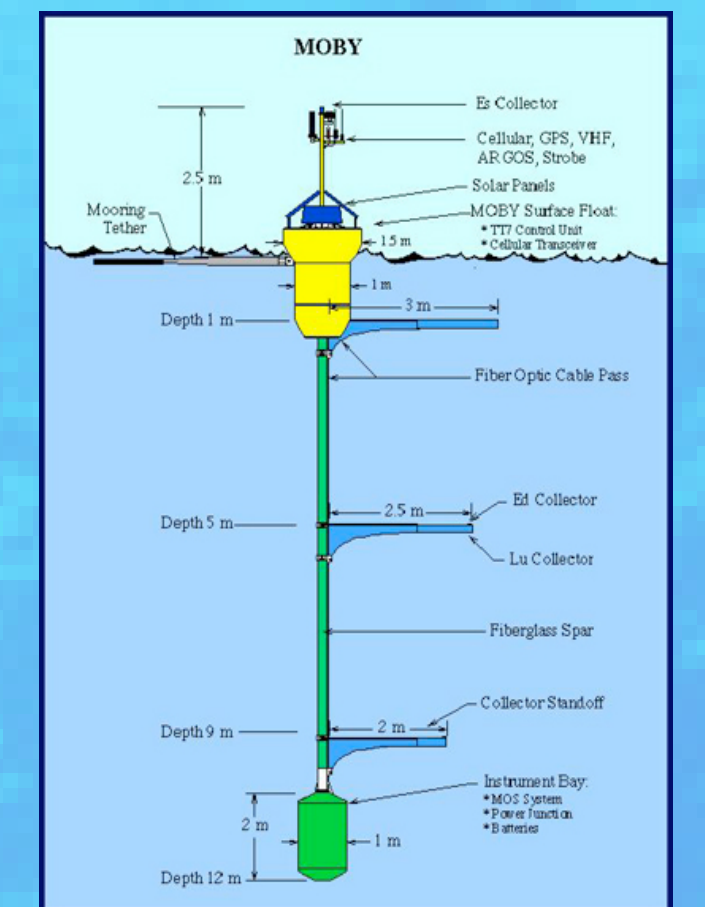
The MOBY system has provided invaluable data to the Ocean Color community for the vicarious calibration of ocean color satellite systems. While it has performed well in the past, many of the components are significantly past their design life time and the need for replacement/updates is critical. We are currently at the beginning of this process as we build up the new optical system and other subsystems in the MOBY platform. This will provide the capability to extend the MOBY time series and continued vicarious calibration capabilities into the future.

References:

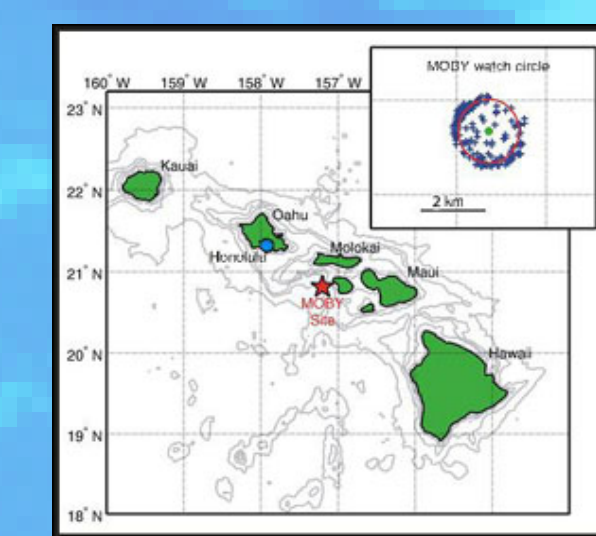
Barnes, R.A., R.E. Eplee, Jr., G.M. Schmidt, F.S. Patt, and C.R. McClain, 2001. The calibration of SeaWiFS, part1: Direct techniques, Appl Opt., 40: 6682-6700.
 Clark, D.K, H.R. Gordon, K.J. Voss, Y. Ge, W. Broenkow and C.C. Trees, 1997. Validation of atmospheric corrections over oceans. J. Geophys. Res., 102:17209-17217.
 Clark, D.K, M.A. Yarbrough, M.E. Feinholz, S. Flora, W. Broenkow, Y.S. Kim, B.C. Johnson, S.W. Brown, M. Yuen and J.L. Mueller 2002. MOBY, a radiometric buoy for performance monitoring and vicarious calibration of satellite ocean color sensors: Measurement and data analysis protocols. Ocean Optics Protocols for Satellite Ocean Color Sensor Validation, Revision 3, Volume 2. J. L. Mueller and G. S. Fraun, Eds. Greenbelt, MD, NASA Goddard Space Flight Center. NASA/TM--2002-21004:138-170.
 Eplee, R.E., Jr., W.D. Robinson, S.W. Bailey, D.K. Clark, P.J. Werdell, M. Wang, R.A. Barnes, and C.R. McClain, 2001. The calibration of SeaWiFS, part 2: Vicarious techniques, Appl. Opt., 40:6701-6718.
 Franz, B.A., S. W. Bailey, P. J. Werdell, and C. R. McClain, "Sensor-independent approach to the vicarious calibration of satellite ocean color radiometry," Appl. Opt. 46, 5068-5082 (2007a).
 Franz, B. A., E. J. Kwiatkowska, G. Meister, and C. R. McClain, "Utility of MODIS-Terra for ocean color applications," Proc. SPIE 6677, 14 pgs (2007b).
 Yarbrough, M., S. J. Flora, M. E. Feinholz, T. Houlihan, Y. S. Kim, S. W. Brown, B. C. Johnson, and D. K. Clark, "Simultaneous measurement of upwelling spectral radiance using a fiber-coupled CCD spectrograph," Proc. SPIE 6680, 6680-6618 (2007).



Mooring configuration for MOBY



Instrument Schematic



Location of MOBY

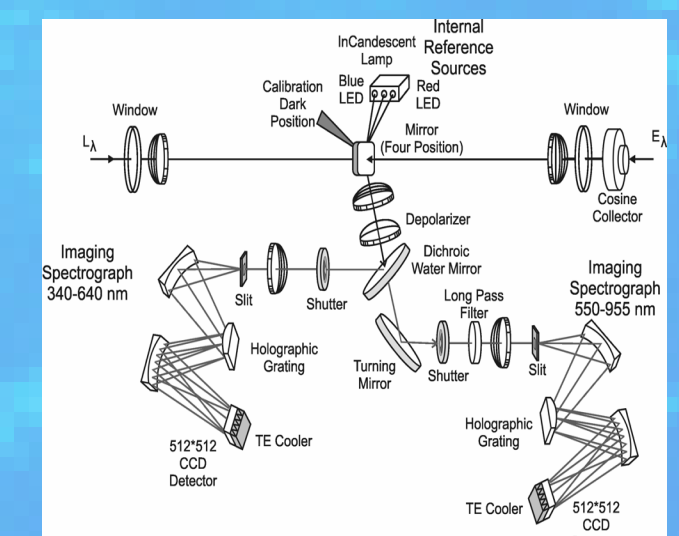
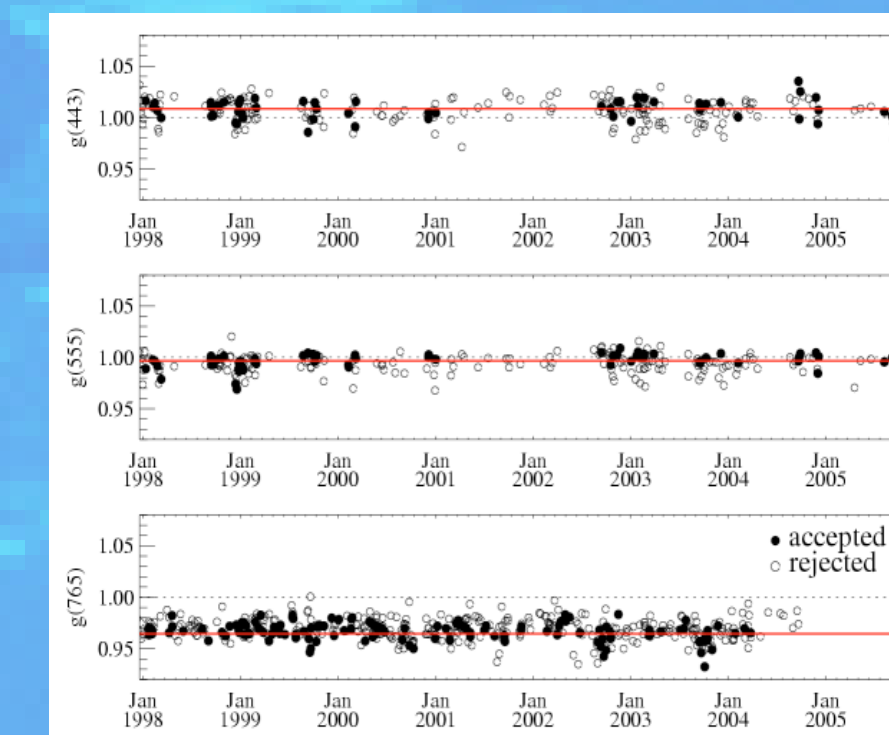
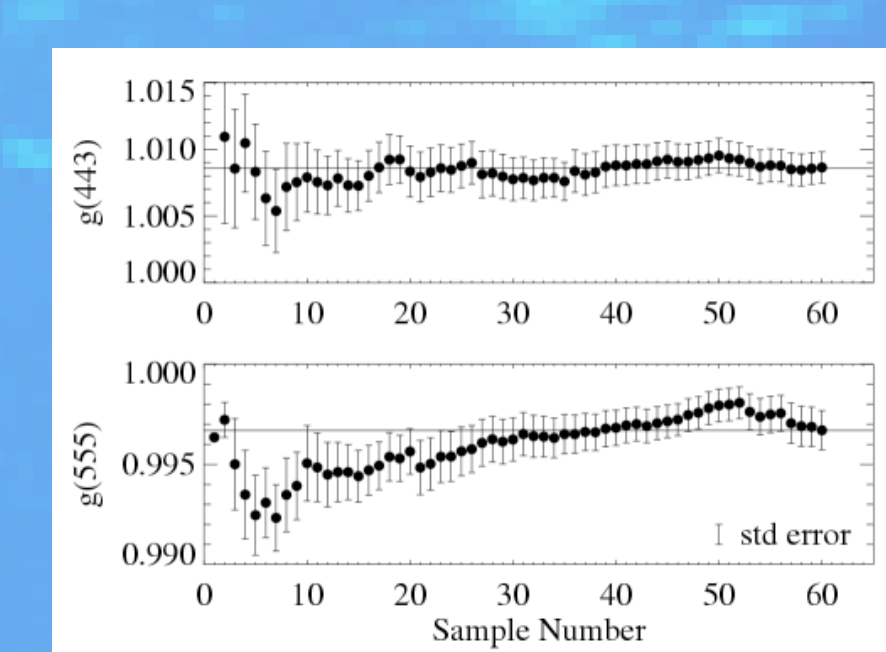


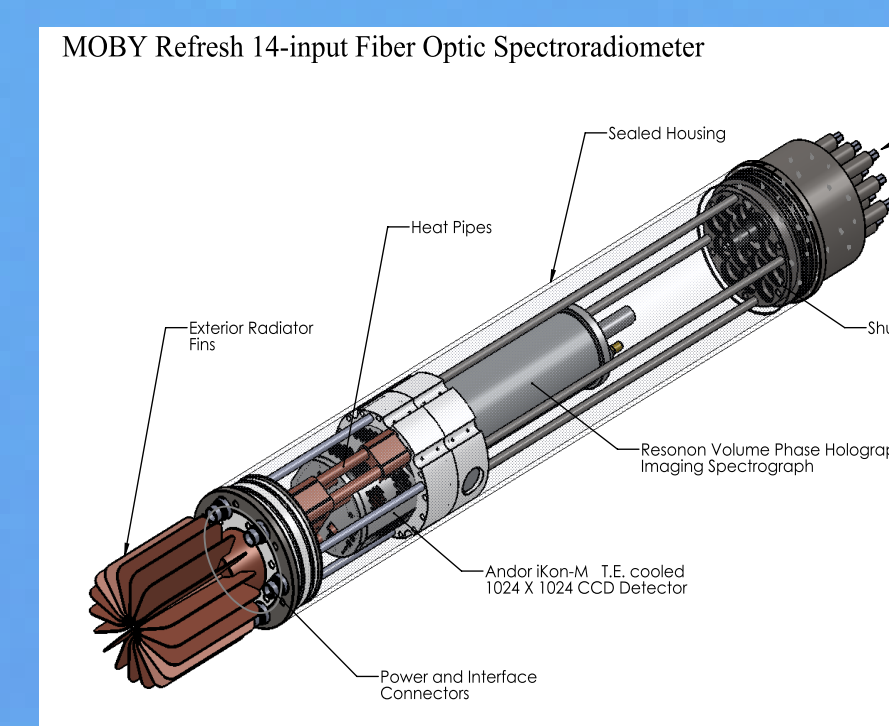
Diagram of current optical system



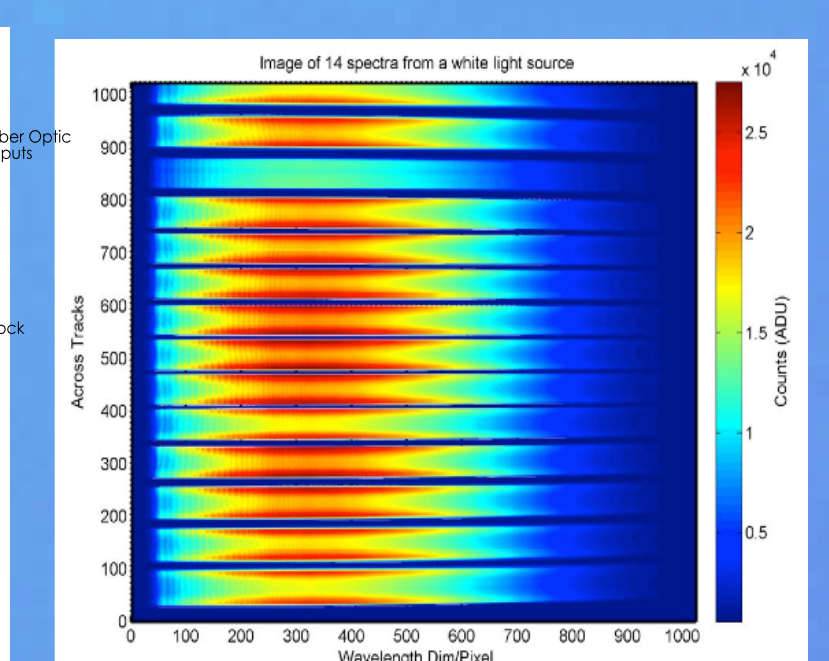
Example of MOBY time Series used in calibration of the SeaWiFS sensor (from Franz et al. 2007a)



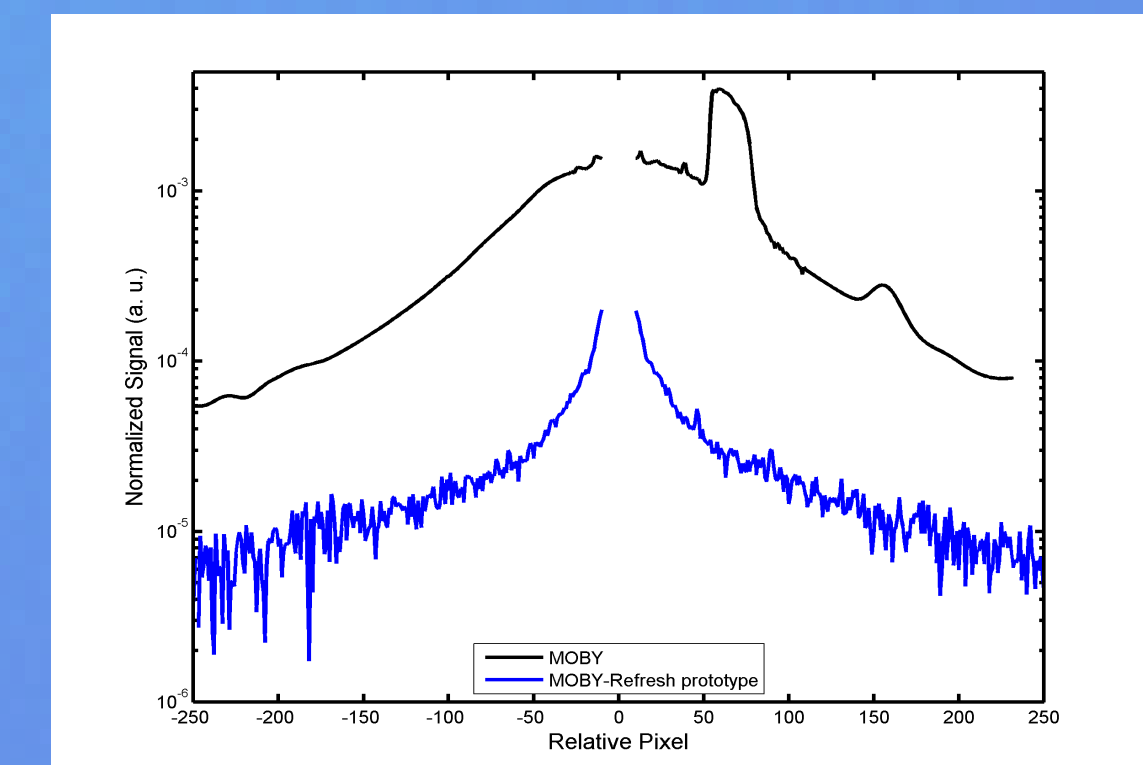
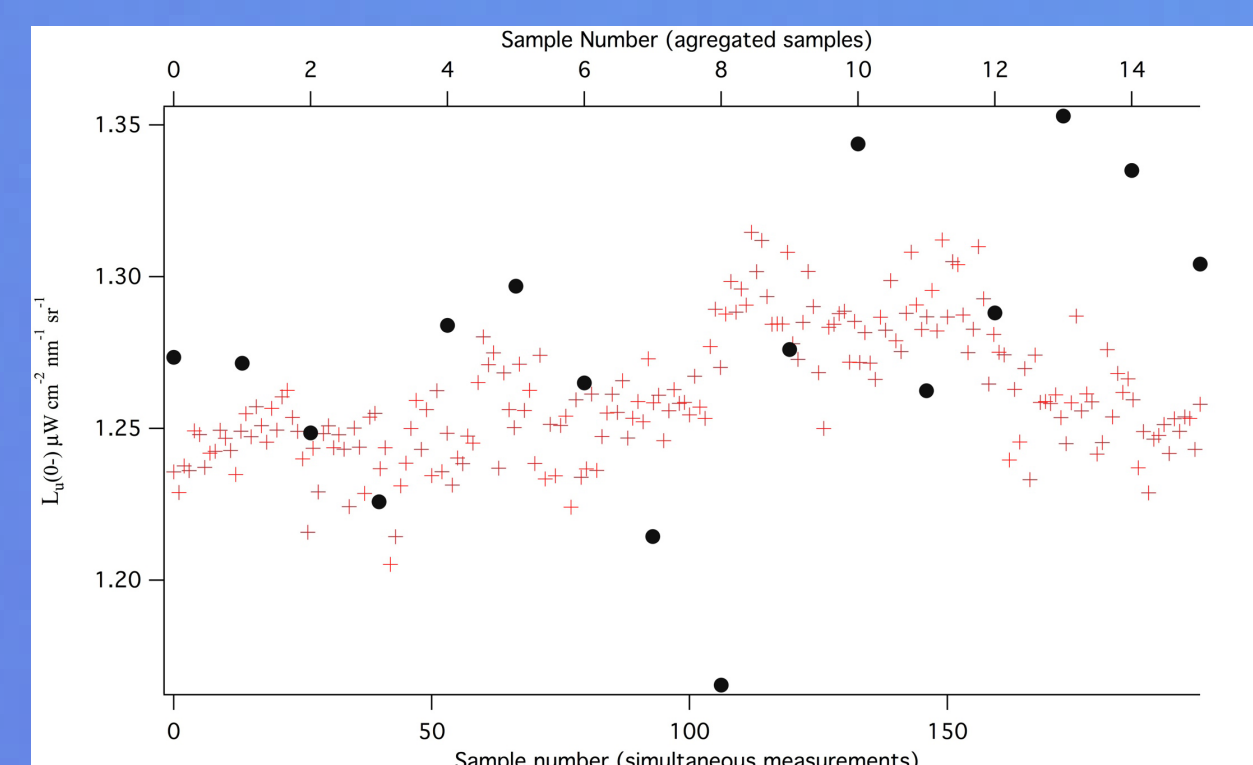
Example of how Satellite calibration converges (with current MOBY data) (from Franz et al. 2007a)



MOBY-Refresh optical system, based on a volume phase spectrograph



Example of the imaging capabilities of the new optical system



Comparison of the stray light exhibited by the current optical system (MOBY) and the new optical system (MOBY-Refresh prototype).

JPSS-1 CrIS Bench Test Data and Preliminary Assessment of the Instrument Stability

Denis Tremblay¹, Yong Han², Yong Chen³, Xin Jin³, Likun Wang⁴

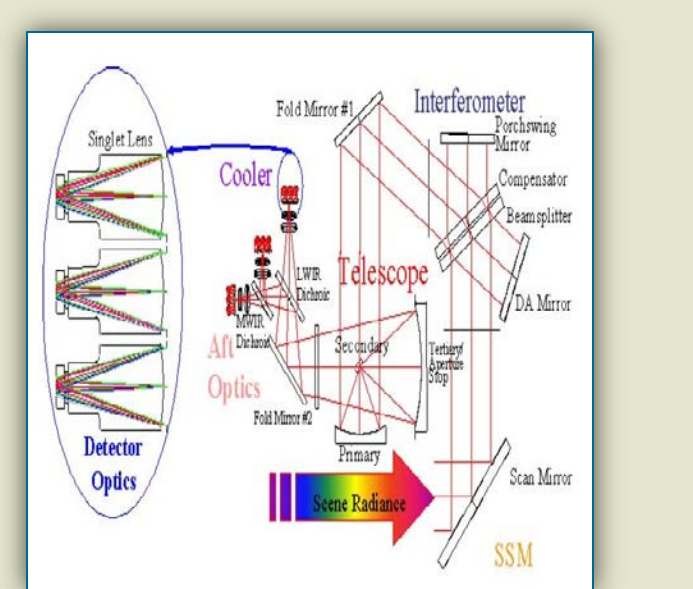
¹ Science Data Processing Inc., ² NOAA/NESDIS/STAR, ³ ERT, ⁴ University of Maryland USA.
Contact: denis.tremblay@noaa.gov

Abstract

The JPSS-1 (or J1) satellite is scheduled for launch in late 2017. One of the instruments on-board this satellite is the CrIS flight module 2 (FM2) which is a Fourier Transform Spectrometer. This CrIS FM2 is a near-clone of the CrIS FM1 that is currently flying on-board the S-NPP satellite. The J1 CrIS underwent a series of tests on the bench which consists in operating the instrument at room temperature with normal atmospheric pressure. This presentation presents analysis results performed on the operational full resolution data set shows that the instrument is very stable and no instrumental artifacts (anomalies) were found. Bench test analysis is essential in characterizing the CrIS instrument.

Instrument Characteristics and Attributes

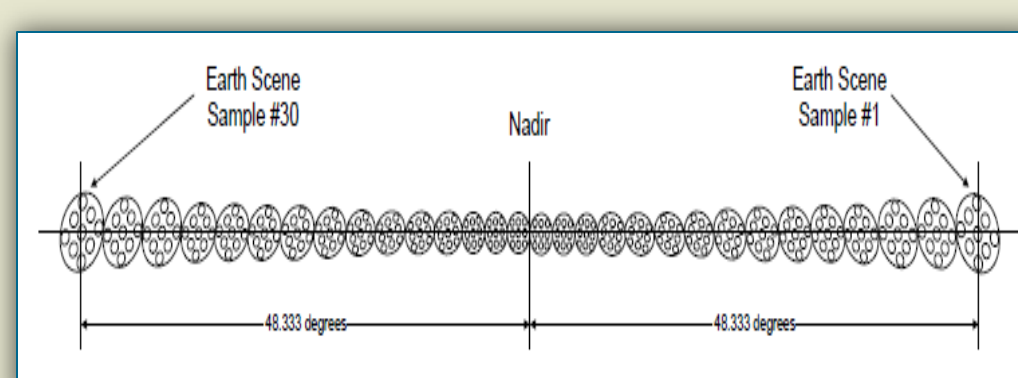
CrIS Optical Schematic



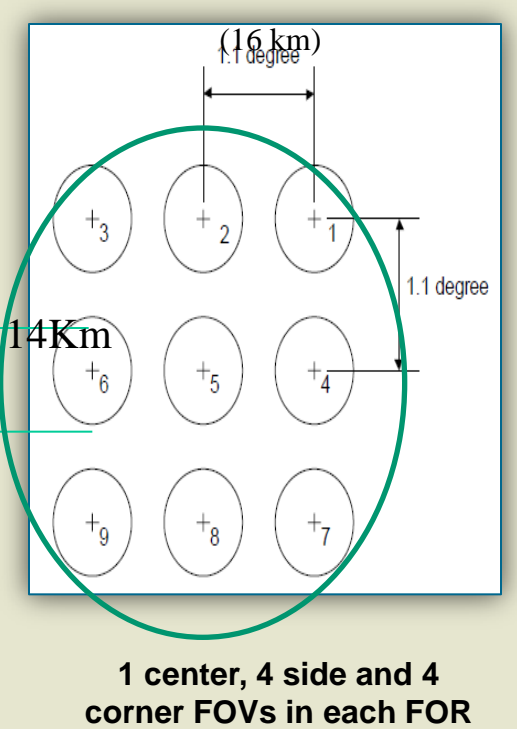
Normal Acquisition Mode

Number of FOV	9
Number of FOR per Scan Line	30
Scan line Acquisition Period	8 seconds
Number of Scan line per day	10800
Number of Frequency Band	3
Total number of Spectra per Day	8.7 Million

Scan Line (2200 Km Swath)

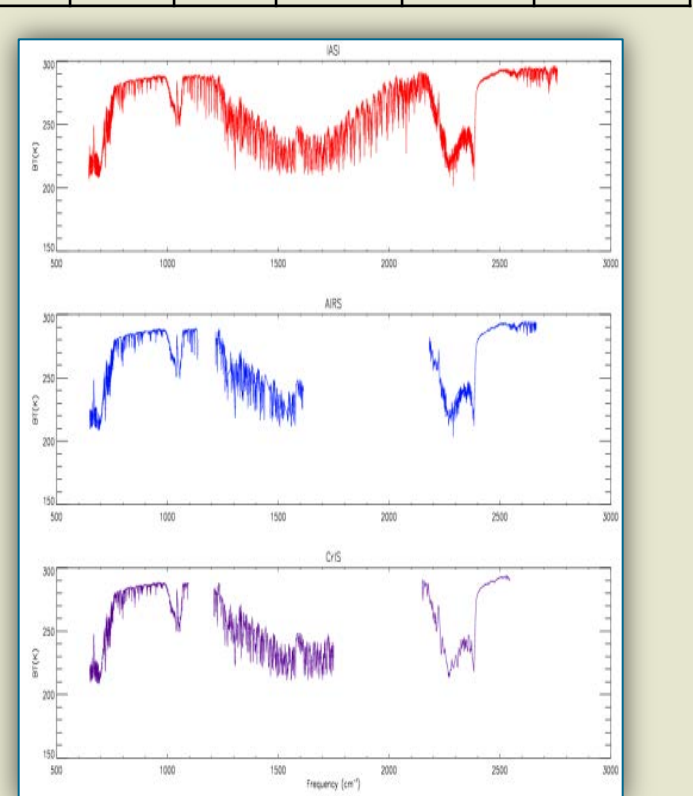


Field Of Regard



Spectral Characteristics

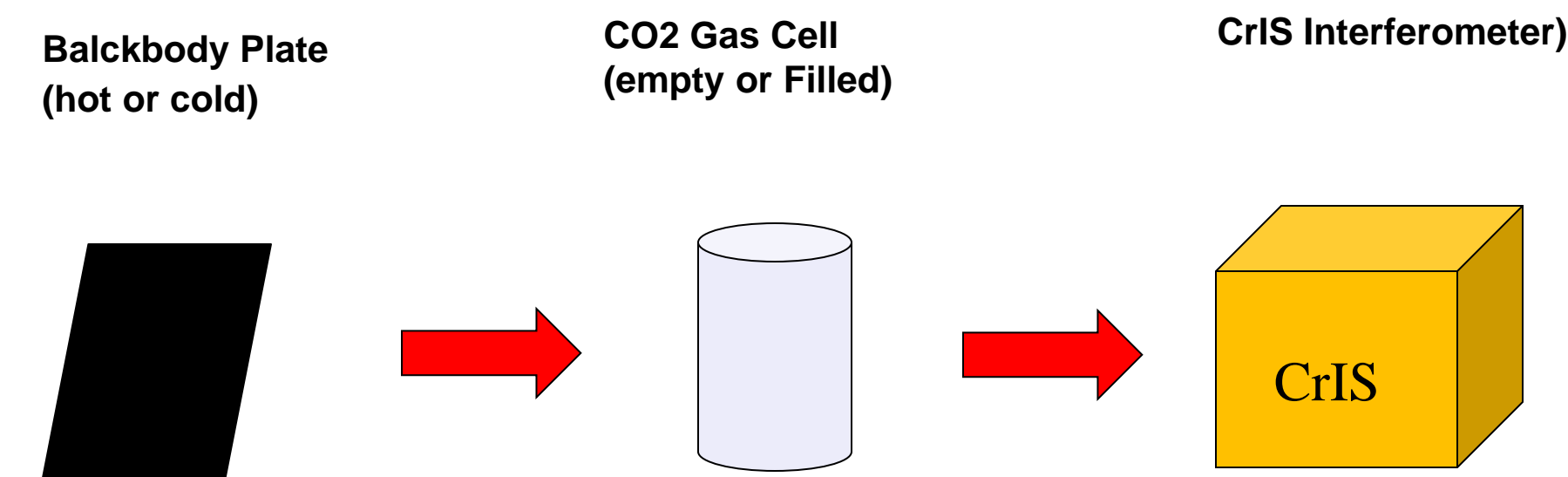
Band	Spectral Range (cm ⁻¹)	Resolution (cm ⁻¹)	Max OPD (cm)
LWIR	605-1095	0.625	0.8
MWIR	1210-1790	0.625	0.8
SWIR	2155-2590	0.625	0.8



- IASI has full spectral coverage from 645 cm⁻¹ to 2760 cm⁻¹.
- AIRS and CrIS have 3 frequency bands as shown.
- CrIS has coarser spectral resolution in MWIR and SWIR. JPSS-1 is expected to download full spectral resolution (0.625 cm⁻¹ all 3 bands). JPSS-1 launch is planned for 2017.

CrIS acquires 8.7 million spectra per day covering over 95% of the Earth surface.

Bench Gas Cell Measurements.



Bench gas cell test setup.

- A blackbody plate is placed. This plate is temperature controlled allowing a cold and hot temperature.
- The gas cell is placed between the blackbody plate and CrIS interferometer. It is empty or filled with CO2 gas for LWIR measurements. The pressure of the CO2 gas is set to 40 Tor.

Data Processing

- Four data sets: (1) Empty-Cold, (2) Empty-Hot, (3) Filled-Cold, (4) Filled-Hot. A total of 320 spectra are averaged for each category.
- The uncorrected transmittance T is

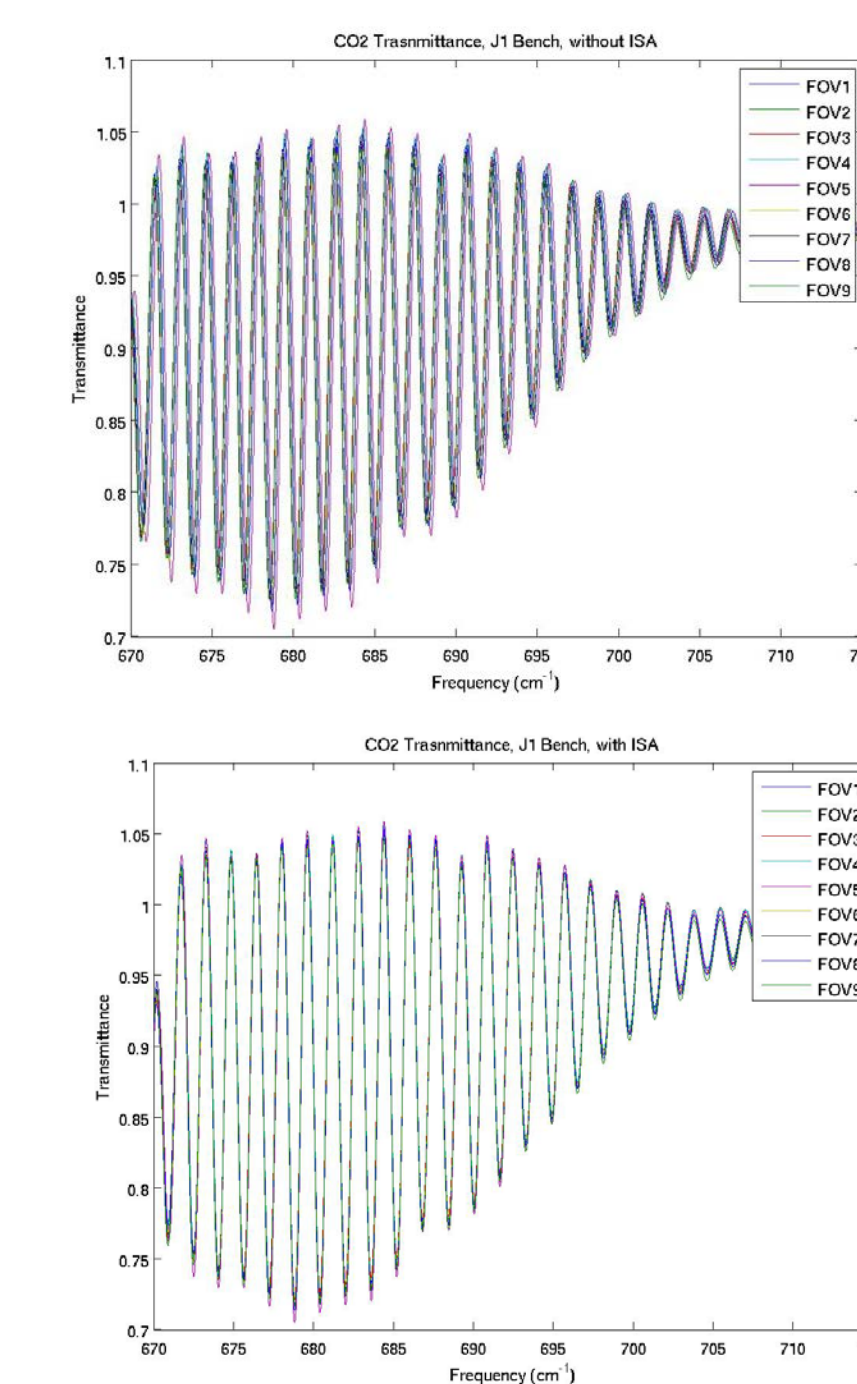
$$T = (FilledHot - FilledCold) / (EmptyHot - EmptyCold)$$

- First order corrected transmittance T* is filtered by the guard band (to dampen the spectrum edges), and multiplied by the inverse self-apodization (ISA) matrix taken from S-NPP TVAC4. The 9 FOVs are shifted to the 'right'. Here no resampling to the user's grid was applied.
- Gas cell measurements will be repeated in TVAC conditions and ILS will be derived. The expected spectral calibration accuracy shall be <10ppm.

$$T^* = ISA * f * T$$

The bench gas cell measurements show a reasonable FOV overlay (Preliminary results).

Result : LWIR FOV overlay in CO₂ region.



All FOV are shifted (no good overlay).

Apparent good FOV overlay

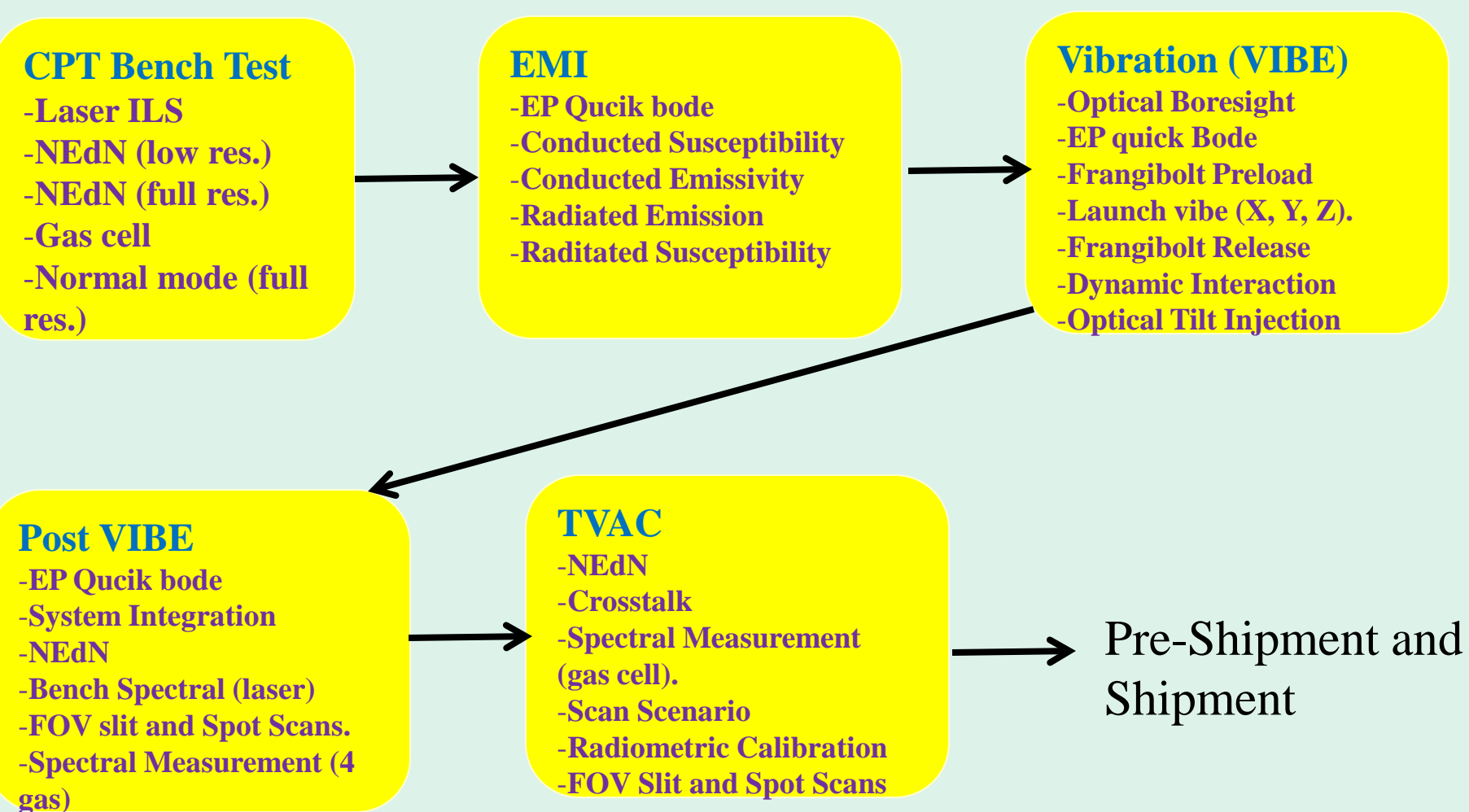
Motivation



The JPSS-1 CrIS instrument will undergo a series of test prior to its delivery. The tests includes: (1) bench, (2) EMI, (3) Vibration, (4) TVAC. After delivery, the CrIS instrument will be subject to additional testing such as satellite integration, geolocation accuracy, additional electro-magnetic susceptibility and many more.

The JPSS-1 CrIS (or Flight Module 2) instrument was put together for the first time in Mid-2013. The first of a series of tests is the so-called 'bench' testing. The instrument is operated on the bench at room temperature and normal atmospheric condition. The goal of the bench test is to assess the interferometer. Bench testing includes Laser ILS, gas cell, normal mode of operation at full spectral resolution, noise (or NEdN), and many others.

JPSS-1 CrIS Pre-launch Testing



PCA Analysis of Normal Mode Acquisition Target Data (full resolution)

Data Processing

Normal mode target (hot blackbody plate) was acquired for a period of over 2 hours on 9/20/2013. In this analysis, 45 minutes of data were processed. First, the ensemble comprised the target views spectra for a given FOV and for the FOR 33 (target) only. This accounts for a total of 360 spectra (or one spectrum every 8 seconds). For LWIR, this forms the matrix A of dimension 864 by 360, the next step is to perform a PCA (or singular value decomposition) of the Matrix A. The results is:

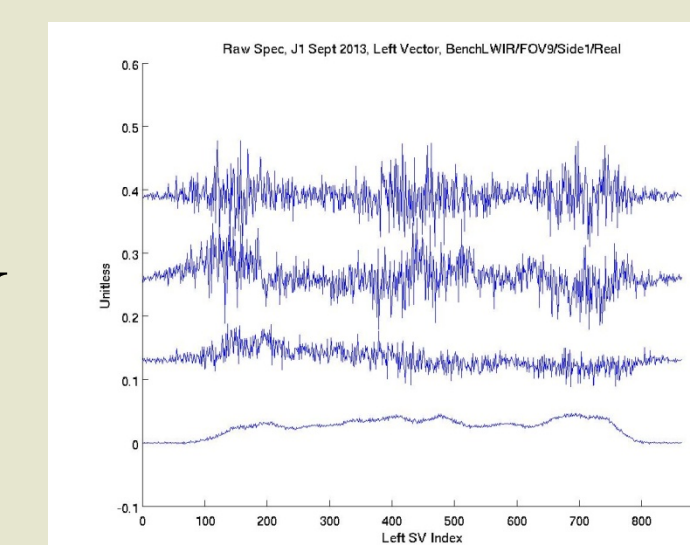
$$A = USV^T$$

The orthogonal matrix U has the dimension 864 by 360 and forms the so-called 'left' eigenvectors. These vectors shows any spectral signal. The diagonal matrix S contains the singular values in increasing order where its dimension is 360 by 360. The orthogonal matrix V has dimension 360 by 360. V has the right vectors which represent the temporal information.

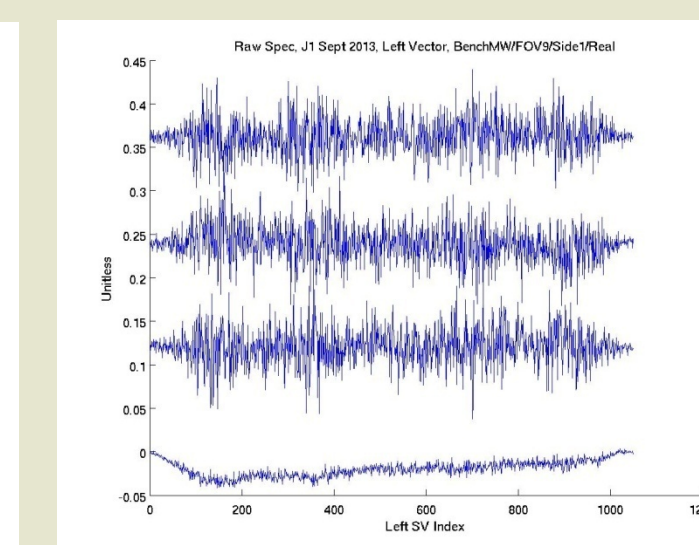
The plots shown here are for FOV 9, all 3 bands, of the right vectors (U), singular values (diagonal of S), and the right vectors V.

Results from FOV5 show similar pattern as FOV9.

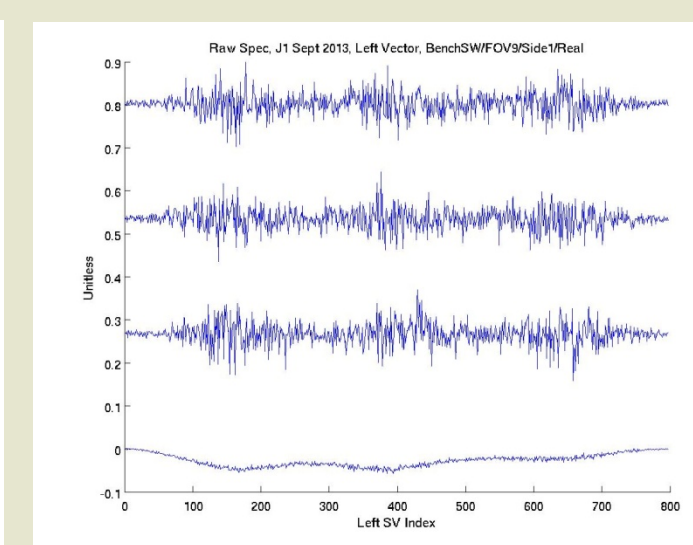
LWIR FOV9



MWIR FOV9



SWIR FOV9



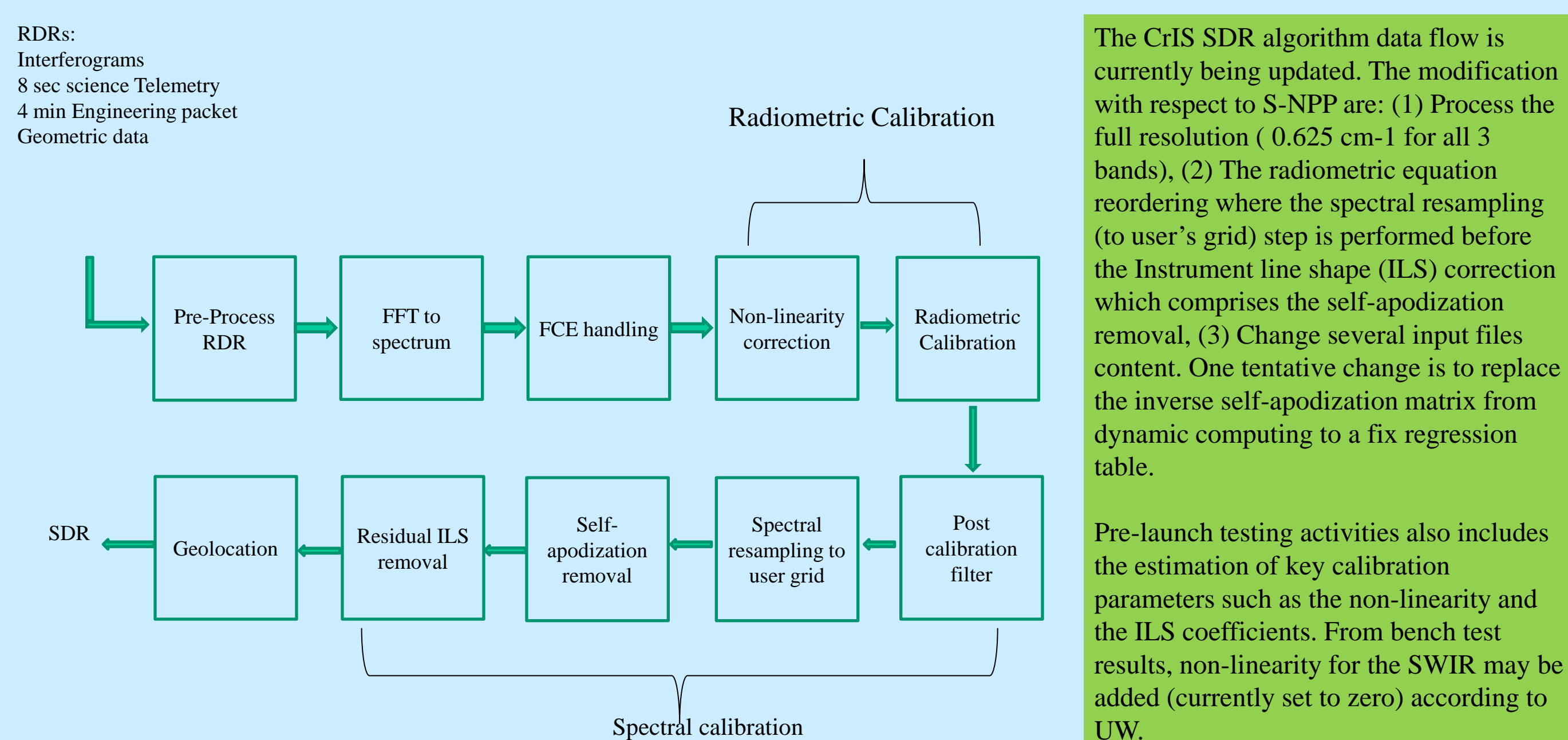
U

S

V

PCA of JPSS-1 target view shows excellent stability with no sign of anomalies (no spectral spikes, no response fluctuation, no gain amplitude variability).

CrIS SDR Algorithm Data Flow



The CrIS SDR algorithm data flow is currently being updated. The modification with respect to S-NPP are: (1) Process the full resolution (0.625 cm⁻¹ for all 3 bands), (2) The radiometric equation reordering where the spectral resampling (to user's grid) step is performed before the Instrument line shape (ILS) correction which comprises the self-apodization removal, (3) Change several input files content. One tentative change is to replace the inverse self-apodization matrix from dynamic computing to a fix regression table.

Pre-launch testing activities also includes the estimation of key calibration parameters such as the non-linearity and the ILS coefficients. From bench test results, non-linearity for the SWIR may be added (currently set to zero) according to UW.

CrIS SDR Algorithm product comprises the radiance, NEdN (noise), geolocation, and data quality flags.

Summary

- Bench testing of JPSS-1 CrIS shows good stability of the instrument.
- Full resolution data are acquired.
- Gas cell measurements show reasonable FOV overlay.

River Runoff Effect on the Suspended Sediment Property in the Upper Chesapeake Bay Using MODIS Observations and ROMS Simulations

Xiaoming Liu and Menghua Wang

NOAA/NESDIS Center for Satellite Applications and Research
E/RA3, 5830 University Research Ct., College Park, MD 20740

Introduction

- Ocean color data derived from MODIS-Aqua from 2002–2012 and simulations from the Regional Ocean Model System (ROMS) are used to study the impact of the Susquehanna River discharge on the total suspended sediment (TSS) concentration in the upper Chesapeake Bay.
- The shortwave infrared (SWIR)-based atmospheric correction algorithm (Wang, 2007) is used to derive $nL_w(\lambda)$. The diffuse attenuation coefficient at the wavelength of 490 nm $K_d(490)$ is derived using the algorithm proposed by Wang et al. (2009), and the TSS is derived using the algorithm proposed by Son and Wang (2012).
- The variations of MODIS-derived TSS climatology and monthly time series are compared with Susquehanna River discharge data at Conowingo Dam from USGS (<http://waterdata.usgs.gov/usa/nwis/>). Since Susquehanna River discharge is dominated by a few high-discharge events each year, ROMS sediment model is used to simulate the response of the upper Bay TSS to the Hurricane Sandy event.

Upper Chesapeake Bay TSS and Susquehanna River Discharge

- MODIS-Aqua-derived monthly climatology TSS concentration in the upper Chesapeake Bay and the Susquehanna River discharge data show similar pattern in seasonal variations: the TSS concentration is low in summer, reaches a peak in December/January, slightly drops in February, and then reaches a second peak in March/April (Fig. 1 and Fig. 2).
- The TSS monthly temporal variation in the upper Chesapeake Bay is also found in phase with the monthly averaged river discharge data (Fig. 3), which indicates strong correlation between the river discharge and the upper Chesapeake Bay TSS concentration.

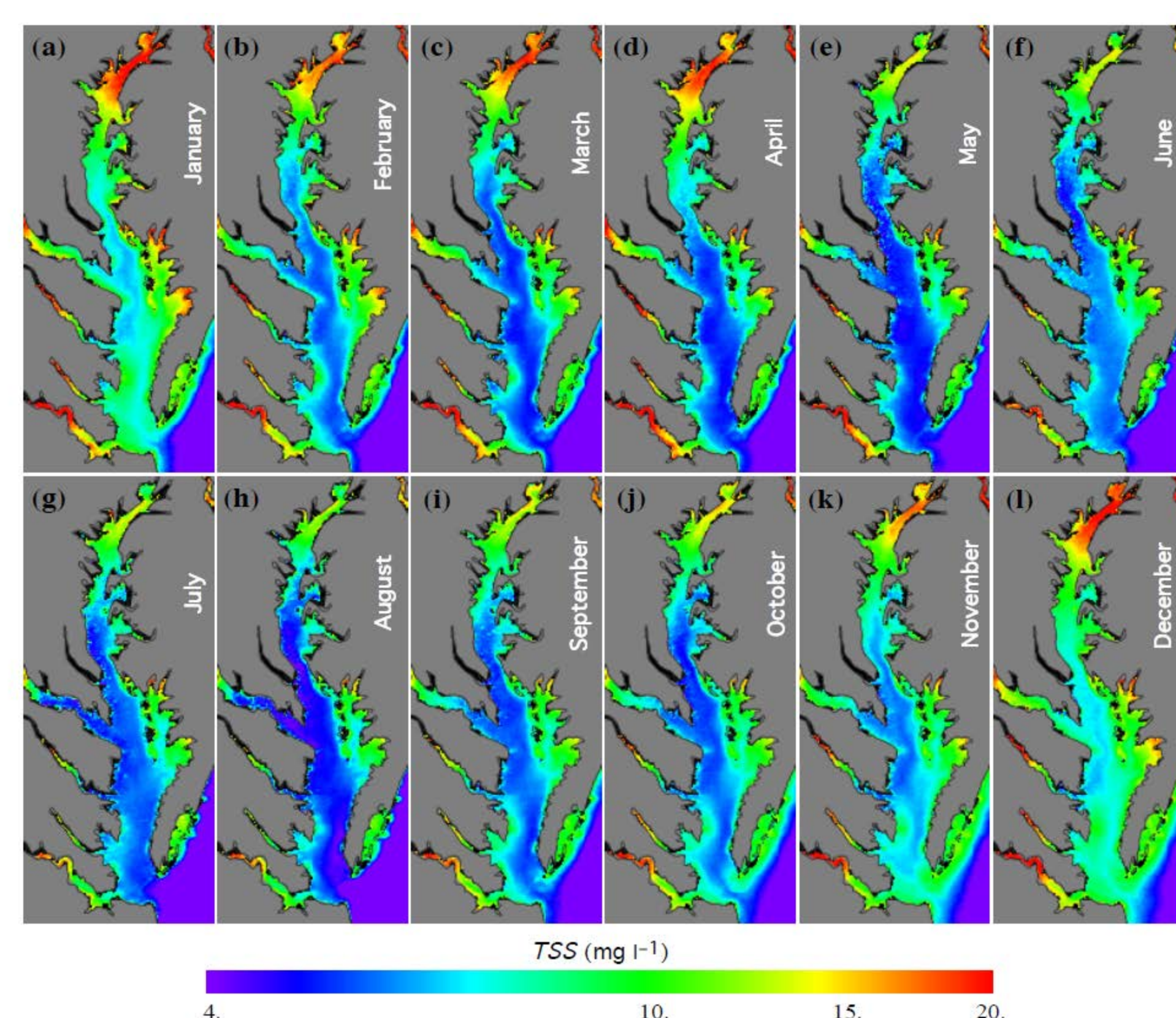


Figure 1. MODIS-Aqua-derived monthly climatology images (2002–2012) of TSS concentration for (a)–(l) as the month of January to December.

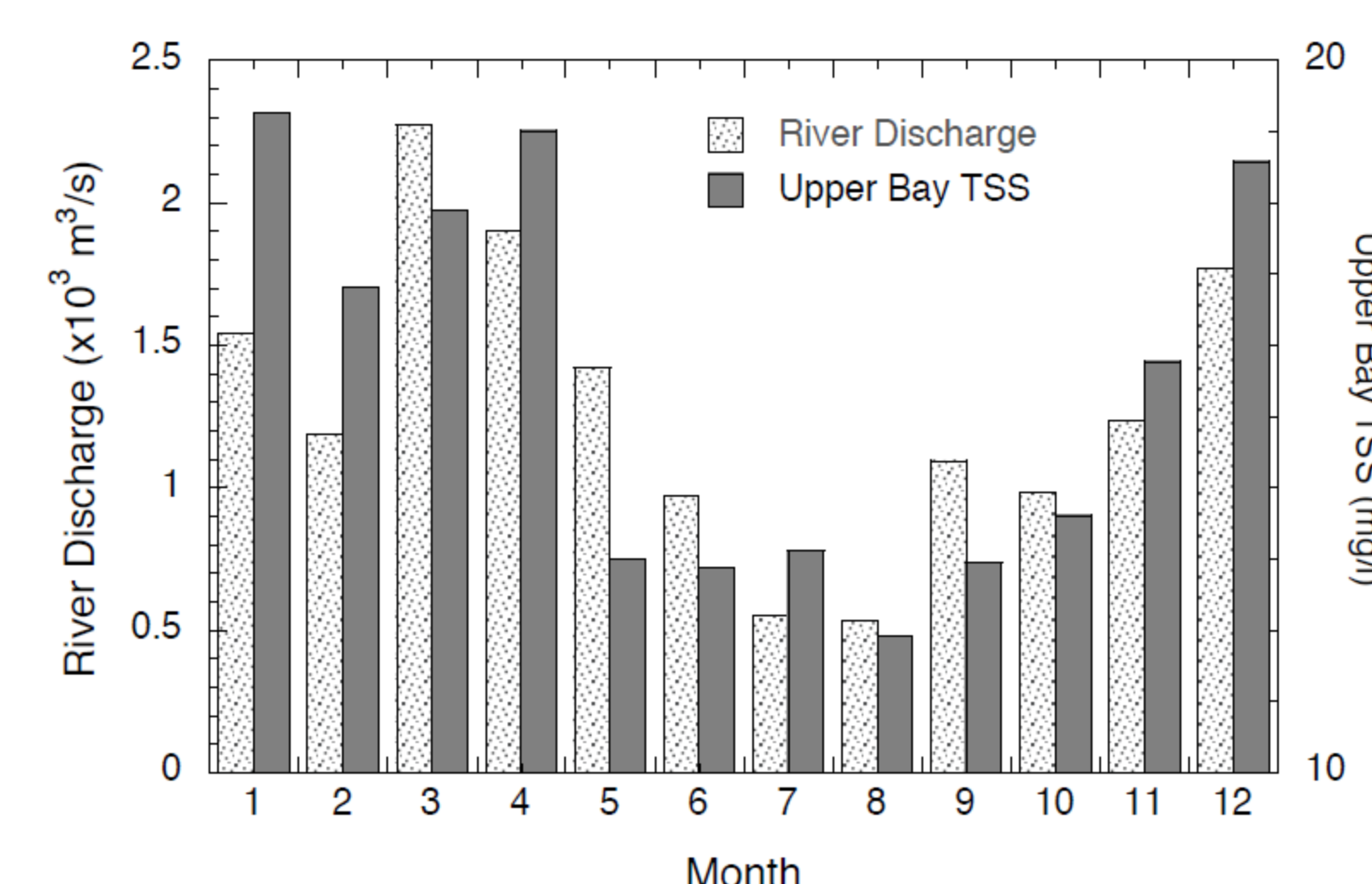


Figure 2. Comparison of the Susquehanna River discharge from year 2002 to 2012 averaged by month (light bars) and MODIS-Aqua-derived monthly climatology TSS concentration in the upper Chesapeake Bay (dark bars).

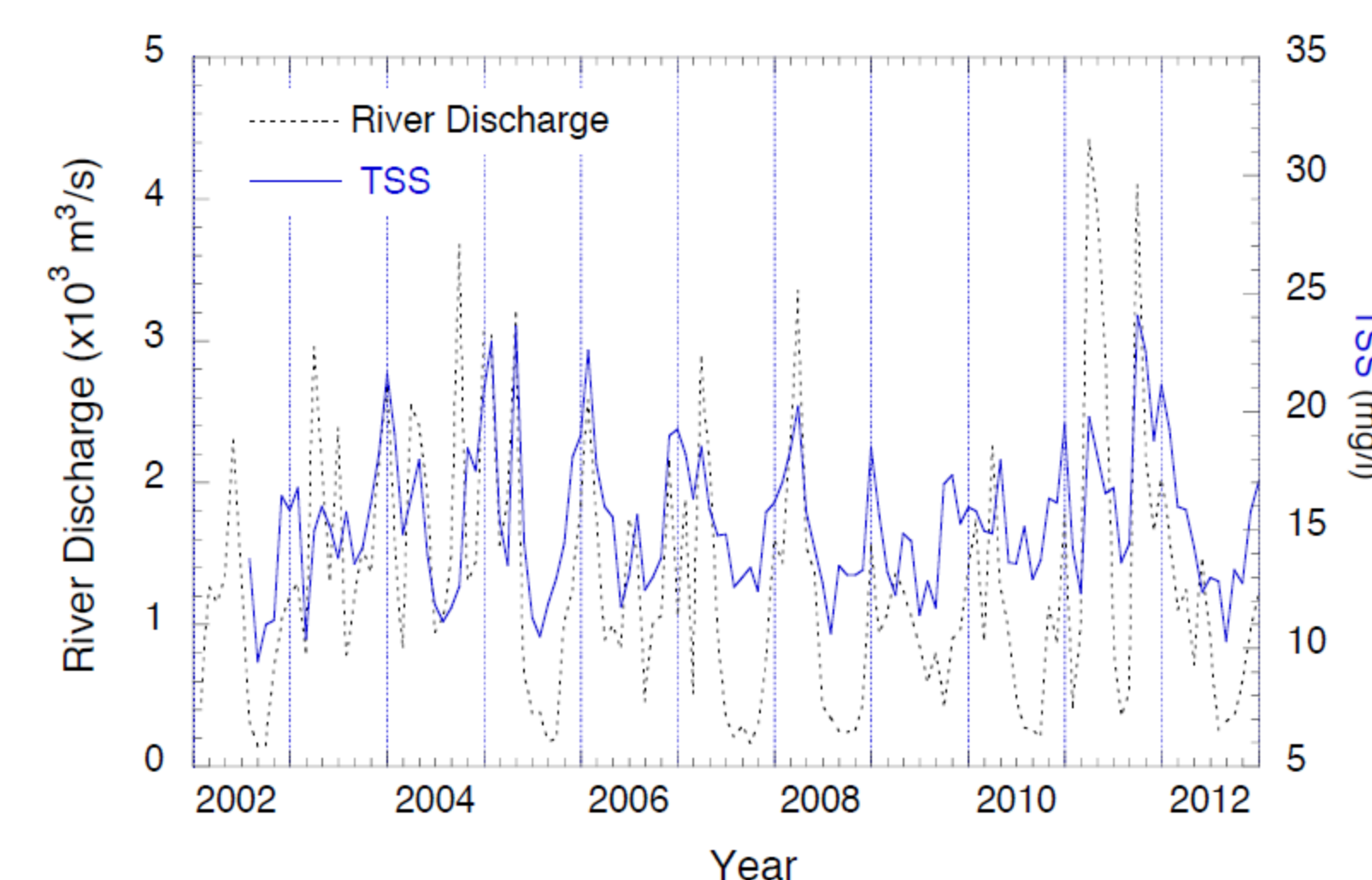


Figure 3. Comparison of time series of monthly averaged Susquehanna River discharge from year 2002 to 2012 (dotted line, scale in left) and time series of monthly averaged MODIS-measured TSS concentration from 2002 to 2012 in the upper Chesapeake Bay (solid line, scale in right).

Impact of High River Discharge Events on the Upper Bay TSS

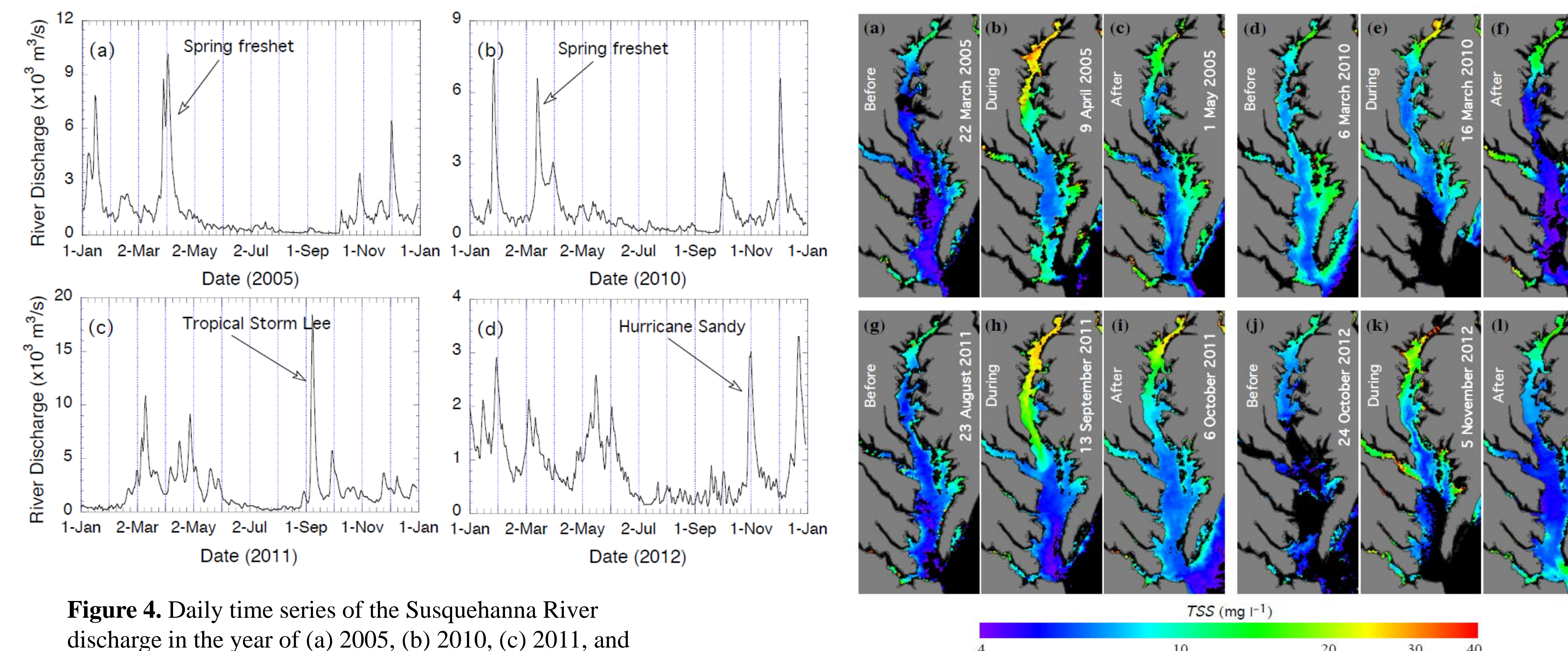


Figure 4. Daily time series of the Susquehanna River discharge in the year of (a) 2005, (b) 2010, (c) 2011, and (d) 2012.

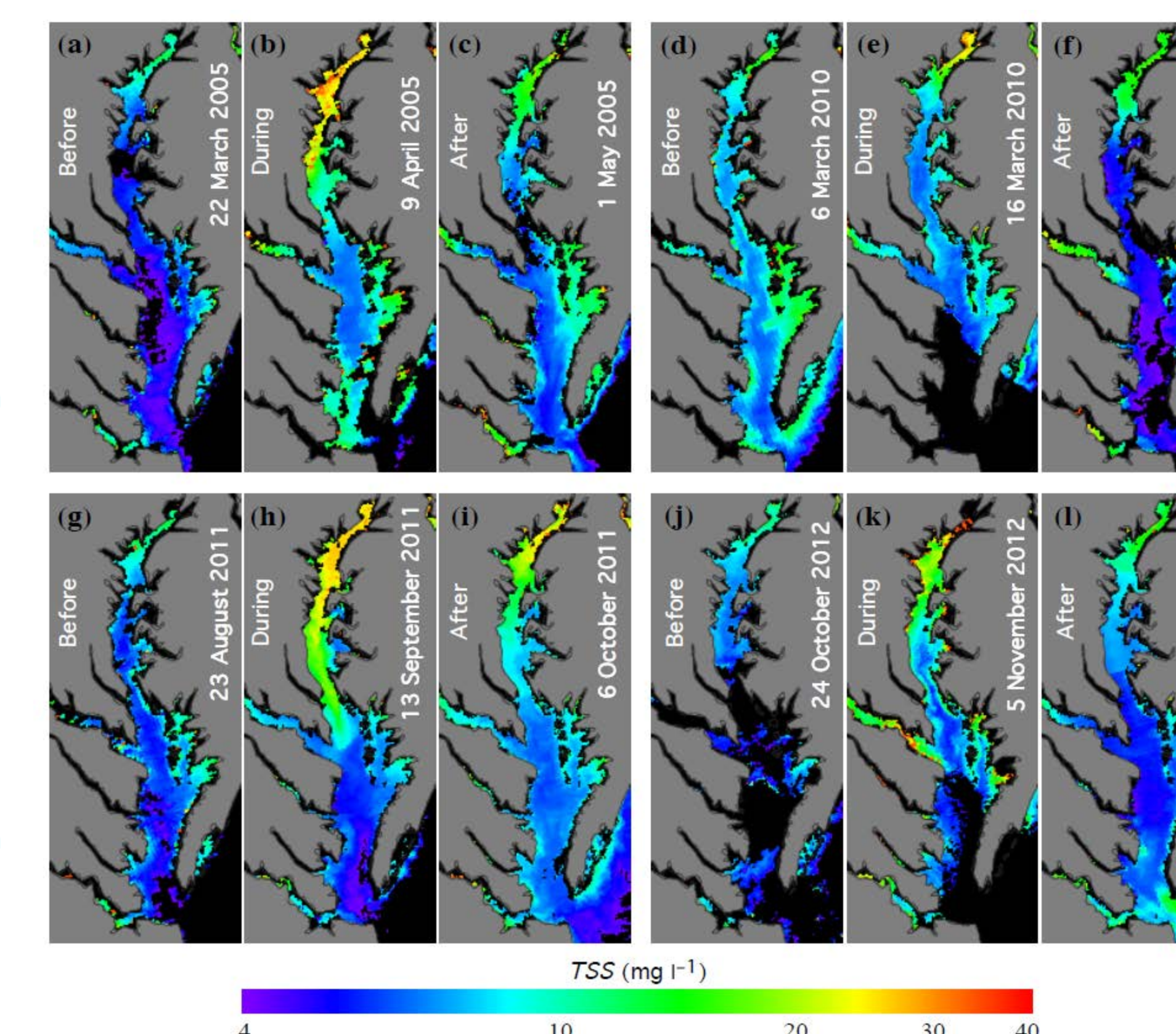


Figure 5. MODIS-Aqua-derived TSS concentration images before, during, and after four high discharge events of the Susquehanna River for the case of (a–c) April 2005, (d–f) March 2010, (g–i) September 2011, and (j–l) November 2012, respectively.

ROMS Simulations

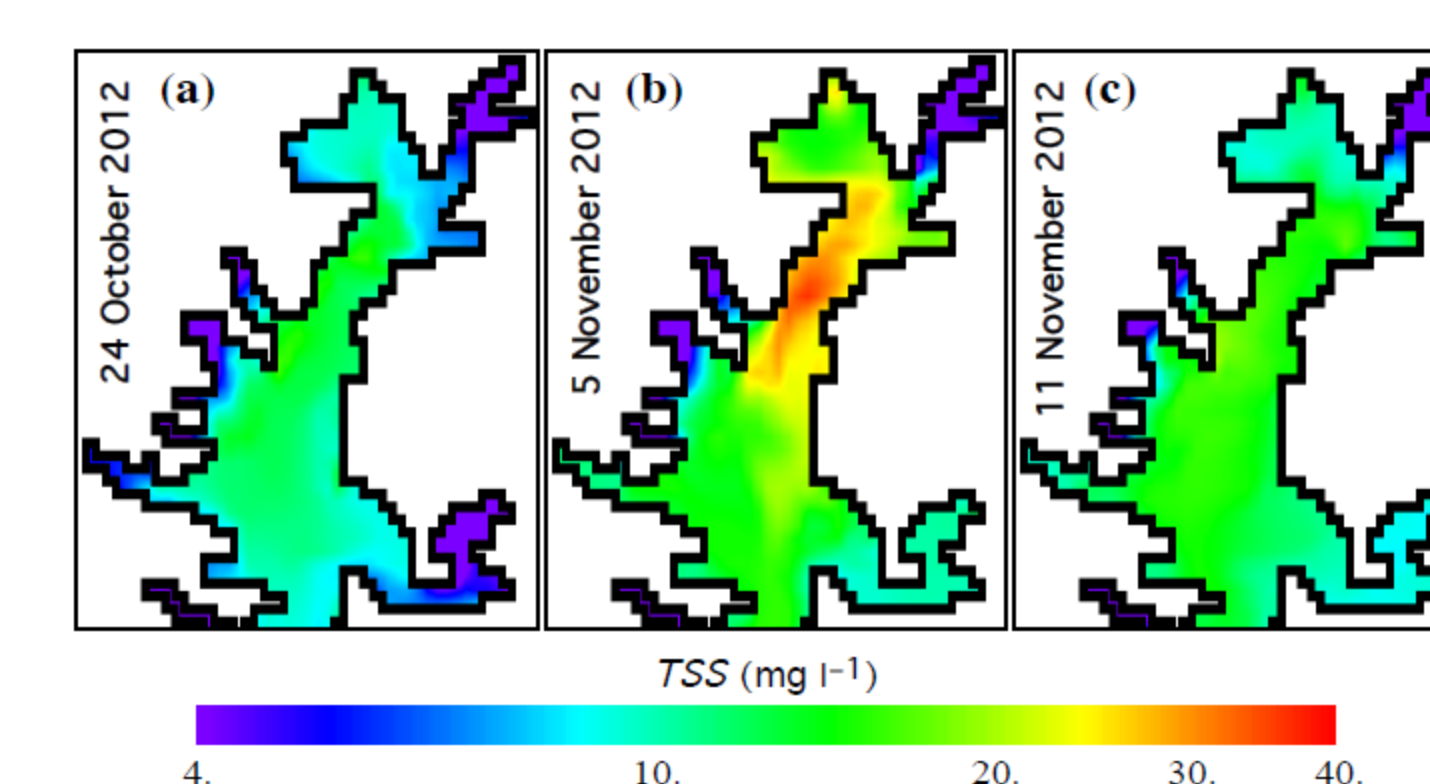


Figure 6. Model simulated TSS concentration in the upper Chesapeake Bay on (a) 24 October, (b) 5 November, and (c) 11 November 2012.

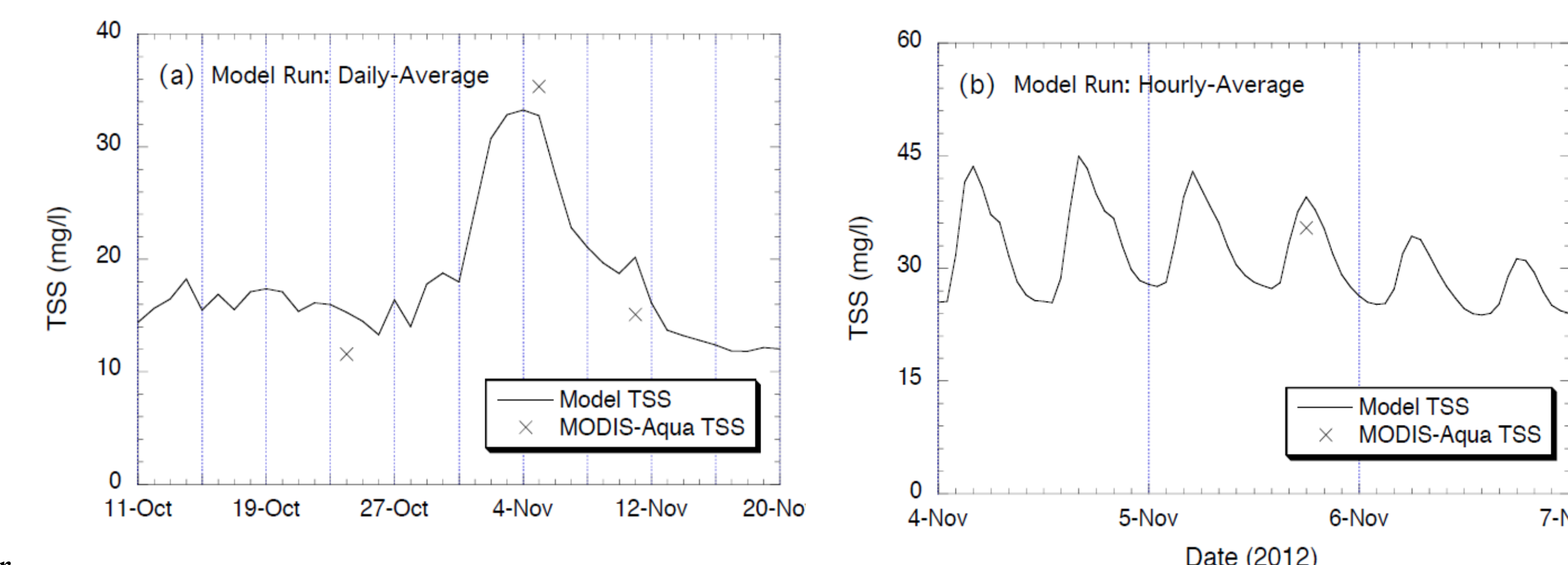


Figure 7. Model-simulated vs. satellite-measured TSS comparison near the center of the ETM zone (39.35°N, 76.14°W) for (a) daily averaged TSS concentration from 11 October 2012 to 20 November 2012 and (b) hourly averaged TSS concentration from 4 November 2012 to 7 November 2012.

Conclusions

- MODIS-Aqua-derived TSS data indicate that the Susquehanna River discharge has strong and direct impact on the variation of TSS concentration in the upper Chesapeake Bay.
- The effect of the Susquehanna River discharge on the upper Bay TSS is mainly through a few high river discharge events in each year, and the TSS is generally low in low river flow conditions.
- Both MODIS-derived TSS data and ROMS simulations show that the Susquehanna River discharge is the dominant factor for the variations of TSS concentration in the upper Chesapeake Bay.

Acknowledgements

MODIS L1B data were obtained from the NASA/GSFC MODAPS Service website.

Progress in Developing a Ground-Based Polarimetric Spectroradiometer to Support J1 VIIRS Validation

Aaron Pearlman¹, Frank Padula¹, Xi Shao¹, and Changyong Cao²
¹ERT, Inc., ²NOAA/NESDIS/STAR

Abstract

J1 VIIRS pre-launch testing showed polarization sensitivity that could lead to radiometric corrections on-orbit, which would rely on understanding the polarization states in the atmosphere. To aid in understanding this phenomenon, we developed a ground-based spectroradiometer for polarization measurements by combining an off-the-shelf spectroradiometer with a rotatable standard camera lens polarizer to allow polarized light into the spectroradiometer. Since these pieces do not combine easily, we built a customized adapter in-house - designed using open source software and built with a 3D printer. Preliminary measurements of the atmosphere using the spectroradiometer show stronger linear polarization (350 nm to ~650 nm) viewing 90° to the sun than towards the sun, which is consistent with polarization dominated by Rayleigh scattering. We plan to further improve the instrument and characterize the atmosphere over a larger range of sun and sensor positions and analyze the measurement uncertainties. This will improve our understanding of polarization states in the atmosphere and contribute to validation efforts of radiative transfer models used in any on-orbit corrections for J1 VIIRS.

Background

Rayleigh Scattering

- Rayleigh scattering linearly polarizes the sun's radiation according to its scattering angle, α :

$$DOLP = \frac{1 - \cos^2(\alpha)}{1 + \cos^2(\alpha) + 2\delta/(1-\delta)}$$

where DOLP is degree of linear polarization and δ is depolarization factor. [Hansen & Travis, Space Science Reviews (1974)]

- With the sensor viewing upward and the sun on the horizon, the photons detected have been scattered at 90°, so are highly polarized.

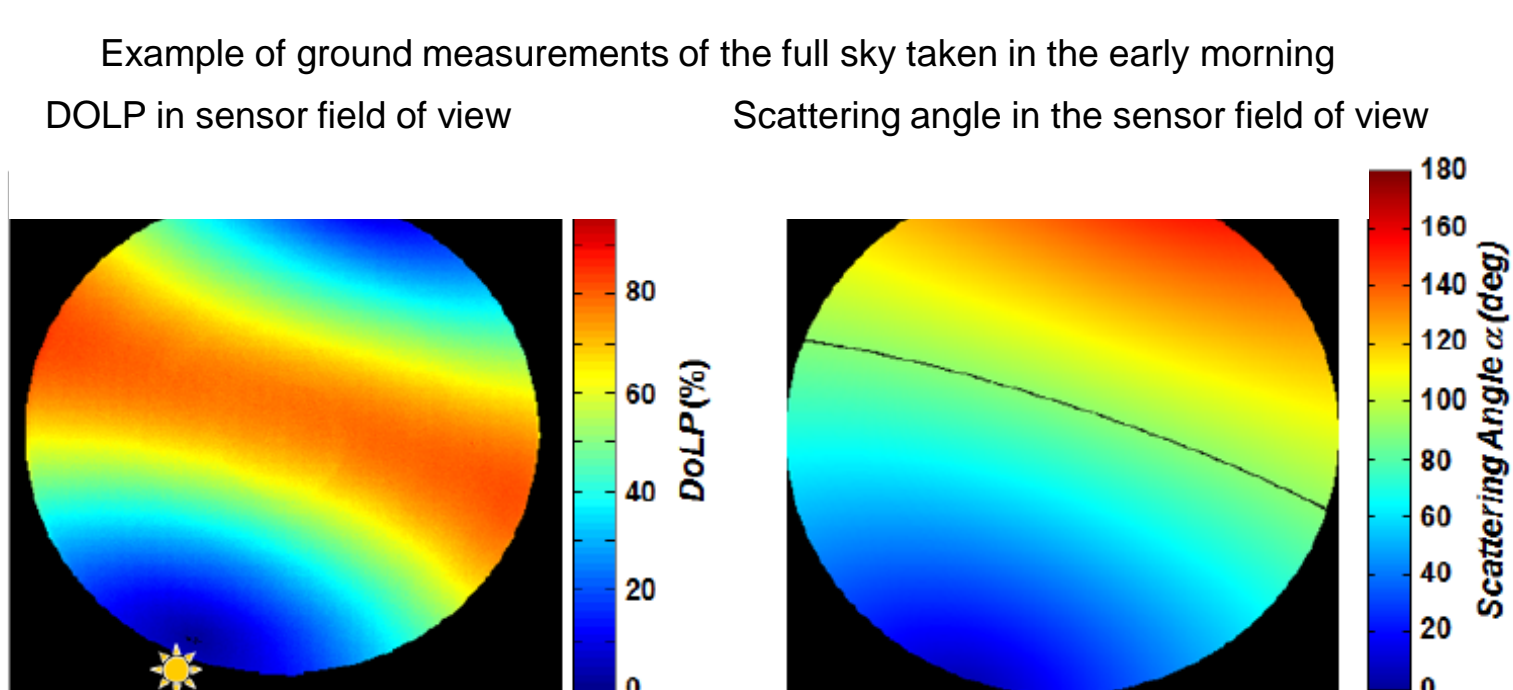
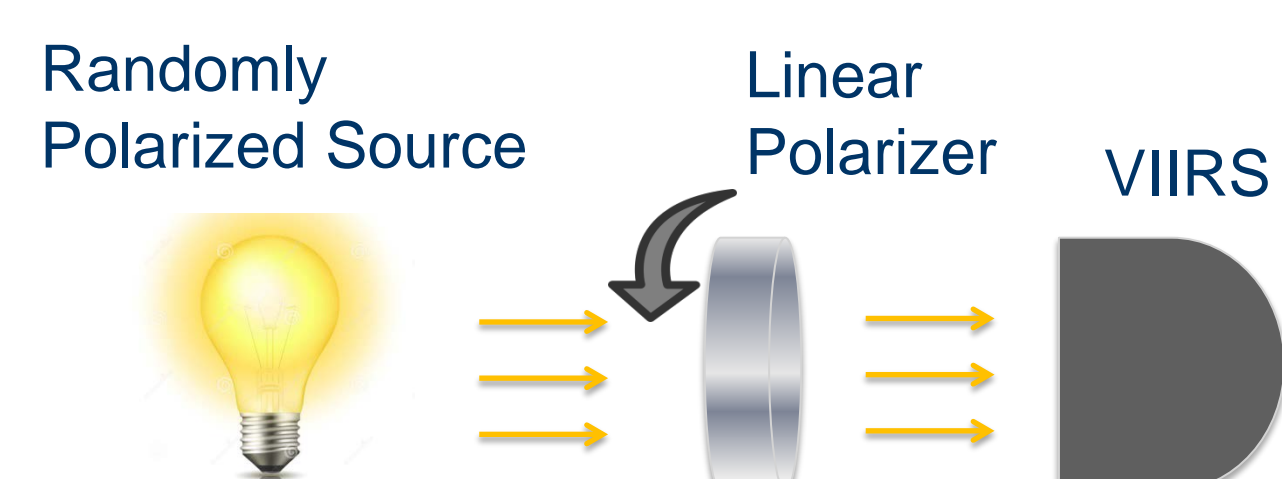


Fig. 4. (a) DoLP image at 700 nm of a clear early morning (23 May 2008) just after sunrise, at around 0620 Hawaiian Standard Time (HST, UTC -10) with the sun to the east. (b) The scattering angle (with respect to the sun) mapped to the fisheye lens image plane.

[Dahlberg et al. Optics Express (2011)]

Pre-launch Polarization Sensitivity Measurements

- Instrument polarization sensitivity contributes to radiometric uncertainty.
- Pre-launch polarization sensitivity measurements found that J1 has higher polarization sensitivity than NPP VIIRS.



NPP VIIRS Pre-launch Measurement Setup and Results

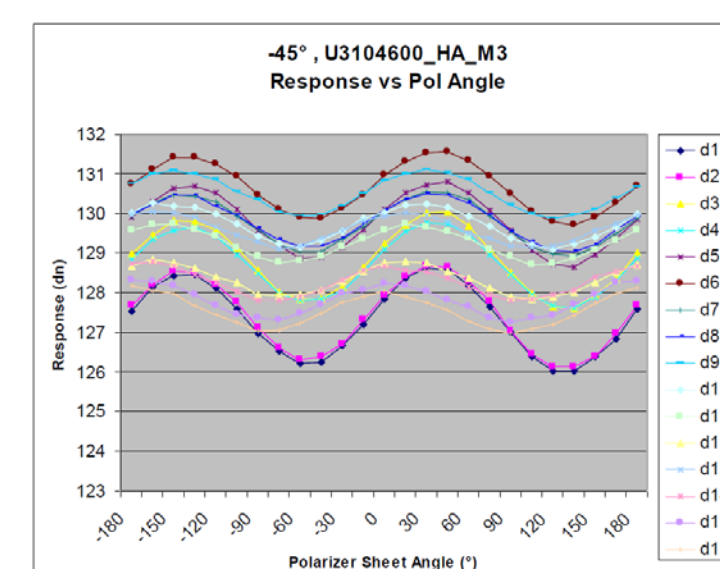
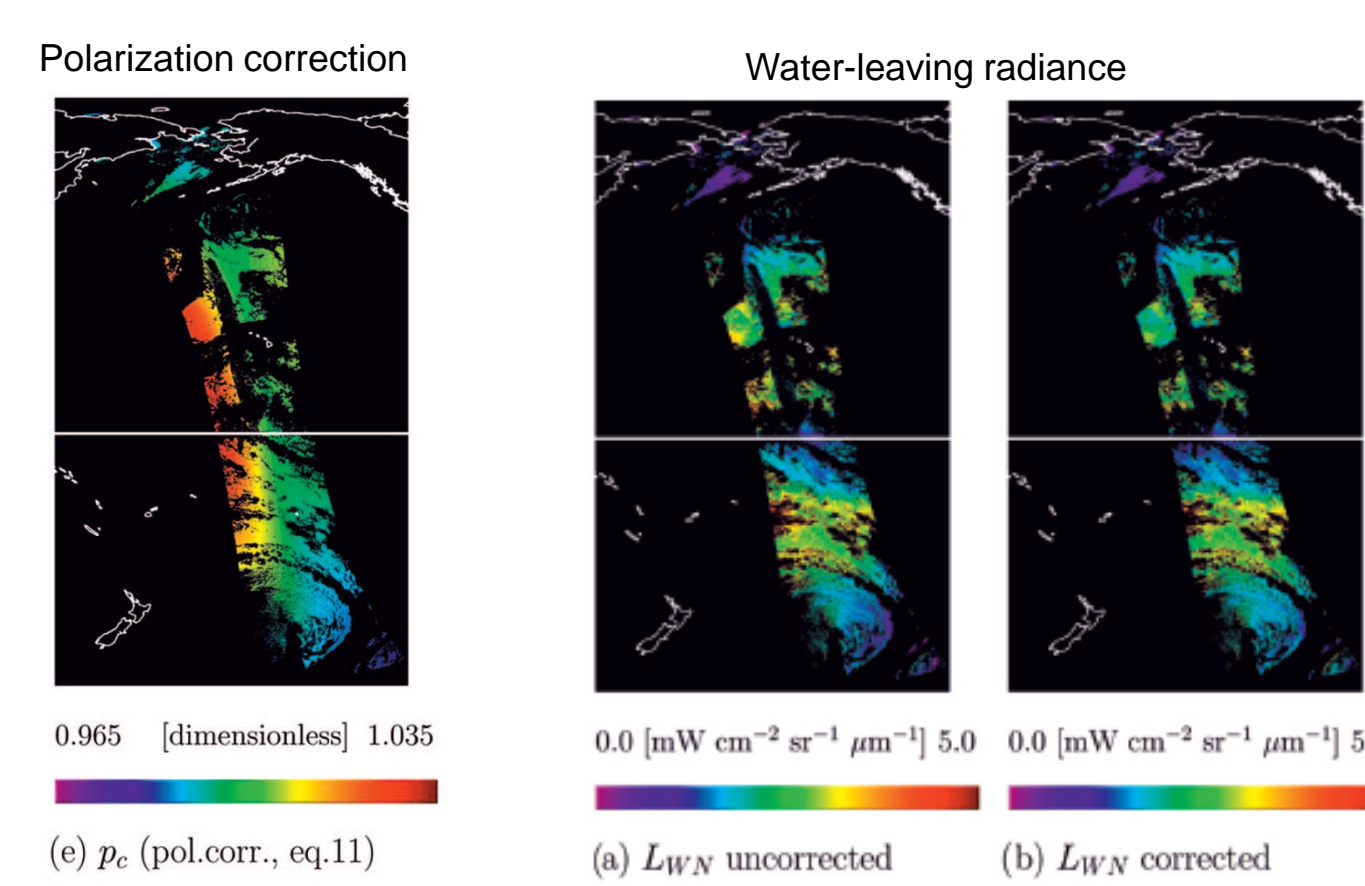


Figure 1. Detector signals, $\Delta I(P)$ as a function of polarizer angle, P . [Novitsky et al. SPIE 2012]

On-orbit Corrections

- On-orbit corrections can be applied at the EDR level:

- Corrections are based on pre-launch polarization sensitivity measurements and atmospheric polarization states (modeled by radiative transfer codes such as 6SV and MODTRAN-P)
- Corrections will most likely be used for J1 VIIRS ocean color channels.



Moderate Resolution Imaging Spectrometer (MODIS) polarization corrections for ocean color [Meister et al. Applied Optics (2005)]

- Developing a polarimetric spectroradiometer to aid in understanding atmospheric polarization phenomenology.

Building a Customized Spectroradiometer for Polarization Measurements

- Objective:** Use ASD[®] spectroradiometer with linear polarizer to create a simple polarimeter that can measure the degree of linear polarization of incoming radiation.
- Challenge:** ASD[®] spectroradiometer provides fiber holder that is incompatible with standard camera lens polarizers.
- Solution:** Design and build custom adapter to connect the ASD with the polarizer

- Designed adapter for holding the rotating polarizer using Blender[®]**
 - Allows unobstructed path between ASD fiber field of view and linear polarizer
 - Fits the rotating stage snugly

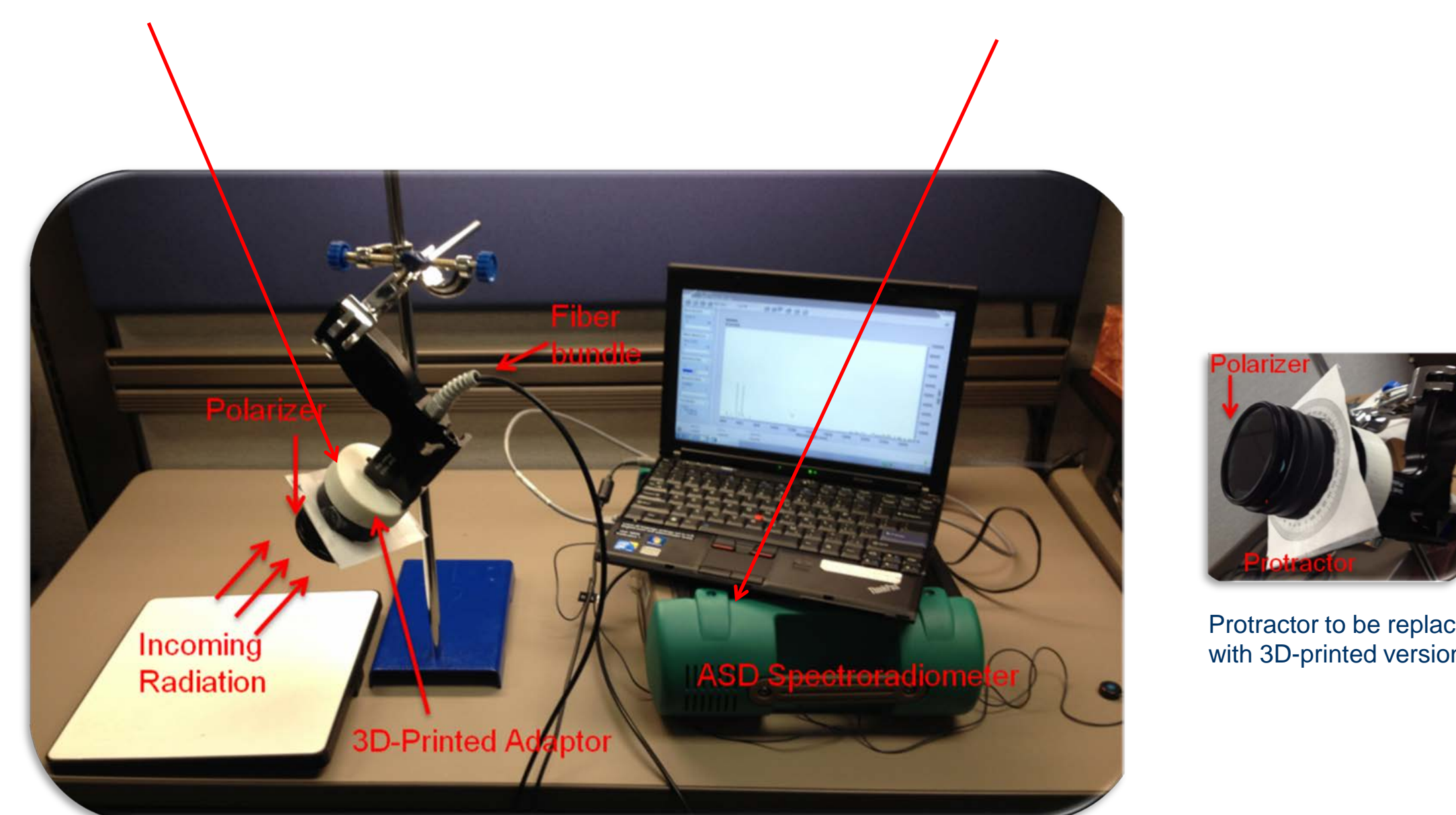


- Used ASD spectroradiometer**
 - Spectral coverage: 350 nm - 2500 nm (2151 bins)
 - Fiber input with FOV = 25°
 - Rugged design
 - Wireless communication capability
 - Calibrated at NIST
 - Low polarization sensitivity



- Built the customized adapter in-house using a 3D printer**
 - Painted black to mitigate reflections
 - Added threads to connect to the fiber holder

- Assembled spectroradiometer for measuring polarization**

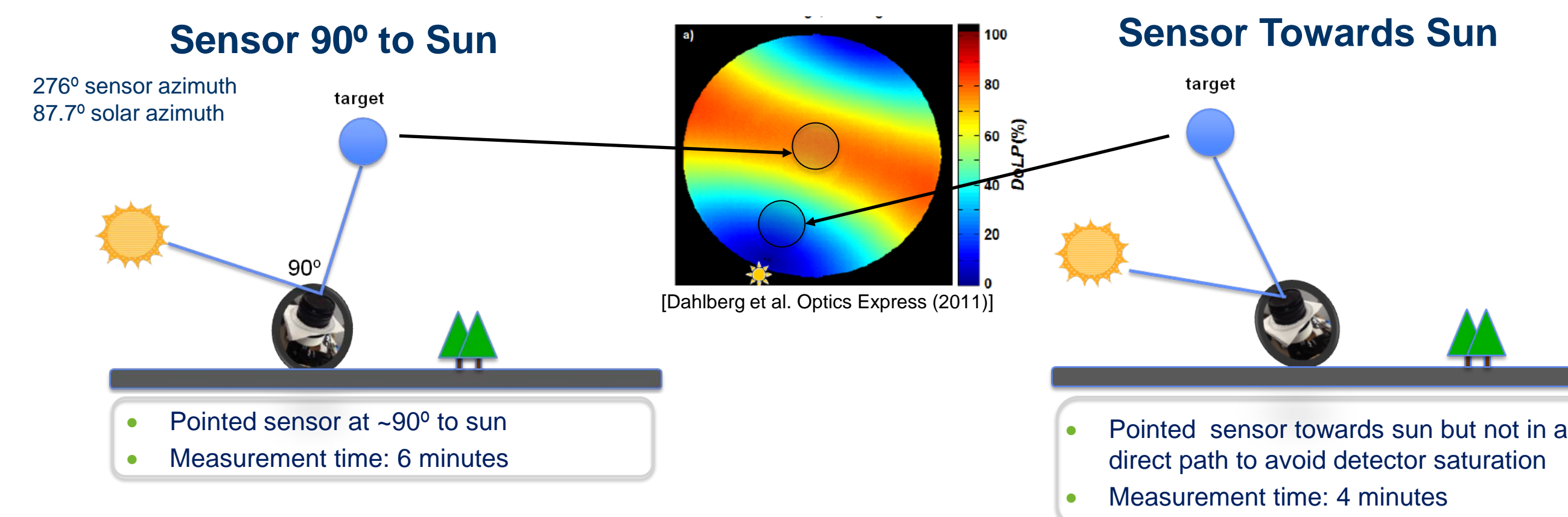


Setup for initial measurement of polarization sensitivity of polarimeter

* Identification is not intended to imply recommendation or endorsement by NOAA.

Taking Measurements of the Atmosphere

- Used polarized sunglasses to locate direction of high and low polarization

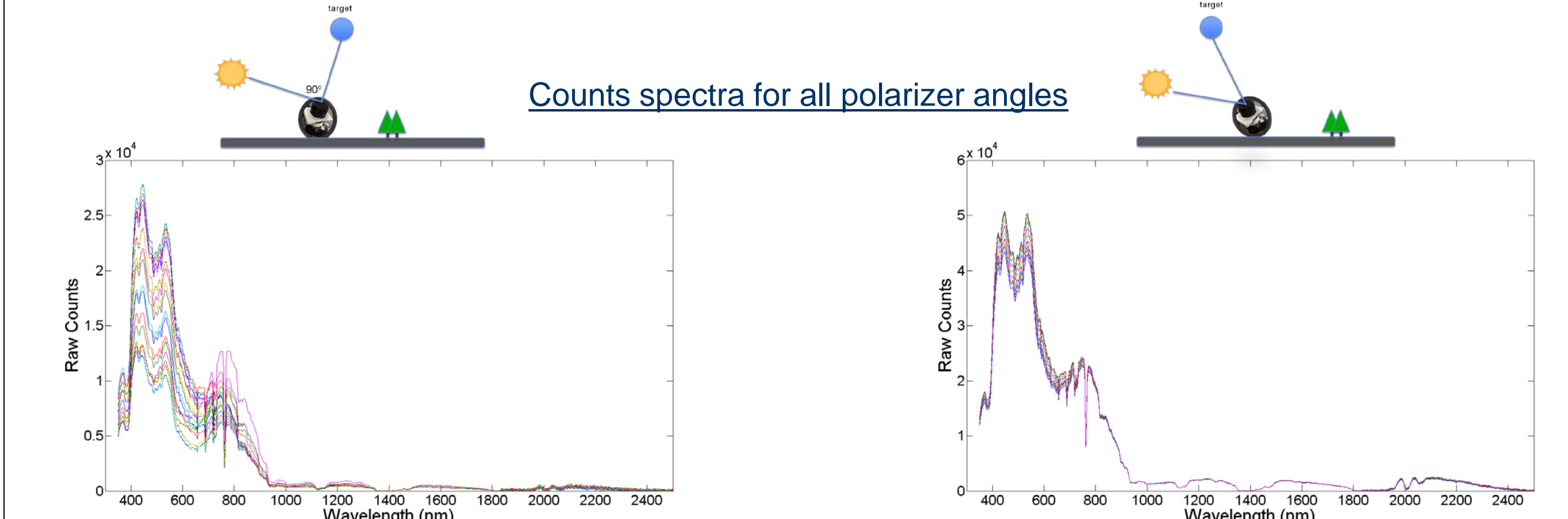


Measurement conditions

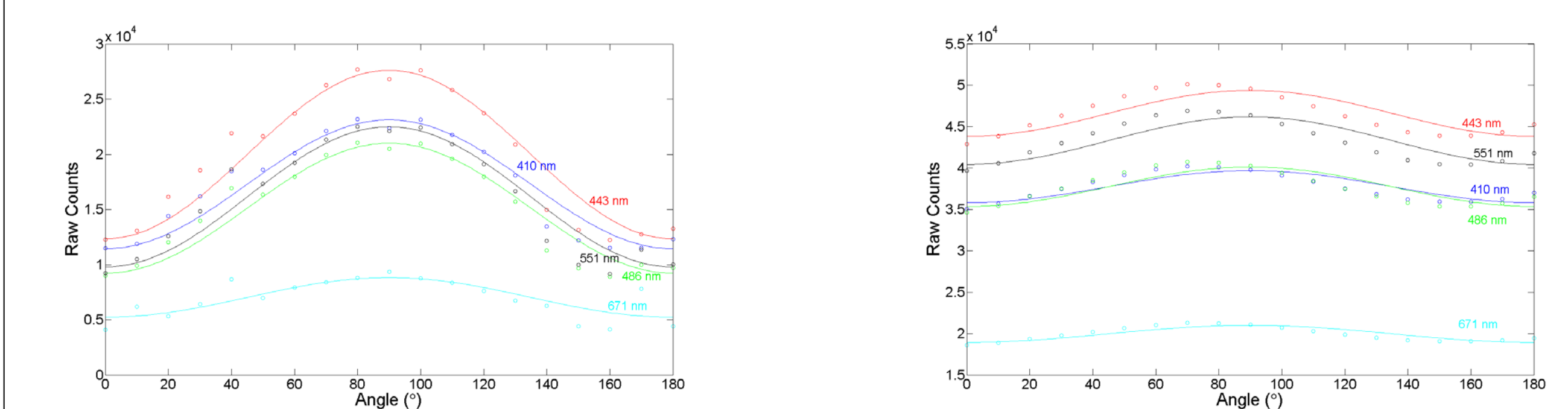


Polarimetric spectroradiometer setup (sensor 90° to sun)

Preliminary Results



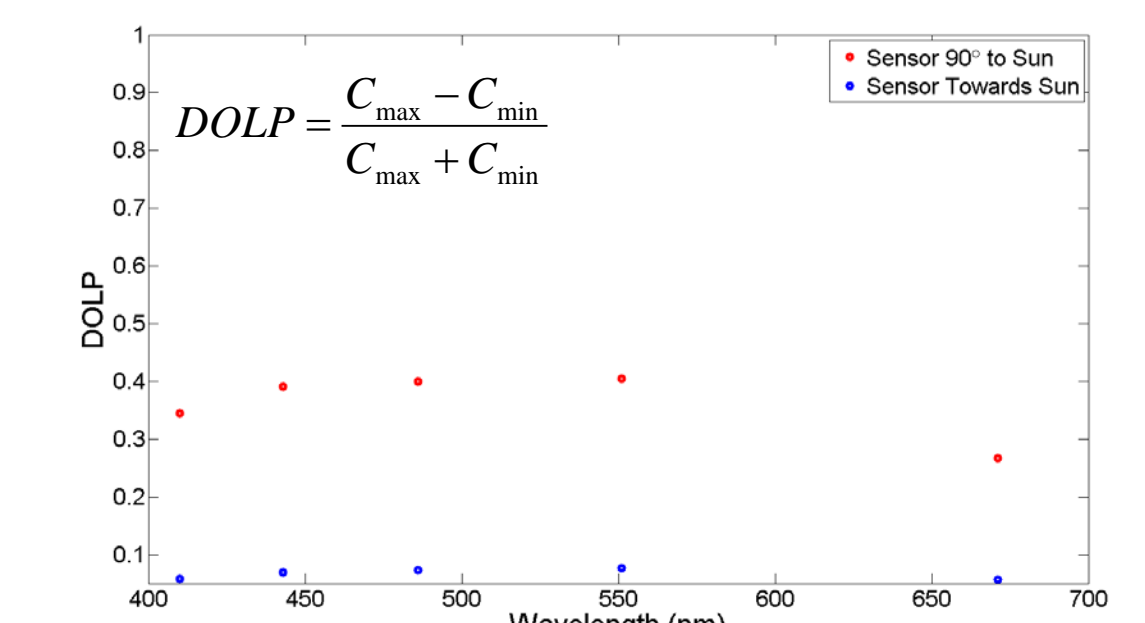
Counts versus polarizer angle for selected wavelengths



Degree of linear polarization (DOLP) at selected wavelengths

- Calculated DOLP values using sinusoidal fits [Novitsky et al. SPIE (2012)]

- Polarization increases with wavelength from 350 to 580 nm:

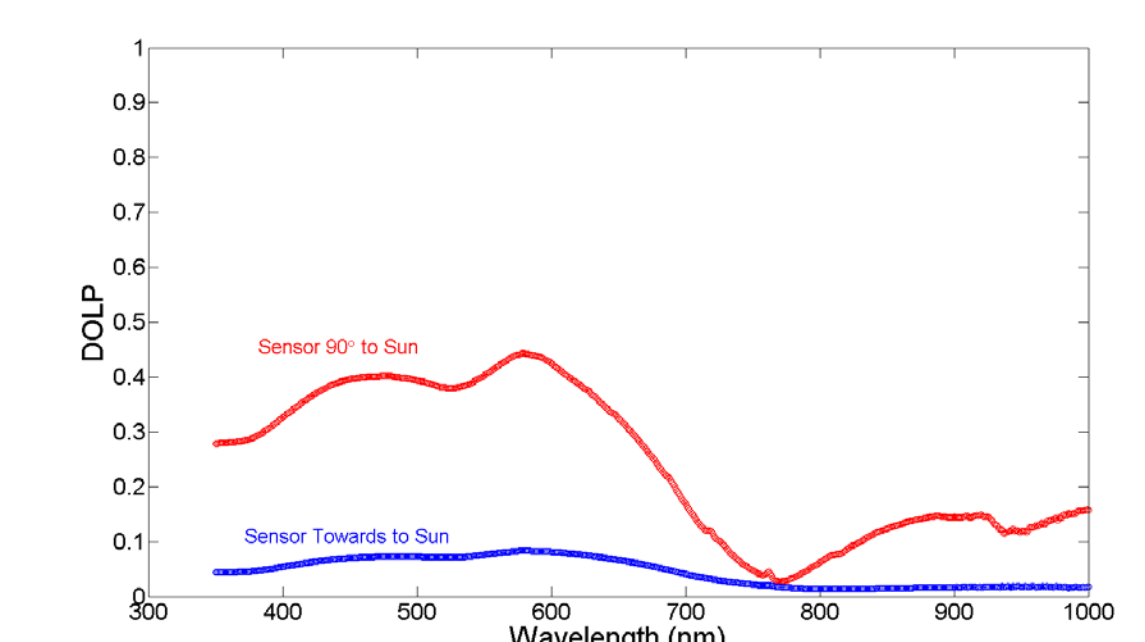


Degree of linear polarization at all wavelengths (< 1000 nm)

- Shows potential of the instrument to measure polarization states with high spectral resolution over a large wavelength range that covers VIIRS ocean color channels.

- Need more measurements to assess wavelength range where the linear polarizer is effective.

- Need further investigation to examine if spectral dependence is consistent with radiative transfer simulation results.



- Results consistent with Rayleigh scattering:**
 - Show that DOLP is higher 90° to sun than towards the sun

Summary and Future Work

Summary:

- Designed and built a customized ASD-based polarimeter that provides a new capability for NOAA to investigate polarization phenomenology in support of J1 VIIRS.
- The preliminary sky measurements established confidence in the proto-type design, which will act as a baseline for advancing atmospheric polarization research and development.

Future work:

- Improve the polarimeter design:
 - Add 3D printed protractor to decrease uncertainty in angle.
 - Add motor control to rotate polarizer to improve efficiency.
- Conduct measurements to gain better understanding of polarization states and assess uncertainties:
 - Continue measuring atmosphere over range of sun angles.
 - Measure polarization of reflected Earth surfaces.
- Work with NIST to calibrate polarimeter
- Validate atmospheric radiative transfer models

Fei Meng^{a, b}, Changyong Cao^c, Xi Shao^a

^aDepartment of Astronomy, University of Maryland, College Park, MD, USA

^bDepartment of Civil Engineering, Shandong Jianzhu University, Jinan, PR China

^cNOAA/ NESDIS/STAR, College Park, MD, USA

Abstract

The spatial and temporal variations in regional aerosol optical thickness (AOT) were investigated over Shandong province of China based upon one year's Visible Infrared Imaging Radiometer Suite (VIIRS) data. The regional forest background annual mean AOT was 0.467 with a standard deviation of 0.339, which was much higher than the background continental AOT level of 0.10. Higher AOT values for the study region were mainly found in the spring and summer, especially from May to August, while the lowest mean aerosol values were seen in November and December. Urban areas all have obviously higher mean AOT values than the rural areas resulting from intense anthropogenic sources. Given that the forest background AOT represents the natural background level, anthropogenic emissions and secondary aerosol generation contribute approximately 0.352 to the aerosol loading in this region. Additionally, strong regional imbalance of AOT was found to be distributed over the study area. The maximum annual average AOT values occurred in inland cities, while the coastal cities usually have lower AOT values.

Introduction

Aerosols are ubiquitous and comprise one important component of the Earth-atmosphere system, and influence air quality, visibility and climate system and human health. It is shown that there is a tendency of increase in the atmospheric aerosol load due to human activities, including the industrial production chains and the operation of various transport systems on the land surface. Because of the role of atmospheric aerosols in human health and climate change, many studies have been carried out on the retrieval of aerosol particle optical properties, their relationship with the PM_{2.5} and PM₁₀ concentrations, temporal and spatial variations, and their influence on the climate system and atmospheric radiation, with the development of new techniques and instruments. However, there are still uncertainties because of the lack of adequate knowledge on the spatial and temporal variability of aerosol properties across the globe. Long-term continuous aerosol observations in a large region are still of great importance for a range of assessments and applications, including satellite aerosol data validation, radiative forcing computations and public health and climate change.

The study area is situated on the eastern coast of China, with an area of 15.6 × 104 km², at latitude 34.26° N–38.42° N, longitude 114.93° E–122.46° E. Fig.1 shows the 18 sites under study, including the regional forest background (FB), Jinan (JNA), Qingdao (QD), Yantai (YT), Weihai (WH), Weifang (WF), Zibo (ZB), Tai'an (TA), Linyi (LY), Jining (JN), Rizhao (RZ), Laiwu (LW), Dezhou (DZ), Liaocheng (LC), Heze (HZ), Zaozhuang (ZZ), Binzhou (BZ) and Dongying (DY)



Fig. 1 Location of the study area. *Forest is the sampling location as forest background.

Methodology and Data

The VIIRS data

The VIIRS aerosol intermediate product (IP) data acquired in Shandong China from January 24 to December 31, 2013 (Fig. 1).

Spectral Range : 410–1250 nm, with 22 channels, of which 16 are M-bands (750 m resolution at nadir) and 5 are I-bands (375 m resolution at nadir)

The combination of aerosol quality flags ≤ 1, cloud detection result quality flags = 0 and turbid/shallow water = 0 were used in AOT retrieval.

Validation

VIIRS derived AOT were compared with those from AERONET ground-based sun photometer data of Beijing and Xianghe sites. The correlation were shown in Fig. 2.

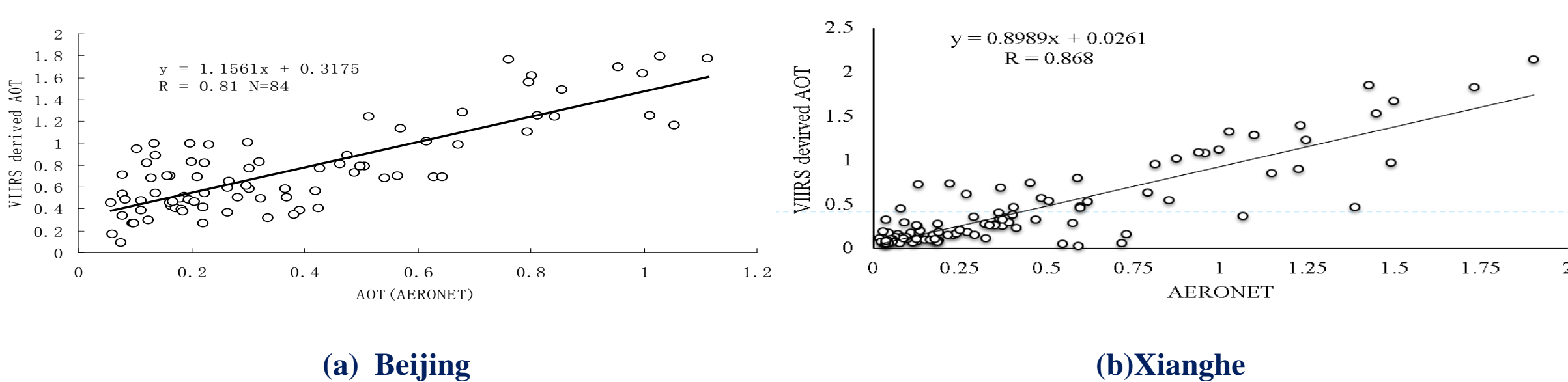


Fig. 2 Comparison of VIIRS AOT with AERONET sun photometer-derived AOT

Results

Annual and seasonal AOT variations for different cities

Averaged over the measurements in 2013, the minimum (Min.), maximum (Max.), mean, standard deviation (Std.) and variance of AOT in 17 cities (Fig.1) are presented in Table 1. In order to better understand the AOT values in different cities, percent days with AOT ≤ 0.5, 1.0 ≤ AOT > 0.5 and AOT > 1.0 respectively in each cities were calculated (Fig.2).

Table 1 Statistical annual AOT data in cities of Shandong province

City	N	Min.	Max.	Mean	Std.	Variance
weihai	201	0.023	1.902	0.540	0.409	0.167
yantai	188	0.071	1.791	0.596	0.409	0.167
qingdao	201	0.050	1.352	0.626	0.322	0.104
Rizhao	189	0.038	1.844	0.713	0.437	0.191
Weifang	193	0.093	1.901	0.747	0.428	0.184
Laiwu	163	0.045	1.731	0.747	0.410	0.168
Binzhou	146	0.048	1.871	0.767	0.500	0.250
Zibo	185	0.074	1.884	0.805	0.454	0.206
Zaozhuang	142	0.084	1.859	0.806	0.435	0.190
Dongying	158	0.086	1.900	0.808	0.504	0.254
Taian	176	0.072	1.964	0.816	0.442	0.195
Jining	165	0.118	1.952	0.823	0.433	0.188
Heze	156	0.168	1.941	0.826	0.441	0.195
Jinan	160	0.113	1.794	0.839	0.448	0.200
Liaocheng	171	0.137	1.894	0.846	0.452	0.204
Dezhou	185	0.096	1.895	0.853	0.478	0.229
Linyi	200	0.126	1.872	0.905	0.418	0.175
Forest	183	0.01	1.583	0.467	0.339	0.115

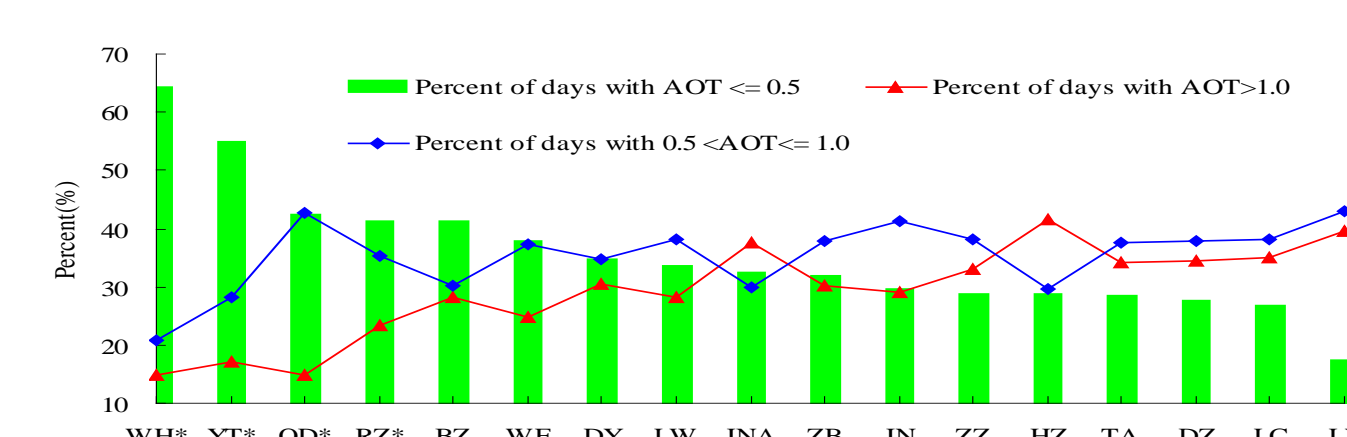


Fig.2 Percent of days with different AOT thresholds. “*” mean coastal city.

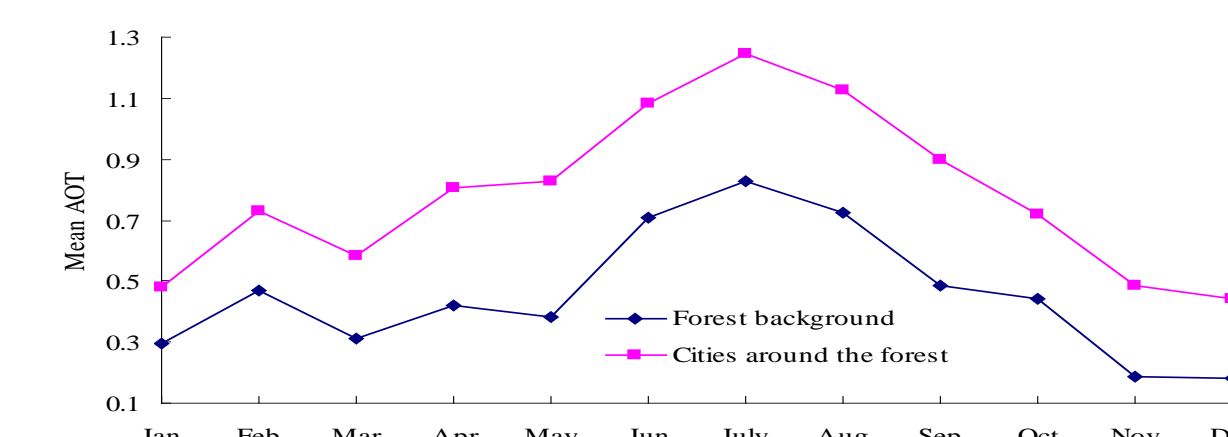


Fig. 3 Monthly mean AOT in the regional forest background and nearby cities

Spatiotemporal pattern of AOT

To investigate the spatial and temporal variation of regional AOT, statistical analysis was performed. 17 main cities plus the forest background were studied. Fig.3 shows variations of monthly mean values of retrieved AOT over the forest background site (FB) and cities around it. Fig.4 also shows a large seasonal variation that AOT varied from 0.260 ± 0.240 (Winter) to 1.226 ± 0.401 (Summer). Urban seasonally averaged in summer was always higher than values in other seasons, varied from 0.754 ± 0.449 (WH) to 1.226 ± 0.356 (JNA). The results in Fig.5 show a seasonal cycle of AOT with the lowest values recorded in winter and autumn and maximum values obtained in summer and spring. The time series of daily AOT and 7-day moving average line from January to December 2013 are illustrated in Fig.6 with a strong seasonal variation in 4 typical cities: Jinan, Linyi, Jining and Weihai. Fig.7 shows the AOT movement between August 17 and 18.

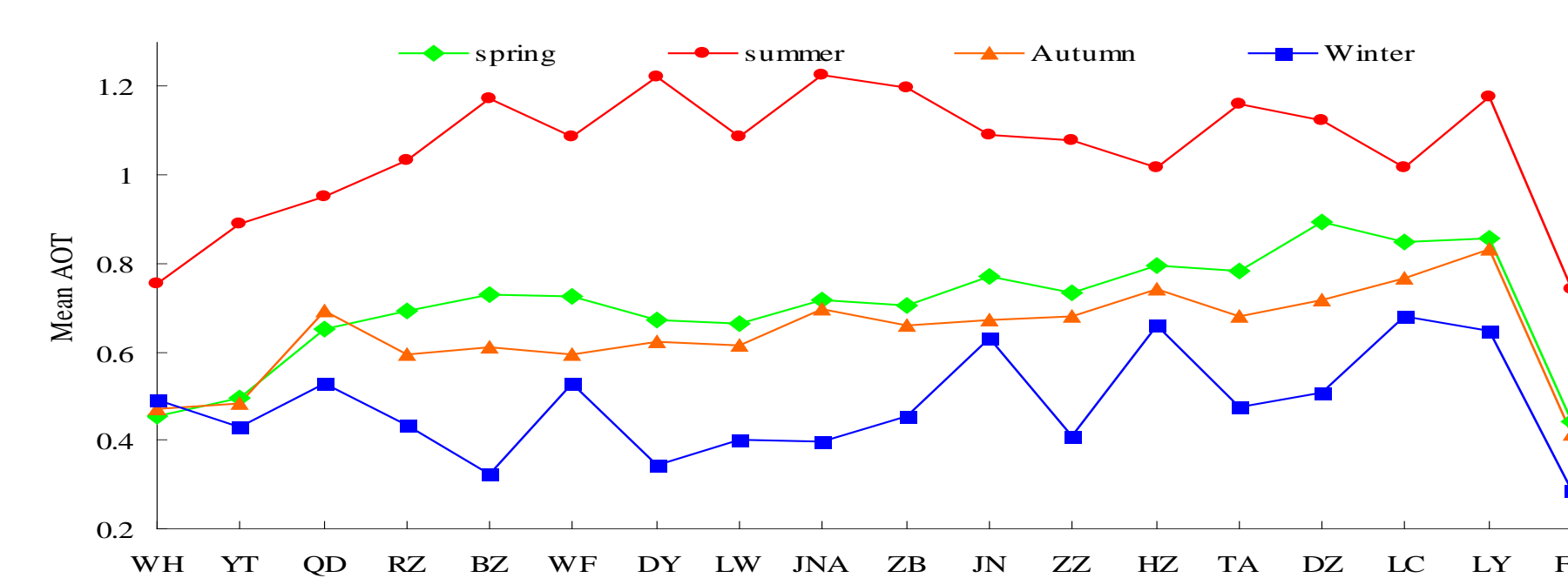


Fig. 4 Statistical seasonal overview of mean AOT in different cities of Shandong

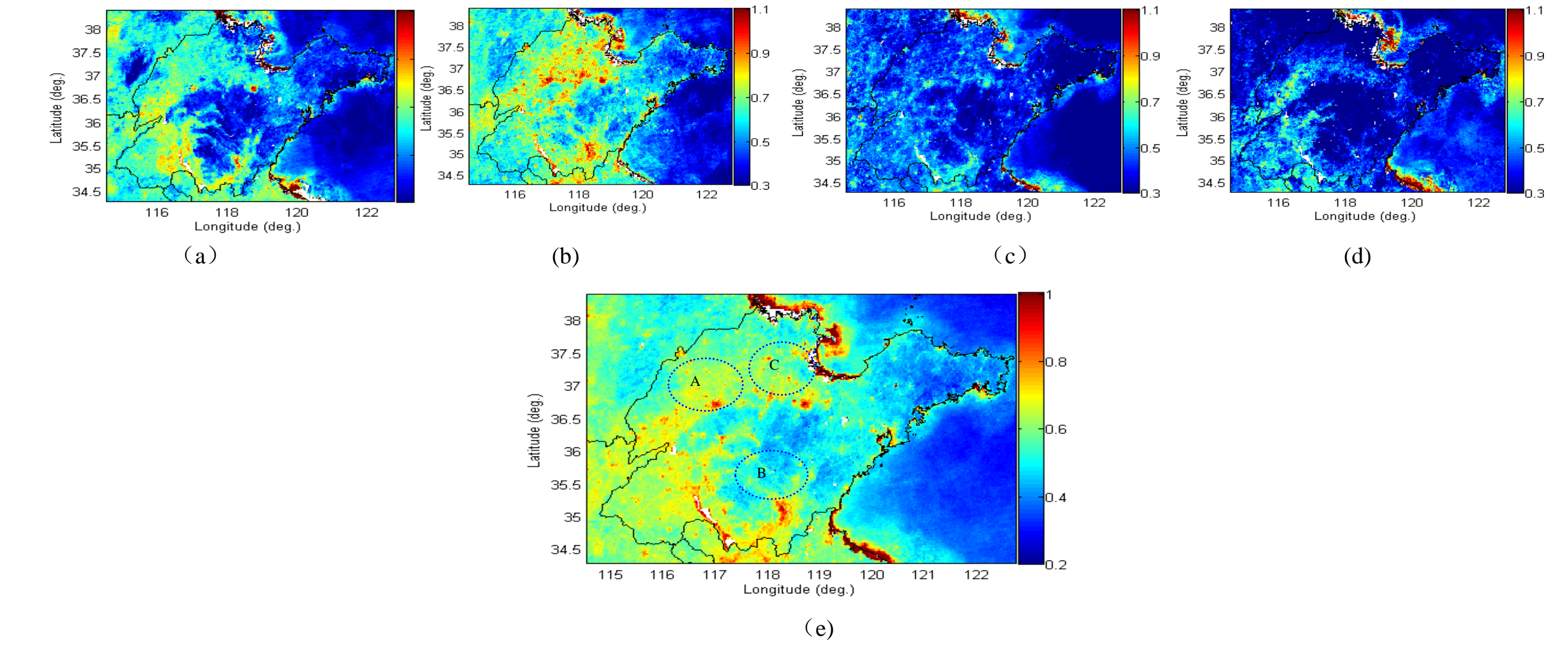


Fig.5 Seasonal mean VIIRS AOT observed in (a) spring (March to May 2013), (b) summer (June to August 2013), (c) Autumn (September to November 2013), (d) winter (December to February, 2013) and (e) annual in 2013. A is Jinan Jinan metropolitan, B is Linyi urban belt and C is Zibo urban belt.

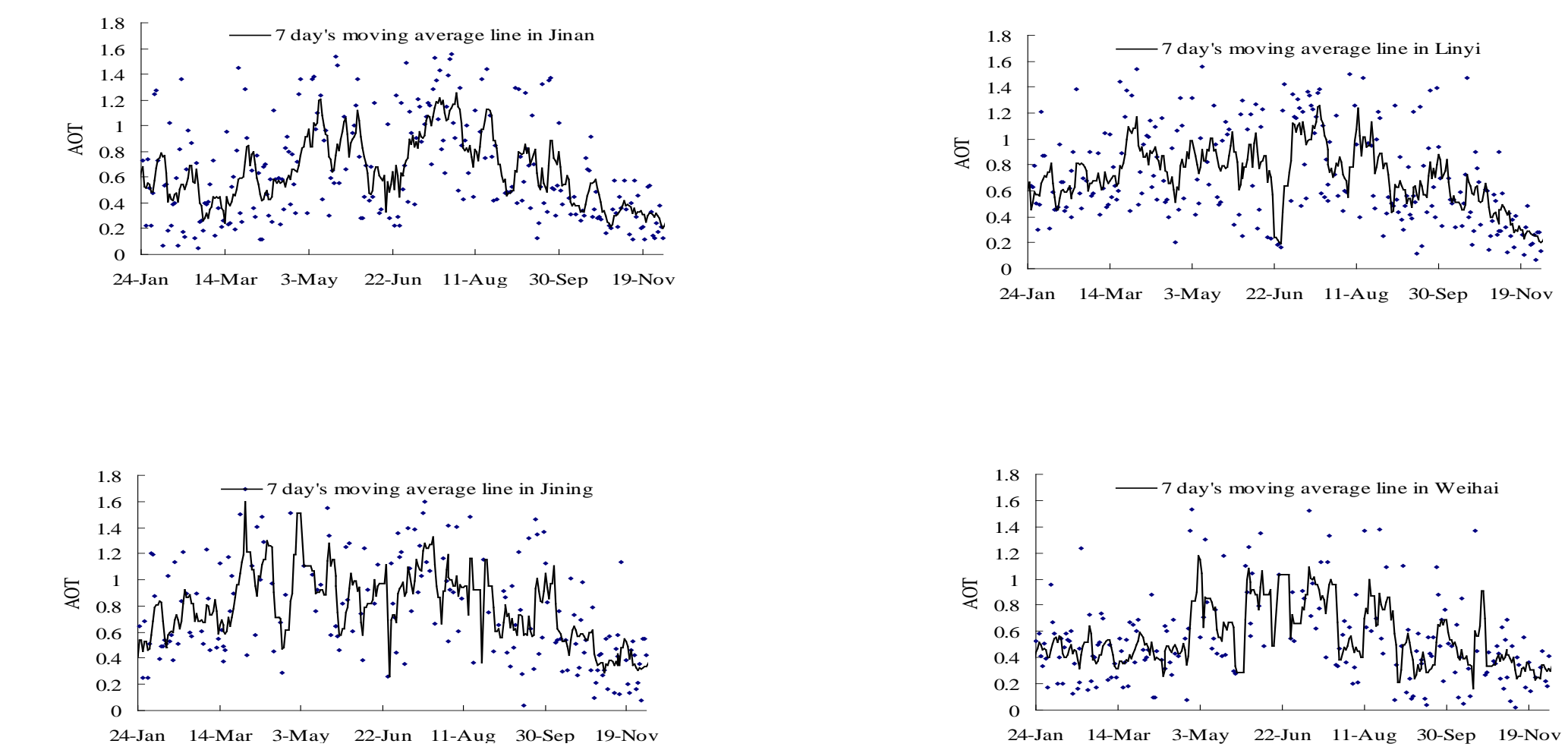


Fig. 6. Scatter plots of daily AOT and 7 day's moving average line of Jinan, Linyi, Jining and Weihai in 2013.

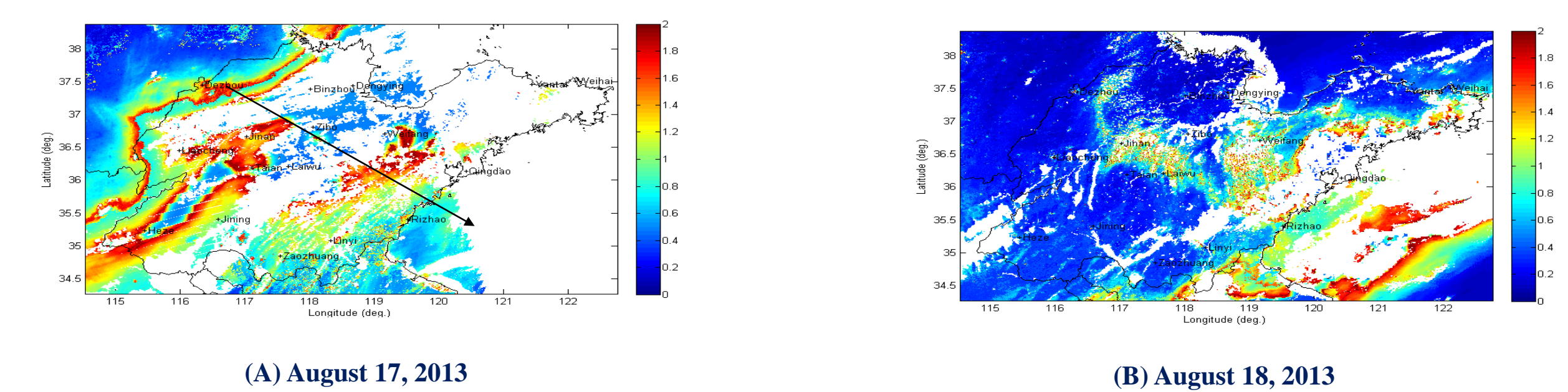


Fig. 7. Distribution of AOT retrieved with VIIRS during a heavy polluted event from August 17 to 18, 2013. The black arrow is the AOT moving direction.

Summary

The forest background annual averaged AOT was 0.467 with a standard deviation of 0.339, which was much higher than the background continental AOT level of 0.10. Higher AOT values for the study region were mainly found in the spring and summer, especially from May to August, while the lowest mean aerosol values were seen in November and December. The sequence of seasonally mean AOT values was summer > spring > autumn > winter. Urban areas all have obviously higher mean AOT values than the rural areas resulting from intense anthropogenic sources. Given that the forest background AOT (annual mean 0.467) represents the natural background level, anthropogenic emissions and secondary aerosol generation contribute approximately 0.352 to the aerosol loading in this region. Strong regional imbalance of AOT was found to be distributed over the study area. The maximum annual average AOT values occurred in inland cities, while the coastal cities usually have low AOT values.



VIIRS Surface Type algorithm refinement and preliminary validation

Rui Zhang¹, Chengquan Huang¹, Xiwu Zhan², Mark Friedl³, Damien Sulla-Menashe³

1. Department of Geographical Sciences, University of Maryland, College Park, MD 20742

2. Center for Satellite Applications and Research, NESDIS, NOAA, College Park, MD 20740

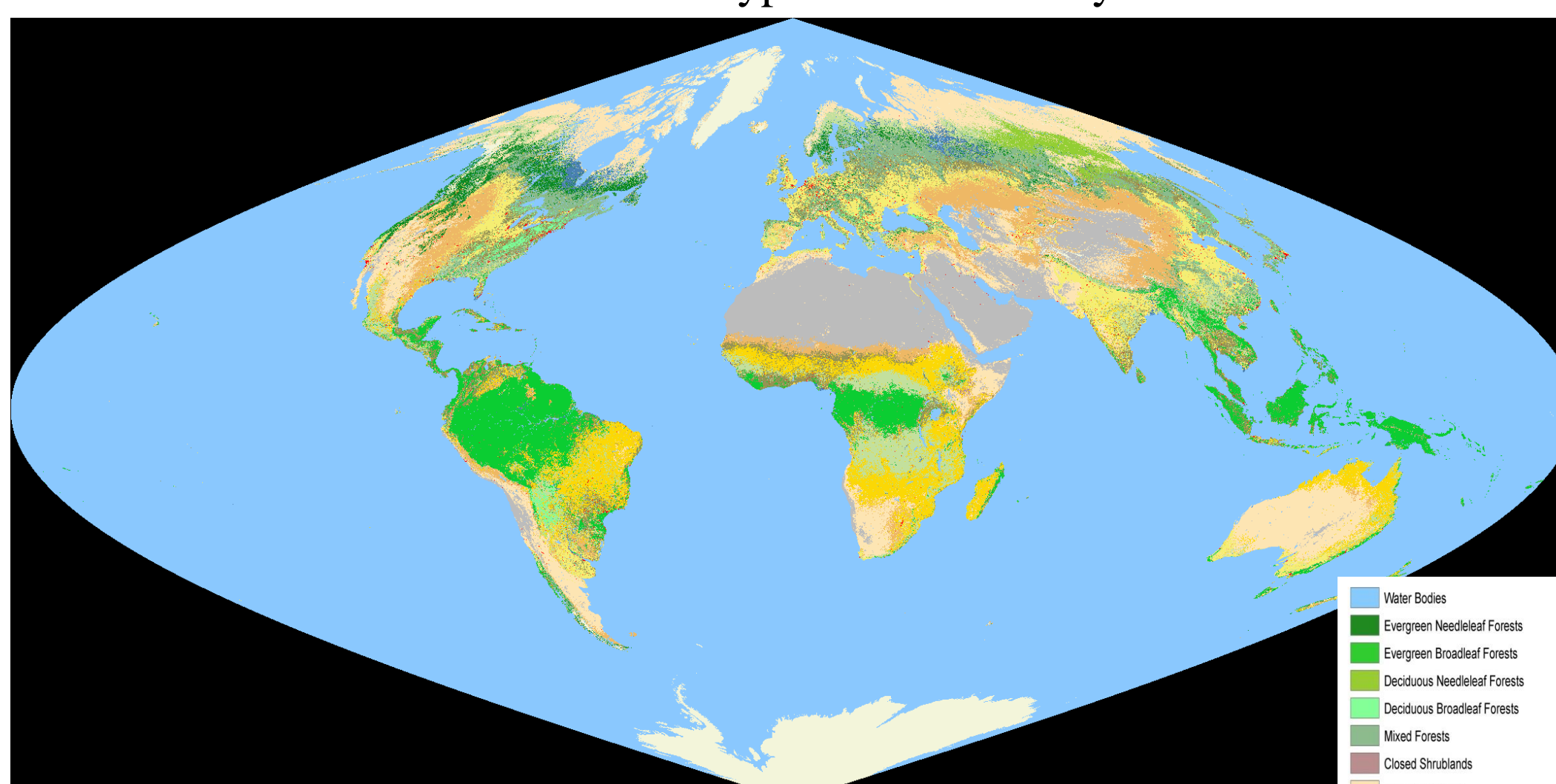
3. Department of Earth & Environment, Boston University, Boston, MA 02215



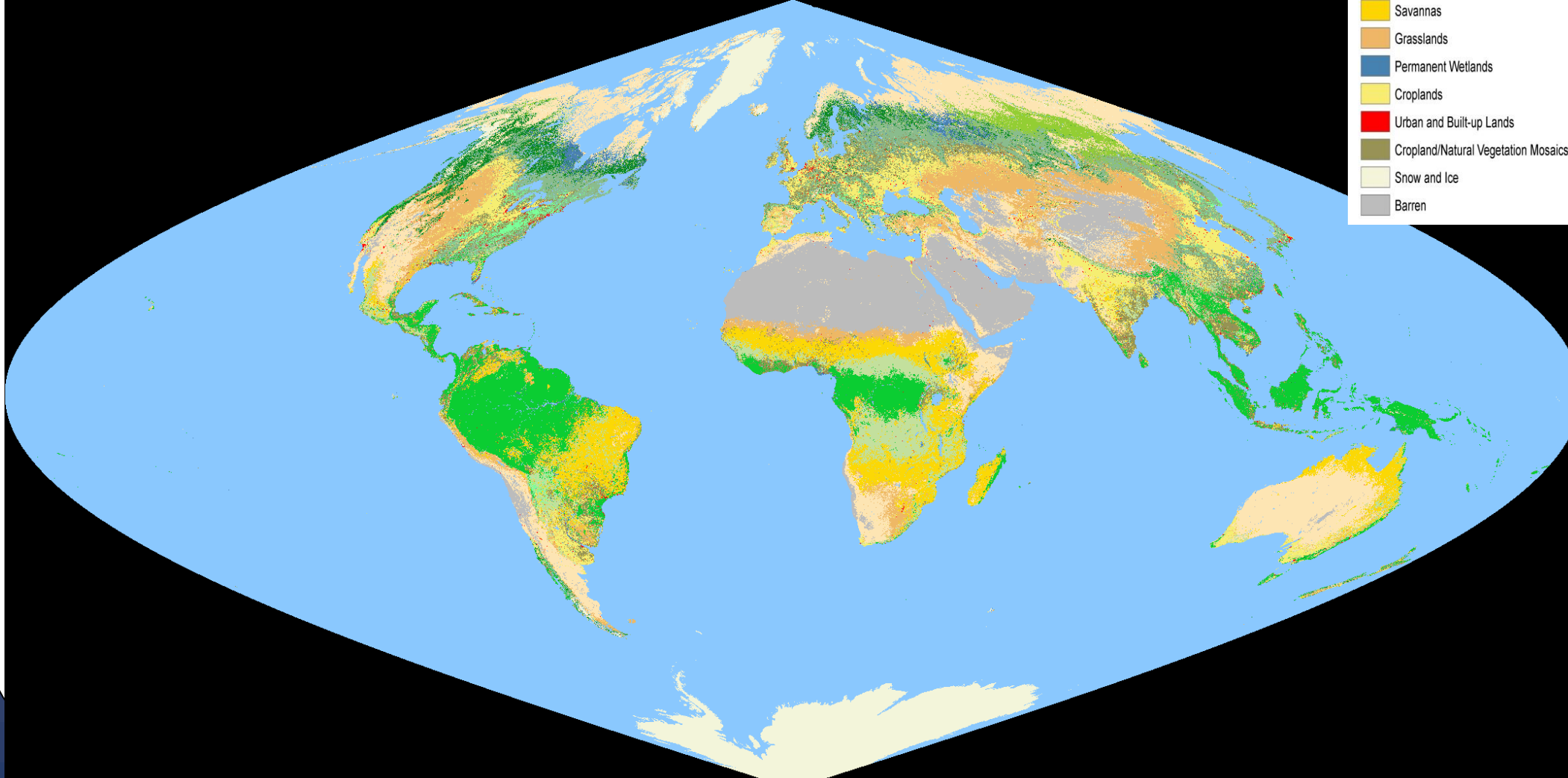
Introduction

VIIRS Surface Type Intermediate Product (IP) and Environmental Data Record (EDR) represent continuity with NASA EOS MODIS and NOAA POES AVHRR land cover products. After the beta delivery, VIIRS Surface Type algorithms are continuously evolving, and many improvements have been applied to the Surface Type IP, and then EDR. Among those improvements, results of a post-classification modeling on top of the original decision tree algorithm outputs, and a new classification algorithm Support Vector Machines (SVM) generated outputs are shown. The necessity of the new SVM in the ST algorithm refinement is that decision tree output requires intensive post processing while SVM may produce better direct output and needs less post processing. Comparisons of IGBP class agreements between SEED delivery and the delivered decision tree result, post-classification modelled result, and SVM result are presented. Preliminary validations performed by BU are also included.

VIIRS Surface Type IP beta delivery

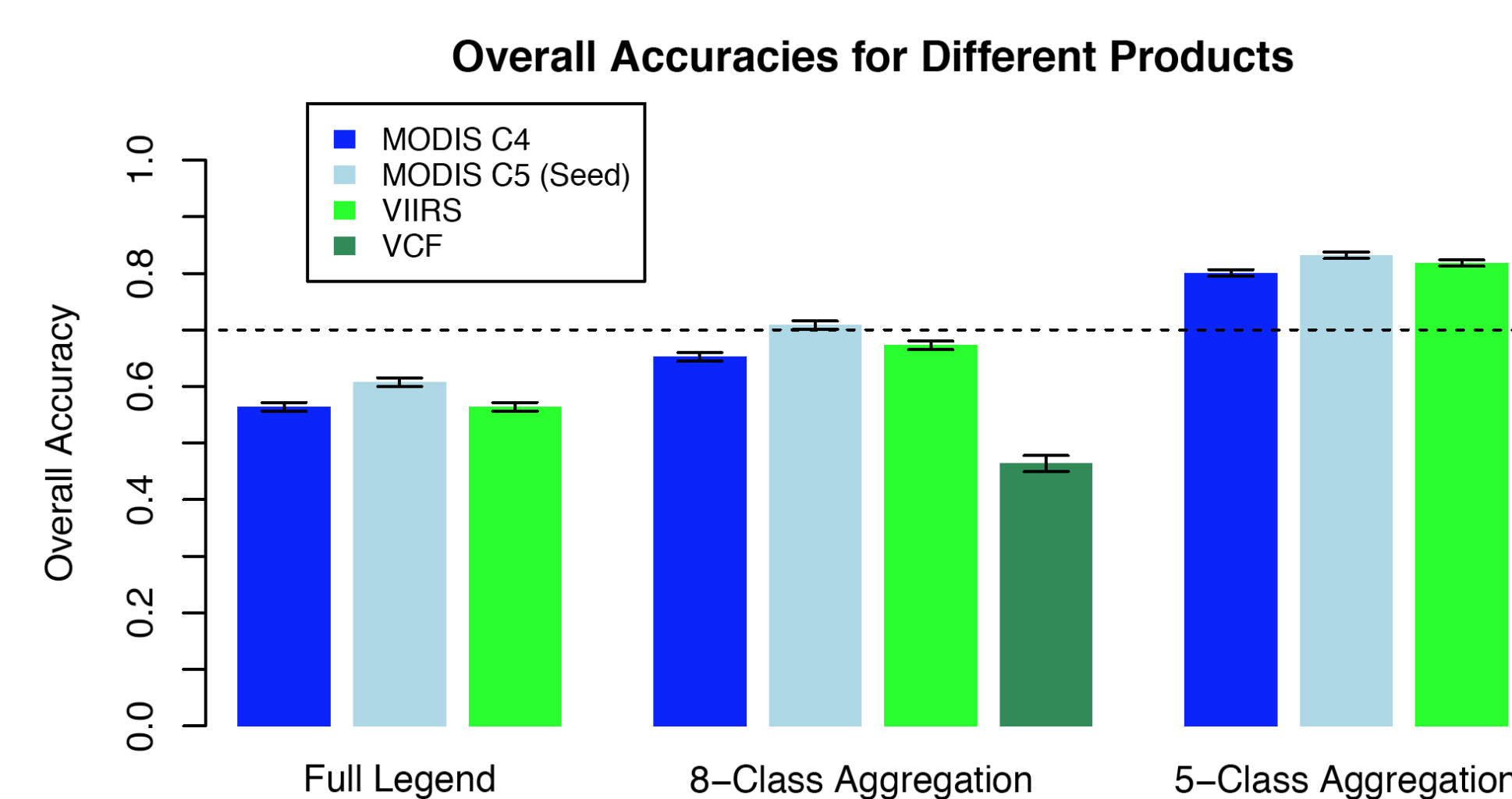
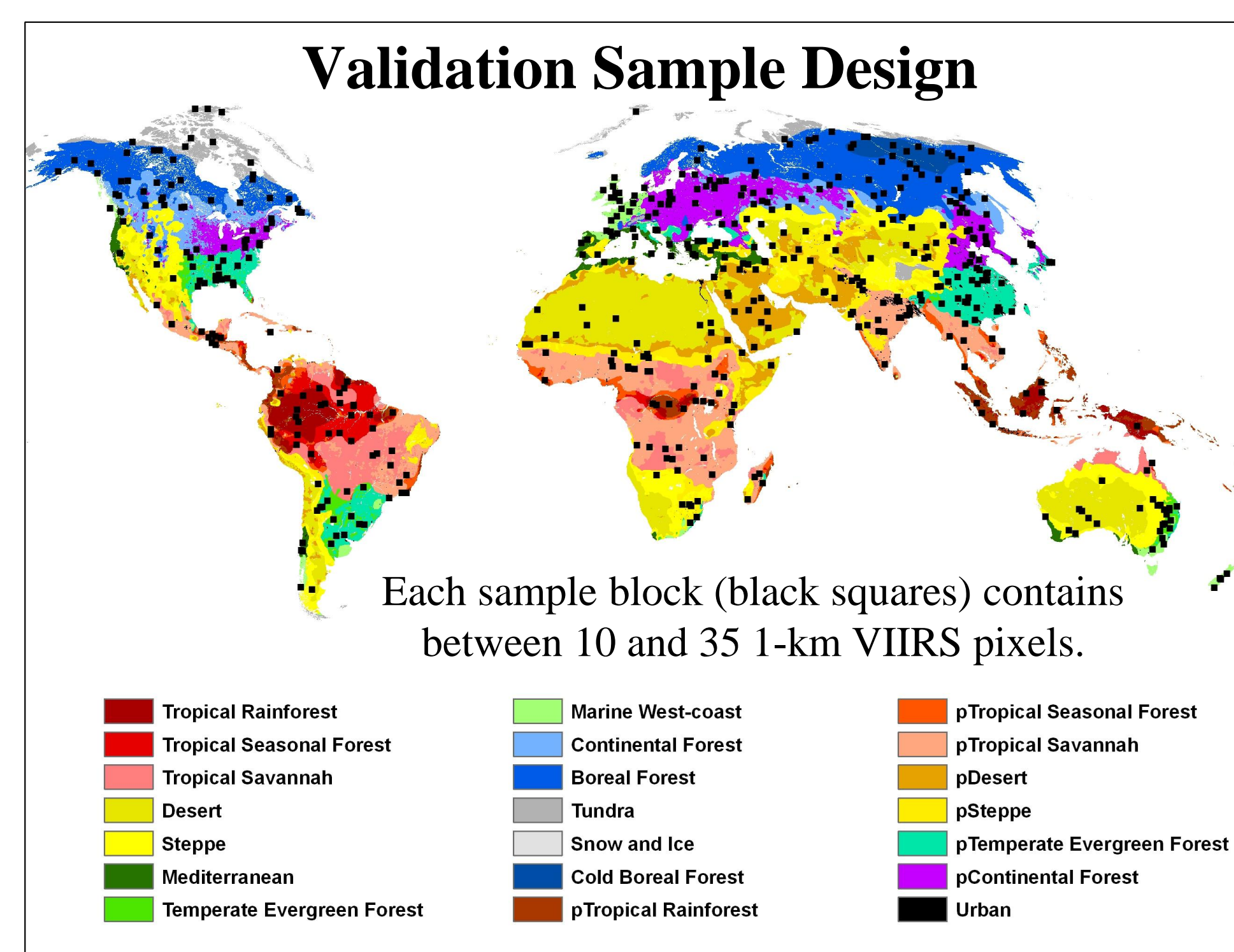


VIIRS Surface Type IP by SVM



Validations

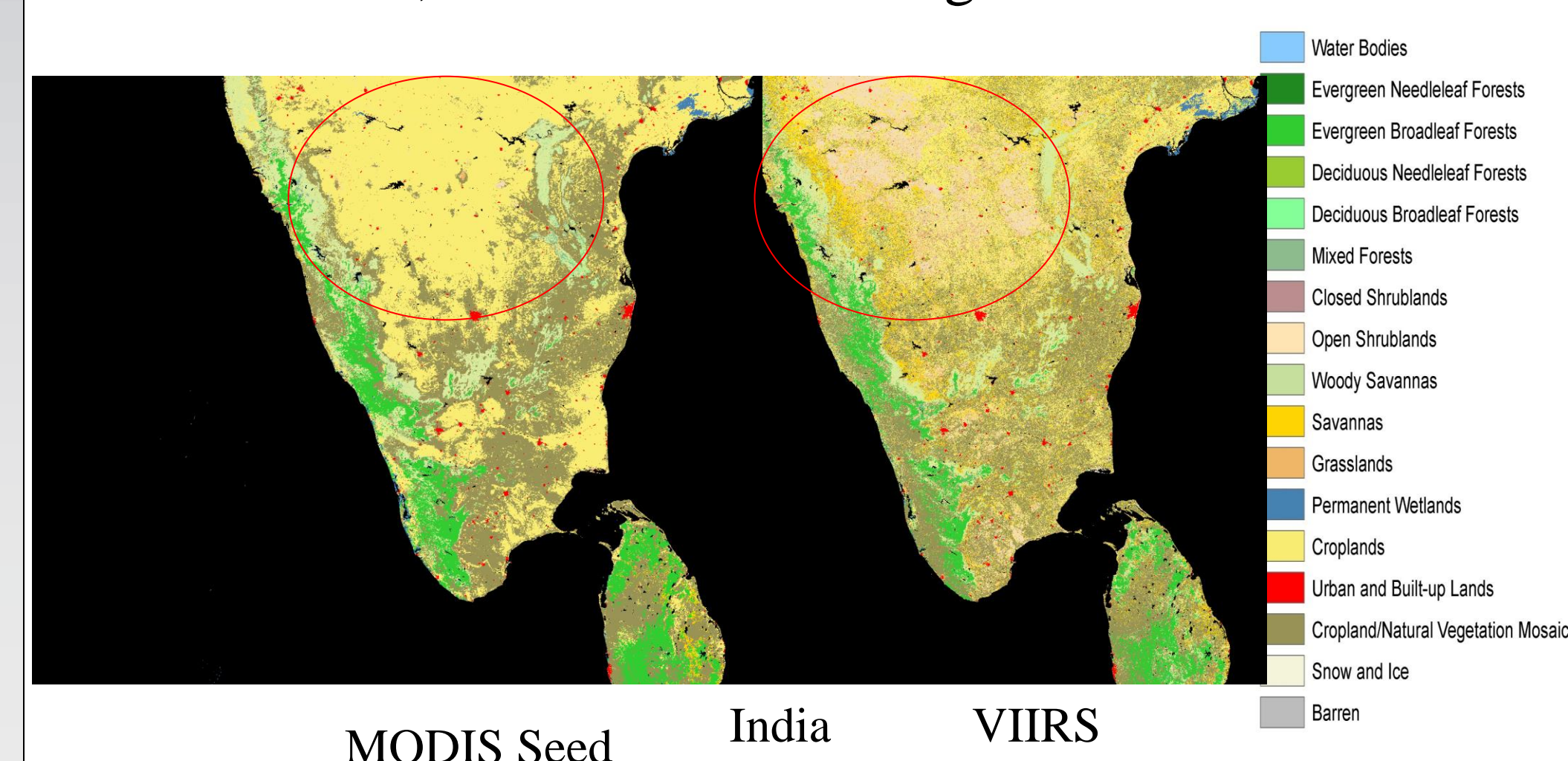
The independent global validation dataset was based on a stratified random sample of 500 blocks, which included 17 IGBP classes. Each validation block contains between 10-35 VIIRS 1km pixels. The validation was performed by human interpretation in high resolution images using a tool built in Google Earth. Validation samples and comparisons of overall accuracies among different products are shown below.



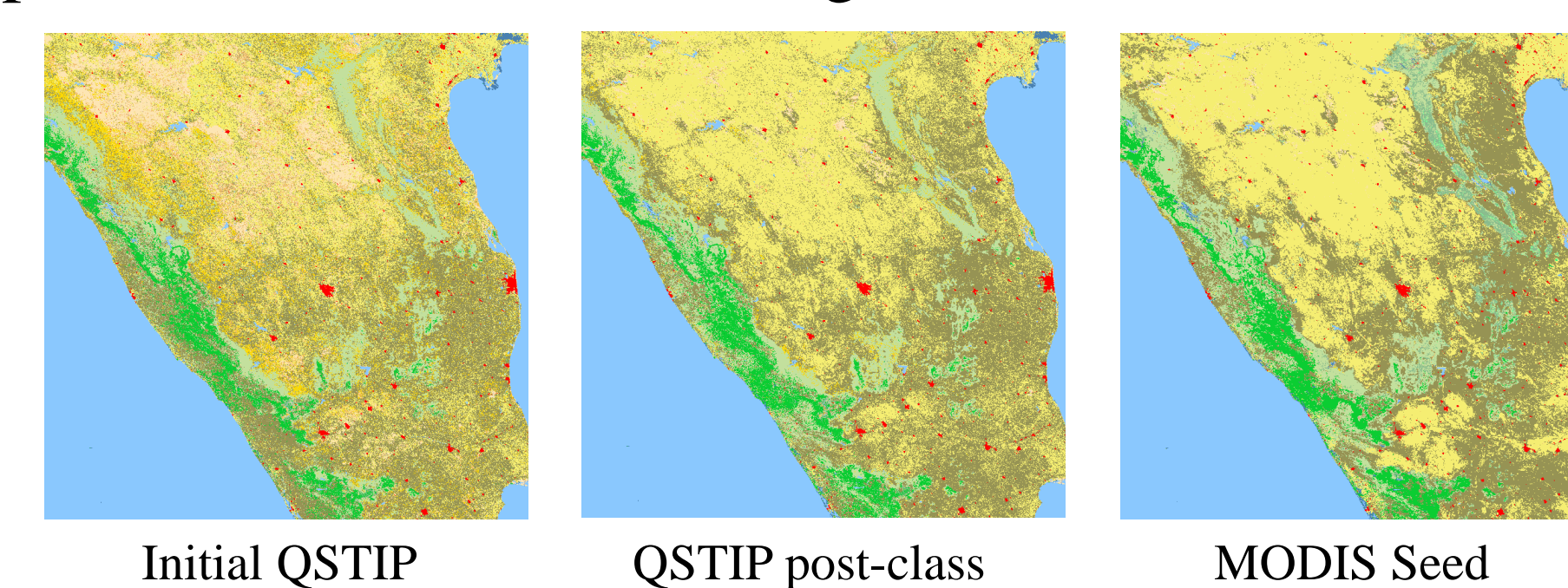
VIIRS QST IP overall accuracy is similar to MODIS C4 and C5 (Seed), and detailed visual interpretation and per-class analyses indicated that the VIIRS QST IP is compatible to MODIS C5 Land cover product.

Refinement

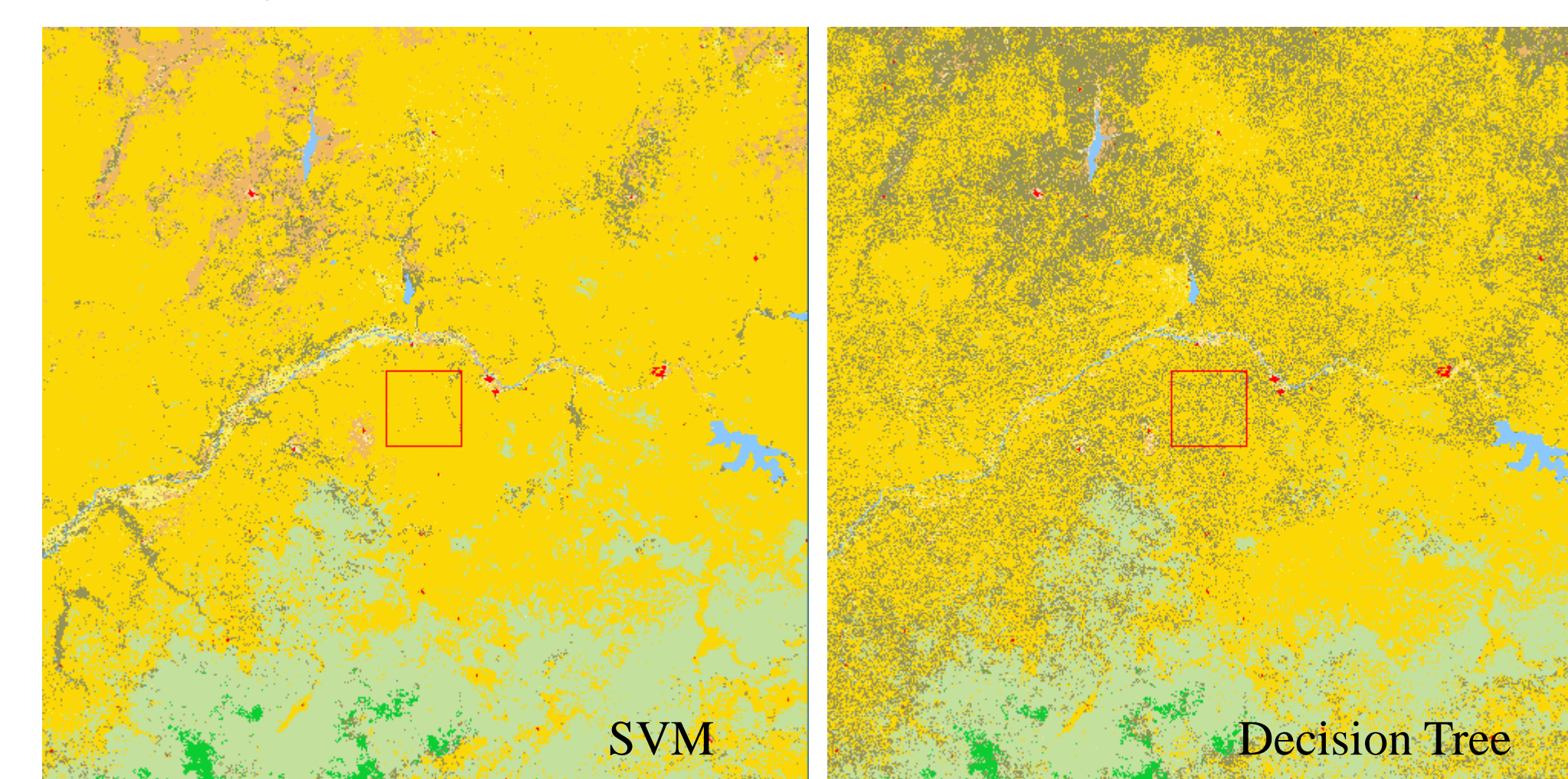
The preliminary validation suggested the new VIIRS QST IP omitted some cropland pixels in India and misclassified some grassland or open shrublands into croplands in high latitude areas, such as southern Argentina.



To improve the accuracy of croplands class, a crop probability product from global cropland extent project of South Dakota State University and an internal multiple products crop distribution agreement data are employed in a post-classification modelling.



Another refinement is the introduction of the SVM algorithm in the generation of QSTIP. Preliminary visual comparisons suggest the SVM yield less speckle noises than original decision tree. A west Africa case showed.



Agreement with MODIS C5

The initial decision tree generated global surface type IP, post-classification modelled QST-IP, and SVM generated QST-IP are compared to MODIS C5 (Seed) Land Cover, and agreements among those datasets are presented. The results indicated both decision tree and SVM are able to generate MODIS C5 compatible VIIRS surface type products, and their agreements are very similar.

17 Class IGBP agreement between SEED and Beta delivery QSTIP in percentage, overall agreement = 92.9841%

	ENF	EBF	DSF	DRF	MF	CS	OS	WS	S	G	PW	C	UB	CN	SI	B	WB
ENF	66.85	0.19	1.34	0.06	5.39	1.14	0.24	3.46	1.04	0.72	3.24	0.08	0	0.20	0	0	0.001
EBF	0.62	90.14	0.01	2.91	2.63	0.30	0	3.29	2.06	0.23	11.42	0.32	0	4.58	0	0	0
DSF	0.46	0	74.63	0	1.25	0.02	1.19	1.48	0.58	0.15	0.42	0.01	0	0.16	0	0	0
DRF	0	0.07	0	53.30	1.53	0.15	0	0.31	0.07	0.05	0.05	0	0	1.17	0	0	0
MF	18.18	1.44	9.86	11.44	75.44	5.95	0.24	4.66	0.42	0.95	2.89	0.44	0	4.64	0	0	0
CS	0.02	0	0.11	0.01	18.37	0.06	0.05	0.04	0.13	0	0.02	0	0	0.01	0	0	0
OS	0.74	0.01	3.07	0.10	0.13	18.30	81.89	2.51	4.29	23.45	8.73	3.09	0	0.63	1.23	5.99	0.02
WS	8.10	2.77	7.45	17.18	6.44	18.57	3.02	63.79	14.02	2.24	10.20	2.45	0	7.29	0.01	0	0
S	0.01	0.49	0.01	5.90	0.13	24.22	3.53	10.57	66.15	6.24	2.05	5.87	0	13.31	0	0.01	0
G	1.25	0.17	0.26	0.23	0.45	7.64	3.79	0.64	1.92	50.65	0.46	7.27	0	3.36	0.02	0.97	0
PW	1.43	0.23	1.80	0.12	0.31	1.11	1.49	0.82	1.13	0.23	48.78	0.23	0	0.22	0	0.02	0.01
C	0.78	0.23	0.23	0.75	1.84	4.72	1.34	2.30	0.90	6.19	3.85	70.32	0	10.13	0.02	0.05	0.01
UB	0	0	0	0	0	0	0	0	0	0	0	0	0	99.76	0	0	0
CN	0.57	4.23	1.24	7.89	4.33	2.14	0.70	5.99	7.34	3.40	4.21	9.80	0	54.17	0	0.02	0
SI	0.35	0	0.03	0	0.04	0.05	0.21	0.06	0.01	2.47	0.13	0	0	0	98.51	0.65	0
B	0.01	0	0	0	0	0.04	2.23	0	0	2.77	0.07	0.02	0	0.11	0.10	92.28	0
WB	0.63	0.02	0.08	0	0.09	0.07	0.08	0.08	0.02	0.15	3.50	0.03	0.24	0.01	0.11	0.02	99.93

17 Class IGBP agreement between SEED and Post-classification modelled QSTIP in percentage, overall agreement = 93.5068%

	ENF	EBF	DSF	DRF	MF	CS	OS	WS	S	G	PW	C	UB	CN	SI	B	WB
ENF	67.71	0.19	1.38	0.07	5.48	1.41	0.26	3.49	1.07	0.79	3.4	0.1	0	0.29	0	0	0.001
EBF	0.62	92.9	0.01	2.94	2.66	0.33	0	3.59	2.19	0.25	11.98	0.39	0	5.96	0	0	0
DSF	0.46	0	75.06	0	1.27	0.02	1.2	1.49	0.59	0.16	0.5	0.01	0	0.19	0	0	0
DRF	0	0.08	0	58.4	1.7	0.23	0	0.37	0.1	0.06	0.09	0.06	0	1.77	0	0	0
MF	18.32	1.48	10.32	12.51	79.43	7.35	0.27	5.23	0.55	1.1	3.38	0.66	0	6.74	0	0	0.001
CS	0.02	0	0	0.12	0.02	20.05	0.07	0.07	0.05	0.14	0.04	0.04	0	0.03	0	0	0
OS	0.76	0.01	3.14	0.12	0.15	18.5	82.8	2.57	4.34	23.65	8.92	1.85	0	0.64	1.23	5.99	0.02
WS	8.16	3.04	7.52	17.59	6.71	16.25	3.07	68.05	14.66	2.41	10.71	2.54	0	9.02	0.01	0	0.001
S	0.02	0.62	0.07	5.97	0.15	24.32	3.56	10.83	70.95	6.37	2.22	4.71	0	14.01	0	0.01	0
G	1.36	0.2	0.36	0.47	0.58	8.51	3.99	0.79	2.15	55.15	0.82	5.96	0	4.71	0.02	0.97	0
PW	1.44	0.31	1.84	0.13	0.35	1.17	1.5	0.87	1.17	0.25	51.92	0.29	0	0.34	0	0.02	0.01
C	0.77	0.05	0.04	0.16	0.53	1.2	0.66	0.98	0.31	3.08	1.34	74.14	0	7.84	0	0.03	0
UB	0	0	0	0	0.02	0.01	0.01	0	0.01	0.01	0.03	0.05	98.74	0.09	0	0	0
CN	0.05	1.1	0.14	1.48	0.82	0.5	0.1	1.52	1.84	1.19	0.94	9.14	0.33	47.62	0	0.01	0
SI	0.35	0	0.03	0	0.04	0.05	0.21	0.06	0.01	2.47	0.14	0	0	0	98.52	0.65	0
B	0.01	0	0	0	0	0.04	2.23	0	0	2.78	0.08	0.03	0	0.12	0.11	92.3	0
WB	0.63	0.02	0.08	0	0.09	0.07	0.08	0.08	0.02	0.15	3.51	0.03	0.24	0.01	0.11	0.02	99.93

17 Class IGBP agreement between SEED and SVM generated QSTIP in percentage, overall agreement = 92.6669%

	ENF	EBF	DSF	DRF	MF	CS	OS	WS	S	G	PW	C	UB	CN	SI	B	WB
ENF	67.03	0.26	1.14	0.06	5.07	0.39	0.19	6.25	1.38	0.66	2.72	0.05	0	0.1	0	0	0.001
EBF	1.1	92.74	0.01	3.03	3.43	0.29	0	4.72	2.87	0.3	9.9	0.23	0	8.47	0	0	0
DSF	0.46	0	78.9	0	1.12	0	1.88	3.87	0.89	0.12	0.96	0	0	0.13	0	0	0
DRF	0	0.1	0	46.85	2.06	0.39	0	0.54	0.12	0.06	0.12	0.12	0	3.03	0	0	0
MF	22.35	1.43	12.83	13.89	78.69	9.04	0.44	7.56	0.54	1.43	4.45	0.52	0	7.4	0	0	0.001
CS	0.01	0	0	0	0.35	0.01	0.01	0	0.01	0	0	0	0	0	0	0	0
OS	1.06	0.01	2.92	0.1	0.21	24.04	83.19	4.27	4.17	23.81	9.95	3.1	0	0.79	1.65	6.07	0.02
WS	2.45	2.17	1.31	27.47	3.42	19.56	1.24	52.43	14.56	1.78	5.15	0.9	0	6.69	0	0	0
S	0	0.44	0.02	3.68	0.13	22.76	2.98	10.19	65.93	6.45	2.1	5.07	0	17.02	0	0	0
G	0.81	0.09	0.27	0.23	0.35	7.07	3.94	0.75	2.72	50.9	0.42	8.16	0	4.73	0.08	1.03	0
PW	1.99	0.46	1.86	0.14	0.61	1.39	1.45	1.84	1.44	0.29	52.67	0.41	0	0.36	0	0.02	0.01
C	0.47	0.12	0.08	1.25	0.84	2.92	1.39	1.48	0.72	5.51	2.75	67.03	0	6.36	0.01	0.1	0.001
UB	0	0	0	0	0	0	0	0	0	0	0	0	0	99.76	0	0	0
CN	0.74	2.05	0.54	3.28	3.93	1.48	0.41	5.91	4.62	2.98	4.98	14.35	0	44.74	0	0.01	0.001
SI	0.58	0.12	0.03	0.01	0.07	0.2	0.32	0.1	0.01	2.89	0.21	0.01	0	0.01	98.09	0.71	0
B	0.01	0	0	0	0	0.03	2.49	0	0.01	2.65	0.12	0.02	0	0.16	0.04	92.04	0
WB	0.63	0.02	0.08	0	0.09	0.07	0.08	0.08	0.02	0.15	3.5	0.03	0.24	0.01	0.11	0.02	99.93

Assessment of S-NPP CrIS Spectral Calibration Accuracy and Stability

Yong Chen¹, Yong Han², Xin Jin³, Likun Wang¹, Denis Tremblay⁴, and Fuzhong Weng²

Contact info: Yong.Chen@noaa.gov

¹ESSIC, University of Maryland, College Park, MD 20740 ²NOAA/NESDIS Center for Satellite Applications and Research, College Park, MD 20740

³ERT, Laurel, MD 20723 ⁴Science Data Processing Inc. Laurel, MD 20723

2014 STAR JPSS Annual Science Team Meeting

Abstract

The Cross-track Infrared Sounder (CrIS) on Suomi National Polar-orbiting Partnership Satellite (S-NPP) is a Fourier transform spectrometer and provides a total of 1305 channels for sounding the atmosphere. Quantifying the CrIS spectral accuracy, which is directly related to radiometric accuracy, is crucial for improving its data assimilation in the numerical weather prediction.

Two basic spectral calibration methods are used to assess the CrIS Sensor Data Records (SDR) spectral accuracy and stability: 1). Relative spectral calibration, which uses two uniform observations to determine frequency offsets relative to each other; 2). Absolute spectral calibration, which requires an accurate forward model to simulate the top of atmosphere radiance under clear conditions and correlates the simulation with the observed radiance to find the maximum correlation. In this study, we use Community Radiative Transfer Model (CRTM) and European Centre for Medium-Range Weather Forecasts (ECMWF) forecast fields to simulate the CrIS radiance over tropical clear scenes over ocean.

CrIS spectral stability is so high that we could detect the Earth-rotation Doppler shift (ERDS) from CrIS observations using the relative spectral calibration method for CrIS band 1.

Spectral calibration results show that CrIS has small and consistent FOV to FOV spectral shift in all three bands. The spectral shift is very stable during the satellite mission and better than the instrument requirement. Long-term CrIS SDR spectral stability is very high.

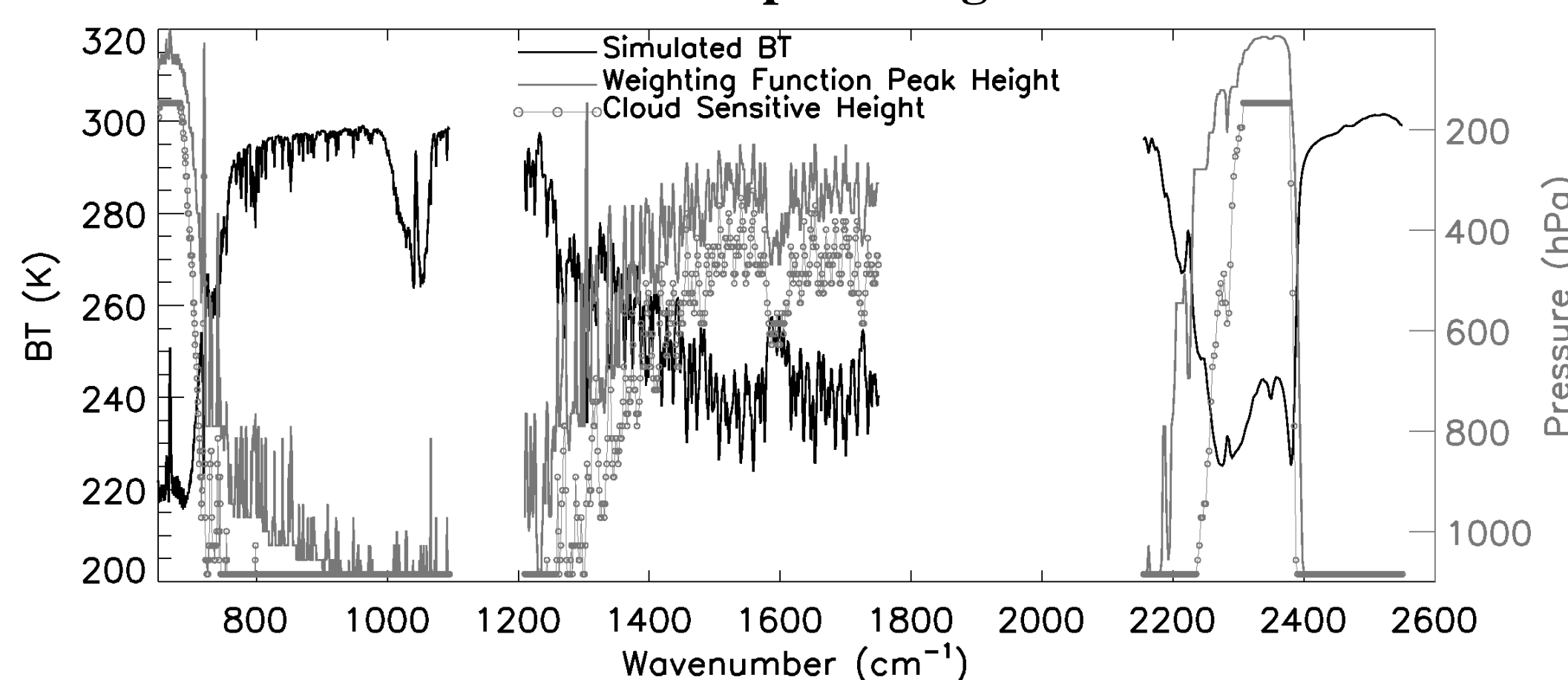
IR Cloud Detection Algorithm

- The channels are first ordered according to their cloud sensitivity (with the highest channels first and the channels closest to the surface last) (McNally and Watts, 2003)
- The overcast variable contains overcast radiances assuming the presence of a black cloud at each of atmospheric layers. The height for a particular channel is assigned by finding the layer where the difference between the overcast and clear radiances is less than 1%.

$$\frac{|R_{clear} - R_{cloudy}|}{R_{clear}} < 0.01$$

- The resulting ranked brightness temperature departures are smoothed with a moving-average filter in order to reduce the effect of instrument noise.

CrIS channel cloud sensitivity height and weighting function peak height



CrIS Spectral Calibration Method

The correlation coefficient between the two spectra can be written:

$$r_{S_1, S_2} = \frac{\sum_{i=1}^n (S_{1,i} - \bar{S}_1)(S_{2,i} - \bar{S}_2)}{(n-1)D_{S_1}D_{S_2}} = \frac{\sum_{i=1}^n (S_{1,i} - \bar{S}_1)(S_{2,i} - \bar{S}_2)}{\sqrt{\sum_{i=1}^n (S_{1,i} - \bar{S}_1)^2 \sum_{i=1}^n (S_{2,i} - \bar{S}_2)^2}}$$

Standard deviation based on the difference of the two spectra:

$$D_{S_1, S_2} = \sqrt{\sum_{i=1}^n [(S_{1,i} - \bar{S}_1) - (S_{2,i} - \bar{S}_2)]^2 / (n-1)}$$

The cross-correlation method is applied to a pair fine grid spectra to get the maximum correlation and minimum standard deviation by shifting one of the spectra in a given shift factor.

Detection of ERDS from CrIS SDRs

Spectral Shift Caused by Earth-rotation Doppler Effect

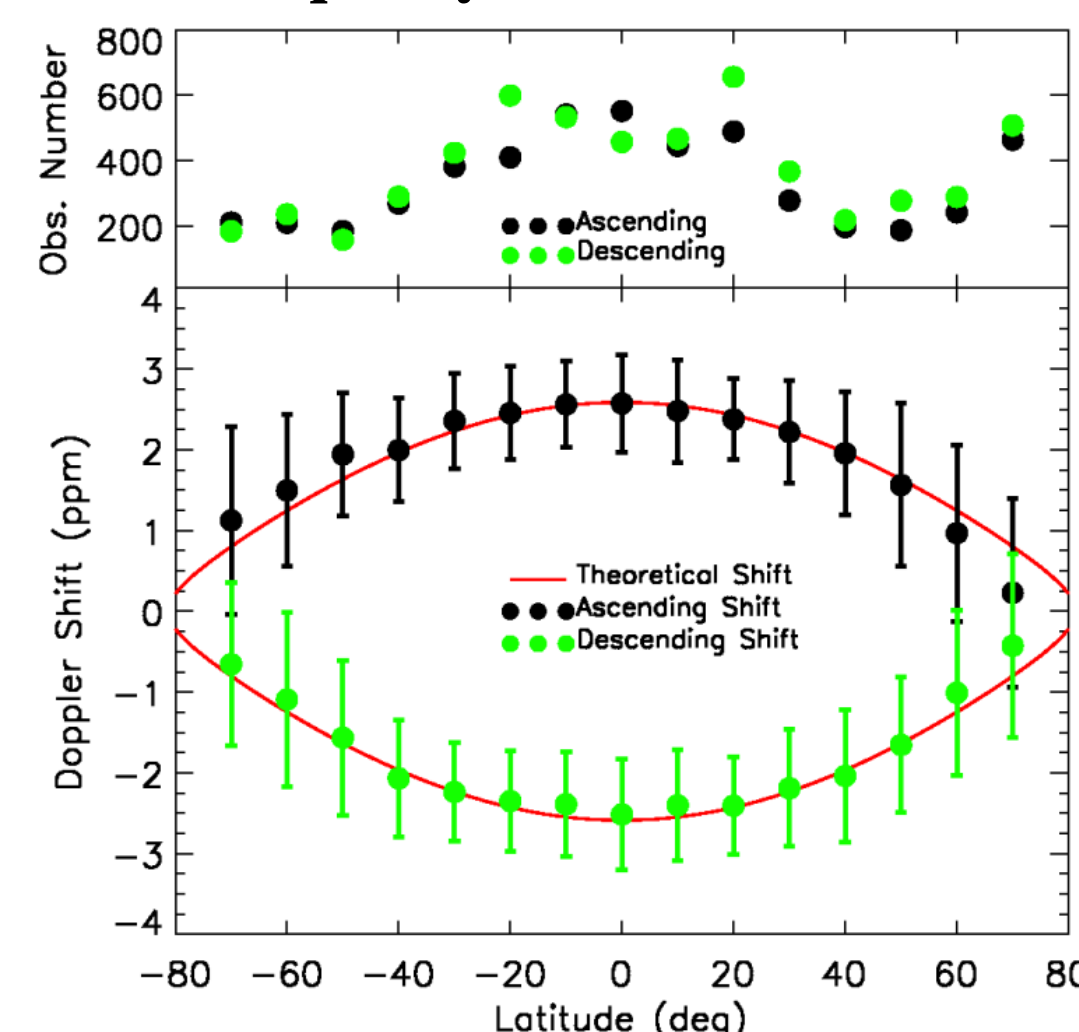
$$\Delta \nu = \pm \frac{v}{c} \Omega R \sin(\theta_{zenith}) \cos(\lambda) |\sin(\phi_{azimuth})|$$

v : channel frequency; Ω : Earth angular velocity

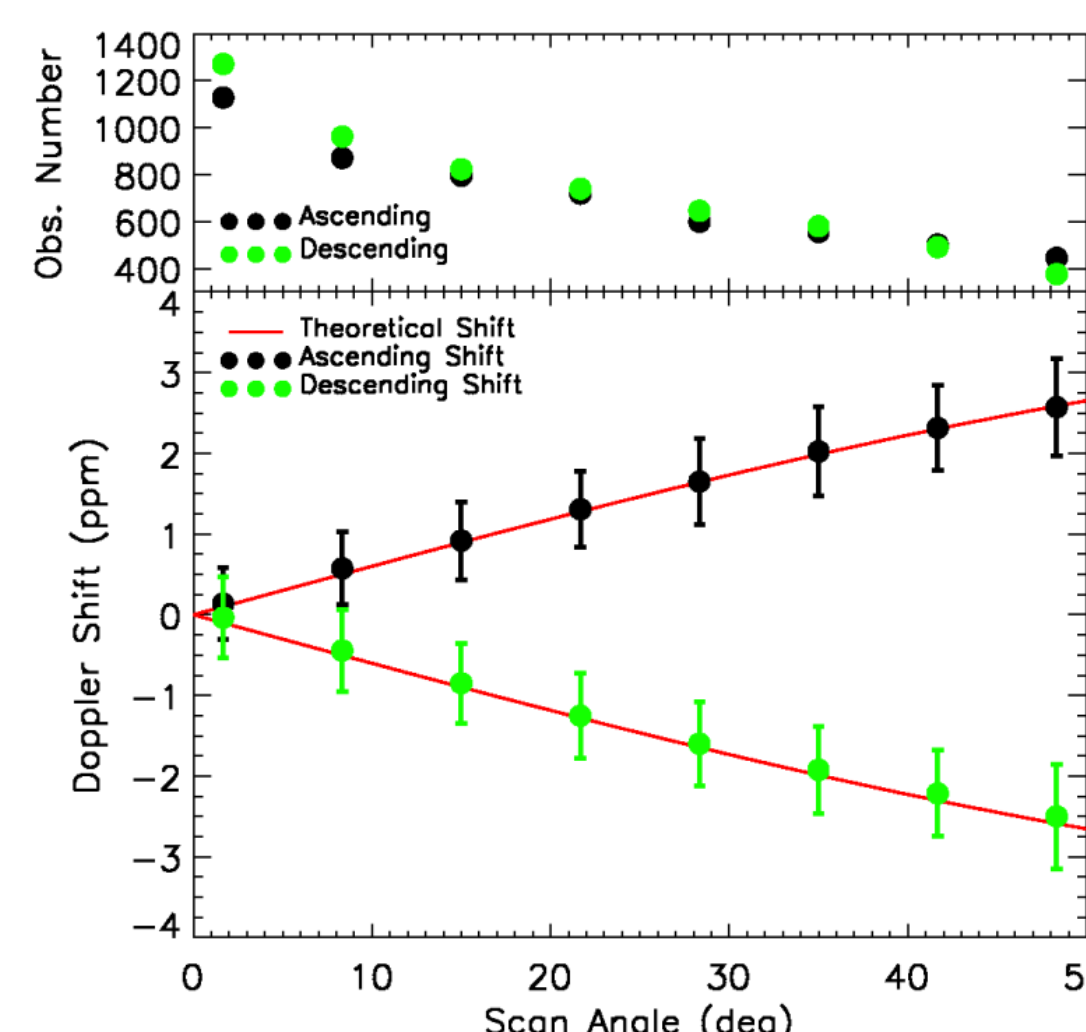
R : Earth's radius; λ : Latitude

$\phi_{azimuth}$: Satellite azimuth angle; θ_{zenith} : Satellite zenith angle.

FOR1 frequency shift relative to FOR30



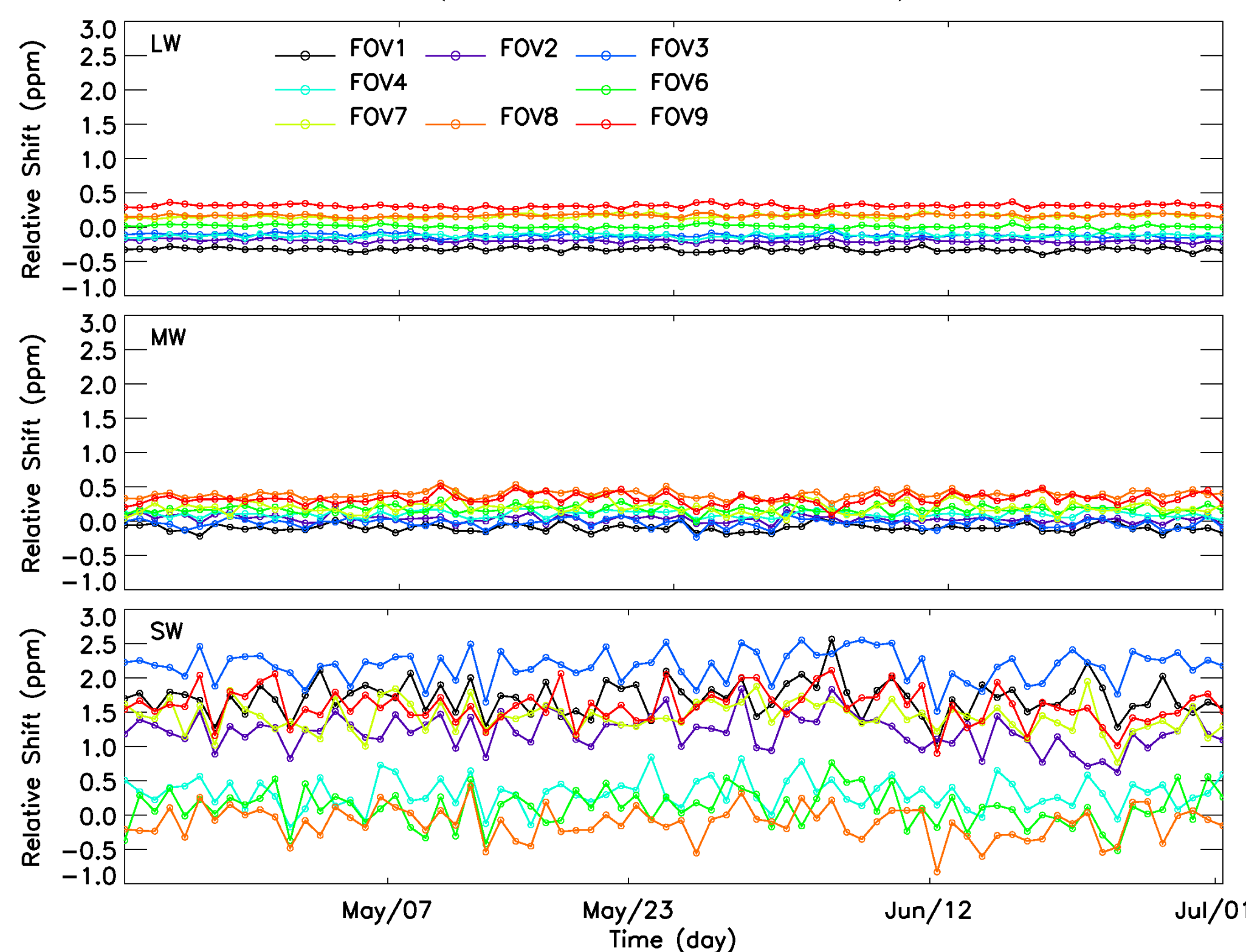
Doppler shift at near Equator



(Chen, et al. 2013)

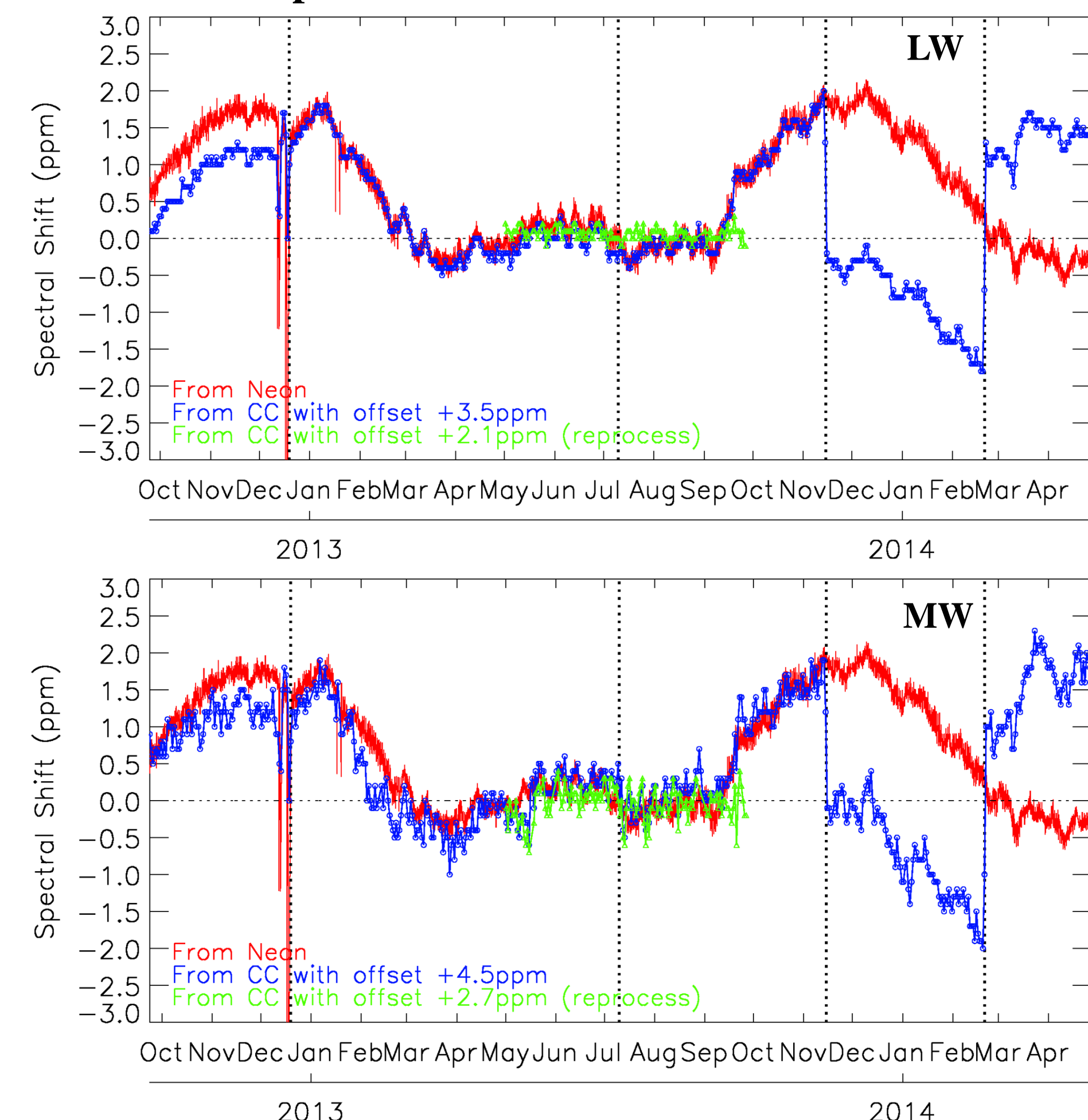
FOV to FOV5 Relative Spectral Shift

Time series of spectral shifts with respect to FOV5 (4/19/2013 to 07/01/2013)

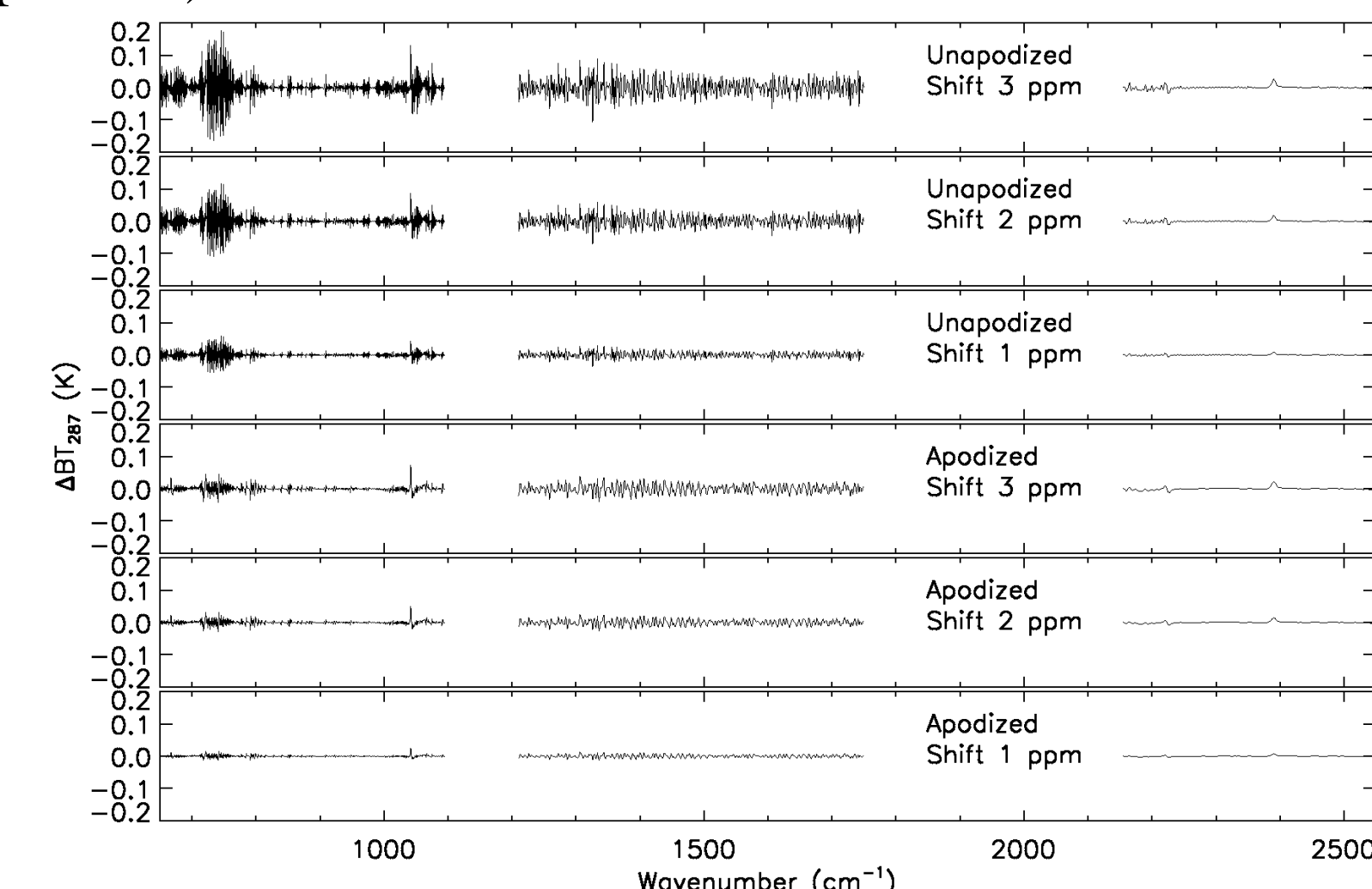


Absolute Spectral Shift

Time series of CrIS spectral shift between observations and simulations



- Time series spectral shift for IDPS SDRs from 09/22/2012 to 04/27/2014, and ADL reprocess SDRs with updated non-linearity coefficients and ILS parameters from 05/01/2013 to 09/26/2013 (with CMO update daily).
- Bands 1 and 2 FOV 5 spectral shift is determined by using cross-correlation (CC) method between CRTM simulations and observations.
- The Neon ZERO shift time is determined by the Correction Matrix Operator (CMO) update on Dec 19, 2012. The vertical lines indicate four CMO update times in IDPS: 12/19/2012, 07/10/2013, 11/14/2013, and 02/20/2014.
- Offsets of +3.5 ppm (2.1 ppm) for band1 and +4.5 ppm (2.7 ppm) for band2 from the CC results are used to match the Neon result in IDPS (ADL reprocess).



Effect of spectral shift on CrIS brightness temperature for a typical warm scene with respect to an effective BT of 287 K for three different spectral shifts (1 ppm, 2 ppm, and 3 ppm) at CrIS three bands for both unapodized and apodized spectra.

Conclusion

This study assesses the CrIS spectral calibration accuracy and stability using relative and absolute correlation methods. Earth-rotation Doppler shift can be detected by using CrIS observations which indicates CrIS spectral is very stable. FOV to FOV relative spectral shift is consistent within 1 ppm for bands 1 and 2. Absolute spectral shift has 3.5 ppm (2.1 ppm) offset wrt CRTM for LWIR, and 4.5 ppm (2.7 ppm) offset for MWIR for IDPS (ADL reprocess). The spectral uncertainty at both bands meet requirement (10 ppm). Long-term CrIS SDR spectral stability is very high during the satellite mission.

OMPS ozone validation by the NOAA ground-based ozone network



By I. Petropavlovskikh^{1,2}, B. Evans², G. McConville^{1,2}, A. McClure^{1,2}, E. Beach³, L. E. Flynn⁴

¹ Cooperative Institute for Research in Environmental Sciences, U. of Colorado, Boulder, CO, 80305

² Global Monitoring Division, NOAA/ESRL, 325 Broadway, Boulder, CO, 80305

³ IMSG, Inc. @ Center for Satellite Applications and Research, NOAA/NESDIS, 5830 University Research Court, College Park, MD 20740

⁴ Center for Satellite Applications and Research, NOAA/NESDIS, 5830 University Research Court, College Park, MD 20740



Abstract. The National Polar-orbiting Partnership satellite (S-NPP) was launched on October 28, 2011. Measurements from the satellite have been used to derive total ozone products (e.g., OMPS-TC-EDR/OOTCO and OMPS-TC-Oz-Fist-Guess-IP/INTCO). Several long-term NOAA Dobson stations were selected for the first round of total column ozone (TCO) validation due to an almost real time processing option that became recently available with the Dobson automation system upgrade at several stations to an automation system designed by the Japanese Meteorological Agency. Three stations are located at MLO, Hawaii (tropics), Lauder, New Zealand (Southern Hemisphere middle latitudes), and in Boulder, CO (Northern Hemisphere middle latitudes), and are part of the WMO/GAW network. Dobson direct sun observations are used to derive the best Dobson ozone product (precision is better than 1%). The TCO observations are typically taken three times a day, excluding overcast conditions and weekends, when Zenith sky measurements are used to derive TCO. The number of direct sun (AD-pair) observations at Boulder, MLO and Lauder observatories in 2012 and 2013 are 1334, 1604 and 475 respectively. These same three stations also make measurements of the Umkehr effect, from which an ozone profile over the station is derived. The overpass satellite product corresponding to the ground-based station value is one determined within 12 hours and within area of +/- 5 degrees in latitude and longitude centered on a station location. During the first stage of the comparisons the OOTCO and INTCO datasets continued to be modified and adjusted through calibration and algorithm changes. It was noticed that the average difference between OMPS and Dobson at MLO prior to middle of June 2013 was at +15DU, while after that, it changed to 4 DU. At the same time difference between OMI (NASA Ozone Monitoring Instrument on EOS Aura) and Dobson at MLO was on average at 13 DU before, and remained close at 11 DU after the change in OMPS output. At MLO the correlation (R^2) between Dobson and INTCO (OMI) is 0.88 (0.9) for the period between January 1 2012 and July 30, 2013, where mean Dobson, OMPS and OMI TCOs are 262, 268 and 273 DU. Similar correlation results are found for Boulder, CO. However, over Lauder station the Dobson TCO daily correlations are 0.98 and 0.97 with OMI and OMPS overpass ozone respectively. The differences could be due to the altitudes of the stations and the surrounding topography: Lauder (370 mmsl) to Boulder (1640 mmsl) and MLO (3400 mmsl). Profile comparisons were also performed for Boulder station and show some biases, most likely due to treatment of the stray light in both satellite and Dobson Umkehr data.

Ground-based validation sites for rapid delivery:
Boulder (40 N, 105W), MLO(19.5 N, 156W) ,
Lauder (45S, 170E)

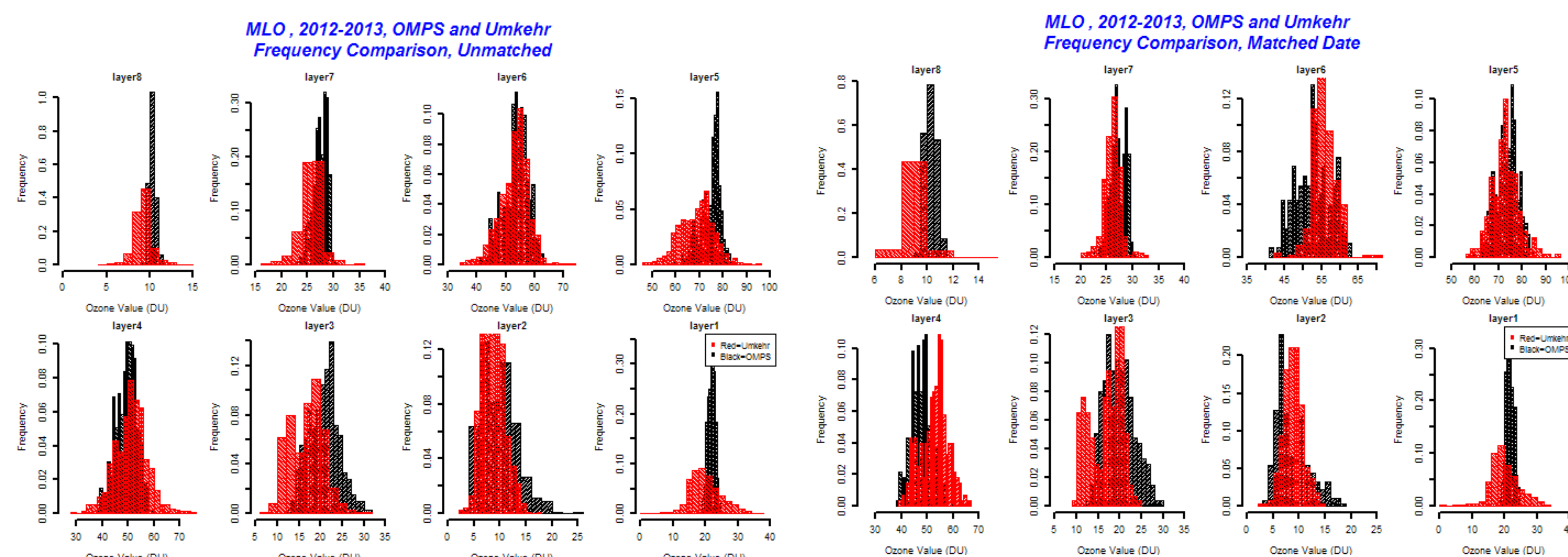
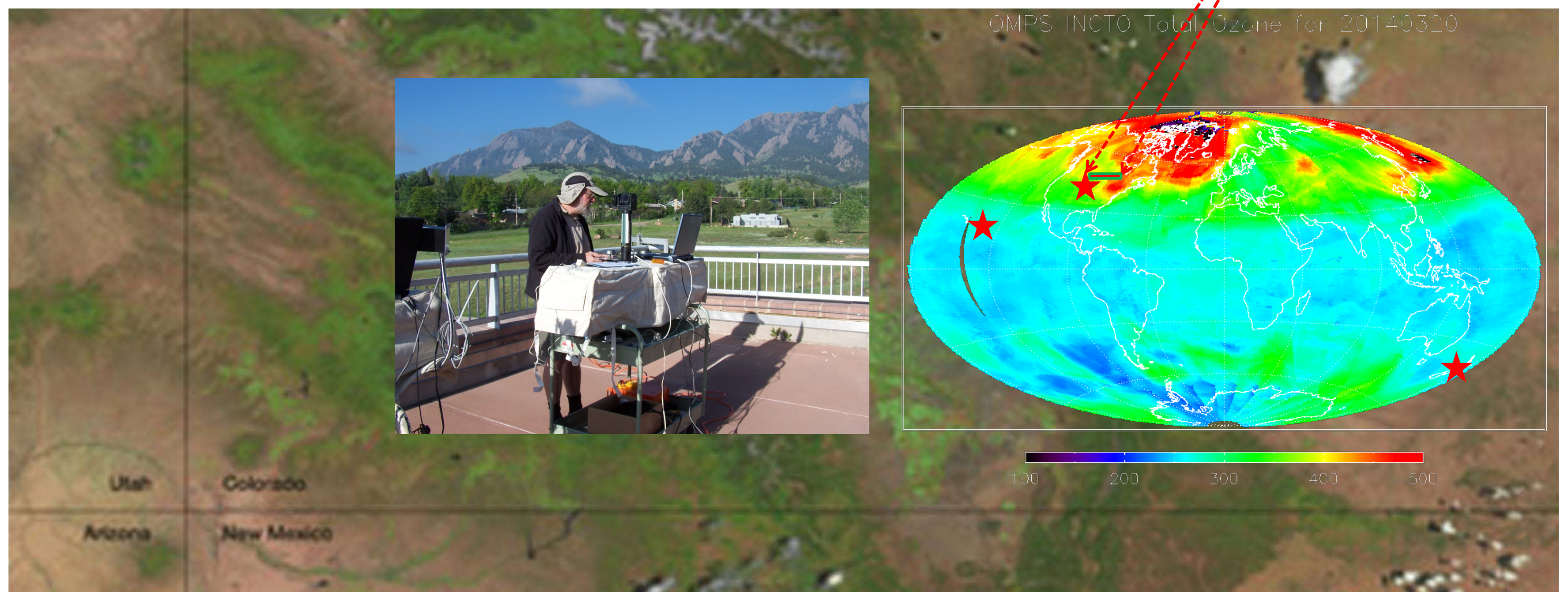


Figure A. Frequency distribution plots to compare Umkehr ozone profiles at MLO and OMPS overpass without date-coincidence matching

Figure B. same as A, but with date coincidence selection applied – clear differences in the tails in layer 6 and layer 3, offset in median value in layer 4.

All Dobson data

Only DS Dobson data

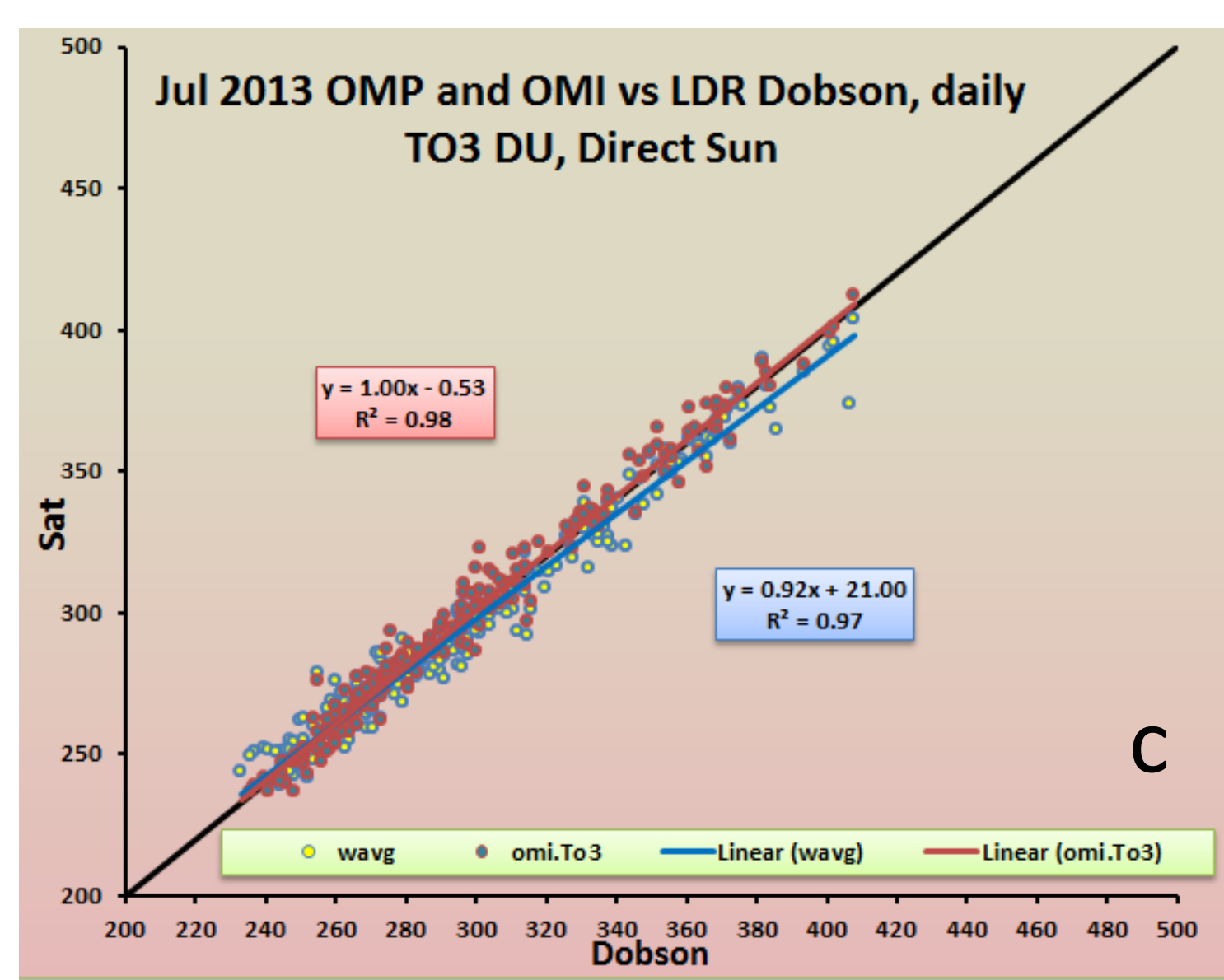
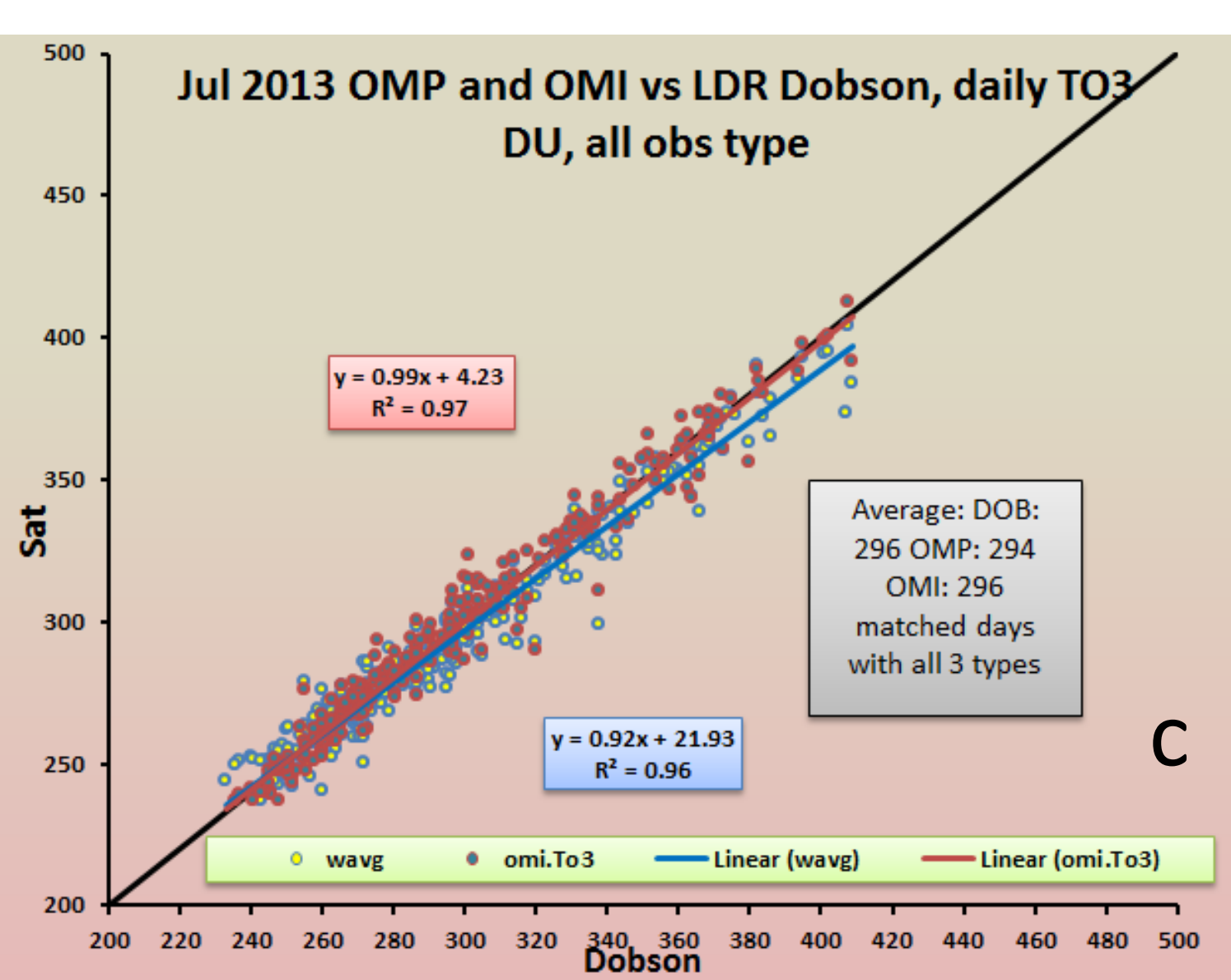
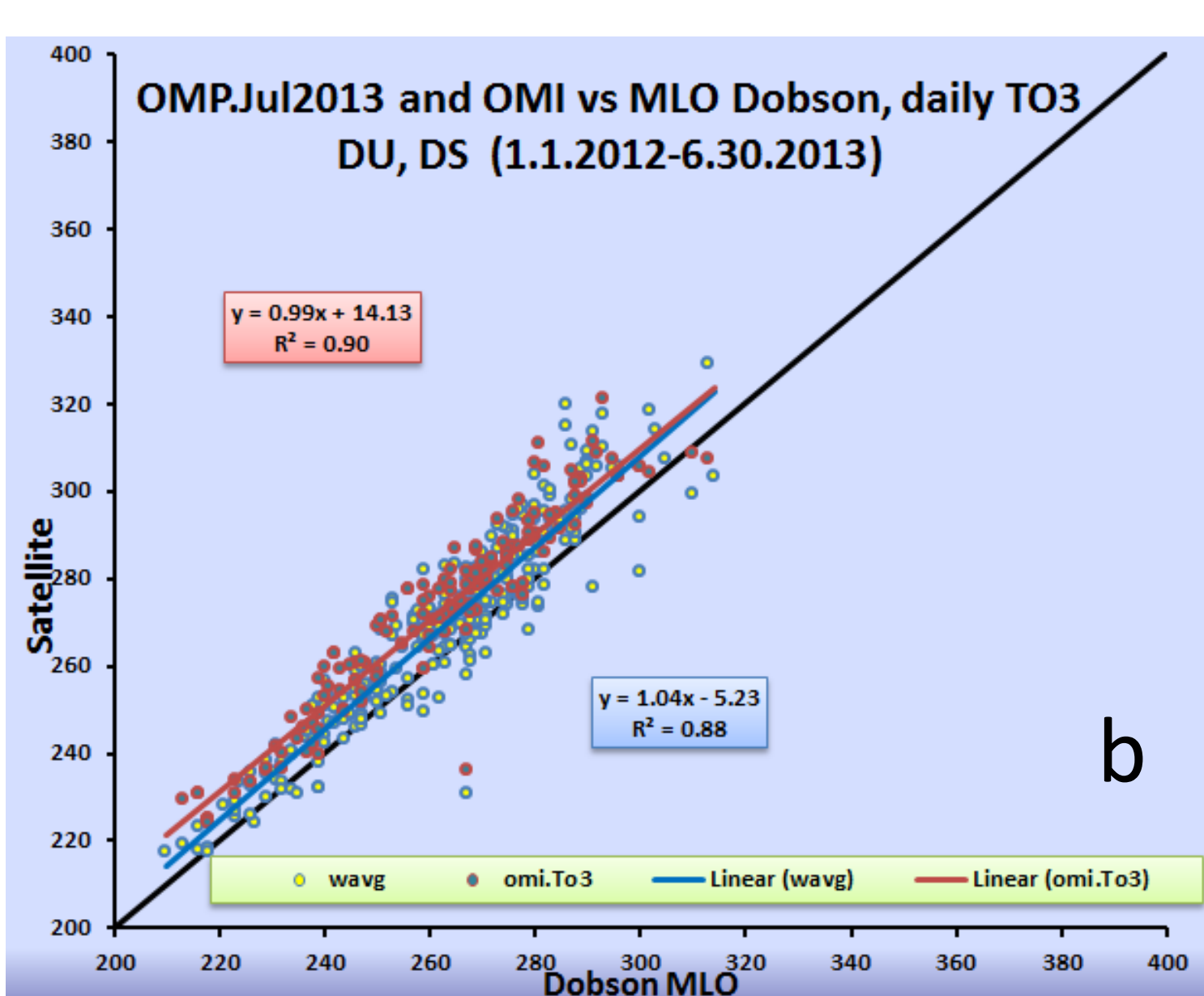
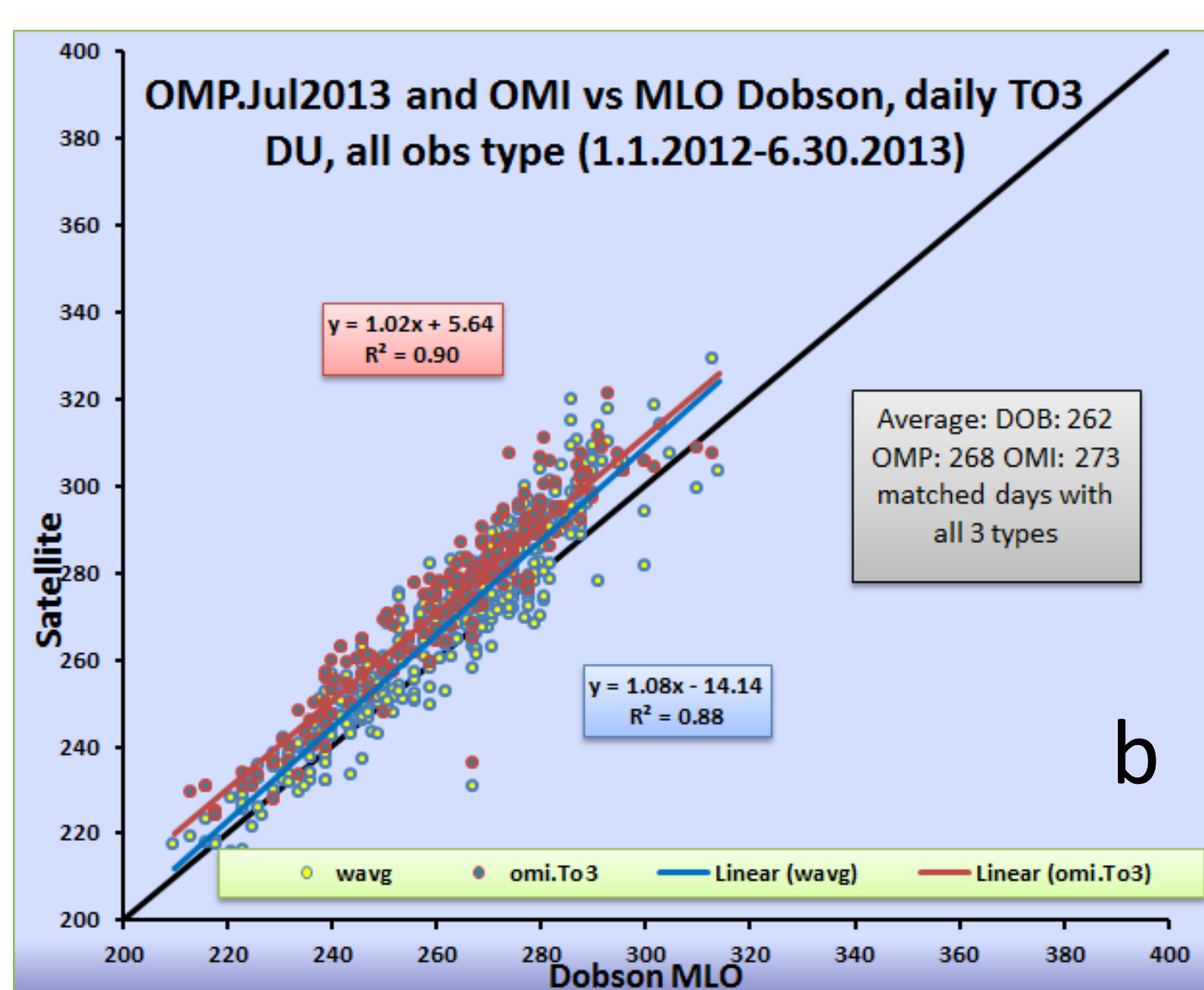
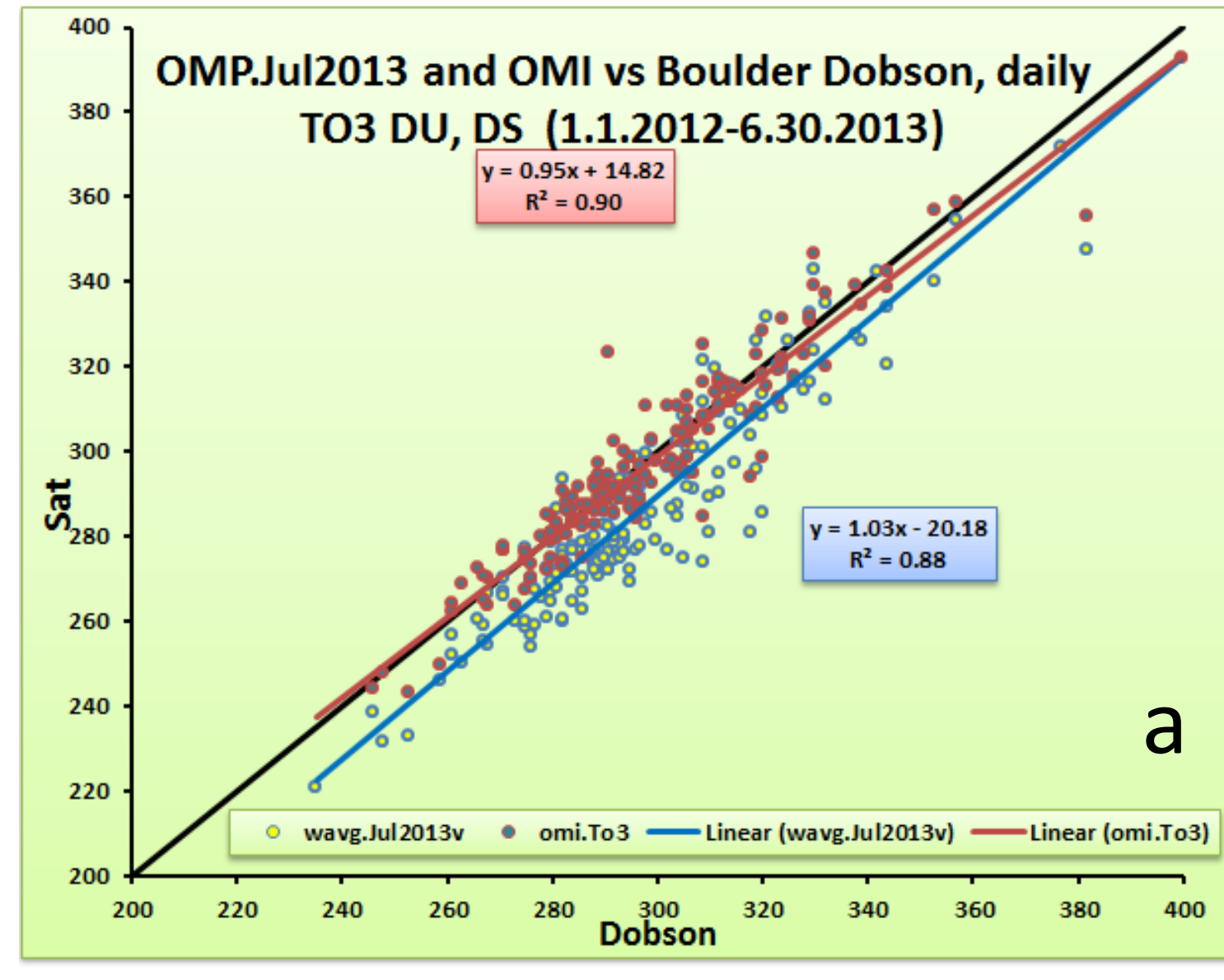
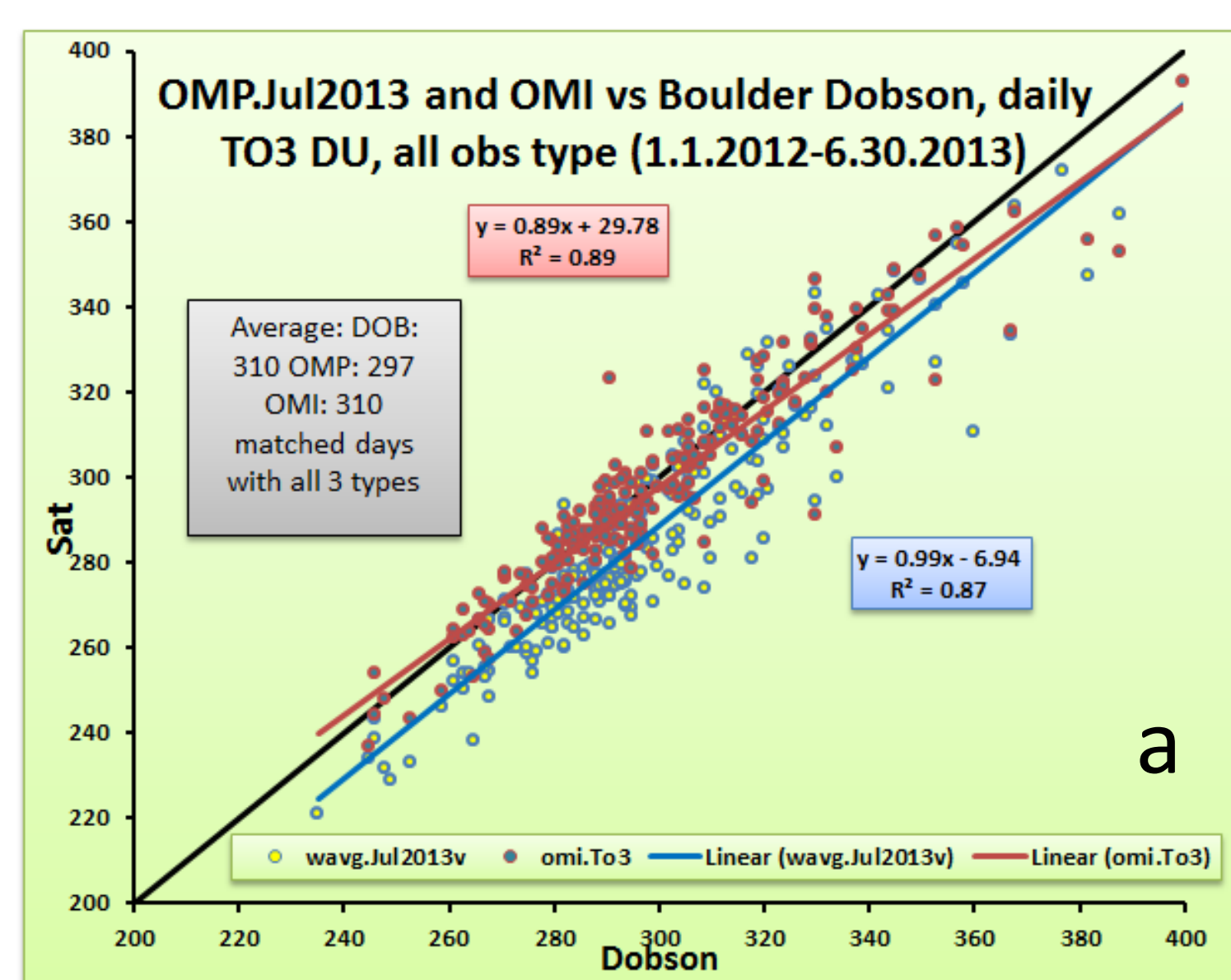


Figure 1 a) Scatter plot between daily Dobson observations and OMPS or OMI overpass over Boulder, CO, b) same as a), but for MLO, HI, c) same as a), but for Lauder, NZ

Figure 2 a) Scatter plot between only direct-sun Dobson observations and OMPS or OMI overpass over Boulder, CO, b) same as a), but for MLO, HI, c) same as a), but for Lauder, NZ

As time series

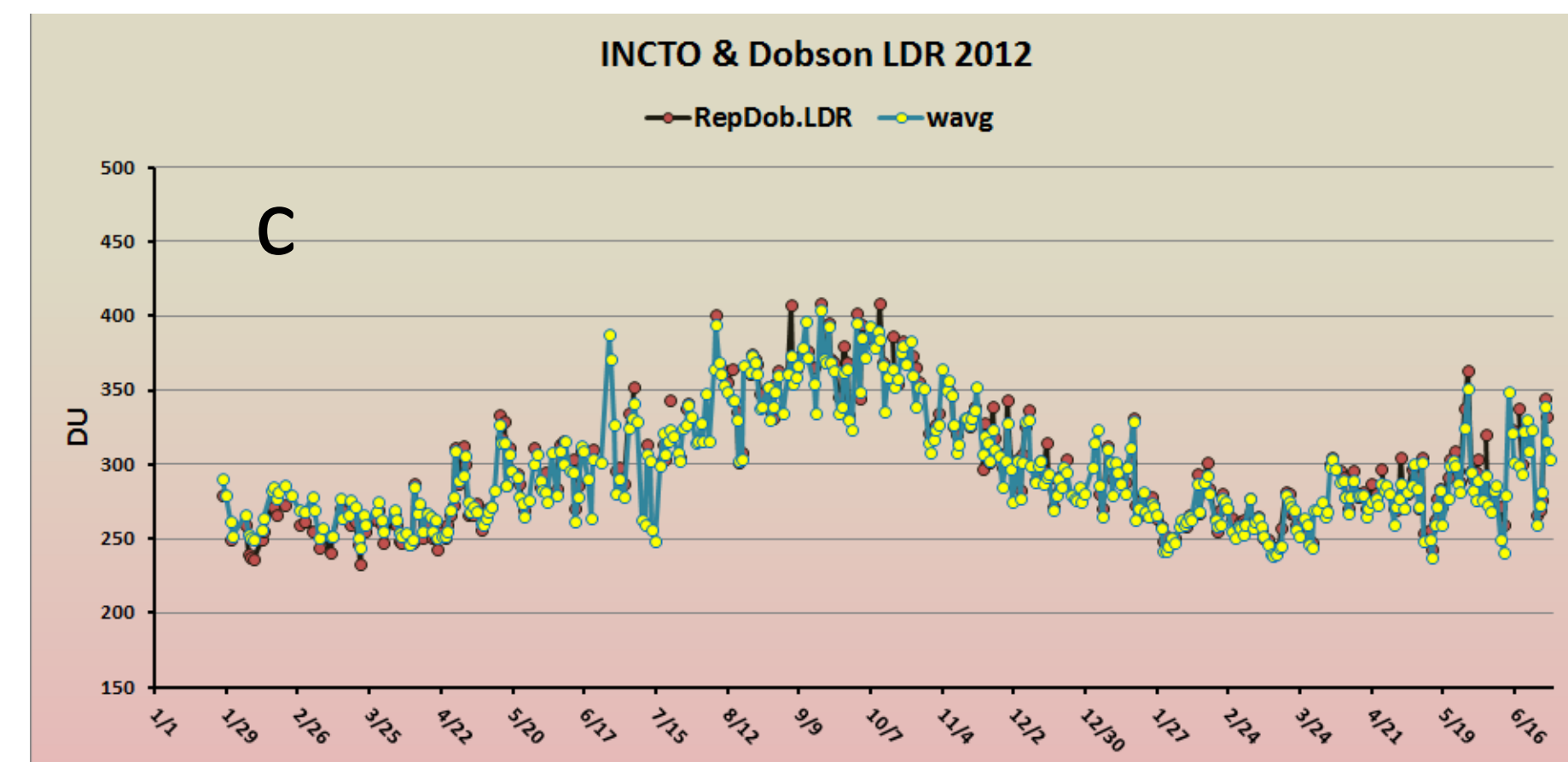
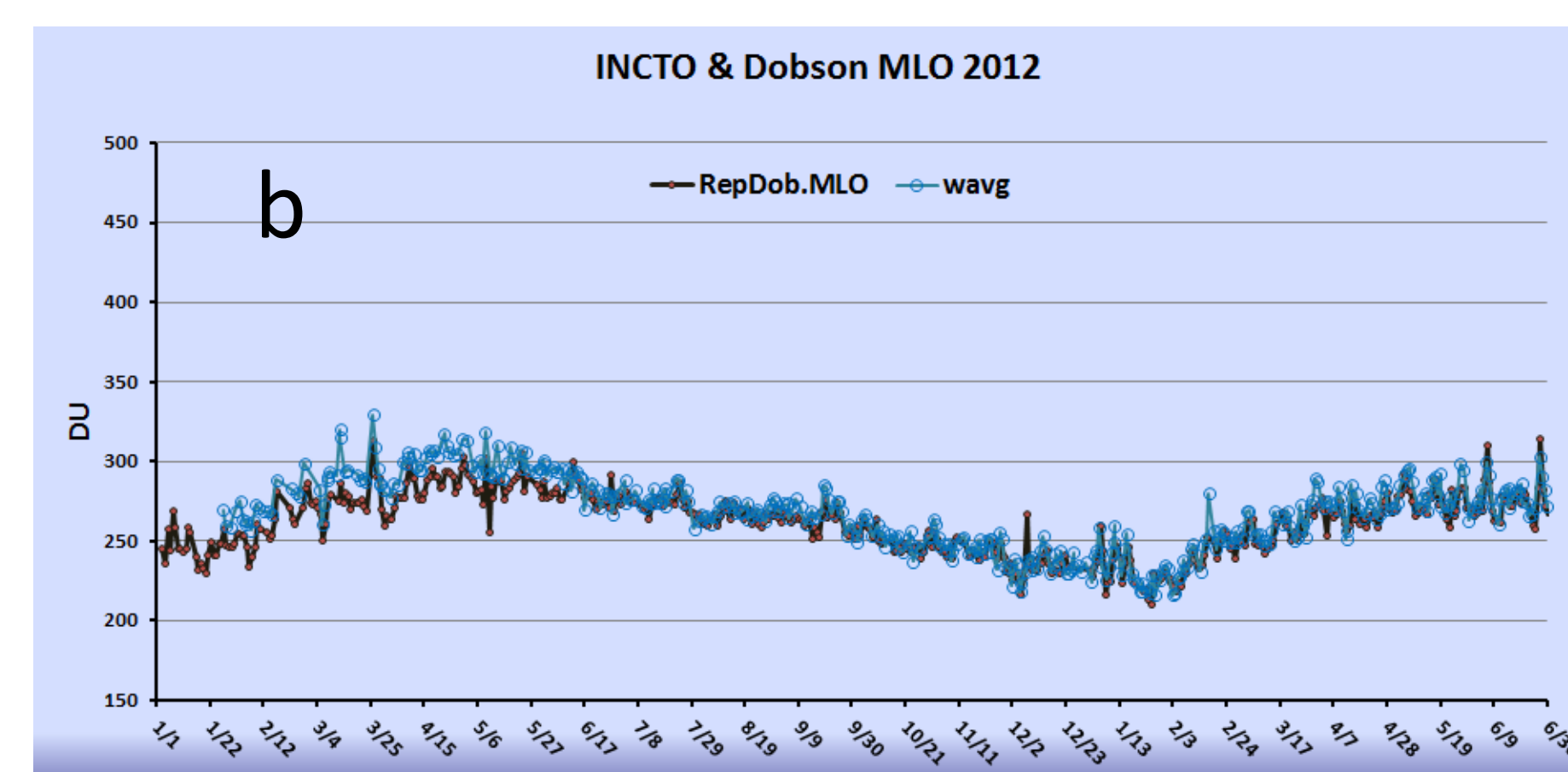
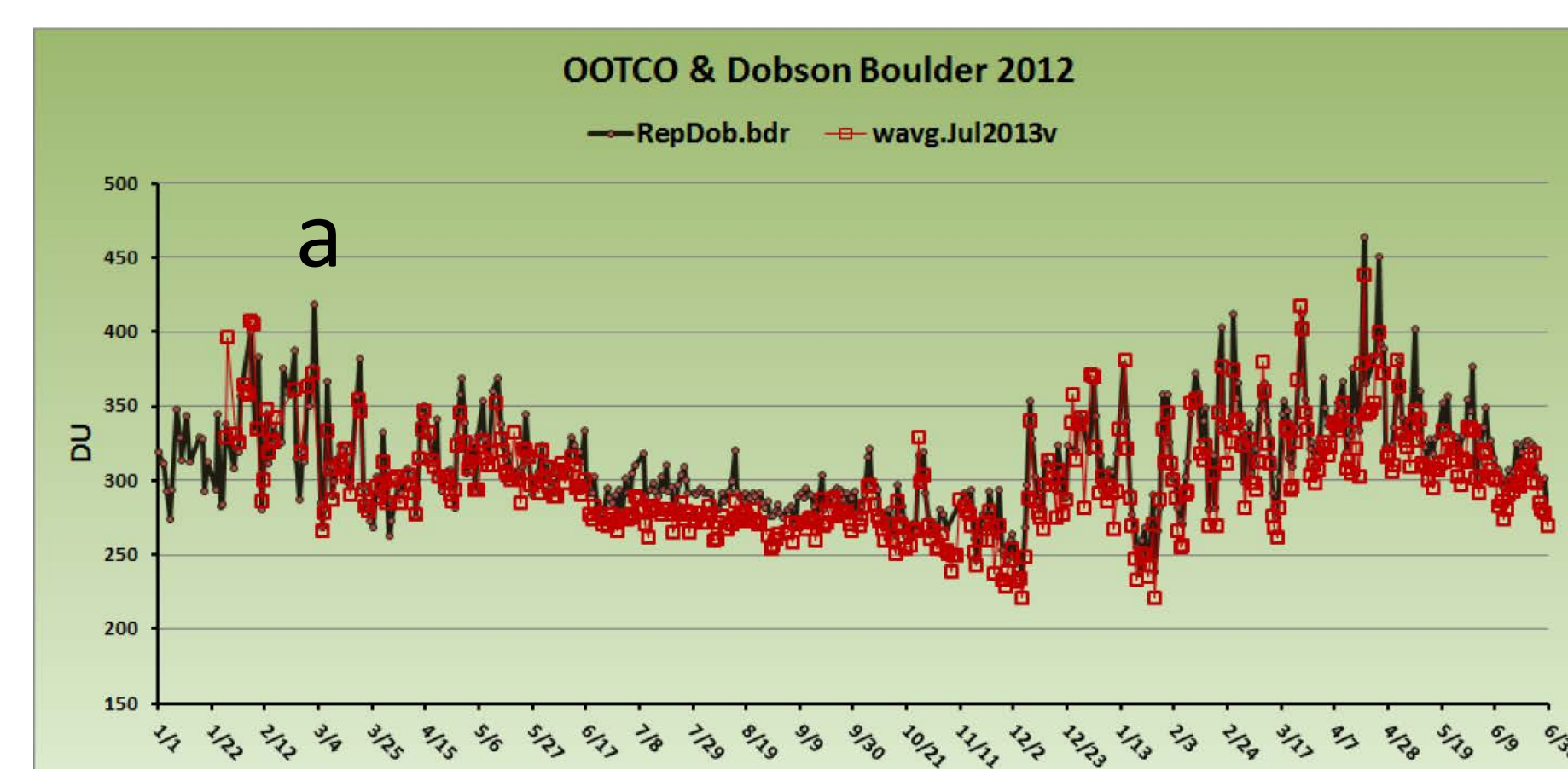


Figure 3 a) Time progression of co-incident measurements by Dobson and OMPS overpass over Boulder, CO, b) same as a), but for MLO, HI, c) same as a), but for Lauder, NZ

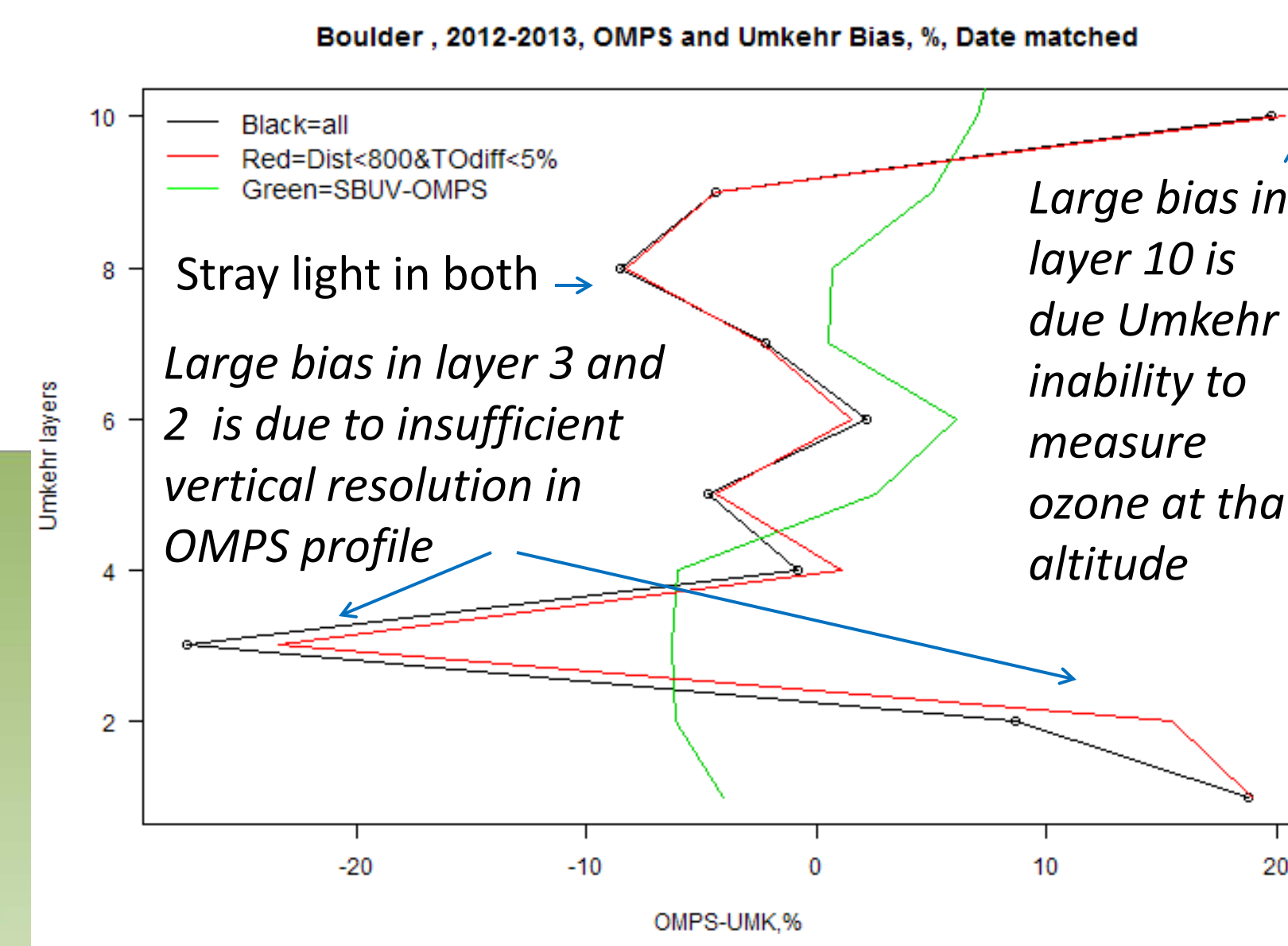


Figure C. Bias between OMPS and Umkehr (black line), difference after restriction was applied (red): on the distance of OMPS pixel from station (<800 km) and difference in Total ozone column (< 5 %), difference between SBUV and OMPS

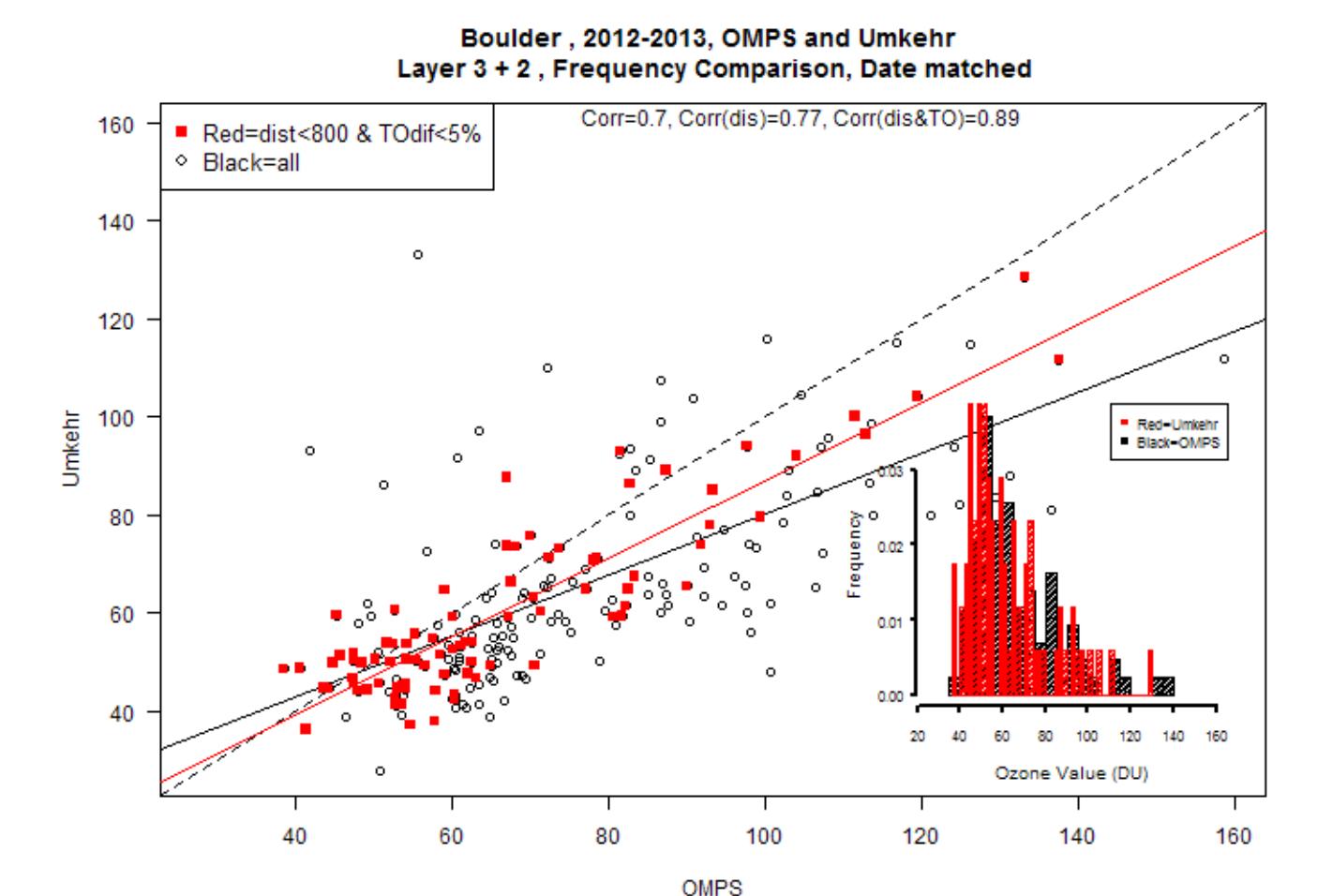


Figure D. Scatter plot between OMPS and Umkehr (black circles) ozone in combined layer 2 and 3 (250-63 hPa), and after restriction was applied (red): distance of OMPS pixel from station (<800 km) and difference in Total ozone column (< 5 %). Correlation for two sets of data is shown in the legend at the top.



NOAA STAR ICVS LTM – Suomi NPP VIIRS WEB PAGE

Vicky Lin², Fuzhong Weng¹, Ninghai Sun², Lori Brown², Jason Choi², Wanchun Chen², Changyong Cao¹

1-- NOAA/NESDIS/STAR ; 2 – NOAA Affiliate



http://www.star.nesdis.noaa.gov/icvs/status_NPP_VIIRS.php

Abstract

The Visible Infrared Imaging Radiometer Suite (VIIRS) is one of the key instruments onboard the Suomi National Polar-Orbiting Partnership (Suomi NPP) spacecraft, which was successfully launched on October 28, 2011.

To support the post-launch calibration and validation of VIIRS, the Integrated Calibration / Validation System Long-Term Monitoring (ICVS-LTM) was developed at NOAA STAR and made available online. This poster introduces the scope of the user friendly STAR ICVS web page, which extends to anomaly detection and future sensor improvements.

The quality of satellite radiances is essential for direct radiance assimilation in numerical weather prediction models, for retrievals of various geophysical parameters, and for climate trend studies. It is also a measurement of the success of the engineering and science efforts of our operational satellite program. Past efforts in post-launch calibration and validation took a piecemeal approach, focusing on onboard calibration, with much less attention paid to the quality of radiance data of earth observations. Many instrument related artifacts were left to the users to discover and evaluate the impacts. The lack of on-orbit calibration standards and methodology for radiance verification also aggravated the problem. In order to meet the challenge of the increasing demand for better satellite data quality, an integrated system that incorporates pre-launch, post-launch, onboard sensor calibration and long-term monitoring, as well as forward calculation of radiances are needed.

The STAR ICVS – VIIRS LTM has become an important tool for monitoring VIIRS data quality and instrument performance. It provides critical support for producing the products of sea surface temperature, ocean color, cloud imagery, vegetation, aerosols, and others, which will improve product quality to meet the growing need for high quality satellite data.

Introduction

Parameters	Descriptions	Dimensions	Measurement
Global True Color Image	Global image from VIIRS M3, M4, and M5 bands	1 map	Cloud distribution, Solar eclipse detection
Global Single Band Image	VIIRS broad spectral coverage for observing the Earth	M1-16, I1-5, Day and Night DNB 23 maps	Atmosphere, land, ocean characteristics
Global SDR Quality Map	Global overall VIIRS SDR quality map	M1-16, I1-5, DNB 22 maps	Daily global data quality
Lunar Intrusion Map	Moon in the Space View	1 band represents all M & I bands	Data contaminated by the Moon
Instrument Temperature	BB, RTA, cavity, HAM, FPA, cooler, Mainframe, Circuit Card Assembly	19 temperature	Electromagnetic radiation
Instrument Status	In flight instrument health status	20 parameters	Voltage, current and motor errors
F factors and H factors	Degradation of Solar bands based on SD signal and SDSM	9 bands	Degradation of reflective solar bands
Solar Diffuser Counts	VIIRS observation delta N of solar diffuser for band I1-I3, M1-M11, DNB over band average	21 bands	Degradation trends
Solar Diffuser NEΔN	Noise NEΔN for solar diffuser signal of solar bands	17 bands	Signal to noise ratio bands
Detector Solar Diffuser Counts	VIIRS observed DN of Solar diffuser from bands I1-I3, M1-M13 over detector average	16 bands	degradation of detector uniformity
SDSM signal	SDSM signal of solar diffuser and the Sun in every orbit	7 bands	SDSM trends
Space View Counts	VIIRS observation Space view DN for I1-I5, M1-M16 bands	21 bands	Background signal
Space View Count NEΔN	Dark Noise NEΔN for space view signal for I1 to I5, M1 to M16 bands	21 bands	Dark noise signal
Blackbody Counts	VIIRS observation blackbody DN for I1 to I5, M1 to M16 bands	21 bands	IR gain derivation
Blackbody Counts NEΔN	Noise NEΔN for black body signal for I1 to I5, M1 to M16 bands	21 bands	IR NEDT derivation

Goals and Objectives

Goals - Build a site that can easily be edited to house an evolving set of metrics for each satellite instrument. Our goal was to build a site that was maintainable, extensible, and simple for instrument monitoring teams to populate and manage.

Objectives –

- 1) Search engine optimization - Better chart metadata and consistent labeling for satellite and instrument names has made the ICVS system very 'discoverable' via web search tools.
- 2) Compliant with Section 508 - STAR ICVS web page is compliant with Section 508 accessibility standards and other requirements associated with a properly compliant government website
- 3) Animation capability - use "Slide Show of All Charts for Selected Date" button
- 4) Browsers and devices support - IE8 and newer; Firefox; Safari; Opera; iPhone and Android mobile devices
- 5) Access to metrics across S-NPP's entire operational history through the calendar
- 6) Intelligent error handling by listing missing files and providing contact e-mail for communication

Detailed Activity Schedule Load Detection

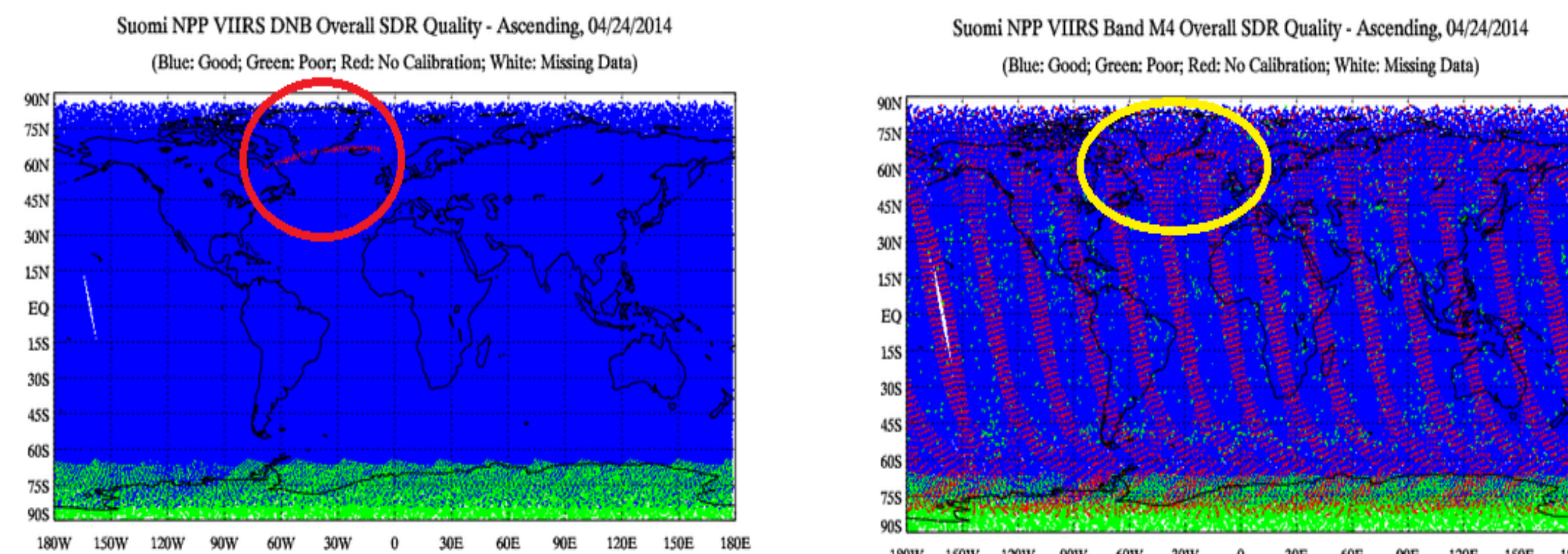


Figure 1. Suomi NPP VIIRS detailed activity schedule (DAS) were uploaded during contact for orbit number 12900 at 15:00 UTC on 24th April. This activity was observed on the VIIRS overall SDR quality map for all bands. A red streak which means no calibration data passed south of Greenland over the North Atlantic Ocean. This is the result of missing thermistor data which is required for calibration processing.

Cross Reference VIIRS SDR Teamwork

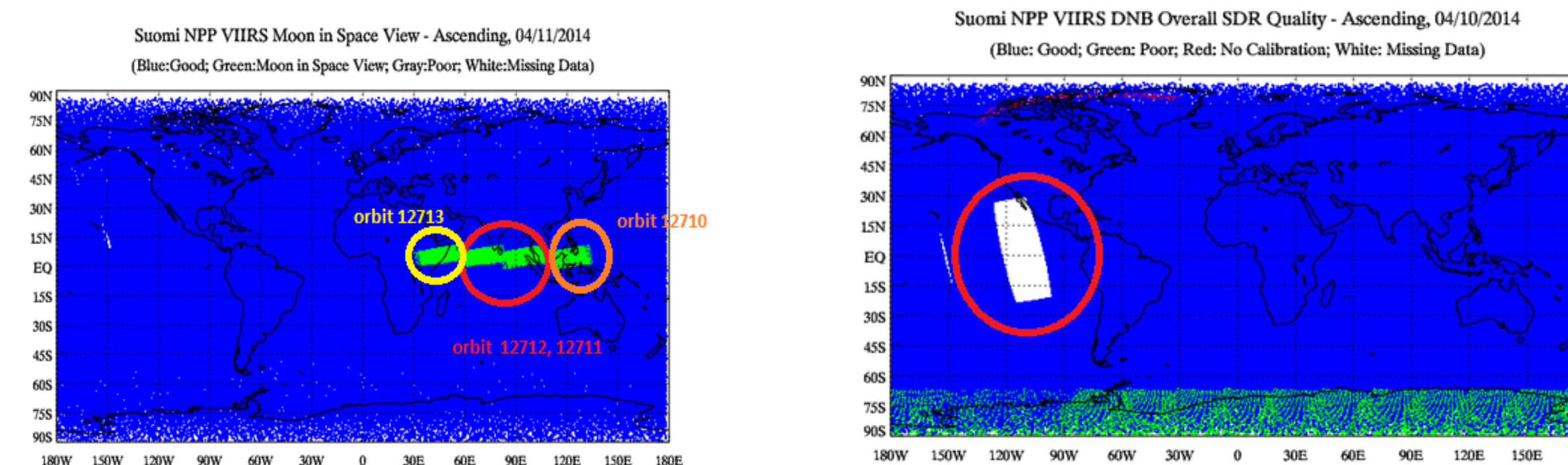


Figure 2. False Suomi NPP VIIRS Lunar Intrusion observed on 11th April - The VIIRS lunar intrusion was expected for two orbits: orbit 12711 from 07:02:52 to 07:03:07 and orbit 12712 from 08:44:37 to 08:44:52 on April 11, 2014. We received good geo-location data for the day. Quality flag two for orbit 12711 (t0701585_e0703227_b12711), which is the right middle rectangle of the four green rectangles, and 12712 (t0844241_e0845483_b12712), which is the left middle rectangle of the four green rectangles, in the above time frame showed the Moon has corrupted the space view. Besides the two predicted lunar intrusion orbits, the adjacent orbits are also contaminated with lunar intrusion. The unpredicted lunar intrusion was observed on the VIIRS Lunar Intrusion map for orbit numbers 12710 (t0048094_e0049336_b12650) and 12713 (t0410080_e0411322_b12652). North Grumman team is aware of the extra lunar intrusion issue and they are working on a solution to fix it.

Figure 3. Suomi NPP VIIRS Lunar Calibration Maneuver on 10th April - Suomi NPP VIIRS performed a maneuver for lunar calibration on orbit 12704 with VIIRS sector rotation (encoder offset) to allow the Moon image to be captured in the middle of Earth view sector (target time 20:53:17 UTC). This includes thirteen minutes of sector rotation, from 20:47:46 to 21:00:47 UTC, which impacted VIIRS SDR and EDR data quality and twelve minutes of geo-location pointing off nadir, i.e. maneuver, from 20:48:16 to 21:00:16 UTC. We received good geo-location data for the day, but the geo-location data received from 20:47:46 to 21:00:50 are not useful (filled values) -- which is the white area on the map where lunar calibration was performed

Monitoring VIIRS Instrument Degradation

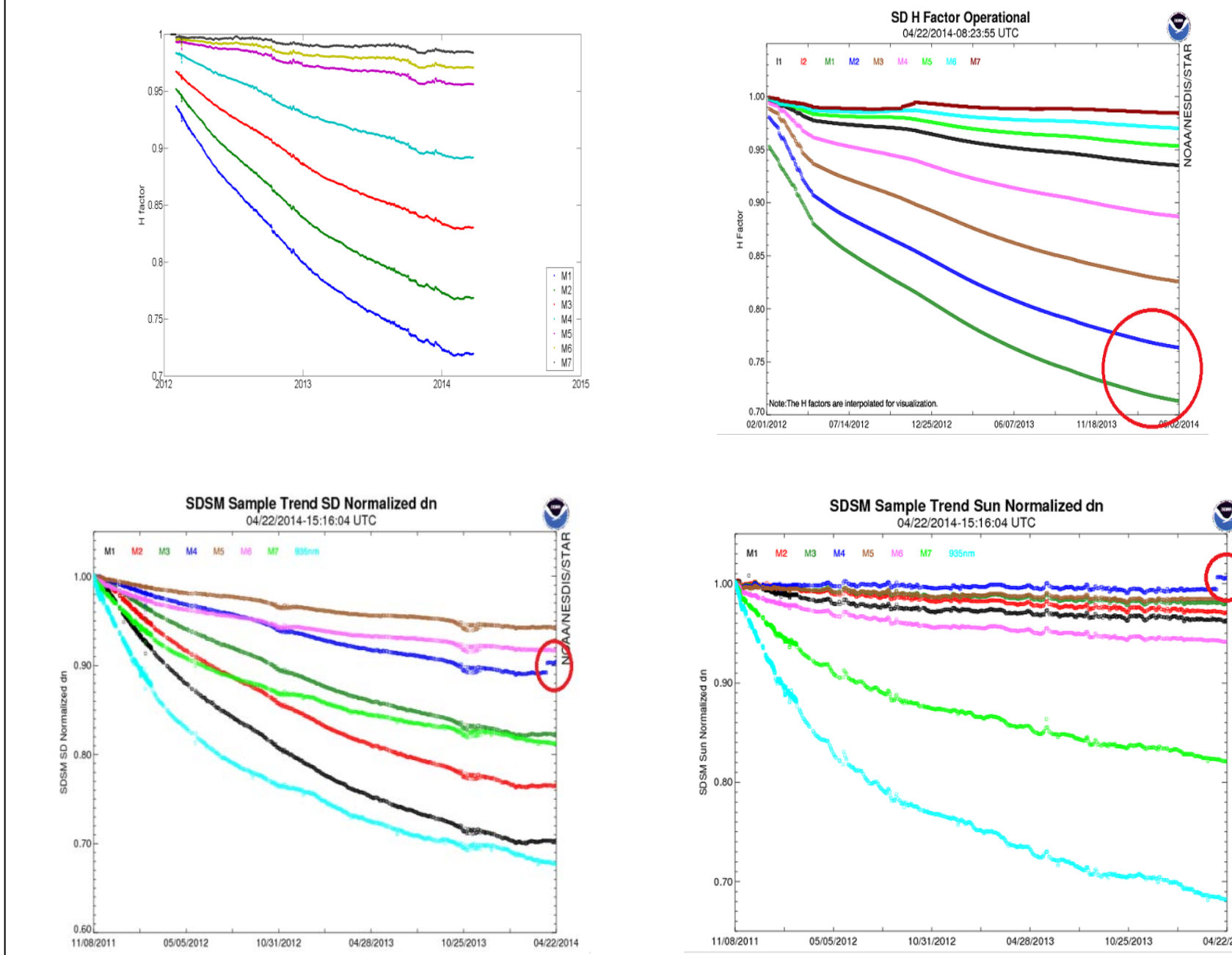


Figure 4. Suomi NPP VIIRS H-Factor trending showed discrepancies from the Aerospace H-Factor trends. The H-Factor from Aerospace (left figure) showed flattened curves in February and March of 2014, especially in the M1 and M2 bands, while the H-Factor from ICVS (right figure) showed decreasing curvature in 2014.

Figure 5. Suomi NPP VIIRS SDSM SD and SDSM Sun Normalized DN showed discontinuity for the M4 band. The discontinuity started on 4th April.

Astronomical Activity Detection

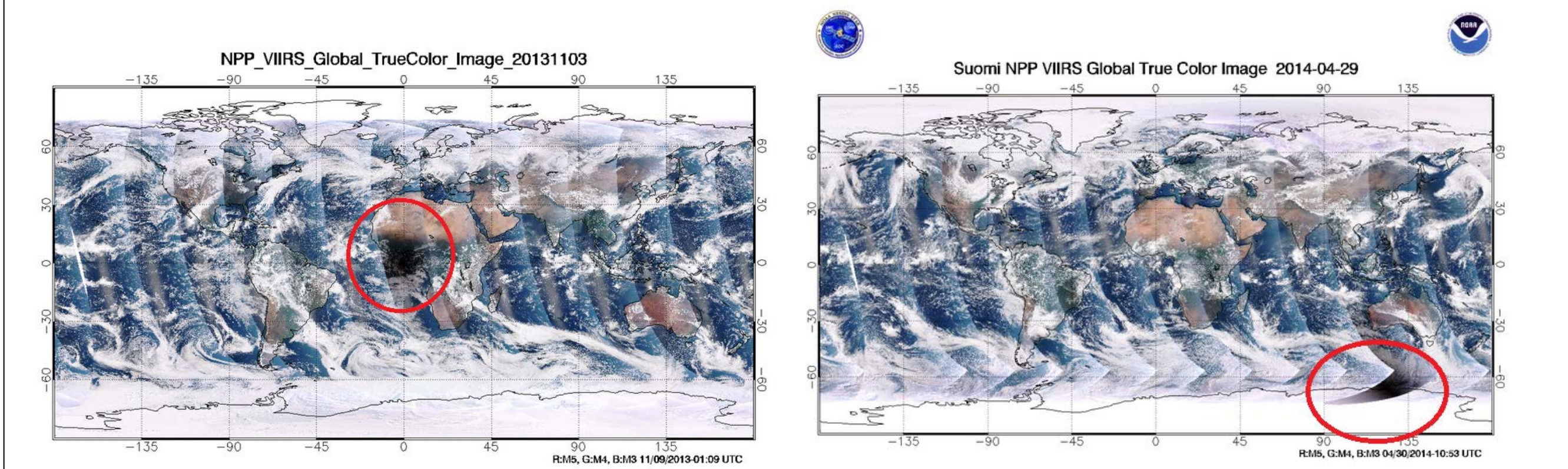


Figure 6. Suomi NPP VIIRS Global Image Captures the Solar Eclipse on the 3rd November 2013 and the 29th April 2014

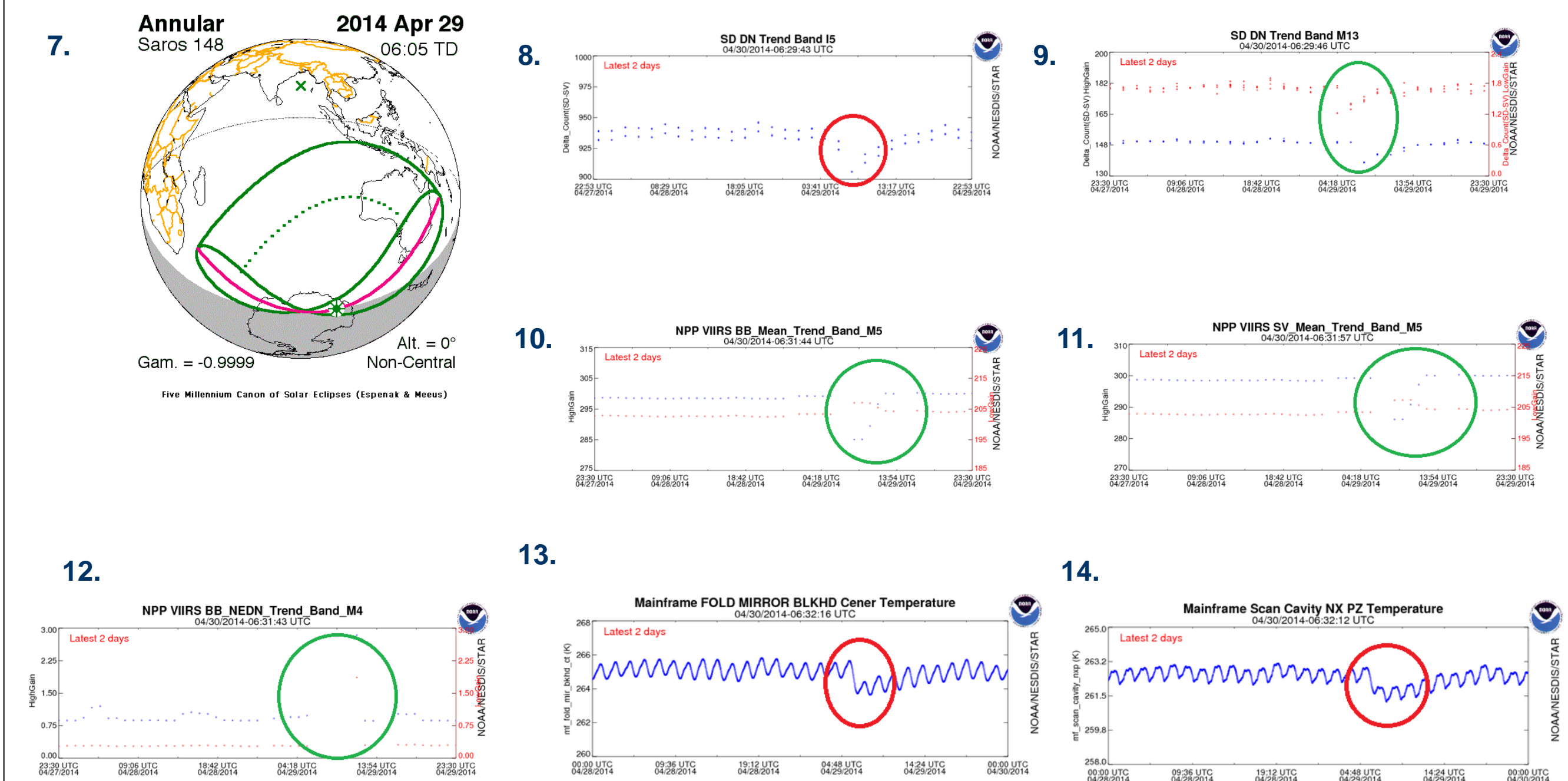


Figure 7. Solar eclipse event on 29 April 2014 - The northern edge of the shadow first touches down in Antarctica at 05:57:35 UTC. The instant of greatest eclipse occurs six minutes later at 06:03:25 UTC the event last seventeen minutes. Figures 8 and 9. VIIRS solar diffuser count for M12 to 16, I4 and I5 bands showed decreased SD count at 5:00 - 7:00 UTC; Figures 10 and 11. VIIRS high and low gain of M4 and M5 bands switch position for blackbody count and space view count after the solar eclipse; Figure 12. VIIRS blackbody count NE delta N for M4, M5 showed data missing during and after the solar eclipse; Figures 13 and 14. VIIRS mirror, telescope, and mainframe scan cavity temperature declined during the solar eclipse.

Future Development

We are looking for anomalies daily through the NOAA STAR ICVS VIIRS web page. The convenience of the NOAA STAR ICVS VIIRS SDR database allows all the scientists to flip through the calendar and find the parameters of interest for their research projects. We received very positive user feedback. The need of VIIRS RDR data monitoring is in high demand in order to find the root causes of instrument malfunction. NOAA STAR ICVS VIIRS team is developing a tool to monitor VIIRS RDR data.

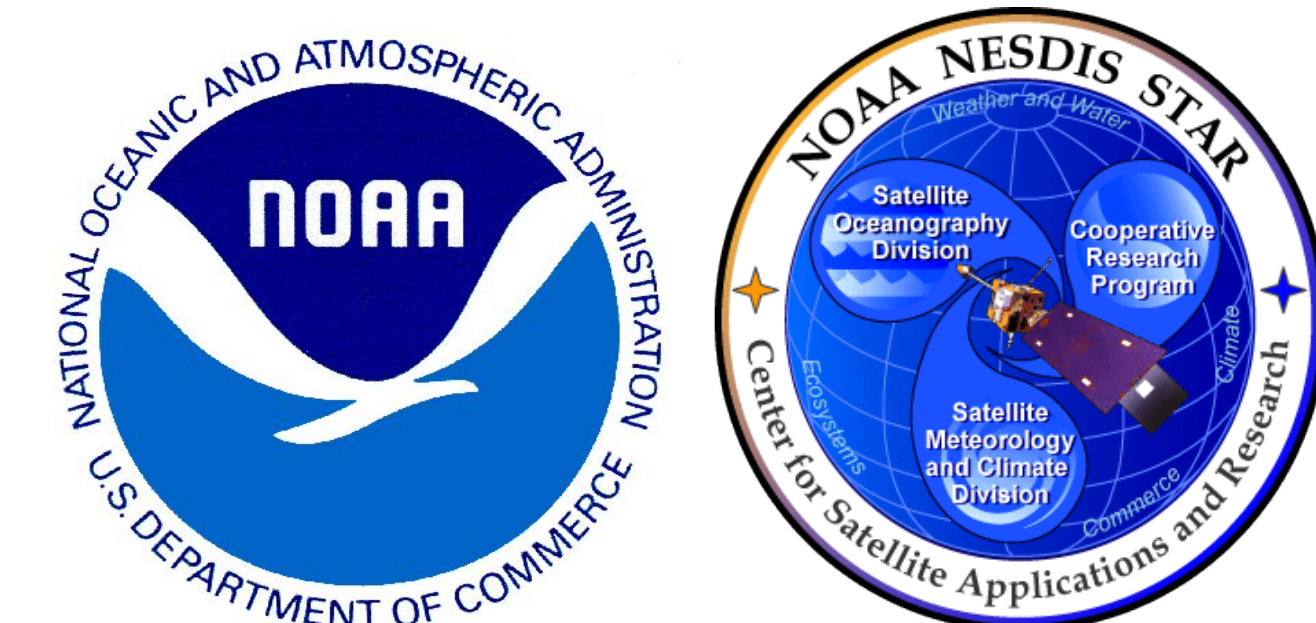


Evaluation of the Performance of VIIRS Top of Canopy Vegetation Indices over AERONET Network

Nikolay Shabanov¹, Marco Vargas²

¹IMSG, ²NOAA/NESDIS/STAR
 nikolay.shabanov@noaa.gov

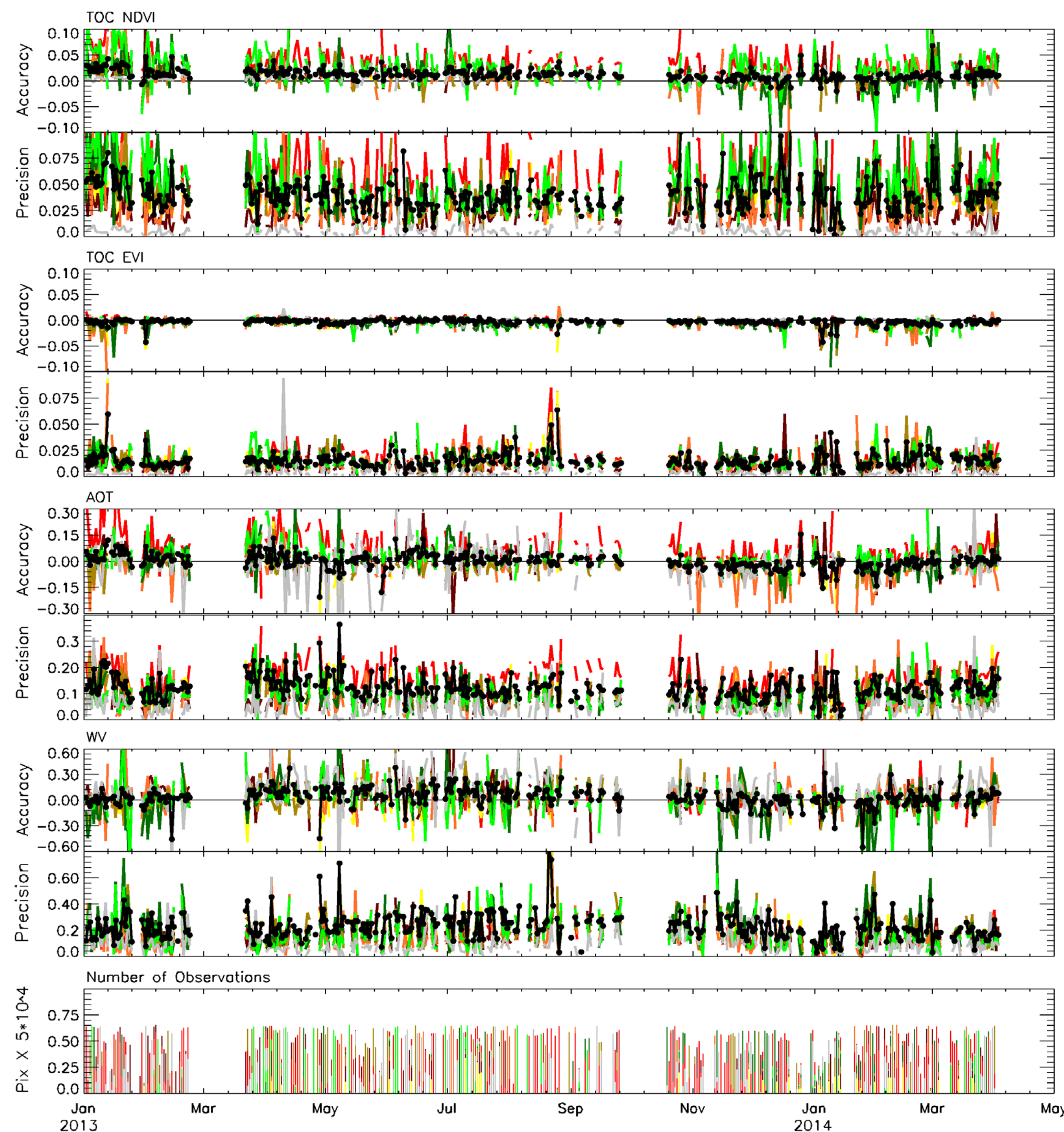
STAR JPSS Annual Science Team Meeting | May 12-16, 2014 | NCWCP, College Park, MD



1. Introduction

In this study we utilized VIIRS Surface Reflectance match-up data set to evaluate Top Of Canopy (TOC) Normalized Difference Vegetation Index (NDVI) and Enhanced Vegetation Index (EVI) at the local scale of Aerosol Robotic NETwork (AERONET) sites. Match-up data are pairs of VIIRS Surface reflectance (SR) and SR derived by atmospheric correction of VIIRS Top Of Atmosphere (TOA) Reflectances using AERONET ground measurements of key input parameters of 6S atmospheric correction algorithm (aerosol, water vapor and others). Match-up data are generated under condition that VIIRS and AERONET measurements fall within +/- 45 min window. Match-up data utilized in this study are 101 x 101 pix subsets at VIIRS Imagery resolution (375m) over period Jan 1, 2013 through March 31, 2014. The overall objective of this study is to characterize the performance of VIIRS TOC VIs at the local scale of AERONET sites as function of performance of atmospheric correction under constrains specified by Cloud Mask, Aerosol Product and Snow Mask.

2. Global Analysis

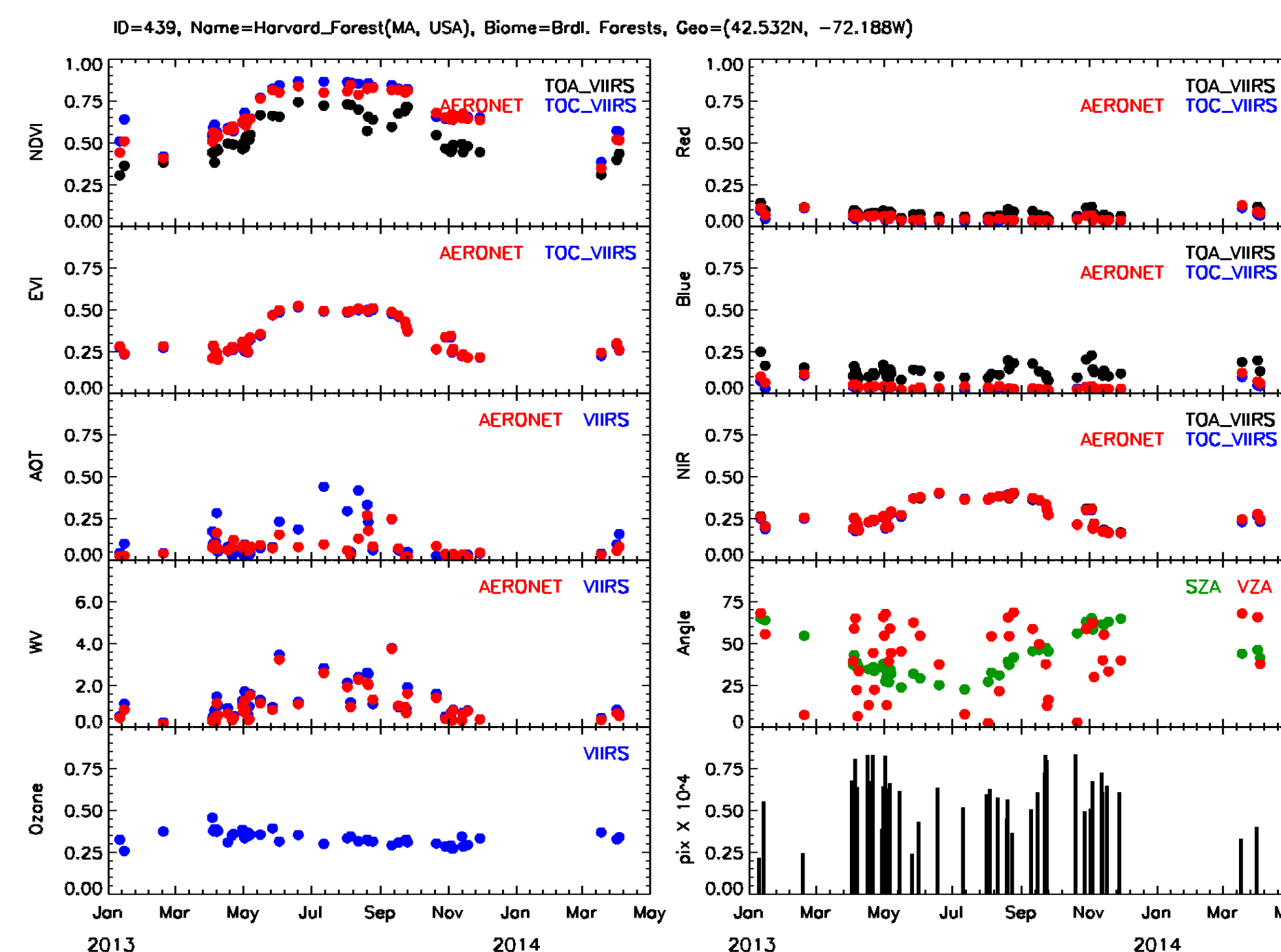


Time Series Accuracy and Precision for TOC NDVI and TOC EVI are shown: while VIIRS TOC EVI matches well to AERONET based reference (low values for accuracy and precision over whole length of time series), TOC NDVI exhibits systematic positive bias and precision value is 3-4 times higher. Analyzing inputs to atmospheric correction algorithm we found that Water Vapor uncertainties are immaterial, but uncertainties in AOT result in overcorrection of visible channels. By design TOC EVI provides resistance to residual atmospheric contamination, however, TOC NDVI does not.

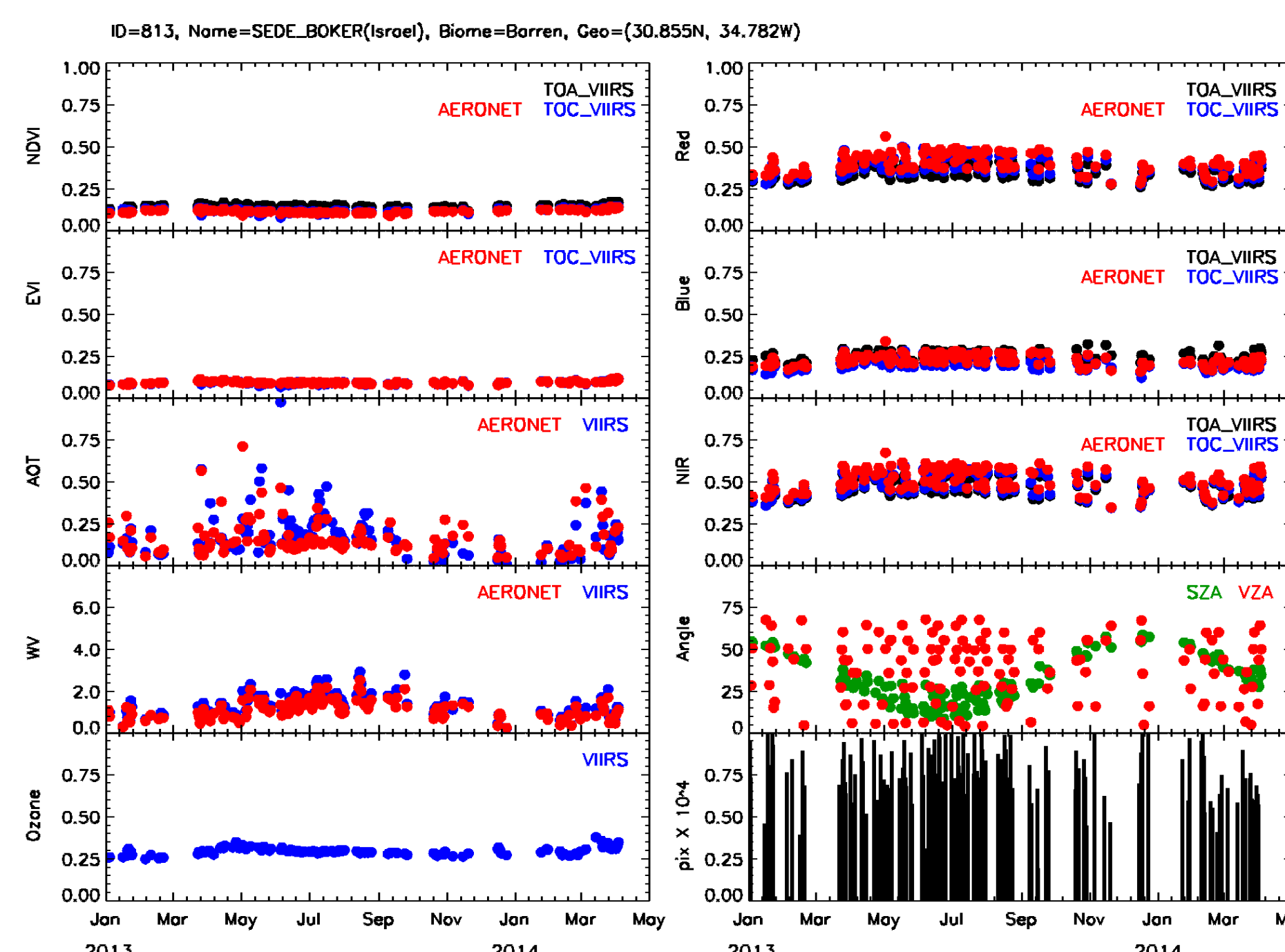
Disclaimer

The views, opinions, and findings contained in this poster are those of the author(s) and should not be construed as an official National Oceanic and Atmospheric Administration or U.S. Government position, policy, or decision.

3. Individual Sites Analysis

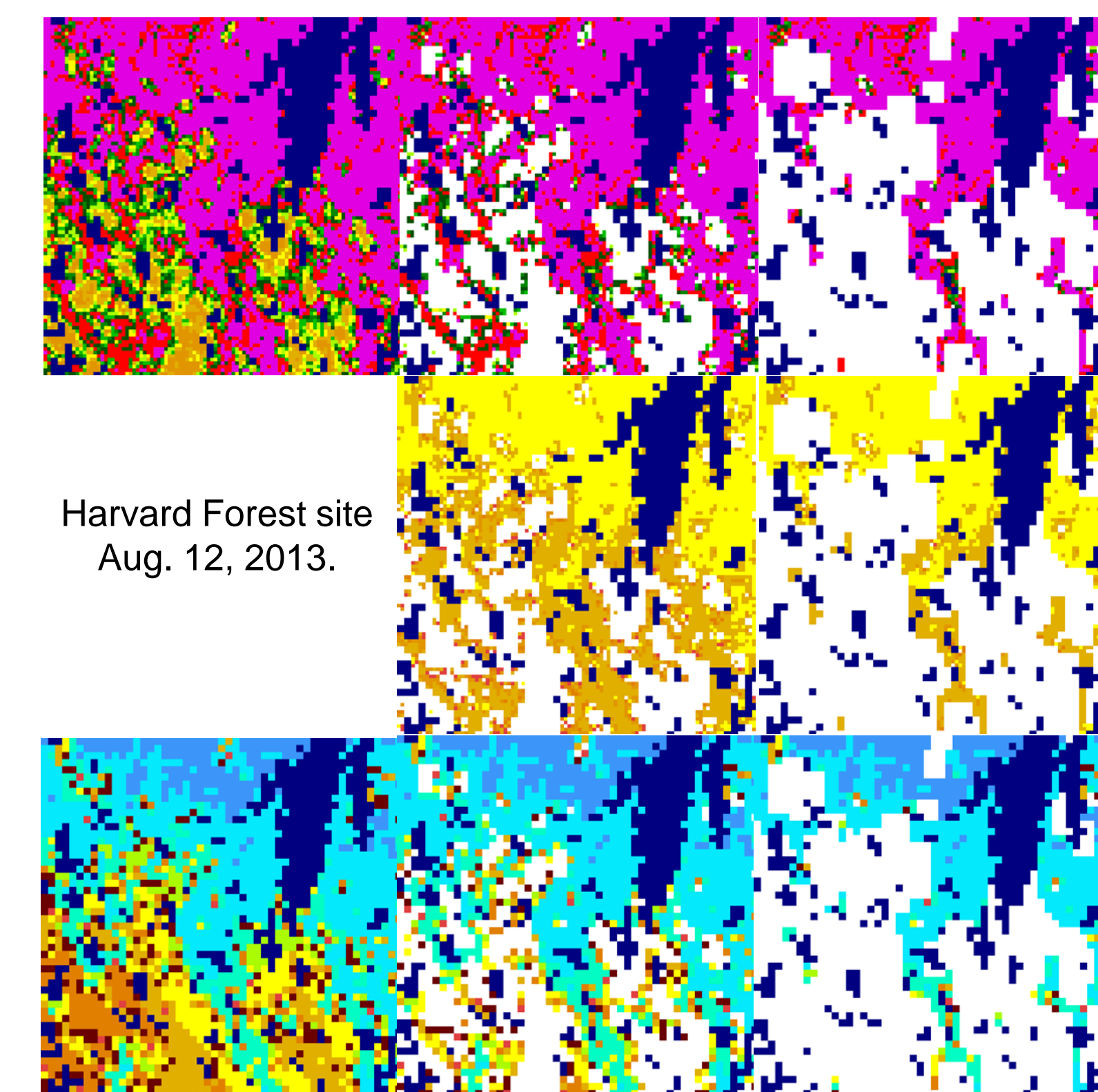


Time Series of VI, SR and key parameters of atmospheric correction algorithm (AOT, Water Vapor) are shown for Harvard Forest site (broadleaf forest) in Massachusetts (42.5328° N, 72.1885° W). Time series of TOC NDVI and TOC EVI exhibit strong seasonality. Effect of atmospheric correction is to increase (already high) TOA NDVI. Time series of AOT from AERONET measurements generally have low values (<0.1), but have significant impact on NDVI over dark target (dense forest). In summer VIIRS tends to overestimate AERONET AOT, however this is artifact of AOT retrievals in vicinity of clouds (c.f. next section). In contrast to TOC NDVI performance, TOC EVI is virtually insensitive to AOT overestimation, therefore VIIRS and AERONET-based TOC EVI match well.



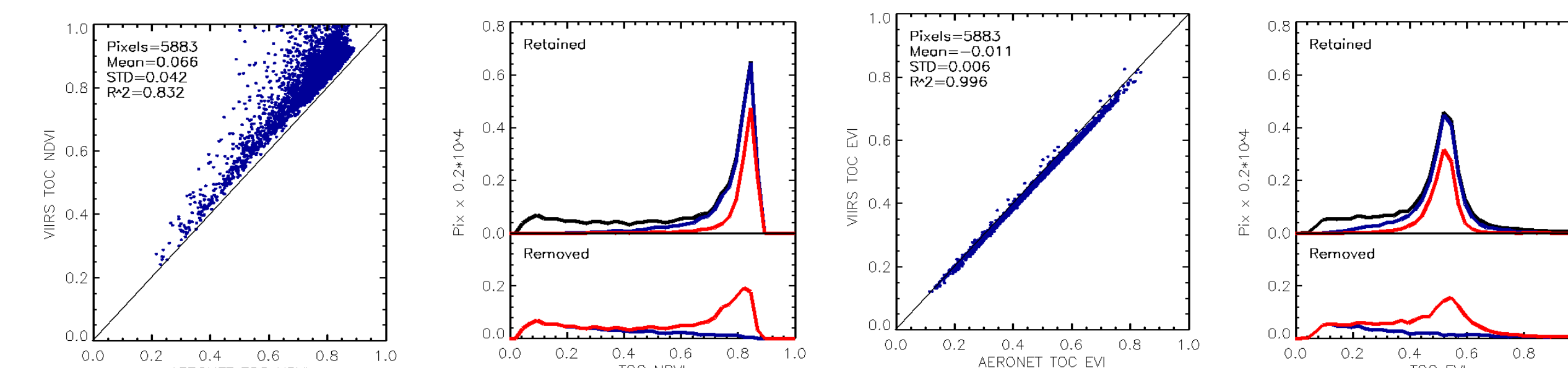
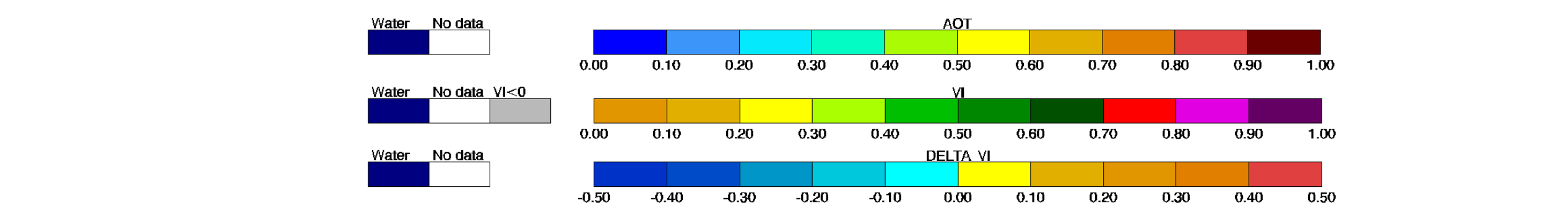
Time Series of VI, SR and key parameters of atmospheric correction algorithm (AOT, Water Vapor) are shown for Sede Boker site (barren) in Israel (30.855° N, 34.782° W). As common to the barren site, Red reflectance is comparable to NIR reflectance. BRDF effect has strong influence on channel data, as VZA form 0-75 form day-to-day. Time series of TOC NDVI and TOC EVI are flat and show very low value. However both TOC NDVI and TOC EVI are insensitive to BRDF effect- time series are flat. Time series of AOT indicates strong variability: usually AOT is ~0.1, however for selected days can rise to 0.25-0.5. This could be due suspended sand in the air. While for majority of days VIIRS and AERONET AOT measurements agree, significant over- under- estimation (up to 0.3 or higher) occurs for selected days. Nevertheless, this inconsistency incurs minor effect both on TOC NDVI and TOC EVI.

4. Sensitivity to Clouds, AOT and Snow



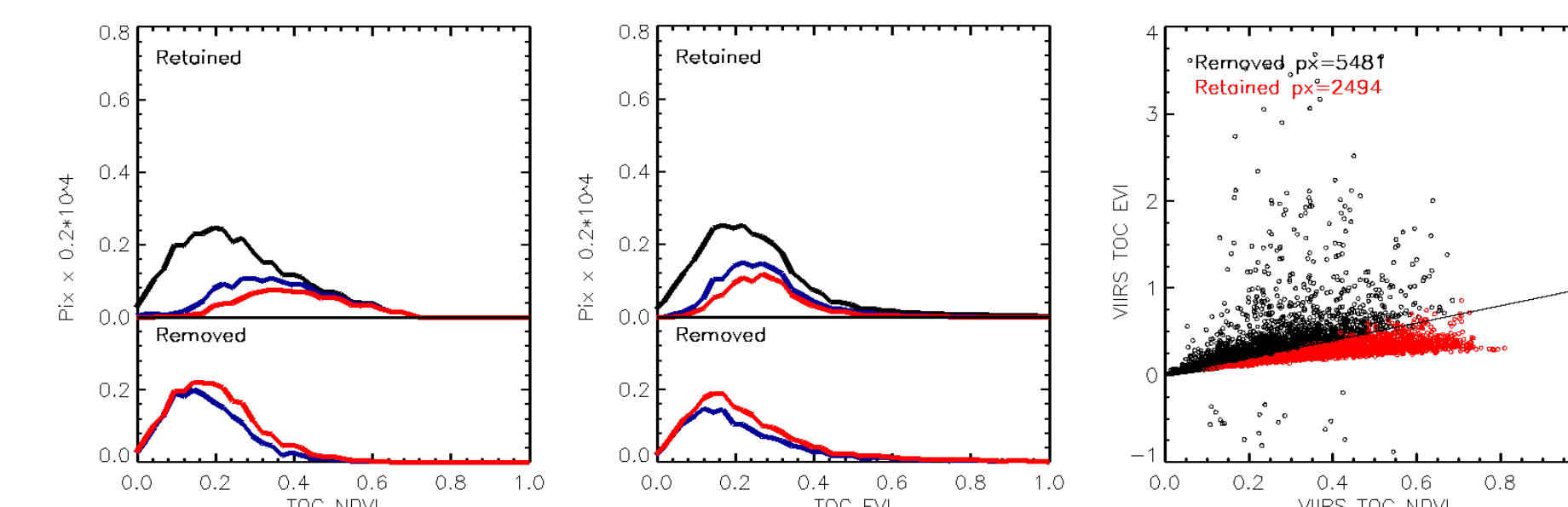
Harvard Forest site
 Aug. 12, 2013.

Match-up data over Harvard Forest were analyzed to understand overestimation of TOC NDVI. Top-left image shows TOC NDVI covered by clouds at bottom-left. Top-middle image shows TOC NDVI screened with Cloud State (only Conf. Clear pixels are retained). Effect of clouds seems screened out. However, constructing anomaly, VIIRS TOC NDVI minus AERONET TOC NDVI and applying the above mask one can see large discrepancies in vicinity of clouds. Those discrepancies are due to abnormally high values of AOT (bottom row) observed in vicinity of clouds. Screening TOC NDVI data with Cloud Shadow and Cloud Adjacency (mask at the right column) helps to minimize anomalies. TOC EVI is not affected by AOT anomalies (cf. plots below)



Match-up data for Harvard Forest were analyzed to evaluate performance of Cloud and Snow masks. In case of TOC NDVI, performance of Cloud and Snow masks is reasonable, without over-screening. Of high values of TOC NDVI (left-most figure below). However, in case of TOC EVI, the mask is efficient to remove snow covered pixels (and especially TOC EVI outliers), however over-screen valid high TOC EVI (middle and right-most figure).

Harvard Forest site
 Feb.18, 2013.



5. Conclusions

Over the length of match-up time series utilized in this study (Jan 1, 2013 - March 31, 2014) APU statistics for TOC NDVI were (0.012, 0.040, 0.040) and for TOC EVI (-0.003, 0.014, 0.013). Those statistics were derived based on screening to retain only Confidently Clear and Snow free regions. The reason for substantial difference in performance of VIs is different sensitivity of VIs to residual atmospheric contamination. Namely, TOC EVI exhibits good resistance to (1) anomalous AOT at cloud edges and resulting visible channels overcorrection and (2) residual snow contamination. While VIIRS VIs will benefit from improvement of Cloud, Aerosol and Snow algorithms, this study also suggest to develop VI-specific Quality Control, which most efficiently screens data for VIs with various sensitivities.

Introduction

S-NPP ATMS takes passive microwave (MW) measurements at certain high frequencies (88.2~183.31 GHz) that are sensitive to the scattering effect of snow particles and can be utilized to retrieve snowfall properties. An ATMS land snowfall rate (SFR) algorithm has been developed in a project supported by the JPSS Proving Ground and Risk Reduction (PGRR) Program. The ATMS SFR, combined with the operational AMSU/MHS (aboard NOAA-18/-19, and MetOp-A/-B) SFR product, can provide up to ten snowfall estimates at any location over global land at mid-latitudes. There are more estimates from overlapping orbits from ATMS and at higher latitudes from ATMS and AMSU/MHS.

Methodology

1. Detect snowfall using principal component analysis (PCA) and logistic regression model (Kongoli et al., 2014). Input includes temperature and water vapor sounding channels. Output is the probability of snowfall. In addition, a set of filters based on NWP model temperature and water vapor profiles are used for further screening. A cold snowfall extension was also developed which is a major advancement compared to the AMSU/MHS SFR.
2. Cloud properties are retrieved using an inversion method with an iteration algorithm and a two-stream Radiative Transfer Model (Yan et. al, 2008).

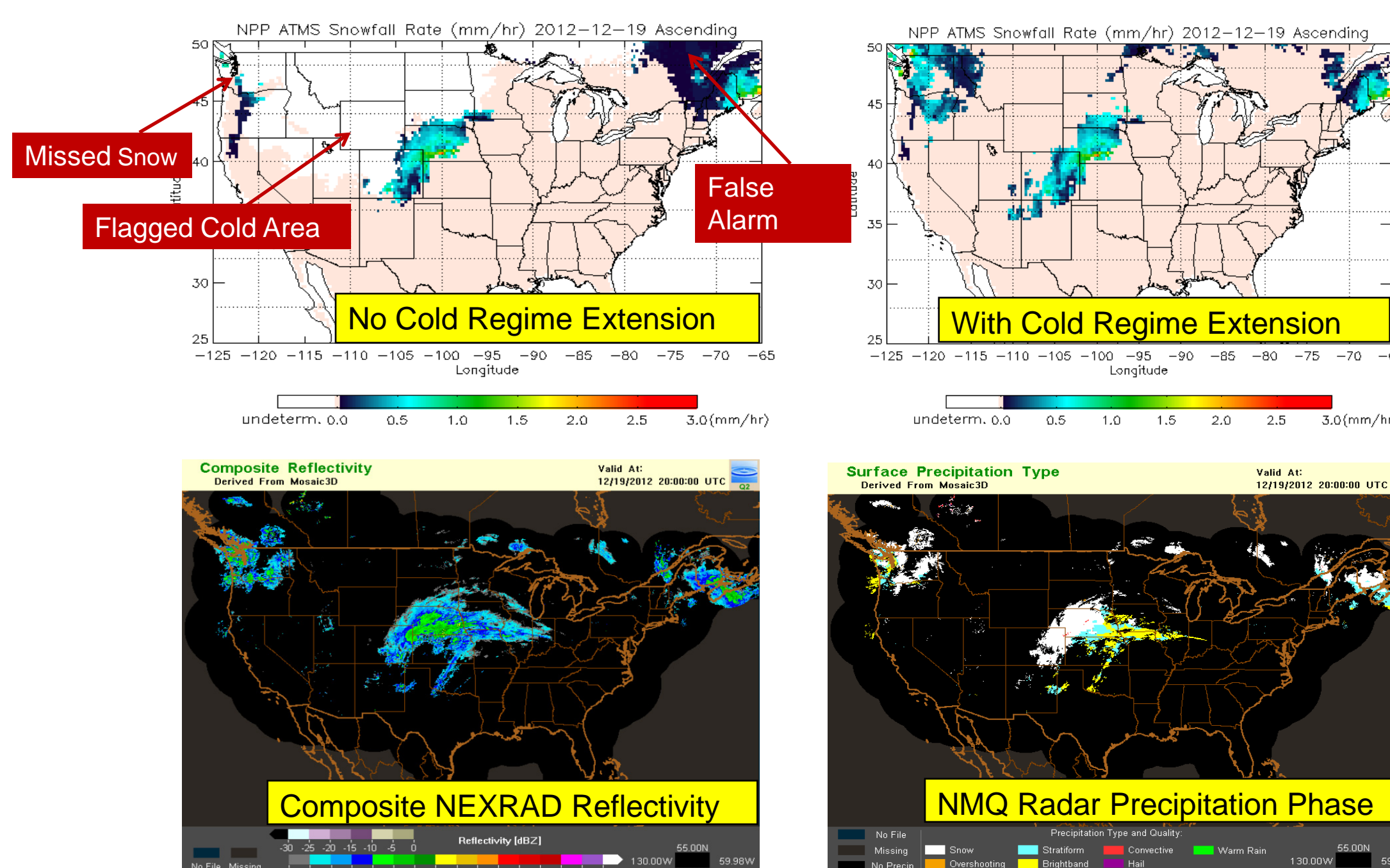
$$\begin{bmatrix} \Delta IWP \\ \Delta D_e \\ \Delta \epsilon_{23} \\ \Delta \epsilon_{31} \\ \Delta \epsilon_{88} \\ \Delta \epsilon_{165} \\ \Delta \epsilon_{183 \pm 7} \end{bmatrix} = (A^T A + E)^{-1} A^T \begin{bmatrix} \Delta T_{B23} \\ \Delta T_{B31} \\ \Delta T_{B88} \\ \Delta T_{B165} \\ \Delta T_{B183 \pm 7} \end{bmatrix}$$

IWP: ice water path
 D_e : ice particle effective diameter
 ϵ : emissivity
 A : Jacobian matrix
 E : error matrix
 T_B : brightness temperature

3. Compute snow particle terminal velocity (Heymsfield and Westbrook, 2010) and determine snowfall rate by numerically solving a complex integral.

- Heymsfield, A.J. and C.D. Westbrook, 2010, Advances in the Estimation of Ice Particle Fall Speeds Using Laboratory and Field Measurements. J. Atmos. Sci., 67, 2469-2482 doi: 10.1175/2010JAS3379.1
 - Kongoli, C., H. Meng, J. Dong, R. Ferraro, N. Wang, 2014, A Snowfall Detection Algorithm over Land utilizing High-frequency Passive Microwave Measurements – Application to ATMS. To be submitted to Journal of Geophysical Research - Atmospheres.
 - Yan, B., F. Weng, and H. Meng, 2008. Retrieval of snow surface microwave emissivity from the advanced microwave sounding unit, J. Geophys. Res., 113, D19206, doi:10.1029/2007JD009559.

ATMS Snowfall Detection With Cold Climate Extension



Statistics of Snowfall Detection Component

	Probability of Detection (%)	False Alarm Rate (%)	Heidke Skill Score
Warm Regime	73	9	0.63
Cold Regime	56	13	0.45

Product Applications

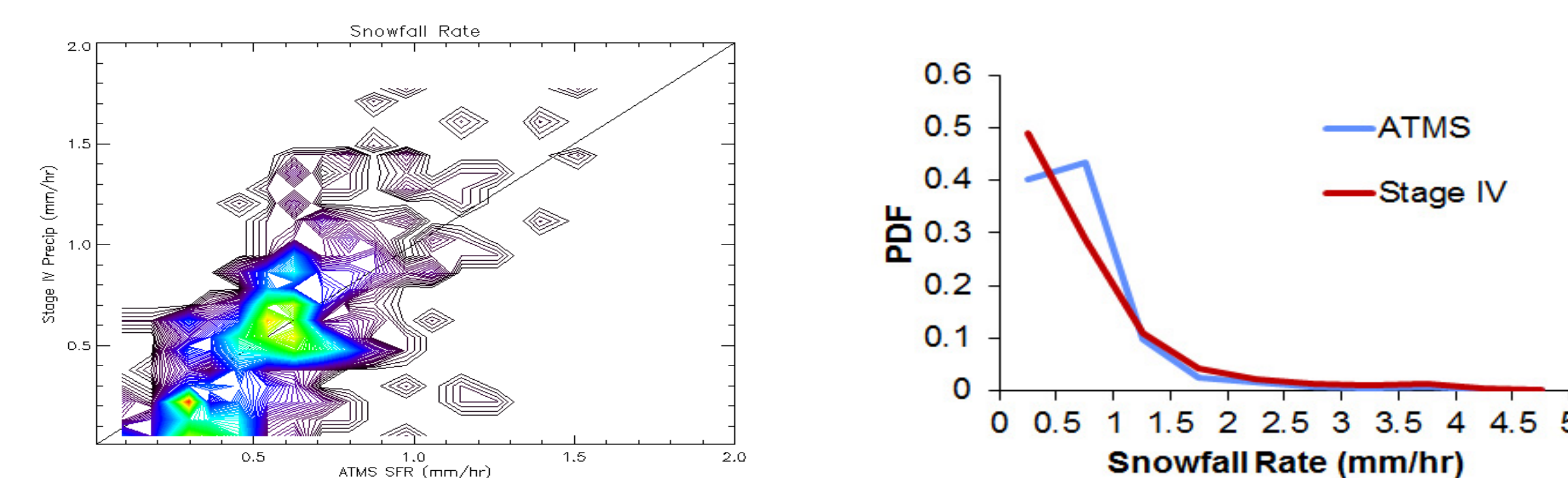
The SFR product can impact users mainly in two communities:

- Global blended precipitation products traditionally do not include snowfall derived from satellites because such products were not available operationally in the past. The ATMS and AMSU/MHS SFR can provide the winter precipitation information for these blended precipitation products. NCEP/CPC CMORPH is the first such data set to include the SFR products.
- The SFR products can fill in the gaps where traditional snowfall data are not available to weather forecasters. The products can also be used to confirm radar and gauge snowfall data. NASA SPOrT led a project to evaluate the AMSU/MHS SFR at NWS Weather Forecast Offices and NESDIS/SAB in the past winter with very valuable feedback. The ATMS SFR will also be evaluated in the next winter in collaboration with SPOrT in a project supported by NASA.

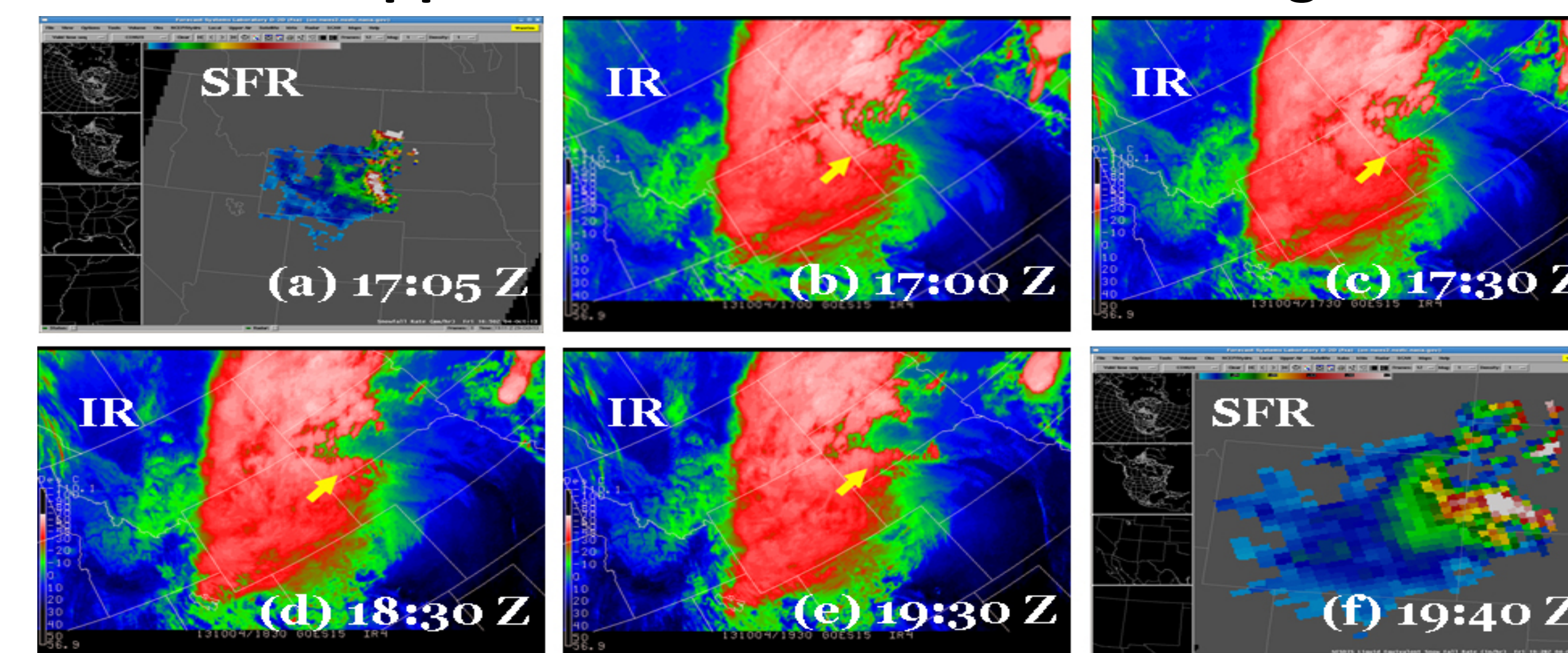
Validation

Limited validation has been conducted for the ATMS SFR product. Validation sources included StageIV radar and gauge combined hourly precipitation data, NMQ radar instantaneous precipitation data, and station hourly accumulated precipitation data. Snowfall product validation is especially challenging due to the spatial and temporal differences between satellite retrieval and validation data, and errors in the validation data etc.

	Correlation Coefficient	Bias (mm/hr)	RMSE (mm/hr)
Stage IV 02/21/2013	0.80	0.05	0.83
Stage IV 3/5/2013	0.65	0.02	0.26
Station	0.80	0.04	0.73



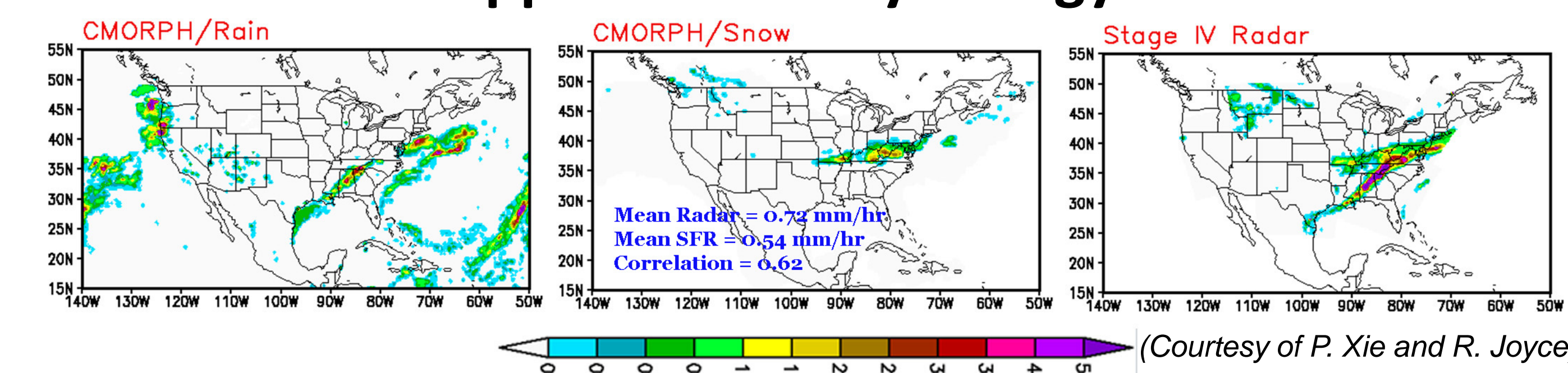
SFR Application in Weather Forecasting



(GOES images are courtesy of M. Folmer)

Time sequence of a snowstorm in the Northern Plains. (a) and (f): the AMSU/MHS SFR product at around 17:05Z and 19:40Z, respectively; (b)-(e) GOES-15 IR images at 17:00Z, 17:30Z, 18:30Z, and 19:30Z, respectively. The yellow arrow points to the most intense snow in the IR images. The IR sequence indicates that the snow max rotated counter-clockwise and moved north between the two SFR observations. This is confirmed by the second satellite pass at 19:40Z.

SFR Application in Hydrology



NCEP/CPC CMORPH blended precipitation product uses both ATMS and AMSU/MHS SFR for its winter precipitation analysis. In this snowfall event, the correlation coefficient between the CMORPH 3-hour precipitation and Stage IV reaches 0.62.

This study was partially supported by NOAA grant NA09NES4400006 (Cooperative Institute for Climate and Satellites -CICS) at the University of Maryland/ESSIC.



Real-time daily rolling weekly green vegetation fraction derived from Suomi NPP satellite

Zhangyan Jiang^{1,2}, Junchang Ju^{1,2}, Marco Vargas¹, Ivan Csiszar¹

¹ NOAA National Environmental Satellite, Data, and Information Service, Center for Satellite Applications and Research, College Park, MD, 20740. ² AER inc. Lexington, MA, 02421

2014 STAR JPSS Science Teams Annual Meeting, May 12-16, NOAA NCWCP, College Park, MD

Introduction

Green Vegetation fraction (GVF) is defined as the fraction of a pixel covered by green vegetation if it were viewed vertically. Real-time GVF is needed in the numeric weather, climate and hydrological models. The current NOAA operational GVF product is derived from AVHRR top of atmosphere NDVI data at 16-km resolution. In the Suomi National Polar-orbiting Partnership (SNPP) era, there is a need to produce GVF as a NOAA-Unique Product (NUP) from data from the Visible Infrared Imager Radiometer Suite (VIIRS) sensor for applications in numerical weather and seasonal climate prediction models at the National Centers for Environmental Prediction (NCEP). The retrieval algorithm uses VIIRS red (I1), near-infrared (I2) and blue (M3) bands centered at 0.640 μm, 0.865 μm and 0.490 μm, respectively, to calculate the Enhanced Vegetation Index (EVI) and derive GVF from EVI. This poster describes the GVF algorithm that is used for GVF retrieval. To meet the data needs of NCEP and other potential users, GVF will be produced as a daily rolling weekly composite at 4-km resolution (global scale) and 1-km resolution (regional scale).

VIIRS GVF Algorithm

The basic retrieval strategy of the GVF processing system is to produce green vegetation fraction from VIIRS observations. Daily VIIRS surface reflectance data are composited weekly and EVI is calculated based on the composited data. GVF is then calculated by comparison of weekly EVI to the global maximum and minimum EVI values.

The GVF processing system generates weekly Green Vegetation Fraction through the following steps:

Step 1: VIIRS swath surface reflectance data in bands I1 (red), I2 (NIR), and M3 (blue) during a calendar day (0000 – 2400 UTC) are mapped to the native GVF geographic grid (0.003 degree plate carree projection) to produce a gridded daily surface reflectance map.

Step 2: At the end of a 7-day period, the daily surface reflectance maps of the 7 days are composited to produce a weekly surface reflectance map using the MVA-SAVI compositing algorithm, which selects, at each GVF grid point (pixel), the observation with maximum view-angle adjusted SAVI value in the 7-day period. The 7-day compositing is conducted daily using data in the previous 7 days as input data, which is called daily rolling weekly compositing.

Step 3: EVI is calculated from the daily rolling weekly composited VIIRS surface reflectance data in bands I1, I2 and M3.

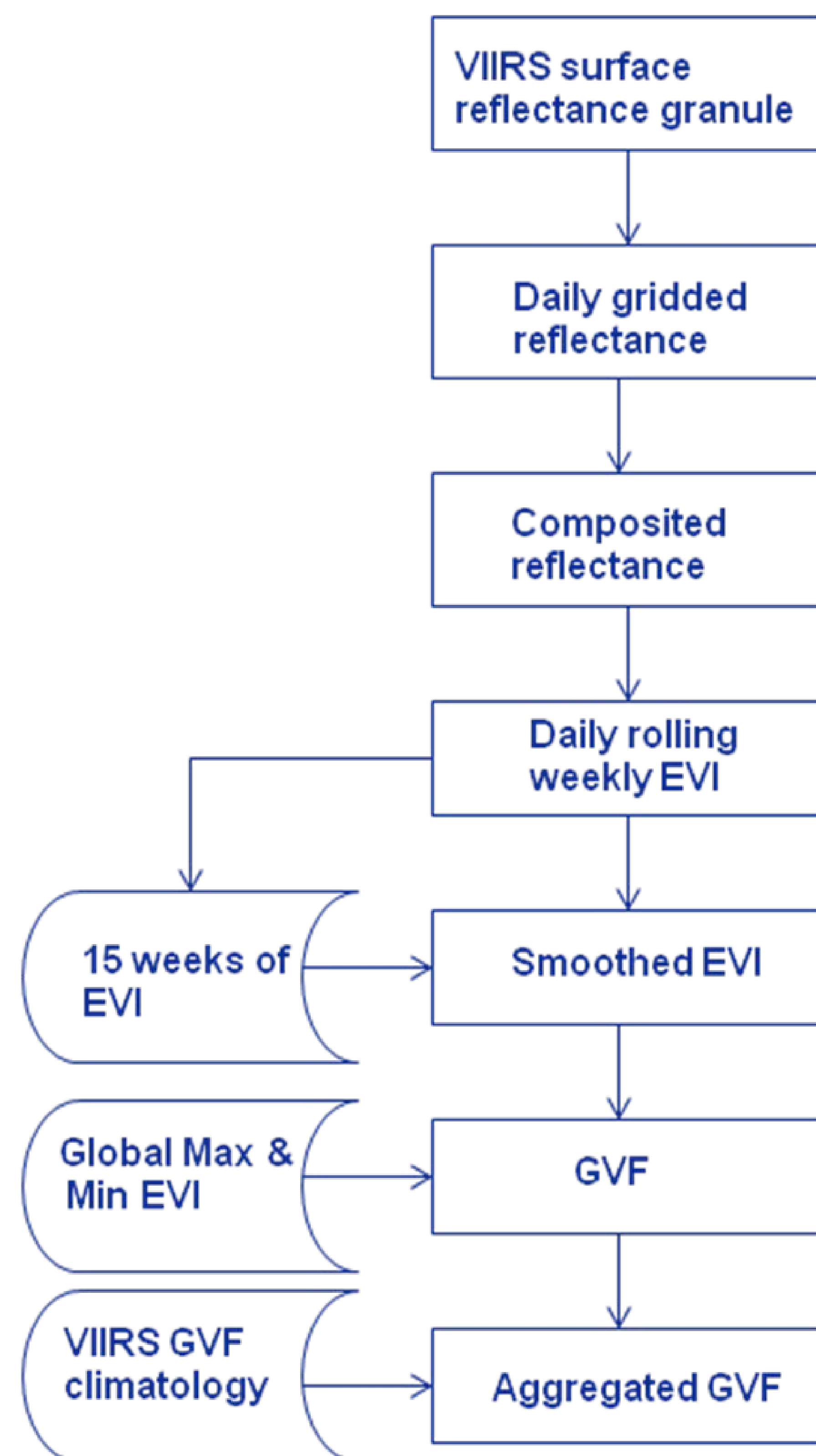
$$EVI = 2.5 \frac{NIR - Red}{NIR + 6Red - 7.5Blue + 1}$$

Step 4: High frequency noise in EVI is reduced by applying a 15-week digital smoothing filter on EVI.

Step 5: GVF is calculated by comparing the smoothed EVI against the global maximum (EVI_∞) and minimum EVI (EVI₀) values assuming a linear relationship between EVI and GVF.

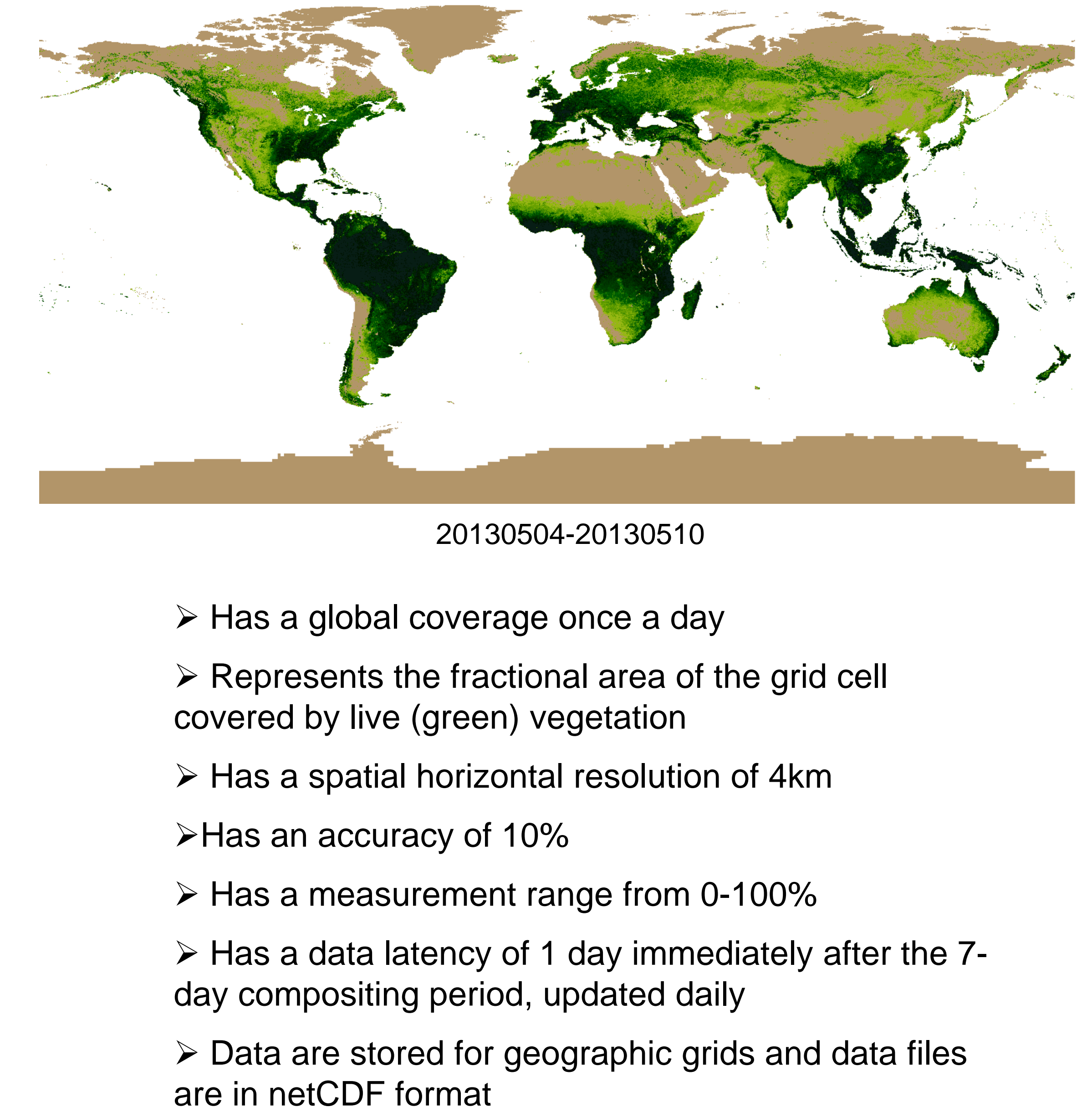
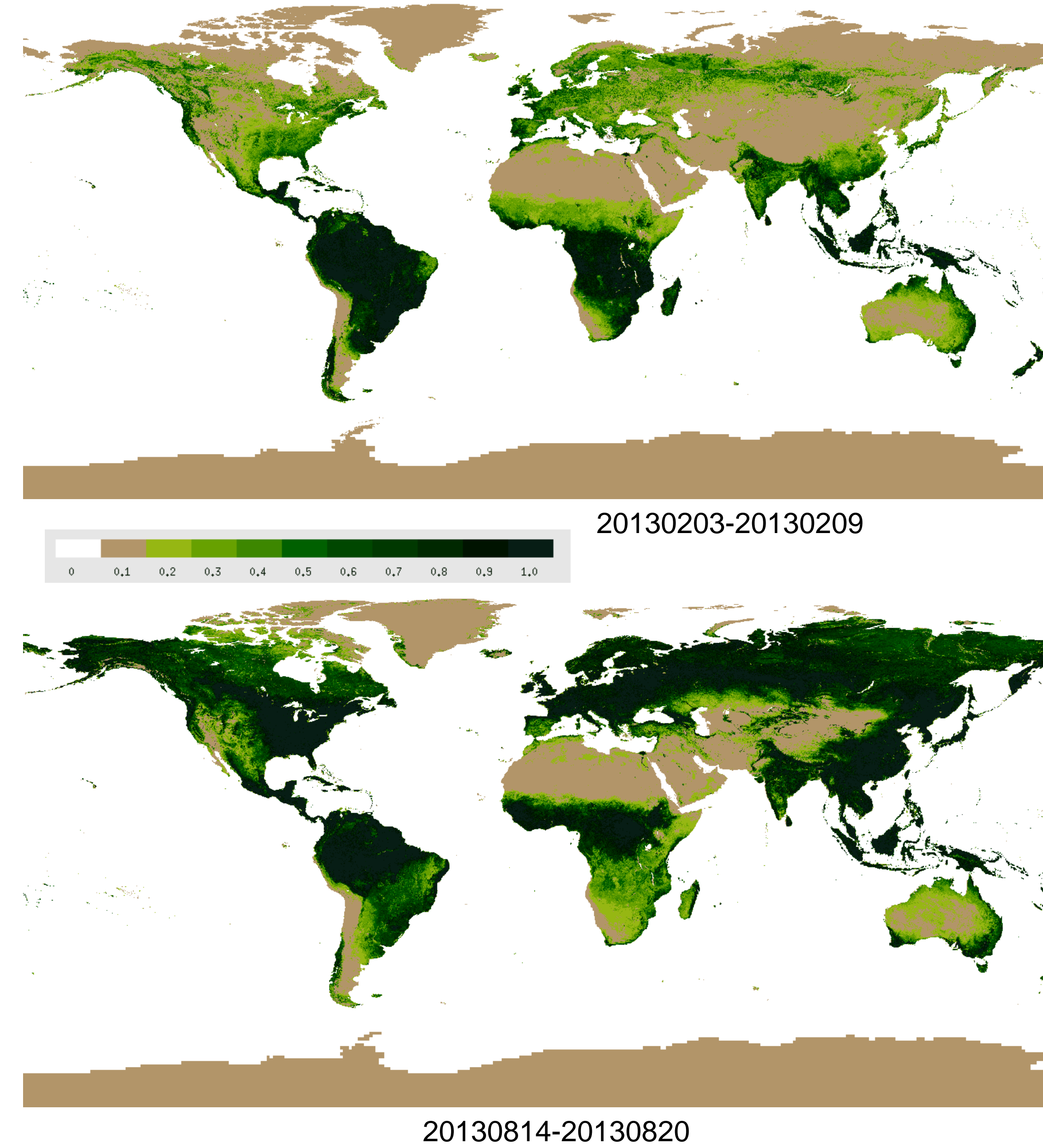
$$GVF = \frac{EVI - EVI_0}{EVI_\infty - EVI_0}$$

Step 6: GVF is aggregated to 0.009 degree (1-km) and 0.036 degree (4-km) resolution for output maps. Potential gaps on the output maps at high latitudes are filled using monthly VIIRS GVF climatology.



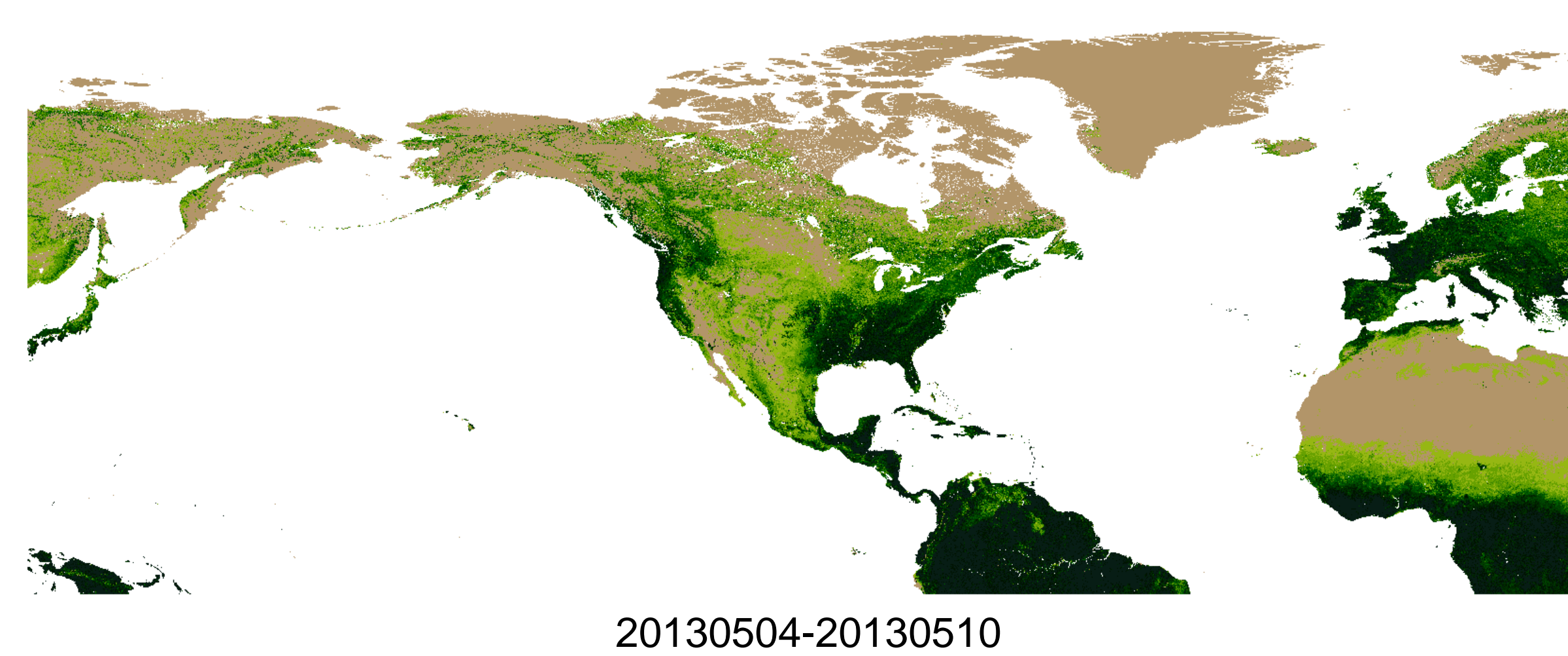
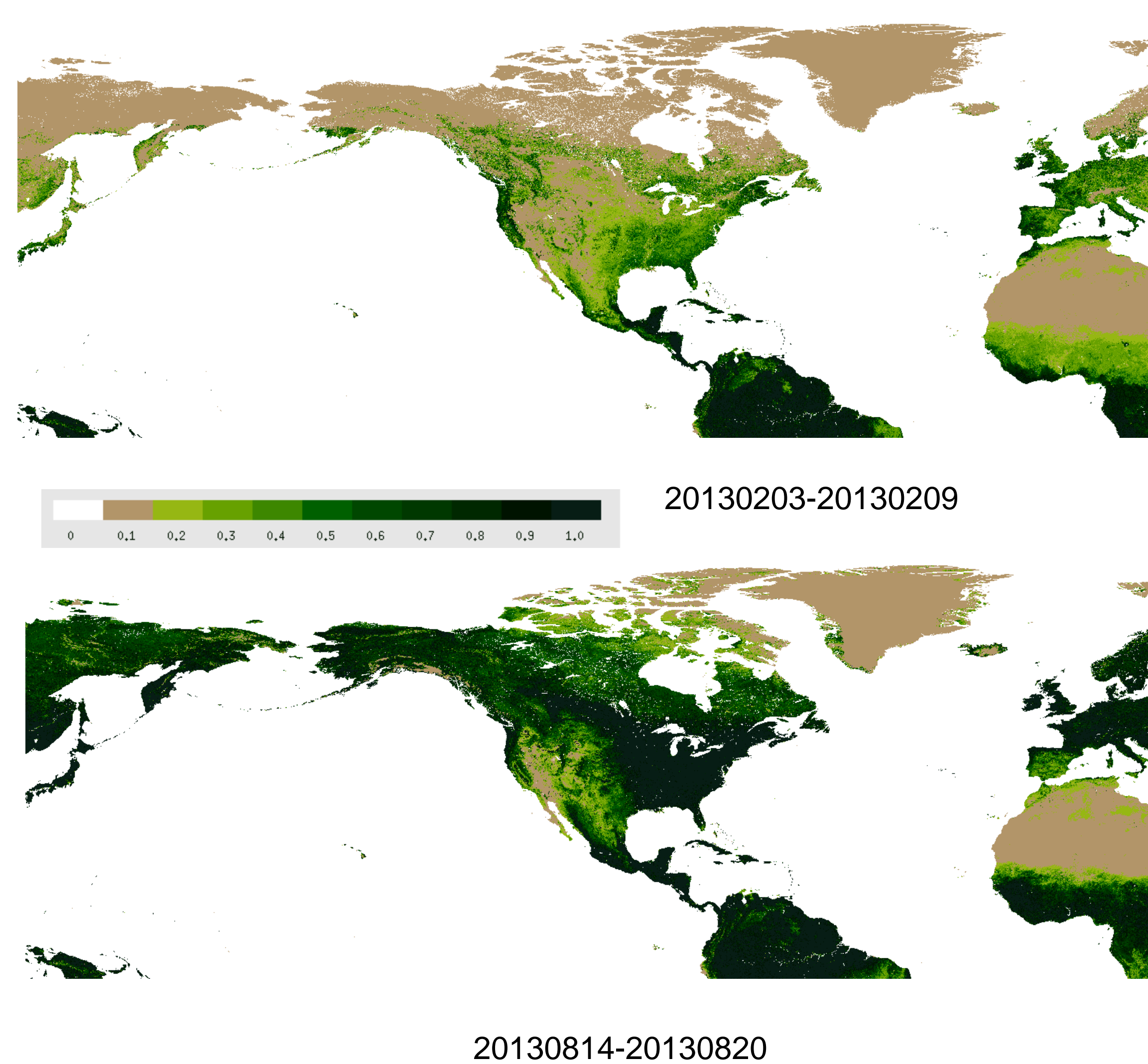
Flow chart of GVF system

Global GVF product

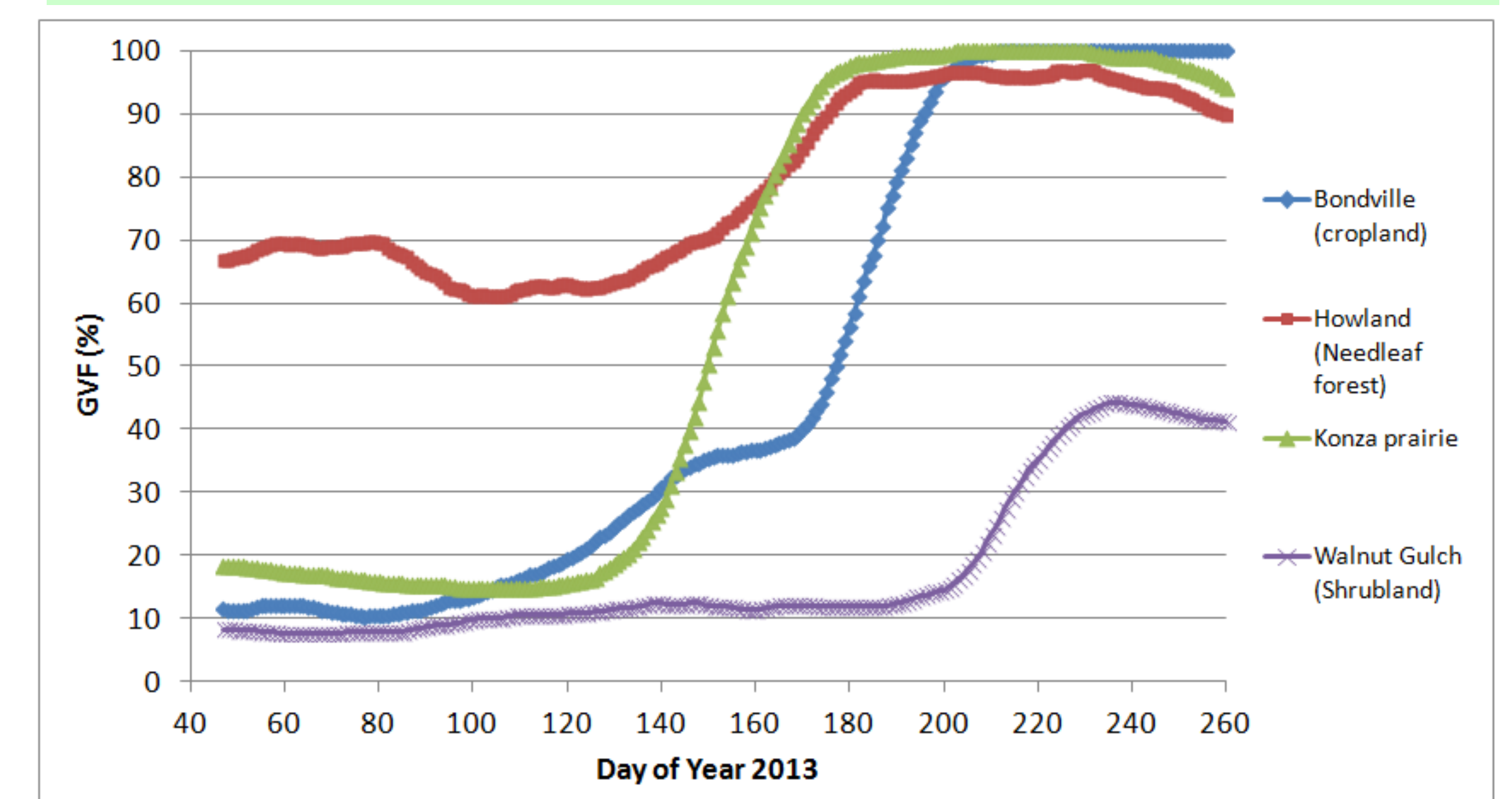


- Has a global coverage once a day
- Represents the fractional area of the grid cell covered by live (green) vegetation
- Has a spatial horizontal resolution of 4km
- Has an accuracy of 10%
- Has a measurement range from 0-100%
- Has a data latency of 1 day immediately after the 7-day compositing period, updated daily
- Data are stored for geographic grids and data files are in netCDF format

Regional GVF product

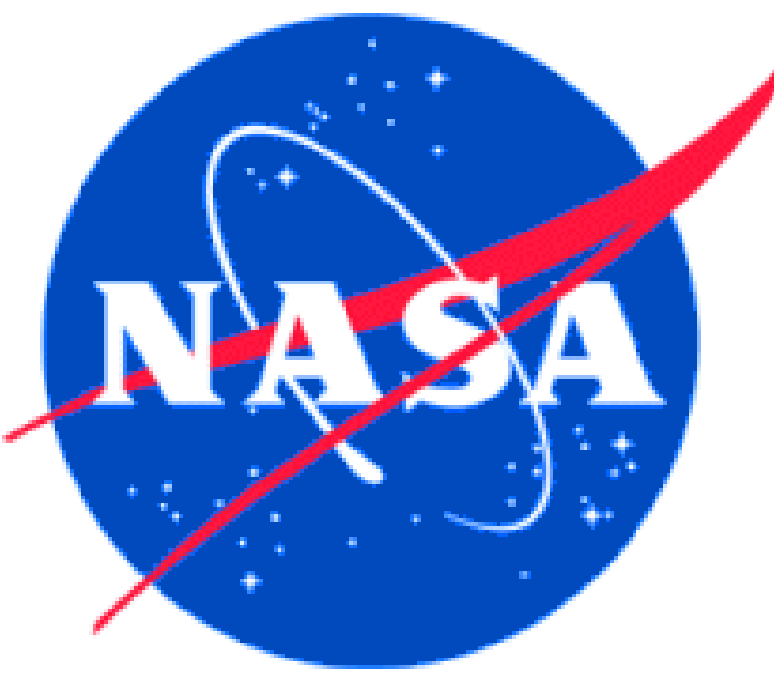


GVF time series



Daily rolling weekly GVF time series over different land cover types

- Has a regional coverage once a day, covering latitude 7.5° S to 90° N degrees, longitude 130° E eastward to 30° E
- Has a spatial horizontal resolution of 1km



VIIRS Lunar Observation and Applications

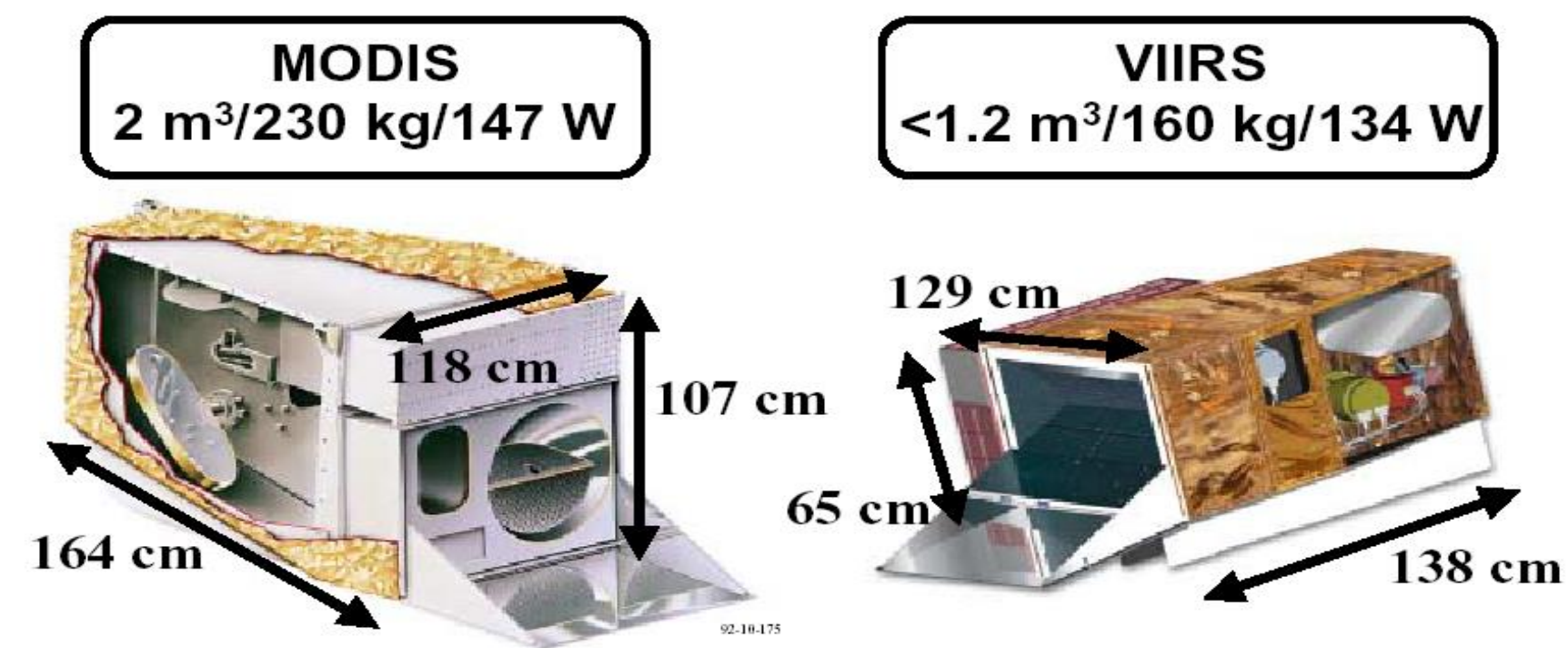
Xiaoxiong (Jack) Xiong*, Zhipeng (Ben) Wang**, Jon Fulbright**, Boryana Efremova** and Hongda Chen**

* Sciences and Exploration Directorate, NASA/GSFC, Greenbelt, MD 20771; ** Sigma Space Corp., Lanham, MD 20706



Introduction - VIIRS

- The Visible Infrared Imaging Radiometer Suite (VIIRS) onboard the Suomi National Polar-orbiting Partnership (S-NPP) spacecraft was launched on October 28, 2011.
- VIIRS consists of 14 Reflective Solar Bands (RSB), 7 Thermal Emissive Bands (TEB) and a Day/Night Band (DNB), covering a spectral range from 0.41 to 12.2 μm .
- The spatial resolutions are 375 m for imagery (I) bands I1-I5 and 750 m for moderate-resolution (M) bands M1-M16.
- VIIRS is calibrated by onboard calibrators – solar diffuser (SD) and SD stability monitor (SDSM) for RSB; blackbody (BB) for TEB.
- The design/operation of VIIRS has strong MODIS heritage:



- The NASA VIIRS Characterization Support Team (VCST) supports VIIRS SDR radiometric / geometric calibration and characterization.

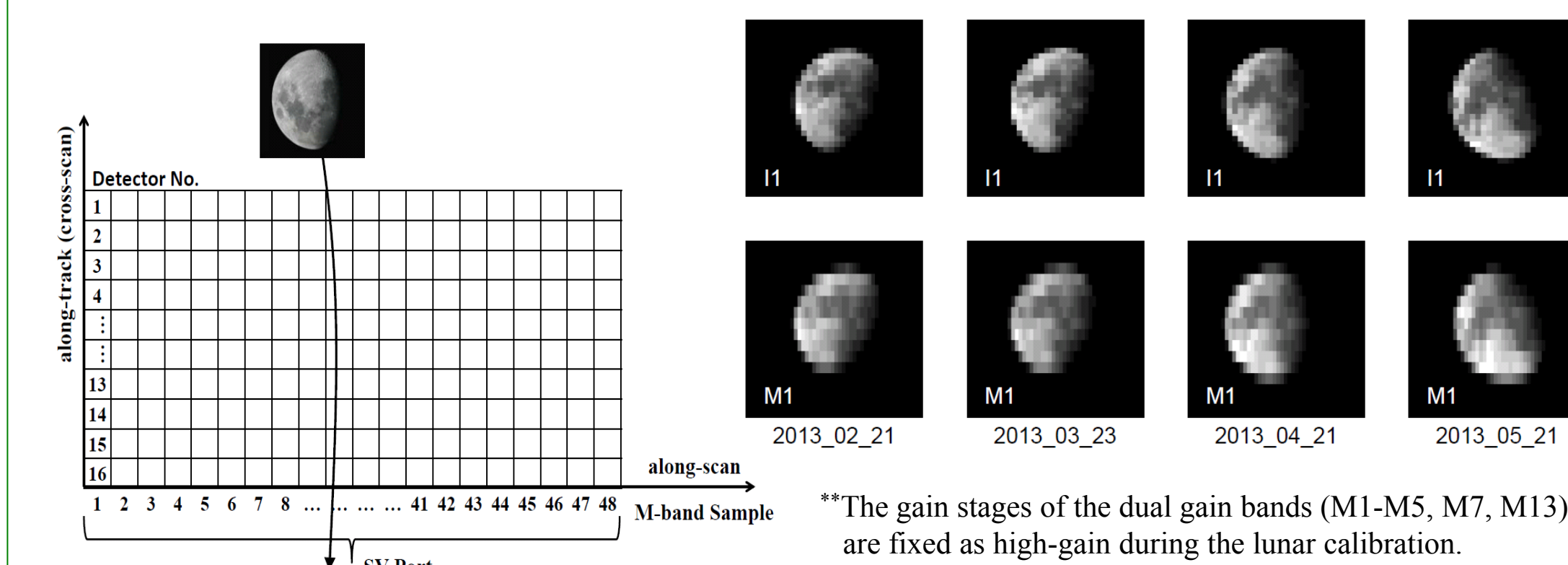
VIIRS Lunar Calibration

- VIIRS lunar observations have been scheduled on a nearly monthly basis since January 2012.
- The lunar phase is within a limited range of [-51.5, -50.5] degrees.

M/D/Y	H:M:S	Roll Angle	Phase Angle	SEaVr Angle	Sector
01/04/2012	08:48:53	-9.490	-55.41	35.9	SV
02/03/2012	04:21:32	-5.445	-56.19	41.3	SV
02/03/2012	06:03:34	-5.279	-55.38	39.6	SV
04/02/2012	23:05:11	-3.989	-51.24	23.0	EV
05/02/2012	10:20:06	-3.228	-50.92	340.2	EV
05/31/2012	14:47:14	-0.081*	-52.97	53.5	EV
10/25/2012	06:58:15	-4.048	-51.02	309.0	EV
11/23/2012	21:18:20	-9.429	-50.74	326.6	EV
12/23/2012	15:00:50	-7.767	-50.90	24.0	EV
01/22/2013	12:13:35	-3.383	-50.81	28.1	EV
02/21/2013	09:31:25	-1.712	-50.71	28.8	EV
03/23/2013	03:29:00	-3.320	-51.15	25.2	EV
04/21/2013	19:47:54	-3.882	-50.82	18.6	EV
05/21/2013	08:43:15	-0.809*	-50.67	335.7	EV
10/14/2013	21:39:19	-1.305	-50.95	305.6	EV
11/13/2013	06:57:41	-7.981	-50.66	314.9	EV
12/12/2013	19:35:46	-9.438	-50.39	334.3	EV
01/11/2014	09:59:45	-6.727	-51.30	25.9	EV
02/10/2014	05:34:12	-3.714	-51.03	29.0	EV
03/12/2014	01:11:43	-3.944	-51.05	28.4	EV
04/10/2014	20:53:17	-4.977	-50.60	22.2	EV

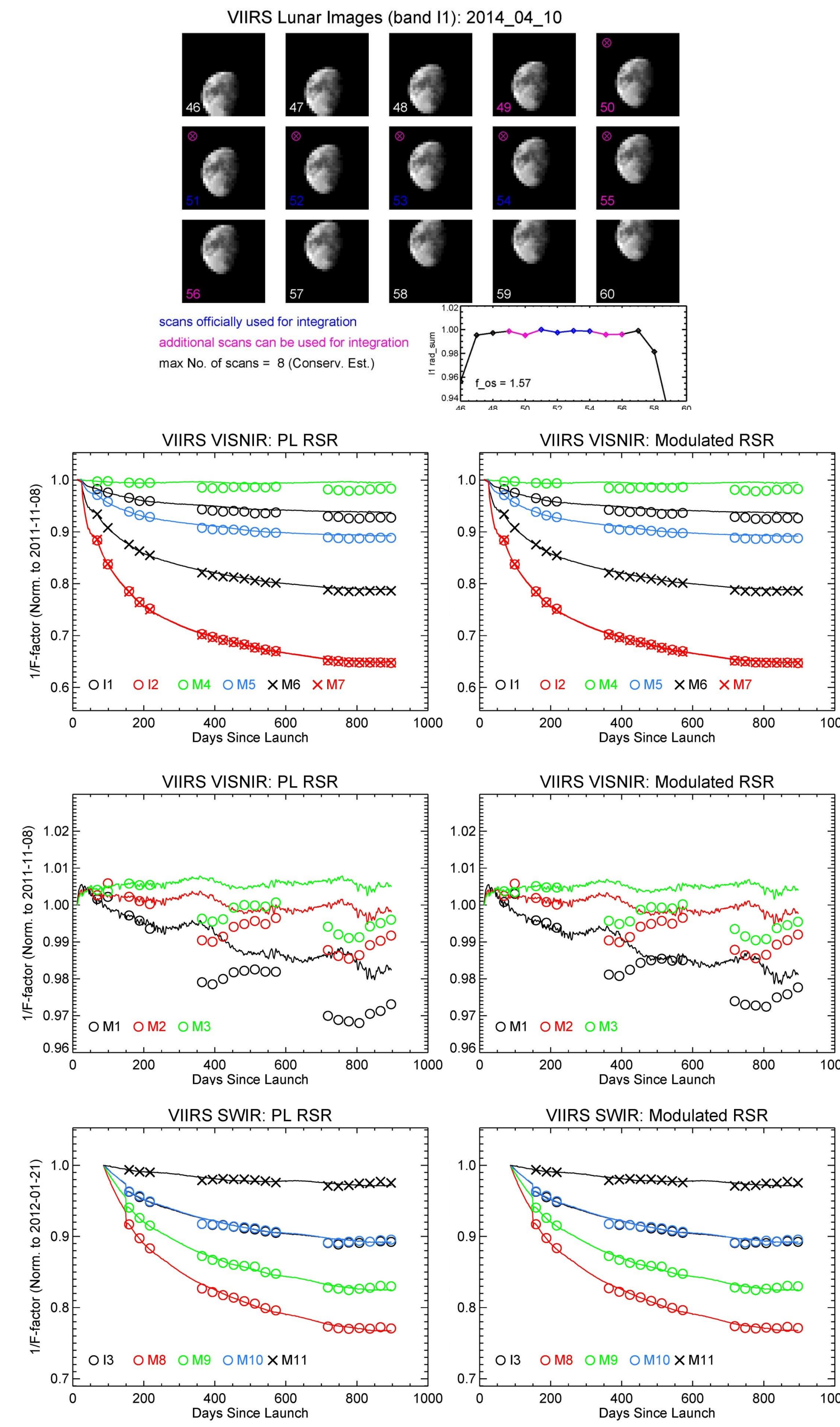
*No roll maneuver performed for small angles.

- Multiple scans of lunar images are captured during each calibration.



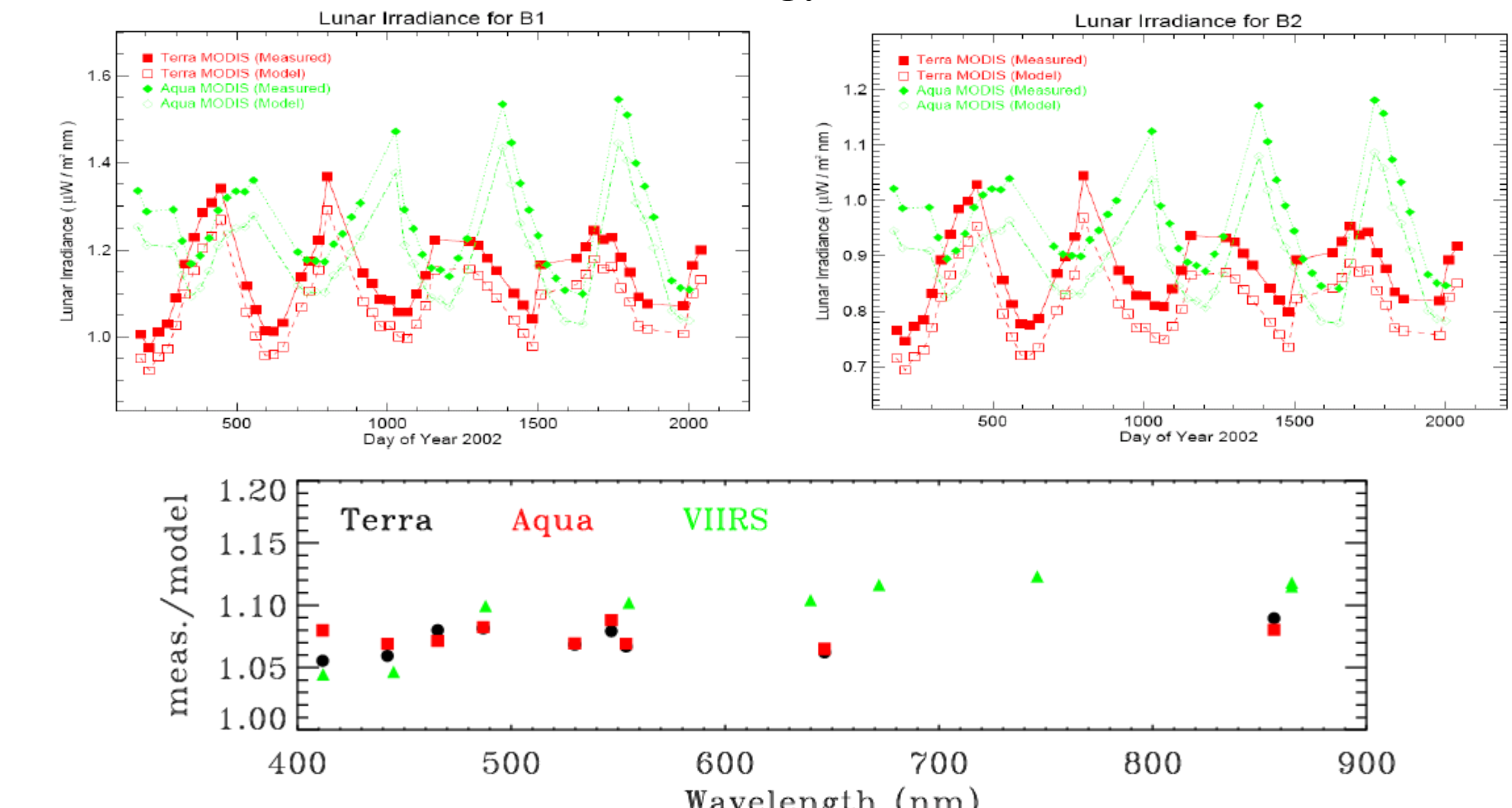
RSB Radiometric Calibration

- The VIIRS lunar spectral irradiance $I_{moon,PL}$ is calculated by integrating lunar images using the pre-launch gain coefficient.
- The actual lunar irradiance I_{ROLO} is predicted by ROLO model.
- The lunar calibration F-factor is the ratio of I_{ROLO} and $I_{moon,PL}$.
- The lunar F-factor and SD F-factor trending should agree.



Inter-comparison with MODIS

- MODIS uses similar methodology RSB lunar calibration method.



RSB Spatial Characterization

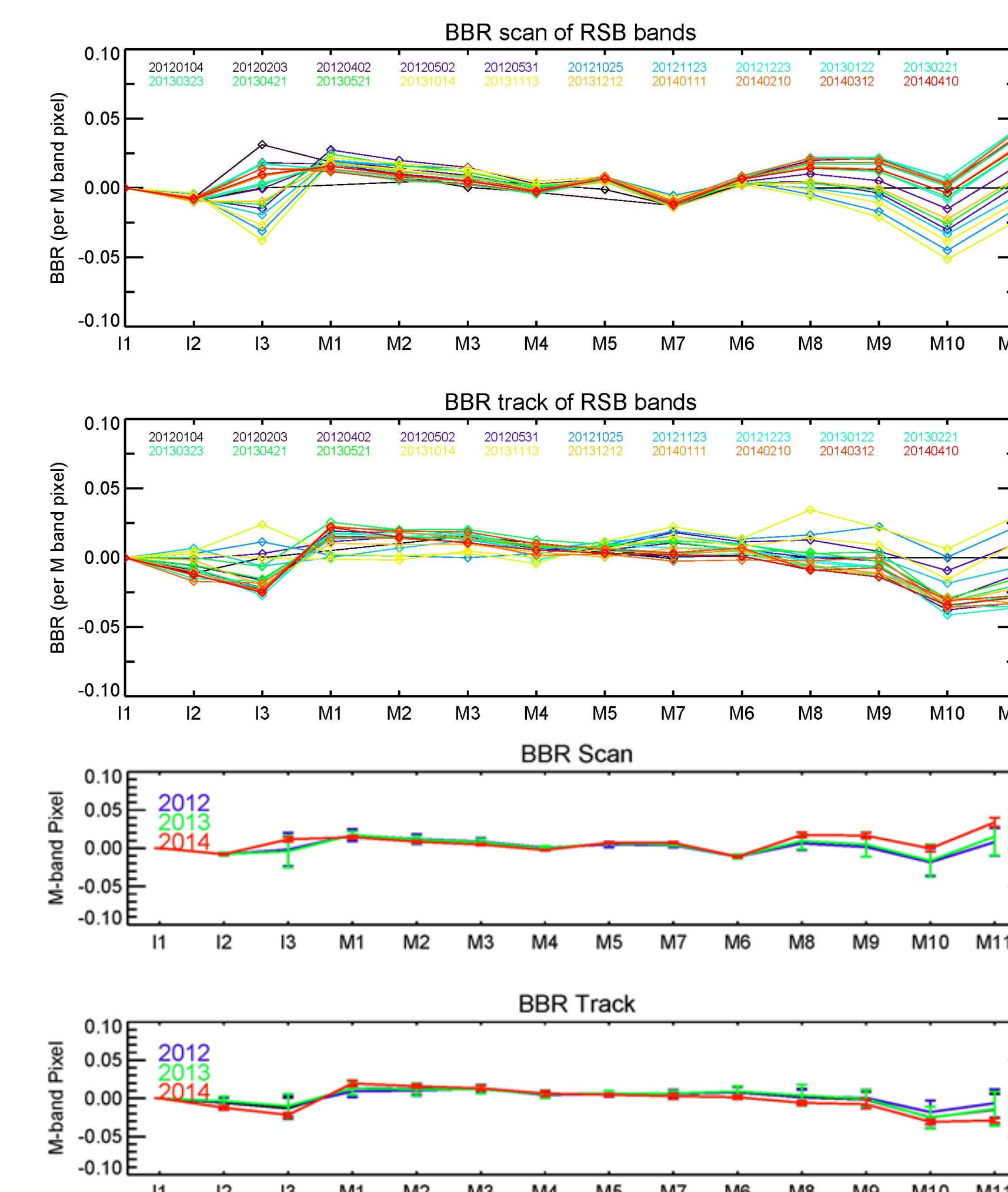
Band-to-Band Registration (BBR)

- The BBR is quantized by the offset Δ between the matching detectors of the two bands.
- The lunar dn is background subtracted and corrected with the detector gain difference.
- The centroid of the 2-D lunar image is

$$f_{B,D} = \frac{\sum_i \left(\sum_j dn_{B,D}^* \right) \cdot f}{\sum_i \sum_j dn_{B,D}^*} \quad s_{B,D} = \frac{\sum_i \left(\sum_j dn_{B,D}^* \right) \cdot s}{\sum_i \sum_j dn_{B,D}^*}$$

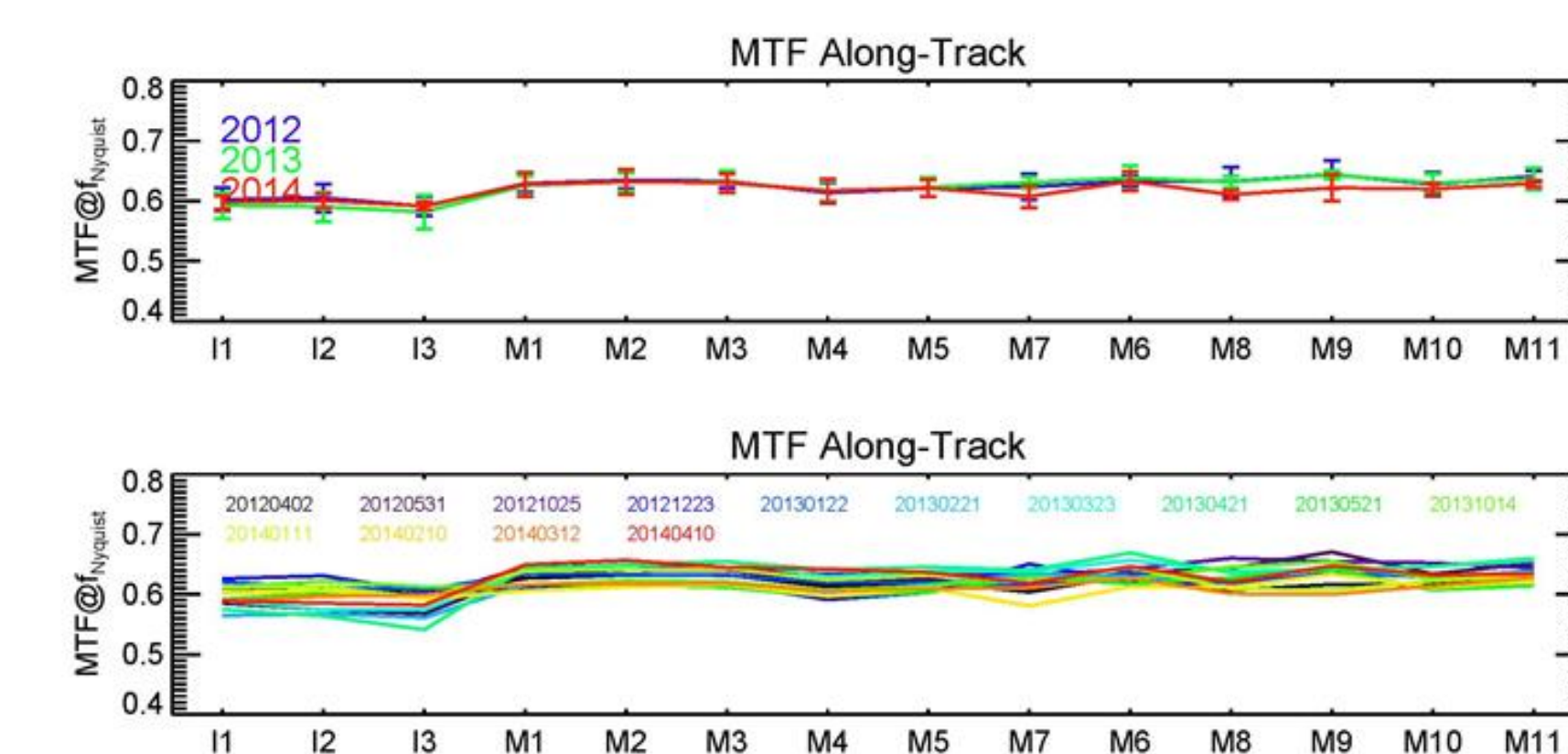
- The BBR offset is calculated by

$$\Delta_{scan} = \overline{f_{B1,D}} - \overline{f_{B2,D}} \quad \Delta_{track} = \frac{\overline{s_{B1,D}} - \overline{s_{B2,D}}}{\beta}$$



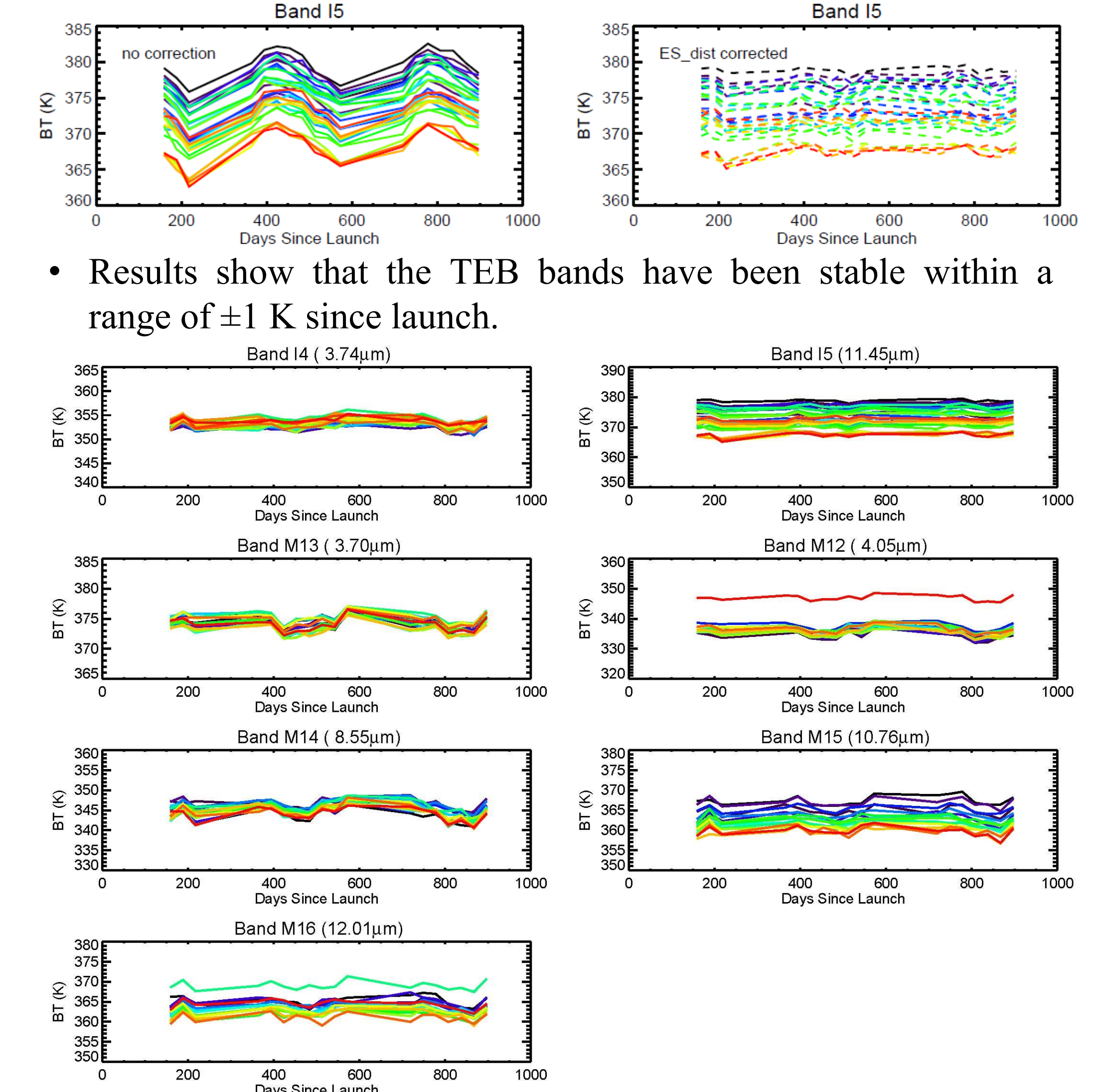
Modulation Transfer Function (MTF)

- MTF is the spatial frequency response of the instrument.
- The edge of the Moon can be used to derive the VIIRS MTF in both along-scan and along-track directions.
- Images of multiple scans need to be aligned and superimposed based on the scan-to-scan movement.
- Along-track MTF is constantly monitored.



TEB Calibration Stability Trending

- TEB is calibrated by an on-board blackbody on a scan basis.
- The Brightness Temperature (BT) of the lunar surface can be retrieved with the calibrated gain coefficient.
- The thermal properties of lunar surface is stable, so the surface BT trending can be used to assess the calibration stability.
- Seasonal oscillation of the BT trending is reduced, mostly by considering the Earth/Moon-Sun distance variation.

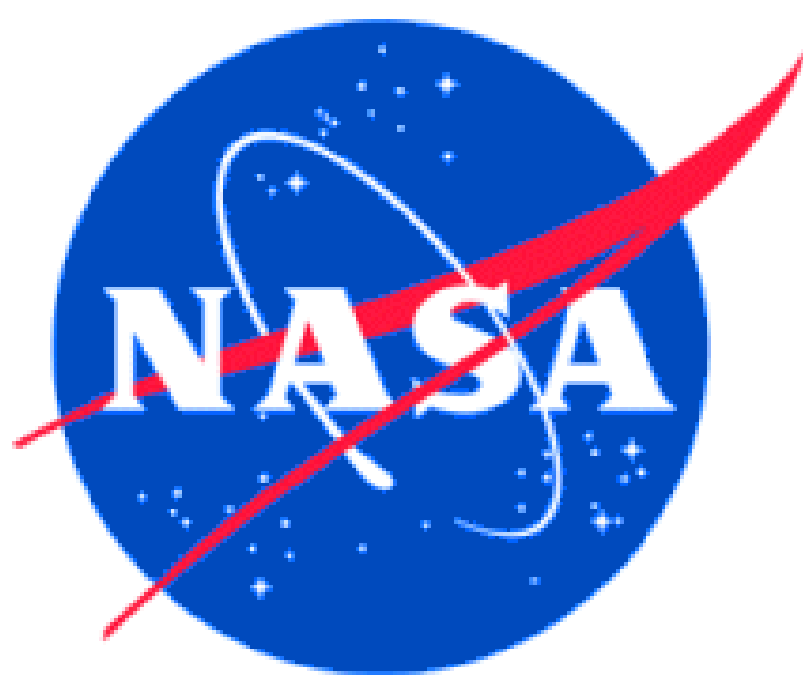


- Results show that the TEB bands have been stable within a range of ± 1 K since launch.

- The accuracy of the trending is limited mainly by the facts of
 - 1) surface temperature varies considerably across the Moon;
 - 2) the lunar images of all TEB detectors are partially saturated;
 - 3) the trended pixels among events are not perfectly registered.

Summary

- Calibration/characterization of some VIIRS on-orbit radiometric and spatial parameters can be performed through the scheduled lunar observation, including
 - 1) determining the RSB radiometric calibration coefficient;
 - 2) calibration inter-comparison with MODIS and other sensors;
 - 3) characterizing the spatial parameters BBR and MTF;
 - 4) tracking the stability of the TEB radiometric calibration.
- These parameters will be continuously monitored throughout VIIRS lifetime.
- Most of these parameters can also be derived from un-scheduled lunar observations.
- The methodologies/algorithms are mainly developed for MODIS lunar calibration and have been successfully extended to VIIRS.
- More lunar calibration applications are under study.



S-NPP VIIRS SDSM Screen Transmittance Determined from both Yaw Maneuver and Regular On-orbit Data

VIIRS Characterization Support Team (VCST), NASA/GSFC

Ning Lei*, Xuexia (Sherry) Chen*, and Xiaoxiong (Jack) Xiong**



Introduction: S-NPP VIIRS uses an on-board solar diffuser (SD) to carry out radiometric calibration of its reflective solar bands (RSB). The SD bidirectional reflectance distribution function (BRDF) degrades over time. An on-board solar diffuser stability monitor (SDSM) is used to determine the degradation coefficient. The SDSM observes the sun through a pinhole screen and the SD at almost the same time and thus is able to determine the SD BRDF degradation. As a result, accurate knowledge of the SDSM screen transmittance is essential to allow the SDSM to determine the degradation coefficient accurately. Yaw maneuver data has large step size in the projected solar horizontal angle and therefore is not able to yield details of the transmittance. We use yaw maneuver data determined SDSM screen transmittances as anchors and use a portion of regular on-orbit data (~ 3 months) data to determine the SDSM pinhole screen transmittance at very fine angular step sizes. The BRDF degradation coefficient versus time curve determined with the new SDSM screen transmittance is much smoother than that computed with yaw maneuver data determined SDSM screen transmittance.

Theory

For an SDSM detector d per unit time:

$$\frac{\tau_{SDSM, eff}(\phi_h(t), \phi_v(t); t)}{\tau_{SDSM, eff}(\phi_h(t_0), \phi_v(t_0); t_0)} = [1 + b_1(t - t_0) + b_2(t - t_0)^2] * \frac{dc_{sun}(t)R^2(t)}{dc_{sun}(t_0)R^2(t_0)}$$

t_0 ~ middle time in the yaw maneuver data or a small segment (in time) of on-orbit data (change in RSR is negligible over the yaw data or a small segment)

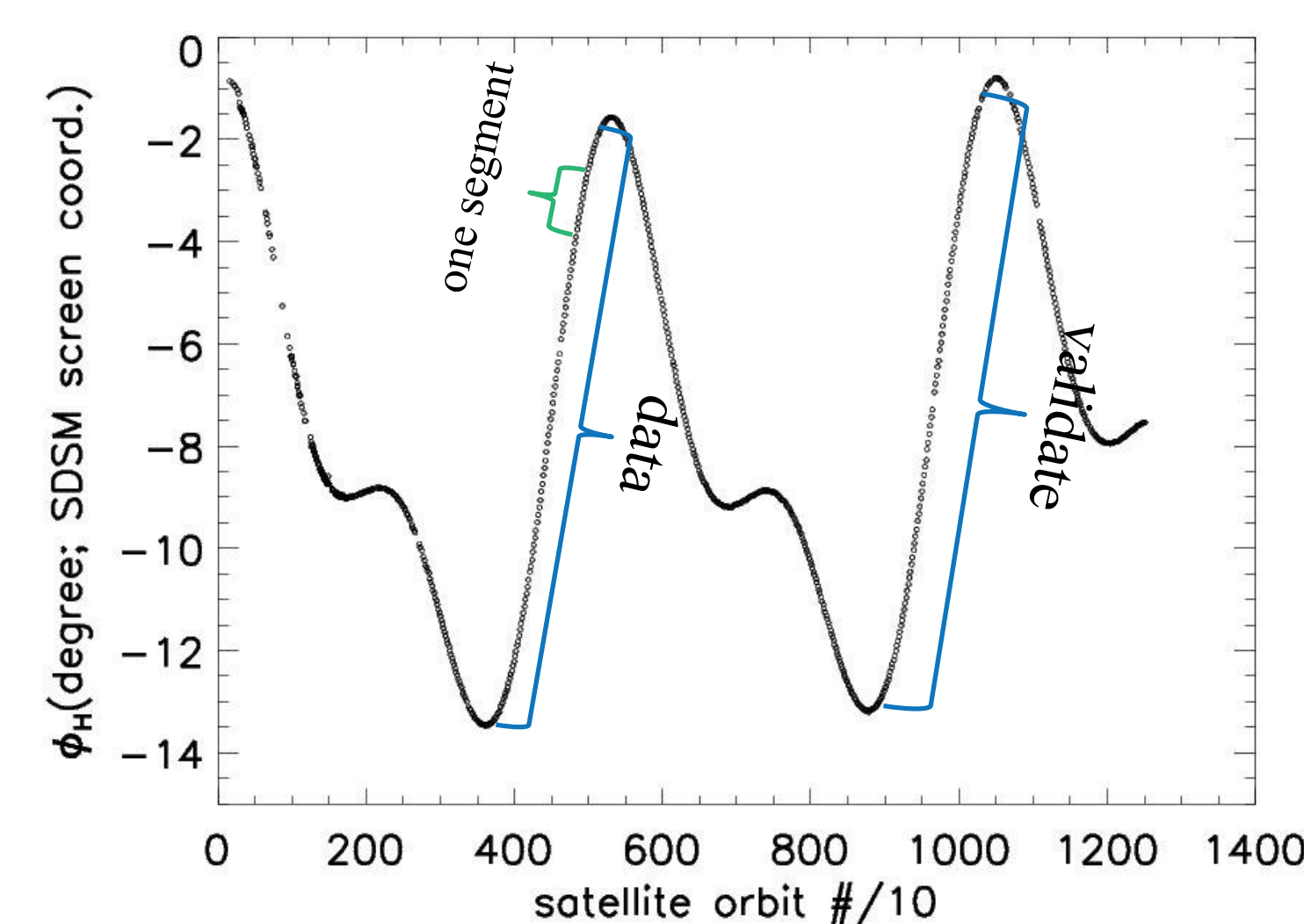
Detector 8 has the largest b_1 and $|b_2|$.

At orbit 1570 (~ yaw maneuvers):

$b_1 = 6.6 \times 10^{-5}/\text{orbit}$, $b_2 = -2.16 \times 10^{-8}/\text{orbit}^2$

(solar spectral power drift is folded in b_1 and b_2)

Regular on-orbit data

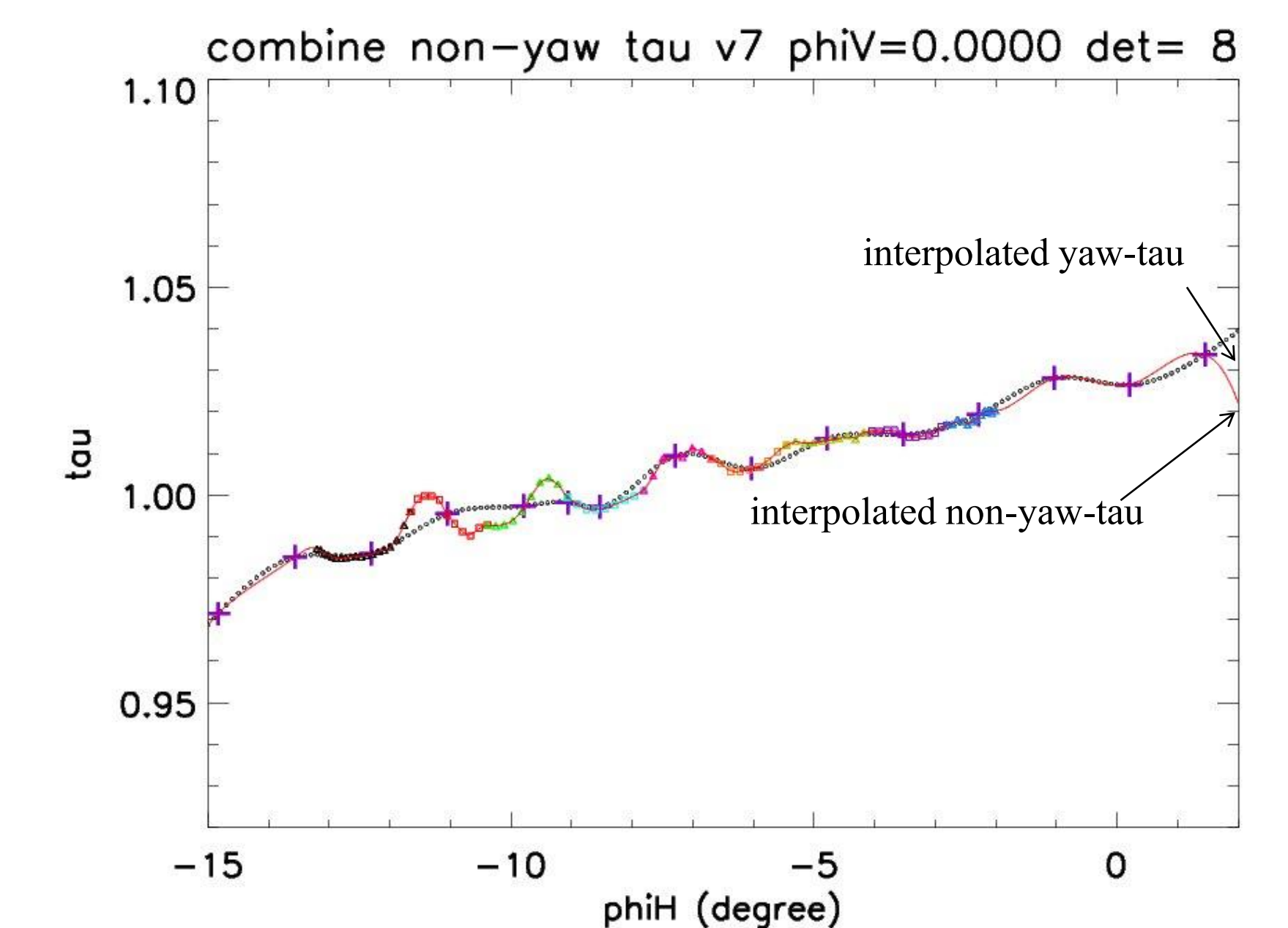


Very fine step size in ϕ_H , able to resolve transmittance in detail.

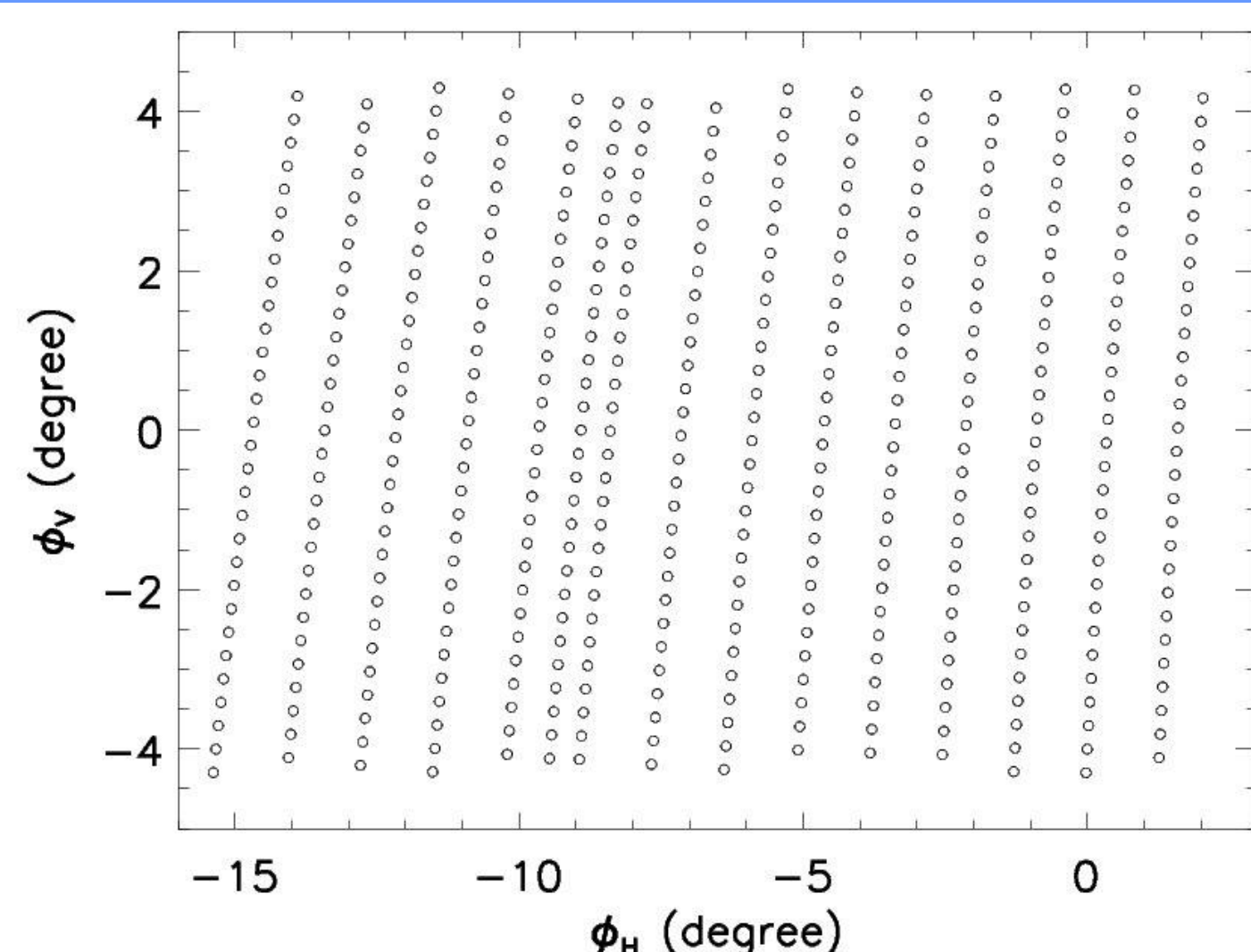
Procedure

- (1) Divide the regular on-orbit data (~3-month) into segments with each covers one yaw maneuver orbit in solar angles.
- (2) Compute transmittance for each segment and interpolate the transmittance at the yaw maneuver solar angles.
- (3) Tau(yaw) and Tau(non-yaw) differ by a scale factor due to drifts in solar power and the SDSM detector gain, find the scale factor through a least-square fit; multiply Tau(non-yaw) by the scale factor.
- (4) Combine tau(non-yaw) with linear adjustments.

Combine non-yaw tau from the segments

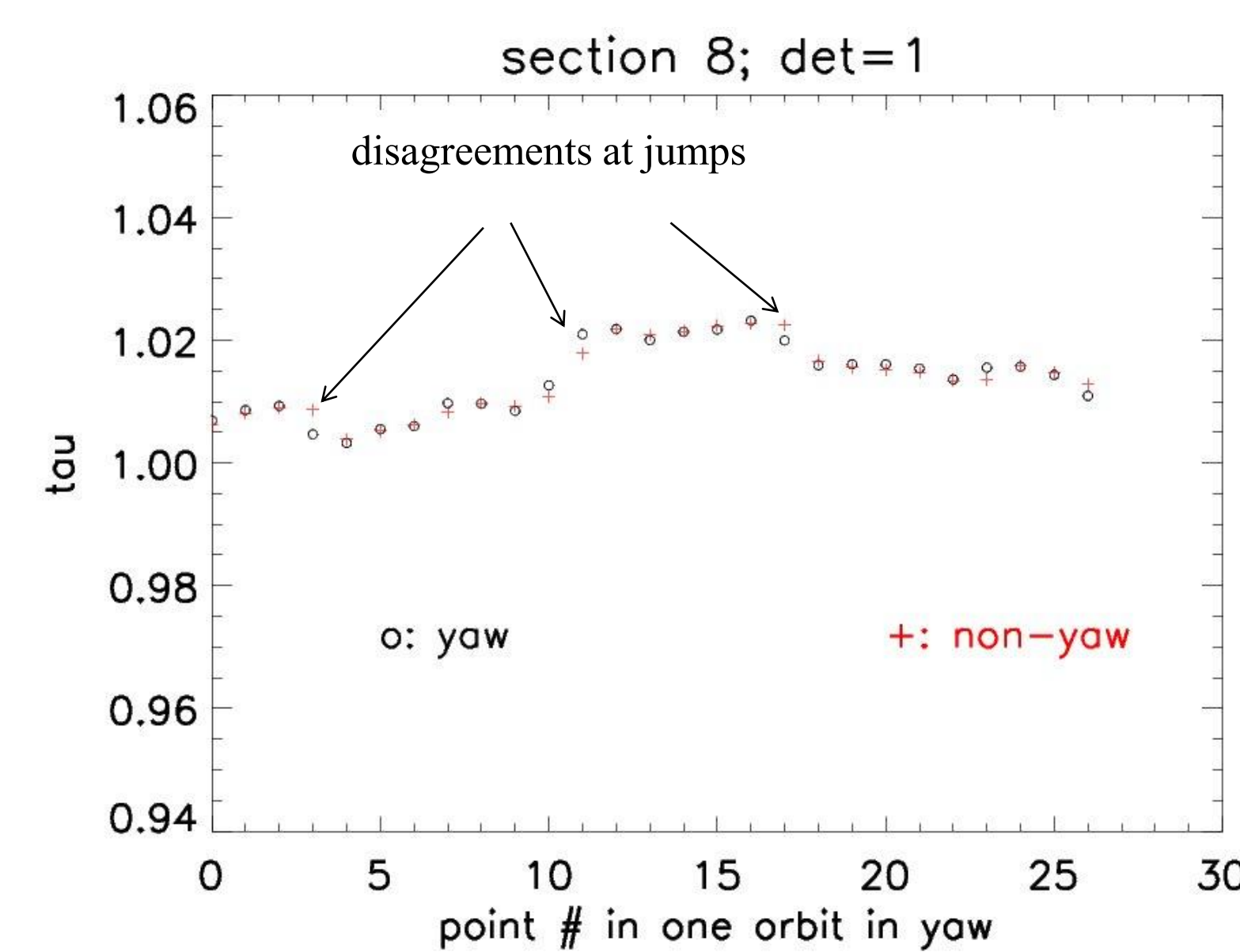


Yaw maneuver data

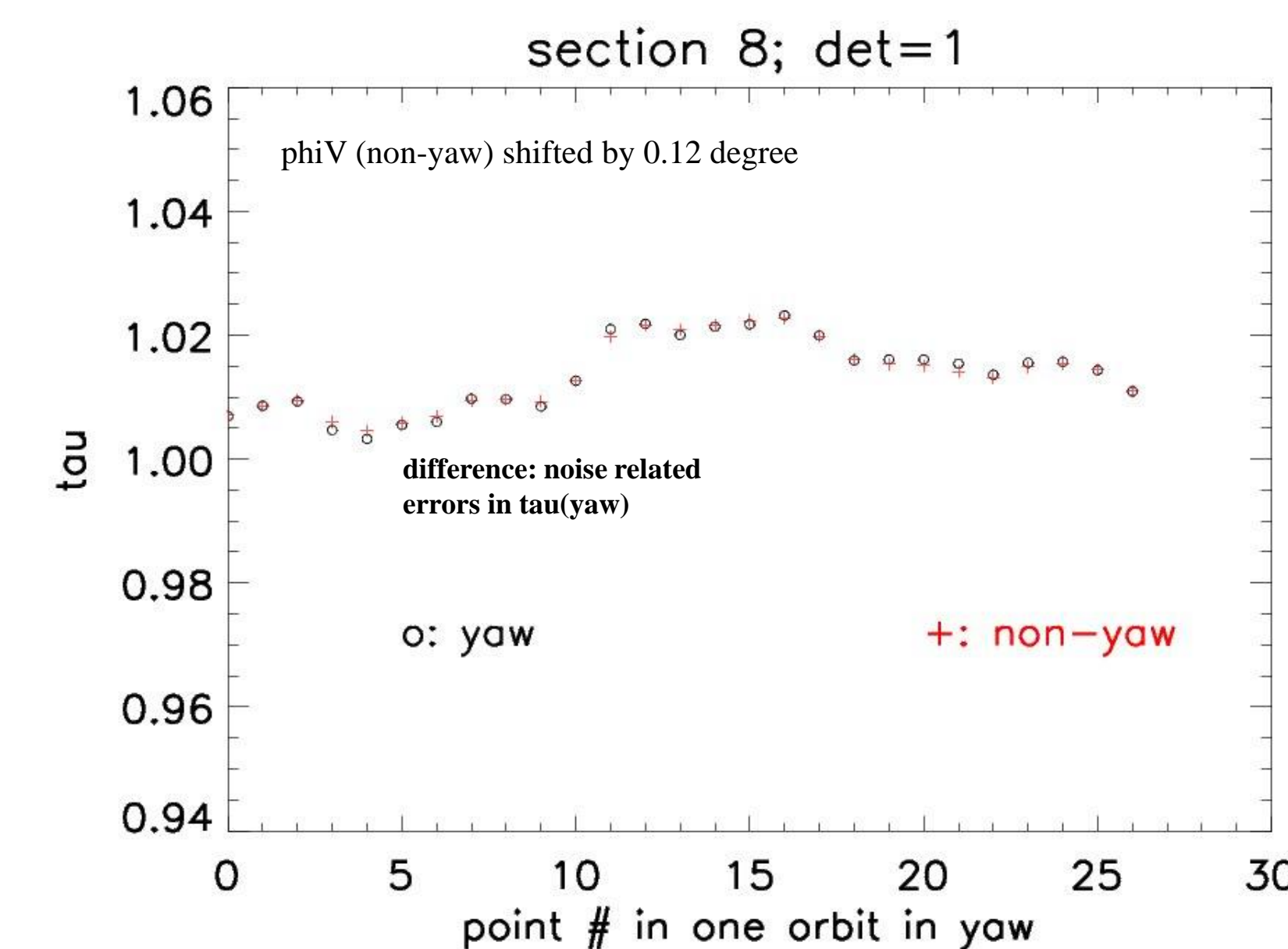


Large step size in ϕ_H , not able to resolve transmittance in detail.

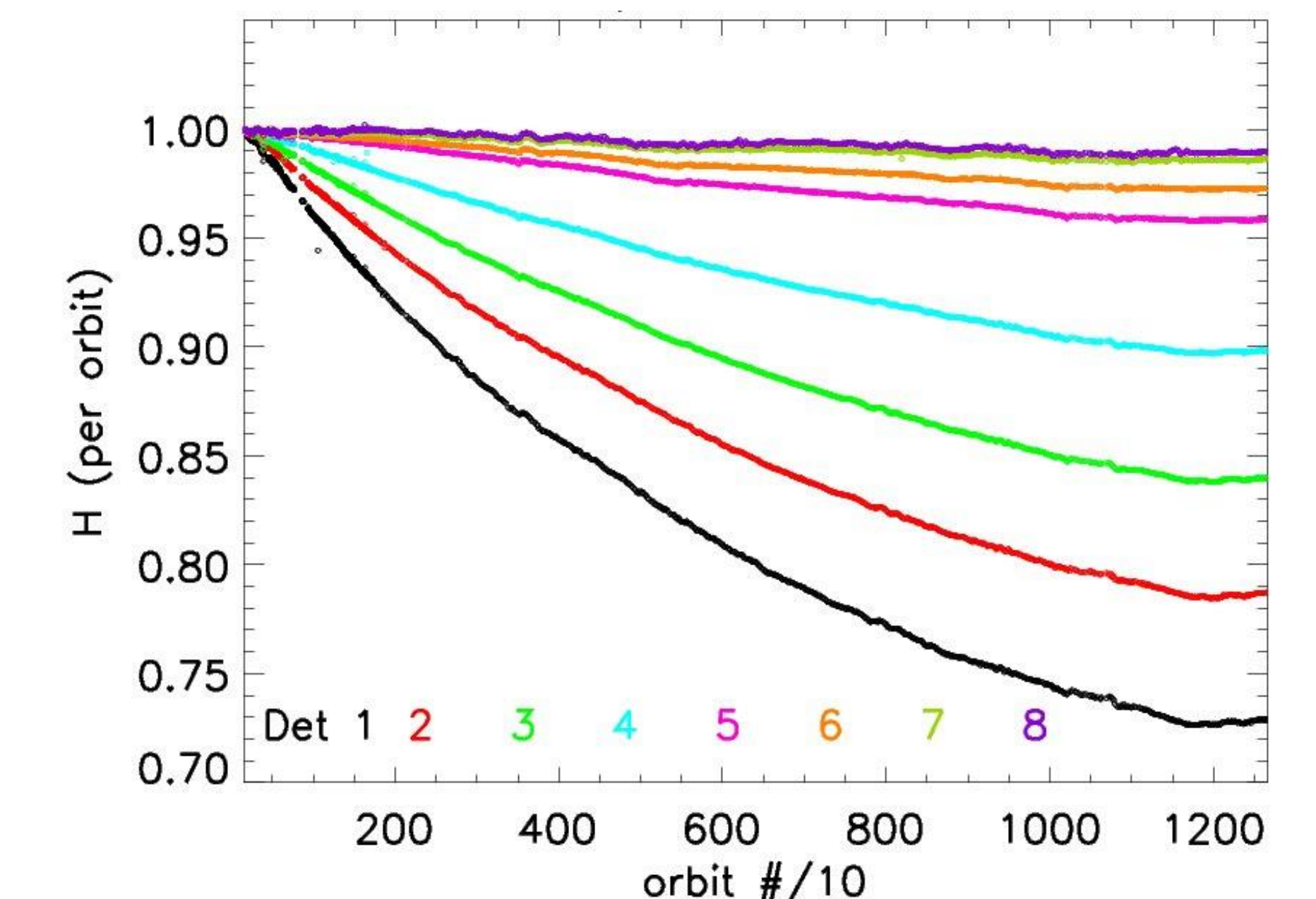
Mismatch at the jumps



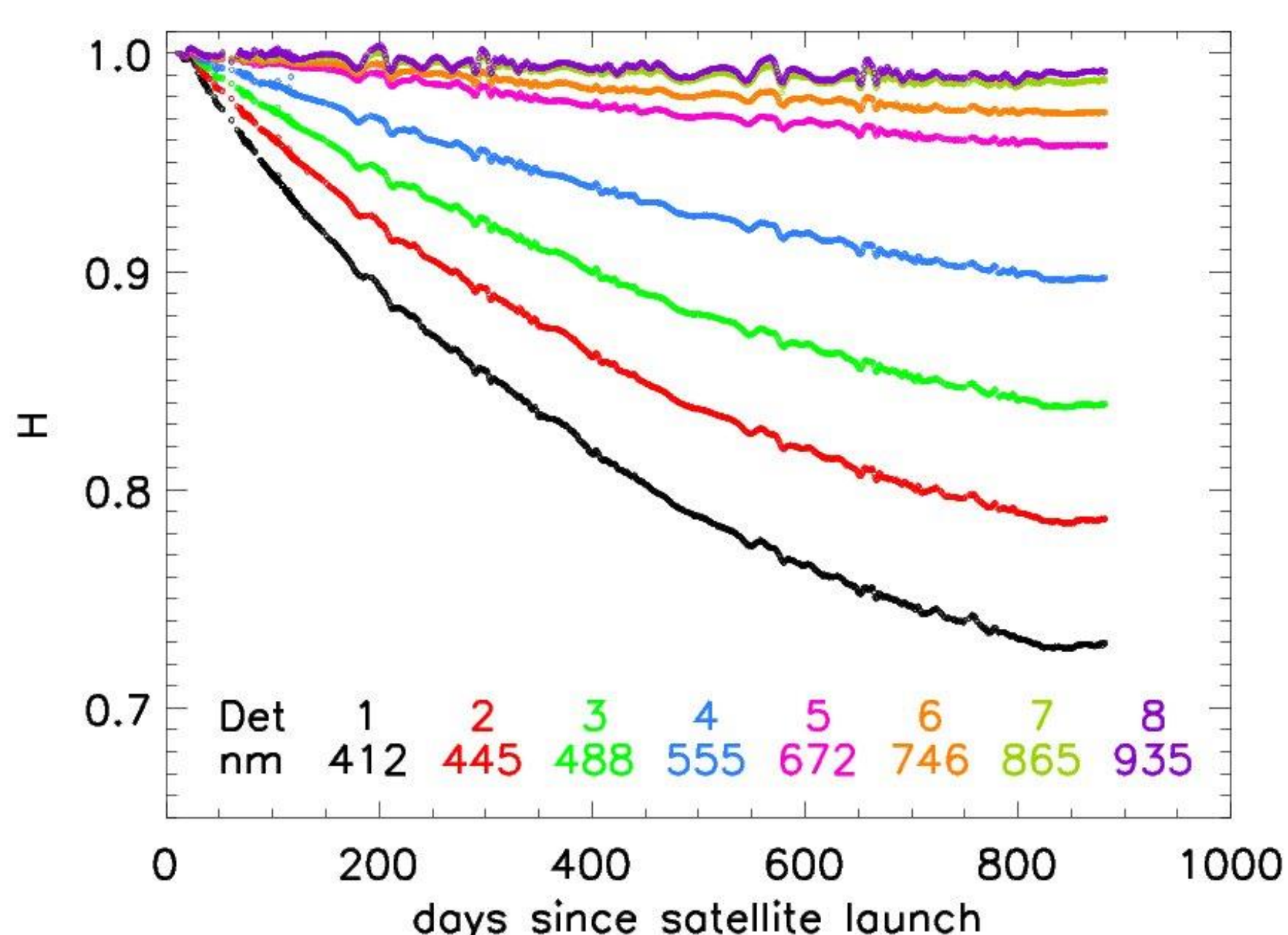
Shift in phiV to make a better match



Smoother BRDF degradation coefficients

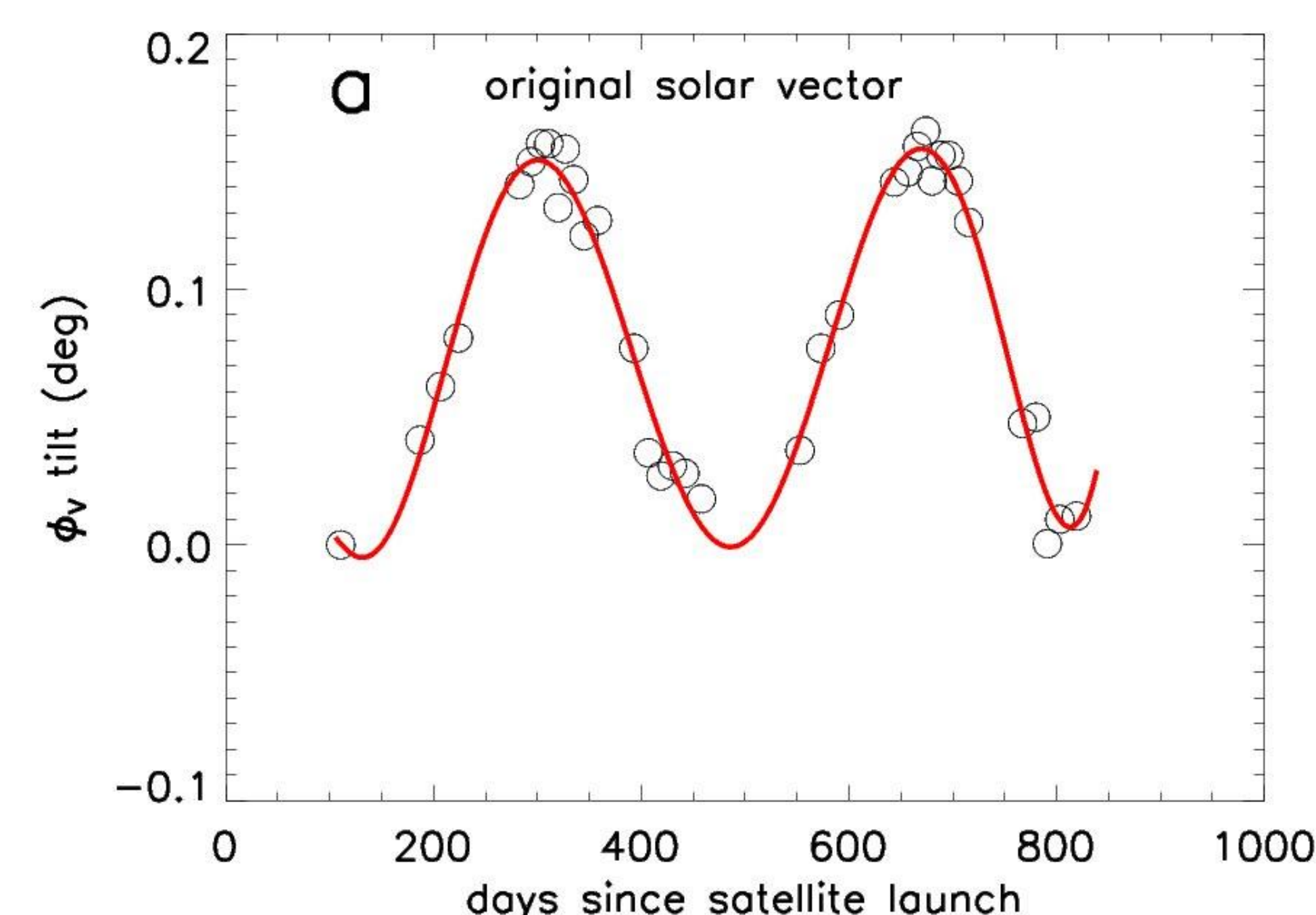


BRDF degradation coefficient

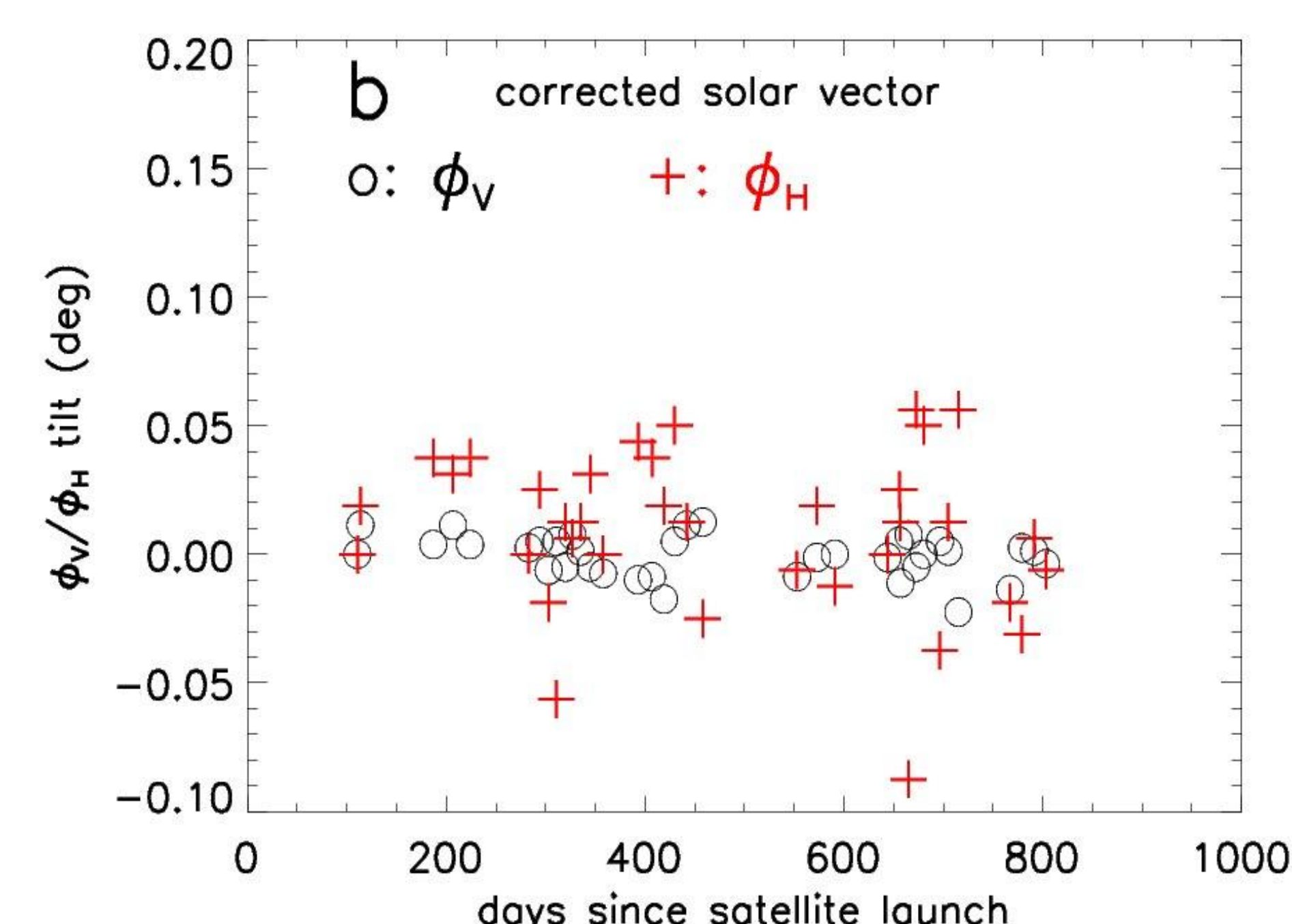


Degradation coefficient curves are not smooth.

phiV shift over time: solar vector error



Solar angle shift with corrected solar vector

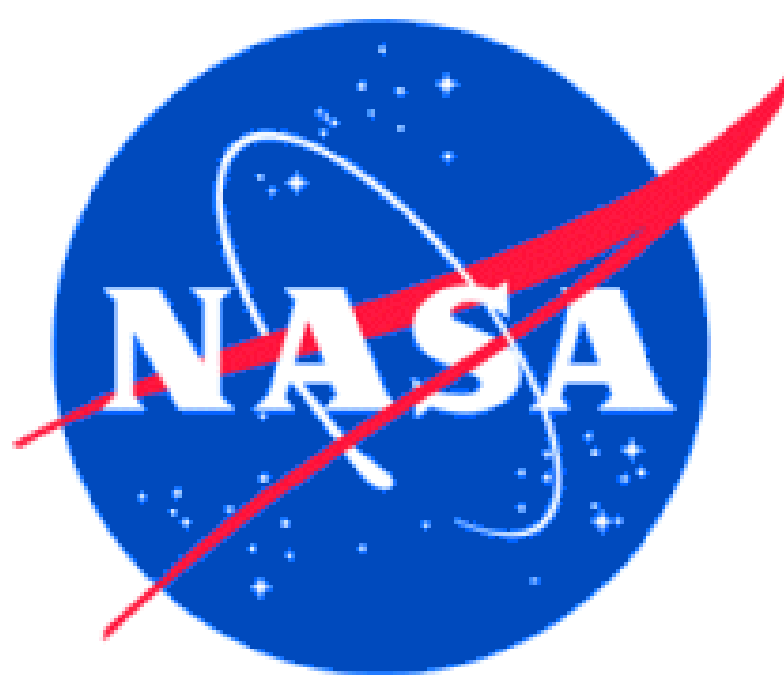


Summary

- (1) SDSM screen transmittance is computed more accurately with 3-month of regular on-orbit data.
- (2) Relative transmittance error standard deviations are computed with the help of validation data at: 0.00059, 0.00045, 0.00039, 0.00035, 0.00033, 0.00033, 0.00058, 0.00099, for SDSM detectors 1 to 8, respectively.
- (3) SDSM screen is stable over time.

Acknowledgement

We thank Samuel Anderson, Jon Fulbright, and Zhipeng Wang of NASA-VCST for providing corrected solar vectors for this work.



S-NPP Solar Vector Error with the Common GEO Code: The Correction and the Effects on the VIIRS SDR RSB Calibration

VIIRS Characterization Support Team (VCST), NASA/GSFC

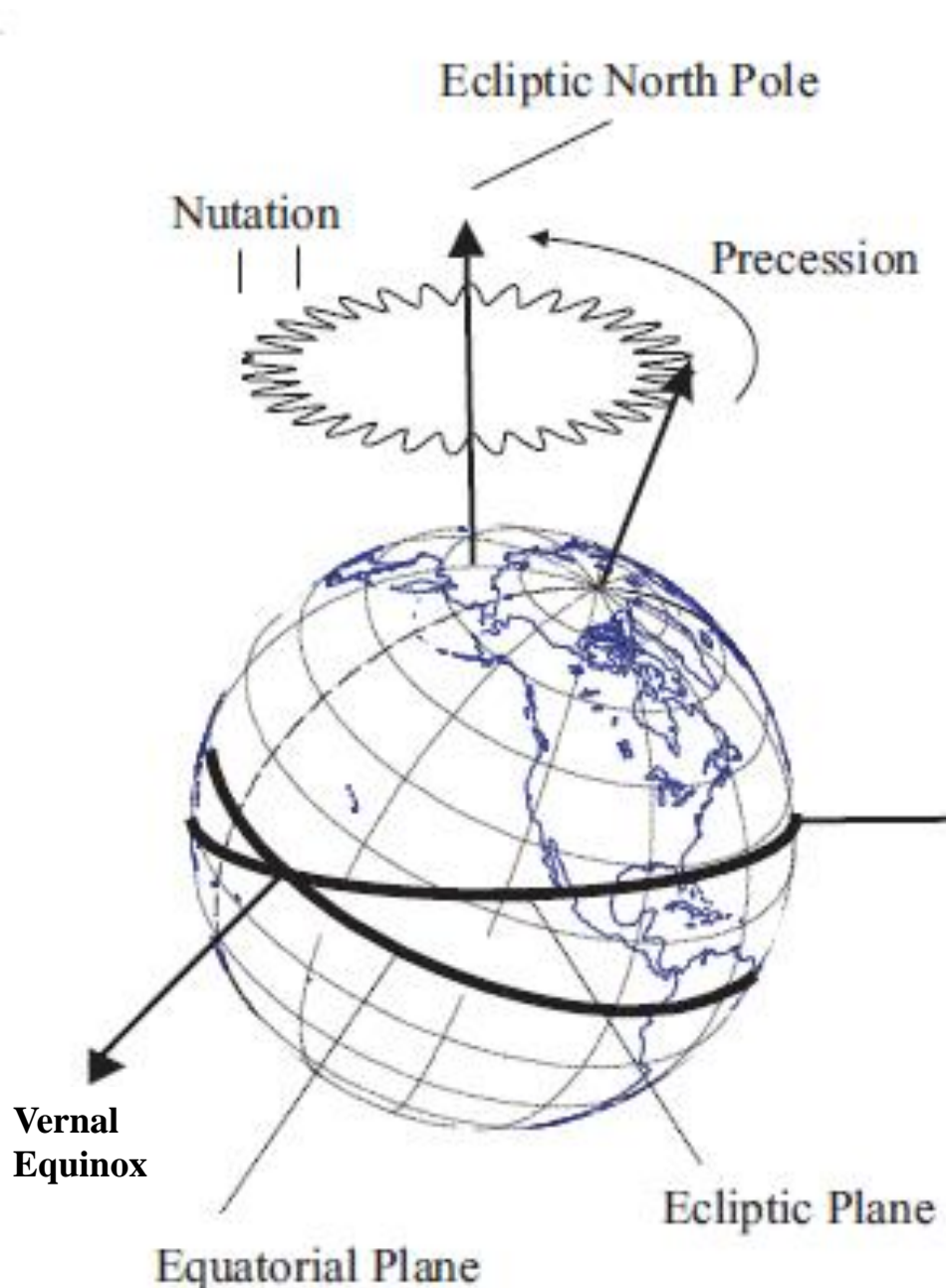
Jon Fulbright*, Samuel Anderson*, Ning Lei*, Boryana Efremova*, Zhipeng Wang*, Jeff McIntire, Kwofu (Vincent) Chiang*, Ning Lei*, and Xiaoxiong (Jack) Xiong**



Introduction

The Visible Infrared Imaging Radiometer Suite (VIIRS) uses the Sun as the primary radiometric calibrator for the Reflective Solar Bands (RSB). The calibration relies upon the once-per-orbit measurements of sunlight incident upon the Solar Diffuser (SD), which happens once per orbit. Further, the status of the reflectivity of the Solar Diffuser relies upon the measurements made with the Solar Diffuser Stability Monitor (SDSM), which also uses the Sun as the calibration light source. Both calibrations, as well as several EDR data products, require an accurate solar (and/or lunar) position vector in order to calibrate their SDR and/or EDR products. The vector is used in the transmission functions of the SD and SDSM screens, the calculation of the SD BRDF, and solar incident angles. In early 2014, it was shown that the NPP solar vector was in error.

Geocentric Inertial Reference Frames



The source of the error is the misuse of two Earth-Centered Inertial (ECI) reference frames. The SDR code was calculating the relative position of the spacecraft and the Sun in "True of Date" (TOD) coordinates, where the x- and z-axes are defined by the direction of the vernal equinox and the North Pole at the ephemeris time. However, the rotation from ECI to the spacecraft coordinates is in J2000 coordinates, where the axes are locked to their positions at 12 UT 01/01/2000.

The TOD and J2000 systems are identical at that time, but drift apart due to the changing orientation of the poles and the orientation of the Earth's orbit. The error in early 2014 had grown to about 0.2 degrees.

Magnitude of the Solar Vector Error

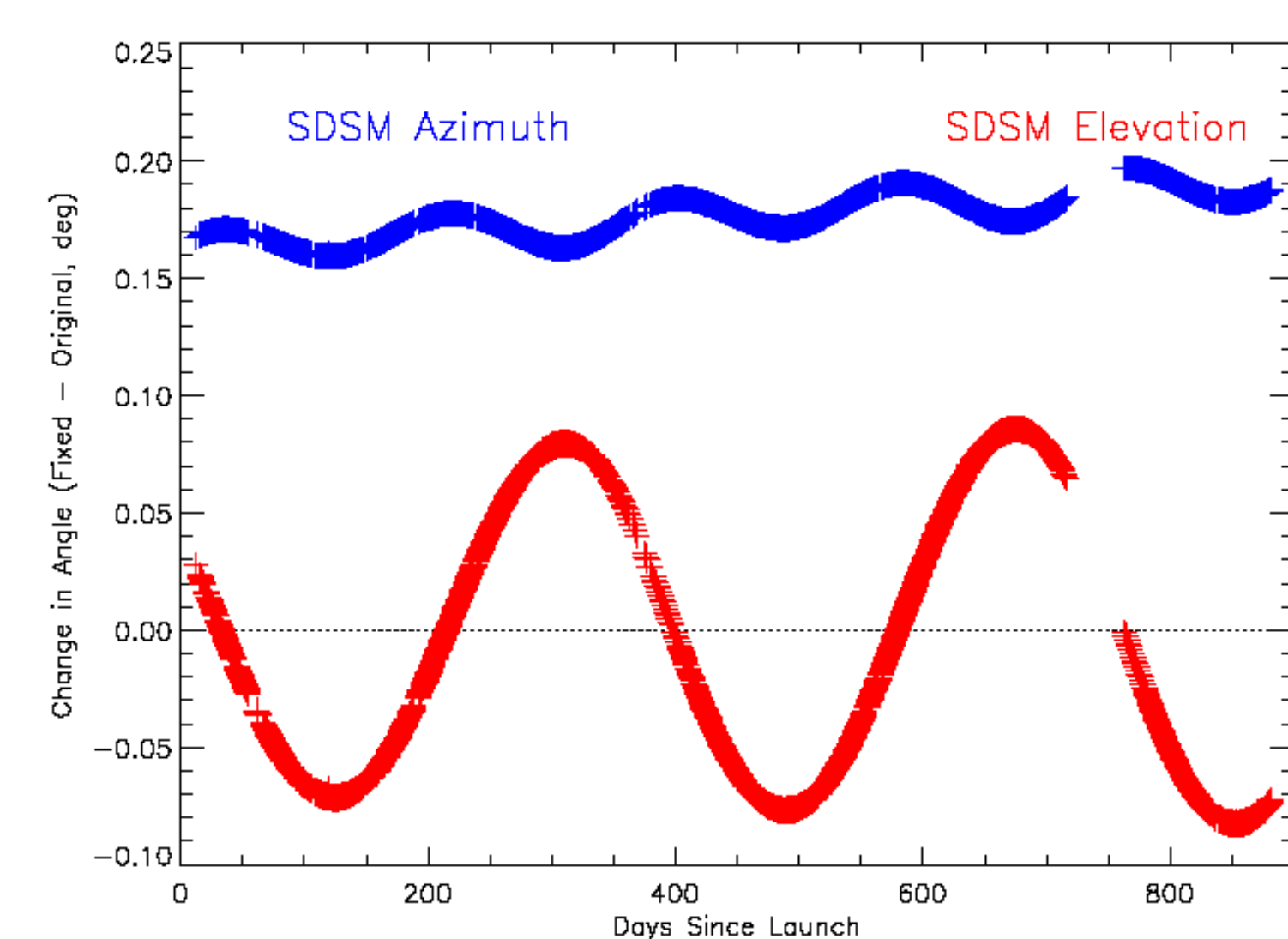


Figure 1. The difference in the SDSM Sun View elevation and azimuth angles as a function of time between the "wrong" value returned by the SDR code and the "fixed" values after recalculation. The error grows with time, but there is also an annual cycle.

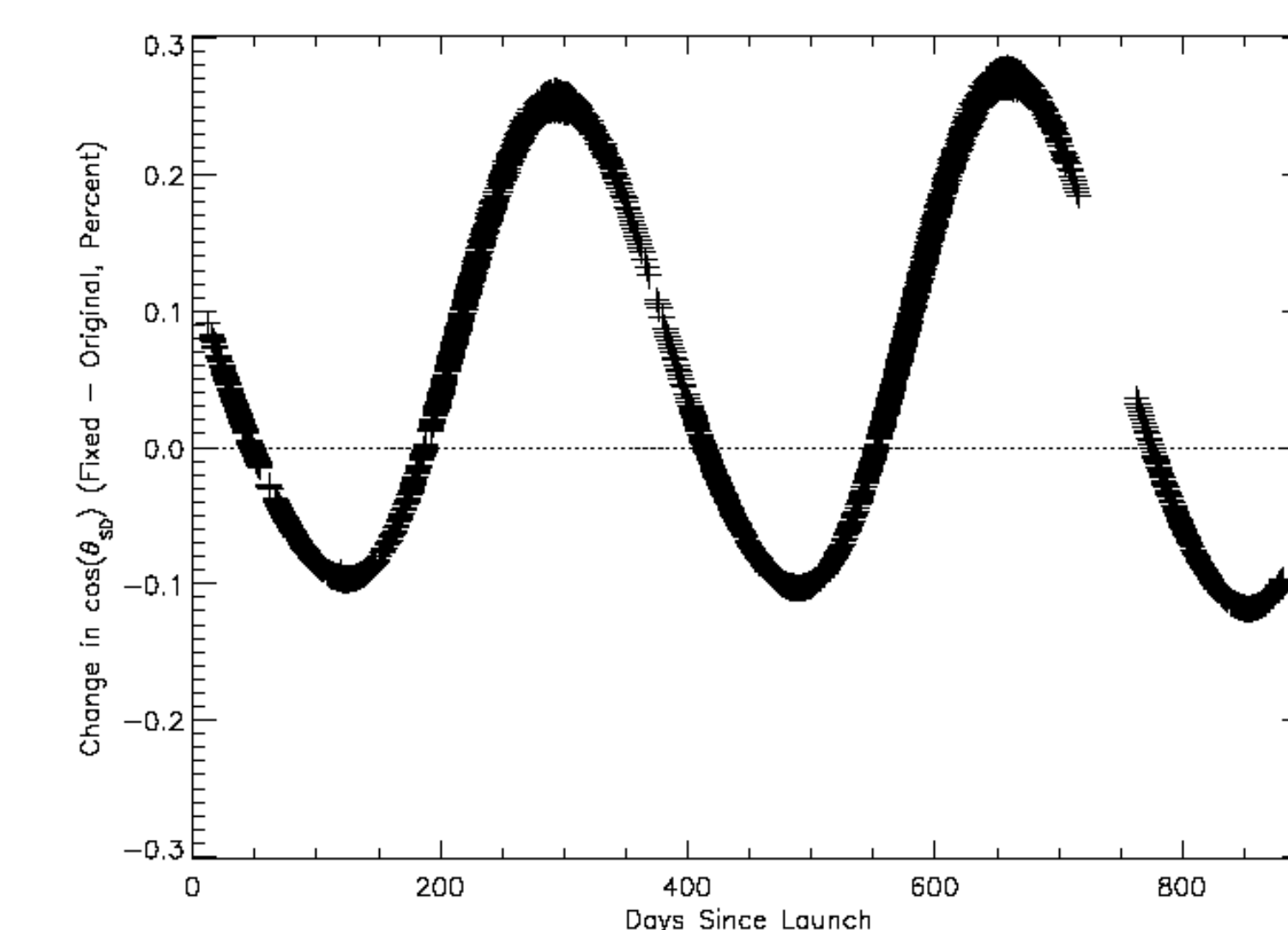


Figure 2. The difference in the cosine of the angle of solar incidence to the SD panel normal. This value is used in both the SDSM and SD algorithms. The magnitude of the change (about 0.4% peak-to-peak) is a potentially larger effect than the angle error to the screen transmission values.

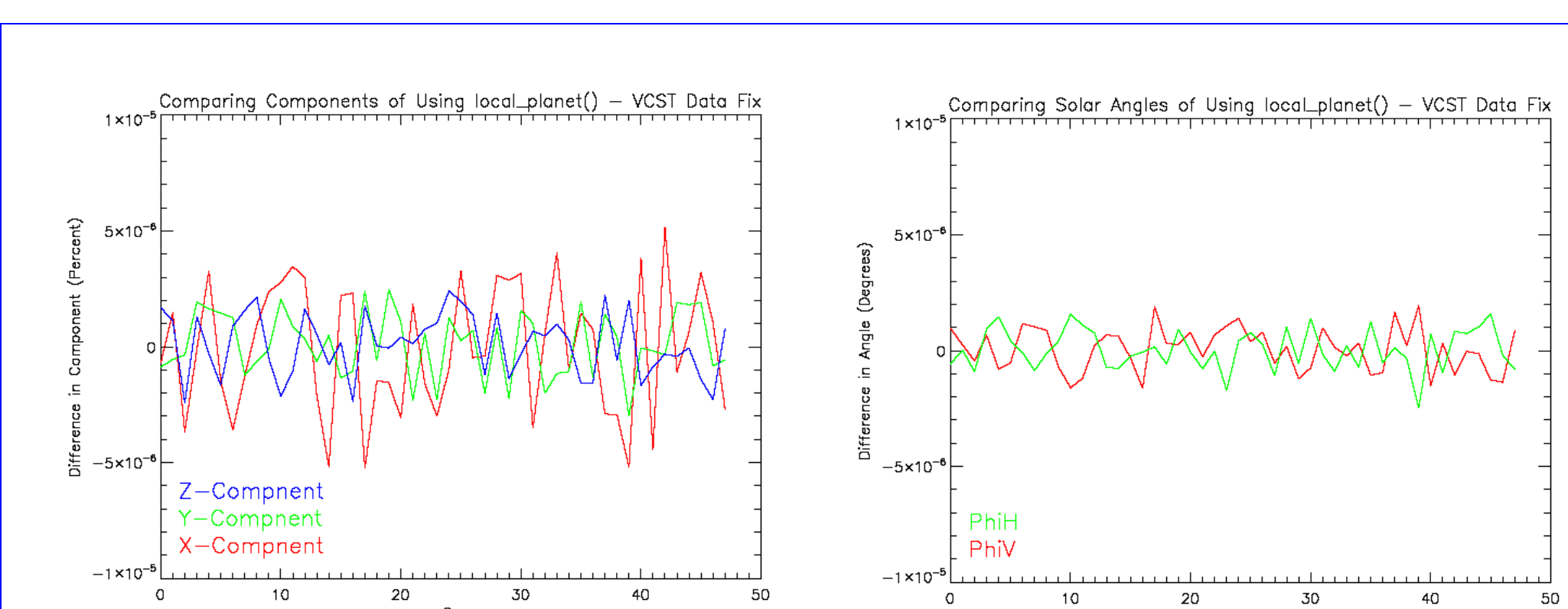
Fixing the Error in the SDR Code

The SDR code calculates the solar vector (the vector from NPP to the Sun) and lunar vector (Moon to NPP) in TOD coordinates using the Common GEO routine `topo_planet()` (from the USNO "NOVAS-C" package). This inputs for this package include the time, the spacecraft position (from the Spacecraft Diary), and polar wander parameters.

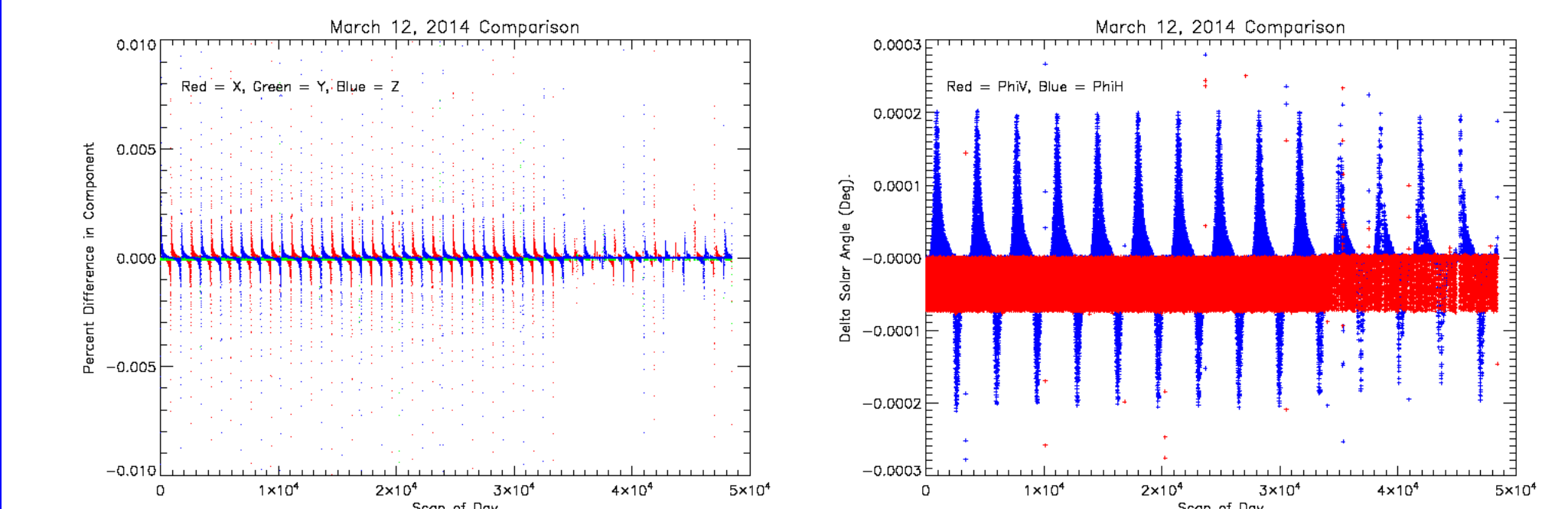
The Common GEO package includes a similar routine called `local_planet()`. It uses the same input parameters, but it produces output in the J2000 coordinate system. Replacing `topo_planet()` with `local_planet()` the two times it occurs in the code fixes the problem.

The fix was tested using routines from the NASA/NAIF "CSPIEC" package. The test data does not include polar wander and invoked a different method to interpolate the spacecraft attitude rotation data, which leads to the small differences seen below.

Comparison of "Fixed" Solar Vectors



Figures 3 (left) and 4 (right). The difference in the solar vector components (in percent; left) and the SDSM Sun View elevation and azimuth angles (in degrees; right) for a sample 48-scan granule.



Figures 5 (left) and 6 (right). The difference in the solar vector components (in percent; left) and the SDSM Sun View elevation and azimuth angles (in degrees; right) for a full day. The periodic larger differences are due to the different quaternion interpolation methods (the VCST method uses the "sleep" method commonly used by 3-D animation software). The offset is due to the VCST method not including polar wander. The differences, however, are much smaller than the 0.02 degree uncertainty in the spacecraft attitude data as given in the Spacecraft Diary.

Revising the Mission Data Archive

The solar vector error has been in the SDR code since launch. All OBCIP files contain this solar and lunar vector error.

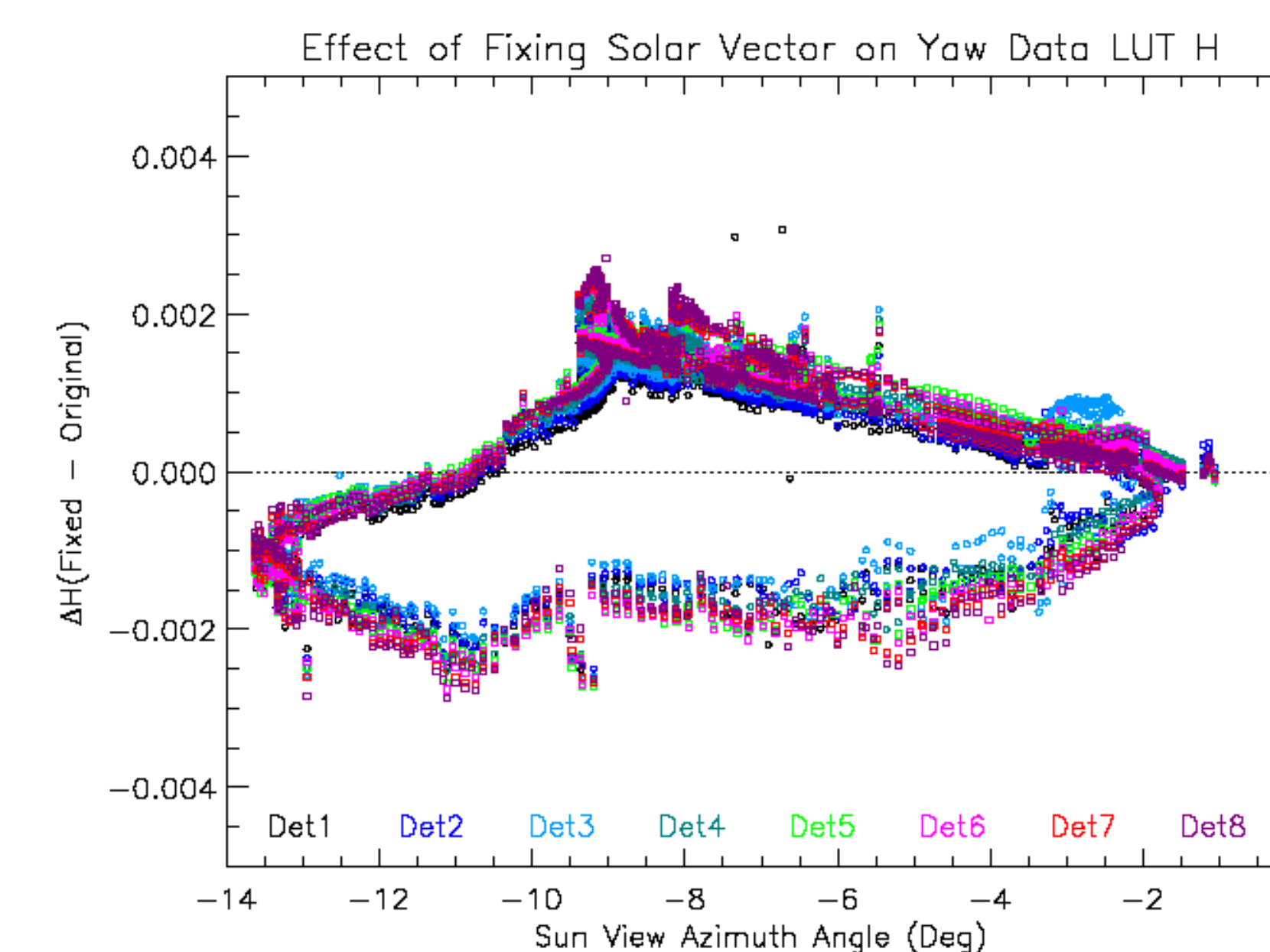
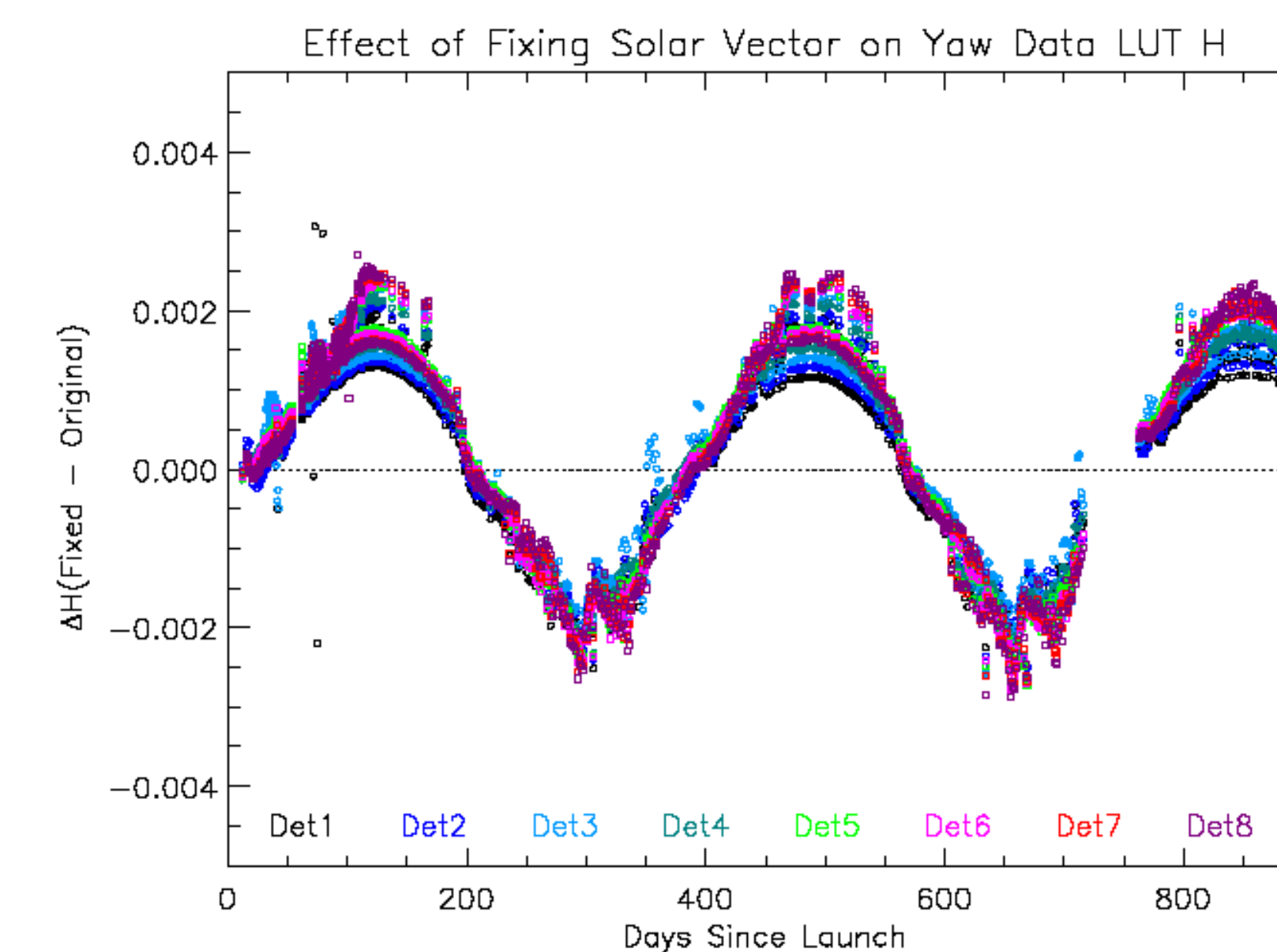
One solution is to recreate all the OBC files using a revised SDR code. There are practical concerns on the amount of computing time and bandwidth necessary for the reprocessing and delivery of the product.

For internal use, VCST has developed an algorithm that takes the present solar and lunar vectors as found in the OBC files as input. These vectors are in spacecraft frame coordinates. They are then "de-rotated" to TOD frame coordinates using Spacecraft Diary information. Then the TOD frame vector is rotated to the J2000 frame by the known transformation between the two. Finally, the Spacecraft Diary attitude data are again used to rotate the vector back into spacecraft frame. This correction is fast and can be done "on the fly" if one has the Spacecraft Diary information available.

Alternatively, a separate solar/lunar vector LUT could be created for each time period (day, orbit, or granule) to be read in replacing the present data.

Note: Many of the calibration algorithms assume "instrument coordinates", which are slightly rotated from "spacecraft coordinates", but this rotation is not presently included in the SDR code.

Effect of Solar Vector Correction on H-factors



Figures 7 (top) and 8 (bottom). The difference in H-factors from before and after the solar vector correction as a function of time (top) and SDSM Sun View azimuth angle (bottom). The change in H-factors over the lifetime of the mission is dominated by the seasonal variation, which is itself dominated by the change in $\cos\theta_{SD}$.

Revising the H-factors requires more than just fixing the input solar vector. The screen transmission functions are defined by data from the yaw-maneuvers and other on-orbit data. If the screens were created with the original solar vector data, then they are incompatible with the new, fixed solar vectors.

Therefore, VCST re-created the τ_{sun} and $\tau_{SD} * BRDF_0$ functions from on-orbit data using the corrected solar vector throughout the process.

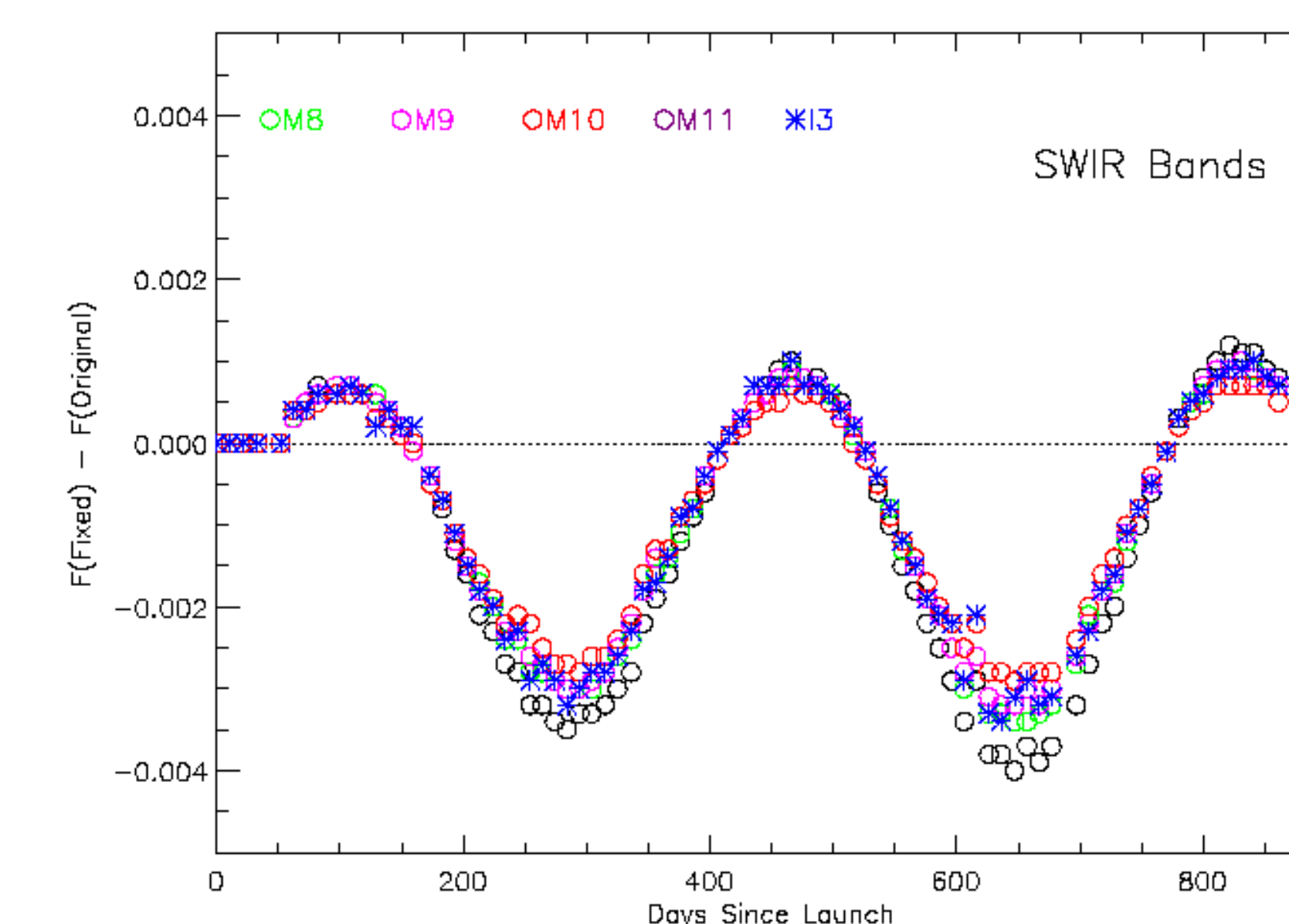
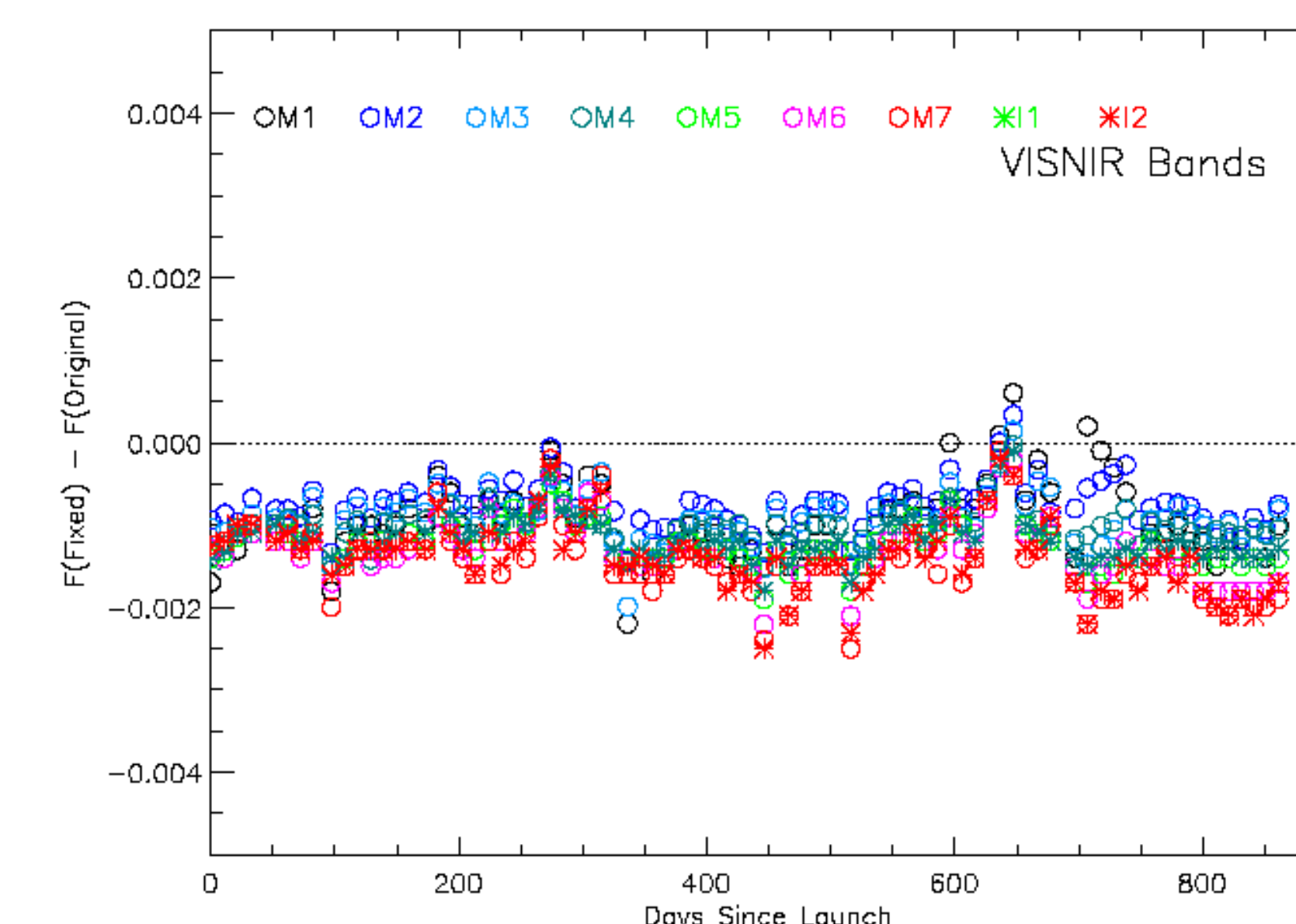
The results are shown above. The dominant feature is the seasonal variation in the change in H-factors, which is a result in the change in $\cos\theta_{SD}$ (see Figure 2). The H-factor is proportional to $1/\cos\theta_{SD}$ which is why the seasonal variations are the opposite of what is seen in Figure 2. There is a slow growing offset, too, but this is small in comparison to the seasonal trend.

The H-factors are normalized to $H = 1$ for all bands at launch. This minimizes the effects of the offset in angles from before launch.

Acknowledgements

We thank members of the VCST GEO Team, especially Masahiro "Mash" Nishihama and Gary Lin for their valuable assistance, especially their help in the identification of `topo_planet()` as the source of the error.

Effect of Solar Vector Correction on F-factors



Figures 9 (top) and 10 (bottom). The difference in f-factors from before and after the solar vector correction as a function of time for the VISNIR bands (top) and the SWIR bands (bottom). The change in $\cos\theta_{SD}$ cancels for the VISNIR bands, but for the SWIR bands, the value of H is forced to be 1.

As for the H-factors, the $\tau_{SD} * BRDF_0$ screen for the main VIIRS detectors had to be derived again from the beginning to incorporate the effects of the change in solar vector. The F-factor is proportional to H and $\cos\theta_{SD}$, and for the VISNIR bands (M1-M7, I1-I2 and the DNB) the H-factor is proportional to $1/\cos\theta_{SD}$, so the effects cancel out. The offset -0.001 offset in the VISNIR bands is due to the renormalization of the H-factors at $t = 0$, which means that normalization factor is not removed.

For the SWIR bands, the assumption is that the SD panel does not degrade at those wavelengths. As a result of that assumption, $H_{SWIR} = 1$. That means there is no canceling of the $\cos\theta_{SD}$ effect.

An important additional note: The change in the F-factors seen here is not enough to resolve the differences between the F-factors derived by lunar and SD methods (see poster by Z. Wang). It will not even directly explain the F-factor seasonal fluctuations over the year for the SD VISNIR bands.

Conclusions and Further Effort

The solar vector error is large enough to require careful consideration of its effects on the RSB calibration. The changes will not cause wholesale revisions of the radiometric calibration, but it may explain some, but not all, of the seasonal variation seen in the F-factors.

There are other aspects of the solar and lunar vector error that are not addressed here (such as the effect on lunar intrusion into the Space View port), so further work is required.

Easy Access to the VIIRS Science Raw Data Record

James C. Biard - CICS-NC
jim.biard@noaa.gov

Linda Copley - CICS-NC
linda.copley@noaa.gov

Drew Saunders - NOAA NCDC
drew.saunders@noaa.gov

Jeff Privette - NOAA NCDC
jeff.privette@noaa.gov

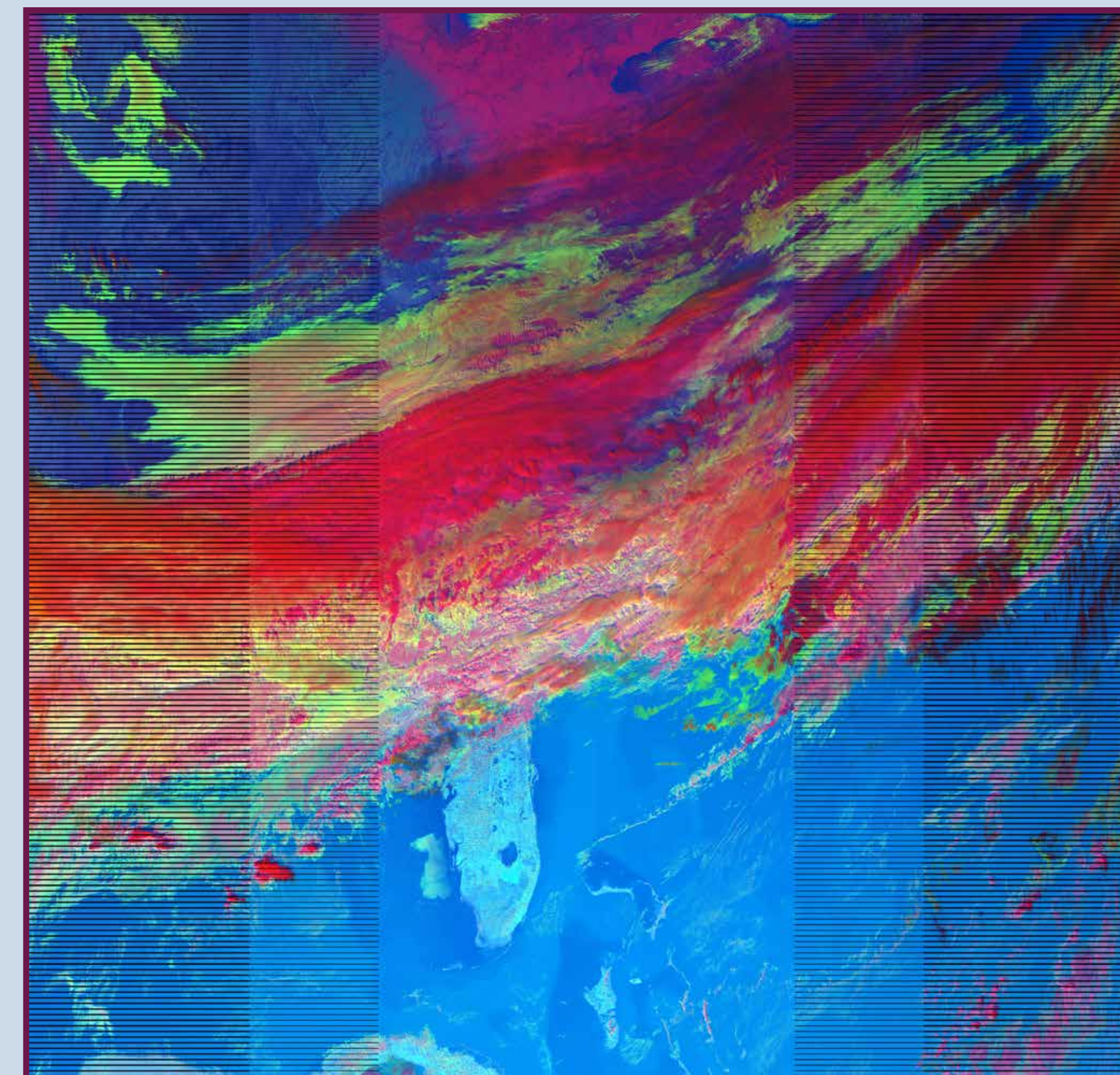
Introduction

The Climate Raw Data Record (C-RDR) Project at NOAA's National Climatic Data Center (NCDC), under the auspices of the Climate Data Record Program (CDRP), is producing a NOAA Level 1b (NASA level 1a) dataset for the VIIRS instrument on the Suomi National Polar-orbiting Partnership (SNPP) satellite. A Level 1b dataset contains "unprocessed data at full resolution, time-referenced, and annotated with ancillary information including data quality indicators, calibration coefficients and georeferencing parameters." [FGDC-STD-012-2002] This dataset is being produced operationally and is being archived and made available for public use.

The NOAA Interface Data Processing Segment (IDPS) produces Raw Data Record (RDR), Sensor Data Record (SDR), and Environmental Data Record (EDR) datasets for the VIIRS instrument. The RDR dataset is processed to NOAA Level 1a (NASA level 0), and it contains time-sequenced and indexed Consultative Committee for Space Data Systems (CCSDS) Space Packets containing the VIIRS engineering and science data. The contents of the CCSDS Space Packets have not been unpacked at this level.

The SDRs contain data that has undergone calibration transformations, some of which are complex, and the engineering data that was used in the operations have not been preserved within the datasets. As a result, those who wish to use different calibration values or algorithms must start from the VIIRS Science RDR, which is complex to use and requires a significant custom code base.

Those who want to do diagnostic studies of the VIIRS instrument have to deal with the same issues as those who wish to produce their own SDRs or EDRs from scratch. The VIIRS C-RDR solves these problems by providing an easy to use source for the raw science and engineering measurements.



False-color image created from the raw band 5, 4, and 2 (used as blue, green, and red, respectively) 375 m resolution pixels extracted from the VIIRS C-RDR file with a start time of 18:24:51 GMT, January 28, 2014.

How Is the VIIRS C-RDR Produced?

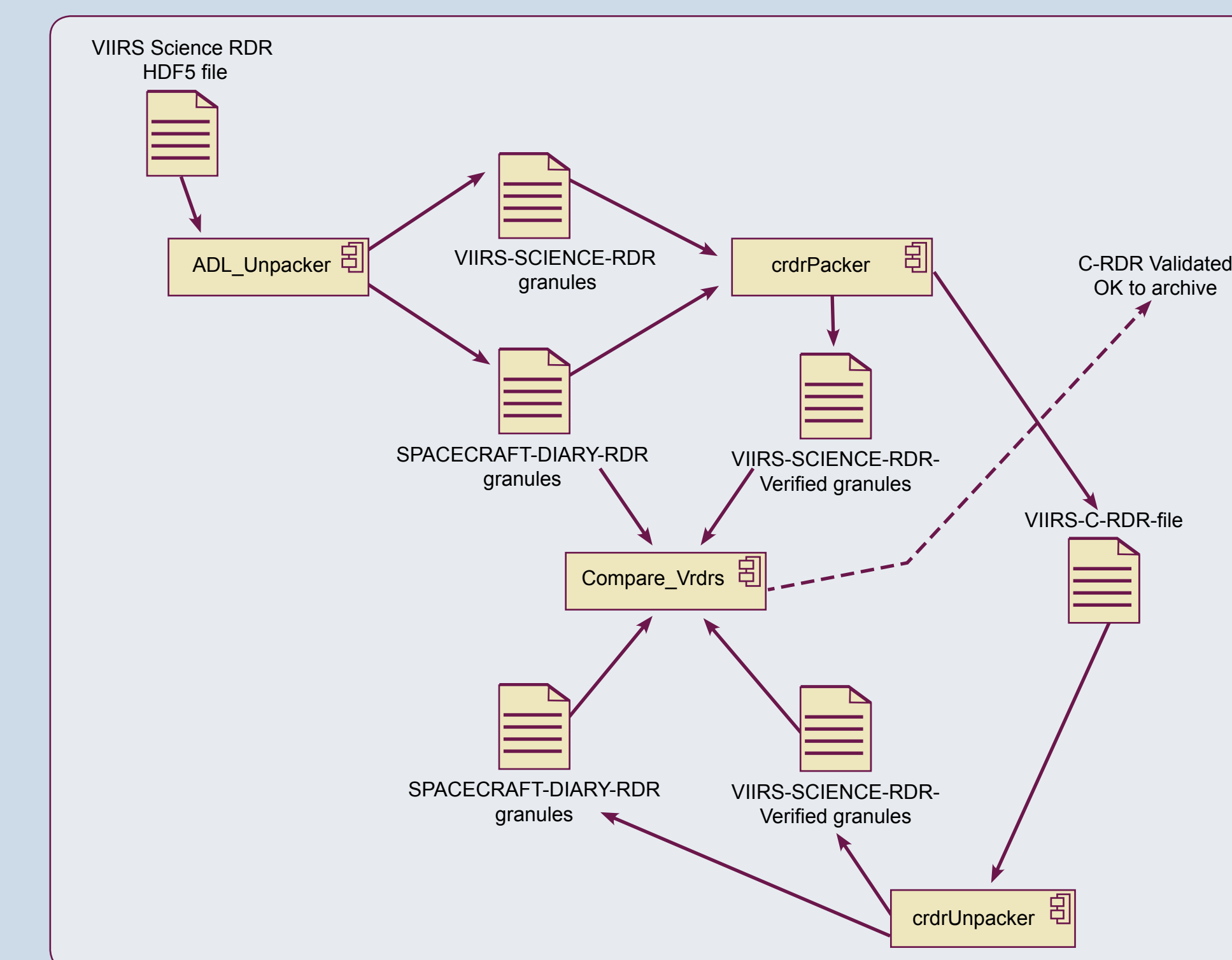
The VIIRS C-RDR is produced by applications developed using the Application Development Library (ADL). ADL provides the data structures and processing framework needed to marshal the VIIRS-SCIENCE-RDR and SPACECRAFT-DIARY-RDR granule inputs. It is generated on a continuous operational basis as files are obtained by subscription from NOAA's Comprehensive Large Array-data Stewardship System (CLASS). The processing includes validation of each VIIRS C-RDR file as part of the workflow.

As each VIIRS Science RDR HDF5 file is obtained from CLASS, it is unpacked into VIIRS-SCIENCE-RDR and SPACECRAFT-DIARY-RDR granule files with accompanying ASCII metadata. The crdrPacker application then reads the granule files, organizes the information into time series arrays, and writes them as variables to a C-RDR file. One VIIRS C-RDR file nominally contains four granules of VIIRS Science RDR data.

The crdrPacker application also produces a set of VIIRS-SCIENCE-RDR-Verified (VRDR) granule files with associated ASCII metadata - one for each VIIRS-SCIENCE-RDR granule. The VRDR granules are the inputs used by all of the IDPS VIIRS SDR algorithms.

The crdrUnpacker application uses the VIIRS C-RDR file just produced to create VRDR and SPACECRAFT-DIARY-RDR granule files with accompanying metadata. The SPACECRAFT-DIARY-RDR granules files and metadata should be identical to those extracted from the VIIRS Science RDR HDF5 file, and the VRDR granule files and metadata should be identical to those produced by the crdrPacker application.

If the VRDR and Spacecraft Diary RDR files are found to match one another, the VIIRS C-RDR file is considered to be validated and is submitted to the archive system for long-term storage and public access.



What Does the VIIRS C-RDR Contain?

The VIIRS C-RDR contains raw, unpacked engineering and science data from VIIRS Science RDR granules, along with satellite position, velocity, attitude, and operation state data from associated Spacecraft Diary RDR granules, stored as time-series variables in Network Common Data Form 4 (netCDF-4) files. The netCDF-4 format is platform-independent, binary, hierarchical, and self-describing. Each variable within a VIIRS C-RDR file is annotated with a description of the measurement it contains, information about the source, and specifications of valid limits and fill values.

The image data, which were differentially encoded and compressed using the RICE algorithm by the VIIRS on-board processing, are decompressed, decoded, and stored as multi-band images in the VIIRS C-RDR files. Each VIIRS C-RDR file also contains 70 elements of file-level metadata conforming to the Climate and Forecast (CF) metadata conventions, the Attribute Convention for Dataset Discovery (ACDD), and the JPSS RDR/SDR metadata standards.

The measurements inside a VIIRS C-RDR file are organized into groups of measurements that share a common type or theme.

VIIRS C-RDR Variable Groups		
Group	Number of Variables	Description
Quality_Measures	4	Per-scan counts of missing packets, bad check-sums, and discarded packets, and the per-scan RDR quality measure.
Engineering_Data	242	All the raw VIIRS engineering measurements with time stamps.
Image_375m	8	The raw earth view and calibration view for the 5 VIIRS imaging-resolution bands, along with time stamps and band control words.
Image_750m_DualGain	10	The raw earth view and calibration view for the 7 VIIRS dual-gain moderate-resolution bands, along with gains, time stamps, and band control words.
Image_750m_SingleGain	8	The raw earth view and calibration view for the 9 VIIRS single-gain moderate-resolution bands, along with time stamps and band control words.
Image_DayNight	12	The raw earth view and calibration view for the VIIRS day/night band, along with time stamps, aggregation mode, active sample counts, and band control words.
Spacecraft_Diary	10	The satellite position, velocity, and attitude vectors, a selection of housekeeping telemetry elements, and accompanying time stamps.
Spacecraft_Diary/ADCS_Hous_keeping_Telemetry	3	Full APID 8 packets, along with the packet sequence counter and fill percentage metadata.
Spacecraft_Diary/Bus_Critical_Telemetry	3	Full APID 0 packets, along with the packet sequence counter and fill percentage metadata.
Spacecraft_Diary/Ephemeris_Attitude_Telemetry	3	Full APID 11 packets, along with the packet sequence counter and fill percentage metadata.

Where Can I Get VIIRS C-RDR Files?

VIIRS C-RDR files can be obtained from the NCDC Hierarchical Data Storage System (HDSS) Access System (HAS). The current holdings start from October 19, 2013, with plans to extend them back to the beginning of VIIRS science mode operation. HAS allows you to search for and order VIIRS C-RDR files based on time. (See the "For more information" section at the end.)

How Do I Read a VIIRS C-RDR File?

Accessing the measurements within a VIIRS C-RDR file is quite straightforward. Since the netCDF-4 format is built on top of the HDF5 format, existing applications that can read either netCDF-4 or HDF5 files can be used to read VIIRS C-RDR files. As an example, IDL and MATLAB both support these formats. The HdfView application produced by the HDF Group can also be used to access and view the contents.

If you are going to write your own application, it takes only a few lines of code to open and read the contents of a variable from a VIIRS C-RDR file. NetCDF-4 and/or HDF5 libraries are available for many languages (C, C++, FORTRAN, Java, and python to name a few). The process is similarly straightforward in other languages.

```
import ucar.nc2.*;
import ucar.ma2.*;

...
// Open the VIIRS C-RDR file.
//
NetcdfFile oDataFile = NetcdfFile.open(sInputFilePath, null);

// Find the calibration view variable for the 750 m dual-gain
// image group. This variable has dimensions of band, calibration
// source, line number, and number of samples.
//
Variable oVar = oDataFile.findVariable("Image_750m_DualGain/calibview");

// Get the dimensions of the variable.
//
int[] anCounts = oVar.getShape();

// Create an array of start indices. They all have the value
// index value of zero.
//
int[] anStarts = new int[anCounts.length];

// Read the values from the variable.
//
Array oValues = oVar.read(anStarts, anCounts);

...
```

Info

For More Information
If you would like to know more about the VIIRS C-RDR, you can go to its NCDC product page at:
<http://www.ncdc.noaa.gov/data-access/satellite-data/satellite-data-access-datasets/c-rdr-viirs>
This page provides links to the data access portal, documentation, and a demonstration Java application that can be used to investigate a VIIRS C-RDR file once you download it. You can also go directly to the HAS data access portal at:
http://has.ncdc.noaa.gov/pls/plhas/HAS.FileAppSelect?datasetname=3658_01



www.ncdc.noaa.gov
www.cicsnc.org

NOAA's National Climatic Data Center Asheville, North Carolina

Protecting the past... Revealing the future

Validation of VIIRS Vegetation Index EDR Using In Situ Radiation Sensor Data

Jiao Wang¹, Tomoaki Miura¹, Anna Kato¹, and Marco Vargas²

- University of Hawaii at Manoa
- NOAA / NESDIS / STAR

Introduction

Satellite vegetation index time series datasets have been used to monitor and characterize seasonal vegetation dynamics in regional to global scales. Visible Infrared Imaging Radiometer Suite (VIIRS) Environmental Data Records (EDR) include two vegetation index (VI) products: Top of the Atmosphere (TOA) **Normalized Difference Vegetation Index (NDVI)** and the Top of the Canopy (TOC) **Enhanced Vegetation Index (EVI)**. Validation of the VI EDR is critical to assure product accuracy and consistency throughout the mission. Ground observation networks are emerging, providing well-calibrated time series measurements at high temporal resolution and data availability, as well as covering a wide range of vegetation types and climates. FLUXNET includes over 500 towers worldwide. Some towers are mounted with sensors measuring radiation which can be processed into VIs.

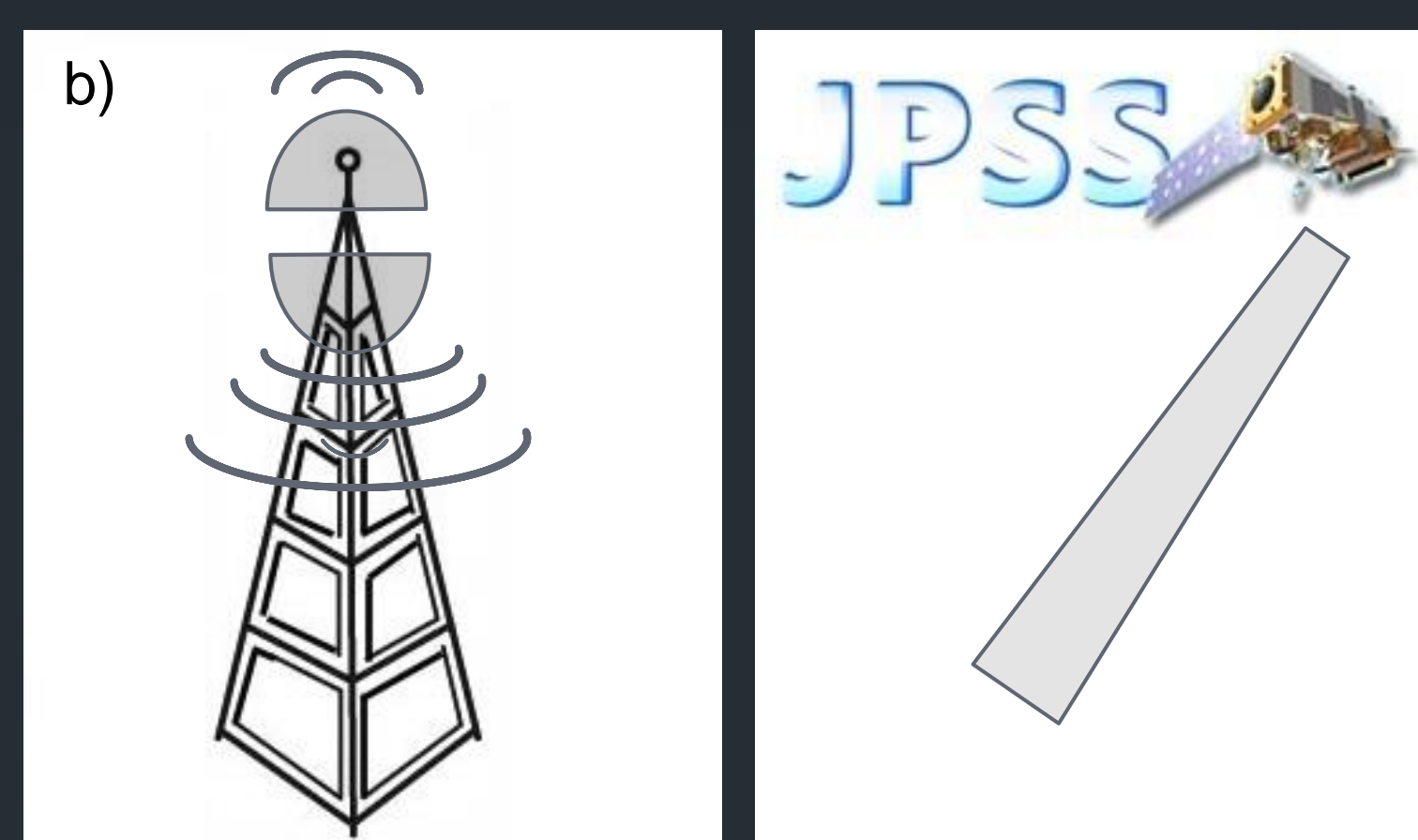
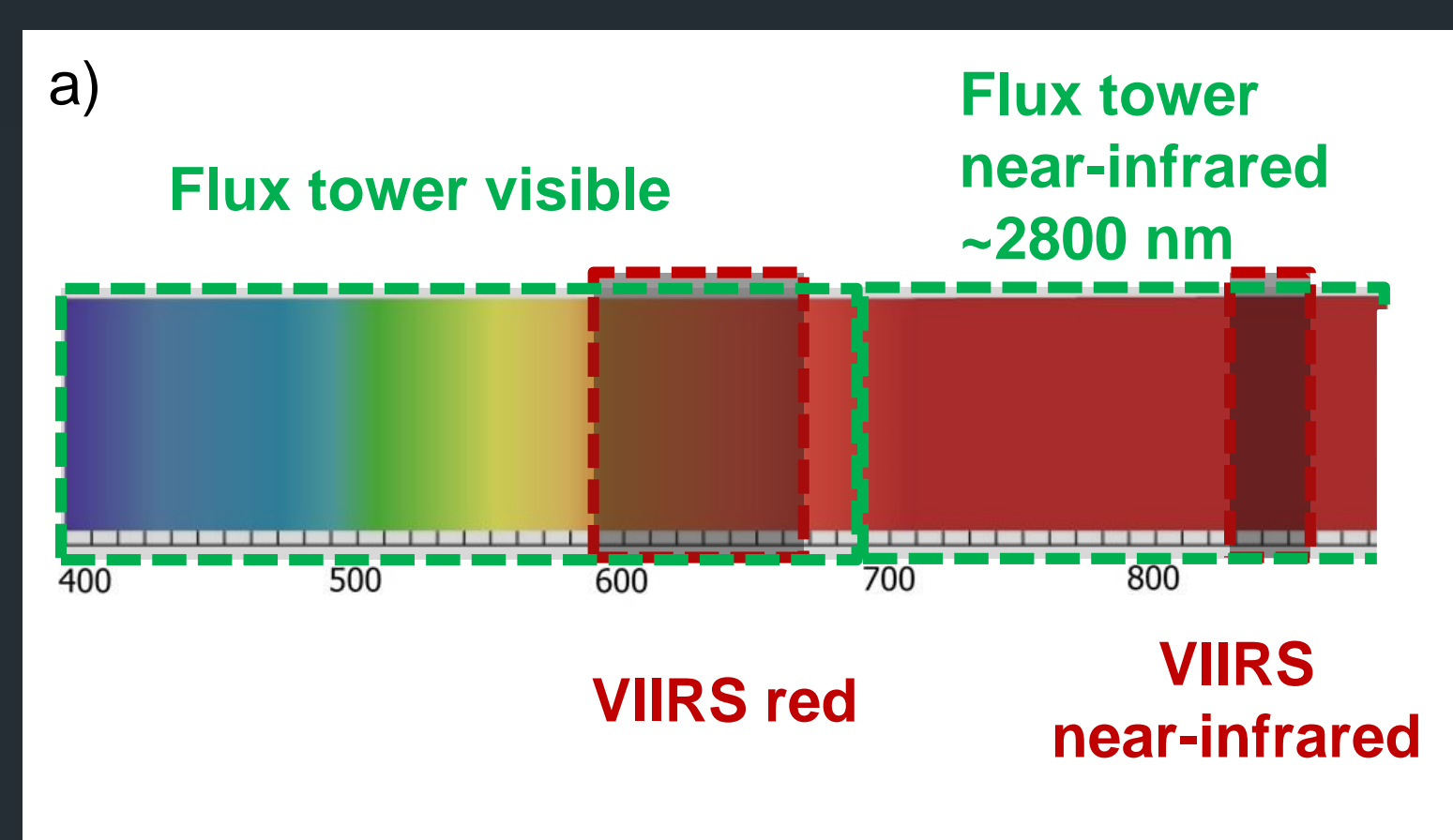
Objectives

The objective of this study was to validate VIIRS VIs (i.e. TOA NDVI and TOC EVI) by evaluating how well VIIRS VIs capture the seasonal dynamics of vegetated surfaces in comparison with those depicted by in situ VI time series measurements from flux towers:

- Visually compare the **seasonal changes** of VIIRS VIs with those from flux tower VIs, depict the seasonal dynamics
- Examine **correlations** between VIIRS and flux tower VIs
- Compare **phenological metrics** (i.e. **SOS: Start of Season** and **EOS: End of Season**) derived from VIIRS and flux tower VIs

Data Compatibility Issues

- Spectral bandpass:** Flux tower broad bandwidth vs. VIIRS narrow bandwidth
- Geometry:** Flux tower hemispherical vs. VIIRS directional



- Footprint size:** Flux tower—varies at each site with radius from 23 m to 293 m, determined by the tower's height
VIIRS—375 meters at nadir
- Land surface:** homogeneous vs. heterogeneous

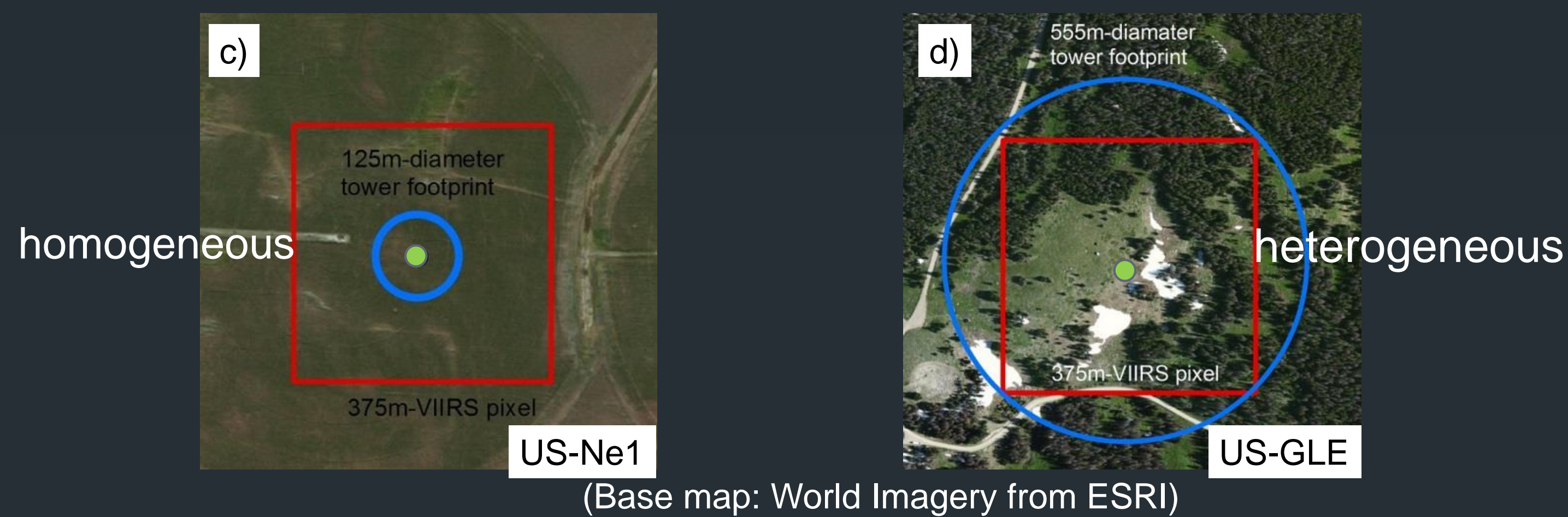


Figure 1. Differences in Spectral bandpass, geometry, footprint and land surface.

Methods

- NDVI and EVI / EVI2

$$NDVI = \frac{R_{nir} - R_{red}}{R_{nir} + R_{red}}$$

$$EVI = 2.0 \cdot \frac{R_{nir} - R_{red}}{R_{nir} + 6 \cdot R_{red} - 7.5 \cdot R_{blue} + 1}$$

$$EVI2 = 2.5 \cdot \frac{R_{nir} - R_{red}}{R_{nir} + 2.4 \cdot R_{red} + 1}$$

Flux tower[1]

$$NDVI = \frac{R_{nir} - R_{vis}}{R_{nir} + R_{vis}}$$

$$EVI2 = 2.5 \cdot \frac{R_{nir} - R_{vis}}{R_{nir} + 2.4 \cdot R_{vis} + 1}$$

- VIIRS Data pre-processing (Quality Flags: ice, snow, and cloud)
- Data post-processing (95% confidence interval for noise removal and moving average for filling missing data)
- Phenological Metrics-SOS and EOS

$$NDVI_{ratio} = \frac{NDVI - NDVI_{min}}{NDVI_{max} - NDVI_{min}}$$

The threshold of 50% of NDVI ratio was used in this study. The increase in greenness is believed to be the most rapid at this threshold[2].

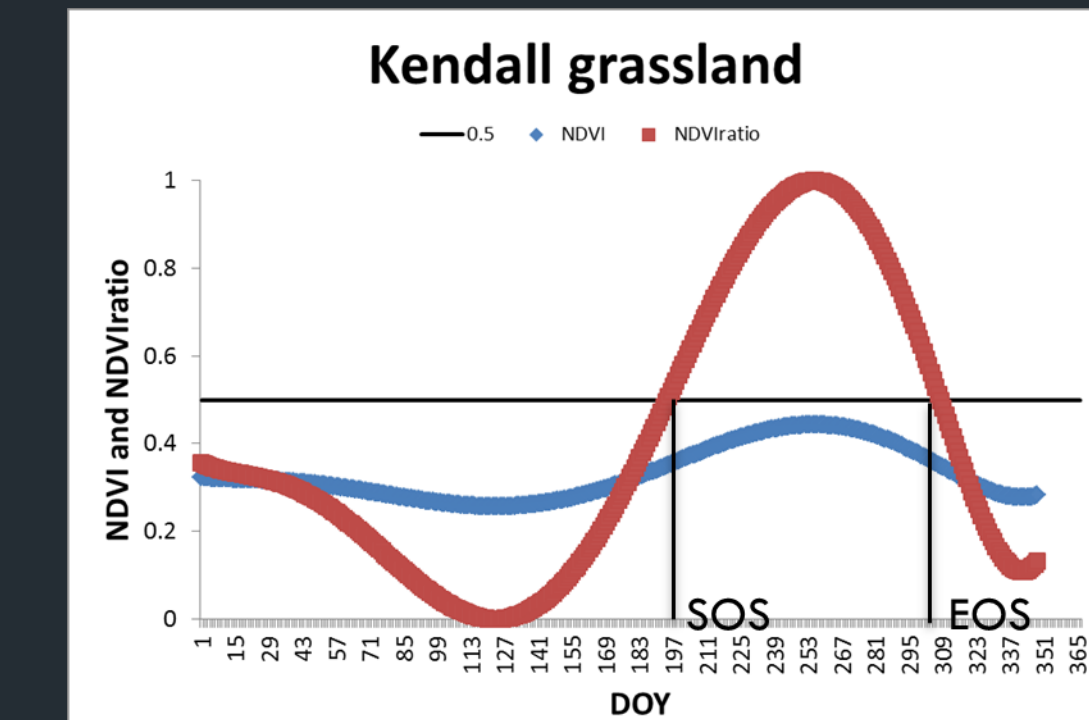


Figure 2. SOS and EOS extraction

Study Sites

Flux towers: 10 Vegetation cover types: 5 Data period: daily from April to December 2012

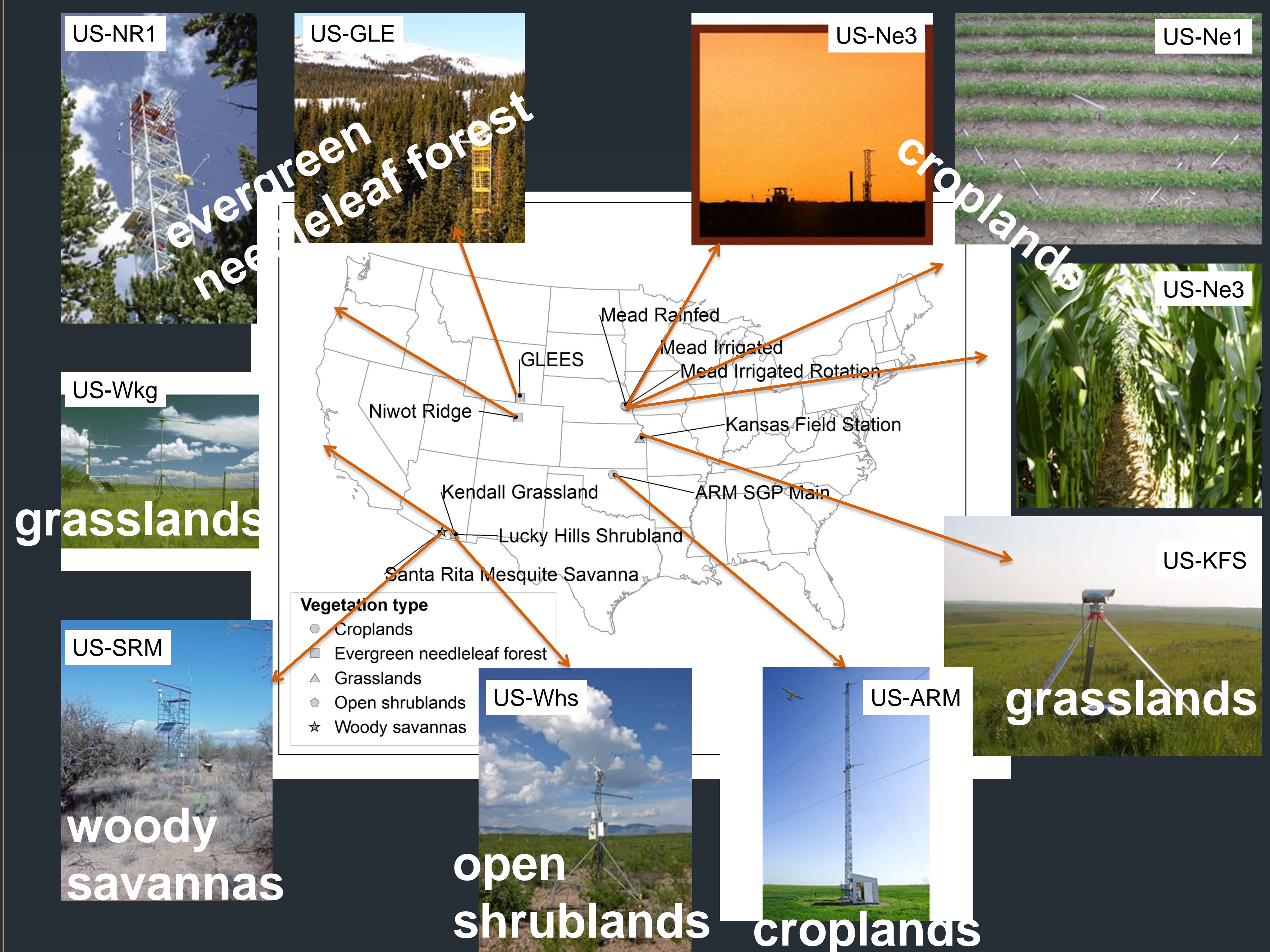


Figure 3. Locations of study sites (Photo credits: Ameriflux website).

Results

- About 1/3 of VIIRS data were left after running with quality flags and noise removal.
- Both flux towers and VIIRS present similar seasonal trends for each site and vegetation cover. At croplands and grasslands, VIs showed a unimodal pattern. At homogeneous evergreen needle forest, VIs were relatively constant. At woody savanna and open shrublands, VIs showed multimodal patterns (Figure 4).
- Scatterplots between VIIRS VIs and flux tower derived VIs showed that these two datasets scattered near the 1:1 line at most sites, except for US-NR1 which is at evergreen needle forest area (Figure 5).
- Out of 10 sites, 4 were used to extract SOS and EOS, including 3 at croplands and 1 at grasslands. At these 4 sites, both VIIRS and flux tower captured the SOS and EOS during the temporal range from April to December. The differences between SOS were from 1 to 10 days, and between EOS were from 0 to 5 days (Table 1 and Figure 6). Sites with SOS earlier than April or no distinct SOS or multi-model growing season were excluded for this study.

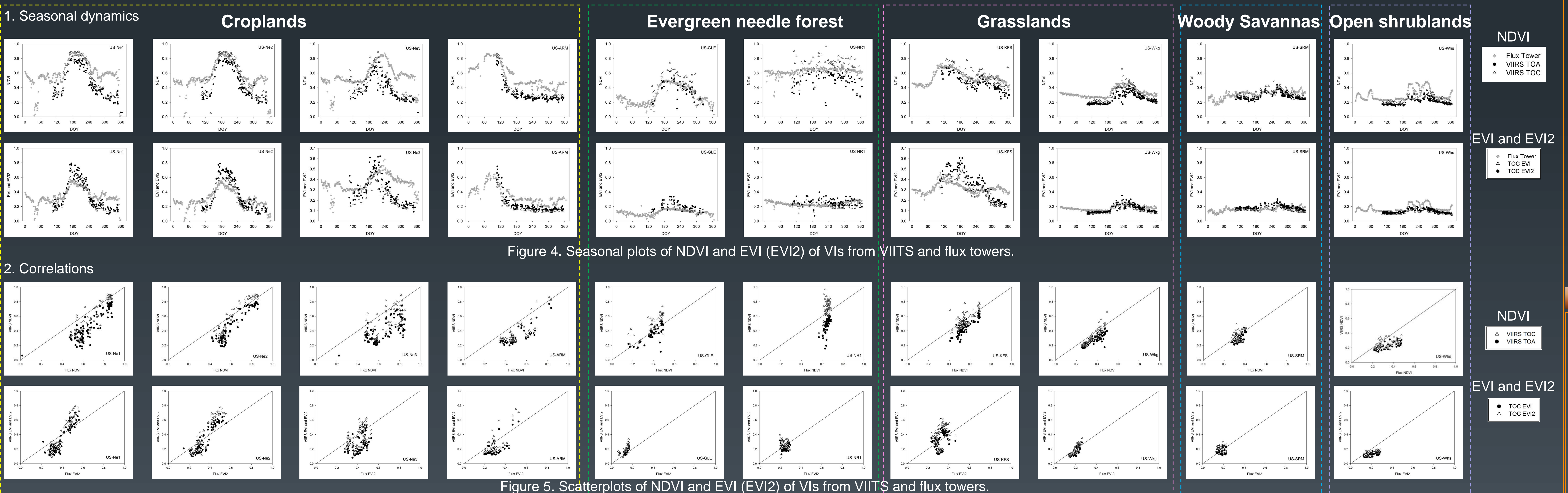


Figure 4. Seasonal plots of NDVI and EVI (EVI2) of VIs from VIIRS and flux towers.

Figure 5. Scatterplots of NDVI and EVI (EVI2) of VIs from VIIRS and flux towers.

- Phenological metrics (showing data for NDVI only, EVI(EVI2) are not shown)

Table 1. SOS and EOS dates for NDVI from VIIRS and flux towers.

SOS (DOY)	TOCNDVI	TOANDVI	FluxNDVI	EOS (DOY)	TOCNDVI	TOANDVI	FluxNDVI
US-Wkg	196	205	195	US-Wkg	304	304	304
US-Ne1	151	151	149	US-Ne1	244	242	246
US-Ne2	153	152	148	US-Ne2	246	244	241
US-Ne3	160	161	168	US-Ne3	254	255	254
Minimum Difference	1	2		Minimum Difference	0	0	
Maximum Difference	8	10		Maximum Difference	5	4	
Mean Difference	0	2.25		Mean Difference	0.75	0	
Standard Deviations	5.60	7.04		Standard Deviations	3.61	3.51	

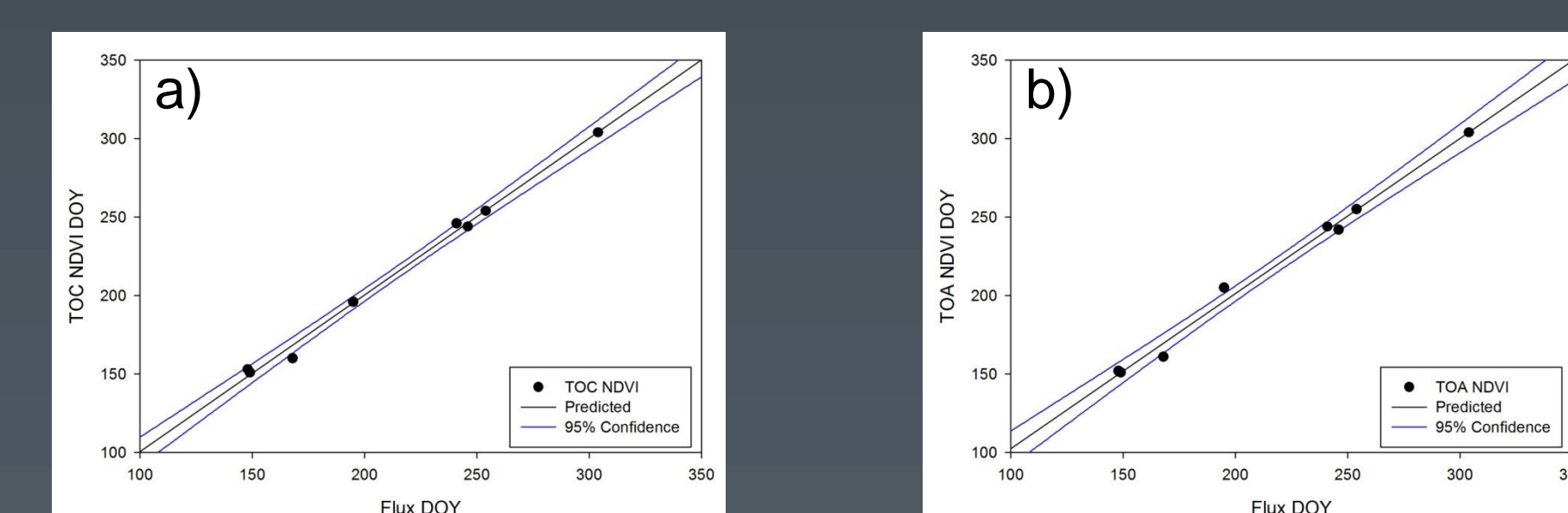


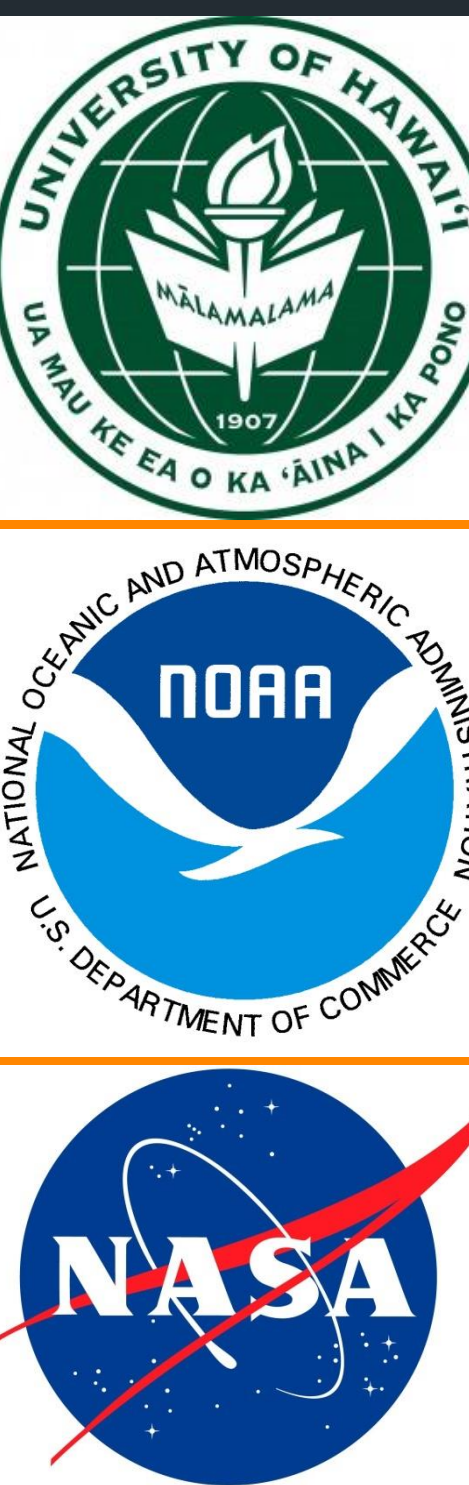
Figure 6. 95% confidence interval for SOS and EOS extracted from NDVI.

Conclusions

- FLUXNET measurements can be used to validate VIIRS VIs.
- Daily VIs from flux towers and VIIRS were comparable and both captured similar seasonal dynamics of vegetation.
- Phenological metrics (i.e. SOS and EOS) extracted from flux towers and VIIRS were within 10-day differences.
- The methodology presented can serve as a basis for validating medium resolution satellite products.

References

- Huemmerich, K.F., Black, T.A., Jarvis, P.G., McCaughey, J.H. and Hall, F.G. 1999. High temporal resolution NDVI phenology from micrometeorological radiation sensors. *Journal of Geophysical Research* 104:27935-27944.
- White, M. A., Thornton, P. E., & Running, S. W. (1997). A continental phenology model for monitoring vegetation responses to interannual climatic variability. *Global Biogeochemical Cycles*, 11, 217-234.



Acknowledgements

We would like to thank Land PEATE for providing the VIIRS VI products used in this study. The flux towers included are part of the AmeriFlux network. We would like to thank the following investigators of these sites for providing their data: US-ARM: Dave Billesbach, Marc Fischer and Margaret Torn; US-KFS: Nathaniel Brunzell; US-GLE: William Massman; US-Ne1, US-Ne2 and US-Ne3: Andrew Suyker; US-NR1: Peter Blanken and Russ Monson; US-SRM, US-Whs; and US-Wkg: Russ Scott

This work was supported by a NOAA STAR JPSS contract and NASA NPP grant NNX11AH25G.

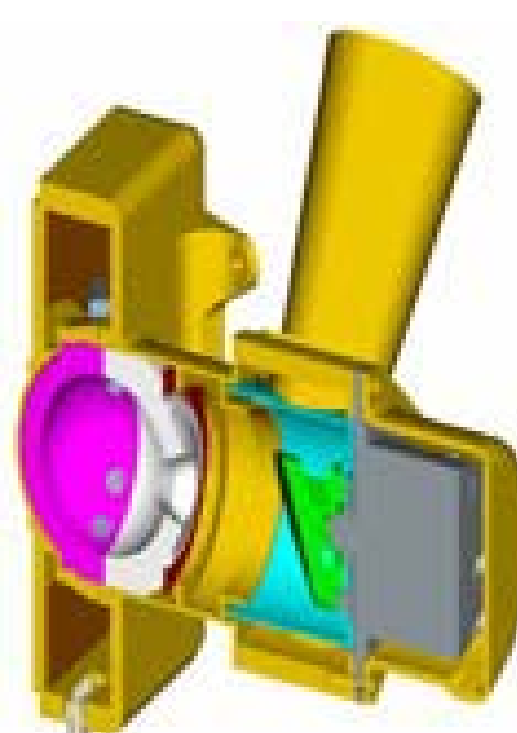
Introduction

- VIIRS is one of five instruments onboard the Suomi National Polar-Orbiting Partnership (SNPP) satellite that launched from Vandenberg Air Force Base, Calif., on Oct. 28, 2011.
- The VIIRS is a whiskbroom radiometer that provides ± 56.28 degree scans of the Earth view (EV) covering a 12 km (nadir) along track by 3060 km along scan swath each scan using a rotating telescope assembly and a double-sided half-angle mirror (HAM).
- VIIRS has 22 spectral bands, among which 14 reflective solar bands (RSB) ranging from 0.41 to 2.25 μm , with spatial resolution of 375 m (bands I1-I3) and 750 m (bands M1-M11).
- RSB are calibrated on-orbit using a Solar Diffuser (SD) with a Solar Diffuser Stability Monitor (SDSM) and near-monthly lunar observations.

SDSM Calibration

- $$H(t) = \frac{\tau_{Sun} \cdot dc_{SD}}{\tau_{SD} \cdot \cos(\theta_{SD}) \cdot BRF_{SDSM} \cdot dc_{Sun}}$$
- BRF_{SDSM} : SD prelaunch BRF for SDSM view
 - τ_{Sun} : VF of the sun view screen
 - τ_{SD} : VF of the SD screen
 - θ_{SD} : AOI on SD surface
 - dc_{SD} : Background subtracted SDSM SD view response
 - dc_{Sun} : background subtracted SDSM Sun view response

SDSM



SD on-orbit degradation

$$h(t) = H(t) / H(t_0)$$

SD Calibration

- $$F(t) = \frac{RVS_{B,SD} \cdot \int RSR_B(\lambda) \cdot L_{SD}(\lambda) \cdot d\lambda}{(c_0 + c_1 \cdot dn + c_2 \cdot dn^2) \cdot \int RSR_B(\lambda) \cdot d\lambda}$$
- $$L_{SD}(\lambda) = I_{Sun}(\lambda) \cdot \tau_{SD} \cdot \cos(\theta_{SD}) \cdot BRF_{RTA} \cdot h(\lambda) / d_{VS}^2$$
- BRF_{SD} : SD prelaunch BRF for RTA view
 - RSR_B : Relative spectral response for band
 - c_0, c_1, c_2 : Temperature effect corrected prelaunch calibration coefficients
 - I_{Sun} : Solar irradiance
 - dn : Background subtracted instrument response
 - $RVS_{B,SD}$: Response Versus Scan angle at AOI of SD for band B
 - d_{VS} : VIIRS-Sun distance

SD



Lunar Calibration

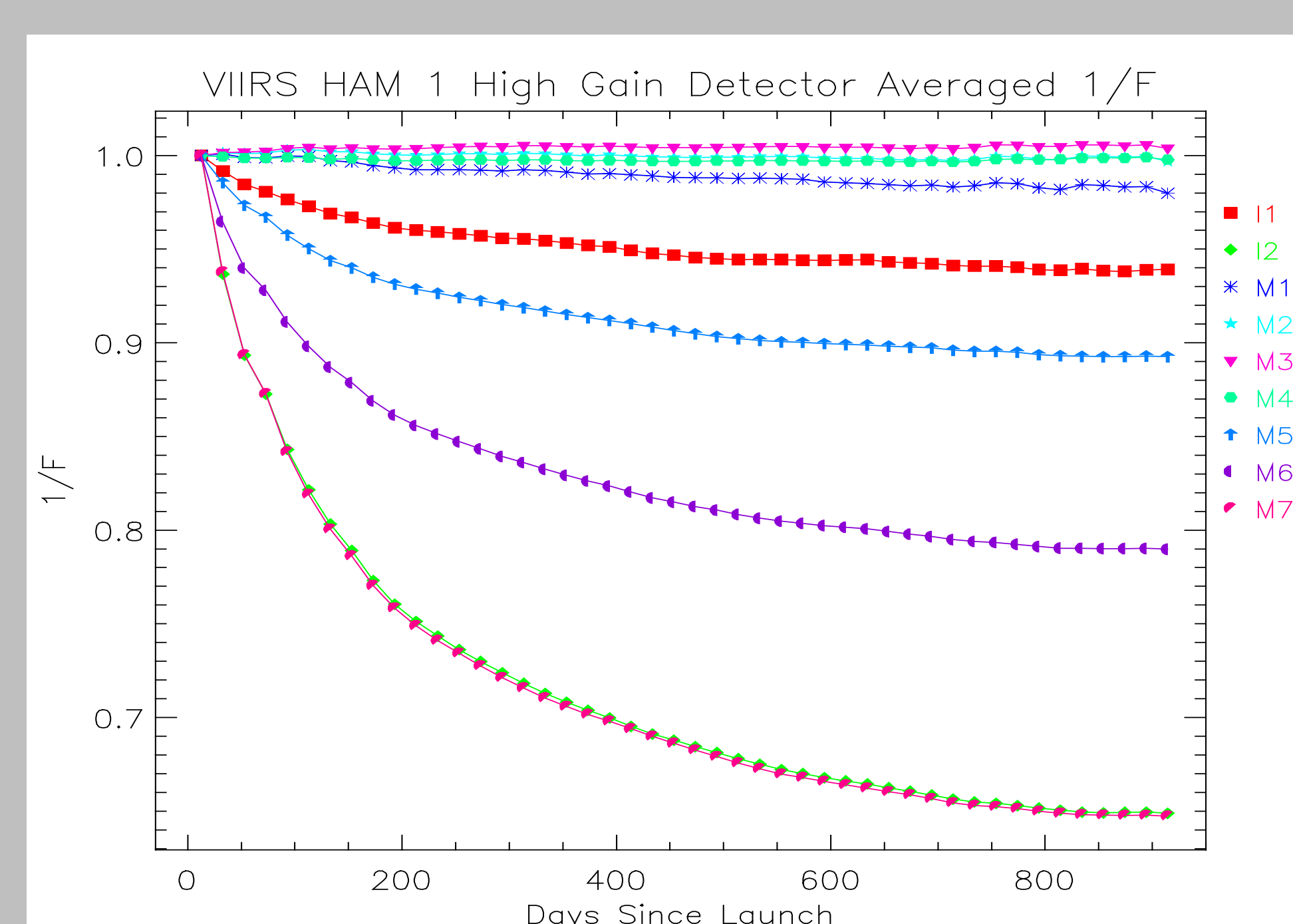
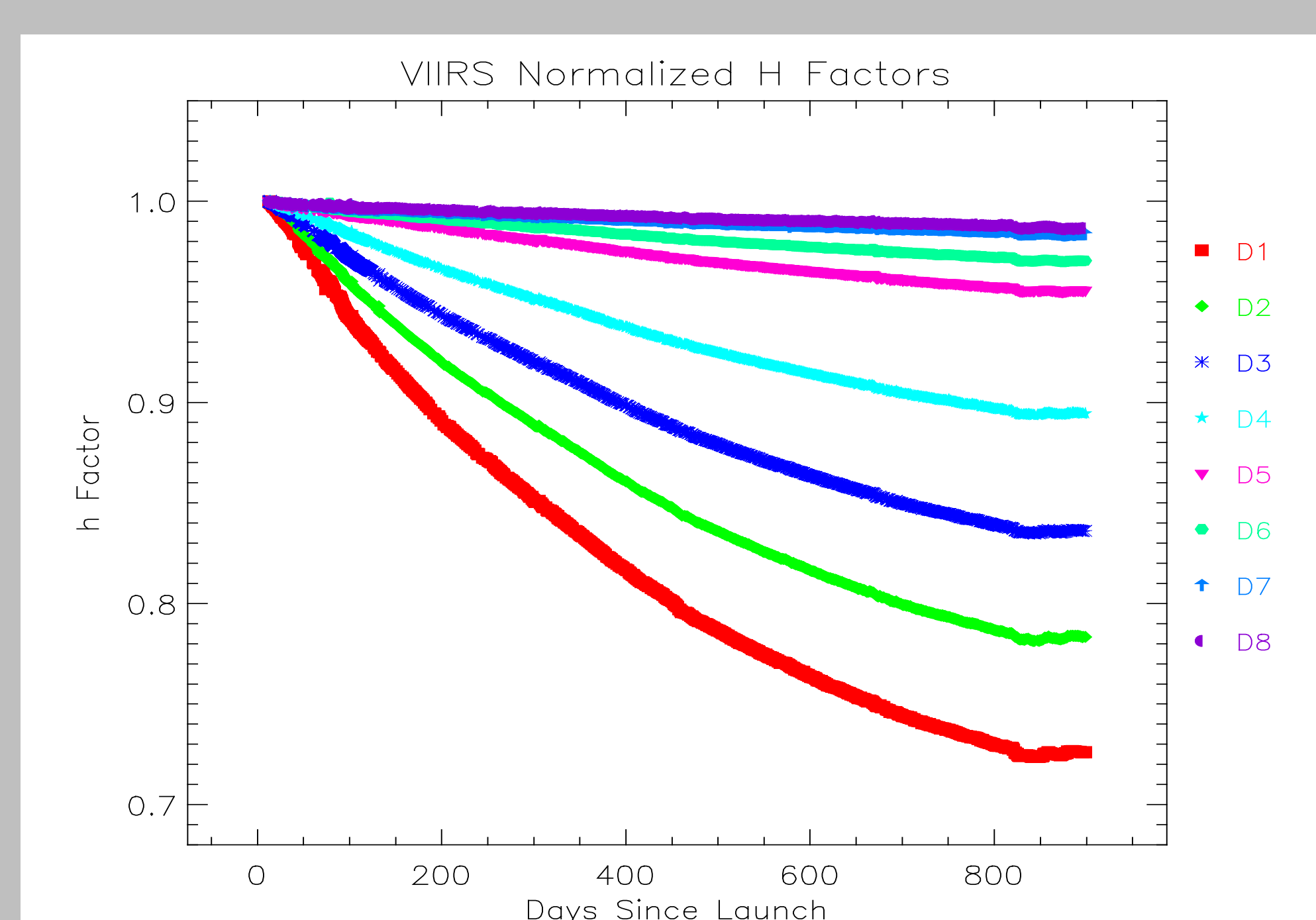
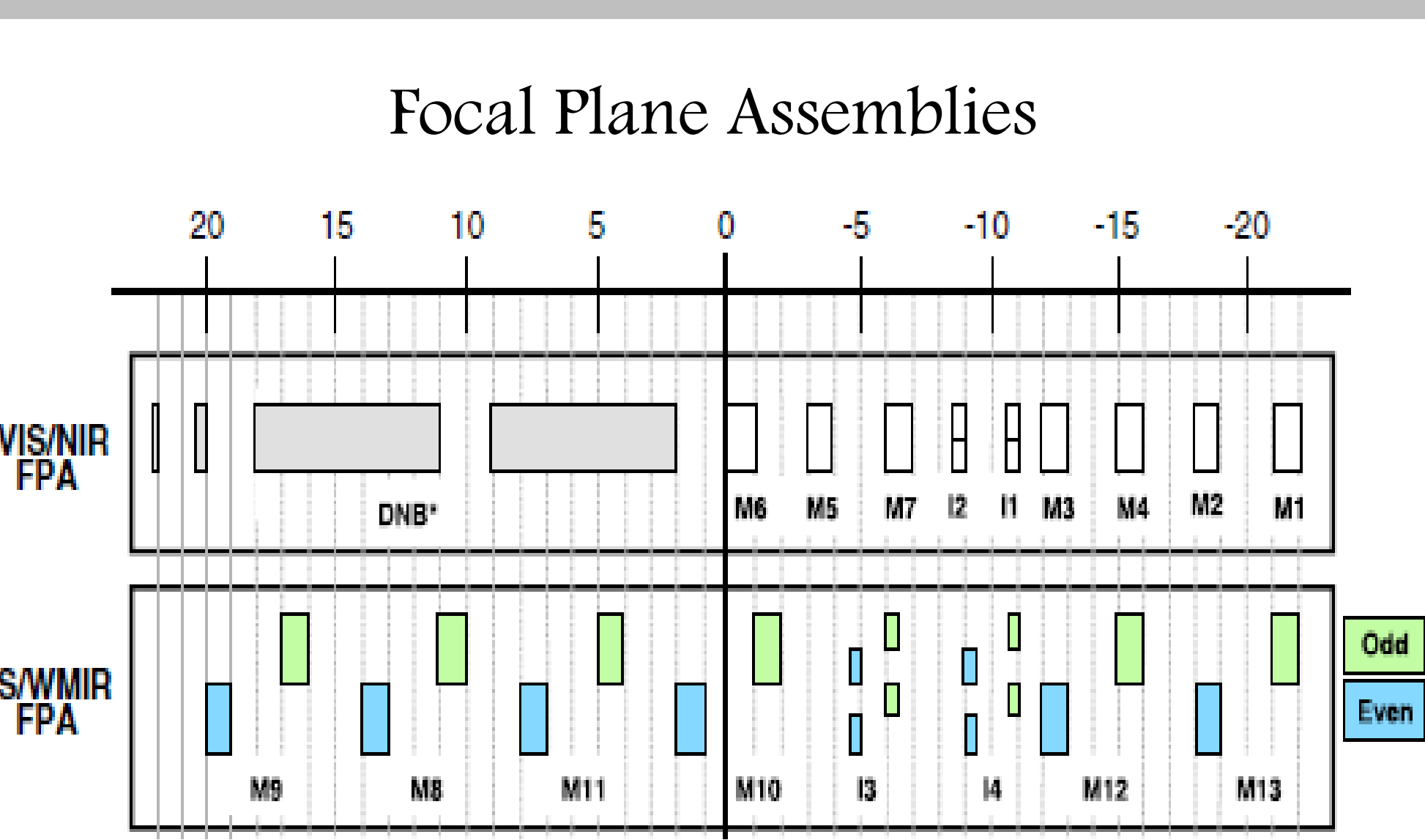
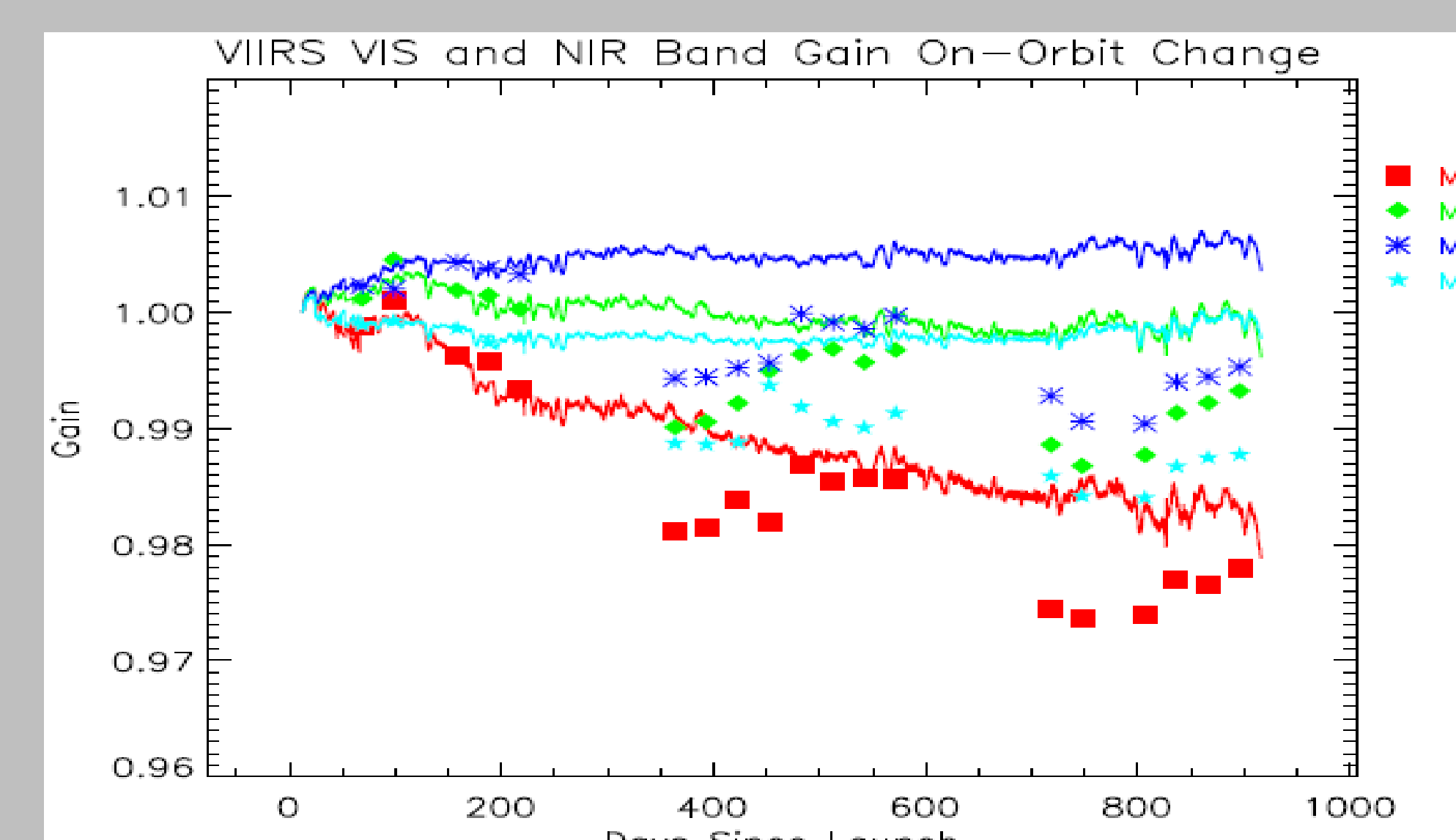
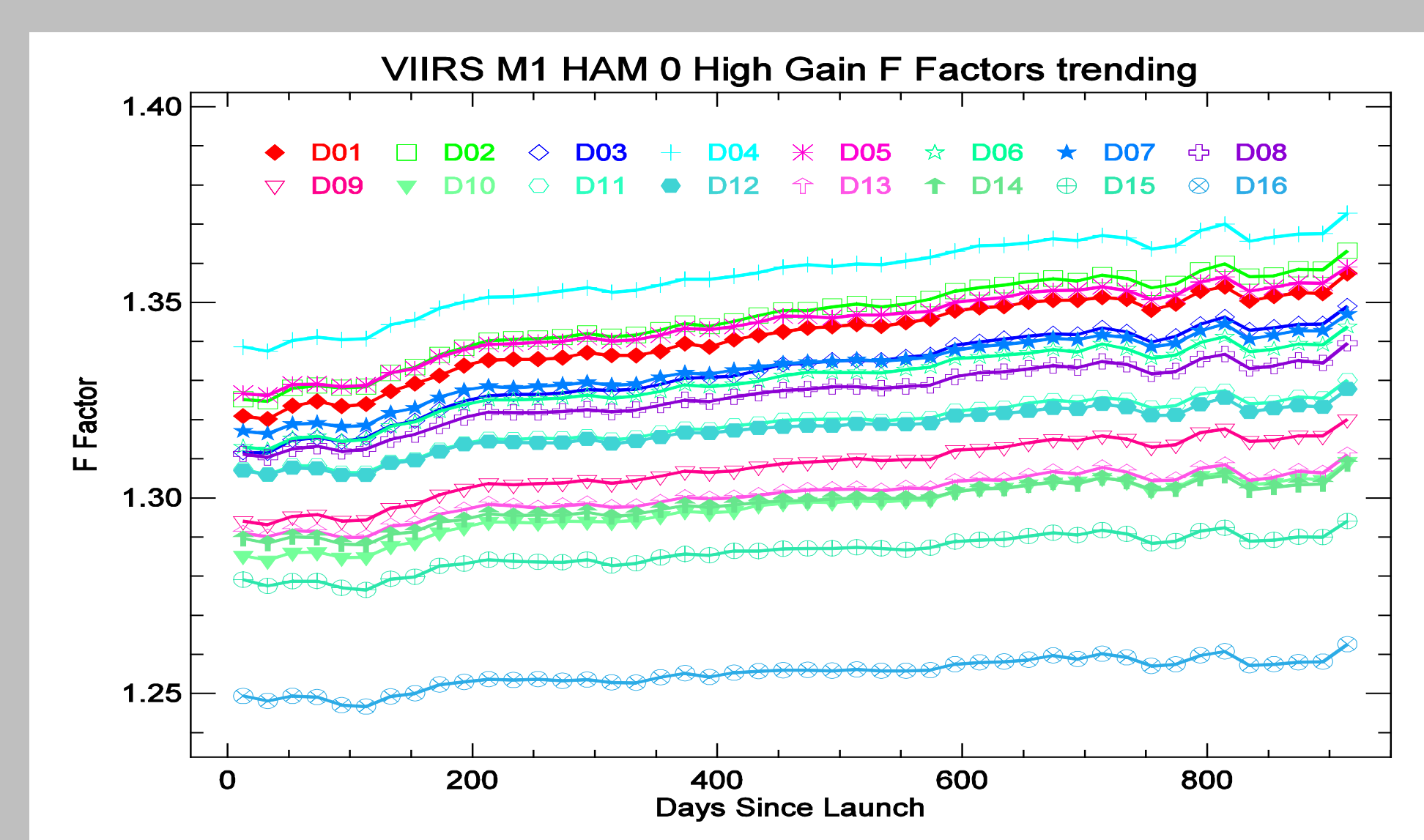
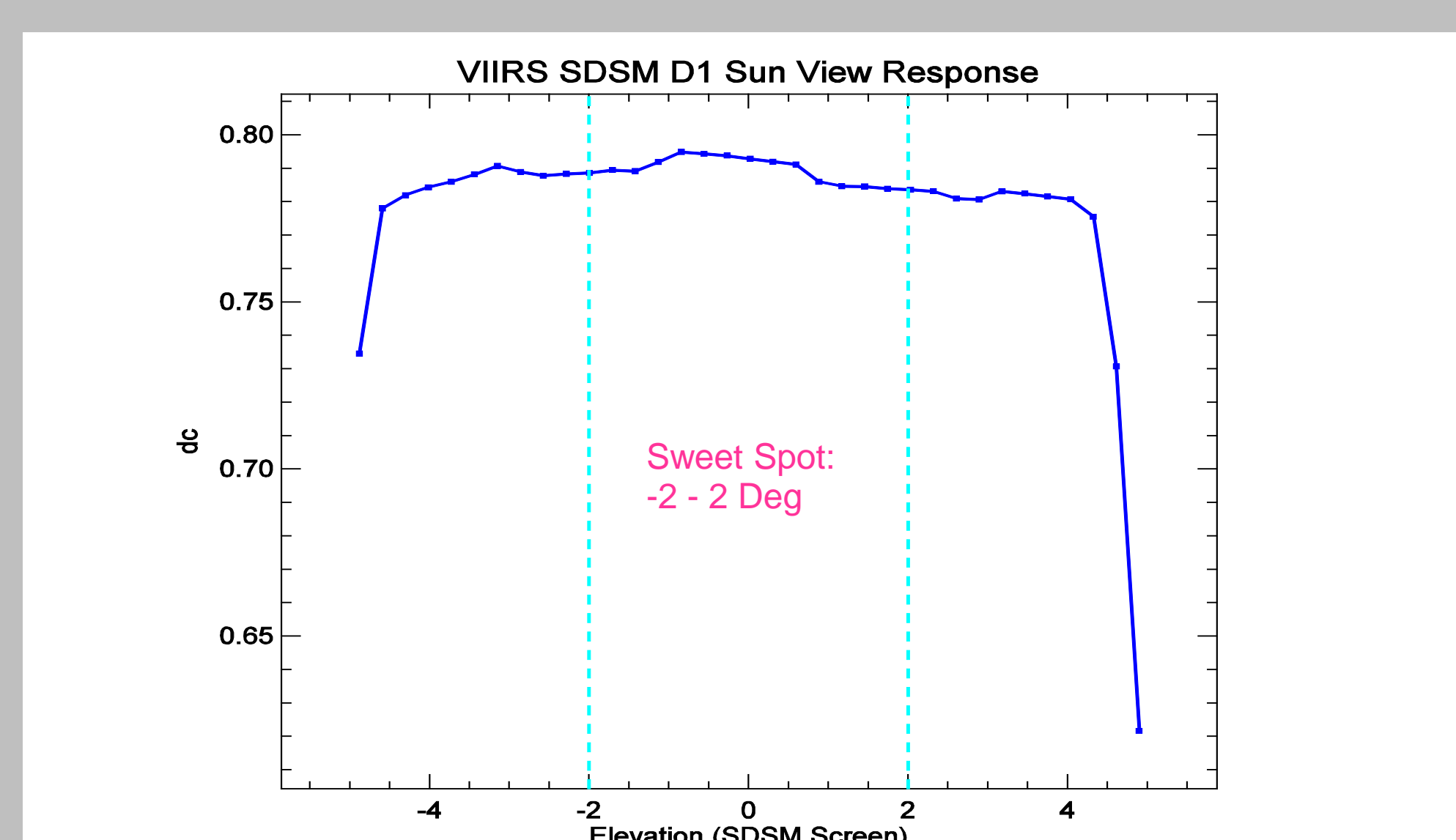
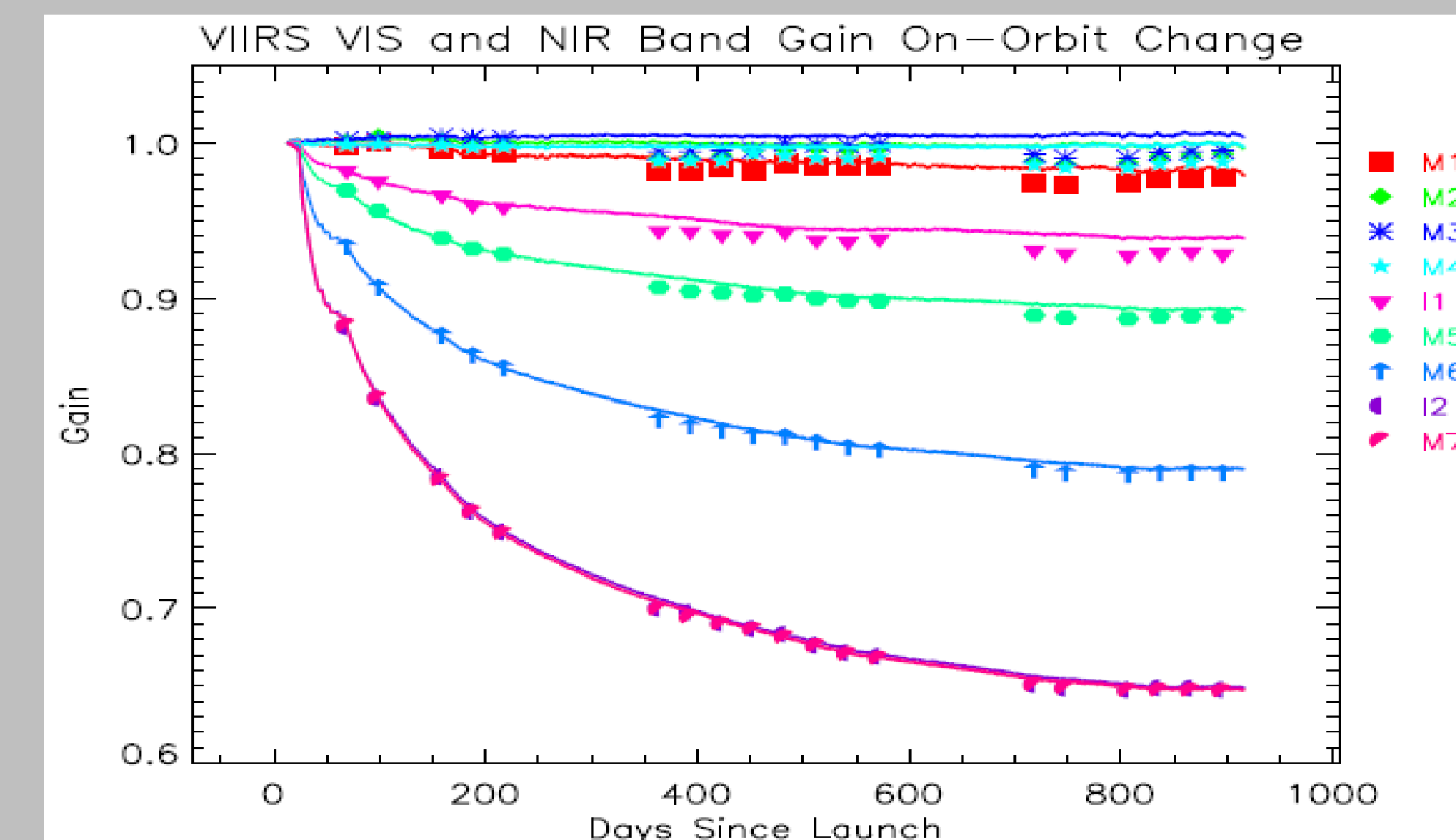
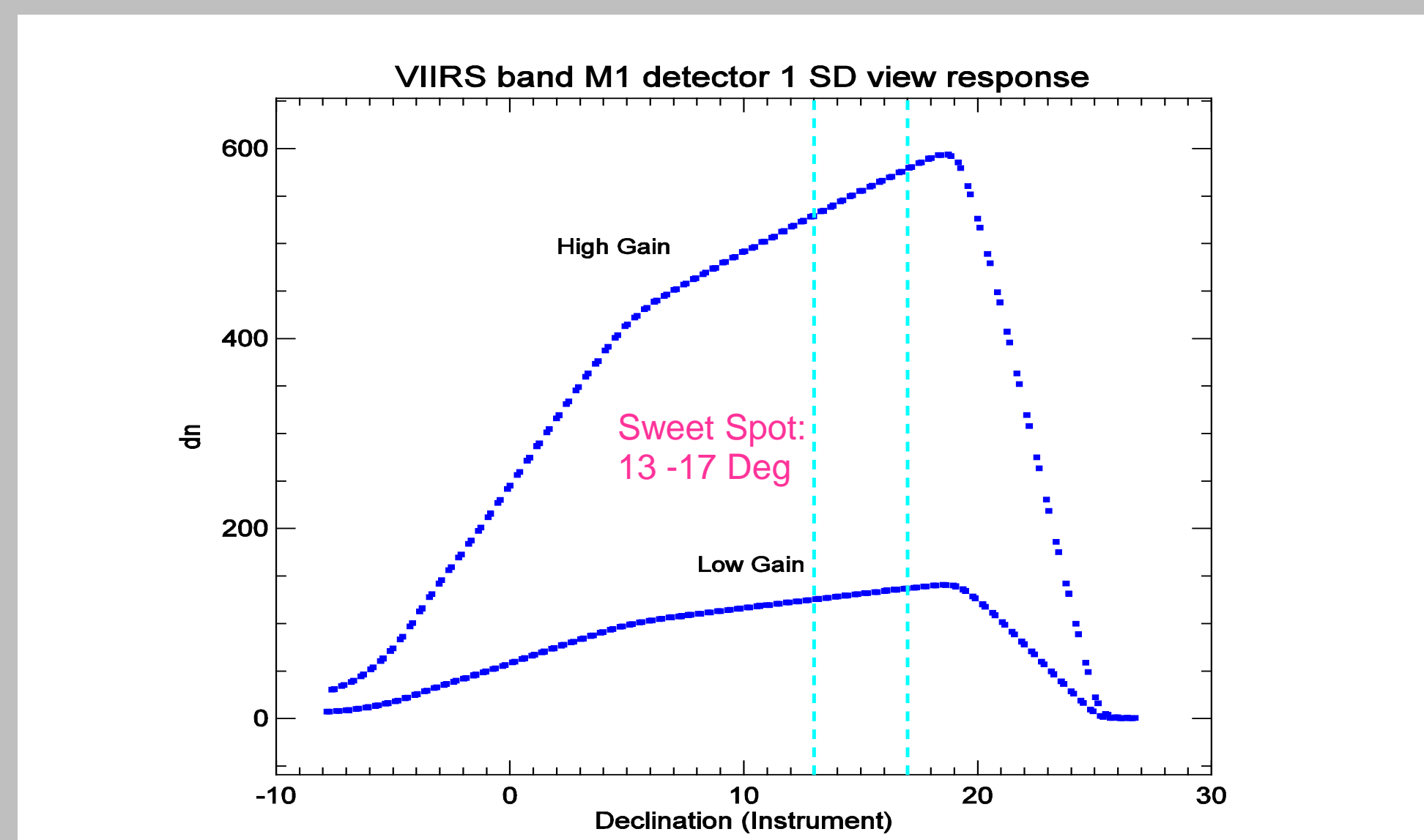
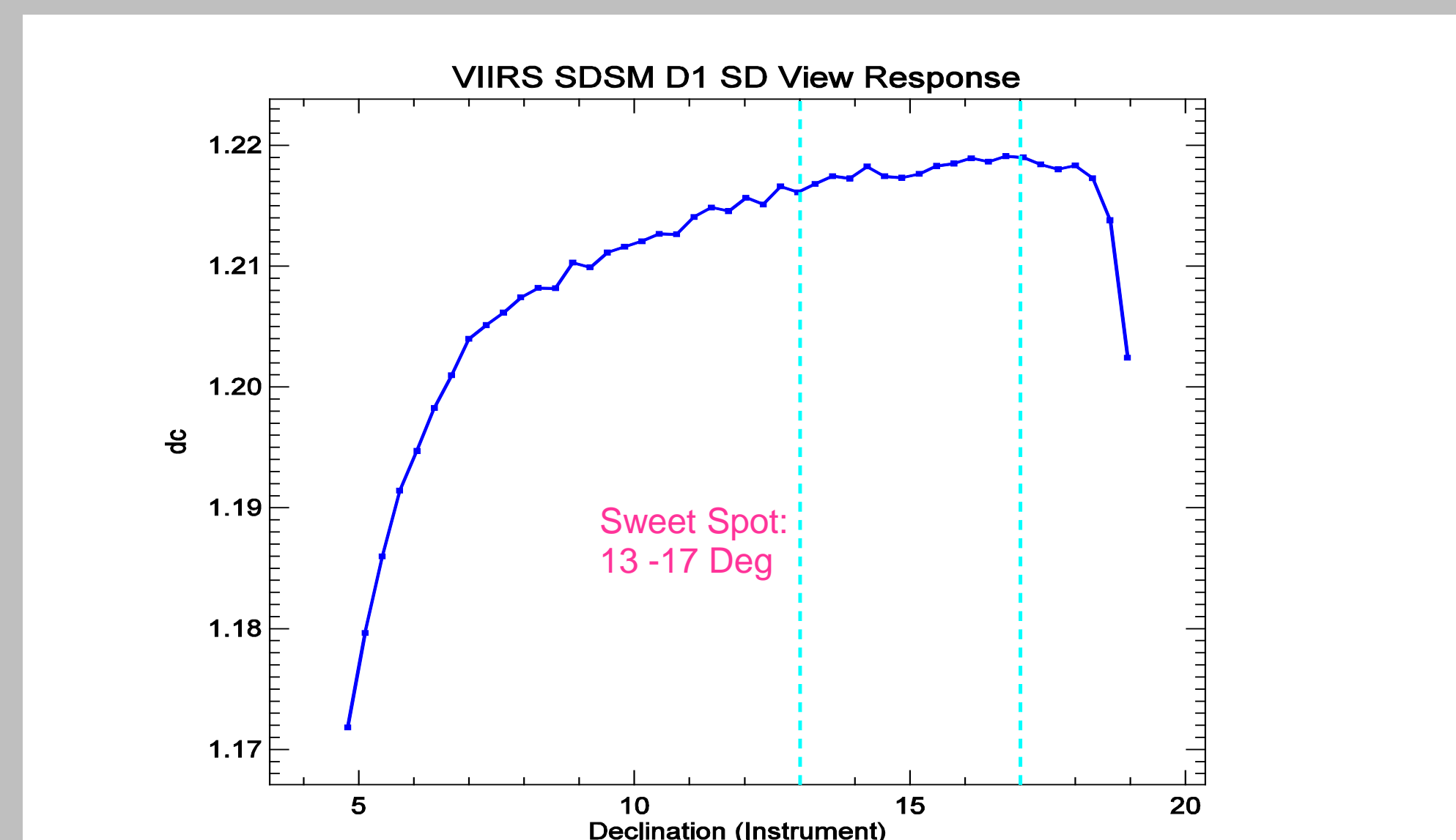
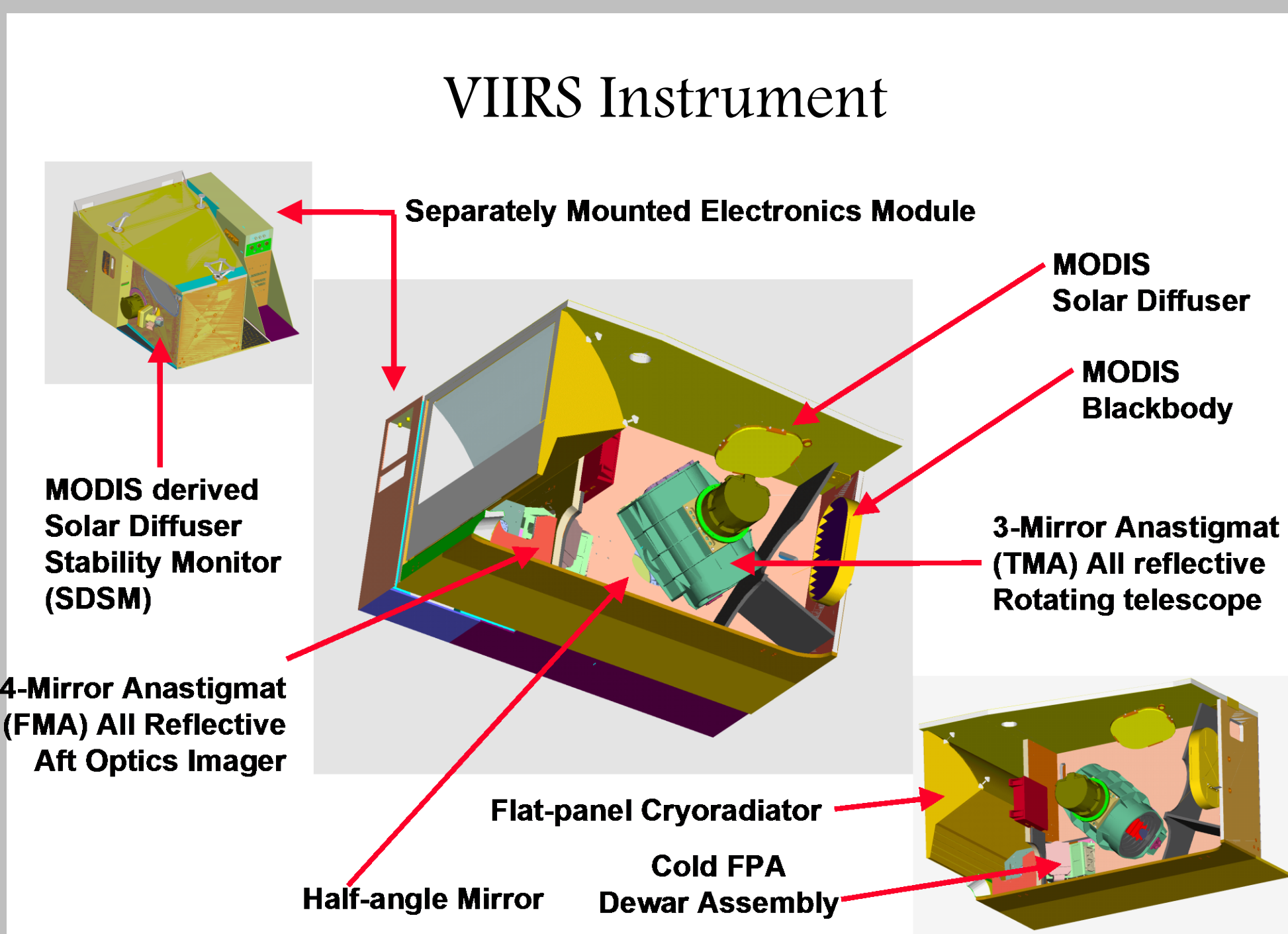
- $$F(B, M, t) = \frac{g(B) \cdot N_M}{\sum_{D,S,n} L_{pl}(B, D, S, n) \delta(M, M_n)}$$
- $$L_{pl}(B, D, S, n) = \sum_{j=0}^2 c_j(B, D, M) dn_{Moon}(B, D, S, n)$$
- B, D, S, n : Band, detector, sample, and HAM side
 - dn_{Moon} : Background subtracted instrument response
 - N_M : Number of scan which views a full Moon with HAM M

Lunar Image



Relative lunar F factor

$$f(B, M, t) = F(B, M, t) / F(B, M, t_0)$$



Summary and Challenges

- The SD degradation has been tracked by the on-board SDSM since SNPP VIIRS launched. The SD degradation is strongly wavelength dependent and it has degraded about 28% at 412 nm in the past 2+ years.
- The SNPP VIIRS RSB are calibrated using the on-board SD. The RSB on-orbit change is also strongly wavelength dependent. The near infrared bands have largest gain decrease, which is about 35% for bands I2 and M7.
- The RSB response changes are also tracked using the scheduled approximately monthly lunar observations. The lunar calibration coefficients matches the SD results reasonably well except for the unexpected seasonal oscillations seen in lunar calibration coefficients.

Key Specifications

Band	Center Wavelength (nm)	Gain Type	Single Gain		Dual Gain			
			Lmin	Lmax	High Gain Lmin	High Gain Lmax	Low Gain Lmin	Low Gain Lmax
M1	412	Dual	-	-	30	135	135	615
M2	445	Dual	-	-	26	127	127	687
M3	488	Dual	-	-	22	107	107	702
M4	555	Dual	-	-	12	78	78	667
M5	672	Dual	-	-	8.6	59	59	651
M6	746	Single	5.3	41.0	-	-	-	-
M7	865	Dual	-	-	3.4	29	29	349
M8	1240	Single	3.5	164.9	-	-	-	-
M9	1378	Single	0.6	77.1	-	-	-	-
M10	1610	Single	1.2	71.2	-	-	-	-
M11	2250	Single	0.12	31.8	-	-	-	-
I1	640	Single	5	718	-	-	-	-
I2	865	Single	10.3	349	-	-	-	-
I3	1610	Single	1.2	72.5	-	-	-	-

Improvements: Sweet spots and new VFs

Improvements: Sweet spot and new VF

Yan Bai^a, Changyong Cao^b, Xi Shao^c, Wenhui Wang^a

^a Earth Resources Technology, Inc., Laurel, Maryland, USA, ^b NOAA/NESDIS/STAR, College Park, MD, ^c University of Maryland, College Park, MD

Abstract

The Visible Infrared Imaging Radiometer Suite (VIIRS) is one of the key instruments onboard the Suomi National Polar-Orbiting Partnership (Suomi NPP) spacecraft, which was successfully launched on October 28, 2011.

To support the post launch calibration/validation of VIIRS, a comprehensive knowledgebase has been developed at NOAA and made available online. This poster introduces the key components of the knowledgebase and its use for data quality assurance, anomaly investigation, and EDR applications.

The calibration knowledgebase has a number of features, including daily orbital prediction, simultaneous nadir overpass (SNO) and SNO extension to low latitude (SNOx) predictions, VIIRS event log database, image gallery, radiometric time series at validation sites, instrument information, and publication references. It has been used extensively for the VIIRS calibration/validation. For example, the event log database contains the monthly lunar calibration events through maneuver from 2012 to current. The database provides the lunar data date and time, location, spectral bands, and event type for users to search the lunar data from the database. This provides important support for lunar data analysis which allows us to independently verify the stability of the VIIRS calibration.

The VIIRS calibration knowledgebase has become an important component for supporting the VIIRS SDR data calibration/validation, monitoring VIIRS data quality and instrument performance. It provides critical support for producing the products of sea surface temperature, ocean color, cloud imagery, vegetation, aerosols, and others, which will improve product quality to meet the growing needs for high quality satellite data.

The URL for the calibration Knowledge Base is <https://cs.star.nesdis.noaa.gov/NCC/VIIRS>

Calibration Knowledge Base Components

VIIRS Event Log Database

The Event log database contains all events that occurred to Suomi NPP VIIRS since launch. This includes major events such as sync loss, single event upset outage, as well as planned events such as lunar maneuvers, blackbody warm-up cool-down (WUCD), star tracker realignment, etc. The event log database is very useful for instrument diagnoses, time series trending and analysis, and future reanalysis and recalibration. We have used the Event log database to collect lunar maneuver data which has been used for the lunar band ratio analysis. It is also used to correlate the time and location of the single event upset outage in instrument anomaly and diagnosis.

Figure 1 shows the distribution of the SBC lockup events from the database and its correlation with the SAA. The event log database is powered by MySQL and was initially designed by a summer intern from the Computer Science Department, University of Maryland.

While the current database only includes instrument related events, the ground processing related events such as MX updates will be added in the near future.

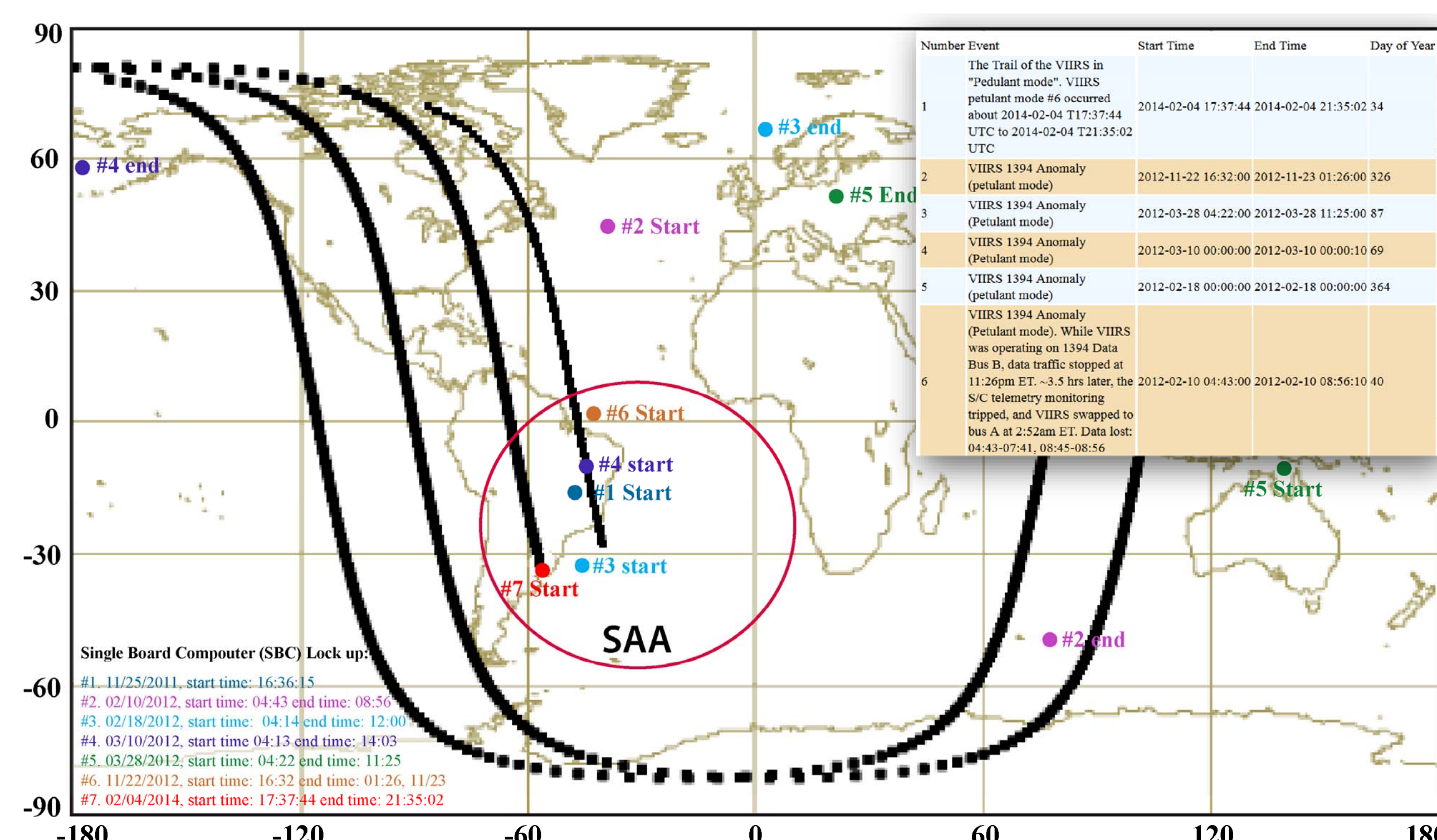


Figure 1. SBC lockups and other events from the event log database

VIIRS Image Gallery

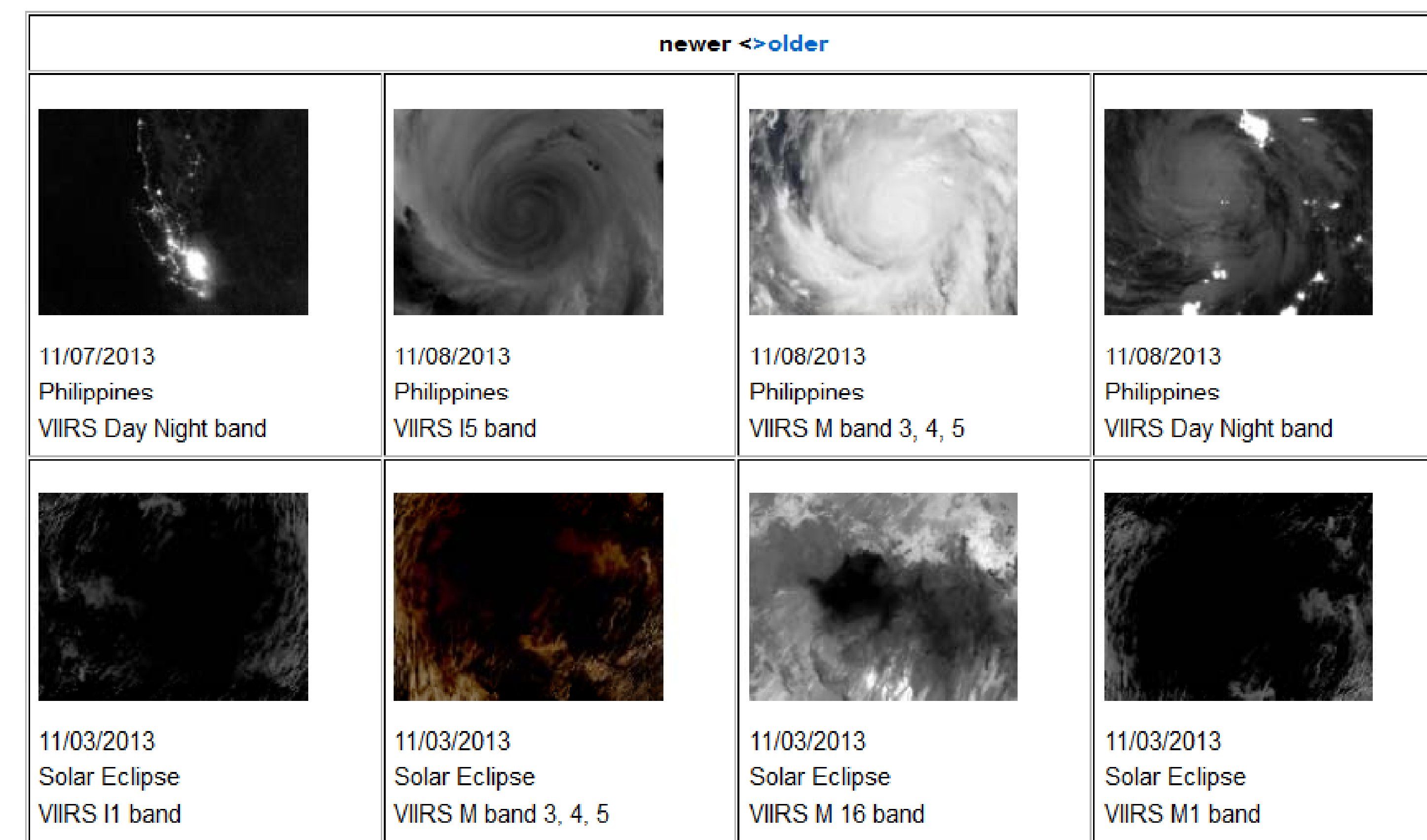


Figure 2. Sample images from the image gallery

The VIIRS image gallery is one of the early features developed for the calibration knowledge base shortly after Suomi NPP launch. The sample images has a collection of observations of major events such as the Hurricane Sandy, Super Typhoon, solar eclipse, and first light images. The DNB sample imagery shows that the quality has improved significantly since launch, with the calibration improvements by updating the look up tables, and with the stray-light correction implementation. Figure 2 shows that the Super Typhoon was over the Philippines on November 8, 2013.

Validation Site Radiometric Time Series

Although VIIRS has onboard calibration for all channels, it is important that the calibrated SDR are independently validated. A major effort towards this end is the development of the world-wide validation site radiometric time series. The goal is to construct the time series for the entire period of the mission over about 30 vicarious sites to monitor the stability of the VIIRS calibration (Figure 3). Many of these sites are endorsed by the Committee on Earth Observation Satellites (CEOS) Working Group on Calibration/Validation (WGCV). Legacy sites such as MOBY are also included. The time series has already been used for diagnoses for the recent H and F factor trend changes. In addition to the ground based sites, the time series also includes the Deep Convective Cloud time series, and the Lunar Band Ratio Time Series.

If any calibration trend is found in the onboard calibration, the vicarious time series will be used to validate the trend. Conversely, if the time series over the vicarious sites show trends, the information will be used for the onboard calibration performance analysis.

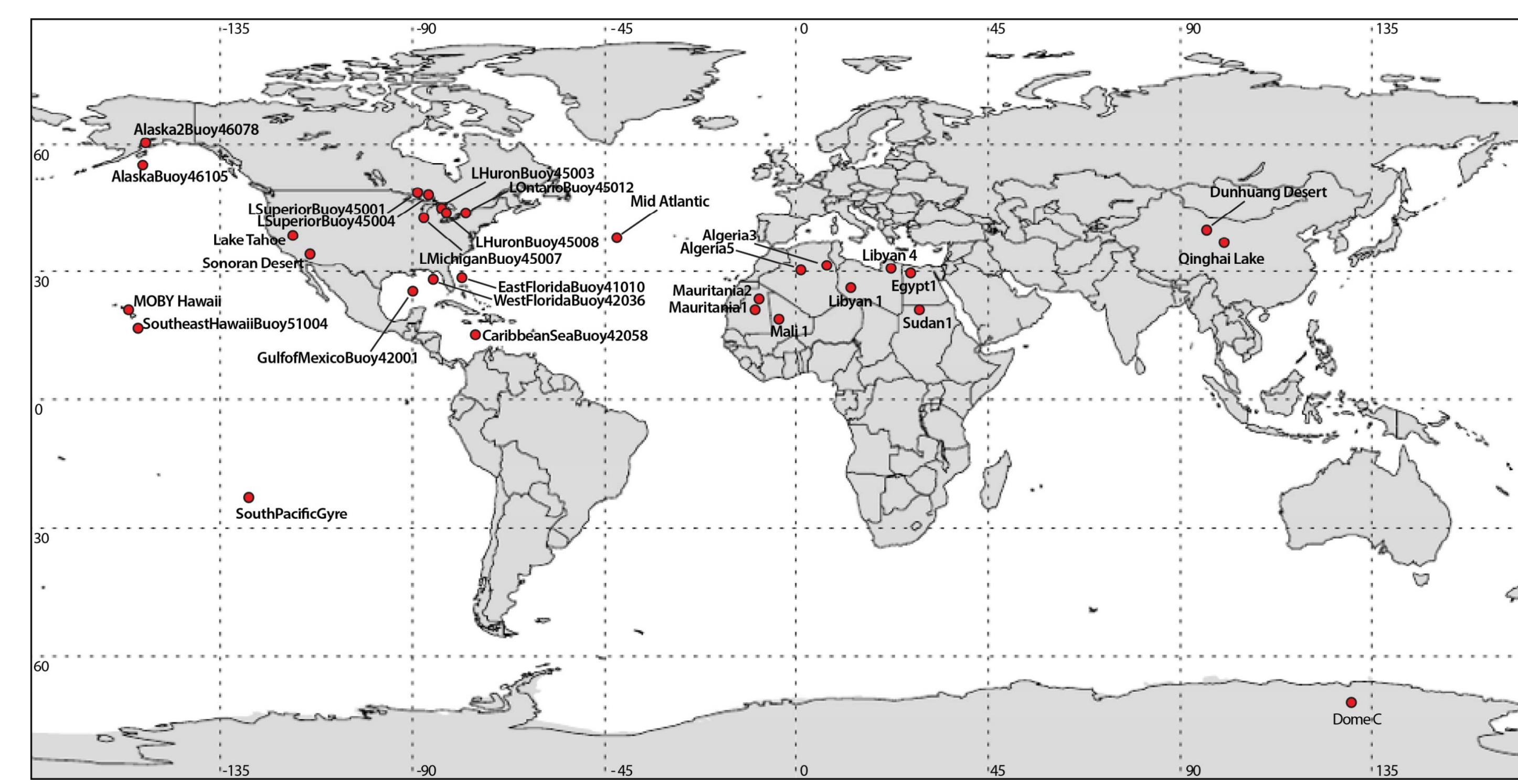


Figure 3. Over thirty validation sites included worldwide

Daily Orbital Track & SNO Predictions

The Suomi NPP orbital ground track has been made available since launch. The prediction is based on the latest SGP4 model and TLEs. This information is used to locate specific data on a daily basis by image analysts (Figure 5).

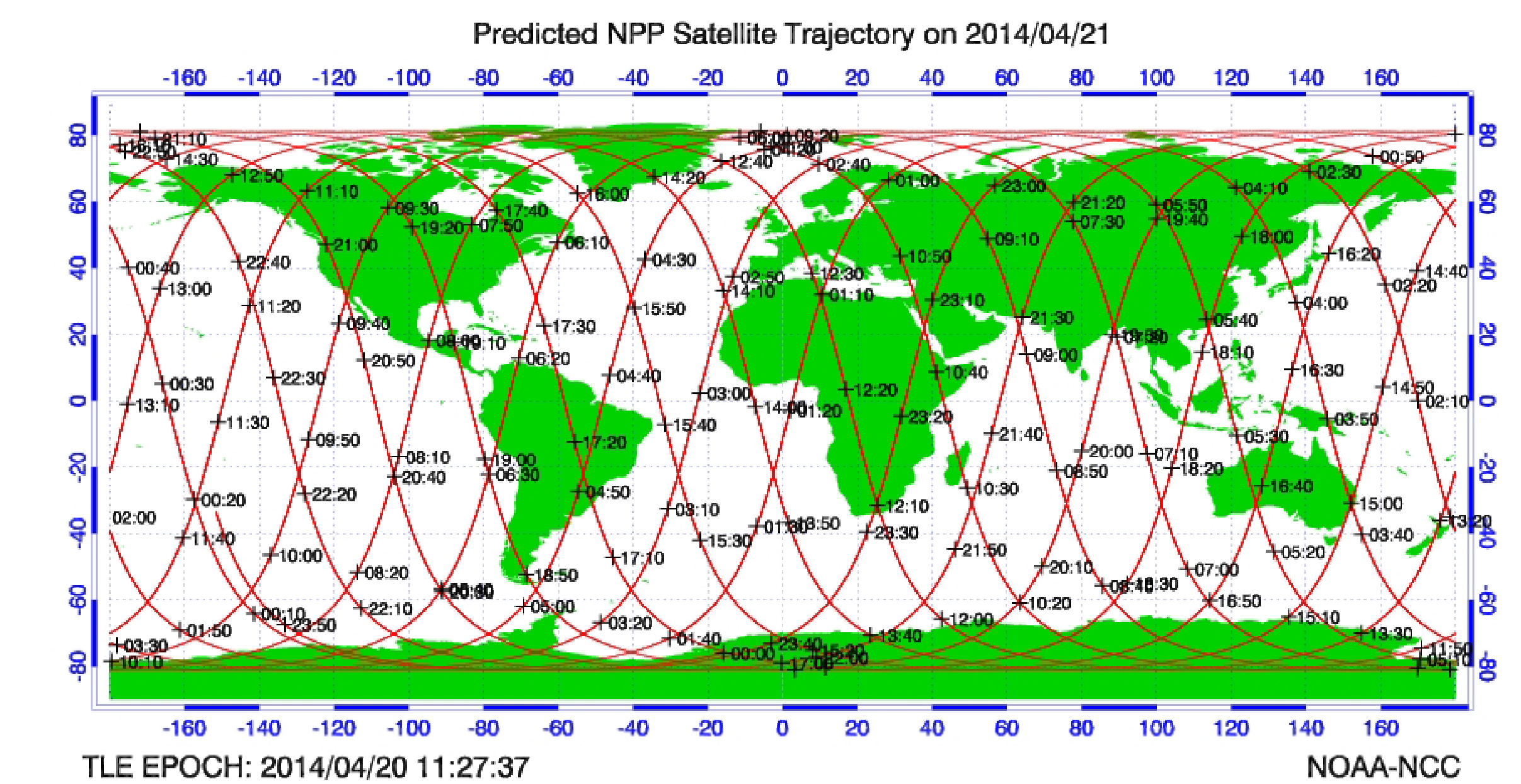


Figure 5. Daily orbital track

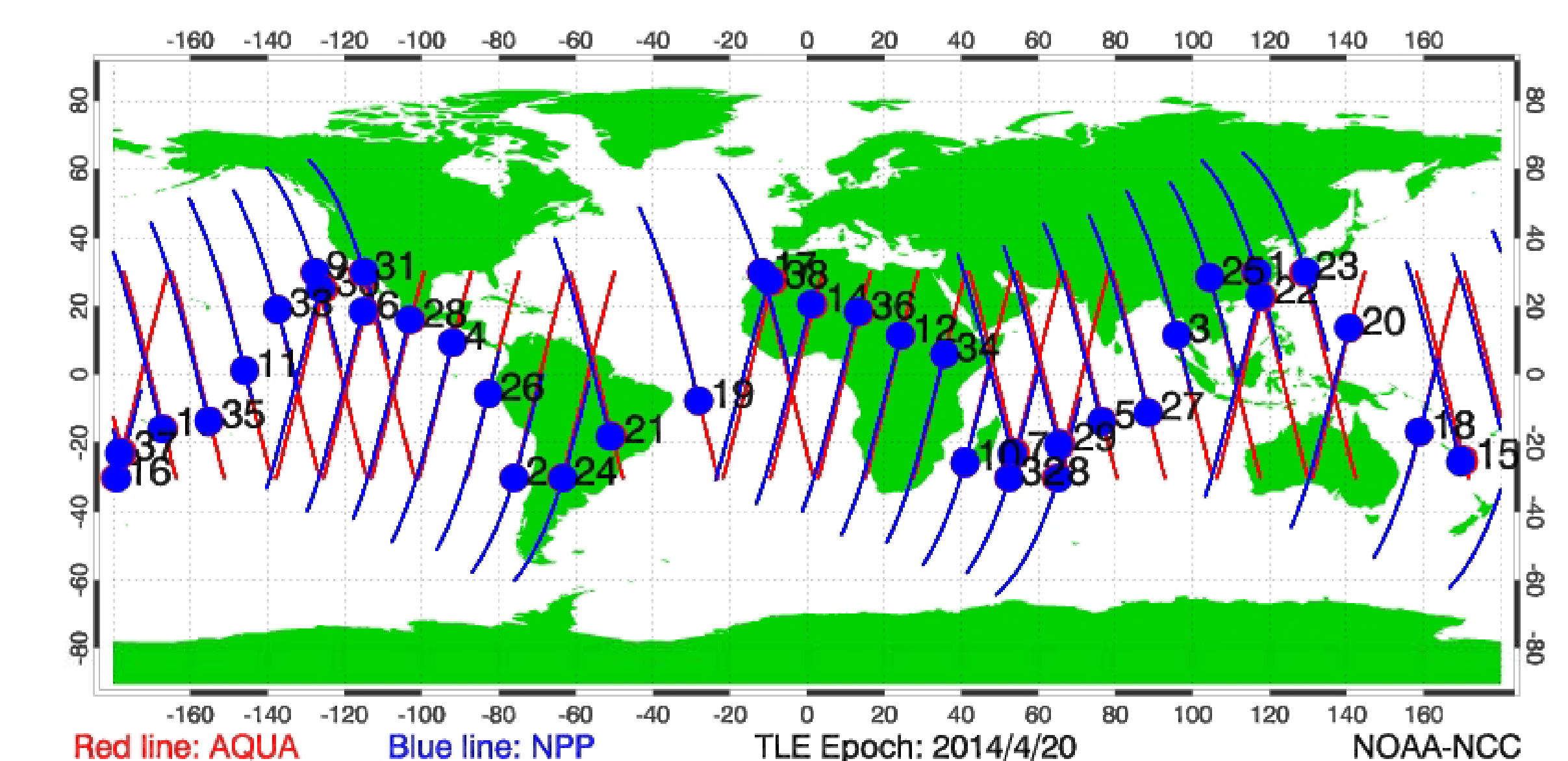


Figure 6. SNOx in the low latitudes.

Similarly, the SNO prediction information has been used for intersatellite comparisons with MODIS and other instruments by VIIRS SDR as well as other SDR teams.

Summary

The Suomi NPP calibration knowledge base provides important information for both VIIRS SDR and EDR users. It has become an indispensable part of the cal/val tool for the postlaunch verification and validation of VIIRS SDR. The event log database keeps track of what happened to the VIIRS in its history of operations, while the validation time series tells us how VIIRS is performing over time. The image quality can be analyzed using the sample data from the image gallery and through comparisons with other instruments at the SNOs.

For additional information about the Calibration Knowledge Base, such as calibration parameters, spectral response functions, publications, documentation, data format, software, as well as links to VIIRS applications, please visit the website at <https://cs.star.nesdis.noaa.gov/NCC/VIIRS>.

References

Cao, C., F. DeLuccia, X. Xiong, et al., Early On-Orbit Performance of the Visible Infrared Imaging Radiometer Suite Onboard the Suomi National Polar-Orbiting Partnership (S-NPP) Satellite, *IEEE Transactions on Geoscience and Remote Sensing*, Volume: 52 Issue: 2 Pages: 1142-1156 Published: FEB 2014, DOI: 10.1109/TGRS.2013.2247768

Cao, C., X. Shao, X. Xiong, S. Blonski, Q. Liu, S. Uprety, X. Shao, Y. Bai, F. Weng, Suomi NPP VIIRS sensor data record verification, validation, and long-term performance monitoring, *Journal of Geophysical Research: Atmospheres*, Volume 118, Issue 20, pages 11,664-11,678, Published: 27 October 2013, DOI: 10.1002/2013JD020418

Cao, C., X. Shao, S. Uprety, Detecting Light Outages After Severe Storms Using the S-NPP/VIIRS Day/Night Band Radiances, *IEEE Geoscience and Remote Sensing Letters*, Volume: 10 Issue: 6 Pages: 1582-1586 Published: NOV 2013, DOI: 10.1109/LGRS.2013.2262258

Uprety, S., C. Cao, X. Xiong, et al., Radiometric Intercomparison between Suomi-NPP VIIRS and Aqua MODIS Reflective Solar Bands Using Simultaneous Nadir Overpass in the Low Latitudes, *Journal of Atmospheric and Oceanic Technology*, Volume: 30 Issue: 12 Pages: 2720-2736, Published: DEC 2013, DOI: 10.1175/JTECH-D-13-00071.1